The Kalahari Copperbelt in central-eastern Namibia

By

Sarah-Jane Gill

A thesis submitted to Birkbeck College, University of London for the degree of Doctor of Philosophy (PhD)

I, Sarah-Jane Gill, confirm that the work submitted in this thesis is my own. Where information has been derived from other sources, this is clearly indicated in the text.

"From an exploration perspective, it is important not to be wedded to a specific model. Multiple working hypotheses not only encourage us to test different controls on metal concentration but also open the mind to other possible mineralised settings which might not yet have been discovered. You can flirt with a model... but don't marry one. "

Ken Maiden, 2011

International Base Metals Ltd.

Australian Institute of Geoscientists Annual Conference

Abstract

The continuity of the Kalahari Copperbelt (KCB) beneath the Cenozoic cover of the Kalahari Group in central eastern Namibia has long been assumed, but was only confirmed by exploration drilling in 2010 when Eiseb Prospecting and Mining (EPM) uncovered Ag-bearing Cu sulfide mineralisation comparable to that found elsewhere in the belt. The geology of this region has not been described in any detail in the literature to date.

Zircon geochronology suggests that sedimentation of the Eiseb started at ~1170 Ma. An uplifted basement horst of deformed acid volcanics marks the western edge of the Eiseb. There is no eastern border to the Eiseb, which extends into the Ghanzi-Chobe Belt of Botswana. Deformation and folding of the belt occurred during the Pan African Damara Orogen which peaked at ~530 Ma. Cu-Ag mineralisation is disseminated across a range of rock types, from the volcanic basement horst, to sandstones and argillites. Mineralisation also occurs in veins, often discordant to stratigraphic boundaries, and within the coarse laminae of interbedded siltstones. The preservation of delicate sulfide replacement textures of evaporite minerals in micro-folded rocks suggests that the mineralisation is largely epigenetic, favouring pressure shadows and foliation on a local scale, and fold-closures, faults and thrusts on a regional scale. Magnetite is commonly associated with with Cu-Ag mineralisation both textually and spatially, across a range of rock types. Paleomagnetic methods were unable to constrain the timing of magnetite growth. The trace element contents of magnetite, as deduced by laser ablation inductive coupled plasma mass spectrometry (ICP-MS), is able to distinguish between barren and Cu-Ag mineralised host-rocks using element ratios. The V vs. Ni binary plot is effective for the acid volcanic rocks, and the V vs. Co plot distinguishes between mineralised and un-mineralised sedimentary rocks. Magnetite trace element concentrations show that it formed from hot (150-250˚C) metalliferous fluids with an IOCG (iron-oxide-copper-gold) affinity. The most likely mechanism for magnetite formation is by replacement of pyrite, with textures suggesting this occurred during deformation, i.e. during the Damara Orogeny.

The syn-deformation, epigenetic Cu-Ag mineralisation recognised in the Eiseb has been reported from numerous other deposits traditionally classified as ‘sediment-hosted stratiform copper’ (SSC). In these deposits mineralisation has been shown to be coeval with regional plate movements and orogenesis, which is fundamentally different to the SSC model where mineralisation is related to diagenetic processes. An alternative mineralisation model is thus proposed, orogenic-sediment-hosted-copper (O-SSC).

Acknowledgements

I would like to express my deep gratitude to my supervisor, Prof. Karen Hudson-Edwards, and to my mentors Tim Smalley, Alan Simmonds and Henrik Veldsman for their invaluable inputs during all stages of this project. Thank you also to Dr Andrew Beard and Steve Hirons for their supervision and guidance.

Special thanks go to Prof. Andrew Carter for his assistance during the zircon geochronology study, and to Dr Martin Rittner who assisted with the LA-IPC-MS study.

My heartfelt thanks are also extended to Dr Jenny Omma from Rocktype Ltd for not only training me in the use of the QEMSCAN and the iDiscover software, but also for taking me on as an intern during the latter part of my studies.

The paleomagnetic study would not have been possible without the assistance of Dr Adrian Muxworthy at Imperial College. His patience, expertise and insights formed a critical part of this study.

Thank you to my colleagues and the staff at Birkbeck College for support during this study.

This study also benefited greatly from discussions with Dr Ken Maiden on the KCB, with David Kossoff on mineral chemistry and statistics, with Sean Johnson on paleomagnetics, and from discussions with Pedro Acosta-Góngora on magnetite geochemistry.

I would like to thank my family and friends for their encouragement, love and support during this project, without which I would have been lost. Special thanks go to my long suffering father whose feedback, advice and sense of humour kept me anchored in rough seas. And lastly, to my husband Gerald, thank you for being the most important rock in my life.

Table of Contents

Abstract **4**

Acknowledgements **5**

Table of Contents **6**

List of Acronyms **10**

List of Figures **11**

List of Tables **29**

1 Introduction **29**

1.1 Aims and objectives 35

2 Literature Review **37**

2.1 Sedimentary-hosted Stratiform Copper Deposits 37

2.1.1 Introduction 37

2.1.2 SSC deposits: Characteristics and Genesis 38

2.2 Regional Geological Setting: The Kalahari Copperbelt 43

2.2.1 Tectonic Setting 46

2.2.2 Cu-Ag Mineralisation 51

2.3 Magnetite 57

2.3.1 Magnetite Geochemistry 57

2.3.2 Rock Magnetism 63

3 Recent Work on the KCB **65**

3.1 Academic work presented at the KCB conference 65

3.1.1 Sulfur Isotopes 66

3.1.2 Oxygen and Carbon Isotopes 67

3.1.3 Fluid Inclusions 68

3.1.4 Rhenium-Osmium Chronometry 68

3.1.5 Discussion 69

3.2 Summary of Eiseb Prospecting and Mining (Pty) Ltd exploration activities 70

3.2.1 Aeromagnetic Data Interpretation 75
3.2.2 Lithotype 76
3.2.3 Mineralisation 79
3.2.4 Magnetic Characteristics 82
3.2.5 Structure 84
3.2.6 Summary of EPM exploration results 87
4 Methodology 88
4.1 Sample Suite 88
4.2 Eiseb Data sets 94
4.2.1 Geophysical Data sets 94
4.2.2 Geochemical Data 94
4.2.3 Geological Data 96
4.3 Zircon U-Pb Geochronology 97
4.4 Electron Microprobe Analyser (EMPA) 98
4.5 Quantitative Evaluation of Minerals by Scanning Electron Microscopy (QEMSCAN®) 99
4.6 Laser Ablation Inductive Coupled Mass Spectrometry (LA-ICP-MS) 102
4.7 Palaeomagnetic Methods 103
5 Results 1: Geology of the Eiseb 106
5.1 Eiseb data sets 106
5.1.1 Stratigraphy and geochemistry 106
5.1.2 Geophysical data interpretation 113
5.2 Geological Mapping 113
5.2.1 Ground-truthing the Lehmann et al. (2015) geological map 115
5.2.2 Structural Mapping 116
5.3 Zircon Geochronology 120
5.4 Petrography: Optical and EMPA 123
5.4.1 Basement volcanics 123

5.4.2 Metavolcanics 132
5.4.3 Hangingwall 137
5.4.4 Interbedded Unit 139
5.4.5 Footwall 153
5.4.6 Unmineralised Central Zone 161
5.4.7 Mineralised Zone 165
5.5 QEMSCAN Textural and Mineralogical Investigation 170
5.5.1 SIP Mineralogy 170
5.5.2 QEMSCAN SIP vs Optical Petrography 187
5.6 Magnetite and Cu(-Fe) sulfide mineralisation 190
5.6.1 Mineralisation within the metavolcanics 192
5.6.2 Mineralisation within the sedimentary rocks 194
5.6.3 Magnetite Petrography 198
6 Results 2: Magnetite 204
6.1 LA-ICP-MS Magnetite Trace Element Geochemistry 204
6.1.1 Glitter™ 204
6.1.2 Data Treatment 205
6.1.3 NIST Standard Reference Material (SRM) 205
6.1.4 Magnetite Trace Element Geochemistry 207
6.2 Palaeomagnetic Investigation 218
6.2.1 Palaeomagnetic Direction 218
6.2.2 Rock Magnetism 221
7 Discussion 224
7.1 Geology of the Eiseb 224
7.1.1 Zircon Geochronology 224
7.2 Magnetite and Cu(-Fe) sulfide mineralisation 231
7.3 Magnetite trace element geochemistry 233
7.3.1 Volcanic and metavolcanic magnetite 233

7.3.2 Sediment-hosted magnetite 241
7.3.3 Summary 255
7.3.4 Palaeomagnetic Investigation 257
8 Synthesis 261
9 O-SSC Deposits 266
10 Recommendations 269
11 References 270
12 Appendices 286
Appendix I: BCR-2 EDS Measurements 286
Appendix II: Borehole Summary Data 287
Appendix III: Zircon Geochronology Results 306
Appendix IV-A: BCR-2 EMPA Area Scan Results 323
Appendix IV-B: Volcanic and Metavolcanic EMPA Area Scan Results (sort applied on total) 324
Appendix V: Primary and Secondary Mineral Groupings 338
Appendix VI-A: LA-ICP-MS Results for Magnetite 340
Appendix VI-B: LA-ICP-MS Excluded Measurements (*n*=30) 393
Appendix VI-C: LA-ICP-MS Measurements of NIST-610 and NIST-612 Standard Reference Material 396

List of Acronyms

1VD	First Vertical Derivative
ARG	Argillite
AS	Analytical Signal
BSE	Back-scatter Electron
CAB	Central African Copperbelt
ChRM	Characteristic Magnetism
CRM	Chemical Remanent Magnetism
EDS	Energy Dispersive Spectra
EMPA	Electron Microprobe Analysis
EPM	Eiseb Prospecting and Mining Pty (Ltd)
FW	Footwall
GCB	Ghanzi-Chobe Belt
GSN	Geological Survey Namibia
HW	Hangingwall
IBU	Interbedded Unit
IOCG	Iron-Oxide-Copper-Gold
KCB	Kalahari Copperbelt
KSG	Khoras-Sinclair-Ghanzi
LA-ICP-MS	Laser Ablation Induced Coupled Plasma Mass-Spectronmetry
MAB	Matchless Amphibolite Belt
MV	Metavolcanic
NP-DK	Ngwako Pan-D'Kar Formations
NRM	Natural Remanent Magnetism
PLT	Phyllite
QAQC	Quality Assurance and Quality Control
QEMSCAN	Quantitative Evaluation of Minerals by Scanning Electon Microscopy
RTP	Reduced-to-Pole
SEM	Scanning Electron Microscope
SIP	Species Identification Protocol
SLT	Siltstone
SMZ	Southern Marginal Zone
SSC	Sediment-hosted Stratiform Copper
SST	Sandstone
TMI	Total Magnetic Intensity
VMS	Volcanogenic Massive Sulfide

List of Figures

1-1: Location of the Kalahari Copperbelt within the crustal framework of southern Africa. The major copper deposits of Zimbabwe, Zambia and the Democratic Republic of Congo are also show. Image taken directly from the website of Porter Geoconsultancy (http://www.portergeo.com.au), accessed 21/05/15. 34

2-1: Map of the world showing the location of the largest, 'supergiant,' sedimentary rock-hosted stratiform copper deposits. 37

2-2: Basin-scale genetic model for SSC deposits. Highland recharge drives meteroric water flow along idealised pathways which may interact with the basement or rift fill sediments. Image taken from Brown (2014). 39

2-3: Typical rift-basin sedimentary sequence which hosts SSC deposits. Evaporite dissolution by diagenetic fluids provides the basinal brines necessary to scavenge and transport metals from the redbed sediments and/or bimodal volcanics (source rocks). Alternatively, fluids are generated through metamorphism, or have a magmatic component, or are possibly a combination of fluids. Growth-faults, bedding planes and brittle fractures in the rocks provide fluid conduits. Metals are scavenged from the source rocks, either from volcanics or redbeds. Convection can be generated by thermal or chemical gradients, or by the loss of pressure due to erosion or fracturing, causing fluids to rapidly ascend and forcing them to interact with reduced sediments/fluids. This is most pronounced at basin edges, where sedimentary units are thinner, or along the edges of basement highs. Precipitation of metal sulfides is initiated by the interaction of the oxidised metal-charged fluid with either a reduced fluid or fixed reductant. Modified after Hitzman et al. (2010). 42

2-4: The Kalahari Group surficial sands, calcretes and silcretes cover extends over large swathes of southern Africa, including Namibia and Botswana. The study area lies within beneath this cover, along the KCB. The KCB is developed along the Khoras-Sinclair-Ghanzi rift between the Kalahari and Congo cratons (insert) after Borg (1988a). 43

2-5: Stratigraphic correlation of the Eiseb deposits with the stratigraphy from Ghanzi, Klein Aub and Witvlei (bold). The logs show Formation names i.e. Doorpoort Formation, Eskadron Formation etc. The dashed lines show correlations after Borg (1988a). 44

2-6: Phases A of the evolution of the basin which hosts the Eiseb deposits. Figure modified after Borg (1988a) in Veldsman et al. (2010). 46

2-7: Phases B of the evolution of the basin which hosts the Eiseb deposits. Figure modified after Borg (1988a) in Veldsman et al. (2010). 47

2-8: Phase C of the development of the basin which hosts the Eiseb deposits was characterised by thermal subsidence and marine transgression. Figure modified after Borg (1988a) in Veldsman et al. (2010).....48
2-9: The termination of rifting along the (Koras-) Sinclair-Ghanzi rift and the initiation of Damaran rifting further north occurred around 750 Ma (Miller, 2008). . Figure modified after Borg (1988a) in Veldsman et al. (2010).....49
2-10: The termination of rifting along the (Koras-) Sinclair-Ghanzi rift was followed by the Damara Orogeny which peaked ~530 Ma (Ahrendt et al., 1978). Figure modified after Borg (1988a) in Veldsman et al. (2010).....50
2-11: Regional tectono-stratigraphic domains of Namibia after Corner (2000) as reported in Miller (2008). 50
2-12: Location of the Boseto Copper Project, Discovery Metals (Pty) Ltd. The Plutus and Zeta deposits are in the Boseto Zone. Maps taken from the Discovery Metals website (2015). 52
2-13: Geological cross-section through the Lake N'gami area Ngwako Pan deposits of Botswana showing its relationship to the Ghanzi-Chobe Ridge (insert). Figure taken from Borg and Maiden (1989).....53
2-14: Bornite mineralised foliation fabric, Zeta Deposit. a: Layer-parallel bornite adjacent to bornite-bearing quartz-calcite vein, hosted within green, reduced sediments. Borehole GDRD1143, 230.5m; b: Zoomed view of 'a'. Borehole GDRD1109, 202m. Photographs taken from Hall (2013). 53
2-15: Disseminated sulfide minerals, Plutus deposit. a): reflected light microphotograph of irregular bornite partially replaced by supergene covellite. Borehole PSRD1254, 462m; b): Reflected light microphotograph of chalcopyrite. Borhole PSDD310, 141m. Microphotographs taken from Hall (2013). 54
2-16: Simplified cross-section of the Klein-Aub orebodies (LEFT) and the main mineralisation styles recorded in the deposit (RIGHT). A: Disseminated; B: brittle fracture and cleavage-hosted; C: Disseminated in laminated slate and massive ore along a (organic-rich) slickenside; and D: Relationship between disseminated and brittle fracture-hosted mineralisation. Figure taken from Borg and Maiden (1989).....55
2-17: Schematic representation of the spinel group minerals. Thick lines illustrate minerals with a complete solid solution, and thin lines depict partial solid solutions. Figure redrawn from Dupuis and Beaudoin (2011). 58
2-18: Log *f*O2-T diagram showing the Fe-Si-O system buffers (LEFT) - HM: hematite-magnetite; FMQ: fayalite-magnetite-quartz; MW: magnetite-wűstite; IW: iron- wűstite; QIF: quartz-iron-fayalite (redrawn after Frost (1991b) and Nadoll et al. (2014)). RIGHT: Schematic phase diagram for the Fe-O-S system in fO_2- fS_2 space (modified after Nadoll et al. (2014)).....59

2-19: Discriminant diagram for average composition of magnetite from various Fe-oxide-containing deposits. A: Ni+Cr vs. Si+Mg to discriminate Ni-Cu deposits; B: Al/(Zn+Ca) vs. Cu/(Si+Ca) to discriminate magnetite from VMS deposits; C: Ni/(Cr+Mn) vs. Ti+V discriminant diagram for average Fe-oxide compositions from Kiruna, IOCG, porphyry Cu, Fe-Ti-V and BIF deposits; and D: Also used to distinguish deposits from Kiruna, , IOCG, porphyry Cu, Fe-Ti-V and BIF deposits, but also skarn deposits. Diagrams C and D should be used in conjunction to disctinguish between BIF, skarn, Archean porphyry deposits and Opemiska-type Cu veins. Images combined from Dupuis and Beaudoin (2011). 61

2-20: Plot of Ti (ppm) versus Ni ratio (un-normalised) in magnetite (mt) to distinguish magmatic (red) and hydrothermal (blue) settings. Figure redrawn from Dare et al. (2014). 62

3-1: Copper exploration licences along the Ghanzi-Chobe Belt in central-eastern Namibia and Botswana circa. 2013. The study area is circled in red (Eiseb licences). Map extracted from Dean (2013). 65

3-2: Sulfur isotope analysis from the KCB in the vicinity of Ghanzi, Botswana. Isotopic delta measurements of sulfur are made relative to Vienna Cañon Diablo troilite (V-CDT). Image extracted from Gorman et al. (2013). 66

3-3: $\delta^{13}C$ and $\delta^{18}O$ results are compared to other Neoproterozoic carbonates (Hendjala, 2010; Morgan et al., 2013). Results reported relative to Vienna Pee Dee Belemnite (V-PDB*)*. Figure taken from Morgan et al. (2013). 67

3-4: Fluid inclusion microthermometry from veins taken from Morgan et al. (2013). 68

3-5: Location map of the study area and known copper occurrences along the KCB prior to exploration commencing in 2008 by EPM. Copper occurrences in Namibia are from the Geological Survey of Namibia (www.mme.gov.na), and for Botswana published occurrences from DML and Hana Mining were used (www.cupriccanyon.com). 70

3-6: Regional airborne magnetic data interpretation method after Veldsman et al. (2010). GSN efers to the Geological Survey of Namibia (www.mme.gov.na). Magnetic and gravity data grids covering Botswana were purchased from Department of Geological Survey (DGS), Lobatse, Botswana (www.gov.bw). 72

3-7: Location of regional soil geochemical surveys carried out by EPM prior to 2012. Image taken from Veldsman et al. (2010). 73

3-8: Location of the IP survey (LEFT) and the gravity surveys carried out by EPM (RIGHT). Images taken from Veldsman et al. (2010) 73

Figure 3-9: Location of the high resolution (GEX) aeromagnetic survey (LEFT) and a ground magnetic survey (ETG5) carried out by EPM (RIGHT). Images taken from Veldsman et al. (2010) 74

3-10: The regional total magnetic intensity (TMI) map of Namibia and Botswana with the geology of Botswana shown (A). Simplified geological map of eastern-central Namibia after Smalley (2012) and of Botswana overlying the TMI for both countries (B). The cross-section is taken from Veldsman et al. (2010). The geology of Botswana shapefile was provided by the Department of Geological Survey, Lobatse, Botswana (www.gov.bw). The regional TMI is a composite of aeromagnetic survey data provided by the Geological Survey of Namibia (www.mme.gov.na) and Department of Geological Survey, Lobatse, Botswana. 75
3-11: Summary of the stratigraphy from the Talismanis area from Dawnborn (2012). 77
3-12: Magnetic profiles A-A' and B-B' lithological cross-sections with magnetic susceptibility shown in blue. Images modified to exclude proprietary information. Images from Dawborn (2014). 78
3-13: Element map of chalcocite showing silver exsolutions along the crystal lattice (LEFT). Chalcocite and bornite exsolution texture (RIGHT). Images taken from Dawborn (2013). 80
3-14: SEM photomicrographs taken from Dawborn (2013). A: Photomicrograph from the hangingwall arkose unit (HWA). B, C and D: Photomicrographs from the lower argillite unit (LAU). 81
3-15: Photomicrograph of the inclusions of copper sulfides. RIGHT: chalcocite and bornite in an exsolution texture. Images taken from Dawborn (2013). 81
3-16: Lithological log with assay results and magnetic susceptibility readings. Modified image based on logs provided by EPM (2012). The blue and brown lines show the positive magnetic susceptibility (brown) and the negative total magnetic field (blue) anomalies.....83
3-17: Lithological log with assay results and magnetic susceptibility readings. Modified image based on logs provided by EPM (2012). The blue and brown lines show the positive magnetic susceptibility (brown) and the negative total magnetic field (blue) anomalies.....84
3-18: A: Schematic section through the Kagas Member of the Klein Aub Mine from Borg (1988b). B: Copper deposit styles in the western Mount Isa block from Maiden and Borg (2011). C: Analytical signal magnetic images from the study area showing 'imbricate-like' splay features and faulting. Image from Smalley (2014). 86

4-1: Summary of the geological information used in this study. The borehole/sample locations are shown on the Analytical Signal aeromagnetic maps of Namibia and Botswana provided by the Geological Survey of Namibia (www.mme.gov.na) and Department of Geological Survey (www.gov.bw), respectively. The boreholes names are shown in bold above the lithological logs, which were provided by EPM (2014). Boreholes are divided into lithotypes according to the geological logs provided by Eiseb Prospecting and Mining. Sample numbers are shown adjacent to the lithotype logs with yellow stars

indicating the approximate position of the sample. Different coloured circles indicate the type of analyses carried out on a given sample. 89
4-2: U-Pb geochronology sample locations shown on the Namibian government regional airborne magnetic survey Reduced-to-Pole image product. 97
4-3: Schematic illustration of areas analysed by QEMSCAN, showing the relationship between the field size, the stepping distance and the number of measurements taken. The black circle represents the sample, red squares show the 1.5mm × 1.5mm fields and the red spots show individual data analysis points for measurement stepping intervals of 50µm, 10µm and 3µm. Image modified from http://www.rocktype.com/qemscan. 99
4-4: Overview of the locations of the boreholes sampled for the paleomagnetic study, as well as where in each borehole samples were taken. The sample numbers should be prefixed with OPS. The maps were made using the GSN regional airborne magnetic survey (www.mme.gov.na) Reduced-to-Pole image. 105

5-1: Correlation of lithological units in the study area with formation names of the Eiseb area. The Footwall is thought to correspond with the Ngwako Pan Formation and the Hangingwall and Interbedded Unit to the D'Kar Formation of the Ghanzi Group. Modified after Dawborn (2014). 107
5-2: Example of the summary lithological and geochemical information contained within Appendix II. The geochemical data were compiled from assay data made available by Eiseb Prospecting and Mining. The location is shown on the Namibian Government airborne magnetic data (www.mme.gov.na) AS image. 108
5-3: Scatterplots of the average Cu vs. Ag (ppm) for the 18 boreholes across the study area showing the strong correlation between these two elements. **A:** Boreholes from the Central Anticline (CA), Eastern Anticline (EA), and North Eastern Anticline (NEA) are highlighted using different colours to demonstrate that mineralisation is present, although variable, in all three anticlines. **B:** Mineralisation is also not restricted to the IBU, but is present in both hangingwall and footwall intersections. 109
5-4: Summary table illustrating the rationale used to map the geology of the Eiseb area. The example images are taken from a regional TMI composite of aeromagnetic survey data provided by the Geological Survey of Namibia (www.mme.gov.na) and Department of Geological Survey, Lobatse, Botswana (1994-2008) (www.gov.bw). 113
5-5: Example of geological mapping of the Eiseb area using Namibian government regional aeromagnetic survey data (www.mme.gov.na). (A) Total Magnetic Intensity (TMI); (B) Analytical Signal (AS); (C) RTP total horizontal derivative (RTP-THD); (D) RTP first vertical derivative (RTP-1VD); (E) Reduced to Pole (RTP); (F) Tilt derivative of the RTP (RTP-TDR). The location shown is the fold closure of the east anticline (EA). 114

5-6: Geological map of the Eiseb section of central Eastern Namibia from Lehmann et al. (2015) (A) was geo-referenced and redrawn using ArcGIS (B) and the colours changed to reflect the convention used for this study. 115
5-7: Geological map of the Eiseb area (after Lehmann et al., 2015) overlain by the Eiseb borehole locations (black dots). The lithotypes first intersected below the Kalahari Group (B) were used to validate the geological mapping in this area. 115
5-8: Deciphering of the sense of shear on the large rotational feature in the Eiseb area using the RTP magnetic image rendered from the Namibian governments regional aeromagnetic survey data (www.mme.gov.na). In this area NE-SW tending faults also show a dextral sense of movement (A). NNW-SSE faults along fold limbs are interpreted as axial planar cleavage on the central anticline (B), although the orientation of these shifts to a more NNE-SSW orientation towards the east (C). Late stage Karroo dolerite dykes are also easily identified in the magnetic image products as these form distinct NW-SE trending lineations which do not appear to disturb the underlying lithotypes (D). Faulting thought to be associated with rheological contrasts is shown as dotted white lines. 116
5-9: RTP image from the Namibian government regional aeromagnetic survey data from the southern portion of the Eiseb (www.mme.gov.na). The long (5-10 km), sinuous NNE-SSW/NE-SW faults contrast the short (2-4 km) axial faulting oriented NNW-SSE. 117
5-10: RTP magnetic image rendered from the Namibian governments regional aeromagnetic survey data (www.mme.gov.na). This shows the overall sense of movement across the Eiseb (black arrows) in relation to the southern Damara Thrust Zone (*pers comm.* Corner, 2015) shown in white. The dotted black line shows the outline of inferred rotated basement horst. 118
5-11: Geology and main structural features of the Eiseb, modified after Lehmann et al. (2015). (A) is shown with a 30% transparency overlain on the RTP image product of the Namibia government's regional airborne magnetic survey data (www.mme.gov.na). The map is also shown without the magnetic image underlay (B). 119
5-12: U-Pb concordia plots of the detrital zircon grains for ZR-01. The red ellipses represent the analyzed grains, and include an internal 2-sigma error. Plot drawn using Isoplot (ver. 4.1)...120
5-13: U-Pb concordia plots of the detrital zircon grains for ZR-02. The red ellipses represent the analyzed grains, and include an internal 2-sigma error. Plot drawn using Isoplot (ver. 4.1)...121
5-14: U-Pb concordia plots of the detrital zircon grains for ZR-03. The red ellipses represent the analyzed grains, and include an internal 2-sigma error. Plot drawn using Isoplot (ver. 4.1)...121
5-15: Cathode luminescence images of zircon grain mounts. A: the metavolcanic sample ZR-01 (WB-1); B: ZR-02 from borehole CZ-1; and C: Sample ZR-03 from borehole NEA-PL-2. 122

5-16: U-Pb ages for detrital zircons in the Eiseb study area. The main age peaks were extracted using the normal mixture modelling algorithm of Galbraith (2005) using the Densityplotter (ver.7.0) (Vermeesch, 2012). 122
5-17: Photomicrograohs of sample KG-1 from the Kgwebe Formation quary in Botswana. Under PPL (A) the growth rims which surround many anorthoclase phenocrysts are seem as white halos. Magnetite often forms embayments into these phenocrysts and is commonly associated with altered epidote (A & B). B taken under XPL. 123
5-18: Backscatter electron microphotograph of the main opaque phases found in KG-1: magnetite and barite. 124
5-19: Photomicrographs of the Oorlogsende Member sample OE-1 showing, A: the common occurrence of the opaque minerals barite and magnetite. The former is present as fine-grained anhedral crystals which are very common in the groundmass and form a weak fabric in the rock by their parallel alignment, and the latter forms euhedral to subhedral crystals commonly associated with the feldspar phenocrysts. B: Calcite is common both within the groundmass of the rock, and along the edges of the phenocrysts. 125
5-20: Backscatter electron microphotograph of OE-1 during EMPA showing the paragensis of anorthoclase ->magnetite ->apatite in this rock.....126
5-21: Photomicrographs taken under XPL of sample OE-2 from the Oorlogsende Member. Micrographitic textures are commonly developed between quartz and alkali feldspars adjacent to mineral aggregates (A). Acicular plagioclase needles are commonly developed in patches throughout the groundmass. Alteration of feldspars to sericite is commonly observed, particularly along grin boundaries and along cleavage planes (B). Zones of altered epidote, calcite, feldspars and equant opaque minerals are common. The bright green mineral in B is zircon. 127
5-22: Backscatter electron photomicrograph of intergranular opaque minerals in the Oorlogsende Member sample OE-2. There is an apparent association between the Pb-Se mineral chlausthalite and magnetite (A). Magnetite forms aggregates within a quartz phenocryst. The aggregate has an ovoid shape. The phenocryst also contains titanite intergrown with magnetite, and an unknown Ce-La-Nd phase (B). 128
5-23: Backscattered electron image of the BCR-2 standard area scans, Spectrum 44-86. The area scan calculates the average composition of each block and the average of all of the blocks is taken as the average of the sample (Beard and Drake *pers comm.*, 2016). 129
5-24: Example of a back scatter electron image showing the overlapping area scans used for the EDS major oxide compositional analysis of the basement rocks (OE-2). Two areas of this size were analysed for each of the basement samples and the results averaged to produce the compositional data in Table 17. 130
5-25: The basement samples are plotted on a TAS diagram for the classification of igneous rocks. Each point represents the average composition for a given sample based on ~80

area scans per sample (Table 18)(Appendix IV-B). KG-1 and OE-1 plot within the rhyolite field and OE-2 plots within the trachyte field bordering on the dacite field. The TAS diagram boundaries are redrawn after Le Maitre et al. (2005). 131

5-26: Magnetic map of the study area showing the location of boreholes WB-1 and WB-2 (INSERT). Background is the GSN regional airborne magnetic survey Analytical Signal (AS) image. 132

5-27: Micro-faulting along a zone of fine-grained quartz off-sets copper sulfides (EPS-02: A: PPL & B: XPL). Alternating bands of coarse silicates and fine-grained phyllosilicates show evidence of micro-folding (EPS-04: C: PPL), and micro-faulting (D: XPL). The opaque phase (bornite) favours the coarse-grained layers. 134

5-28: Bornite and magnetite micro-textural relationship along zones of increase porosity from EPS-04, WB-2. Photomicrographs taken during EMPA. 134

5-29: Pyrite contains inclusions of quartz and plagioclase (A). An alteration halo is developed around this mineral of a fine-grained unidentified iron-oxide, and calcite (EPS-03, WB-2). B: Microscopic cobaltite and bornite were identified using EMPA (EPS-02, WB-1). 135

5-30: The metavolcanic samples are plotted on a TAS diagram for the classification of igneous rocks. EPS-01 and EPS-03 are from similar depths and both plot within the dacite field of the TAS diagram. Samples EPS-02 and EPS-04 are from shallower depths in the boreholes (WB-1 and WB-2) and plot in the Trachyte and Trachyandesite fields respectively. Boundaries redrawn after Le Maitre et al. (2005). 136

5-31: Photomicrographs from the hanging wall sandstones in the east of the study area. A: Subhedral to anhedral quartz and sericitised feldspar are common in OPS-11 (EA-NL-1). B: Muscovite is commonly bent, but forms long laths up to 0.4mm (OPS-14). Photomicrographs taken in XPL. 138

5-32: Photomicrographs of the subarkose hangingwall sandstone (OPS-6, CA-PL-1) under transmitted light in PPL (A) and XPL (B). The dashed lines show the development of a very weak foliation. 139

5-33: Photomicrographs of the IBU sandstones. A: A weakly developed foliation is defined by fine-grained platy minerals (white dashed lines). Many of the quartz grains show undulose extinction (OPS-8). B: Much of the plagioclase in OPS-8 has been altered to sericite, and those which have not been altered commonly show deformation twinning. C: The alignment of detrital muscovite and some of the felsic minerals suggest relict bedding in the rock was at an angle to foliation developed by fine-grained platy minerals in OPS-10. 141

5-34: Photomicrographs of the IBU siltstones (foliation shown by white dashed lines). A: Under reflected light the opaque minerals in the eastern anticline (EA) were identified as galena. Photomicrograph from OPS-13. B: Many of the siltstones show interbeds of coarser and finer material. The fabric developed in the fine-grained layer is at an angle to

that developed in the sandy unit (PST-2D2-2). C: Biotite appears to be detrital in most of the siltstones, demonstrating the orientation of the original bedding at an angle to the foliation (PST-4D2-1). D: The opaques in NEA are magnetite and anhedral chalcocite, covellite and bornite intergrowths (PST-4D2-3). 143

5-35: EMPA photomicrographs of the complex textural intergrowths between galena (very bright), chalcocite (medium brightness) and magnetite (low brightness) in sample PST-2D2-1 from the IBU. 144

5-36: Photomicrographs of the phyllite units within the IBU in the eastern study area. A: Magnetite growth is elongated parallel to the main foliation developed in the rock, but some large porphyroblasts show an orientation at ~45˚ to this fabric. Sulfide minerals are common parallel to the foliation and in the pressure shadows of magnetite porphyroblasts (PST-4D1-2). B: Two generations of biotite are evident, one parallel to the main fabric in the rock, and the second at an angle to it (PST-4D1-3). 145

5-37: Magnetite occurs as euhedral to subhedral crystals (A) parallel to the fabric of the rock, and with quartz pressure shadows. (B) Ce-La-Nd minerals occur between magnetite grains and as stringers parallel to the fabric. Photomicrographs taken using the EMP, both images are from sample OPS-4. 147

5-38: Magnetite clearly post-dates bornite in sample OPS-2. Photomicrographs taken during EMPA.....148

5-39: Photomicrographs from the hanging wall siltstone in the central study area. A: Fine-grained phyllosilicates define a strong fabric with opaques and biotite aligned to this foliation. Photomicrograph taken from OPS-1 under PPL B: Compositional layers have preserved relict bedding which is at an angle to the foliation of the rock. Photomicrograph taken from OPS-3 under PPL C: Biotite and opaque minerals show the development of pressure shadows parallel to the foliation. Photomicrograph taken from OPS-1 under XPL D: Biotite and calcite form elongate subhedral crystals parallel to foliation which have quartz grown in their pressure shadows. Photomicrograph taken from OPS-3 under XPL.....149

5-40: EMP Photomicrographs from EMPA of OPS-3 showing apatite (A), magnetite, and the Ce-bearing vein (B). 150

5-41: Element map of magnetite which is spatially associated with copper sulfide minerals. Native silver does not occur within the chalcocite inclusion, but occurs with the chalcocite on the magnetite grain boundary. 151

5-42: Photomicrographs from the interbedded unit argillite EPS-12 in the central study area. A: In PPL under transmitted light the two main litho-types are distinguished from each other and the quartz vein on the basis of colour. The vein is clear, the chlorite-rich unit is green and the muscovite-sericite unit is dusty brown. B: In XPL the quartz vein is clearly

visible as euhedral to subhedral grains which fine towards the edge of the vein to form polygonal quartz with triple junctions. 152
5-43: Photomicrographs from the interbedded unit argillite EPS-18 in the central study area. A: In PPL under transmitted light the calcite-rich bands are distinguished on the basis of their light colour relative to the muscovite-sericite bands which are a dusty brown colour. B: In XPL the calcite-rich units are more readily identified due to the high birefringence colours of calcite. In both XPL and PPL it is evident that this rock is strongly foliated. 153
5-44: Photomicrograph of the main textural and mineralogical features of the footwall in the east of the study area. Image taken from OPS-12. 155
5-45: Photomicrographs from the footwall sandstone lithotypes in the central study area. A: Typical sandstone composition of plagioclase and quartz showing sutured boundaries, sub-grain formation and fine-grained polygonal felsic aggregates along grain boundaries (recrystallization). Photomicrograph from OPS-5 in XPL. B: Quartz-calcite vein cross-cutting the footwall sandstone. Photomicrograph from OPS-5 in XPL. C: Contact between the sandstone and fine-grained argillite unit from OPS-7. Remnant cross-bedding is visible, as well as a strong schistose fabric in the argillite. Photomicrograph from OPS-7 in PPL. D: A thin layer of titanite is micro-folded and deflected around angular quartz grains. Photomicrograph from OPS-7 in PPL. 158
5-46: Covellite shows a strong alignment to the foliation in the fine-grained sediment layer within sample OPS-7. Photomicrographs taken during EMPA. 159
5-47: Magnetite intergrown with Ce-La-Nd minerals in footwall sample EPS-13, CA-PL-9. Photomicrograph taken during EMPA. 160
5-48: Subhedral to anhedral ilmenite was identified in sample EPS-19, CA-PL-6. Apatite, euhedral galena and zincian-greenockite were also identified in this rock. Photomicrograph taken during EMPA. 160
5-49: Barite is a fairly common opaque mineral in the footwall sample from EPS-05, about 15m below EPS-19, CA-PL-6. Magnetite reports high Ti values which may suggest exsolutions of ilmenite. Photomicrograph taken during EMPA. 160
5-50: Borehole CZ-1 is located to the WNW of the Central Anticline. Background is the GSN regional airborne magnetic survey Analytical Signal (AS) image. 161
5-51: Photomicrographs from sample EPS-14 showing the texture of the rock in XPL (A) and the magnetite bands associated with muscovite and sercite (B). 162
5-52: Magnetite forms subhedral to cubic aggregates which show brittle fracturing (A & B). An Fe-oxide phase has exsolved from biotite along cleavage planes (C). Zircon has also undergone brittle fracturing (D). In this sample a single grain of almost pure Nickel was also identified. Photomicrographs taken during EMPA on sample EPS-14, CZ-1. 163

5-53: Pyrrhotite defines a foliation in the rock which is distorted by a second foliation which deforms the first (A). Pyrite occurs in lenses parallel to the foliation (B). Both images taken in XPL. 164
5-54: Pyrrhotite forms elongate bodies parallel to the foliation. Photomicrographs taken during EMPA. 165
5-55: Photomicrographs from the mineralised siltstones and phyllites of the eastern study area. A: The ore minerals chalcocite and bornite are replacing biotite/chlorite blocky laths parallel to the foliation. Photomicrograph from sample PST-4D1-4, borehole NEA-PL-1, taken in PPL. B: Occassional plagioclase grains are preserved and show characteristic twinning. Detrital muscovite grains are rarely aligned to the foliation. Photomicrograph from sample PST-4D1-4, borehole NEA-PL-1, taken in XPL. C: Felsic minerals (white) form thin layers which indicate original sedimentary bedding. Opaque minerals favour the coarse felsic band where they form lenses parallel to the foliation. Photomicrograph from sample PST-7D1-1, borehole EA-SL-1, taken in PPL. D: Biotite, altering to/from chlorite, shows a strong spatial association with copper mineralisation. Photomicrograph from sample PST-4D1-4, borehole NEA-PL-1, taken in PPL. 167
5-56: A: Bornite and chalcocite commonly form exsolutions textures. Native silver is within chalcocite grains. B: Galena forms inclusions within bornite and magnetite grains. Magnetite and chalcopyrite share a straight boundary. Photomicrographs taken from sample PST-4D1-4 from borehole NEA-PL-1. 168
5-57: EMPA photomicrograph (A) of a mineralised layer from PTS-2D2-4 from EA-PL-1. Apatite, goethite/lepidocrocite and chalcocite form the main constituents of the ore assemblage in this rock. B: Photomicrograph of the same view taken under reflected light. The iron-oxides appear light grey, and the copper sulfides as blue (chalcocite) to orange (bornite). 168
5-58: False colour mineral maps of PB-6 (sandstone), PB-8 (siltstone) and PB-9 (phyllite). 171
5-59: False colour mineral maps of PB-10 (phyllite), PB-12 (phyllite) and EPS-14 (siltstone). 171
5-60: False colour mineral maps of OPS-11 (sandstone), EPS-04 (Metavolcanic) and OPS-7 (siltstone). 172
5-61: Modal abundance (volume per cent) for the whole rock sample set using the secondary SIP groupings. 173
5-62: Grain mount sample MG-12 showing the same grain at different stepping intervals. Magnetite is shown as the maroon pixels, cyan shows albite inclusions within the grain, and the highly reflective mineral inclusions shown in the BSE image (right) have been mapped by the SIP in black to denote that the pixels are 'unclassified.' Albite inclusions in magnetite are not detected in the 50µm scan, but are clearly seen in both the 5µm and 1µm scans. 175
5-63: False colour mineral maps of MG-1 at a stepping interval of 50µm (LEFT), 5µm (CENTRE) and 1µm (RIGHT). 175

5-64: False colour mineral maps of MG-3 at a stepping interval of 1µm (LEFT), 50µm (CENTRE), and 5µm (RIGHT).....176
5-65: False colour mineral maps of MG-5 at a stepping interval of 50µm (LEFT), 5µm (CENTRE) and 1µm (RIGHT).....177
5-66: False colour mineral maps of MG-6 at a stepping interval of 50µm (LEFT), 5µm (CENTRE) and 1µm (RIGHT).....177
5-67: False colour mineral maps of MG-9 at a stepping interval of 50µm (LEFT), 5µm (CENTRE) and 1µm (RIGHT).....178
5-68: False colour mineral maps of MG-10 at a stepping interval of 50µm (LEFT), 5µm (CENTRE) and 1µm (RIGHT).....178
5-69: False colour mineral maps of MG-12 at a stepping interval of 50µm (LEFT), 5µm (CENTRE) and 1µm (RIGHT).....179
5-70: False colour mineral maps of MG-13 at a stepping interval of 50µm (LEFT), 5µm (CENTRE) and 1µm (RIGHT).....179
5-71: Modal abundance (volume per cent) for the grain mount sample set using the secondary SIP groupings.....180
5-72: False colour mineral maps showing only the unclassified pixels in black for PB-8 and EPS-04. 186
5-73: False colour mineral maps showing only the unclassified pixels in black for MG-1 and MG-9. 187
5-74: Photomicrograph of polished section OPS-11 from a hangingwall arkosic sandstone (borehole EA-NL-1). The rock shows evidence of brittle fracturing (dashed lines), sutured grain boundaries and recrystallization, as well as undulose extinction. This suggests that this rock has undergone deformation by compaction. The image was taken in XPL. 188
5-75: Photomicrograph from polished section OPS-7 in the footwall of borehole CA-PL-1 under PPL. The sample marks the contact between a competent quartzitic schist and a very fine-grained micaceous phyllite. Opaque minerals are present parallel to the foliation (yellow dotted lines) of both lithotypes, but within the phyllite preferentially aggregate in the pressure shadows of quartz grains in occasional sandy lenses. The opaque phases are most concentrated along the contact between the two lithotypes. 188
5-76: Photomicrograph from polished section EPS-14, the hangingwall sandstone from borehole CZ-1. The opaque minerals which define the banding in this rock are black in this PPL image. The strongly sericitised nature of the feldspars in this sample is seen as a dusty coating over many of the grains. Under XPL this was identified as sericite/muscovite. 189
5-77: Photomicrograph from polished thin section EPS-04 (borehole WB-2). The mineralisation in this sample is strongly segregated to coarser mineral units defined by quartz and feldspar. Fine-grained magnetite is present both proximal to interstitial bornite, and as

fine-grained euhedral crystals within the muscovite/sericite/chlorite bands. Image taken in PPL. 190

5-78: False colour mineral maps showing the an overview for PB-10 and PB-12 (TOP-LEFT and TOP-CENTRE), and selective mineral maps for PB-10 (BOTTOM-LEFT), PB-12 (BOTTOM-CENTRE) and EPS-14 (RIGHT) showing only the minerals magnetite, bornite, chalcocite/digenite, covellite and Cu-Fe sulfide (T). Dashed lines indicate the general trends of the minerals shown. 191

5-79: False colour mineral maps for three whole rock samples, OPS-11, EPS-04 and OPS-7. The maps show only magnetite and the copper(-Fe) minerals. Dashed lines have been included to indicate the trends of these minerals. 192

5-80: Photomicrographs from the metavolcanic sample suite showing opaque minerals. A: EPS-02 shows brittle fracturing at an angle to the quartzo-feldspathic layer within the rock. Phenocrysts do not show any displacement along fractures. Magnetite and Cu(-Fe) sulfides occur within the foliation parallel quartz-feldspathic layers. These layers appear to texturally precede brittle fracturing in this rock. Image taken under XPL. B: EPS-03 shows the rotation of a sandine phenocryst into the foliation. Magnetite micrporphyroblasts occur in the calcite and phyllosilicates-rich layers of the rock. Image taken under XPL. C & D: EPS-04 under PPL (C) and XPL (D) showing the preferential concentrations of magnetite and Cu(-Fe) sulfides within the quartzo-feldspathic layers of the rock. The finer units are primary comprised of phyllosilicates and calcite, and chlorite. The dashed lines indicate microfolding in the rock. Dynamic deformation is suggested by the multiple hinge zones developed from the micro-fold. 193

5-81: False colour mineral maps of magnetite particles from MG-3. Bornite-Cu-Fe sulfide occur interstitially to magnetite (A), as inclusions (B, D, E and F), as fracture-fill (C), and as embayments into magnetite grains (F). 194

5-82: Photomicrographs of the main mineralisation styles encountered in the Eiseb (meta-) sedimentary rocks. A&B: Bornite and chalcocite, which form exsolutions textures (insert B), are disseminated within the coarse-grained part of the rock (PST4-D1-4). C: Quartz-calcite veins containing bornite and magnetite (EPS-07). In D bornite and magnetite are concentrated on the edge of a folded and fractured quartz-carbonate vein (EPS-09). E: Bornite and chalcocite, which form exsolutions textures (insert E) occur parallel to the foliation (E & F) and along the hinge zone of a fold (E) (PST2-D2-4). G & H: The foliation forms at an angle to the relict bedding with sulfides elongated parallel to the foliation (PST7-D1-1). Borg (1988a) interpreted similar txtures from the Klein Aub and Lake Ngami deposits as chalcocite pseudomorphs after evaporite minerals such as gypsum. 195

5-83: Photomicrographs of thin sections from the Lake Ngami area (Botswana) from Borg (1988a) (A & B), and from sample OPS-3 from borehole CA-PL-3 (C & D) in the Eiseb showing (opaque) Cu sulfides concentrating in the coarser layers of laminated rocks,

along with calcite, and in OPS-3 also magnetite. Cu sulfides from both the Lake Ngami area, and from the Eiseb, are interpreted as pseudomorphs after evaporite minerals (e.g. gypsum). In photomicrograph A the Cu sulfides have been stretched and pressure shadows are evident, suggesting replacement of evaporite minerals took place prior to deformation in the rock, however, in the Eiseb (C) no pressure shadows are developed on the Cu sulfides, suggesting syn-deformation replacement of evaporite minerals. The scale bars in A & B are 5mm. 196

5-84: Photomicrograph of a magnetite crystal from the grain mount sample MG-5 from borehole NEA-PL-1 showing moderate oxidation of magnetite (pink) to hematite (yellow) along lattice planes (TOP). The level of oxidation for magnetite in every polished thin section was categorised using a scale devised for this study based on the percentage of hematite in any given magnetite grain (BOTTOM). 198

5-85: Photomicrographs of magnetite from OPS-2 from borehole CA-PL-2 showing fine-grained magnetite stringers parallel to the foliation of the rock (Type 1) and a magnetite porphyroblast (Type 2) with pressure shadows developed parallel to the foliation of the rock. Images taken in PPL (A) and under reflected light (B). 202

5-86: Photomicrographs showing the relationship between magnetite and Cu(-Fe) sulfides in Type 3 magnetite under reflected light. A: Weakly martitised magnetite shares straight boundaries with bornite which is partly altered to covellite along its edges (EPS-04). B: Magnetite and the Cu-sulfides are aligned parallel to the foliation developed in sample PST-4D1-2. Magnetite shows pressure shadow development parallel to the foliation. These pressure shadows are filled by quartz and the chalcocite showing alteration to covellite. Magnetite also contains inclusions of chalcocite altering to covellite. These inclusions are rounded and elongated parallel to the foliation. 202

6-1: Box and whisker plots show the variability in Al, Si, Ti, V, Cr, Mn, Co and Ni concentrations for the magnetite bulk samples. 208

6-2: Median minor and trace element concentrations in magnetite plotted for each of the sample locations. A solid line is drawn at 1ppm and dashed lines at 0.01 and 100 ppm, an order of magnitude above and below 1 ppm. 212

6-3: Magnetite median results (D) normalised to BCC (A), BMS (B) and IBZ (C). 214

6-4: Scattergrams of spinel elements from all of the magnetite grains analysed for this study for: Mn-Mg (A), Mn-Co (B), V-Cr (C), Ni-Co (D), Ga-Zn (E) and Ni-Ti (F). The element concentrations are on a log scale. See text for explanation of groupings and arrows. 216

6-5: Sediment-hosted magnetite measurements are compared and distinguished based on lithotype for the element ratios V-Co (A), Mn-Co (B), V-Cr (C) and Ni-Co (D). The abbreviations used are PLT - phyllite, SLT - siltstone, SST - sandstone. 217

6-6: Examples of orthogonal plots for AF (top) and thermal demagnetisation (bottom) methods for specimens a) OPS-6; b) OPS-7; c) OPS-8 and d) OPS-15. The solid symbols represent horizontal projections, defined by North (N), East (E), South (S) and West (W); the open symbols represent the vertical projections along North (N), Down (D), South (S) and Up (U) axes. All axes are expressed in mT. 218

6-7: Thermal step demagnetisation of sandstone example sub-samples from OPS-6 (A), -8 (B), -10 (C) and -14 (D). Each black square represents a step in demagnetisation process. Axial intensity values (J) are expressed as a ratio of the natural remanent magnetisation (NRM) intensity (J_{NRM}). 219

6-8: Equal area stereonet mean ChRM directions for each sample, as well as the site mean. The error on the mean is illustrated by the 95% confidence cone (red). 220

6-9: Hysteresis plots for two representative samples, OPS-02 and OPS-12. The narrow shape of these plots is suggestive of multi-domain magnetite (MD).....222

6-10: Curie temperature plots for two representative samples, OPS-02 (LEFT) and OPS-10 (RIGHT). The plots show a single drop-off and a relatively stable return cooling path. 222

7-1: Regional distribution of the Kgwebe Formation and published zircon ages for the Oorlogsende Member (Hegenberger and Burger, 1985); the Mabeleapodi Hills outcrop (Schwartz et al., 1996) and the Eiseb metavolcanic, ZR-01 (yellow circles). The samples used in this study for whole rock geochemistry are indicated in bold, KG-1, OE-1 and OE-2, and EPS-01-EPS-04. EPS-01 and ZR-01 were sourced from the same 10cm of drill core.....224

7-2: Stratigraphic correlation of the Eiseb deposits with the stratigraphy from Ghanzi, Klein Aub and Witvlei (bold). The logs show Formation names i.e. Doorpoort Formation, Eskadron Formation etc. The dashed lines show the preferred correlations from the results of the current study. Basement and Kuke Formation correlatives in the Eiseb are not confirmed so denoted by '?.' The correlations are modified after Borg (1987). 225

7-3: The basement horst is bordered to the north and to the east by the southern Damara thrust zone (SDTZ) (white dashed lines), and to the west by metavolcanics which form long NNE trending linear ridges. The arrows indicate the zone of uplift associated with a possible basement inlier at depth. Background map: Namibian Government regional airborne magnetic data (www.mme.gov.na), AS-image product. 226

7-4: Residual Bouguer Gravity map showing the location of the basement horst and a possible basement high in Botswana, near Ghanzi. Gravity data compiled by Corner (2000) and reported in Miller (2008). 227

7-5: The Gondwana supercontinent during the Early Cambrian (1); geological map of the Lufilian and Zambezi Belts (2); and the location of the Eiseb basement horst (black circle)

between two regional Damaran thrusts (white) on the GSN regional aeromagnetic RTP map (3). Image 1 and 2 are taken directly from Milani et al. (2015). 227

7-6: TAS diagram comparing the volcanic (OE-1 & OE-2) and metavolcanic (EPS-01 – EPS-04) samples from the Eiseb to published data for the Kgwebe Formation and the Nauzerus Formation using the data presented in Table 34: Kgwebe Hill, Mapeleapodi Hills, Makgabana Hills and Ngwenelekau Hills (Kampunzu et al., 1998); and the Nauzurus Group in Namibia: Opdam Formation (Becker at al., 2005), Langberg Formation (Becker et al. 2005) and Nückopf Formation (Ziegler and Stoessel, 1993). The volcanic samples from the Eiseb plot within the rhyolite and trachyte fields, as do those of the Kgwebe. The metavolcanic samples which host mineralisation, EPS-02 and EPS-04, plot in the high alkali trachyte field, and trachyandesite fields, respectively. TAS boundaries redrawn after Le Maitre et al. (2005). 228

7-7: TAS diagram showing the changes in SiO_2 and alkali elements for the metavolcanic samples from the same boreholes (blue dashed lines) and the volcanic samples KG-1 and OE-1 during alteration to OE-2 (brown dashed line). TAS boundaries redrawn after Le Maitre et al. (2005). 230

7-8: Reflected light photomicrographs of sulfide mineralogy within veins (A & C) compared to disseminated mineralisation (B & D) for EPS-09 (A & B) and OPS-5 (C & D). Insert C showing the typical exsolution textures between chalcocite and bornite. 232

7-9: Plot of Ti (ppm) versus Ni/Cr ratio in magnetite as determined by LA-ICP-MS. The fields for magmatic and hydrothermal magnetite are drawn after Dare et al. (2014). Cr was not detected in 12 of the magnetite grains analysed and 9 grains contained no detectable Ni. ..233

7-10: Median trace element concentration (ppm) for magnetite from the metavolcanic samples MG-1 and MG-3, and the altered rhyolite OE-2, normalised against OE-1. All of the samples show systematic variations in W, Cu and Ti relative to OE-1, as highlighted by grey bars. With the exception of V there is a general increase in the slope from Ti to Cr reflecting the increased concentration of these elements as a function of their compatibility into magnetite. 234

7-11: Schematic illustration of the effects of alteration and deformation relative to the composition of magmatic magnetite. Alteration and deformation of the host-rock result in a net loss of W and Ti, relative to magmatic magnetite, and the addition of Cu. Alteration alone produces magnetite with higher V concentrations than either magmatic magnetite, or magnetite in the deformed rocks. Where the host-rock has undergone deformation only, magnetite is enriched in Co, Ni and Cr. In the sample which hosts significant Cu concentrations, magnetite is characterised by significantly lower Pb concentrations. 235

7-12: Vanadium versus Ni concentrations (ppm) for the magnetite sampled from the metavolcanic rocks (MG-1 & MG-3) and the rhyolite samples (OE-1, OE-2 and KG-1). The

V/Ni ratio for each of the environments sampled are clearly illustrated dashed circles enclosing magnetite analyses from each location. The Ni content of the rhyolites which have not undergone deformation/metamorphism, show a fair amount of spread in the data, but have fairly narrow ranges in terms of V concentrations. Magnetite from the metavolcanics which have undergone deformation/metamorphism (MG-1) and contain mineralisation have very narrow ranges for both V and Ni concentrations. 236

7-13: A: Sn vs. Ga concentrations for magnetite from the volcanic and metavolcanic samples measured. The fields shown on the diagram were interpreted from the data of Nadoll et al. (2014) which showed magnetite associated with BIF either had low, or below detection limit concentrations of Sn and Ga. The concentration of Sn for both BIF/iron ore and Ag-Pb-Zn hydrothermal vein type magnetite rarely exceeded 10ppm, although higher concentrations of Ga are associated with the veins. Magnetite from the igneous Henderson Climax-type Mo deposit has the highest Sn and Ga concentrations, (generally >100 ppm). Igneous and hydrothermal porphyry magnetite is characterised by high Ga concentrations, but lower Sn contents than the Henderson -type magnetite. B: This same relationship has been shown for the Al + Mn vs Ti + V concentrations of known ore-deposits, with higher concentrations in all elements thought to represent higher temperatures of formation. The temperature ranges are based on information published by Nadoll et al. (2014) for the same deposits described in A. 239

7-14: Nb vs. Y for magmatic magnetite (OE-1) compared to whole rock data from Kampunzu et al. (1998) for Kgwebe Hills, Makgabana Hills, Mapeleapodi Hills and Ngwenelekau Hills. Diagram boundaries after Pearce et al. (1984). 240

7-15: Median spinel trace element concentrations for magnetite from the sedimentary samples (A) and the metavolcanic samples (B) normalised against BCC (bulk continental crust) using the values from Rudnick and Gao (2003). Magnetite from the sedimentary rocks (MG-4 to -14) shows strong depletions in Al, Mg, Ti and V relative to BCC, and similar enrichments for Zn, Co and Ni. Manganese and Cr show the most variability, although by less than an order of magnitude. The magnetite from MG-3 is depleted in all of the spinel group elements relative to BCC. MG-1 shows depletions for all of the elements relative to BCC, but also enrichments in Ti, Co, V and Cr. C: The median values for 20 of the elements measured, with no normalisation, show the overall consistency of the data. 241

7-16: Photomicrographs of the textural association between magnetite and pre-deformation biotite from A: PST4-D2-2 (NEA-PL-1), B: EPS-20 (CA-PL-6), C: OPS-3 (CA-PL-3), and D: OPS-1 (CA-PL-2). Pressure shadows are commonly associated with biotite when it is oriented parallel to the foliation, Type 2 magnetite shows similar pressure shadows which means that it either formed prior to deformation, as part of a pre-deformation assemblage which included biotite, or magnetite growth replaces biotite during

metamorphism and the pressure shadows are inherited. All photomicrographs taken under XPL. 245
7-17: Vanadium vs. Ni binary plot for sediment-hosted magnetite samples relative to the volcanic and metavolcanic samples OE-1, OE-2, KG-1, MG-3 and MG-1. The mineralised sediment-hosted magnetite samples MG-6, MG-10 and MG-12 cannot be distinguished from un-mineralised samples on the basis of this diagram. 246
7-18: Vanadium vs. Co for the sediment-hosted magnetite samples distinguishes mineralised from non-mineralised host-rocks. MG-10 shows a strong linear relationship between Co and V. 247
7-19: Median trace element concentrations from magnetite are compared to whole-rock assay results from the same depth (dashed line), and the average for the specific stratigraphic unit the sample was taken from (solid black line). A: MG-3; B: MG-6; C: MG-10; and D: MG-12. The stratigraphic units used for comparison were the median values taken from Table 15 (for the MV MG-3). IBU-CA (MG-6 & MG-12) and IBU-NEA (MG-10). 248
7-20: Silver vs. Cu plots for all of the magnetite from the sedimentary samples. Most samples shows an erratic relationship between these elements, magnetite from MG-6 and MG-13, however show a linear relationship. 249
7-21: Median oncentrations of some spinel elements in magnetite from two siltstone samples with variable levels of martitisation. MG-14 is from a hangingwall (HW) siltstone (SLT) which shows moderate to high levels of martitisation for magnetite (borehole CZ-1). MG-13 is from a footwall (FW) siltstone which shows low levels of martitisation. 250
7-22: Tin vs. Ga (A) and Al + Mn versus Ti + V (B) for the sediment-hosted magnetite samples indicating restricted formational temperatures for this type of magnetite. 251
7-23: Ni + Cr vs. Si + Mg plot (A) and Al / (Zn + Ca) vs Cu / (Si + Ca) plot (B) of the Eiseb data using the fields defined by Dupuis and Beaudoin (2011) to discriminate between Ni-Cu sulfide deposits, and VMS deopsits. All elements calculated as weight percentages. 252
7-24: Ni/(Cr+Mn) vs Ti+V (A) and Ca+Al+Mn vs Ti+V (B) discriminant plots to distinguish magnetite from Kiruna, IOCG, porphyry Cu, Fe-Ti-V and BIF deposits. In A the Eiseb data plot mostly between the BIF and IOCG fields, with the mineralised metavolcanic sample (MG-3) plotting in the skarn field at low Ti +V, and the basement rhyolites (KG-1, OE-1 and OE-2 plotting in the same field but with higher Ti+V and lower Ni/(Cr+Mn). MG-10 and MG-13 show variable Ti+V and plot within the skarn field. B suggests that the Eiseb magnetite has an overwhelmingly IOCG signature, with minor scatter into the skarn and BIF fields. The sandstone of MG-4 and the mineralised metavolcanic MG-3 plot partly inside, but mostly outside, of the BIF field. The basement sample OE-1 plots mostly within the porphyry field, as do some MG-12 grains. 253
7-25: Comparison diagrams of the normalised trace element patterns for magnetite from the Eiseb with A: Banded Iron Formation (BIF) and B: Iron-oxide Copper Gold (IOCG)

deposits. The data have been normalised to bulk continental crust using values from Rudnick and Gao (2003), and the compositional fields for BIF and IOCG deposits are after Dupuis and Beaudoin (2011).....254

7-26: The APWPs for Gondwana constructed using the fitted spherical spline path (a) and the Running Mean path (b) methods. The white shading shows the 95% confidence ovals for the input poles and the grey shading shows the α_{95} ovals after a sedimentary inclination correction as been applied. The results of this study were plotted using the APWP spline path in (a). Figures taken from Torsvik et al. (2012). 259

7-27: Pole position (red dot) from the Eiseb plotted on the APWP (spline path) of Torsvik et al. (2012) (blue line). The α_{95} confidence ellipse is plotted as a red circle around the pole. 259

9-1: Schematic diagram of O-SSC deposits showing the main features which should be tested for exploration purposes. The rift basin is exposed to regional compression (red arrows) during orogenesis which causes folding of the basin sedimentary rocks, as well as associated thrusting and faulting (dashed lines), potentially reactivating deep-seated syn-rift faults which tap the bimodal basement and focus fluid flow (blue lines). Uplifted basement fragments also contain fault networks which may channel fluid flow to the overlying rift sediments. The basement may contain a pre-enrichment of ore minerals (red crosses) from a previous mineralising event which may have been leached by hydrothermal fluids, and transported via seismic pumping to the overlying sedimentary sequences. Syn-deformational intrusions may have provided important heat sources to drive hydrothermal fluids, as well as the uplift of basement segments. Within the folded sedimentary sequences rheological contrasts and redox boundaries play a role in metal precipitation (red lines), particularly where brecciation, faulting, thrusting and fold closures have contributed to secondary permeability development. 268

List of Tables

1: Stratigraphic subdivisions after Miller (2008) for the Sinclair Supergroup and the lower Damara Sequence in the Eiseb area. Dashed lines represent unconformities. * Includes the Oorlogsende Member as this is a lateral correlative of the Langberg Formation. 44

2: Generalised lithostratigraphy and interpretation of the sedimentary depositional environments (modified after Modie, 1996). 45

3: Summary of drilling carried out by EPM from 2010 to the end of 2014.....74

4: Assay results from a single drill hole along a limb from the central study area antiform (CA: central antiform). Table extracted from Smalley et al. (2012).....79

5: Summary information on the samples used during this study. The copper and silver ppm values were obtained from the Eiseb database. The 'Palaeo-mag' column refers to samples used for the palaeomagnetic study. 90
6: Certified Reference Material used for QAQC. 96
7: Example of blank chips used as reference material for QAQC procedures. 96
8: Summary of the samples used for Pb-U zircon geochronology. 97
9: Summary statistics for the EDS QAQC using the BCR-2 reference material. The mean refers to the mean from the 10 repeat analyses, Stdev refers to the standard deviation for the repeat measurements, and BCR-2 shows the recommended values for oxides published by Wilson (1997). 99
10: Samples analysed using QEMSCAN. All samples prefixed with 'PB' are polished blocks and the whole rock samples are polished thin sections. Grain mount samples prefixed with 'MG' are thin sections. 101
11: Operational parameters summarised for the measurements taken during this study using the QEMSCAN. 101
12: ICP-MS sample list. 102
13: Summary of the samples used for palaeomagnetic testing. 104
14: Summary geochemical information grouped by rock type and stratigraphic unit for the 18 boreholes sampled by Eiseb. All values are reported in ppm. ARG=argillite, PLT=phyllite, SLT=siltstone, SST=sandstone, MV=metavolcanic, IBU=interbedded unit, FW=footwall, HW=hangingwall, IBU = Interbedded unit, FW = footwall, HW = hangingwall, n=number of samples above detection limit, AVG=average, Min=minimum, Max=maximum, Med=median. 111
15: Summary geochemical information grouped by stratigraphic unit and location for the 18 boreholes sampled by Eiseb. All values are reported in ppm. ARG=argillite, PLT=phyllite, SLT=siltstone, SST=sandstone, MV=metavolcanic, IBU=interbedded unit, FW=footwall, HW=hangingwall, n=number of samples, AVG=average, Min=minimum, Max=maximum, Med=median. 112
16: The published oxide weight % values for the BRC-2 standard and associated standard deviation values (±) compared to the results of the area scans using EMP. The standard deviation between the published results and the area scans show good agreement between the results for all of the oxides analysed. 129
17: Major element oxide compositions for the three basement samples KG-1, OE-1 and OE-2 as determined by EDS area scans. Values are averages. AI has been determined by Na_2O+K_2O/Al_2O_3 using weight percentages and ASI=Al_2O_3/CaO + Na_2O+K_2O. 130
18: Major element oxide compositions for the four metavolcanic samples EPS-01 – EPS-04 as determined by EDS area scans. Values are averages. AI has been determined by Na_2O+K_2O/Al_2O_3 using weight percentages and ASI=Al_2O_3/CaO + Na_2O+K_2O. 136

19: Samples analysed using QEMSCAN. All samples prefixed with 'PB' are polished blocks and the whole rock samples are polished thin sections. Grain mount samples prefixed with 'MG' are thin sections. 170
20: Summary modal mineralogy for the whole rock sample set using the secondary SIP. The table includes only entries >0.0051 %. The suffix (T) denotes trap definitions. 174
21: Summary modal mineralogy for the MG sample set using the secondary SIP for stepping interval of 50µm, 5µm, 1µm and the standard deviation between them. Table derived using the iDiscover software from QEMSCAN data. 181
22: Summary information for the modal abundance of trap definitions and unclassified material for the whole rock polished sections as calculated using the primary SIP. 185
23: Summary information for the modal abundance of trap definitions and unclassified material for the grain mount polished sections as calculated using the primary SIP for the 5µm scans. 186
24: Summary table of the petrographic characteristics of magnetite in the polished thin sections from the Eiseb Deposits. BH=borehole; MG=magnetite, MS=magnetite stringer; MP=magnetite porphyroblasts; RF=rock fabric (foliation or lepidoblastic texture); PS-MP=pressure shadows developed on magnetite porphyroblasts; MP-F=magnetite porphyroblasts parallel to the fabric of the rock; CFS=copper-iron sulfides; OX=oxidation level based on the chart presented in Figure 5-83. X=magnetite not present; *=magnetite not observed under reflected light, but confirmed using EMPA. 199
25: FeO weight percentages obtained during EMPA averaged over ten magnetite grains per sample. 206
26: Summary statistics for the standard reference materials analysed during LA-ICP-MS analysis, NIST-610 and NIST-612. 207
27: Mean, minimum and maximum minor and trace element compositions for magnetite from each sample location. Samples where no measurement was taken are marked by an '\'. 'dl' refers to the detection limit, reported as a minimum and maximum for the sample suites in the table. 209
28: Median of minor and trace element concentrations (in ppm) for magnetite per polished thin section. The highest value for each element is emphasised in bold. The number of measurements above the detection limit (dl) for each site is shown as a percentage. 211
29: Normalisation values used for this study were from bulk continental crust (BCC) (Rudnick and Gao, 2003), and from magnetite standards. The magnetite standards used were median values from burial metamorphic magnetite (BMS) from the Belt Supergroup (Nadoll et al., 2012), and the Inner Zone Batholith from Japan (IBZ) (Spong, 1998). 213
30: Site mean characteristic remanent magnetisation (ChRM) directions. Sites which produced incoherent or aberrant directions are not included. The *n* column indicates the number of specimens used to calculate the mean declination (dec) and inclination (inc)

for each site. The α_{95} in degrees is the radius of the 95% confidence cone about the mean, while *k* is the precision parameter of Fisher (1953). 220

31: Mean VGP for each of the samples. The site latitudes are shown in column λ, the longitudes in column ϕ, and the VGP latitude and longitude as VGP λ and VGP ϕ respectively. The first semi-axis of the VGP confidence ellipse is shown in column dp and the second semi-axis of the VGP confidence ellipse in column dm. 221

32: Summary VGP results and Fisher statistics (Fisher, 1953). Dec = declination; inc = inclination. 221

33: Curie temperatures for each of the five samples were calculated using the second derivative method of Tauxe (1998) and a running average of 3. 222

34: Geochemical results for the acid volcanics (KG-1, OE-1 & OE-2) and metavolcanics (EPS-01-EPS-04) from this study and published select major oxide geochemistry for the acid volcanics from the Kgwebe Formation outcrops in Botswana: Kgwebe Hill, Mapeleapodi Hills, Makgabana Hills and Ngwenelekau Hills (Kampunzu et al., 1998); and the Nauzurus Group in Namibia: Opdam Formation (Becker at al., 2005), Langberg Formation (Becker et al. 2005) and Nückopf Formation (Ziegler and Stoessel, 1993). 229

1 Introduction

The Kalahari Copperbelt (KCB) is composed of a series of late-mid Proterozoic basins which stretch discontinuously for ~800 km, roughly NE-SW across Namibia and into north-western Botswana (Maiden and Borg, 1989). Exploration along the KCB in Namibia led to the discovery of Cu-Ag mineralisation within the Tsumis Group meta-sediments of the Sinclair Supergroup, which are lateral equivalents to the ~Neoproterozoic metasedimentary Ghanzi Group in Botswana. These deposits are broadly contemporaneous and geologically similar to the copper-cobalt deposits of the Central African Copperbelt (CAB) of Zambia and Democratic Republic of Congo (Schwartz et al., 1996; Sillitoe *et al.*, 2010). Deformation and metamorphism during the Pan African (~530 Ma) assembly of the Gondwana supercontinent affected both the KCB and CAB as a series of orogenic belts, the Damara Orogeny affecting the former, and the Lufilian Orogeny affecting the latter (e.g. Miller, 1983; Porada and Berhorst, 2000).

The CAB deposits, although diverse on a local scale, have mostly been classed as sediment-hosted stratiform copper (SSC) deposits, although debate on this classification is ongoing (McGowan et al., 2006; Sillitoe et al., 2015, 2010). SSC are low-grade - high tonnage low temperature deposits which represent significant resources of copper on a global-scale (Brown, 1997; Hitzman et al., 2005). The copper occurrences along the KCB share many similar characteristics to SSC deposits in that they occur primarily as broadly stratiform deposits, are hosted within sediments and concentrate largely along perceived regional oxidation-reduction (redox) boundaries.

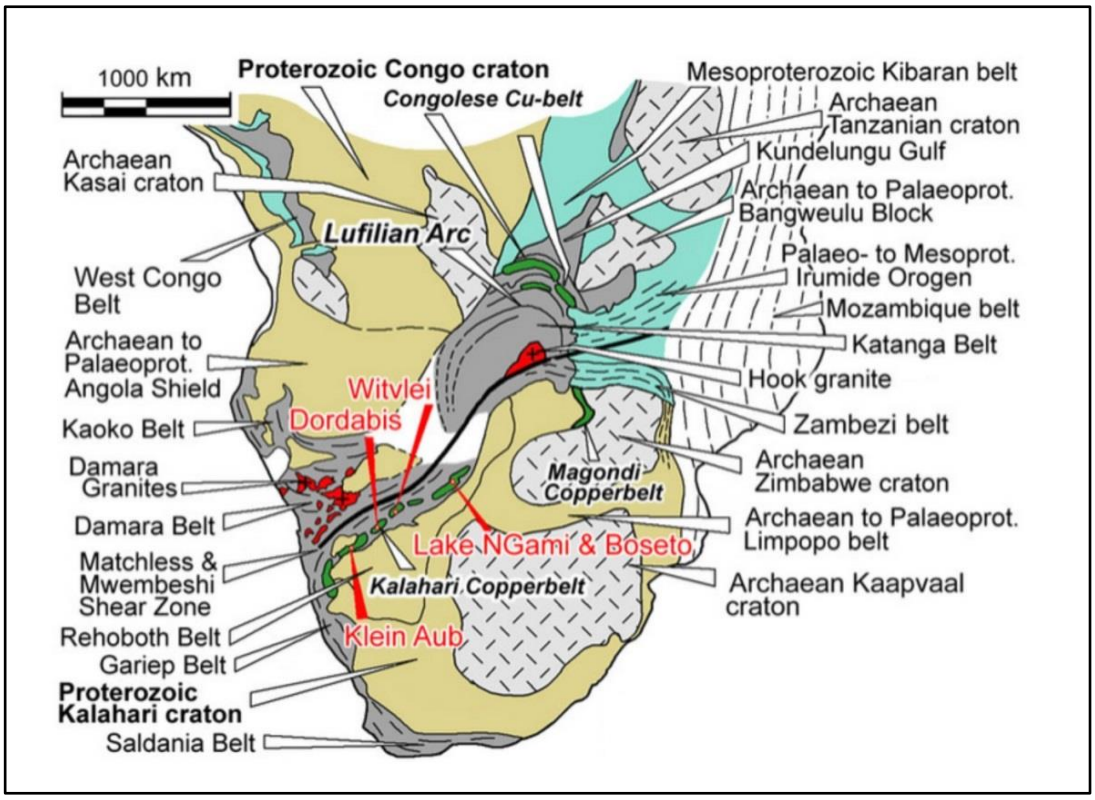

Figure 1-1: Location of the Kalahari Copperbelt within the crustal framework of southern Africa. The major copper deposits of Zimbabwe, Zambia and the Democratic Republic of Congo are also show. Image taken directly from the website of Porter Geoconsultancy (http://www.portergeo.com.au), accessed 21/05/15.

In Botswana Cu-Ag mineralisation was discovered in 1962 in the region of Lake Ngami by Johannesburg Consolidated Investments (JCI). This irregularly developed mineralisation was identified straddling the contact between the clastic continental lithologies of the D'Kar Formation and the reduced lacustrine/marine lithologies of the Ngwako Pan Formation (Ghanzi Group) (Modie, 1996; 2000).

During the 1960s and 1970s regional exploration in Namibia was focussed on locating copper mineralisation associated with the Southern Margin Zone (SMZ) and the Matchless Amphibolite Belt (MAB) where numerous copper deposits had been identified (e.g. Sinclair, Gorob, Hope, Otjihase). Copper was reportedly being shipped to Europe from Sinclair Mine as early as 1850 (Schneider and Seeger, 1992).

In both central eastern Namibia and much of Botswana the thick Cenozoic Kalahari Group sand and calcrete, which in places reaches >100m thick, limited exploration of this region to the edges of the Kalahari where exposures could be accessed (Anglo-Vaal SWA, 1967-71; US Steel, 1972-1978; Anglo American Botswana (Pty), 1990-93). By the 1970s the first connections were being made between the Mesoproterozoic basins of Namibia and Botswana (Toens, 1975), and by 1989 Borg and Maiden published the term 'Kalahari

Copperbelt,' officially linking the deposits of Klein Aub, Dordabis and Witvlei in Namibia with the Lake Ngami and Goha Hills deposits in Botswana. Exploration along the KCB in Namibia, however, remained bound to the discovery of MAB-type Cu mineralisation along the edges of the Kalahari Group, with little consideration given to locating KCB-type deposits. This pursuit of a MAB model proved ultimately unsuccessful, and as a result few exploration companies have been willing to tackle this part of Namibia.

The first exploration aimed specifically at KCB-type Cu-Ag mineralisation beneath the Kalahari Group in central eastern Namibia was started in 2009 by Eiseb Prospecting and Mining Pty (Ltd) (hereafter referred to as EPM). Drilling in October 2010 provided the first evidence of KCB-style mineralisation between the known deposits at Ngami Lake and Witvlei.

By January 2015 a total of 344 holes had been drilled and over 66,600m of geology exposed. This study has been done in collaborate with EPM under the guidance of three geologists who have worked in Cu-exploration in Namibia collectively for almost a century: Hendrik Veldsman, Alan Simmonds and Tim Smalley. They made two key observations which formed the basis of this study, firstly, that magnetite appears to have an association with mineralisation, and secondly, that an exploration model based an SSC origin for Eiseb deposits has met with little success in locating Cu-Ag mineralisation. These were used to guide the aims and objectives of this project.

1.1 Aims and objectives

The aims of this study are two-fold. The first is to characterise the geological setting of Cu-Ag mineralisation in a heretofore unexplored part of the KCB in central eastern Namibia.

This aim is achieved through:

- utilising the geochemical, geological and geophysical (aeromagnetic) datasets of EPM to characterise the stratigraphy of the study area and create a regional geological and structural map across this portion of the KCB;
- using zircon U-Pb geochronology to confirm that the sediments in the Eiseb study area are lateral correlatives to the Ghanzi Group in Botswana;
- detailed petrography of rock types occurring across the study area using reflected and transmitted light, electron microprobe analayses (EMPA) and quantitative evaluation of minerals by scanning electron microscopy (QEMSCAN);

- using reflected and transmitted light, EMPA and QEMSCAN to characterise Cu-Ag mineralogy and textures

The second objective is to investigate the use of magnetite as a petrogenetic indicator to fingerprint the geological setting of the Eiseb. This includes using petrography and trace element geochemistry to distinguishing magnetite from barren and mineralised areas, which could be used as an exploration tool.

The second aim is achieved through:

- characterising the occurrences of magnetite within different lithotypes in terms of levels of oxidation, morphology and textural relationships to Cu-Ag mineralisation;
- using EMPA and LA-ICP-MS to characterise the trace element contents of magnetite from different locations and lithotypes within the basin;
- using palaeomagnetic analysis to determine whether magnetite has remanence, and if so, to constrain the timing of magnetite growth, and potentially also the Cu-Ag mineralisation by proxy.

The overarching aim of this work is to critically address the hypothesis that the Kalahari Copperbelt fits into the SSC classification of ore deposits.

2 Literature Review

2.1 Sedimentary-hosted Stratiform Copper Deposits

2.1.1 Introduction

Sediment-hosted stratiform copper (SSC) deposits are characterised by copper and copper-iron sulfide mineralisation. Mineralisation is broadly stratiform (peneconcordant), occurring as both disseminations and within veins, and may or may not be of an economic grade (Brown, 1997; Hitzman et al., 2005; Robb, 2009). On a global scale these deposits are second only to porphyry copper deposits in terms of copper production, and account for ~23% of the world's Cu production and known reserves (Robb, 2009; Singer, 1995). These deposits are the most important global source of cobalt and can contain significant concentrations of other metals, such as Ag, Pb, Zn and U, and in some cases PGEs (platinum group elements) and Au (e.g. Lubin-Sieroszowice, Poland; and Kolwezi, Congo). The largest of these, the 'supergiant' deposits, occur in the Neoproterozoic Katangan Basin of the Central African Copperbelt (CAB); the Permian Kupferschiefer deposit, and the Palaeoproterozoic Kodaro-Udokan Basin of Siberia (Figure 2-1). Other large deposits include the Devonian to Carboniferous Chu-Sarysu basin in Kazakhstan, the Middle Proterozoic White Pine deposit in the United States, and the Neoproterozoic-Cambrian basin in Afghanistan (Brown, 1997; Hitzman et al., 2005, 2010).

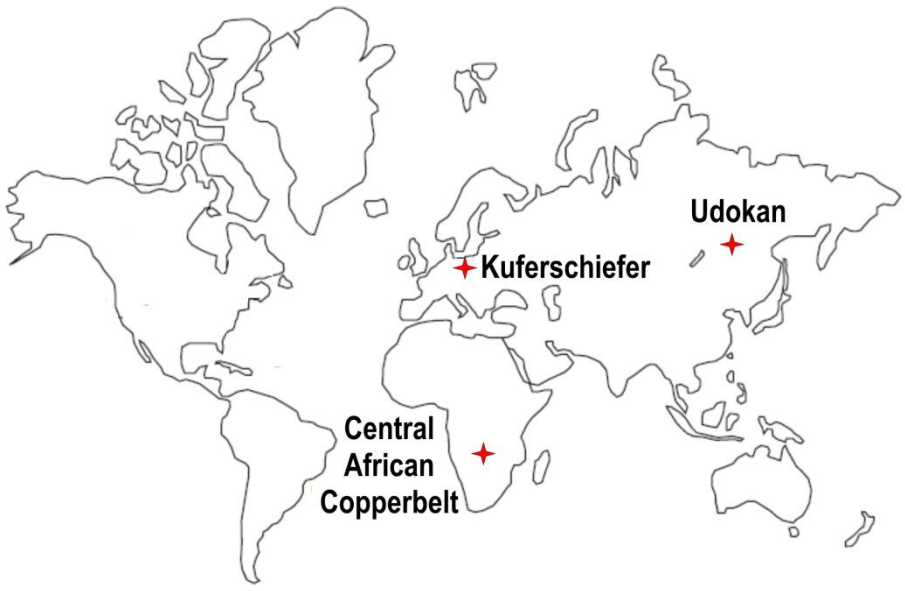

Figure 2-1: Map of the world showing the location of the largest, 'supergiant,' sedimentary rock-hosted stratiform copper deposits.

Although these deposits cover a wide range of characteristics, with ideas about the genesis of mineralisation ranging from early diagenetic to basin inversion and metamorphism, and cover a wide range of temperatures from 50˚ - 400˚C, variable salinities and basinal settings, most of these deposits share incredibly similar morphology, styles of mineralisation and mineralogy. In the following sections the main characteristic of these deposits are described and discussed.

2.1.2 SSC deposits: Characteristics and Genesis

SSC deposits are commonly hosted within rift-related sedimentary basins in an intra-continental setting, with fairly consistent volcano-sedimentary successions. In general the early rift sediments are immature and underlain by mafic to bimodal volcanic sequences. The overlying successions are composed of thick (km-scale) oxidised (hematite-bearing) siliciclastic rocks (redbeds). These are overlain by fine-grained marine to lacustrine, chemically reduced sediments, which represent syn- to post-rift phases of basin fill. In the Katangan (CAB) and Zechstein (Kupferschiefer) basins the marine/lacustrine sediments are interfingered and overlain by evaporitic sequences. SSC mineralisation within these basins typically occurs in thin (<3m) zones which can form laterally extensive sheet-like deposits, or irregular to tabular deposits (Brown, 1997; Hitzman et al., 2005, 2010).

SSC deposits share similar characteristics in terms of the main copper sulfides they contain, i.e. chalcopyrite ($CuFeS_2$) - bornite (Cu_5FeS_4) - chalcocite (Cu_2S); as well as the style of mineralisation. Mineralisation falls into two broad categories: disseminated (<cm-scale) and vein-hosted (>cm-scale). These textures have led to two main schools of thought about the genesis of SSC deposits with the disseminated mineralisation being used to argue for a syn-sedimentary to diagenetic origin for mineralisation, whereas the presence of Cu-Ag mineralisation within veins has been used to argue for a late introduction of metal-bearing fluids.

The favoured geological model for SSC formation is that Cu mineralisation occurred during diagnenesis, where Cu is sourced from the continental clastic redbed sediments and transported by mildly oxidised basinal brines (Figure 2-2). The source rocks are both hematite stable and contain minerals which can be leached of their metals and sulfur (i.e. from minerals in ferromagnesian, mafic and pyritic rocks) (Brown, 1997; Haynes, 1986a, 1986b, Haynes and Bloom, 1987a, 1987b, Hitzman et al., 2005, 2010; Sillitoe et al., 2010).

In a diagenetic model the mineralising process may be summarised as the interaction of two fluids: a mobile oxidised fluid carrying copper as a chloride complex and a reduced fluid (or fixed/ in situ reductant) within the host-rock (Brown, 2014; Cox et al., 2003). In most SSC deposits, where lacustrine and marine sediments immediately overlie continental siliciclastic beds, there is evidence for evaporation exceeding rainfall (aridification of the environment), which would increase the salinity of inland seas. The circulation of this fluid through large volumes of redbed sediments would buffer the basinal fluids to an oxidising state (Hitzman et al., 2010).

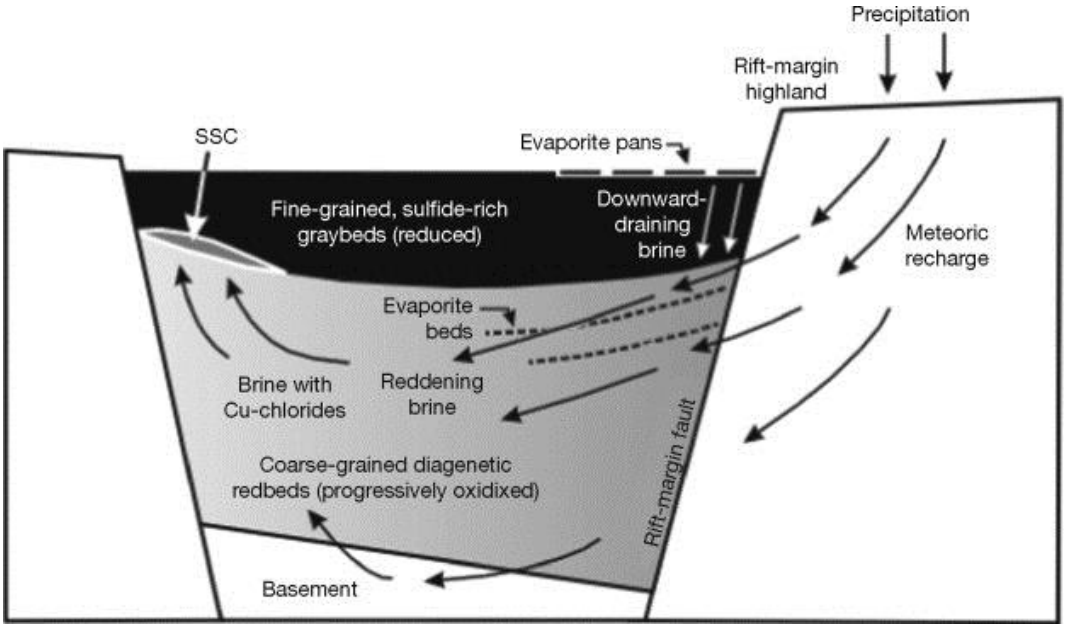

Figure 2-2: Basin-scale genetic model for SSC deposits. Highland recharge drives meteroric water flow along idealised pathways which may interact with the basement or rift fill sediments. Image taken from Brown (2014).

At moderately low pH the process of leaching and transporting copper in solution can be described as:

(1) $$Cu_2O + 6\ Cl^- + 2\ H^+ = 2\ CuCl_3^{2-} + H_2O$$

Connate (formational) fluids have been implicated as the transporting fluid for the deposition of diagenetic, disseminated copper sulfide mineralisation. Burial and time result in a reduction of porosity in sediments, and the production of fluids. Hanor (1979) has shown that at the early stages of burial shales can release up to 3500 litres of water for each m^3 of

sediment deposited. Sandstones, which are initially less porous than shales, will release 700 litres of water for the same volume of sediment deposited. At greater burial depths, where temperatures increase to 50-100˚C, water bound within the clay particles of argillaceous sediments, begins to be released (Robb, 2009). This generally produces a volumetrically much smaller amount of fluid, with the true volume depending on the specific characteristics of the sediment and the local geothermal gradient.

A reduced environment at the site of deposition could be generated by any fluid in equilibrium with pyrite, or the presence of liquid or gaseous hydrocarbons, or fluids interacting with organic-rich shales and carbonate rocks (Cox et al., 2003). The interaction of this fluid (with organic matter acting as the reductant) with the oxidising fluid in (1) will produce native copper, and can be described as:

(2) $$2\ CuCl_3^{2-} + 2\ H_2O + C = 2\ Cu^0 + 1\ CO_2 + 4\ H^+ + 6\ Cl^-$$

For the formation of a copper sulfide, for example, by interacting with bacterially reduced sulphate, the following equation applies:

(3) $$2\ CuCl_3^{2-} + S^{2-} = Cu_2S + 6\ Cl^-$$

Where sulphate ions are contained within the brine, the mixing of this copper-bearing brine with a reduced fluid will result in the following:

(4) $$2\ CuCl_3^{2-} + SO_4^{2-} + CH_4 = Cu_2S + CO_2 + 2\ H_2O + 6\ Cl^-$$

A key feature of these deposit types is thought to be the presence of redox boundaries, with oxidation-reduction reactions driving the precipitation of metals/sulfides (Brown, 1997; Cox et al., 2003; Haynes and Bloom, 1987b; Hitzman et al., 2005, 2010). The reductants in these deposit types can be either *in situ* (organic matter, pyrite), or mobile (i.e. having migrated to

the ‘trap’ area). In parts of the Zambian Copperbelt and the Kupferschiefer hydrogen sulfide (or sour gas) is implicated as the reductant (Hitzman et al., 2010). Equally important to the formation of an SSC deposit is focussed fluid flow along areas of stratal pinch out, or linear structural zones where the fluid is forced to interact with reduced strata. Changes in temperature, pressure, fluid chemistry or host-rock chemistry will also result in the precipitation of the fluid’s metal contents (Hitzman et al., 2005, 2010).

There are numerous aspects to SSC deposits which complicate their otherwise simple shared characteristics. The overall implication in the case of both the Kupferschiefer and the CAB deposits is that mineralisation likely began during early sedimentation of these basins and continued late into the basin's history (Hitzman et al., 2010). This idea of mineralisation spanning millions of years is used to explain the different styles of mineralisation, with the disseminated type sulfides occurring during diagenesis, and later regional metamorphism and deformation locally remobilising disseminated mineralisation into veins (Hitzman et al., 2005). The common association between Cu and uranium-bearing minerals (U-Pb uraninite/rutile) in parts of the Lufilian Fold Belt however, have been used in an attempt to resolve some of issues around the timing of mineralisation (Selley et al., 2005). Age dating places the deposits between 670 ± 20 Ma (Cahen et al., 1971) and 496 ± 1 Ma (Richards et al., 1988). These ages are largely derived from vein or fracture-hosted minerals which generally post-date peak metamorphism (~530 Ma). The Kambove deposit (Congolese Copperbelt) shows an association between Cu and Co, and Co and U which Cahen et al. (1971) used to date this deposit at 555 ± 10 Ma, right in the middle of the Pan African event. In an SSC model such as that favoured by Hitzman et al. (2005, 2010, 2012 and references herein), it is argued that these dates only capture the final mineralising event, and do not negate an earlier diagenetic, or even syngenetic emplacement for the mineralisation.

Robb and Boshoff (1993); Smalley (1998); McGowen et al. (2006); Sillitoe et al. (2010) and Maiden and Borg (2011) contest the syngenetic and diagenetic models in favour of a late stage introduction of metal-bearing fluids with no diagenetic component, as the CAB age constraints would suggest. As evidence for this Sillitoe et al. (2010) have shown that there is an overwhelming consistency between the sulfide mineral assemblages present in both the veins and disseminations for a given rock, which would imply that these formed at the same time. Robb and Boshoff (1993) recognised four main styles of mineralisation from the Lake Ngami deposit in Botswana, namely bedding plane disseminations and lamellae (quartz rich); foliation oriented disseminations, rare breccia fillings and cross-cutting or bedding-parallel,

quartz-calcite rich veins. Through a detailed petrographic study these authors concluded that these mineralisation styles could all be attributed to syntectonic-epigenetic processes possibly associated with metamorphism rather than remobilisation or post-tectonic emplacement. Diagenetic/syngenetic processes may have been responsible for bedding parallel sulfides, but the textural characteristics of the sulfides strongly suggest a syntectonic timing for the mineralisation.

The distinctions between the different contributing factors driving the formation of SSC deposits are summarised in Figure 2-3. For a given deposit, several drivers may be important, whereas for others only one or two will be relevant. Untangling these factors is an ongoing challenge for scientists attempting to understand these deposit types.

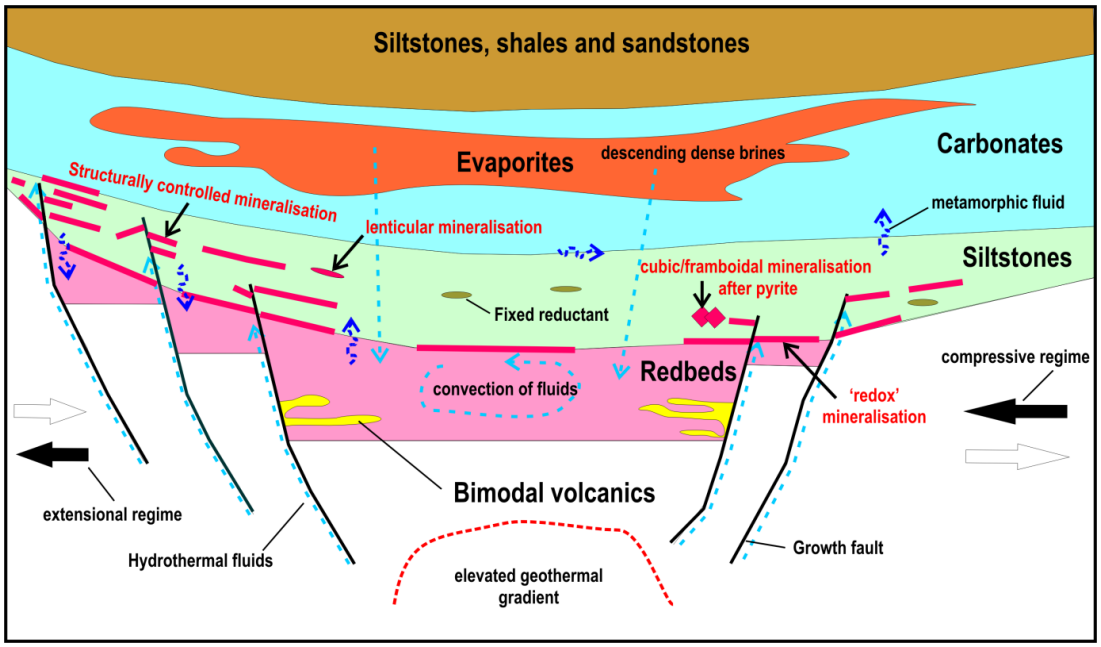

Figure 2-3: Typical rift-basin sedimentary sequence which hosts SSC deposits. Evaporite dissolution by diagenetic fluids provides the basinal brines necessary to scavenge and transport metals from the redbed sediments and/or bimodal volcanics (source rocks). Alternatively, fluids are generated through metamorphism, or have a magmatic component, or are possibly a combination of fluids. Growth-faults, bedding planes and brittle fractures in the rocks provide fluid conduits. Metals are scavenged from the source rocks, either from volcanics or redbeds. Convection can be generated by thermal or chemical gradients, or by the loss of pressure due to erosion or fracturing, causing fluids to rapidly ascend and forcing them to interact with reduced sediments/fluids. This is most pronounced at basin edges, where sedimentary units are thinner, or along the edges of basement highs. Precipitation of metal sulfides is initiated by the interaction of the oxidised metal-charged fluid with either a reduced fluid or fixed reductant. Modified after Hitzman et al. (2010).

2.2 Regional Geological Setting: The Kalahari Copperbelt

The Ghanzi Chobe Belt (GCB) is an elongate NE trending ridge zone (~100km wide) of deformed volcano-sedimentary rocks which extends across Botswana from the Goha and Shinamba Hills in the NE to Mamuno in the SW, near the Namibian border, and forms part of the Pan African Mobile Belt (Figure 2-4) (Borg and Maiden, 1989; Maiden and Borg, 2011; Modie, 1996; Schwartz et al., 1995). The GCB forms part of a larger system referred to as the Kalahari Copperbelt (KCB) which extends from the southern Namibia to northeastern Botswana. This belt follows the northern and western edges of the Kaapvaal (Kalahari) Craton, along the southern margin of the Pan-African Damara Orogenic Belt (Borg, 1988a; Miller, 2008; Modie, 2000). The KCB incorporates a series of deposits which share similarities in age, lithology and structure. Included in the KCB are the Sinclair, Klein Aub, Dordabis and Witvlei deposits in Namibia, as well as the Lake Ngami, Boseto, Goha Hills and Shinamba Hills deposits in Botswana. The KCB follows a regional rift system identified by Borg (1988a) as the Khoras-Sinclair-Ghanzi (KSG) Rift (insert: Figure 2-4).

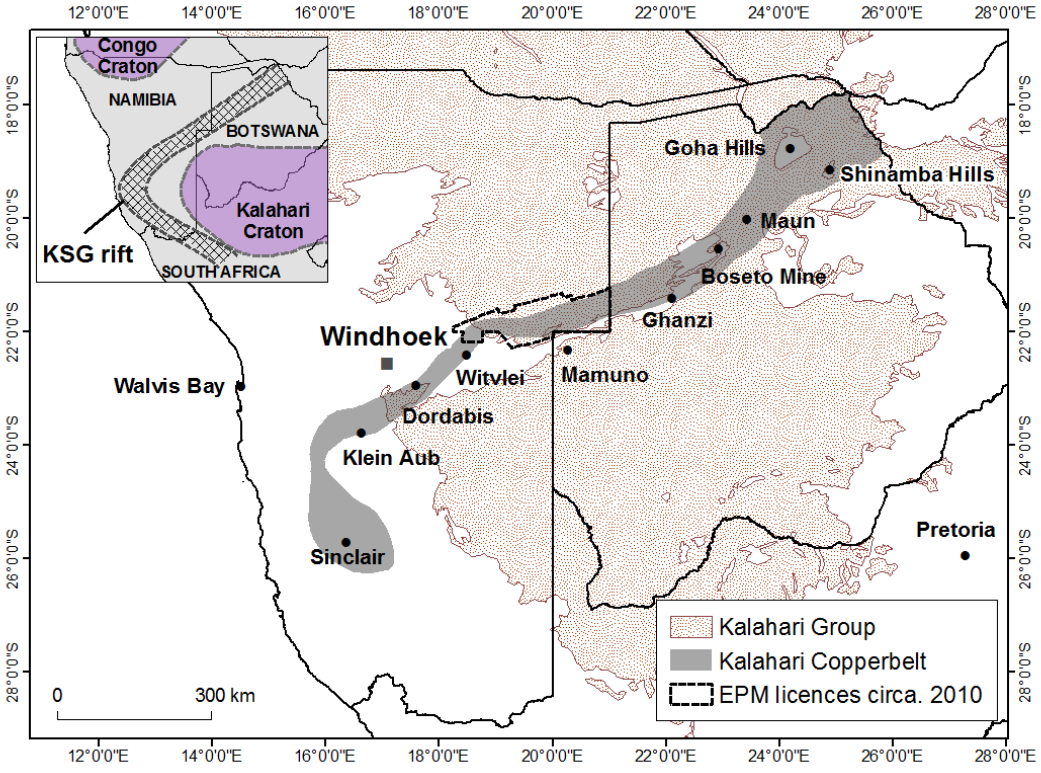

Figure 2-4: The Kalahari Group surficial sands, calcretes and silcretes cover extends over large swathes of southern Africa, including Namibia and Botswana. The study area lies within beneath this cover, along the KCB. The KCB is developed along the Khoras-Sinclair-Ghanzi rift between the Kalahari and Congo cratons (insert) after Borg (1988a).

The stratigraphy of the Sinclair Supergroup is presented Table 1, and the correlations between the laterally equivalent Namibian and Botswanan basins are presented in Figure 2-5 (Borg, 1988a; Hutchins and Reeves, 1980; Meixner and Peart, 1984). In Namibia the Klein Aub –

Doornpoort – Eskadron Formations have been correlated with the Ngwako Pan and D'Kar Formations of the Ghanzi Group (also possibly the Kuke Formation). The Kgwebe Formation of Botswana is correlated with the Nückopf Formation in Namibia, and also to the Oorlogsende Member, an isolated unit in the eastern Rehoboth Region (Borg, 1988a; Borg, 1988b; Borg and Maiden, 1989; Kampunzu et al., 1998; Miller, 2008).

Table 1: Stratigraphic subdivisions after Miller (2008) for the Sinclair Supergroup and the lower Damara Sequence in the Eiseb area. Dashed lines represent unconformities. * Includes the Oorlogsende Member as this is a lateral correlative of the Langberg Formation.

DAMARA SEQUENCE	NOSIB GROUP	DURUCHAUS FORMATION
		KAMTAS FORMATION
SINCLAIR SUPERGROUP	TSUMIS GROUP	KLEIN AUB FORMATION
		DOORNPOORT/ESKADRON FORMATION
	NAUZERUS GROUP	SKUMOK FORMATION
		OPDAM FORMATION
		LANGBERG FORMATION *
		GRAUWATER FORMATION
		NŰCKOPF FORMATION

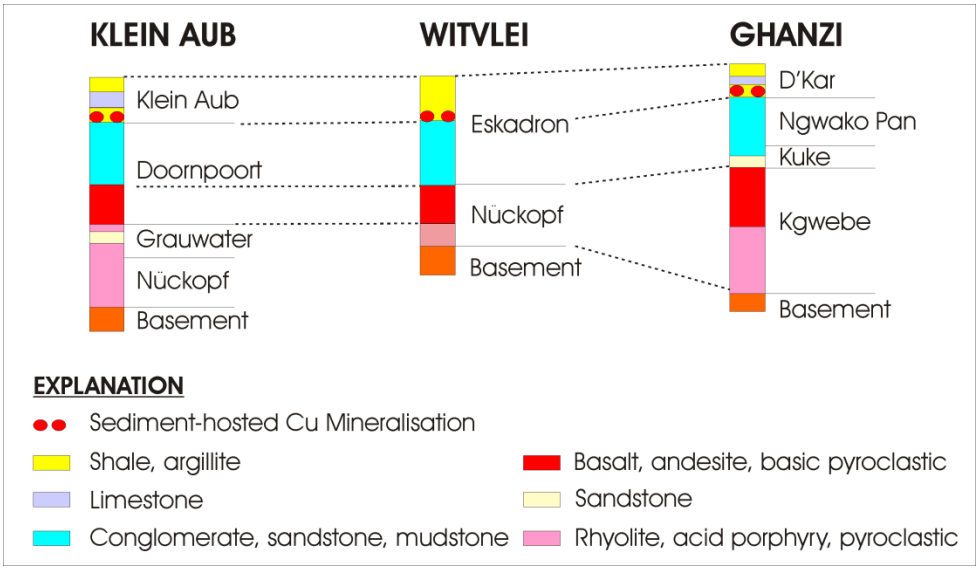

Figure 2-5: Stratigraphic correlation of the Eiseb deposits with the stratigraphy from Ghanzi, Klein Aub and Witvlei (**bold**). The logs show Formation names i.e. Doorpoort Formation, Eskadron Formation etc. The dashed lines show correlations after Borg (1988a).

The geological logs illustrated in Figure 2-5 can broadly be summarised as rhyolites, acid porphyries and pyroclastics overlain by a sequence of basalts, andesite and basic pyroclastics overlain by sedimentary sequence of red to pink-brown conglomerate, sandstone and mudstone. Interbeds of the sedimentary rocks between the volcanic units are not uncommon. The basal mafic and felsic sequences are refered to herein *senso lato* as 'basement' although they are not true basement *senso stricto*. The coarse package of continental clastics is overlain by reducing marine and/or lacustrine sediments such as siltstone, argillite and in some instances, carbonates. These sediments are typically green to grey. Mineralisation is generally hosted in these finer-grained units proximal to the contact with the underlying coarser sediments (Borg, 1988a; Borg and Maiden, 1989; Kampunzu et al., 1998; Meixner and Peart, 1984; Modie, 2000, 1996).

In Botswana the Kgwebe Formation bimodal volcanics form the basement sequence to the GCB basins, and have been dated as Late Mesoproterozoic ~1106 ± 2 Ma (Schwartz et al., 1996). Unconformably overlying the Kgwebe Formation are the various siliciclastic, argillaceous and carbonate rocks, known as the Ghanzi Group (Table 2). The age of this Group has been constrained between *c.* 530 Ma and ~1020 Ma (Ahrendt et al., 1978; Mapeo et al., 2000). As the Eiseb deposits are considered to form the western extension of the GCB into Namibia, the nomenclature of the Ghanzi Group will be used herein to describe the Eiseb geology.

Table 2: Generalised lithostratigraphy and interpretation of the sedimentary depositional environments (modified after Modie, 1996).

AGE		UNIT	DESCRIPTION	DEPOSITIONAL ENVIRONMENT
LATE	GHANZI GROUP	Unconformity **MAMUNO FORMATION** **~1,500m**	Interbedded sandstone, siltstones, shales and occasional limestone	Nearshore to shoreline environment, passive margin sedimentation
NEO-PROTEROZOIC		**D'KAR FORMATION** **~1,500 - 2,500m** **Cu-Ag mineralisation**	Interbedded quartzite and argillite layers. Quartzite units pinkish-brown fining-upward. Argillites are greenish and fine grained with a strongly developed foliation	Enlargement of basin and major marine transgression. Deposition of sediments in a shallow shelf environment
		NGWAKO PAN FORMATION **0 - 3,500m**	Quartzite units grey to pink. Interbedded siltstone and mudstone	Extensional faulting and initial deposition of sediments in the basin. Alluvial fan to lacustrine depositional environment
EARLY		**KUKE FORMATION** **500m**	Basal conglomerate overlain by grey quartz-arenites and red sandstone	Channelised flow fluvial to beach sub-environment
LATE MESO-PROTEROZOIC		Unconformity **KGWEBE FORMATION** **0 - 2,500m**	Rhyolite, acid porphyry and pyroclastic deposits interlayered with basic volcanics	Bimodal volcanism with occasional periods of sedimentation. Lacustrine to fluvial to beach depositional environments

2.2.1 Tectonic Setting

The volcano-sedimentary sequences of the Eiseb deposits occur within the elongate Late Mesoproterozoic KCB, which extends from Sinclair in southern Namibia, to the Goha and Shinamba Hills in NE Botswana, along the KSG Rift system (Figure 2-4) (Borg, 1988a). The location of this rift, between the Kaapvaal and Congo cratons, suggests a link to an older suture produced during continental assembly. The Sinclair-Ghanzi system is characterised by a series of block faulted troughs or grabens. During early rifting and extension, bimodal volcanics (Kgwebe Formation), as well as some clastics, were the primary basin fill (Phase A) (Figure 2-6). In the Klein Aub area, and possibly elsewhere along the Belt, this block faulting produced major basement highs which focussed the movement of both the extrusive and intrusive magmatic pulses (Borg, 1988a; Borg, 1988b; Borg and Maiden, 1989). As denudation of the rift flanks and basement high(s) progressed clastic sedimentary contributions dominated these basins (Ghanzi Group, Phase B).

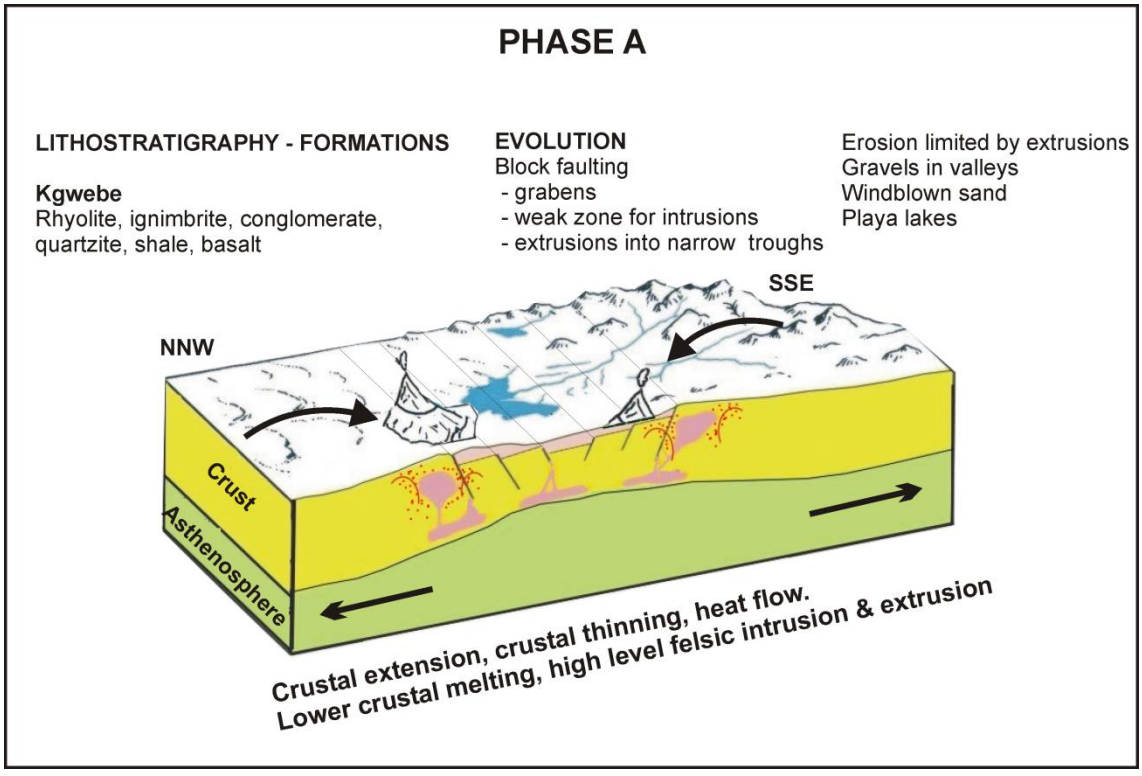

Figure 2-6: Phases A of the evolution of the basin which hosts the Eiseb deposits. Figure modified after Borg (1988a) in Veldsman et al. (2010).

Block faulting eased off at this stage but regional uplift encouraged laterally extensive deposition of coarse clastics across these basins (Phase B) (Figure 2-7) (Borg, 1988a, Borg, 1988b; Borg and Maiden, 1986; Modie, 1996).

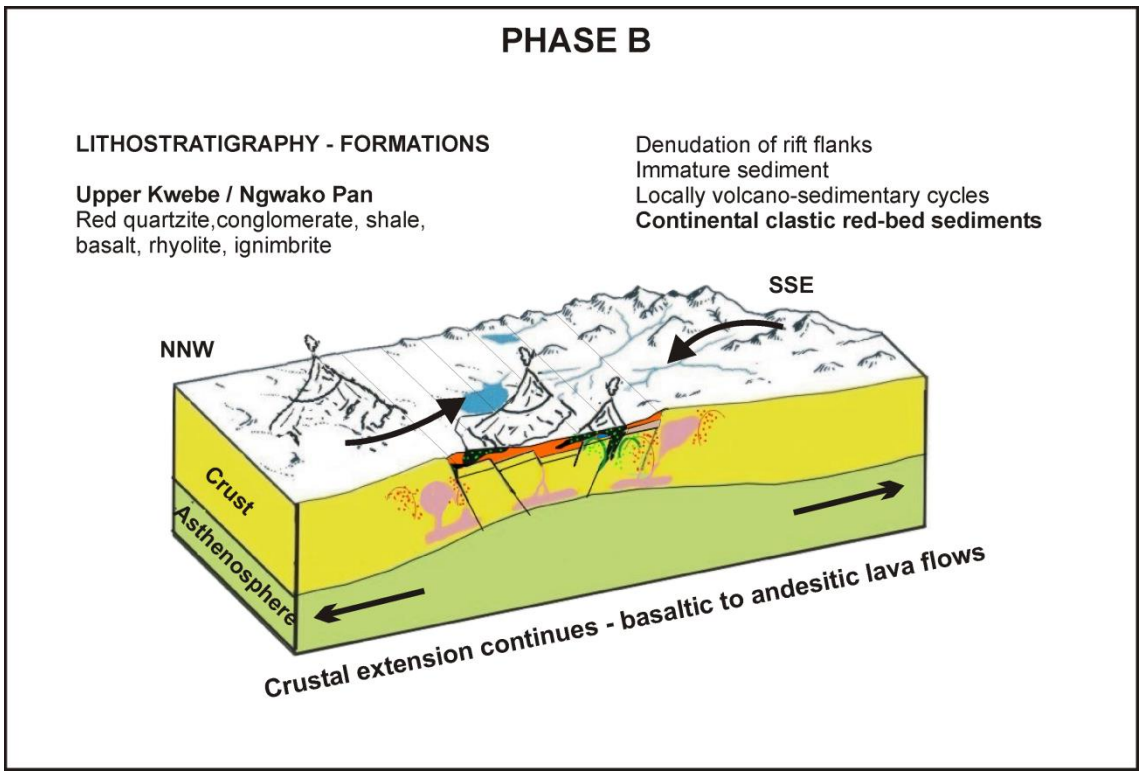

Figure 2-7: Phases B of the evolution of the basin which hosts the Eiseb deposits. Figure modified after Borg (1988a) in Veldsman et al. (2010).

During Phase C, the 'sag' (thermal subsidence) phase of this rift system, marine transgression was initiated and resulted in the deposition of carbonate sequences, and later, as aridification progressed, of lacustrine sediments (Figure 2-8) (Borg, 1988a, Borg, 1988b; Borg and Maiden, 1989). Synsedimentary faults had a strong influence on sedimentary facies distributions throughout rift evolution, which spanned from ~1200 to 950 Ma.

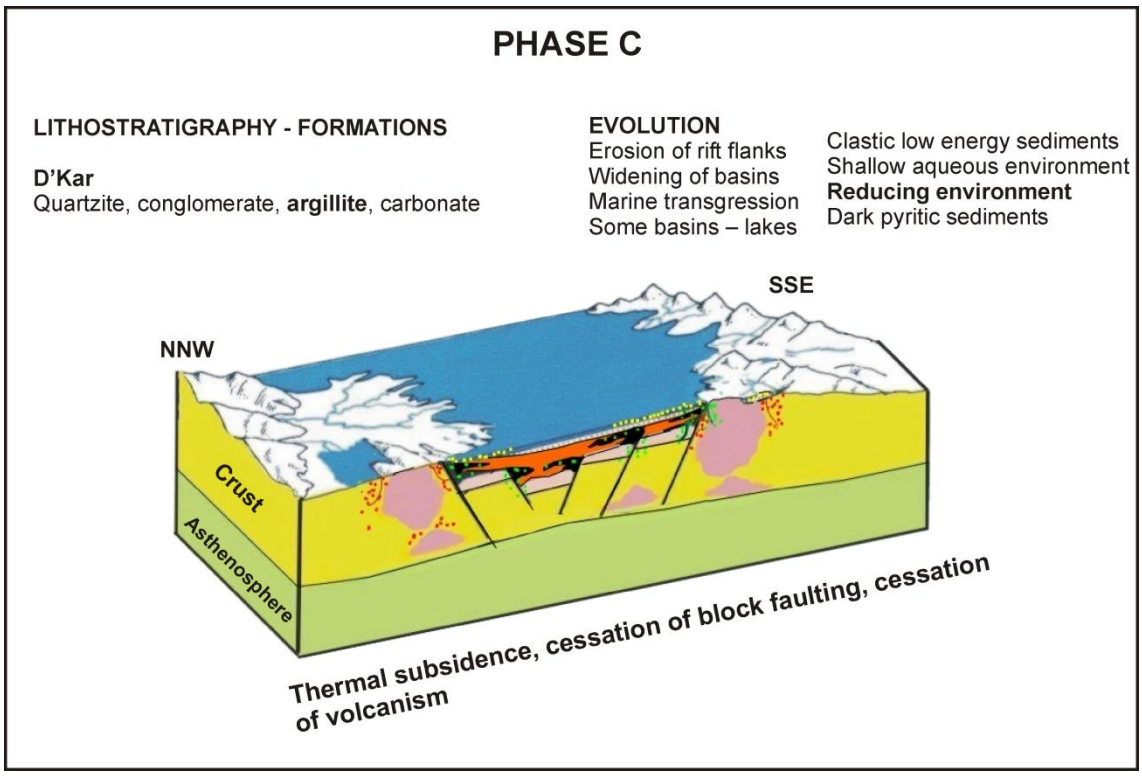

Figure 2-8: Phase C of the development of the basin which hosts the Eiseb deposits was characterised by thermal subsidence and marine transgression. Figure modified after Borg (1988a) in Veldsman et al. (2010).

Early Damara rifting thought to have started around 750 Ma to the north of, but parallel to, the KCB's northern margin (Figure 2-9) (Miller, 2008). There is no evidence of a prominent compressional phase marking the transition between these two rifting events, a situation which prompted Borg (1988a) to suggest plate migration over a stationary mantle plume thermally initiating rifting from Khoras to Sinclair to Ghanzi, and then the Damara rift. Borg (1988a) was also misled by poor Rb-Sr data which suggested a younging of the rocks towards the north-east. This highlights one of the key points of debate in the literature, prior to Damara rifting: What initiated the KSG rift? The main models are an intracontinental or anorogenic setting and that rifting occurred along an active continental margin/collision zone (orogenic model). Borg (1988a) was in favour of the former, while others, such as Watters (1977), favoured the latter. Through geochemical analyses Kampunzu et al. (1998) were able to show that the Kgwebe (and therefore the Nauzerus Group) bimodal suite was produced as a result of extensional collapse linked to the Kibaran collision along the Namaqua-Natal Belt in southern Namibia/South Africa. Authors such as Becker et al. (2005) and Becker (2008) interpret the volcanics of the KSG as the result of a magmatic arc.

Regardless of the initial causes of rifting, by the end of the Precambrian when the Pan African Damaran-Lufilian Orogeny began, rifting had not progressed to the stage of sea-floor

spreading. The Sinclair-Ghanzi system can therefore be considered as a failed (most likely intracratonic) rift system (Modie, 1996).

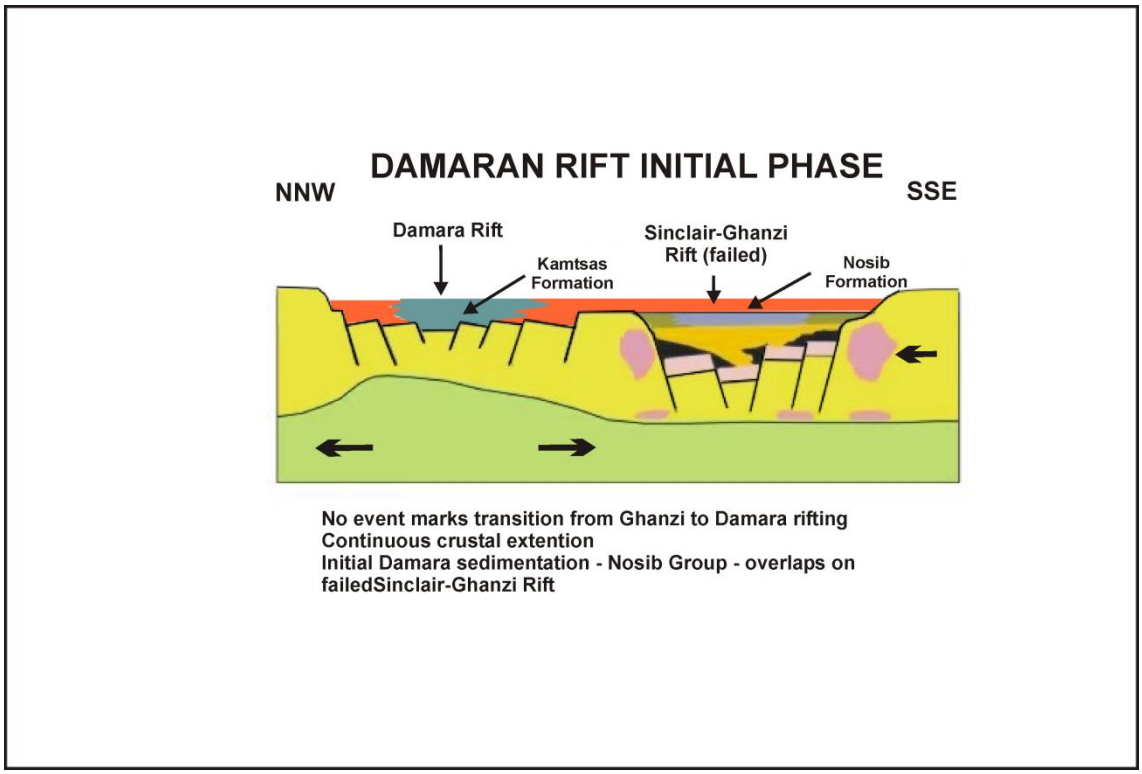

Figure 2-9: The termination of rifting along the (Koras-) Sinclair-Ghanzi rift and the initiation of Damaran rifting further north occurred around 750 Ma (Miller, 2008). . Figure modified after Borg (1988a) in Veldsman et al. (2010).

The assembly of the Gondwana supercontinent during the Pan African initiated the Damara Orogeny, which peaked at ~530 Ma (Figure 2-10) (e.g. Miller, 1983; Porada and Berhorst, 2000). On a local scale the Damara Orogen reactivated basin faults and caused the propagation of reverse, strike-slip and thrust faulting throughout the Damara and KSG Rift basins (Borg, 1988a, Borg, 1988b). On a regional scale the effects of the Damara Orogen were widespread, with the reactivation of regional scale thrusts or lineaments subdividing Namibia into tectono-stratigraphic domains, namely the Southern Margin Zone, Southern Zone, Southern Central Zone, Southern Foreland, Northern Central Zone, Northern Zone, Northern Margin Zone and the Koako Zone (Corner, 2000). The basin which hosts the Eiseb deposits is wedged between the frontal thrust along the south of the SMZ and the Southern (Nama) Foreland (Figure 2-11).

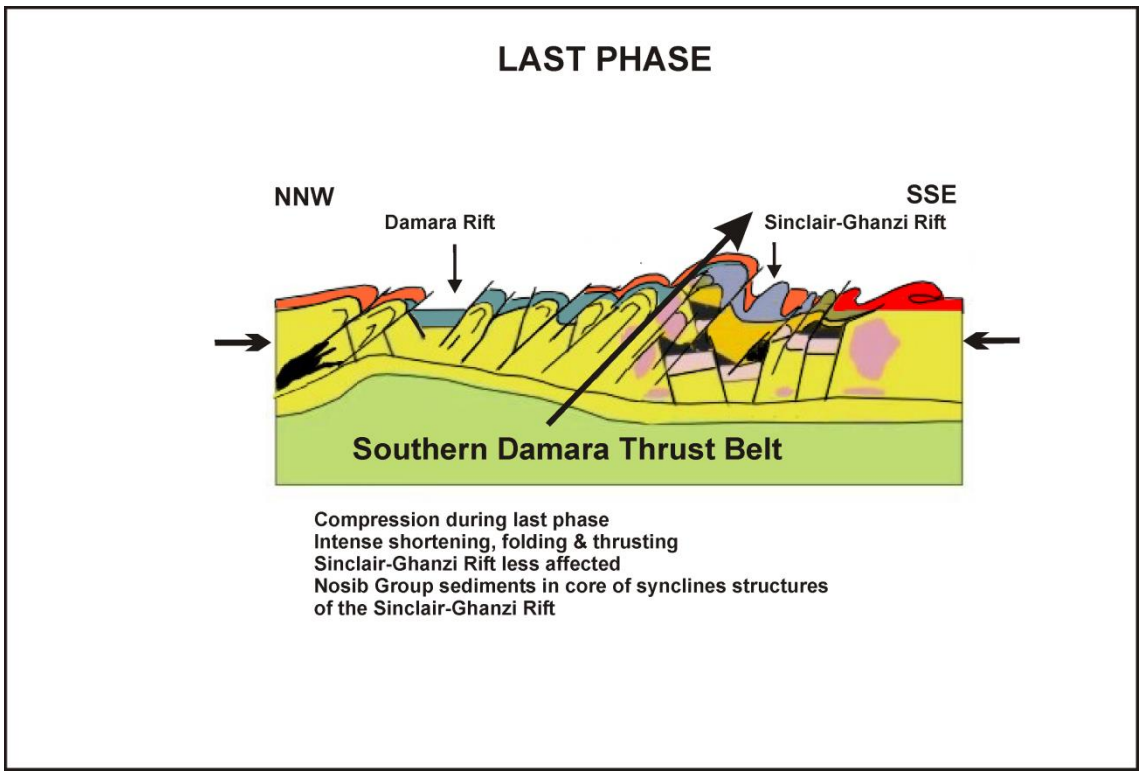

Figure 2-10: The termination of rifting along the (Koras-) Sinclair-Ghanzi rift was followed by the Damara Orogeny which peaked ~530 Ma (Ahrendt et al., 1978). Figure modified after Borg (1988a) in Veldsman et al. (2010).

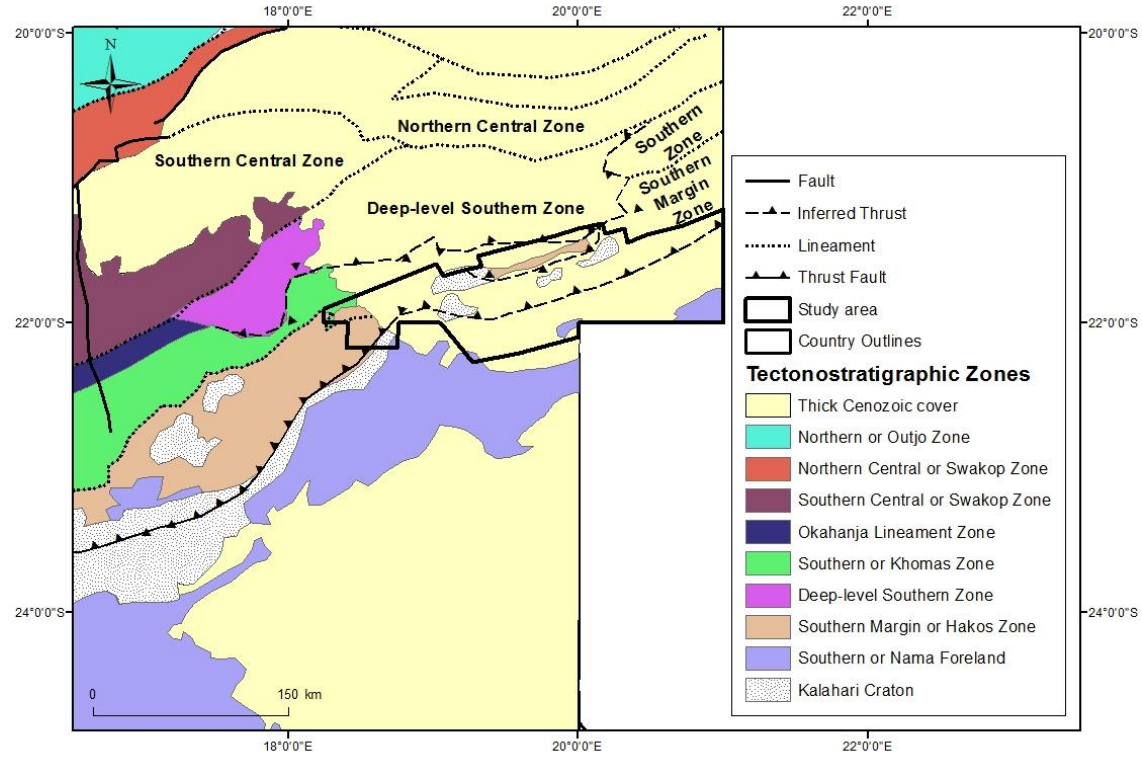

Figure 2-11: Regional tectono-stratigraphic domains of Namibia after Corner (2000) as reported in Miller (2008).

The Damaran Orogeny lasted from roughly 560 to 530 Ma and affected the rocks of the Sinclair-Ghanzi Rift less than those of the Damaran Rift where the rocks show intense shortening (>50%), folding and thrusting (Borg, 1988a; Frimmel et al., 2011; John et al., 2004). Southeastward directed compression along the Sinclair-Ghanzi Rift produced upright isoclinal to angular folds and associated thrusts which have axes striking northeast-southwest to east-west (Modie, 1996; Schwartz et al., 1996, 1995). These rocks underwent greenschist facies metamorphism, and hydrothermal events associated with this deformation have been dated between 507 and 649 Ma (Ahrendt et al., 1978; Schwartz et al., 1995). Lower greenschist facies metamorphism is dated at ~530 Ma ± 10 Ma, with temperatures reaching ~350˚C producing muscovite, biotite, chlorite, actinolite, clinozoizite, zoisite, calcite and rutile (Ahrendt et al., 1978; Schwartz et al., 1996). As with other SSC deposits, mineralisation within the KCB has been linked to early diagenesis, synorogenic and late orogenic emplacement mechanisms. The main deposits in the region of Lake Ngami and Klein Aub have been reviewed extensively in the literature and will herein be used to summarise the main styles and models for SSC-style mineralisation along the KCB.

2.2.2 Cu-Ag Mineralisation

The Cu-Ag mineralisation associated with the KCB is largely hosted by chemically-reduced, transgressive marine fine-grained argillitic sediments of the D'Kar Formation (and its Namibian equivalents) as either disseminations, or as cleavage/fracture/vein-hosted. Mineralisation is usually associated with the contact between the reduced facies and underlying coarse-grained, oxidised continental clastic sediments of the Ngwako Pan Formation, along a redox interface (Modie, 2000, 1996). Vein and fracture-hosted mineralisation, however, can be transgressive and discordant to lithological boundaries. Occurrences of copper sulfides within the basaltic flow breccias of the Kwebe Formation have been recorded, but are rare. Although intermittently developed, mineralisation along the belt is characterised by extensive strike lengths measuring tens of km (eg: Borg, 1988a; Borg and Maiden, 1986, 1989; Maiden and Borg, 2011; Modie, 1996, 2000; Schwartz et al., 1995, 1996).

In the Ngwako Pan deposits of the Lake Ngami area (Zeta and Plutus Deposits) the mineralisation is characterised by copper-silver sulfides, minor Pb and Zn sulfides, and secondary copper minerals (malachite, azurite and chrysocolla) (Figure 2-12) (Hall, 2013).

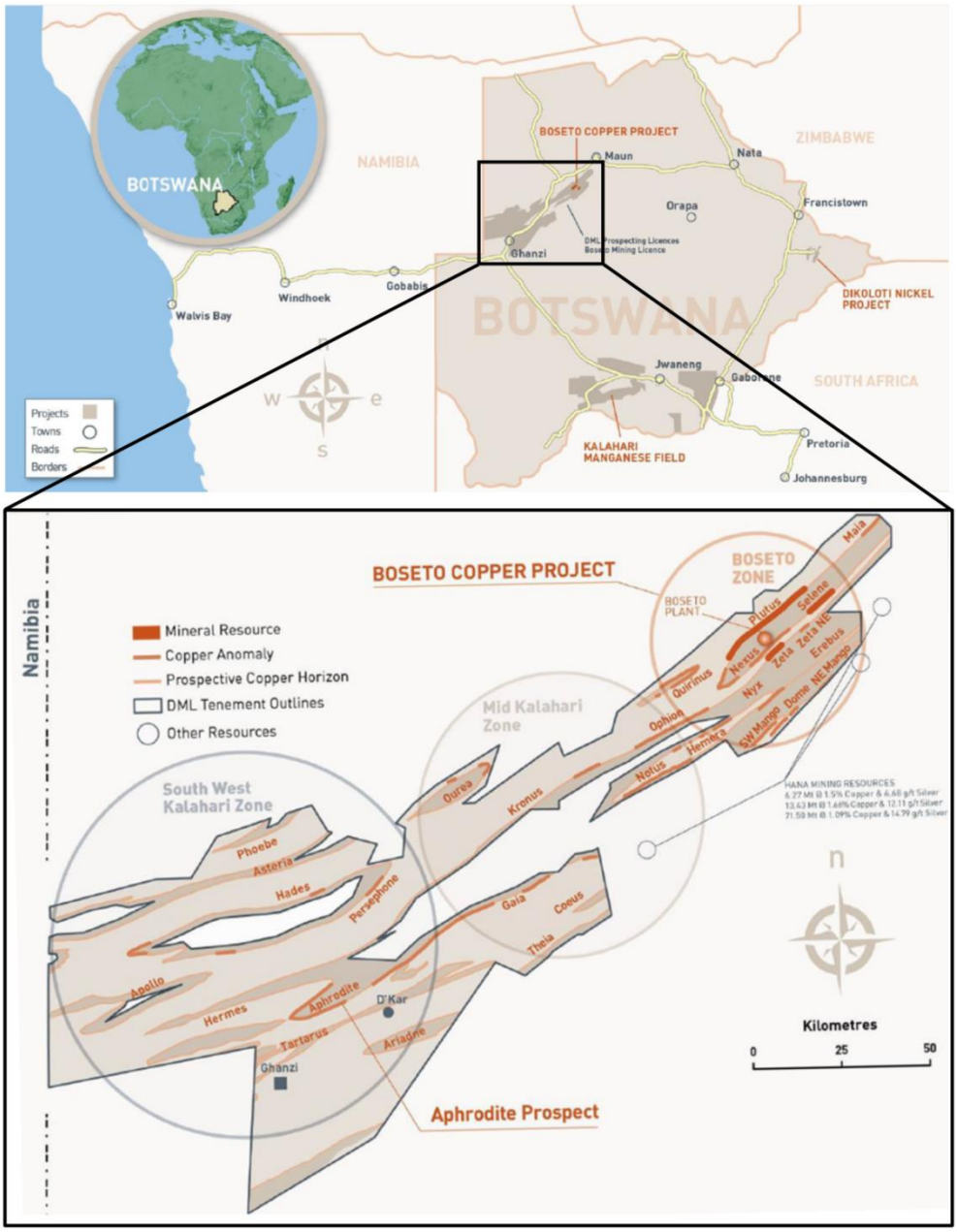

Figure 2-12: Location of the Boseto Copper Project, Discovery Metals (Pty) Ltd. The Plutus and Zeta deposits are in the Boseto Zone. Maps taken from the Discovery Metals website (2015).

Mineralisation appears superficially laterally extensive, but is irregularly developed, focussing on the contact between reduced and oxidised facies of the lower D'Kar Formation (Figure 2-13). The main sulfide minerals are chalcocite, hematite, bornite, chalcopyrite, pyrite, digenite and minor sphalerite and galena. Mineralised intersections can contain up to 2% Cu and reach thicknesses of 20m (Modie, 2000). Borg and Maiden (1989) refer to the Zeta deposit as showing vertical zonation from a lower chalcocite-hematite zone to an upper bornite-chalcopyrite-sphalerite zone. Coarse-grained barite (up to 7000ppm) is commonly associated with mineralisation at Zeta.

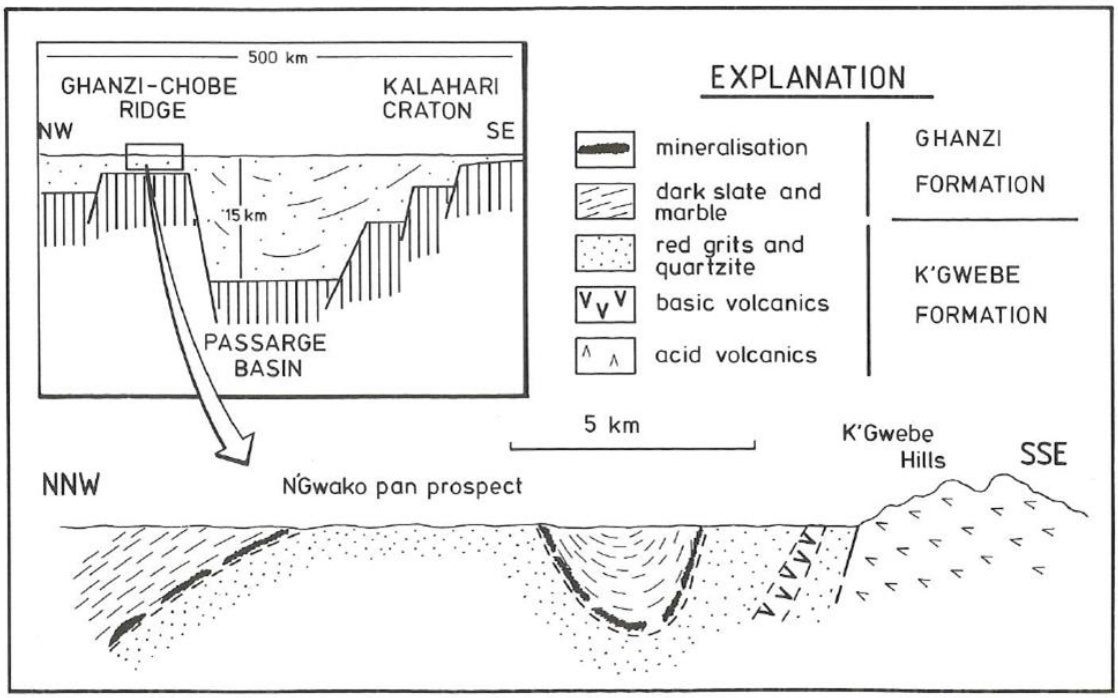

Figure 2-13: Geological cross-section through the Lake N'gami area Ngwako Pan deposits of Botswana showing its relationship to the Ghanzi-Chobe Ridge (insert). Figure taken from Borg and Maiden (1989).

Hall (2013) describes mineralisation from the Zeta deposit in the Boseto Mine area, as being both (stratiform) disseminated, and vein/shear-band-hosted (Figure 2-14 & Figure 2-15).

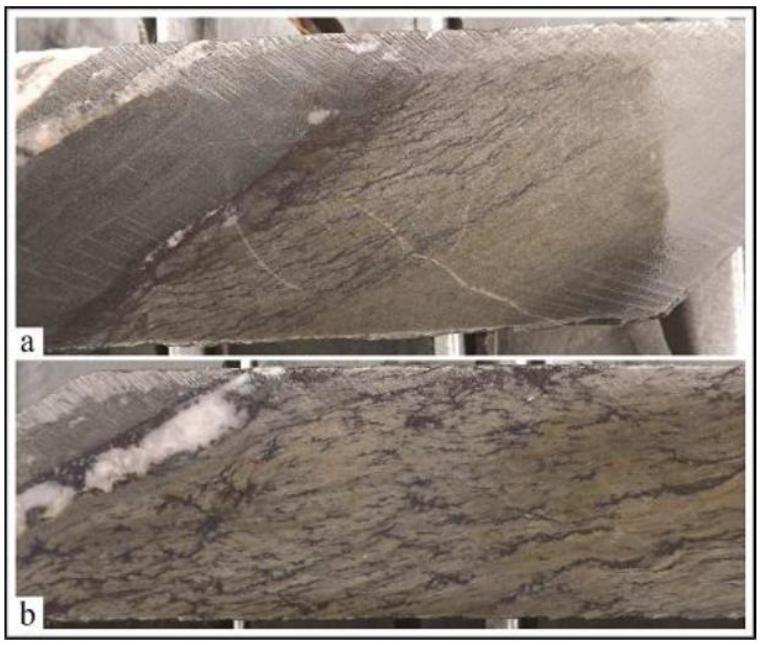

Figure 2-14: Bornite mineralised foliation fabric, Zeta Deposit. **a**: Layer-parallel bornite adjacent to bornite-bearing quartz-calcite vein, hosted within green, reduced sediments. Borehole GDRD1143, 230.5m; **b**: Zoomed view of 'a'. Borehole GDRD1109, 202m. Photographs taken from Hall (2013).

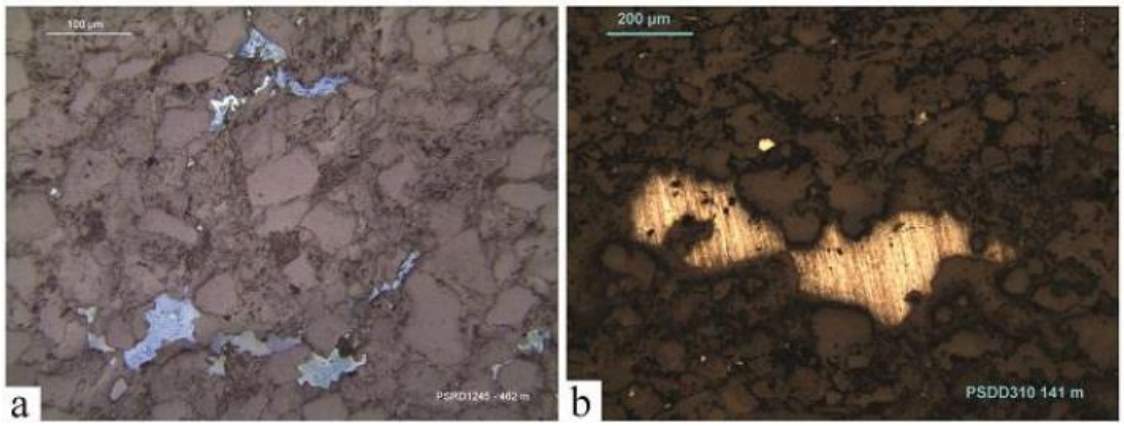

Figure 2-15: Disseminated sulfide minerals, Plutus deposit. **a)**: reflected light microphotograph of irregular bornite partially replaced by supergene covellite. Borehole PSRD1254, 462m; **b)**: Reflected light microphotograph of chalcopyrite. Borhole PSDD310, 141m. Microphotographs taken from Hall (2013).

Hall (2013) interpreted mineral textures in the Zeta deposit as suggestive of copper sulfides replacing authigenic mineral cements and diagenetic pyrite, favouring an early diagenetic mineralising event. Re-Os model ages for the disseminated mineralisation at Zeta however, are bracketed between 914 and 1106 Ma, ages roughly coincident with the formation of the rift basin, suggesting this data is to be viewed with caution. Re-Os dating of the Plutus deposit suggests a much younger age for the vein-hosted mineralisation at 459 ± 37 Ma, which would only just tie it into the last phases of the Damara Orogeny. Hall (2013) argues that the precipitation of mineralisation was driven by episodic changes in pressure linked to layer-parallel shearing, arguing for a recrystallization and reprecipitation of the earlier sulfides producing the economic grades currently mined. The highest concentrations of copper and silver in these deposits are within the chalcocite-hematite cements of tectonically brecciated slates, lending support to a late/syn-tectonic emplacement of the mineralisation.

In the Klein Aub area chalcocite is the dominant ore mineral and occurs primarily within dark green-grey laminated slates interbedded with pyritic quartzites and rarely, marble. The mineralisation at Klein Aub has an association with hematite, and contains localised occurrences of native copper and silver. Although similar in style to the Lake Ngami deposit, i.e. mineralisation occurs as disseminations, cleavage-parallel lenticles, and as brittle fracture fillings, the Klein Aub deposit shows strong genetic links to late tectonic wrench faulting (Figure 2-16)(Borg et al., 1987a). Borg et al. (1987b) found that the deposits at Klein Aub, in addition to Cu-Ag, also contained anomalous concnetrations of PGE's and Au.

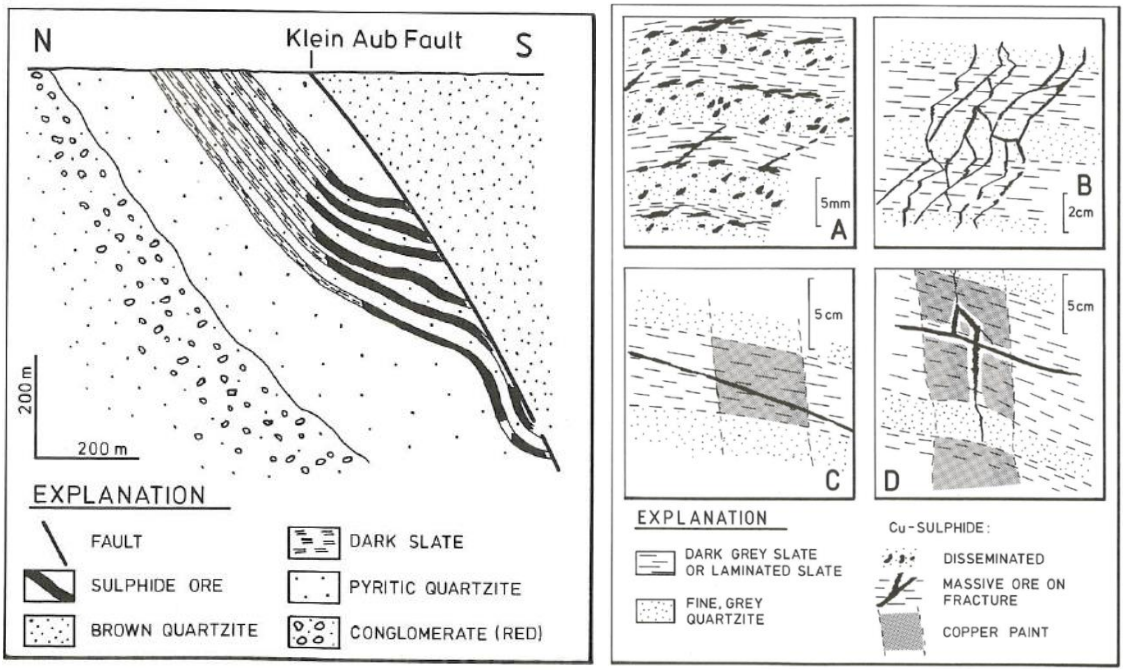

Figure 2-16: Simplified cross-section of the Klein-Aub orebodies (LEFT) and the main mineralisation styles recorded in the deposit (RIGHT). A: Disseminated; B: brittle fracture and cleavage-hosted; C: Disseminated in laminated slate and massive ore along a (organic-rich) slickenside; and D: Relationship between disseminated and brittle fracture-hosted mineralisation. Figure taken from Borg and Maiden (1989).

Textural evidence from this deposit shows that Cu-Ag mineralisation, particularly disseminations, occur within marginally coarser laminae in slates, but in quartzites these minerals commonly occur as nodular to lenticular aggregates. Within such quartz beds, proximal to the main ore horizons, chalcocite appears to pseudomorph diagenetic pyrite (Borg, 1988a; Borg and Maiden, 1989). Borg (1988a) has demonstrated that chalcocite mineralization at Klein Aub post-dates deformation since diagenetic pyrite cubes have been replaced by chalcocite without the soft and ductile chalcocite being deformed but retaining their cubic (pyrite) shapes.

Borg and Maiden (1989) summarise the main controls on mineralisation within the belt as:

- **oxidation-reduction interfaces:** whether considering regional or local scales, are encountered proximal to mineralisation throughout the belt;
- **permeability:** mineralisation seems to favour areas with enhanced permeability. This includes sandy/silty laminae within finer units, and zones were structural features produce permeability, such as brittle fractures, tectonic breccias, and slate cleavage;
- **paleotopography:** basement highs are spatially associated with mineralisation on a regional scale in both the Klein Aub and Lake Ngami area;
- **structure:** structurally induced permeability is one aspect of structure contributing to mineralisation, by creating pathways for metal-charged fluids, but another is related to the creation of basement highs. Evidence suggests that basement highs were horst

blocks actively rising during sedimentation. Synsedimentary block faulting, and the later reactivation of these faults during Damara deformation, likely played an important role in tapping into deep, hot mineralising fluids. Thinning and pinching out (onlap) of sediments along these highs also contributes to focussing fluid flow.

These controls remain valid whether a multi-stage or single stage mineralising event is favoured because any model presented would have to account for the different styles of mineralisation observed on both a local and regional scale along the belt and account for the laterally extensive nature of these deposits. However, determining the dominant controls for a particular deposit will help to constrain the timing of mineralisation, which is critical for understanding the deposit genesis and for successful exploration in the region. An exploration program which targets sedimentary controls (stratiform), such as oxidation-reduction interfaces, or coarse laminae within reduced sediments (strata-bound), will miss mineralisation controlled by structures, and vice versa.

Maiden and Borg (2011) have suggested that stratiform mineralisation in the KCB may represent the selective replacement of reactive mineral laminae such as precursor sulfides, carbonates or feldspars. There is also no evidence of these disseminated/laminar mineralised zones remobilising to form structurally-hosted ore zones in fractures and breccia. Sillitoe et al. (2010) have shown that there was no discernible mineralogical or geochemical difference between disseminated and structurally-hosted ore minerals. This suggests that these styles were contemporaneous, and late in the history of these basins. Both Sillitoe et al. (2010) and Maiden and Borg (2011) emphasise the importance of expanding exploration and mineralisation models away from traditional definitions of SSC deposits.

Constraining the timing of mineralisation is critical to defining both geological and exploration models for the KCB. One way in which this can be done is to understand the mineral assemblages associated with the Cu-Ag mineralisation. For the Eiseb deposits magnetite appears to have an association with the mineralisation. In the following section the significance of magnetite as a petrogenetic indicator will be discussed.

2.3 Magnetite

Magnetite (Fe_3O_4) is the most commonly occurring magnetic mineral in nature, occurring in almost every rock type. It forms and accumulates in a wide range of ore-forming environments including:

- banded iron formations (BIF) (e.g. Thompson Ni-Belt, Canada);
- Ag-Pb-Zn veins (e.g. Coeur d'Arlene, USA);
- porphyry Cu-(Au)-(Mo) deposits (e.g. Morococha, Peru);
- skarn deposits (calcic and magnesian) (e.g. Chino/Santa Rita, New Mexico);
- iron oxide Cu-Au deposits (IOCG) (e.g. Ernest Henry, Australia);
- Fe-Ti-V-P deposits hosted in mafic-ultramafic layered intrusions (e.g. Bushveld Complex, South Africa);
- Ni-Cu-platinum-group-elements (PGE) deposits (e.g. Sudbury, Canada);
- sediment-hosted stratiform Cu-Ag deposits (e.g. Spar Lake, USA);
- magnetite-apatite deposits (e.g. Kiruna, Sweden and Bafq, Iran)

Studies on magnetite have been numerous and varied. From an economic geology perspective, one of the core foci in recent years has been the development of methods to fingerprint magnetite from different magmatic and hydrothermal geological settings (Acosta-Góngora et al., 2014; Dare et al., 2014; Dupuis and Beaudoin, 2011; Nadoll et al., 2014, 2012). The magnetic properties of magnetite also produce distinct geophysical signatures, which in turn can be used to identify, delineate and characterise potential orebodies.

2.3.1 Magnetite Geochemistry

Magnetite is a spinel mineral with an inverse spinel structure and forms a natural solid solution with numerous spinel components, as depicted in Figure 2-17 (Waychunas, 1991). Its stoichiometry is generally in the form AB_2O_4 ($Fe^{2+}Fe_2^{3+}O_4$). Spinels are characterised by the presence of at least two cations, or one cation with at least two valencies in the ratio of 2:1. In the case of magnetite 'A' represents a divalent cation and 'B' a trivalent one, with the ferric (Fe^{3+}) iron occupying the tetrahedral sites and a mix of ferrous (Fe^{2+}) and ferric iron occupying the octahedral sites (Waychunas, 1991). Substitution of iron is common with ferric iron replaced by e.g. Al, V, Ga or Cr; and ferrous iron replaced by Mg, Mn, Zn, Co, or Ni for example.

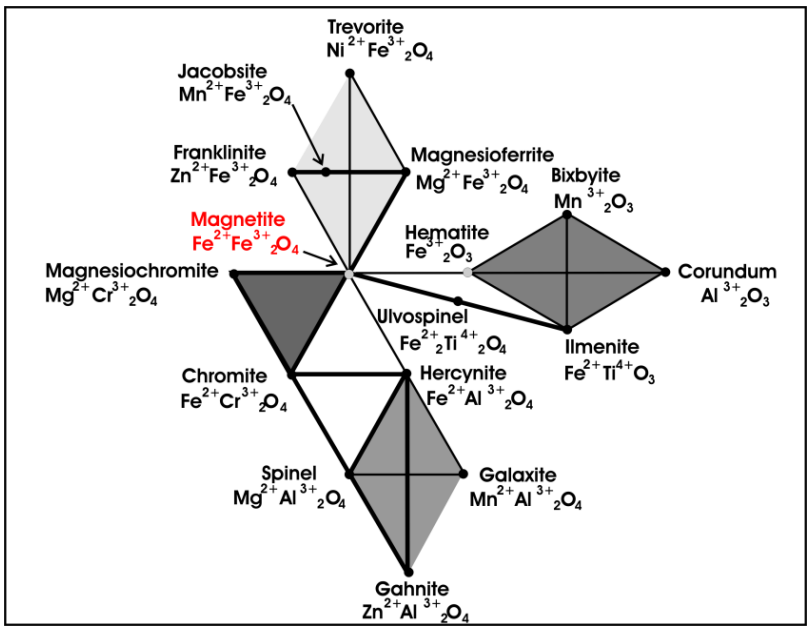

Figure 2-17: Schematic representation of the spinel group minerals. **Thick lines** illustrate minerals with a complete solid solution, and **thin lines** depict partial solid solutions. Figure redrawn from Dupuis and Beaudoin (2011).

In high temperature (>800˚C) silicate melts magnetite can fractionate out either as an accessory phase, or form concentrated segregations. Magnetite can also precipitate under low temperatures from hydrothermal fluids (<200˚C). Metamorphic magnetite is very homogenous, forming nearly pure Fe_3O_4. This is mostly due to re-equilibration on cooling, which also causes magnetite to expel Ti. In sedimentary rocks magnetite is usually introduced as a detrital mineral, or through metamorphic and/or hydrothermal processes (Deer et al., 1992; Frost, 1991a).

The partitioning of trace elements between magnetite precipitating from hydrothermal fluids is not well studied. Magnetite formation and the behaviour of trace elements in igneous systems is however, well documented (Frost, 1991b). It is thought that magnetite geochemistry in hydrothermal systems will be governed by the same controls as an igneous system, namely (Dare et al., 2014; Nadoll et al., 2014):

- oxygen and sulfur fugacity (fO_2 and fS_2respectively);
- silica activity;
- temperature;
- pressure;
- fluid/melt composition;
- cooling rate;
- host rock buffering (particularly for hydrothermal magnetite;
- re-equilibration processes;
- intrinsic crystallographic controls such as ionic radius and charge balance.

The effects of temperature and fO_2 are illustrated in Figure 2-18, and the influence of fO_2 and fS_2 on magnetite formation shown by schematic phase diagram for the Fe-O-S system in the same figure.

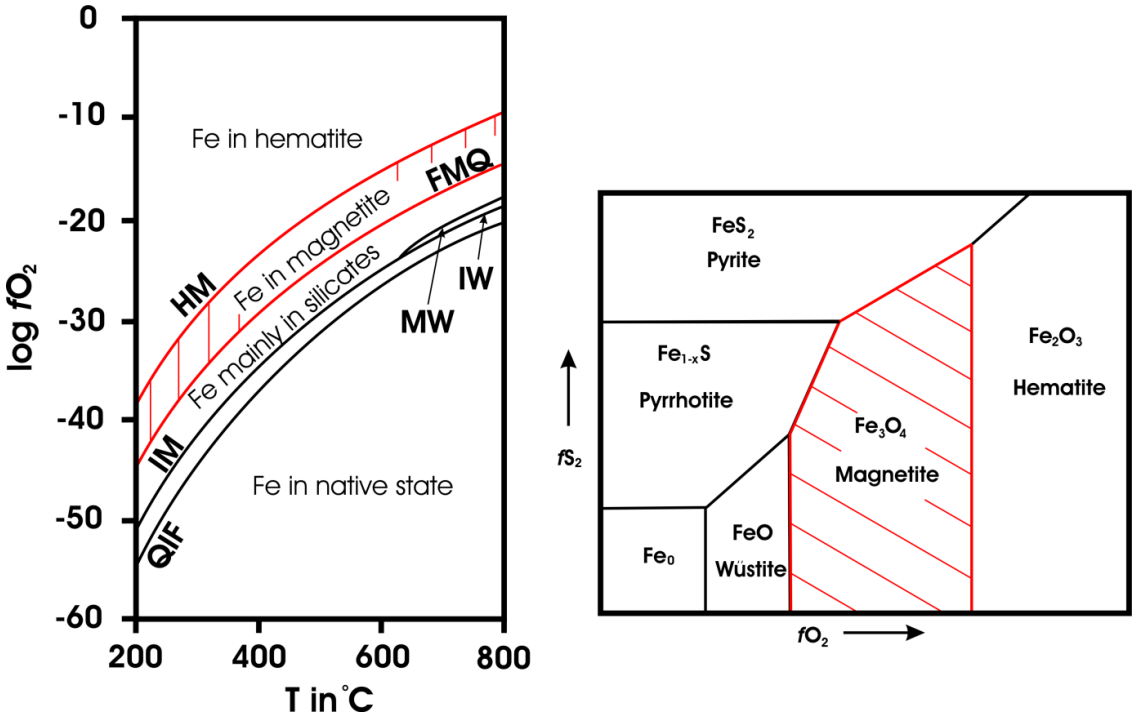

Figure 2-18: Log *f*O2-T diagram showing the Fe-Si-O system buffers (**LEFT**) - HM: hematite-magnetite; FMQ: fayalite-magnetite-quartz; MW: magnetite-wűstite; IW: iron- wűstite; QIF: quartz-iron-fayalite (redrawn after Frost (1991b) and Nadoll et al. (2014)). **RIGHT**: Schematic phase diagram for the Fe-O-S system in fO_2- fS_2 space (modified after Nadoll et al. (2014)).

Whether iron occurs as a metal (Fe_0), or in it's 3+ (ferric) or 2+ (ferrous) oxidation state is strongly influenced by oxygen fugacity and temperature. At very low fO_2 iron will be present in its native state, with increasing fugacity leading to both divalent and trivalent states of iron. Magnetite formation across a broad range of temperatures is limited by the iron-magnetite (IM) or magnetite-wűstite (MW) buffers which represent the minimum fO_2 at which magnetite is stable. Below the fayalite-magnetite-quartz (FMQ) buffer however, Fe is incorporated mostly into silicates.

$$2\ Fe_3O_4 + 3\ SiO_2 = 3\ Fe_2SiO_4 + O_2$$

magnetite quartz fayalite

The production of magnetite would consume free oxygen in the fluid/melt, producing a relative reduction, which, if the fluid contains very little oxygen, can dramatically change the

fO_2 without producing much magnetite (Frost, 1991a). The opposite is also true, in a system where magnetite is being consumed oxygen will be liberated, producing a relative oxidation of the fluid. More significant quantities of magnetite can be produced/consumed where buffer-type equilibria intersect the hematite-magnetite buffer (HM):

$$FeO + Fe_2O_3 = Fe_3O_4$$

in silicate hematite magnetite

Above this threshold Fe is incorporated into hematite and magnetite is no longer stable, driving the reaction to the left. The effects of sulfur activity on the formation of magnetite shown in Figure 2-15 remain valid over a range of temperature, with Fe favouring sulfides under low fO_2 as sulfur activity increases.

Numerous attempts have been made to use the distribution of trace elements within magnetite as a tool for determining the origin of the magnetite, particularly where magnetite is associated with ore deposits. Carew (2004) recognised that trace element patterns could be used to discriminate between barren and mineralised IOCG deposits. Singoyi et al. (2006) expanded this through a detailed review of the trace element geochemistry of magnetite in volcanogenic massive sulfides (VMS), skarn, iron-oxide copper gold (IOCG) and Broken-Hill type Pb-Zn deposits. In their study they determined that Sn/Ga vs. Al/Co plots could be used to discriminate between these deposit types.

Nadoll et al. (2012) used the Belt terrane deposits of the Proterozoic Belt Supergroup in the USA as a case study for investigating the distribution of the trace elements in magnetite. The Belt terrane was chosen for its wide range of deposits including, hydrothermal Ag-Pb-Zn veins, post metamorphic igneous intrusions, burial metamorphic rocks and sediment-hosted Cu-Ag deposits. Magnetite from across this terrane showed only very subtle differences in trace element concentrations. These were deciphered using a statistical approach which enhances these subtle differences, using principal component (factor) analysis.

Dupuis and Beaudoin (2011) used elements and/or element ratios to discriminate between magnetite from different sources by studying a broad range of deposit types. They defined compositional fields for magnetite from (Figure 2-19):

- Ni-Cu-PGE deposits using : Ni + Cr vs. Si + Mg
- Cu-Zn-Pb VMS using: Al/(Zn + Ca) vs. Cu/(Si + Ca)
- IOCG, Kiruna, porphyry Cu, BIF, skarn, Fe-Ti, V deposits using either:
    - Ni/(Cr + Mn) vs. Ti + V **OR**
    - Ca + Al + Mn vs. Ti + V

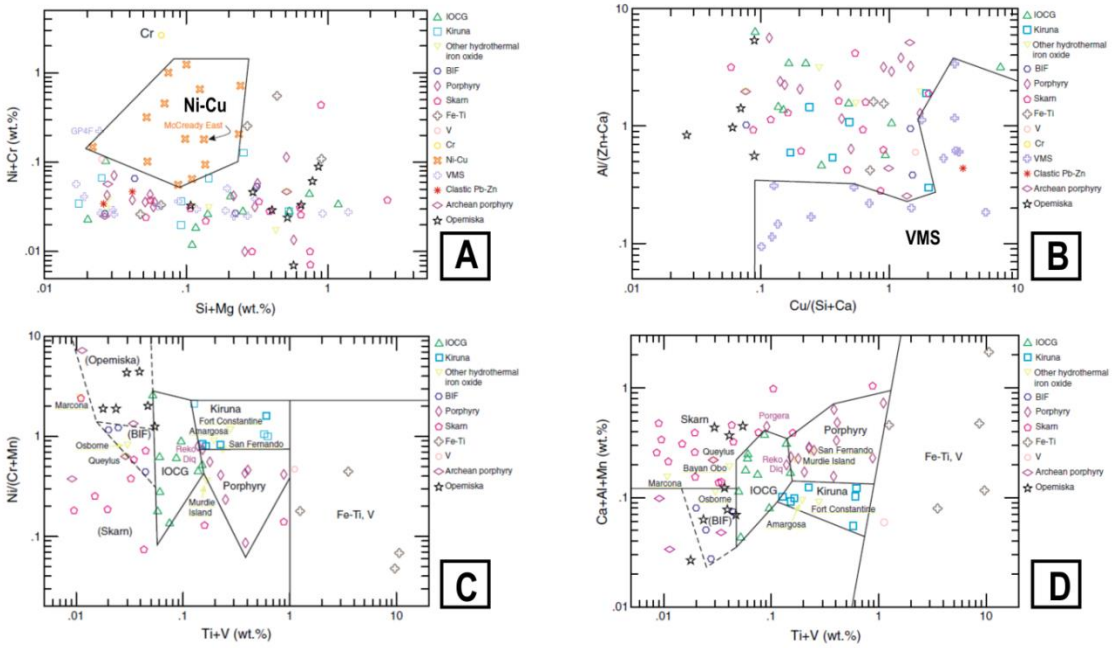

Figure 2-19: Discriminant diagram for average composition of magnetite from various Fe-oxide-containing deposits. **A:** Ni+Cr vs. Si+Mg to discriminate Ni-Cu deposits; **B:** Al/(Zn+Ca) vs. Cu/(Si+Ca) to discriminate magnetite from VMS deposits; **C:** Ni/(Cr+Mn) vs. Ti+V discriminant diagram for average Fe-oxide compositions from Kiruna, IOCG, porphyry Cu, Fe-Ti-V and BIF deposits; and **D:** Also used to distinguish deposits from Kiruna, , IOCG, porphyry Cu, Fe-Ti-V and BIF deposits, but also skarn deposits. Diagrams C and D should be used in conjunction to disctinguish between BIF, skarn, Archean porphyry deposits and Opemiska-type Cu veins. Images combined from Dupuis and Beaudoin (2011).

Dare et al. (2014) developed a method to systematically discriminate between magnetite grains formed in different geological environments using trace element concentrations. In their study they used well known examples to distinguish between magnetite formed in a magmatic environment from hydrothermal magnetite. Dare et al. (2014) recognised that although the processes that govern the distribution of trace elements in magnetite are complex and varied, distinctive chemical signatures will still arise from grains that formed under similar physio-chemical conditions.

Dare et al. (2014) produced a 25-element diagram to highlight this partitioning where elements are plotted in order of increasing compatibility into magnetite. The shape of the graph can therefore be used to comment on the abundances of different trace elements in the liquid, or highlight when competition for an element occurs due to other phases co-crystallising with magnetite, such as sulfides. An important finding from their study was the distinction between high temperature hydrothermal and magmatic magnetite on the basis of Ni and Cr ratios. Due to the coupled compatible behaviour of Ni and Cr in silicate magmas the Ni/Cr ratios are ≤1, whereas in hydrothermal systems this behaviour is decoupled and the ratio shifts to ≥1. By plotting Ti versus this ratio the two types of magnetite can be distinguished, as shown in Figure 2-20.

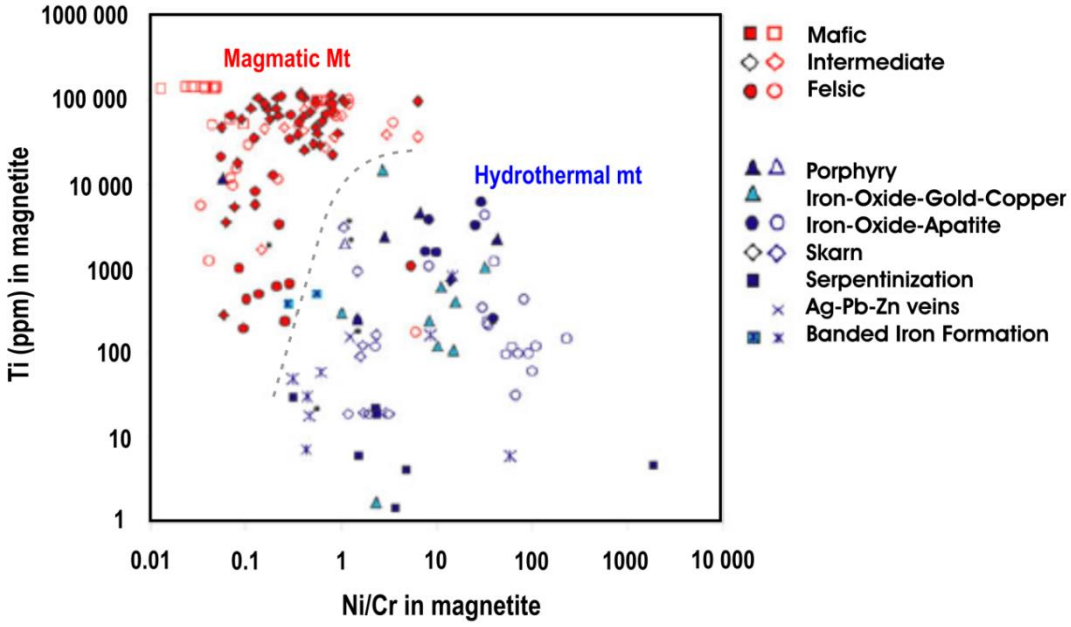

Figure 2-20: Plot of Ti (ppm) versus Ni ratio (un-normalised) in magnetite (mt) to distinguish magmatic (red) and hydrothermal (blue) settings. Figure redrawn from Dare et al. (2014).

Compositional fingerprinting of magnetite trace element concentrations is an emerging field with much of the focus on known igneous and hydrothermal occurrences. To date only one study has been carried out on the trace element geochemistry of magnetite from an SSC deposit, that of Nadoll et al. (2012) for the Spar Lake and Rock Creek deposits of northern Montana. There is also a lack of empirical data supporting the assumption that trace elements partition in the same way in hydrothermal fluids as they would in a melt, although this assumption is based on first principles, below 600˚C few thermodynamic constraints have been set (Frost, 1991a). Understanding the geochemical controls on the formation of magnetite in a rock is half of the story; the other half is understanding how these controls influence the distribution and abundance of magnetite on a regional scale, and thereby the

rock's magnetism. Together these are referred to as magnetic petrology. In the following section the role of magnetite in rock magnetism will be discussed.

2.3.2 Rock Magnetism

The magnetic properties of rocks are controlled by the magnetism of the minerals within the rock. These magnetic minerals can potentially record the Earth's geomagnetic field at the time of their formation, and retain this remanent magnetisation over geologically signficant timescales. The ability of a mineral to retain a stable remanent magnetisation is governed by three main types of magnetic behaviour (Dentith and Mudge, 2014; Tauxe, 2010):

- **Diamagnetism:** All atoms are diamagnetic; according to Lenz's Law atoms produce a magnetic response in opposition to any applied field. This is a weak magnetic effect, but dominates the magnetic response of minerals such as such as quartz, calcite, feldspar, galena, sphalerite and some of the clays. These minerals do not carry magnetic remanence.
- **Paramagnetism:** These minerals have permanent magnetic moments that become aligned with the direction of applied magnetic fields. Minerals in this category have potentially significant but weak positive magnetic susceptibilities, the strength of which is directly proportional to the iron content of the mineral. Minerals in this category include olivine, pyroxene, amphibole, garnet, mica, pyrite, chalcopyrite, arsenopyrite and pure ilmenite. The minerals also do not carry remanence.
- **Ferromagnetism:** This group of minerals retain a spontaneous magnetisation in the absence of an external magnetic field, due to quantum mechanical coupling between atomic magnetic moments. Ferromagnetic minerals (s*enso lato)* retain a record of their magnetic history, and may carry remanence. This group includes ferromagnetic materials (*senso stricto*) such as metallic iron, **ferrimagnetic** minerals such as magnetite, maghemite and monoclinic pyrrhotite and the **antiferromagnetic** minerals such as hematite.

Grain size plays an important role in the ability of a grain to retain its remanence. Below a critical size (~100 nm for magnetite), the magnetisation in a crystal is uniform, and the particles are said to be single domain. Large single domain particles are very stable, but as the particle size decreases the magnetisation is unstable due to thermal fluctuations; such particles are referred to as superparamagnetic. In coarser grains the magnetisation breaks up into regions of uniform magnetisation (domains), and the structures are said to be

multidomain. The stability of multidomain magnetisation is governed only by the movement of internal magnetic structures.

There are a number of types of remanent magnetisation, each reflecting the conditions under which the Earth's magnetic signature was 'fixed'. These are (Dunlop, 1990; Tauxe, 2010):

- **Natural remanent magnetisation (NRM):** This is a blanket term used to describe a rock which has magnetic remanence. The remanence may have been acquired through any of the following mechanisms below, however, until the source of the remanence is known, the rock is referred to as simply having NRM.
- **Thermoremanent magnetisation (TRM):** Magnetic minerals formed in igneous rocks will partially align in the earth's magnetic field as the rock cools from above the Curie temperature.
- **Depositional remanent magnetisation (DRM):** Detrital magnetic minerals partially align to the Earth's magnetic field (or an applied field) during settling in a sedimentary environment.
- **Chemical remanent magnetisation (CRM):** This type of magnetisation is produced by chemical alteration through low-temperature oxidation, exsolution, diagenesis or dehydration. CRM is either acquired as the result of the alteration of a pre-existing parent magnetic mineral within a magnetic field (aCRM), or by a new magnetic mineral precipitating/nucleating out of solution and growing through a critical volume (gCRM). aCRM is particularly difficult to unravel as the newly recrystallized phase may be influenced by both the parent phase and the external field.
- **Viscous remanent magnetisation (VRM):** When a mineral is exposed to a constant magnetic field at ambient temperatures over a prolonged period this type of magnetisation is acquired.
- **Isothermal remanent magnetisation (IRM):** Magnetic remanence can be produced by lightning strikes. Partial or total remagnetisation can occur when this happens, often masking the primary magnetisation of the rock.
- **Thermo-viscous remanent magnetisation (TVRM):** Magnetisation of this kind can be acquired when a mineral/rock is subjected to elevated temperatures for a geologically significant time period.

Palaeomagnetic studies are concerned with determining the orientation of the NRM and the underlying mechanism causing the NRM. Such studies can provide valuable information about the timing and nature of magmatic, tectonic and mineralising events. Magnetite within the Eiseb is investigated through a combination of trace element geochemical analyses, petrography and palaeomagnetics, as discussed in Section 6.

3 Recent Work on the KCB

This project has been carried out in collaboration with EPM; therefore the main findings of their exploration work will be summarised herein as pertains to the current aims and objectives for this study. This review is not exhaustive but limited to a handful of company reports and spreadsheets that were consulted for this review. These are referenced where applicable and available for consultation at the discretion of EPM.

Recent work carried out on the Kalahari Copper Belt (KCB) in Botswana by other companies and individuals was presented during an informal KCB conference held in Maun from 25-27 July 2013. This included presentations from EPM, Discovery Metals Limited (DML), Cupric Africa/Hana Mining Ltd geologists, MSc students from Leicester University working in collaboration with Hana Mining on their Khoemacau Project, and a student from Colorado School of Mines working with DML on Boseto Mine (Figure 3-5). This work is summarised herein.

3.1 Academic work presented at the KCB conference

The academic work presented at the KCB conference discussed here is from Gorman et al. (2013) and Morgan et al. (2013) who worked on the western Hana Mining licence areas, and Hall (2013) who worked on the license areas of Discovery Metals (Figure 3-1).

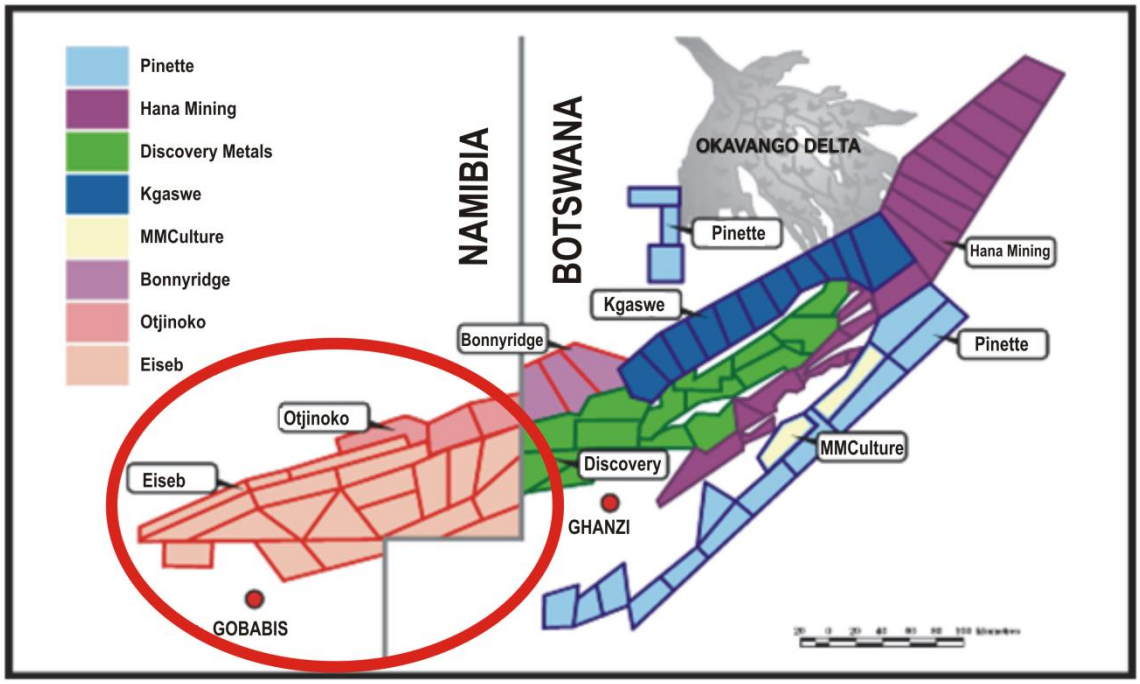

Figure 3-1: Copper exploration licences along the Ghanzi-Chobe Belt in central-eastern Namibia and Botswana circa. 2013. The study area is circled in red (Eiseb licences). Map extracted from Dean (2013).

3.1.1 Sulfur Isotopes

Gorman et al. (2013) sampled 16 boreholes from three zones along the KCB between Kuke and Toteng in Botswana (Figure 3-2). Sulfur isotopes ($\delta^{34}S$) were analysed from three different sulfide occurrences: disseminated (*n* = 4), main stage veins (*n* = 12), and late stage veins (*n* = 3). The results overlap, but the spread of the data is wide, ranging from -45.7‰ to +0.4‰ (V-CDT), with a data gap between -39 and -20‰. These sulfur isotope values are attributed to the source of sulfur being bacterial sulphate reduction (BSR) (Harrison and Thode, 1958; Kaplan and Rittenberg, 1964; Ohmoto et al., 1990). The results are comparable to the Kupferschiefer deposit in Poland, which are thought to be consistent with BSR of Neoproterozoic seawater. Results from the disseminated and vein-hosted mineralisation suggest a single source of sulfur.

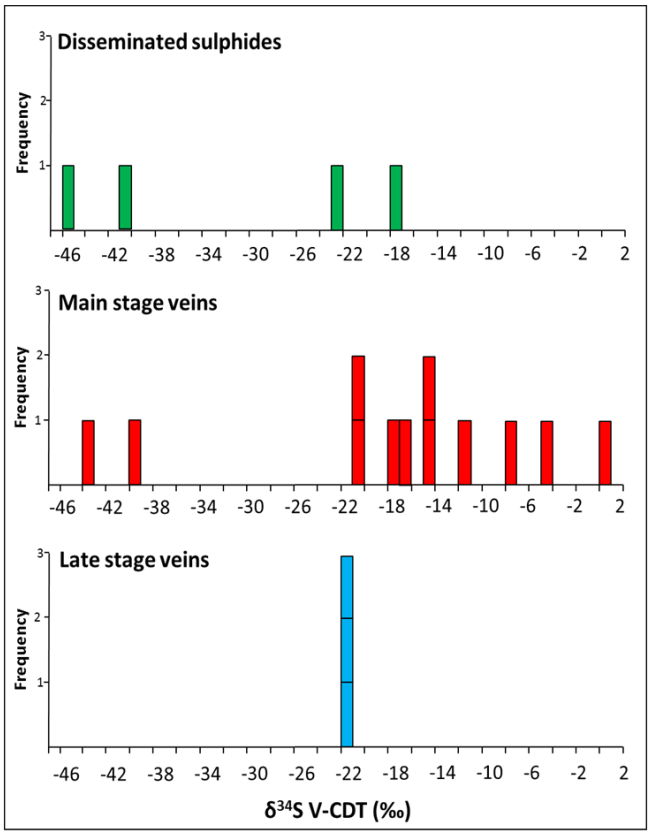

Figure 3-2: Sulfur isotope analysis from the KCB in the vicinity of Ghanzi, Botswana. Isotopic delta measurements of sulfur are made relative to Vienna Cañon Diablo troilite (V-CDT*)*. Image extracted from Gorman et al. (2013).

Hall (2013) obtained similar results from work carried out on the Boseto Project near Maun in Botswana. Hall (2013) however, attributed the overlap in signatures between the disseminated and vein-hosted mineralisation to indicate that the sulfur in the veins was sourced from the disseminations, i.e. dissolution of disseminated sulphide mineralisation and reprecipitation within veins.

3.1.2 Oxygen and Carbon Isotopes

Morgan et al. (2013) examined $\delta^{18}O$ and $\delta^{13}C$ from calcite in the veins which host mineralisation (*n* = 7). The $\delta^{18}O$ values are negative, falling within the -18 to -12‰ range. The $\delta^{13}C$ results range from +4 to -12‰ (Figure 3-3). The results are compared to Neoproterozoic carbonates from mineralised and unmineralised intersections. The $\delta^{18}O$ values are slightly more negative, but the $\delta^{13}C$ fall within a comparable range to other Neoproterozoic carbonates.

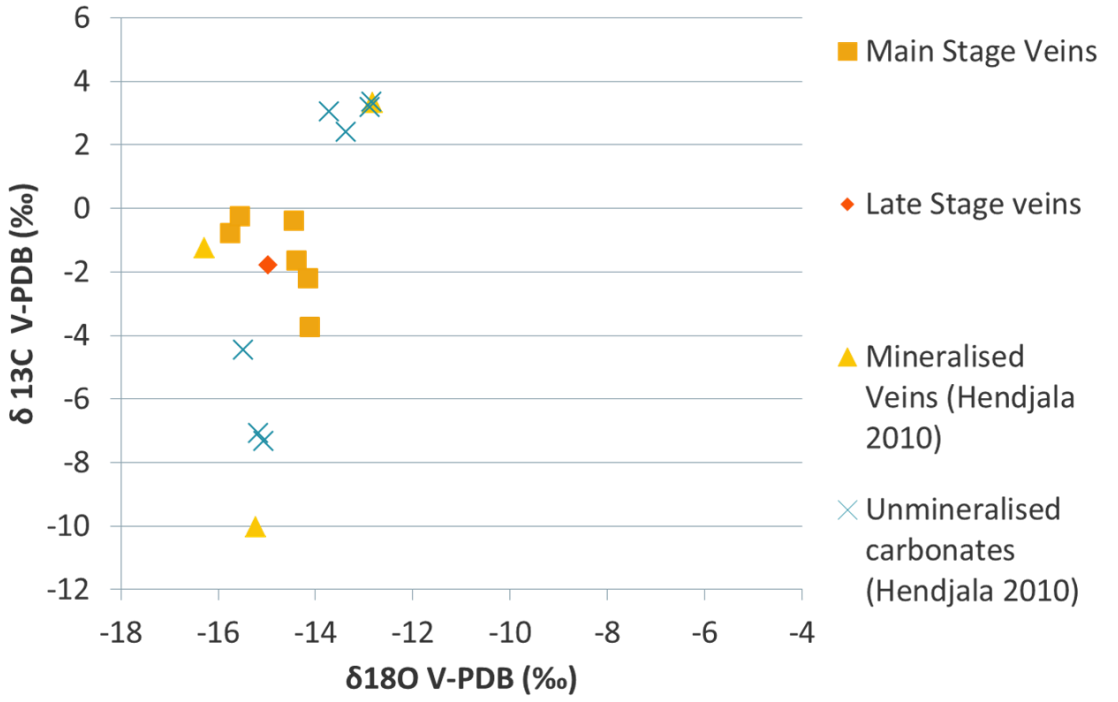

Figure 3-3: $\delta^{13}C$ and $\delta^{18}O$ results are compared to other Neoproterozoic carbonates (Hendjala, 2010; Morgan et al., 2013). Results reported relative to Vienna Pee Dee Belemnite (V-PDB*)*. Figure taken from Morgan et al. (2013).

Isotope analyses carried out by Hall (2013) on vein-hosted minerals from the Boseto project have similar $\delta^{13}C$ values to those shown in Figure 3-3, but are significantly different for $\delta^{18}O$. The $\delta^{18}O$ values range from +11.6‰ to +22.1‰. This variability in the $\delta^{18}O$ was interpreted by Hall (2013) as indicative of metamorphic recrystallization of carbonate minerals and reaction with metamorphic fluids.

3.1.3 Fluid Inclusions

Fluid inclusion microthermometry suggests homogenisation temperatures between 93.9-296˚C (after pressure correction 280-350˚C), with calcite-quartz geothermometry indicating temperatures in the range of 355-375˚C (Morgan et al., 2013).

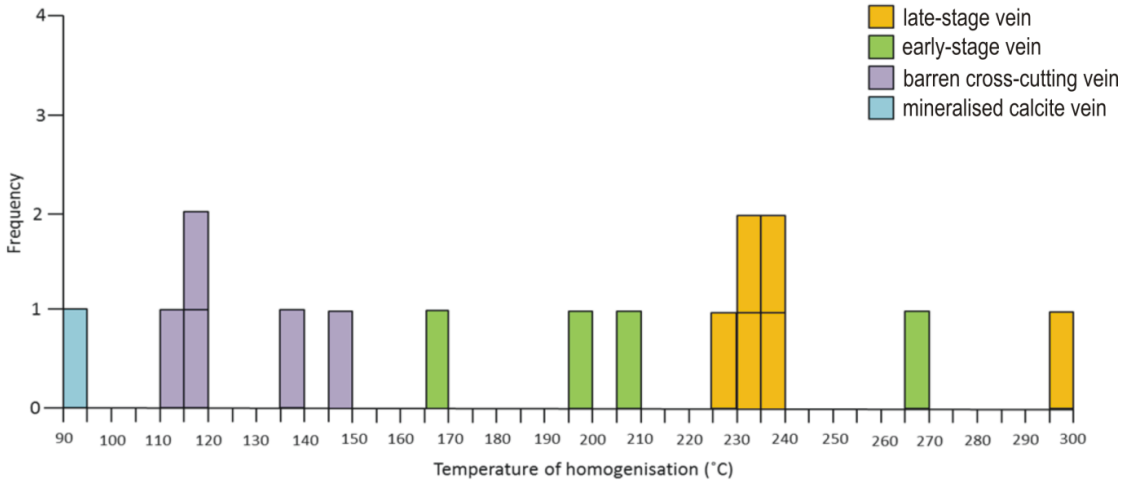

Figure 3-4: Fluid inclusion microthermometry from veins taken from Morgan et al. (2013).

Fluid salinity was also investigated by Gorman et al. (2013). Their results indicate a fluid salinity between 4 and 24 eq. wt. % NaCl (*n* = 19), and a fluid with the composition $CaCl_2$-NaCl-H_2O.

Hall (2013) also attempted to characterise the fluids of the KCB using the crush-leach process which measures bulk fluid compositions. This was carried out on quartz, calcite, bornite, chalcopyrite and pyrite mineral separates from Boseto. The data suggest enrichment in Ca and Na in the Boseto fluids, relative to modern seawater and sedimentary brines. Hall (2013) interprets these characteristics as indicative of metamorphic fluids.

3.1.4 Rhenium-Osmium Chronometry

Hall (2013) carried out a Re-Os chronometry on three sulfide samples from Boseto. This method was chosen due to the robust nature of Re and Os in sulfide minerals, the radiometric clock will only reset when complete chemical dissolution of the sulfide crystal has occurred. The results from vein-hosted bornite and chalcopyrite suggest model ages of 1012 ± 17Ma and 914 ± 4 Ma for samples taken from deformed rocks, and 459 ± 37Ma for the sample taken from a less deformed sequence. The resultant Re-Os model ages are reported as median ages

calculated using an assumed initial $^{187}Os/^{188}Os$ value of 0.2 and 1.0, thought to represent ancient bulk continental crustal compositions. Hall (2013) interpreted the older model ages as indicative of diagenetic sulfides being locally recrystallised and incorporated into veins, and the complete recrystallization and precipitation of sulfides during the waning stages of the Damaran Orogeny producing the younger age.

3.1.5 Discussion

The results of Gorman et al. (2013) argue strongly for a BSR source for the sulfur within the basin, but the data sets used to interpret the temperatures of formation and fluid sources show a wide spread for both Hall (2013) and Morgan et al. (2013). This is most likely a function of sample density, and the inherent complexity associated with a basin of considerable age. Hall (2013) identified a possible metamorphic source for the fluids.

The Re-Os results are even less clear. Hall (2013) uses the younger age to suggest the Damara Orogeny (~530 Ma) drove sulfide precipitation, but that the more deformed rocks contained sulfides mobilised by partial dissolution of existing diagenetic/syngenetic sulfides, which were then incorporated into veins.

Overall, the results obtained from the academic studies discussed provide little to suggest that these techniques would produce meaningful and useful data for the current study. These techniques have therefore not been pursued for the Eiseb study area.

3.2 Summary of Eiseb Prospecting and Mining (Pty) Ltd exploration activities

EPM was awarded Exclusive Reconnaissance Licences (ERLs) in 2007, and between 2008 and 2010 were awarded 19 Exclusive Prospecting Licences (EPL) for base metal exploration in this relatively unexplored region of the KCB (Figure 3-5).

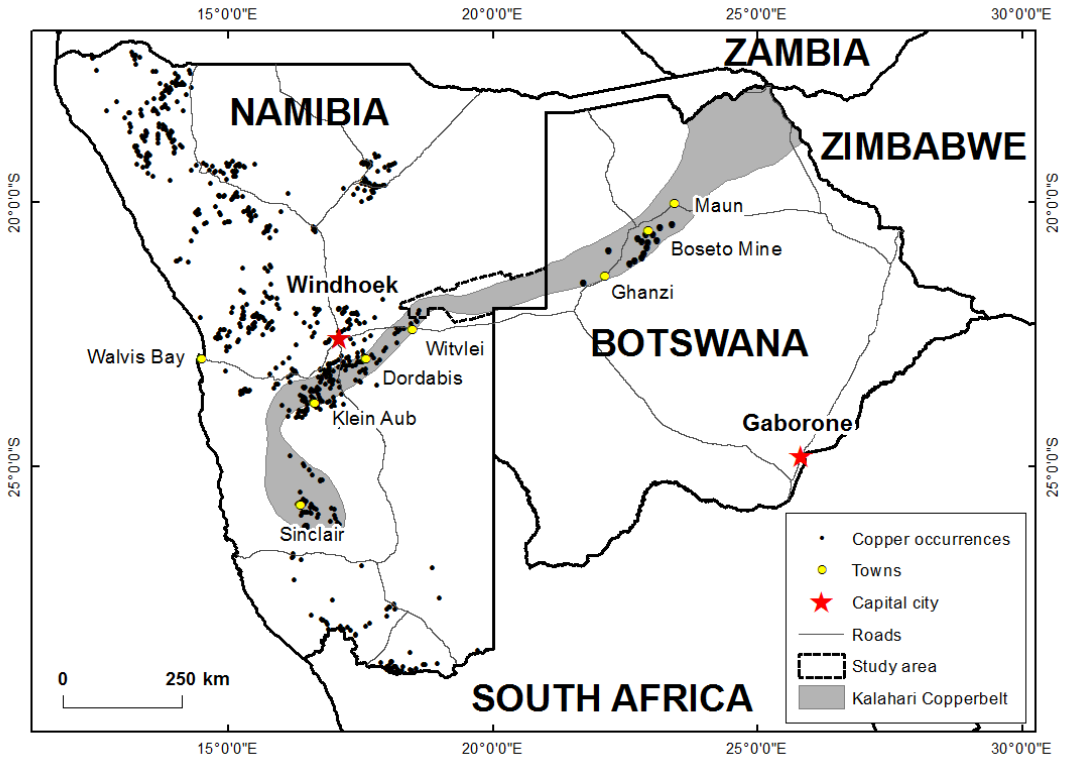

Figure 3-5: Location map of the study area and known copper occurrences along the KCB prior to exploration commencing in 2008 by EPM. Copper occurrences in Namibia are from the Geological Survey of Namibia (www.mme.gov.na), and for Botswana published occurrences from DML and Hana Mining were used (www.cupriccanyon.com).

During their first few years EPM carried out an extensive review of previous mineral exploration carried out within and adjacent to their licenses by the companies (summarised in Veldsman et al., 2010):

- FEDSWA
- B & O Minerals
- Goldfields of South Africa
- Anglovaal Namibia Limited
- BHP Billiton Plc

These reports were often of little use as the companies involved had been targetting MAB type mineralisation hosted in the amphibolites, schists and magnetite quartzites of the Matchless Member of the Kuiseb Group (Veldsman et al., 2010).

Early reconnaissance exploration by EMP combined detailed airborne magnetic survey interpretations with follow-up geochemical soil sampling (Figure 3-6 & Figure 3-7). The surveys used were:

- Composite, coarse national magnetic grids for Botswana and Namibia;
- Thumbnails of 1:250 00 scale datasets from the Geological Survey of Namibia (GSN) website (gravity and magnetics) (www.mme.gov.na);
- Published 1:250 000 scale sheets of airborne magnetics from the GSN (2120, 2118, 2218 and 2316);
- High resolution magnetic grid data covering the licence area, purchased by EPM from GSN (www.mme.gov.na);
- High resolution magnetic grid data covering the GCB in Botswana (Department of Geological Survey, Lobatse, Botswana) (www.gov.bw).

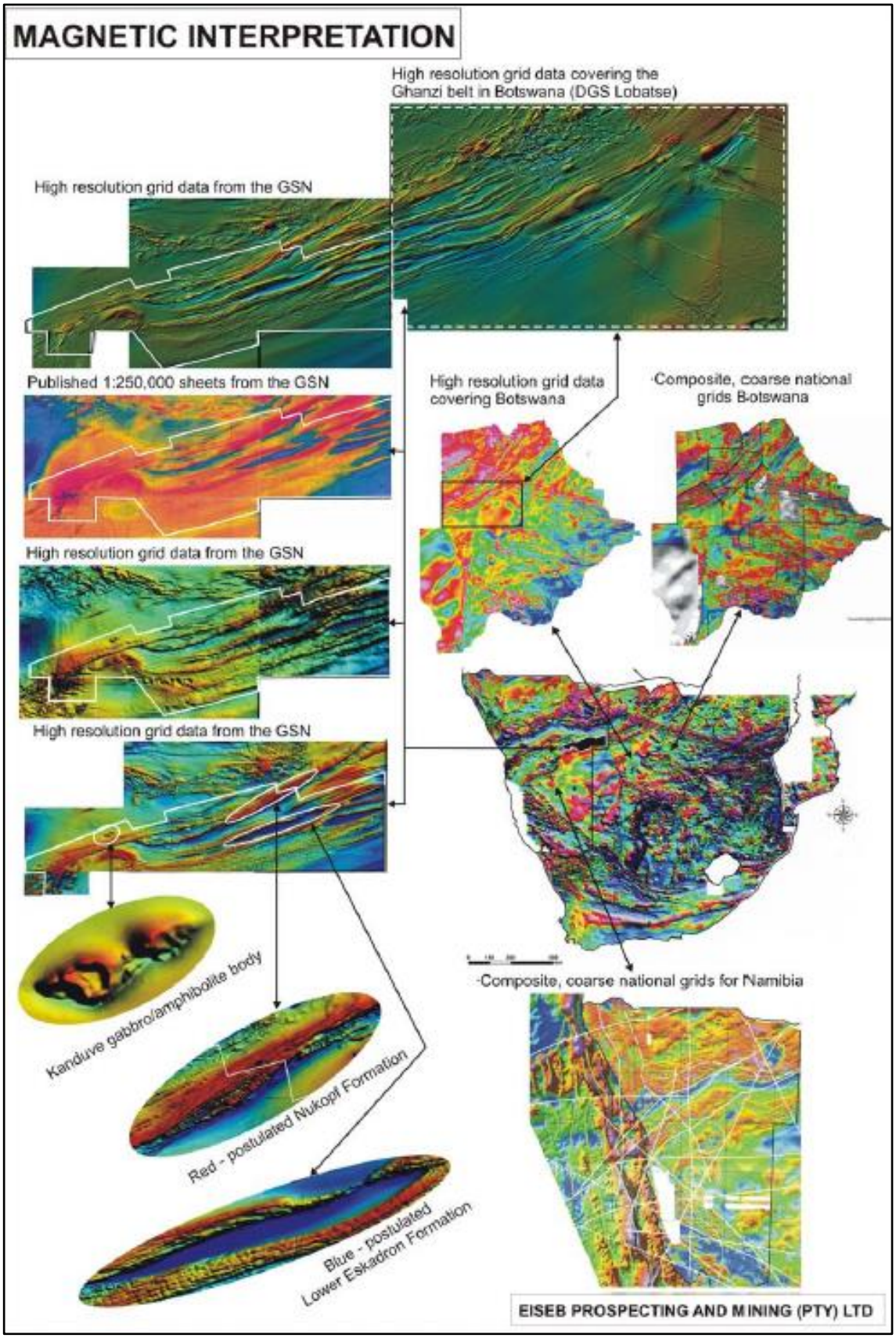

Figure 3-6: Regional airborne magnetic data interpretation method after Veldsman et al. (2010). GSN efers to the Geological Survey of Namibia (www.mme.gov.na). Magnetic and gravity data grids covering Botswana were purchased from Department of Geological Survey (DGS), Lobatse, Botswana (www.gov.bw).

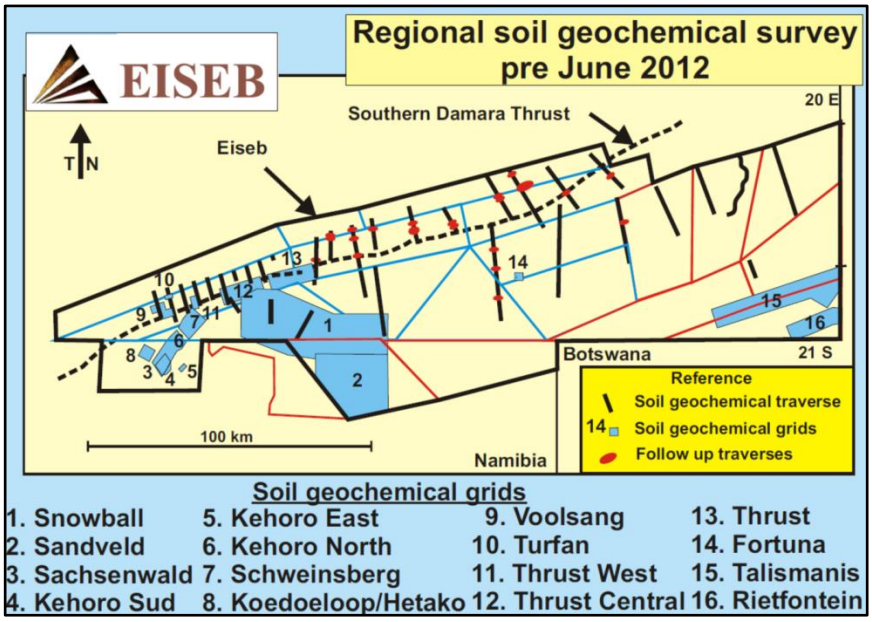

Figure 3-7: Location of regional soil geochemical surveys carried out by EPM prior to 2012. Image taken from Veldsman et al. (2010).

In general soil sampling identified only low order geochemical copper anomalies (>10ppm), which when later drilled, showed no relationship to bedrock. Soil geochemical sampling using conventional analytical methods was therefore largely unsuccessful. In addition to soil geochemical surveys, an IP survey and a regional gravity survey were carried out in the southwest of the licence area (Figure 3-8).

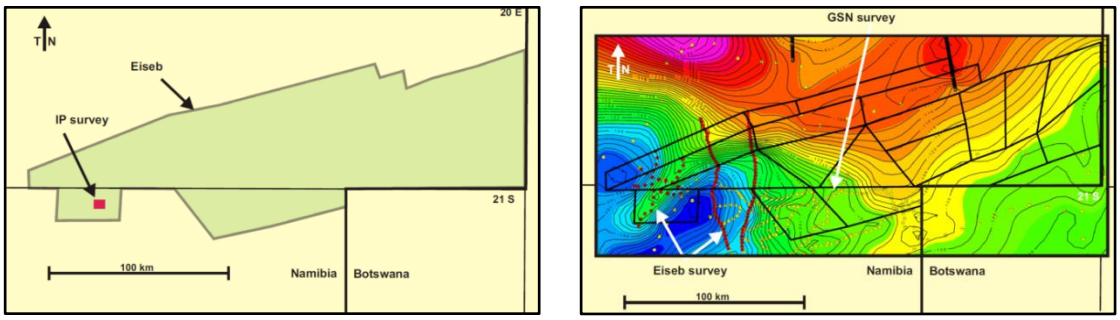

Figure 3-8: Location of the IP survey (LEFT) and the gravity surveys carried out by EPM (RIGHT). Images taken from Veldsman et al. (2010)

A high resolution aeromagnetic survey was also flown across part of the study area, and this was augmented by follow-up ground magnetic surveys (Figure 3-9).

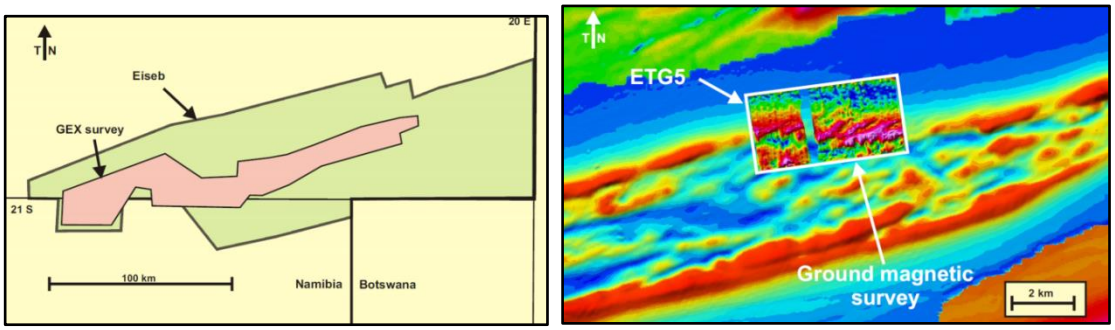

Figure 3-9: Location of the high resolution (GEX) aeromagnetic survey (LEFT) and a ground magnetic survey (ETG5) carried out by EPM (RIGHT). Images taken from Veldsman et al. (2010)

In 2010 EPM intersected their first copper-silver mineralisation comparable to that of the KCB in Botswana, the so called 'Ghanzi-style' mineralisation. By the end of 2014 a total of 334 holes had been drilled across the licence area using a combination of reverse circulation (RC), percussion (PD) and diamond drilling (DD) (Table 3).

Table 3: Summary of drilling carried out by EPM from 2010 to the end of 2014.

Drilling Type	Total meters drilled	Number of holes
Reverse circulation	44843	213
Percussion	9809	77
Diamond	11952	44
TOTAL	**66604**	**334**

In total 195 holes were subsampled and sent laboratories to test for Ag, As, Bi, Co, Cu, Mo, Ni, Pb and Zn, and 65 were also tested for Au, Pt and Pd. Quality assurance and quality control measures (QAQC) were monitored by EPM, as discussed in Section 4.2.2.3. XRF analyses were also done on these rocks, but these will not be discussed in detail as they do not form a part of the current study.

Additional work was carried out Toby Dawborn on the eastern portion of the study area as part of the joint venture between EPM and Antofagasta Minerals. Dawborn (2013) investigated the geochemistry and mineralogy of the eastern licence areas using a scanning electron microprobe (SEM) and x-ray diffraction (XRD) analyses. These, and the work of EPM, will be discussed in more detail as pertains to the local geology and exploration results.

3.2.1 Aeromagnetic Data Interpretation

Several significant steps were taken by EPM in unravelling the geology of the study area. Smalley (2013) produced a geological map for the area using interpreted regional and high resolution aeromagnetic survey data tying it in to the published sub-Kalahari geology map from the Botswana Geological Survey (Figure 3-10).

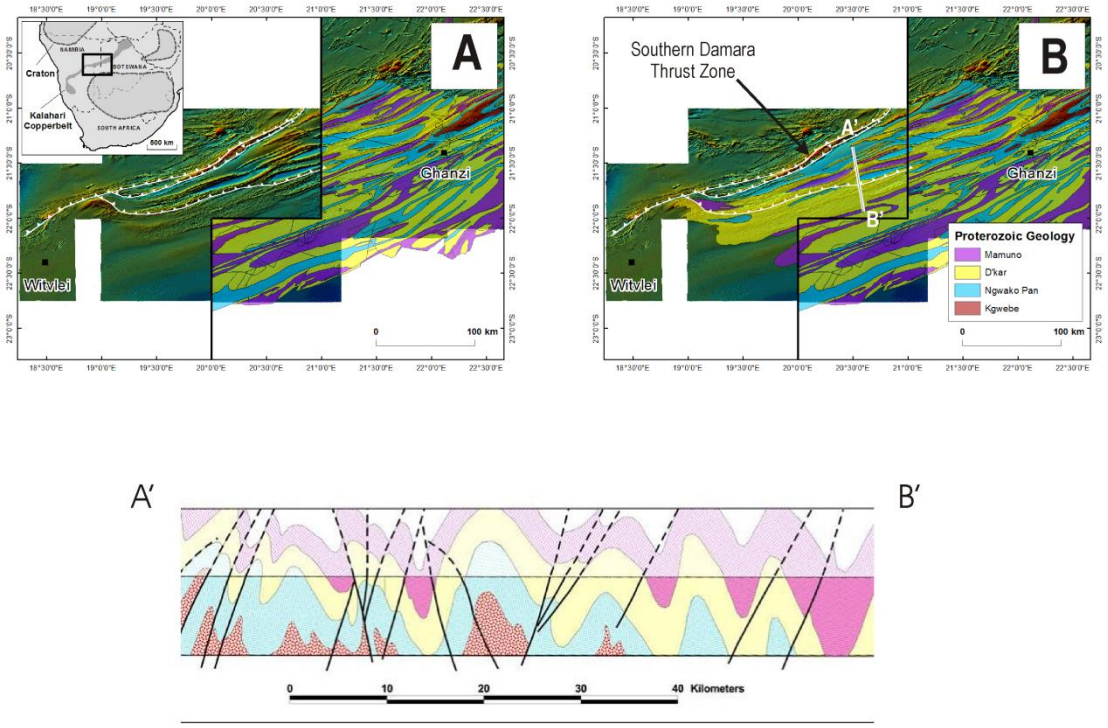

Figure 3-10: The regional total magnetic intensity (TMI) map of Namibia and Botswana with the geology of Botswana shown (A). Simplified geological map of eastern-central Namibia after Smalley (2012) and of Botswana overlying the TMI for both countries (B). The cross-section is taken from Veldsman et al. (2010). The geology of Botswana shapefile was provided by the Department of Geological Survey, Lobatse, Botswana (www.gov.bw). The regional TMI is a composite of aeromagnetic survey data provided by the Geological Survey of Namibia (www.mme.gov.na) and Department of Geological Survey, Lobatse, Botswana.

In order to enhance geological and structural features observed in the magnetic data, a private contractor, Gregory Symons, created over 20 different magnetic image products from the airborne and ground magnetic data including: analytical-signal (AS), reduced-to-pole (RTP), first vertical derivative (1VD), total-magnetic-intensity (TMI), and various derivatives of these (1vd-RTP, etc.)(2011 to 2014). Other data enhancement products were also generated, such as Laplacian reductions and total horizontal derivative (THD) (Smalley, 2013). The main image products used to map the geology and structures were (Kahle, 2013; Smalley, 2011):

- **TMI:** Indicates the overall magnetic character of the lithotype;
- **RTP:** Places the magnetic feature above its causative body;
- **RTP-1VD:** Emphasises near surface features, aides fabric mapping;

- **AS:** Emphasises near surface features by making them positive magnetically. Good for contact mapping;
- **THD:** emphasises shallow linear trends, enhances contacts

3.2.2 Lithotype

Dawborn (2012) carried out several detailed logging exercises in the central parts of the study area, and along the Botswana border (Talismanis area) in an attempt to correlate lithotypes across the area and define stratigraphic unit names where possible. Using colour, grain size, assay data and magnetic susceptibility data Dawborn (2012) defined 6 local stratigraphic units beneath the Kalahari overburden (Figure 3-11 & Figure 3-12):

- **Interbedded Unit (IBU):** Siltstones and argillite interbedded with grey magnetite-bearing quartzite. Quartz-carbonate veins contain pyrite and minor chalcopyrite and are both foliation parallel and cross cutting. Relatively high magnetic susceptibility;
- **Hanging Wall Quartzite (HWQ):** Medium to fine-grained pinkish sandstone unit containing graded heavy mineral (depositional) magnetite bands. Quartz-carbonate veins contain specular hematite.
- **Upper Argillite Unit (UAU):** Fine grained siltstone with interbeds of finer and more silty units. Siltstone is foliated and light green. Minor pyrite and copper sulfides observed. Carbonate alteration present along the upper contact.
- **Hanging Wall Arkose (HWA):** Pink medium to fine-grained arkosic sandstone containing graded magnetite bands (depositional). Specular hematite is observed in the quartz-carbonate veins. Albite alteration is pervasive and the rock appears recrystallized.
- **Lower Argillite Unit (LAU):** Dark green to bright green fine-grained siltstone with a strong foliation. Interbeds of silty and sandy units. Foliation in the silty units produces a phyllitic texture. Chlorite alteration pervasive and carbonate alteration limited to lower contact. Rare interbeds of recrystallized sandstone contain cubic pyrite. Quartz-carbonate veins are foliation parallel and occasionally cross-cutting. Mineralisation occurs as foliation parallel disseminations, veins and stringers in the form of chalcocite, bornite and chalcopyrite.
- **Footwall Quartzite (FWQ):** Generally grey medium-grained sandstone with occasional red spots of hematite after magnetite. Towards the west this becomes more reddish-orange. Graded heavy mineral bands of magnetite at an angle to fabric are present. Quartz-carbonate veins contain specular hematite. Very homogenous unit with little to

no feldspars. Fine-grained pervasive magnetite alteration concentrated near the contact with LAU.

The exploration terms 'hangingwall' and 'footwall' are used throughout this text. These terms have no structural connotations and refer only the rocks above (hangingwall) and below (footwall) mineralised intersections.

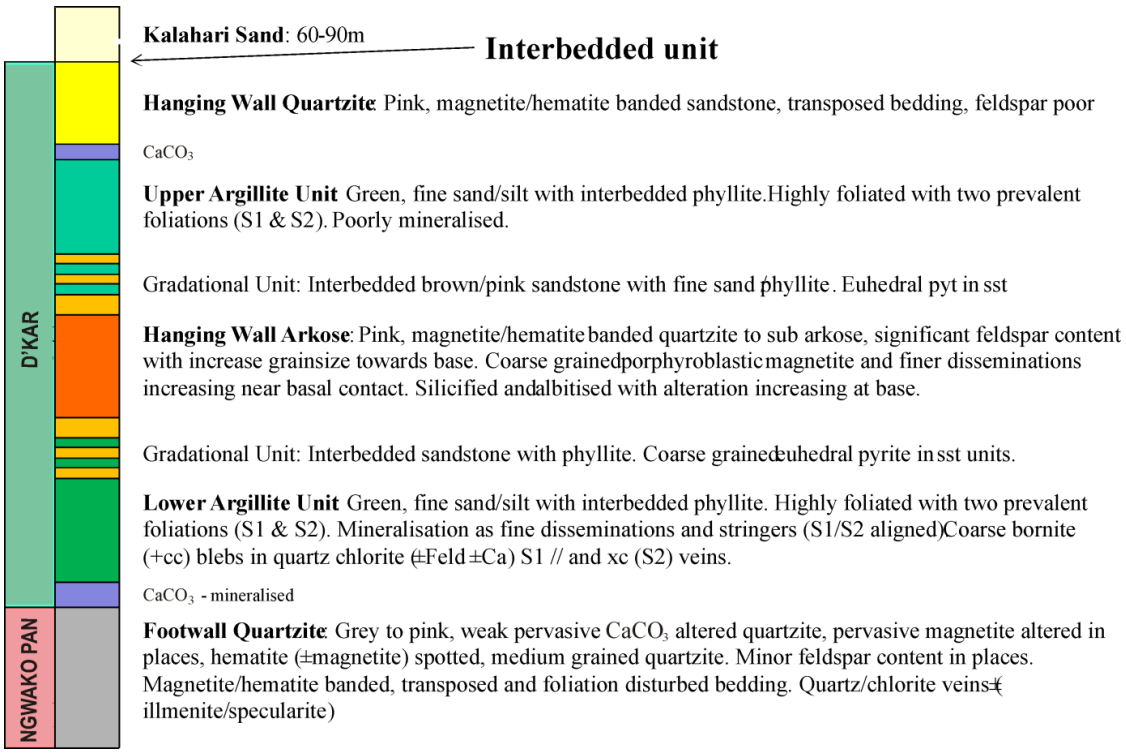

Figure 3-11: Summary of the stratigraphy from the Talismanis area from Dawnborn (2012).

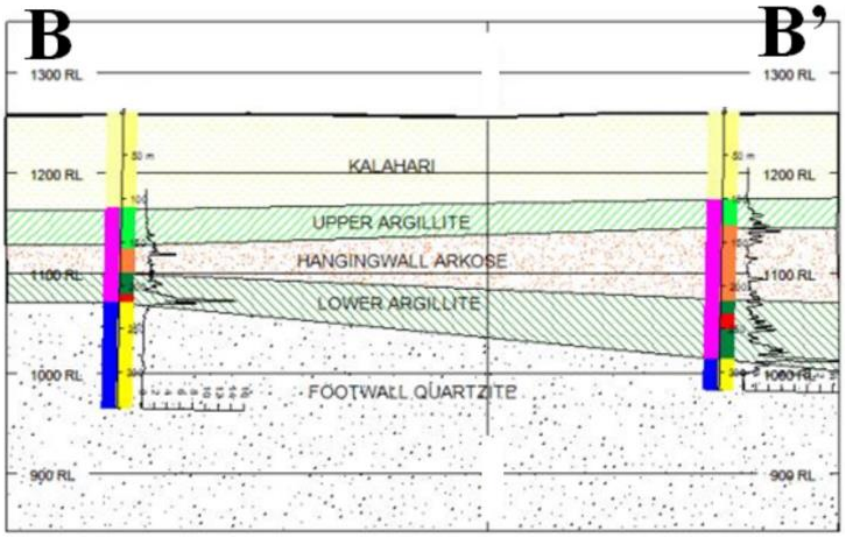

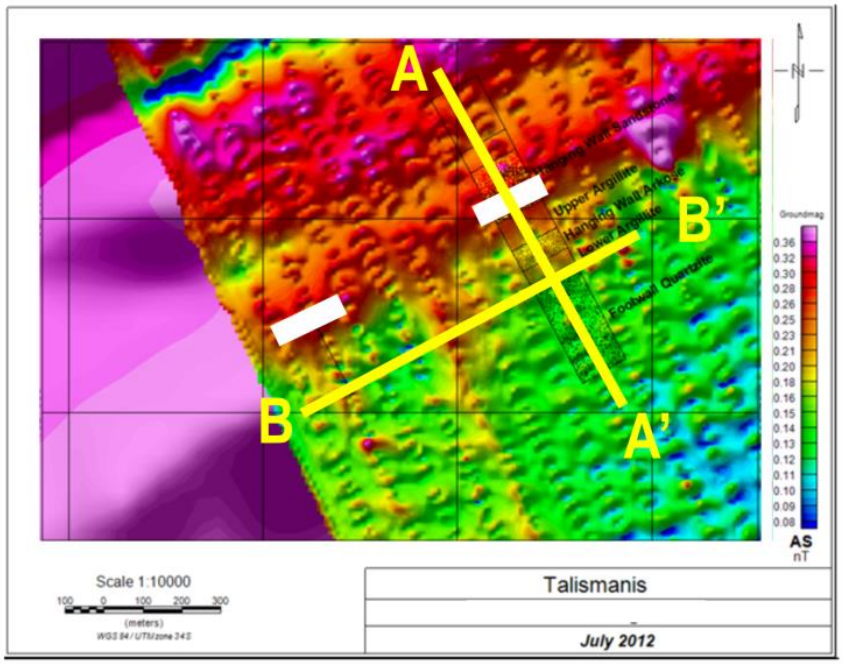

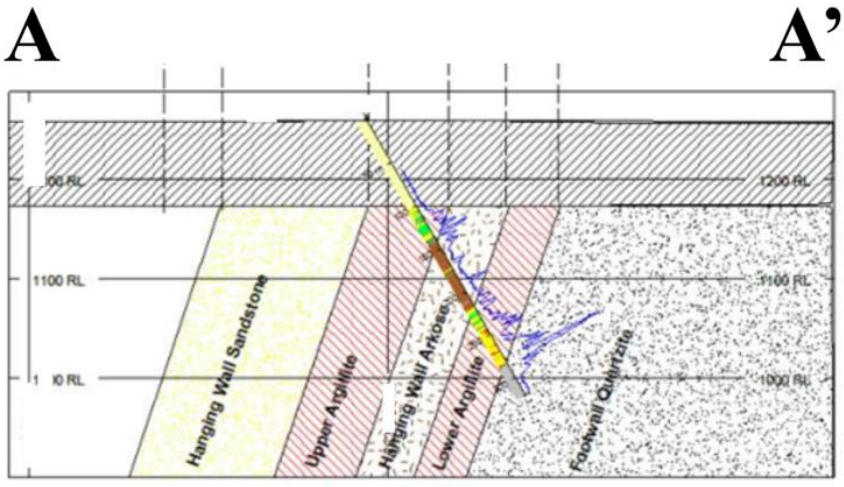

Figure 3-12: Magnetic profiles A-A' and B-B' lithological cross-sections with magnetic susceptibility shown in blue. Images modified to exclude proprietary information. Images from Dawborn (2014).

3.2.3 Mineralisation

The mineralisation associated with the KCB in Botswana is referred to as 'Ghanzi style/type' mineralisation. In Botswana Smalley (1998) identified the presence of mineralisation straddling the contact between the magnetically contrasting Ngwako Pan and D'Kar Formation in the dark greenish siltstones of the latter, Dawborn's (2012) LAU. Mineralisation was observed to focus on the flanks of antiform/synform structures. Overall the mineralisation within the Eiseb occurs in two broad categories (Dawborn, 2012; Veldsman et al., 2010):

- **Disseminated Copper:** Mineralisation, in the form of chalcocite (cc), bornite (bn) or chalcopyrite (chp) (± silver), disseminated within phyllites and argillites, usually inter-layered with quartzites in the LAU. Fine-grained quartzites may also host mineralisation. Coarse disseminations are usually present as aggregates within quartz/feldspar pressure shadows. Disseminations are usually developed in close proximity to veins.
- **Vein-hosted/cleavage parallel:** Copper (± silver) can occur within cleavage-parallel lenticles, brittle fractures, tectonic breccias zones and within quartz-carbonate veins, both parallel and transgressive to bedding. Veins can be foliation parallel or at a low angle to bedding in secondary cleavages. Bornite within quartz carbonate veins is also occasionally reported from sandstone units. This is accompanied by ~foliation parallel disseminations of bornite.

Table 4 shows typical grades recovered from the central study area. Similar results were obtained from a borehole 2km further westwards along strike, suggesting lateral continuity of the mineralisation.

Table 4: Assay results from a single drill hole along a limb from the central study area antiform (CA: central antiform). Table extracted from Smalley et al. (2012)

Depth (m) From	Depth (m) To	Ag (g/t)	Cu ppm	Zn ppm
148	149	50	2820	146
149	150	47	3870	156
150	151	133	7140	162
151	152	338	18900	138
152	153	134	10100	160
153	154	394	25800	160
154	155	14.5	1300	88

The Cu and Ag grades are appreciably higher than in Botswana, reaching 1 % Cu and 100 g/t Ag, while in Botswana the grades are ~1 % Cu and 10g/t Ag (www.cupriccanyon.com/development-exploration/zone-5-resources).

SEM work suggests that silver does not form discrete minerals but exsolves as a pure metal along the crystal lattice of chalcocite (Dawborn, 2012). Exsolution textures are also common between chalcocite and bornite (Figure 3-13).

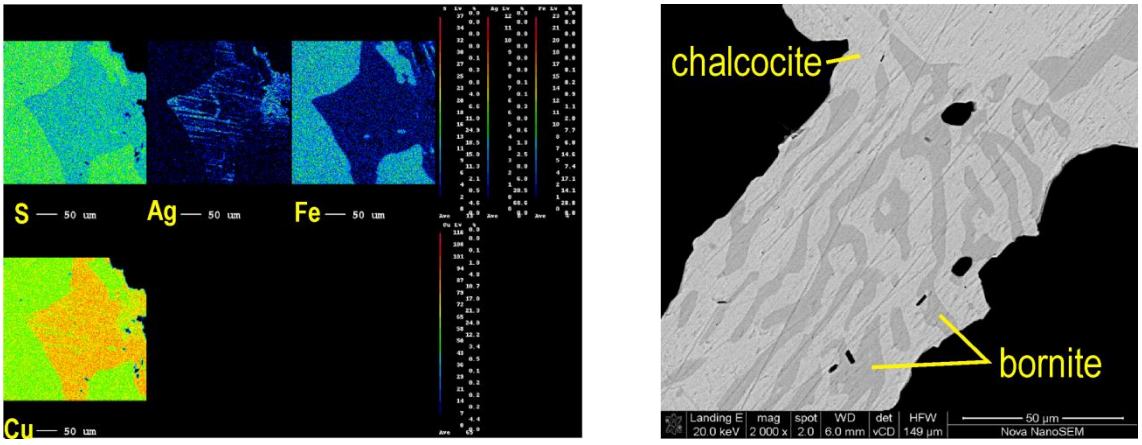

Figure 3-13: Element map of chalcocite showing silver exsolutions along the crystal lattice (LEFT). Chalcocite and bornite exsolution texture (RIGHT). Images taken from Dawborn (2013).

Microprobe data were also used to demonstrate the pervasiveness of the mineralising event(s) throughout this area, by comparing the hanging wall and lower argillite unit mineralogy. Both above and within ore mineralised horizons the same mineral assemblages were observed, mainly titanite and quartz/albite (Figure 3-14).

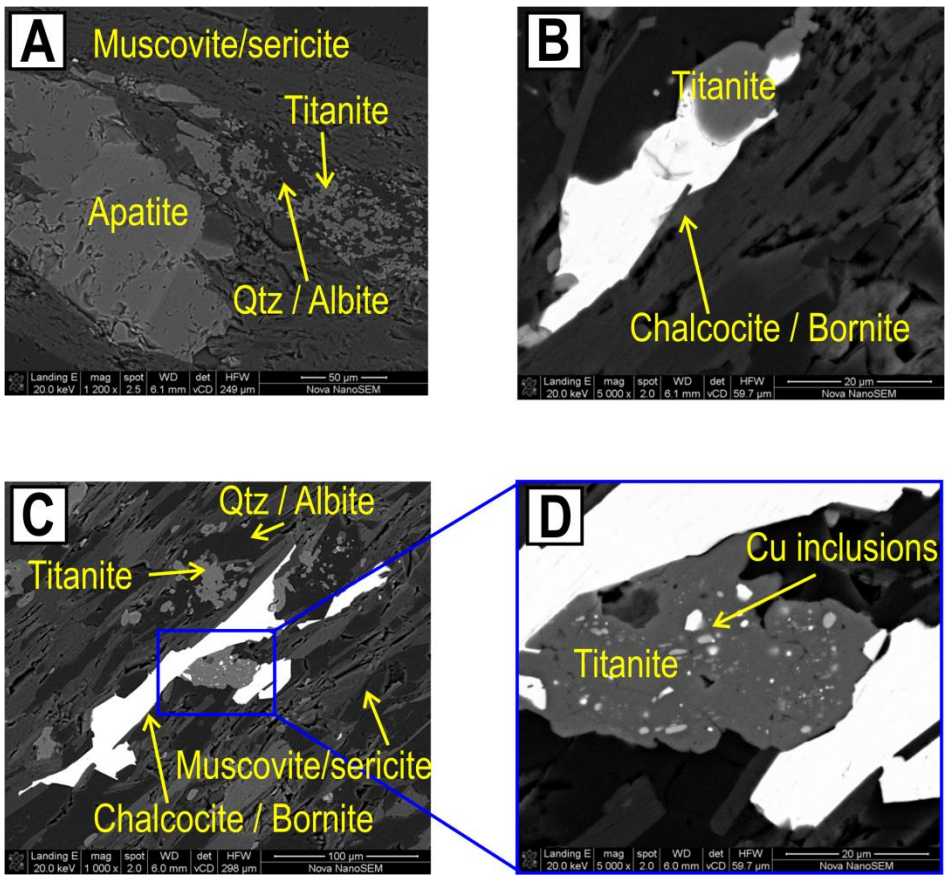

Figure 3-14: SEM photomicrographs taken from Dawborn (2013). **A:** Photomicrograph from the hangingwall arkose unit (HWA). **B**, **C** and **D**: Photomicrographs from the lower argillite unit (LAU).

Of interest are the noticeable amounts of magnetite often associated directly with the sulfides in the fine-grained argillites, and also disseminated through the neighbouring horizons, regardless of rock type (Smalley et al., 2012). Dawborn (2013) speculated that magnetite formed part of the alteration assemblage associated with the mineralisation (Figure 3-15). This is explored throughout this work and discussed in detail in Sections 7.3.2 and 8.

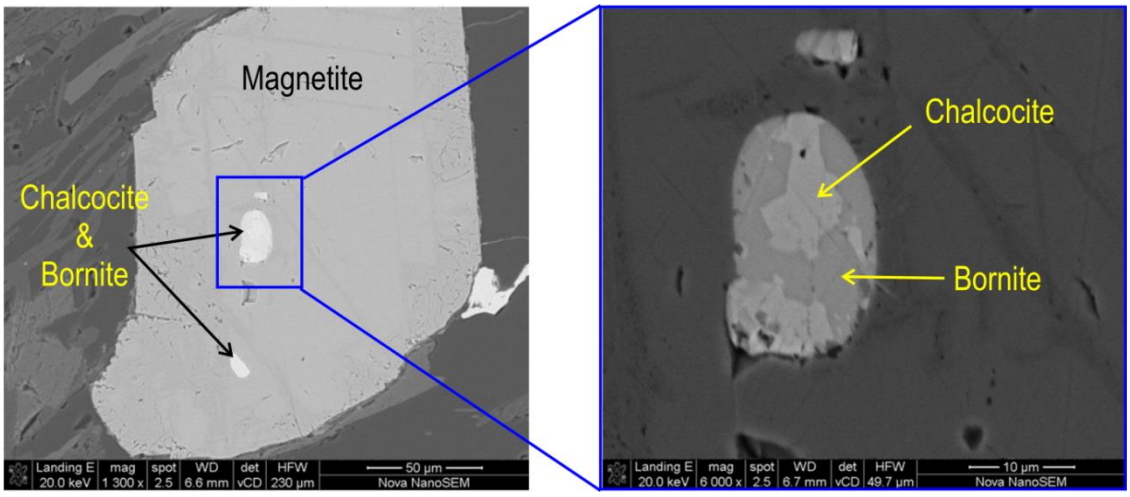

Figure 3-15: Photomicrograph of the inclusions of copper sulfides. RIGHT: chalcocite and bornite in an exsolution texture. Images taken from Dawborn (2013).

3.2.4 Magnetic Characteristics

The magnetite content of the Ngwako Pan and D'Kar Formation strata are thought to account for their distinctive magnetic signatures. The Ngwako Pan Formation is magnetically quiet, and the D'kar Formation is magnetically active. On a regional scale this contrast was used to map out the major boundaries between these formations based on sub-surface interpretations.

Smalley (2013) saw this strong magnetic link as a potential tool to locate mineralisation. To this end additional magnetic information was also gathered by measuring down-hole magnetic susceptibilty variations and by taking hand-held readings of magnetic susceptibilities directly from drill core and chips. It was found that positive susceptibility anomalies and negative total magnetic field anomalies were coincident with Cu-Ag sulfide-bearing strata (Smalley, 2013) (Figure 3-16 & Figure 3-17).

Down-hole magnetic susceptibility results correlated with readings taken on the drill core, indicating that the magnetic units are remnant, in other words, they produce a magnetic signal in the absence of an applied field, and the signal is negative/destructive compared to today's magnetic field (Dawborn, 2014). Smalley (*pers comm.,* 2013) speculated that the magnetite associated with the Cu-Ag mineralisation was most likely precipitated during the Damara Orogeny (~530Ma).

In general the magnetically quiet footwall sandstones of the upper Ngwako Pan Formation correlate with incidences of uncharacteristically high magnetic susceptibility near the contact with the D'Kar Formation and mineralisation (Figure 3-16). However, sudden increases in magnetic susceptibility are not isolated to the mineralised zones proximal to the NP-DK boundary, but to a variety of strata proximal to mineralisation, regardless of this boundary (Figure 3-17).

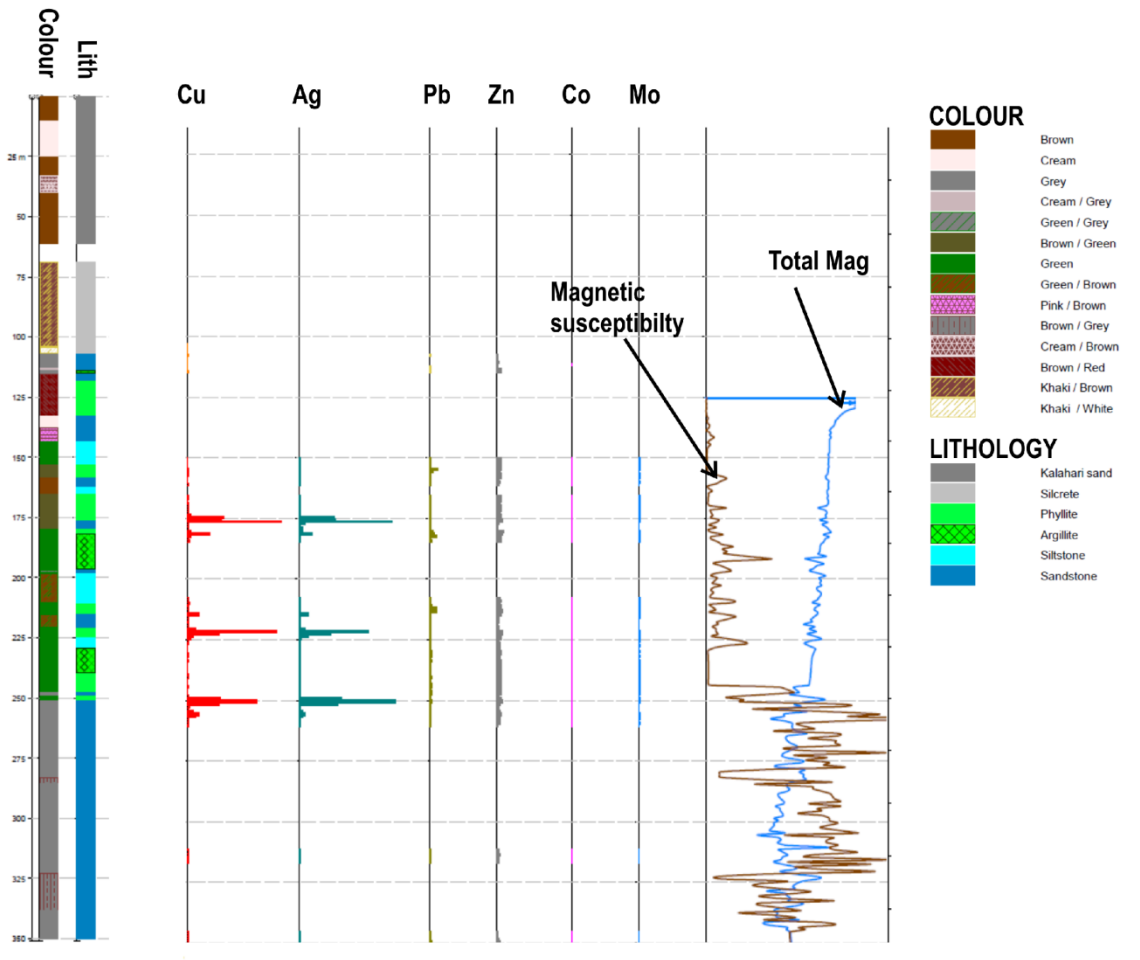

Figure 3-16: Lithological log with assay results and magnetic susceptibility readings. Modified image based on logs provided by EPM (2012). The blue and brown lines show the positive magnetic susceptibility (brown) and the negative total magnetic field (blue) anomalies.

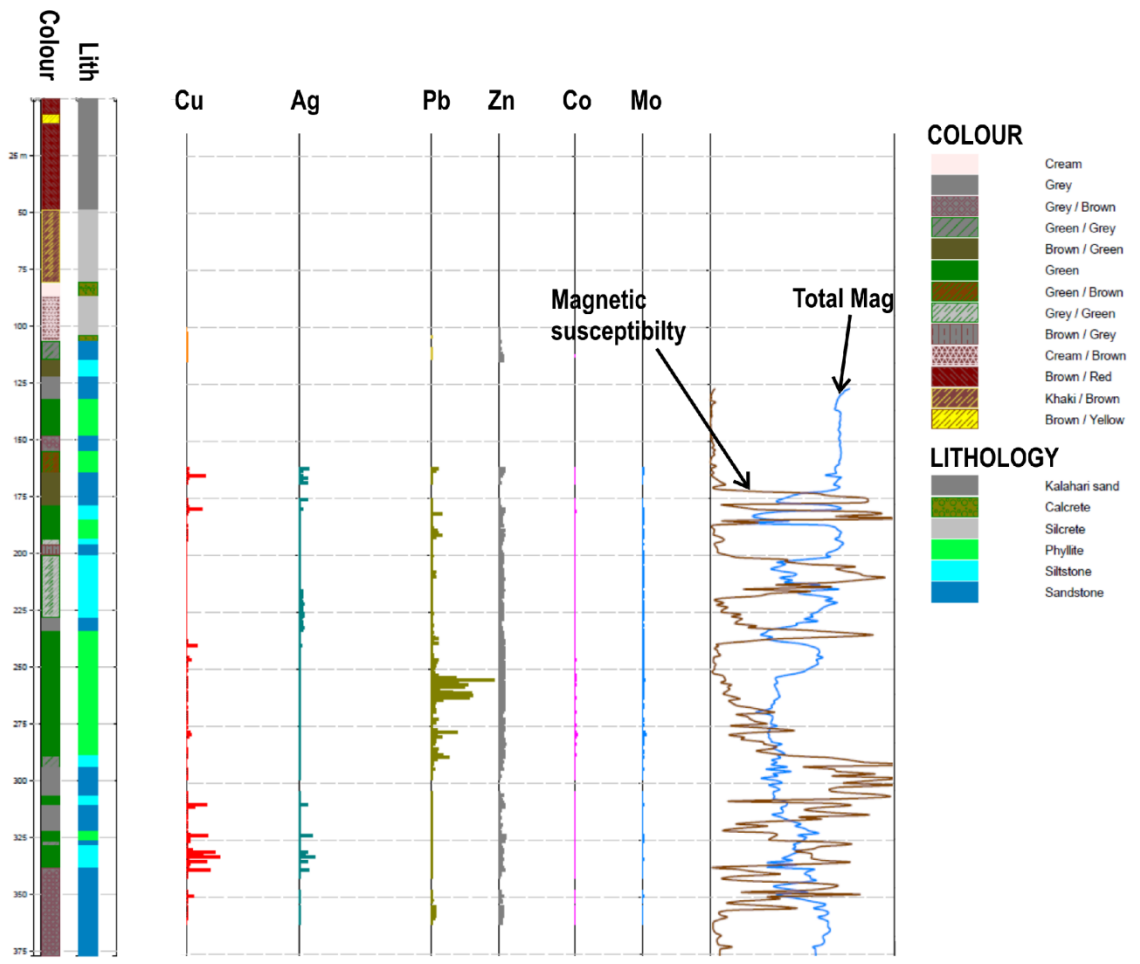

Figure 3-17: Lithological log with assay results and magnetic susceptibility readings. Modified image based on logs provided by EPM (2012). The blue and brown lines show the positive magnetic susceptibility (brown) and the negative total magnetic field (blue) anomalies.

Although the magnetic characteristics are similar for the two intersections shown, i.e. positive magnetic susceptibility anomalies and negative total magnetic field anomalies, only in Figure 3-2 is this near the NP-DK boundary. Both, however, are associated with the mineralisation. This implies that the cause of the magnetic anomalies is linked only to the mineralisation, rather than the stratigraphy unit or the lithological host of the mineralisation.

3.2.5 Structure

The study area underwent prolonged transpression with the main stress directed from the north as part of the Damara Orogeny. The strata were folded and their long axes stretched in an ENE direction in a series of doubly plunging (WSW and ENE) antiforms and synforms. Short axes are generally oriented to the NNW. The northern limbs to these folds are linear and often truncate hangingwall lithotypes, implying some development of NNW dip directed thrusts (Dawborn, 2014).

Proximal to the Southern Damara thrust zone, which marks the northern limit of the study area, southern limbs are generally overturned, but to the south these limbs are normal. This suggests a decrease in the intensity of tectonic activity southward from the main thrust (Smalley et al., 2012). The northern limbs dip between 45˚ and 65˚, while the southern limb, when not overturned, dip on average ~75˚ (Catterall, 2014). The contact zone along the NP-DK boundary shows high strain, especially between rheologically contrasting units. The coarse sandstone units show brittle fracturing and cross-cutting veining, whereas the finer units have variably developed foliation at an angle to bedding (Dawborn, 2012).

Primary bedding (S0) is preserved in some of the quartzite units as heavy mineral/magnetite bands, but in the finer grained silstones and argillites bedding is not preserved. In these units a composite S0/S1 foliation has been observed, which occasionally develops into an S2 cleavage. Mineral growth in this orientation (S1) is sometimes observed in phyllites. Through the use of oriented core to take structural reading Dawborn (2014) found that S2 cleavage was axial planar to the orientation of the regional antiform. Dawborn (2014) suggests that this cleavage development provided the necessary permeability for metal-bearing fluids to interact with the country rock.

Structural complexity is often temporal with fold closures, and generally higher grades of mineralisation. Smalley (2014) draws analogies from the Mount Isa model which was successfully applied to the Klein Aub deposit (Maiden and Borg, 2011) (Figure 3-18). The mineralisation at Mount Isa in Australia is controlled primarily by feeder faults and focussed by localised areas of dislocation or splays. In this model the rheological contrast between different rock units facilitates fluid flow and the chemical (redox) contrasts between units cause metal precipitation. This is fundamentally different to the diagenetic SSC model because mineralisation is controlled by structure and rheology, not just redox conditions.

Down-hole optical investigations were carried out on several boreholes to investigate structures found that the majority of the strata dip steeply to the NNW with some minor southerly dips as well.

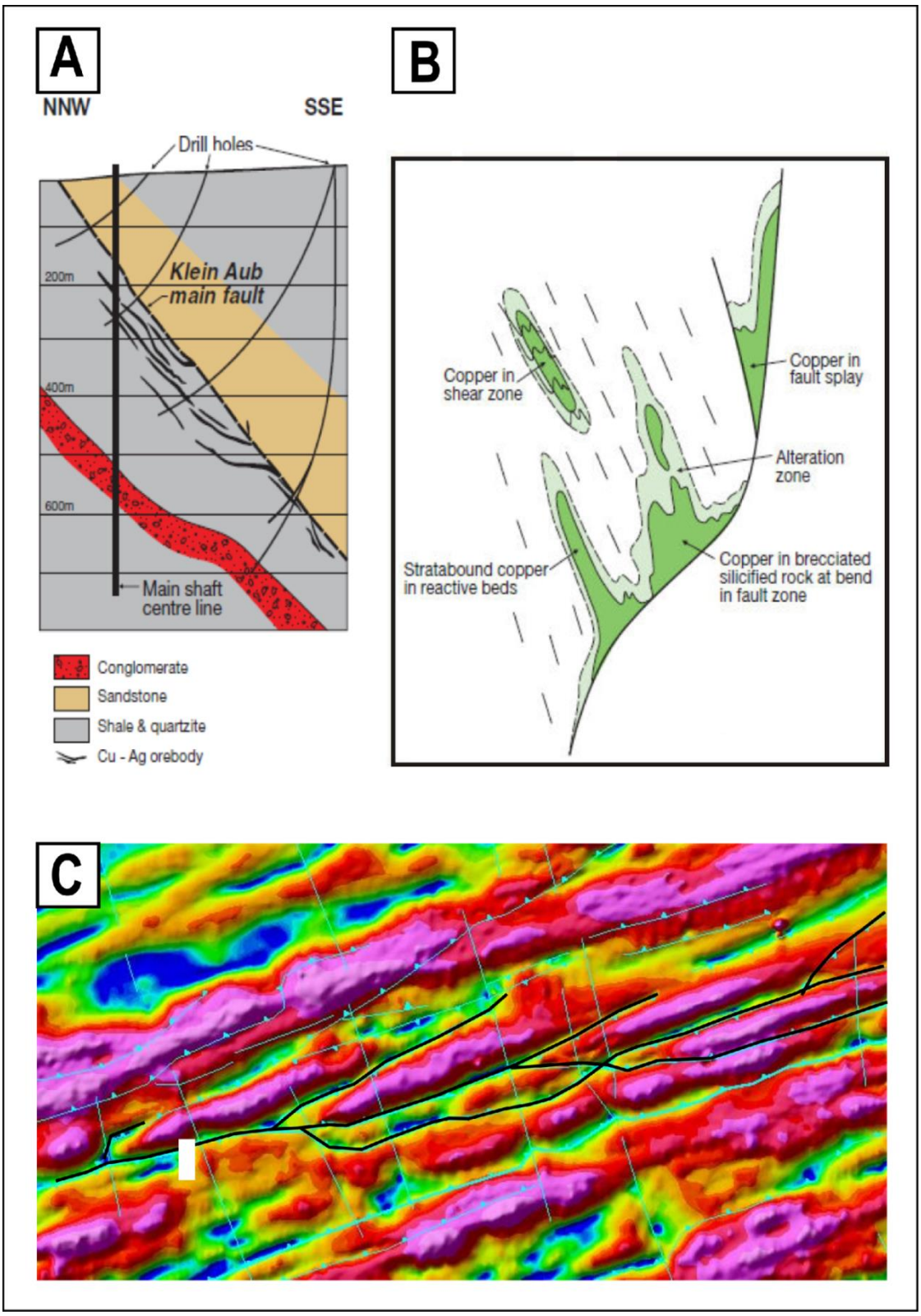

Figure 3-18: A: Schematic section through the Kagas Member of the Klein Aub Mine from Borg (1988b). **B:** Copper deposit styles in the western Mount Isa block from Maiden and Borg (2011). **C:** Analytical signal magnetic images from the study area showing 'imbricate-like' splay features and faulting. Image from Smalley (2014).

3.2.6 Summary of EPM exploration results

On the basis of the work carried out by EPM, some general statements can be made:

- The contrasting magnetic signatures of the Ngwako Pan and D'Kar Formations can be used to map the sub-surface geology (and structures) of the study area using a combination of magnetic image products.
- Locating mineralisation using conventional geochemical soil sampling techniques is ineffective in this area due to thick pervasive sandy cover.
- Lithological units can be distinguished at depth and correlated over large strike distances, however, in areas of structural complexity this becomes increasingly challenging.
- Cu-Ag mineralisation occurs as disseminations and within veins and is broadly focussed along the interpreted magnetic boundary between the NP-DK Formations.
- The ratio of Cu:Ag is an order of magnitude higher in the study area than in Botswana.
- Silver does not form separate minerals but concentrates along the crystal lattices of chalcocite as mative silver.
- Chalcocite and bornite commonly form exsolution textures.
- Overturned limbs contain little to no mineralisation.
- There are strong mineralogical similarities between the hanging wall and mineralised zone; including the occurrence of titanite, and magnetite, chlorite and sericite.
- Magnetite shows an association with the mineralisation, containing inclusions of chalcocite and bornite.
- Positive magnetic susceptibility and negative total magnetic field anomalies are commonly coincident with or proximal to mineralisation.
- There is a direct correlation between mineralised coarser sandstone units and higher magnetic susceptibility.
- Airborne and ground magnetic surveys suggest that the magnetic units are remanent.
- There is a general N-NNW dip to the fabric of the northern limb strata.
- There is a potential link between mineralisation and imbricate/splay structures, such as those found in the Mount Isa or Klein Aub deposits.

4 Methodology

4.1 Sample Suite

In total 64 polished thin sections and 6 polished blocks from 23 sites (20 boreholes, 3 outcrop) were used for this study to describe the range of rock types, mineralised intersections, and degree of deformation across the Eiseb (Figure 4-1;Table 5). This included:

- Six PB (polished block) samples used for automated mineralogical quantification using a QEMSCAN (Section 4.5).
- Eleven MG (magnetite) grain mount polished thin sections from bulk magnetic separates for magnetite trace element analyses by LA-ICP-MS (Section 4.6).
- Fifteen OPS (oriented polished sections) samples for the palaeomagnetic study (Section 4.7).
- Three polished thin sections from outcrops of basal volcanic rocks. One was taken from the Kgwebe Formation in Botswana, and two from the Oorlogsende Member in Namibia (OE-1 & OE-2), a Kgwebe Formation equivalent (Section 5.4.1).

The borehole names have been changed from the Eiseb naming convention in order to reflect the location of a given sample. The study area has been divided into an eastern anticline (EA); north-east anticline (NEA); central anticline (CA); western border zone (WB), and central zone (CZ). The second part of the name further reflects the location as being either on a northern or southern limb (NL/SL), or near the supposed plunge line (PL) or along the hinge zone (HZ) of a fold; e.g. EA-NL-2 refers to borehole 2 from the northern limb of the eastern anticline. This nomenclature is used throughout. In the EPM nomenclature Eatern Anticline and North East Anticline correspond to the Talismanis exploration area, the Central Anticline is equivalent to Fortuna-Fiesta, and Western Block is in the vicinity of Sachsenwald.

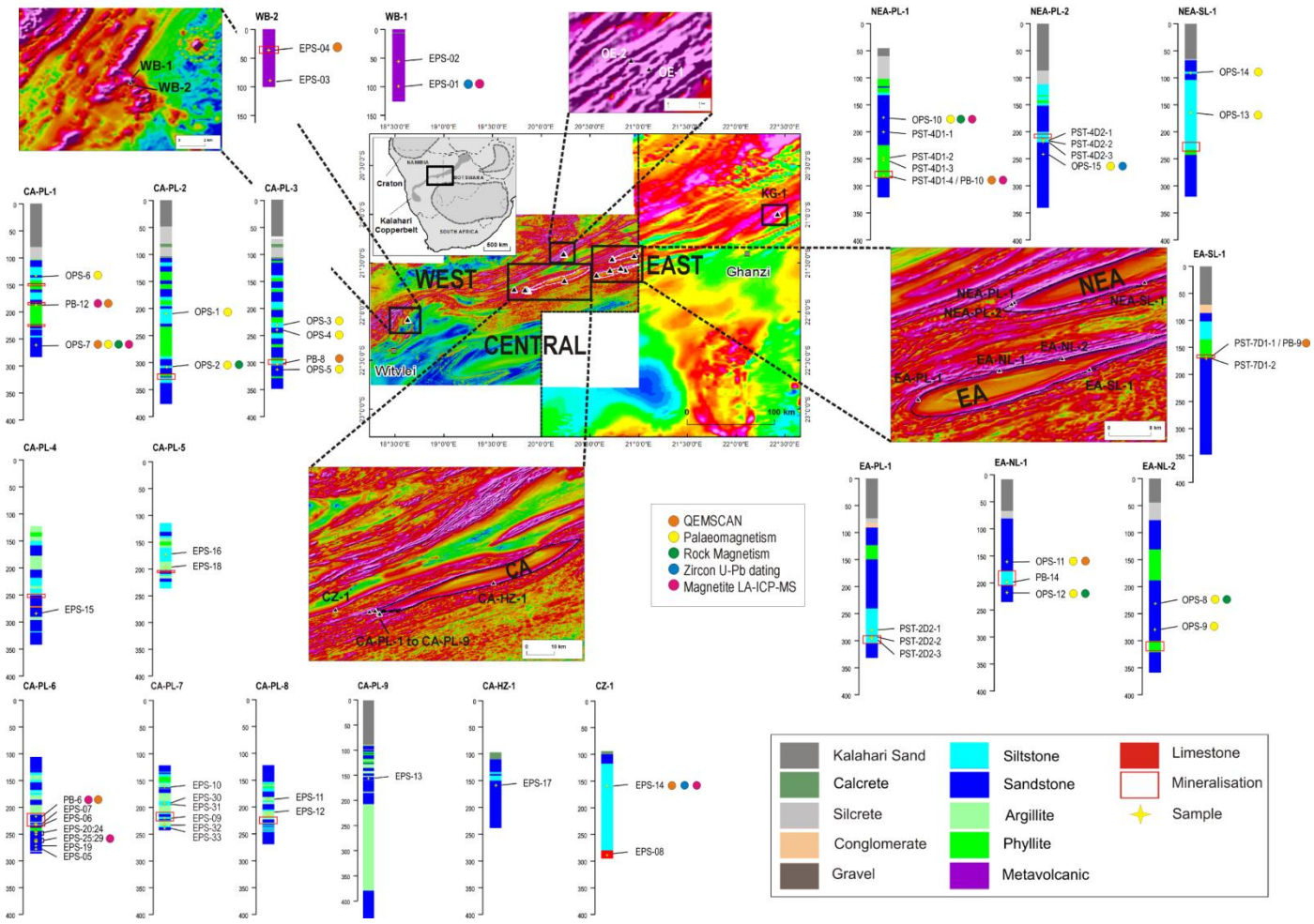

Figure 4-1: Summary of the geological information used in this study. The borehole/sample locations are shown on the Analytical Signal aeromagnetic maps of Namibia and Botswana provided by the Geological Survey of Namibia (www.mme.gov.na) and Department of Geological Survey (www.gov.bw), respectively. The boreholes names are shown in bold above the lithological logs, which were provided by EPM (2014). Boreholes are divided into lithotypes according to the geological logs provided by Eiseb Prospecting and Mining. Sample numbers are shown adjacent to the lithotype logs with yellow stars indicating the approximate position of the sample. Different coloured circles indicate the type of analyses carried out on a given sample.

Table 5: Summary information on the samples used during this study. The copper and silver ppm values were obtained from the Eiseb database. The 'Palaeo-mag' column refers to samples used for the palaeomagnetic study.

Sample	Drillhole	Lithotype	Stratigraphy	Depth	Cu ppm	Ag ppm	MG sample	ICP-MS	Palaeo-mag	Zircon	QEMSCAN
EPS-01	WB-1	MV	MV	98	112	BD	MG-1	√		ZR-01	
EPS-02	WB-1	MV	MV	64	432	BD					
EPS-03	WB-2	MV	MV	85	\	\					
EPS-04	WB-2	MV	MZ	33	32800	12.4	MG-3	√			√
EPS-05	CA-PL-6	SBX	FW	283	\	\					
EPS-06	CA-PL-6	SST	IBU	236	30	BD					
EPS-07	CA-PL-6	SLT	IBU	231.3	102	BD					
EPS-08	CZ-1	LST	FW	287.1	\	\					
EPS-09	CA-PL-7	SLT	IBU	219.3	1680	3.5					
EPS-10	CA-PL-7	SST	IBU	161.8	\						
EPS-11	CA-PL-8	ARG	IBU	188	36	BD					
EPS-12	CA-PL-8	ARG	IBU	214	22	BD					
EPS-13	CA-PL-9	SST	IBU	164.38	\	\					
EPS-14	CZ-1	SLT	HW	166	\	\	MG-14	√		ZR-02	√
EPS-15	CA-PL-4	SST	IBU	287	461	BD					
EPS-16	CA-PL-5	SLT	IBU	175	\	\					
EPS-17	CA-HZ-1	SST	FW	162.8	\	\					
EPS-18	CA-PL-5	ARG	IBU	196.5	31	BD					
EPS-19	CA-PL-6	SLT	FW	277.2	\	\					
EPS-20	CA-PL-6	SST	FW	245	\	\					
EPS-21	CA-PL-6	SST	FW	246	\	\					
EPS-22	CA-PL-6	SST	FW	247	\	\					
EPS-23	CA-PL-6	SST	FW	249.7	\	\					
EPS-24	CA-PL-6	SST	FW	250.8	\	\					
EPS-25	CA-PL-6	SLT	FW	260	\	\					

Table 5: *Continued*.

Sample	Borehole	Lithotype	Stratigraphy	Depth	Cu ppm	Ag ppm	MG sample	ICP-MS	Palaeo-mag	Zircon	QEMSCAN
EPS-26	CA-PL-6	SST	FW	262	\	\					
EPS-27	CA-PL-6	SST	FW	263	\	\	MG-4	√			
EPS-28	CA-PL-6	SST	FW	264	\	\					
EPS-29	CA-PL-6	SST	FW	265	\	\					
EPS-30	CA-PL-7	SLT	IBU	191	66	BD					
EPS-31	CA-PL-7	SLT	IBU	194	3	BD					
EPS-32	CA-PL-7	ARG	IBU	233	145	BD					
EPS-33	CA-PL-7	SST	FW	238	\	\					
KG-1	BM	V	BM	\	\	\	KG-1	√			
OE-1	BM	V	BM	\	\	\	OE-1	√			
OE-2	BM	V	BM	\	\	\	OE-2	√			
OPS-1	CA-PL-2	SLT	IBU	210.48	24	2			√		
OPS-2	CA-PL-2	SLT	IBU	310.26	1960	BD					
OPS-3	CA-PL-3	SLT	IBU	233.62	218	BD			√		
OPS-4	CA-PL-3	SST	IBU	242	88	BD			√		
OPS-5A	CA-PL-3	SST	FW	313.6	1250	BD			√		
OPS-5B	CA-PL-3	SST	FW	313.6	1250	BD			√		
OPS-6	CA-PL-1	SST	HW	133.94	8	BD			√		
OPS-7	CA-PL-1	SLT	FW	266.49	\	\	MG-13	√	√		√
OPS-8	EA-NL-2	SST	IBU	234.14	\	\			√		
OPS-9	EA-NL-2	SST	IBU	280.49	\	\			√		
OPS-10	NEA-PL-1	SST	IBU	176.98	\	\	MG-5	√	√		
OPS-11	EA-NL-1	SST	HW	155.43	\	\			√		√

Table 5: *Continued*.

Sample	Borehole	Lithotype	Stratigraphy	Depth	Cu ppm	Ag ppm	MG sample	ICP-MS	Palaeo-mag	Zircon	QEMSCAN
OPS-12	EA-NL-1	SST	FW	215.32	\	\			√		
OPS-13	NEA-SL-1	SLT	IBU	166.82	39	0.5					
OPS-14	NEA-SL-1	SST	HW	87.41	\	\			√		
OPS-15	NEA-PL-2	SST	FW	238.75	\	\			√	ZR-03	
OPS-12	EA-NL-1	SST	FW	215.32	\	\			√		
OPS-13	NEA-SL-1	SLT	IBU	166.82	39	0.5			√		
OPS-14	NEA-SL-1	SST	HW	87.41	\	\			√		
OPS-15	NEA-PL-2	SST	FW	238.75	\	\			√	ZR-03	
PB-12	CA-PL-1	PLT	MZ	186	16900	78	MG-12	√			√
PB-14	EA-NL-1	SLT	MZ	194	5420	62.4					
PB-6	CA-PL-6	SST	MZ	222.72	10400	17.5	MG-6	√			√
PB-8	CA-PL-3	SLT	MZ	305	6560	14					√
PST-2D2-1	EA-PL-1	SLT	IBU	280.83	148	15					
PST-2D2-2	EA-PL-1	SLT	IBU	293.5	132	1.5					
PST-2D2-4	EA-PL-1	SLT	MZ	303.6	6730	73.5					
PST-4D1-1	NEA-PL-1	SST	IBU	200.52	10	BD					
PST-4D1-2	NEA-PL-1	PLT	IBU	248.75	942	10.5					
PST-4D1-3	NEA-PL-1	PLT	IBU	255.72	92	1.5					
PST-4D1-4/ PB-10	NEA-PL-1	PLT	MZ	279.36	6040	75.2	MG-10	√			√
PST-4D2-1	NEA-PL-2	SLT	IBU	215.67	797	8					
PST-4D2-2	NEA-PL-2	SLT	IBU	215.82	446	4.5					

Table 5: *Continued*.**

Sample	Borehole	Lithotype	Stratigraphy	Depth	Cu ppm	Ag ppm	MG sample	ICP-MS	Palaeo-mag	Zircon	QEMSCAN
PST-4D2-3	NEA-PL-2	SLT	IBU	218.9	1980	15					
PST-7D1-1/ PB-9	EA-SL-1	PLT	MZ	168	3777	29.6					√
PST-7D1-2	EA-SL-1	PLT	MZ	170.5	3546	27.5					

4.2 Eiseb Data sets

An integral part of this study has been the utilisation of the geophysical, geochemical and geological information acquired by EPM over the last eight years (2008-2016). The geophysical data sets used during this study were primarily the airborne magnetic images: analytical-signal (AS), reduced-to-pole (RTP), total-magnetic-intensity (TMI), and various derivatives of these (1vd-RTP, etc.).

The geochemical data used for this study were from diamond drill core processed by accredited laboratories, while the geological data were gathered on-site during drilling by geological field teams.

4.2.1 Geophysical Data sets

The magnetic image products used during this study were based on composites compiled and processed by Greg Symons between 2011 and 2014 (Section 3.2.4). The composite were derived from high resolution airborne geophysical surveys carried out by the Namibian government's Geological Survey Department. These surveys were carried out between 1994 and 2008 at a 200m line spacing and a ground clearance level of 80m. Data were collected using fixed-wing aircrafts equipped with cesium-vapour magnetometers which sampled every 0.05 - 0.1 second. Tie-lines were spaced at 2500m, and the surveys were flown in a north-south orientation.

Greg Symons also compiled composites and processed high resolution aeromagnetic grid data purchased by Eiseb from the Geological Survey of Botswana. These surveys were flown between 1994 and 2004 by fixed-wing aircrafts using the Scintrex CS-2 magnetometer. Data was acquired using 250m line spacings at an average height of 75-80m above the ground. A sampling rate of 0.1 seconds was used, and tie-lines were spaced at 2500m.

4.2.2 Geochemical Data

4.2.2.1 Core Sampling Protocol

All diamonds drill core was split into equal halves. Samples were taken in the region of mineralisation with sample intervals not exceeding 1m in length and not less than 40 cm. Mineralised intersections were determined by the on-site geological team and core halves sent for analysis accordingly.

4.2.2.2 Laboratory Methodology

The Eiseb geochemical analyses on drill core, percussion and RC rock chips were processed by different laboratories at different times. The labs used were all accredited laboratories, and included Genalysis Laboratory Services, Bureau Veritas and ActLabs in Canada.

The laboratories used all followed similar methodologies; the methodology of Bureau Veritas is included herein as an example of the procedures used:

The samples have been sorted and dried. The primary preparation has been by crushing the whole sample and where necessary, samples have been split using a riffle splitter. The samples have then been pulverised in a vibrating disc pulveriser.

The samples have been analysed by firing a ~40 g portion of the sample. This is the classical fire assay process and will give total separation of gold, platinum and palladium in the sample. Au, Pt and Pd have been determined using Inductively Coupled Plasma (ICP) Optical Emission Spectrometry.

The sample(s) have been digested with mixtures of acids including hydrofluoric, nitric, hydrochloric and perchloric acids. This digest approaches a total digest for many elements, but some refractory oxides are not completely dissolved. Using this digest, some sulfur losses may occur if the samples contain high levels of sulfide.

Ag, As, Bi, Co, Mo, Ni and Pb concentrations have been determined by Inductively Coupled Plasma (ICP) Mass Spectrometry.

Cu and Zn have been determined using Inductively Coupled Plasma (ICP) Optical Emission Spectrometry.

4.2.2.3 Eiseb Quality Assurance and Quality Control (QAQC) Protocol

International standards, blanks and field duplicate samples were systematically inserted into the sample stream at a rate of 5% each. QAQA was carried out on each sample returned before results were entered into the database. The following criteria were used:

- Certified standards: If the result falls outside of the mean by more than three times the standard deviation then the batch has failed;
- Certified standards: If two or more consecutive results fall two standard deviations outside of the mean, on the same side of the mean, then the batch has failed;
- Blanks: If the result falls outside ten times the detection limit, then it is considered a warning.

If results failed the QAQC entire batches were re-submitted for analysis. The Certified Reference Material used are summarised in Table 6, and examples of blank chips in Table 7.

Table 6: Certified Reference Material used for QAQC.

Code	Certified Reference	Method	Cu	2SD	Unit
AMIS0036	Copper Sulfide Ore Kansanshi Mine, Zambia	ICP-OES	13806	630	ppm
AMIS0119	Copper Sulfide Ore, Reference Material From Kansanshi, Zambia	ICP-OES	6370	540	ppm
AMIS0128	Copper Sulfide Ore Reference Material from Kansanshi, Zambia	ICP-OES	15500	780	ppm
AMIS0161	Copper cobalt oxide ore Mukondo, DRC	ICP-OES	4535	200	ppm
AMIS0358	Copper cobalt oxide ore Mashitu project, DRC	ICP-OES	7580	314	ppm
AMIS0356	Rare Earth Elements Wigu Carbonatite Complex, Tanzania	ICP	\	\	ppm

Table 7: Example of blank chips used as reference material for QAQC procedures.

Code	Certified Reference	Method	Cu	SD	RSD%	Unit
AMIS0405	Blank Chips	ICP	8.6	2.6	30.6	ppm
AMIS0439	Blank Chips	ICP	6.7	2.4	36	ppm

4.2.3 Geological Data

Logs were compiled during drilling to record the changing geology. These logs always include information on depth, main lithotype, secondary lithotype, colour, shade, grain size and texture. The logs also contained information on structures, such as the angle of foliation/ bedding, or information about the perceived degree of weathering. However, due to the sporadic nature of these entries only the seven criteria listed were used in the data analysis, primarily the main lithotype and the colour.

4.3 Zircon U-Pb Geochronology

Three sites were selected from across the study area for detrital zircon U-Pb geochronology using LA-ICP-MS to determine likely provenance sources and maximum ages for the footwall, the hangingwall and the metavolcanics encountered in the west (Table 8: Summary of the samples used for Pb-U zircon geochronology.Table 8). These sites were selected in order to test the hypothesis that the footwall unit corresponds to the Ngwako Pan Formation, that the hangingwall corresponds to the D'Kar Formation, and to see how the age of the metavolcanic relates to these and known volcanic units in the region. A metavolcanic sample was sourced from WB-1 in the west (ZR-01), hangingwall from the central study area (ZR-02) and footwall from the east (ZR-03), as shown in Figure 4-2.

Table 8: Summary of the samples used for Pb-U zircon geochronology.

Sample	Borehole	Depth (m)	Lithotype	Location
ZR-01	WB-1	98	Metavolcanics	Metavolcanics
ZR-02	CZ-1	166	Siltstone	Hangingwall
ZR-03	NEA-PL-2	239	Sandstone	Footwall

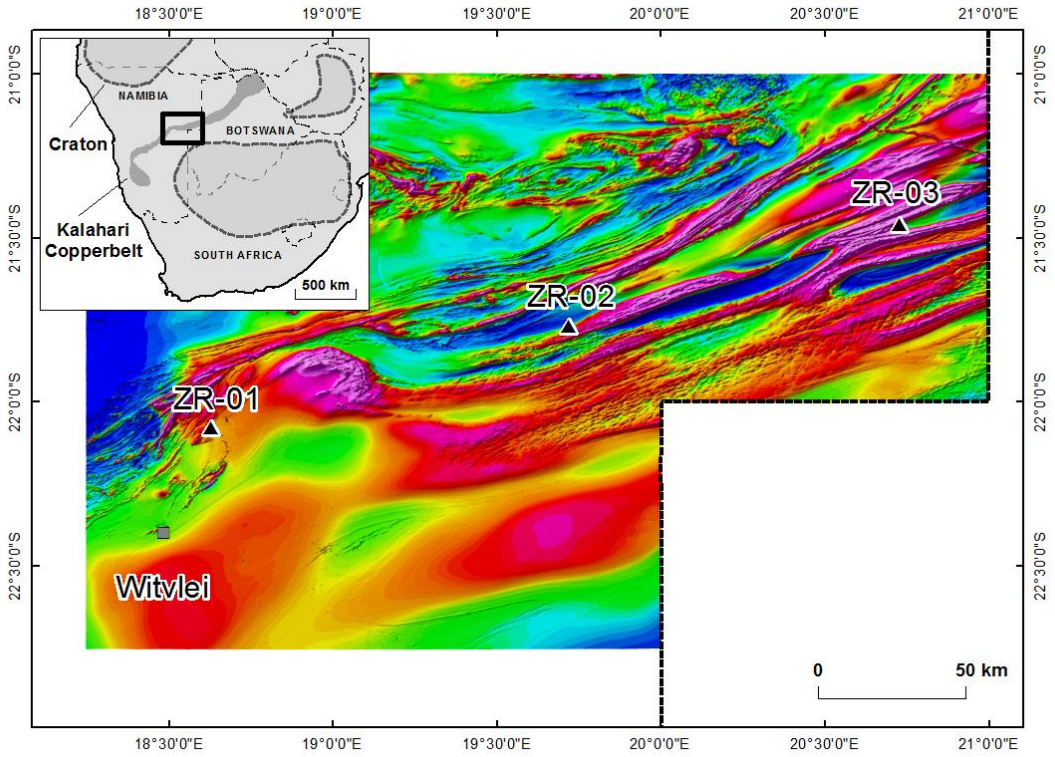

Figure 4-2: U-Pb geochronology sample locations shown on the Namibian government regional airborne magnetic survey Reduced-to-Pole image product.

In order to obtain a zircon-rich concentrate for zircon U-Pb dating each sample was crushed and milled to a medium sand grain size (0.063 mm to ~0.35 mm) and sieved down to remove

grains >300µm, as these are generally composite grains. U–Pb dating analyses were performed on polished grain mounts by laser ablation-inductively coupled plasma mass spectrometry (LA-ICP-MS) using a New Wave 193 nm aperture-imaged, frequency-quintupled laser ablation system, coupled to an Agilent 7700 quadrupole-based ICP-MS. The equipment is housed in the London Geochronology Centre at University College London. Real time data were processed using the GLITTER™ software package. Repeated measurements of external zircon standard Plesovice (TIMS age 337.13 ± 0.37 Ma; Sláma et al., 2008) and NIST 612 silicate glass (Pearce et al., 1997) were used to correct for instrumental mass bias and depth-dependent inter-element fractionation of Pb, Th and U. Use of time-resolved signals that record the evolving isotopic ratios with depth enabled data filtering to remove spurious signals related to boundaries between inheritance and overgrowths, or inclusions or hidden fractures. Data were filtered using standard discordance tests with a 15% cut-off.

In order to achieve 95% certainty that no fraction ≥ 5% of a given sample population was missed (Vermeesch, 2004) showed that at least 117 grains must be analysed per sample. This method provides a statistically robust image of what is potentially a complex source terrain, and was used to guide the number of grains analysed for this study.

The microprobe suite at Birkbeck College was used to take cathodoluminescence (CL) images of zircon grains to enable discrimination between inherited ages and later overgrowths.

4.4 Electron Microprobe Analyser (EMPA)

EMPA was carried out on almost all of the samples used for reflected and transmitted light work (Table 6). Mineral identifications were confirmed and augmented using the microprobe suite at Birkbeck College, University of London, which consists of a Jeol 8100 Superprobe with the attached Oxford Instrument energy dispersive system (EDS) using an INCA micro-analytical system.

EDS analyses were carried out using at an accelerating voltage of 15kV and a current of 1µA. Spectral information was gathered using a beam with a 1µm diameter using counting times of 20s for all elements on the peak and 10s each on the high and low backgrounds. EDS analyses were calibrated against standards of natural silicates, oxides and Specpure® metals with the data corrected using a ZAF program. Thirty repeat analyses were carried out on BCR-2 using EDS (Appendix I). The standard deviation on the results was <1 wt.% for all the measurements, and the results within the reported error limits for BCR-2 for all the oxides measured (Table 9)(Wilson, 1997).

Table 9: Summary statistics for the EDS QAQC using the BCR-2 reference material. The mean refers to the mean from the 10 repeat analyses, Stdev refers to the standard deviation for the repeat measurements, and BCR-2 shows the recommended values for oxides published by Wilson (1997).

		Na_2O	MgO	Al_2O_3	SiO_2	P_2O_5	K_2O	CaO	TiO_2	FeO
BCR2	Wt. %	3.16	3.59	13.5	54.1	0.35	1.79	7.12	2.26	12.4
	±	0.11	0.05	0.2	0.8	0.02	0.05	0.11	0.05	0.2
QAQC (*n*=40)	Wt. %	3.46	3.71	13.9	55.1	0.32	1.82	6.96	2.33	12.1
	±	0.09	0.07	0.13	0.44	0.06	0.06	0.11	0.10	0.21
Stdev	Wt. %	0.22	0.08	0.26	0.68	0.02	0.02	0.11	0.05	0.25

4.5 Quantitative Evaluation of Minerals by Scanning Electron Microscopy (QEMSCAN®)

QEMSCAN (Quantitative Evaluation of Minerals by Scanning Electron Microscopy; an FEI Inc. technology) combines a scanning electron microscope with automation software to allow ultrafast collection and processing of chemical and mineralogical data from a flat, carbon coated material (e.g. rock) surface. QEMSCAN provides rapid, automatic characterisation of different minerals/inorganic species on the basis of chemical spectra, combining SEM and EDS technology. The data produced by the QEMSCAN are quantitative and statistically robust, as well as visual, providing detailed chemical-mineralogical maps of a given sample (Wanhainen et al., 2014).

QEMSCAN collects data by scanning each sample as a series of fields (1.5 x 1.5mm) which overlap by a few µm. The stepping interval the user selects will determine the number of data points analysed within a field, i.e. the pixel size. In this study samples were scanned on a QEMSCAN Wellsite Instrument housed at University College London within the Department of Earth Sciences. Stepping intervals of 50µm, 10µm, 5µm and 1µm were used. A 10µm scan yields approximately 22,500 analysis points per field, as illustrated Figure 4-3.

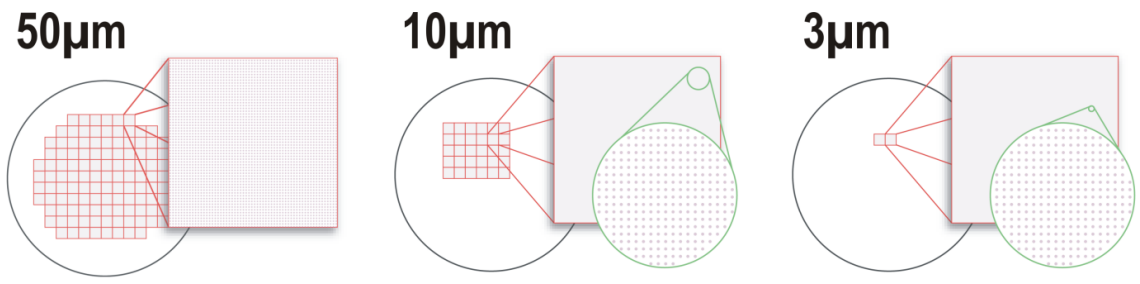

Figure 4-3: Schematic illustration of areas analysed by QEMSCAN, showing the relationship between the field size, the stepping distance and the number of measurements taken. The black circle represents the sample, red squares show the 1.5mm × 1.5mm fields and the red spots show individual data analysis points for measurement stepping intervals of 50µm, 10µm and 3µm. Image modified from http://www.rocktype.com/qemscan.

Initially backscatter electron images (BSE) are generated for each field to exclude areas with low BSE values, i.e. resin surrounding the sample, from the x-ray analysis. The electron beam

then scans areas of high BSE and dwells on each analysis point until sufficient x-ray counts (2000 spectra) have been recorded and the X-rays have been gathered by the EDS detectors. This information is then fed through an extensive X-ray spectral library of known mineral phases (Species Identification Protocol or SIP list), and a 'first match' principal is applied to identify the mineralogy of each analysis point, or pixel. These pixels combine to build up a detailed mineral map of the sample. Pixels which have low BSE are assigned to background and porosity. Pixels which have low count rates, or which returned low confidence results are mapped accordingly (http://www.rocktype.com).

The SIP identifies minerals in three broad phases. The SIP first compares the acquired spectra against known mineral compositions, if it is unable to match the spectra it moves to the second phase of identification which compares the spectra against synthetic mineral compositions. If the SIP is still unable to match the spectra the spectra are compared against what are called ‘trap definitions.’ The first type of classification is the most reliable in terms of mineral identification, while the trap definition has the loosest boundaries on its compositional requirements, and is therefore usually the least reliable. Trap definitions, however, are also used to define pixels along grain boundaries or rims where spectra may be mixed, or to account for mixed spectra due to textural intergrowths on a scale which is finer than the pixel size. If the SIP is unable to allocate the acquired spectra to any mineral definition, trap or otherwise, then the pixel is classed as ‘unclassified.’ Part of the process of authenticating the SIP results is reviewing the types of ‘trap’ definitions and their contribution to the modal mineralogy, and quantifying the unclassified material. It is important to note that the SIP is not a 'built in' feature of the QEMSCAN; it is something which is developed by the user to process the spectra collected by the QEMSCAN. As such, the SIP forms an integral part of the IP of any company using this technology.

This study was carried out in collaboration with Rocktype Ltd., a mineralogical company which specialises in QEMSCAN technology. Rocktype Ltd. not only provided access to their QEMSCAN Wellsite, but also allowed this project to benefit from the use of their SIP.

In this study measurements were gathered from eight grain mount polished thin sections and nine whole-rock samples. The grain mounts were prepared from crushed and milled rocks from which the magnetic fraction was separated using a hand-held magnet. During the milling process metal shavings from the mill discs were introduced into the samples. FEI’s iDiscover 5.4 software was used to identify and separate out this contamination and designate the pixels as ‘mill fragments.’ Of the 17 samples analysed using the QEMSCAN, five of the whole-rock samples are from rocks that were crushed for the grain mounts as per Table 10. The whole

rock samples were all measured at a stepping interval of 10µm, while for the grain mount (MG) samples stepping intervals of 50µm, 5µm and 1µm were used.

Table 10: Samples analysed using QEMSCAN. All samples prefixed with 'PB' are polished blocks and the whole rock samples are polished thin sections. Grain mount samples prefixed with 'MG' are thin sections.

Sample No.	Borehole	Lithotype	Location	Scan stepping interval	Representative whole-rock sample	Scan Stepping interval
MG-1	WB-1	Metavolcanic	Footwall	50µm, 5µm, 1µm	/	/
MG-3	WB-2	Metavolcanic	Mineralised zone	50µm, 5µm, 1µm	EPS-04	10µm
MG-5	NEA-PL-1	Sandstone	Hanging wall	50µm, 5µm, 1µm	/	
MG-6	CA-PL-6	Sandstone	Mineralised zone	50µm, 5µm, 1µm	PB-6	10µm
MG-9	EA-SL-1	Phyllite	Mineralised zone	50µm, 5µm, 1µm	PB-9	10µm
MG-10	NEA-PL-1	Phyllite	Mineralised zone	50µm, 5µm, 1µm	PB-10	10µm
MG-12	CA-PL-1	Phyllite	Mineralised zone	50µm, 5µm, 1µm	PB-12	10µm
MG-13	CA-PL-1	Sandstone	Footwall	50µm, 5µm, 1µm	OPS-7	10µm
PB-08	CA-PL-3	Siltstone	Mineralised zone	10µm	/	
OPS-11	EA-NL-1	Sandstone	Hangingwall	10µm	/	
EPS-14	CZ-1	Siltstone	Hangingwall	10µm	/	

Measurements for 34 elements were taken during this study: Na, Mg, K, Ca, Ti, V, Cr, Mn, Fe, Ni, Cu, Zn, Al, Si, P, S, Cl, C, O, F, Sr, Y, Zr, Ba, La, Hf, W, Sn, Pb, Ce, Th, Nd, U and Yb. The measurements were gathered using a beam current of 36 µA running at 15 keV (Table 11).

Table 11: Operational parameters summarised for the measurements taken during this study using the QEMSCAN.

	Whole Rock Measurements	Grain mounts (MG) measurement	Grain mounts (MG) measurement	Grain mounts (MG) measurement
Pixel size (µm)	10	50	5	1
Magnification (×)	125-173	266	266	266
Number of Pixels	2-6 million	40-110k	500-660k	2-4 million
Total Fields scanned	99-273	437-651	49	9

4.6 Laser Ablation Inductive Coupled Mass Spectrometry (LA-ICP-MS)

Grain mount polished sections from twelve locations were used for magnetite trace element analysis by LA-ICP-MS. Samples from the footwall and mineralised zone in boreholes CA-PL-6 and CA-PL-1 were used, as were footwall and mineralised zone samples from the metavolcanics in boreholes WB-1 and WB-2. The latter samples are considered as a continuous section as WB-1 and 2 are <50 m apart. The hangingwall and mineralised zone of NEA-PL-1 were also sampled, and one sample was analysed from siltstone of the barren hole CZ-1. Three outcrop samples were also taken from known Kgwebe Formation and Oorlogsende Member volcanics (Table 12).

Table 12: ICP-MS sample list.

Sample No.	Borehole	Depth (m)	Lithotype	Zone
MG-1	WB-1	98	Metavolcanic	Footwall
MG-3	WB-2	33	Metavolcanic	Mineralised zone
MG-4	CA-PL-6	263	Sandstone	Footwall
MG-6	CA-PL-6	222.72	Sandstone	Mineralised zone
MG-5	NEA-PL-1	176.98	Sandstone	Hanging wall
MG-10	NEA-PL-1	279.36	Phyllite	Mineralised zone
MG-12	CA-PL-1	186	Phyllite	Mineralised zone
MG-13	CA-PL-1	266.49	Sandstone	Footwall
MG-14	CZ-1	166	Siltstone	N/A
KG-01	\	0	Volcanic	Basement
OE-1	\	0	Volcanic	Basement
OE-2	\	0	Volcanic	Basement

The analyses were performed using an ESI NWR193 aperture-imaged frequency-quintupled laser ablation system (193 nm), coupled to an Agilent 7700x quadrupole-based ICPMS at the London Geochronology Centre, University College London. The beam size was set to 35µm with a pulse repetition rate of 9 Hz and an acquisition time of 35 s. Energy density was ~3.8kJ/cm^2. Background gas signals were measured for 20 s between individual analyses.

The following masses were measured: ^{24}Mg, ^{27}Al, ^{28}Si, ^{43}Ca, ^{45}Sc, ^{47}Ti, ^{51}V, ^{52}Cr, ^{55}Mn, ^{59}Co, ^{60}Ni, ^{63}Cu, ^{66}Zn, ^{69}Ga, ^{72}Ge, ^{89}Y, ^{90}Zr, ^{93}Nb, ^{95}Mo, ^{107}Ag, ^{118}Sn, ^{178}Hf, ^{181}Ta, ^{182}W, ^{208}Pb and ^{232}Th. Element concentrations were calculated based on these isotopes, assuming natural isotopic abundances. Repeated measurements of the National Institute of Standards and Technology (NIST) 610 and 612 synthetic glasses were used for quantification and to correct for instrumental mass bias and mass fractionation (Jochum et al., 2011).

Magnetite grains were scrutinised using EMPA prior to analysis to ensure that inclusions were identified and their hosting grains avoided during the LA-ICP-MS analysis. Nano-scale

inclusions could not be identified in this way, however. Therefore, the possibility of these being included in any given analysis cannot be excluded, but is assumed to constitute a negligible contribution to the overall results. No growth zones or ilmenite exsolutions were identified. The decision was therefore taken to do point analyses using the laser, rather than running trenches across grains to homogenise any compositional zonation or exsolutions. The resultant data were processed using GLITTER ™(Griffin et al., 2008).

4.7 Palaeomagnetic Methods

The paleomagnetic method is concerned with deciphering the 'magnetic memory' of a rock by determining the declination and inclination of the geomagnetic field of the Earth as recorded by the rock at the time of its formation (Dunlop and Özdemir, 2001; Tauxe, 2010). The ancient geomagnetic field for a given place on the Earth's surface can be used to locate the corresponding dipole axis known as a virtual geomagnetic pole (VGP). The strength of this method lies in the essentially centred dipole nature of the geomagnetic field, producing an axis of rotation which can then be used to determine the movements of tectonic plates and terrains through time and space (Dunlop and Özdemir, 2001; Tauxe, 2010).

Eight boreholes were used for palaeomagnetic testing from the central and eastern part of the study area (Figure 4-4). The selection of boreholes was based firstly on the availability of diamond drill core; and secondly on whether the orientation of the borehole had been surveyed. These criteria excluded core from mineralised zones because this core had already been halved and sometimes quartered for geochemical laboratory testing. There was also a limited amount of oriented core available from boreholes drilled on the southern limbs of the anticlines sampled, with the majority coming from northern limbs in the vicinity of the fold closures.

Where sufficient drill core was available a number of 10cm sections were extracted for a total of 12 core samples as summarised in Table 13. Four paleomagnetic specimens were drilled from each core sample for a total of 48 specimens. The specimens were cut to a non-standard size of 26mm and trimmed to 25mm lengths for laboratory testing.

Table 13: Summary of the samples used for palaeomagnetic testing.

Site No.	Sub-samples	Borehole	Depth (m)	Dip (˚)	Azimuth (˚)	Lithotype	Location
OPS-2	4	CA-PL-2	310	-70.3	153	Siltstone	Interbedded Unit
OPS-4	4	CA-PL-3	242	-72.9	153	Sandstone	Interbedded Unit
OPS-5	4	CA-PL-3	313	-70.2	153	Sandstone	Footwall
OPS-6	4	CA-PL-1	134	-72.4	174	Sandstone	Hangingwall
OPS-7	4	CA-PL-1	266	-68.4	172	Siltstone	Footwall
OPS-8	4	EA-NL-2	234	-66.6	178	Sandstone	Interbedded Unit
OPS-9	4	EA-NL-2	280	-65.9	179	Sandstone	Interbedded Unit
OPS-10	4	NEA-PL-1	177	-63.9	160	Sandstone	Interbedded Unit
OPS-11	4	EA-NL-1	155	-71.3	182	Sandstone	Hangingwall
OPS-12	4	EA-NL-1	215	-70.9	181	Sandstone	Footwall
OPS-14	4	NEA-SL-1	87.2	-71.6	339	Sandstone	Hangingwall
OPS-15	4	NEA-PL-2	239	-62.8	154	Sandstone	Footwall

The stability of the natural remanent magnetisation (NRM) was determined using two different techniques. Initially the NRM was determined by subjecting three of the four subsamples from each site to stepwise demagnetisation using alternating-field (AF) demagnetisation techniques, and one of the four subsamples to step-wise progressive thermal demagnetisation (Butler, 1992). For the AF technique the magnetic remanence was measured within a dynamic Helmholtz cage (<30 nT) at Imperial College London using the Agico JR5A. The Molspin Tumbling AF demagnetiser was used to AF demagnetise the samples in steps starting at 0 mT, 2 mT, 4 mT, 6 mT, 8 mT, 10 mT, 12 mT, 18 mT, 25 mT, 35 mT, 50 mT, 75 mT and 100 mT.

Thermal demagnetisation was carried out using a maximum of 15 steps using the ASC TD48 palaeomagnetic oven. The thermal demagnetisation steps were between 100˚C and 690˚C with reducing steps from 50˚C to 30/25˚C steps with increasing temperature. These steps were selected to cover the diagnostic unblocking temperatures of common magnetite minerals i.e. goethite (80-140˚C), pyrrhotite (260-340˚C), magnetite (500-580˚C) and hematite (600-675˚C) (Özdemir and Dunlop, 1997). To identify whether any laboratory induced magnetisation had been acquired through the heating or demagnetisation processes the subsamples were systematically re-oriented by 180˚ between steps.

Chips of rock from five samples were used to characterise the magnetic mineralogy (OPS-2, -7, -8, 10 and OPS-12). Chips were not necessary from all of the sites because of the proximity of these five samples the other sites, it was assumed that the results would be sufficiently representative of the area as a whole. They represent 5 of the 8 boreholes sampled and cover each of the three anticlines sampled. Magnetite had also already been identified using petrography, therefore the characterisation of the magnetic mineralogy was to confirm this

and ascertain whether any other minerals might also be contributing to the magnetic character of these rocks. Rock magnetic measurements were made on a Princeton Measurements Vibrating Sample Magnetometer (VSM), which measured room-temperature hysteresis curves using a maximum applied field of 700 mT. Thermomagnetic curves were conducted on these samples in a helium environment (to minimise alteration by oxidation) with an applied field of 100mT up to a maximum temperature of 720˚C and temperature step size of 1˚C.

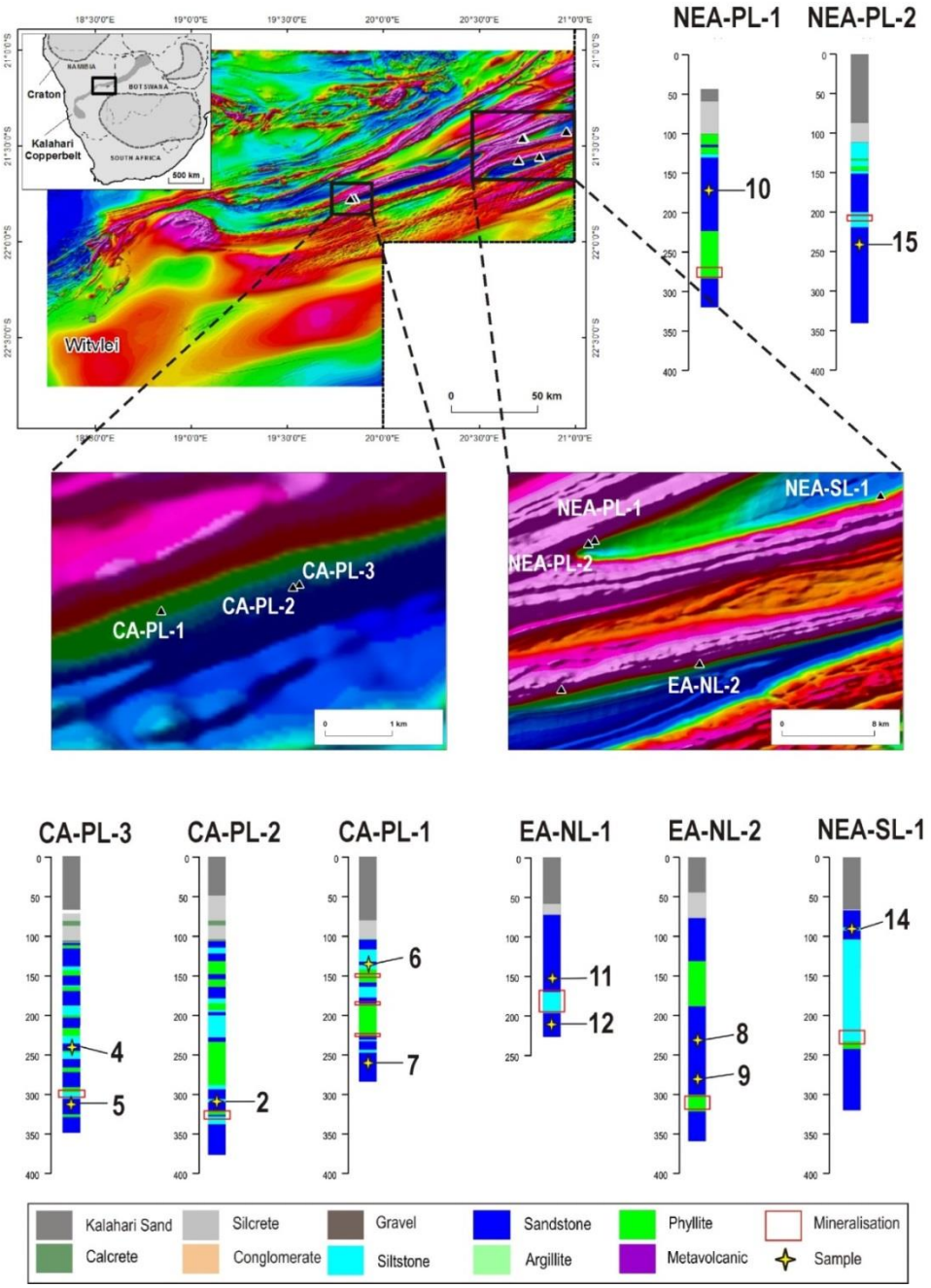

Figure 4-4: Overview of the locations of the boreholes sampled for the paleomagnetic study, as well as where in each borehole samples were taken. The sample numbers should be prefixed with OPS. The maps were made using the GSN regional airborne magnetic survey (www.mme.gov.na) Reduced-to-Pole image.

5 Results 1: Geology of the Eiseb

5.1 Eiseb data sets

5.1.1 Stratigraphy and geochemistry

5.1.1.1 Geological Logs

The rock types identified in the geological logs are volcanics, siltstones, sandstones, quartzites, argillites, phyllites and the Kalahari Group sediments (sand, calcrete and silcrete). An effort was made by the onsite geologists to distinguish between quartzites and sandstones, but because of the subjective nature of these divisions they have all been combined into sandstone for the purposes of this study. The terms argillite and phyllite are equally subjective. Phyllites were identified as very fine-grained (micaceous) 'schistose' rocks, while argillites were identified as very-fine grained but finely laminated, possibly even bedded rocks (Smalley, pers. comm., 2016). These distinctions, although admittedly subjective, have been retained because they potentially suggest something about the degree of deformation in these rocks.

Although all of the rocks within the Eiseb are known to have undergone regional greenschist facies metamorphism, the metamorphic overprint is weak and has generally not obstructed the recognition of the original rock types for either the volcanic or sedimentary rocks. The original rock names are thus used throughout and the prefix 'meta' omitted. The volcanic rocks from the western portion of the study area, however, show a much higher degree of deformation that the volcanics samples from the Oorlogsende Member and Kgwebe Formation to the north and east. The prefix 'meta' is therefore retained for the volcanics from the western block only.

5.1.1.2 Stratigraphic subdivisions

Dawborn (2012) divided the geology of the Eiseb area into 6 local stratigraphic units, as described in Section 3.2.2. Although valid for many areas within the Eiseb, these units often become difficult to distinguish where they have undergone complex structural deformation. These units were therefore simplified into the following (Figure 5-1):

- **Kalahari Group**: Sand, calcrete and minor silcrete;
- **Hangingwall**: Sandstone with occasional siltstone interbeds;
- **Interbedded Unit (IBU)**: Siltstone, argillite and phyllites interbedded with arkosic sandstones;
- **Footwall**: Sandstone to quartzite.

The Footwall units are tentatively correlated with the Ngwako Pan Formation and the Hangingwall and IBU with the D'Kar Formation after Dawborn (2012).

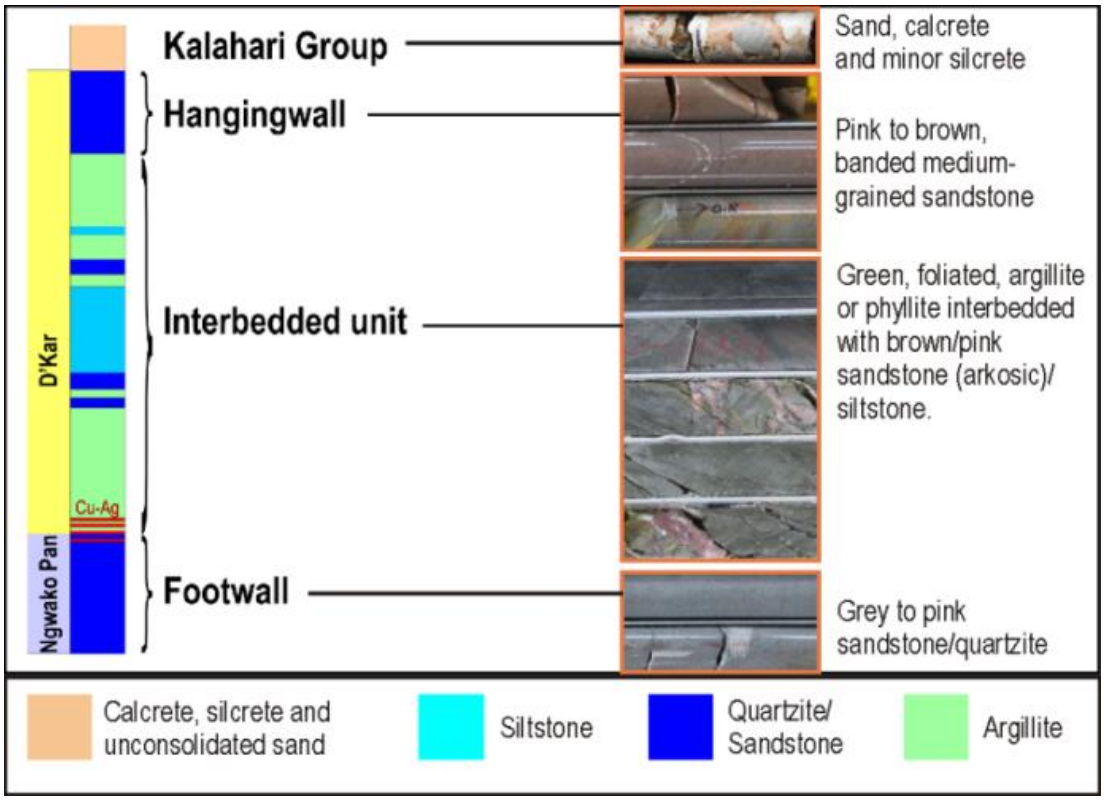

Figure 5-1: Correlation of lithological units in the study area with formation names of the Eiseb area. The Footwall is thought to correspond with the Ngwako Pan Formation and the Hangingwall and Interbedded Unit to the D'Kar Formation of the Ghanzi Group. Modified after Dawborn (2014).

Borehole summaries, which include stratigraphic subdivisions, lithological logs, idealised cross-sections and assay data for copper and silver, can be found in the Appendix II (Figure 5-2). The stratigraphic subdivisions devised in this way have been used throughout this work.

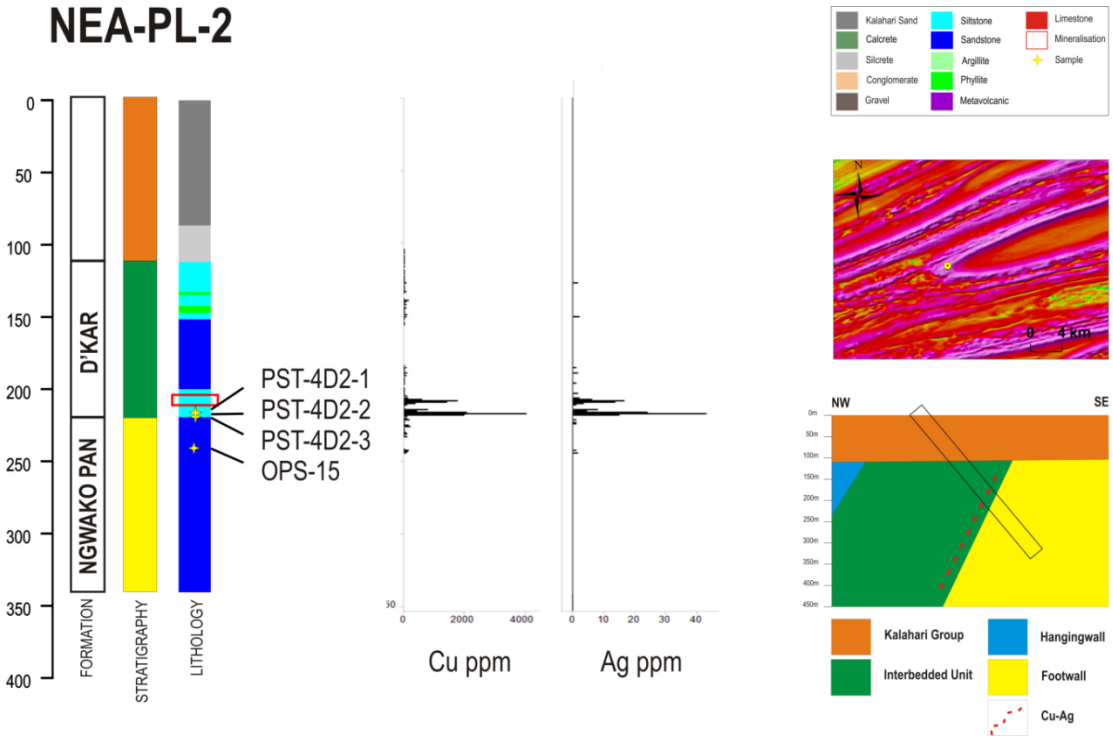

Figure 5-2: Example of the summary lithological and geochemical information contained within Appendix II. The geochemical data were compiled from assay data made available by Eiseb Prospecting and Mining. The location is shown on the Namibian Government airborne magnetic data (www.mme.gov.na) AS image.

5.1.1.3 Geochemistry

Assay data were made available for this study, but these data do not cover continuous intersections downhole, and they only cover 18 of the 20 holes investigated for this study (i.e. there are no data for CZ-1 and CA-HZ-1). Analyses were restricted to intersections either thought to be mineralised on the basis of the working assumption that mineralisation would be located in the fine-grained sediments immediately above the footwall sandstones (quartzites), or where mineralisation was observed in hand specimen. This has produced a somewhat erratic and biased dataset in favour of the Interbedded Unit. The elements analysed included Ag, Co, Cu, Mo, Ni, Pb and Zn. Data for the economically important elements Cu and Ag are presented in Figure 5-3, and these demonstrate a strong log-linear relationship between Cu and Ag (r^2=0.751).

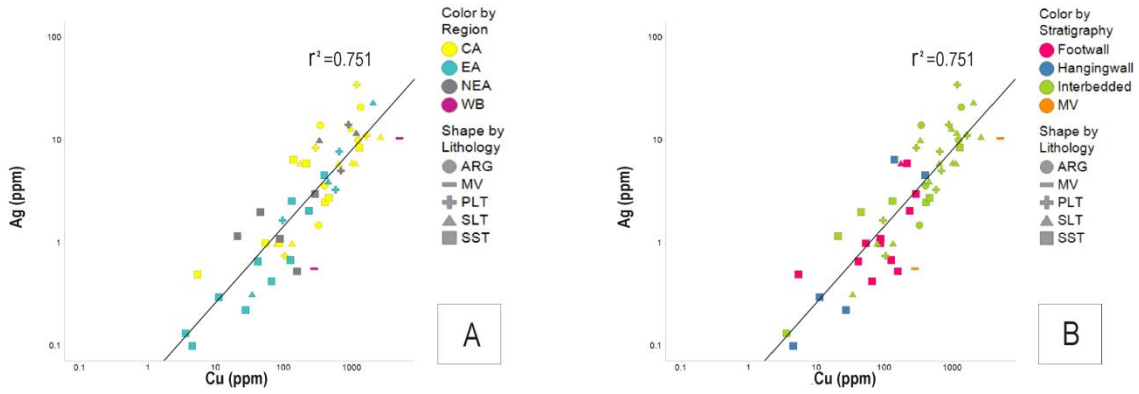

Figure 5-3: Scatterplots of the average Cu vs. Ag (ppm) for the 18 boreholes across the study area showing the strong correlation between these two elements. **A:** Boreholes from the Central Anticline (CA), Eastern Anticline (EA), and North Eastern Anticline (NEA) are highlighted using different colours to demonstrate that mineralisation is present, although variable, in all three anticlines. **B:** Mineralisation is also not restricted to the IBU, but is present in both hangingwall and footwall intersections.

The concentration of these elements appears to be lowest in the boreholes from Eastern Anticline; although the siltstones, which contain the bulk of the mineralisation report a range of values from 0.1 to 62.7 ppm for Ag; and 1 to 6584 ppm for Cu within the Interbedded Unit. The Central Anticline appears to have a higher portion of mineralised rocks from a range of rock types, but this may be an artefact of sampling density. The most important features of these graphs is that they demonstrate that mineralisation spans over all five major rock types (metavolcanic, argillite, phyllite, siltstone and sandstone) recorded in the Eiseb, and that mineralisation is present to some extent in all three stratigraphic horizons (Interbedded Unit, Footwall and Hangingwall).

Each stratigraphic unit contains a number of different rock types; therefore, trying to ascribe general geochemical characteristics to a stratigraphic unit is problematic, and by the same token, characterising rock types without reference to stratigraphic horizons also produces misleading results. The geochemical data are thus presented in two tables, one which illustrates how each element varies by rock type within each stratigraphic unit (Table 14), and the other which presents summary geochemical data for each stratigraphic unit in terms of its location within the basin (Table 15). A 'mineralised zone' has not been separated out in these tables as mineralisation occurs within a range of stratigraphic units, and lithotypes.

Table 14 shows that on average the highest Ag values are from the argillites of the Interbedded Unit at 11.1 ppm. These rocks also contain the highest average values for Co and Ni at 18.8 and 36.2 ppm, respectively. The phyllites of the Interbedded Unit have the highest average Zn (137 ppm), and the phyllites within the Footwall, the highest average Pb contents (235 ppm). The highest concentrations of Cu are from the metavolcanics, which contain an average of 1290 ppm. The metavolcanics, however, contain the lowest average concentrations

of Ni, Pb and Zn at 11.8, 7.32 and 42.6 ppm, respectively. These values are similar to those for the sandstone Hangingwall Units which contain average Ni, Pb and Zn concentrations of 13.9, 12.6 and 44 ppm, respectively. On average the lowest concentrations of Ag, Co, Cu and Mo are from the sandstone units within both the Footwall and Hangingwall Units. The Footwall contains on average 1.50 ppm Ag and 7.38 ppm Co, and the Hangingwall 99 ppm Cu and 0.81 ppm Mo.

The average values for Ag, Co, Mo, Ni, Pb and Zn shown in Table 15 are highest in the Interbedded Unit, particularly in the boreholes from the North East Anticline. The Interbedded Unit within the North East Anticline contains an average of 11.4 ppm Ag, which is very similar to that for the Central Anticline which reports 9.94 ppm Ag on average. The same is true for Co and Ni where the values for North East Anticline and Central Anticline are within ~5 ppm of each other. Average Mo values for the Interbedded Unit are also highest in the North East Anticline at 7.92 ppm, but are within 0.5 ppm of the North East Anticline Footwall Unit at 7.26 ppm. Zn is highest in the Interbedded Unit from the Eastern Anticline at an average of 144 ppm, similar to the 138 ppm from the Interbedded Unit within the North East Anticline. Pb values are also similar for the North East Anticline and the Eastern Anticline within the Interbedded Units at 129 ppm and 127 ppm, respectively. The highest average Cu is from the Metavolcanics at 1290 ppm, followed by the Interbedded Unit. Within the Interbedded Unit the average Cu contents is similar for all three locations sampled with the North East Anticline reporting 736 ppm Cu, the Eastern Anticline 562 ppm Cu and the Central Anticline at 652 ppm Cu. On average the lowest assay results are from the Hangingwall of Eastern Anticline for the elements Ag, Co, Cu, Ni, Pb and Zn. The lowest average Mo is the Eastern Anticline with the footwall containing 0.52 ppm and the Hangingwall 0.53 ppm. The low Ni and Pb concentrations from the Eastern Anticline Hangingwall (10.5 ppm and 6.8 ppm, respectively) are similar to the Metavolcanics which contains 11.8 ppm Ni and 7.32 ppm Pb.

Table 14: Summary geochemical information grouped by rock type and stratigraphic unit for the 18 boreholes sampled by Eiseb. All values are reported in ppm. ARG=argillite, PLT=phyllite, SLT=siltstone, SST=sandstone, MV=metavolcanic, IBU=interbedded unit, FW=footwall, HW=hangingwall, IBU = Interbedded unit, FW = footwall, HW = hangingwall, n=number of samples above detection limit, AVG=average, Min=minimum, Max=maximum, Med=median.

		Ag (n=669)					Co (n=1363)					Cu (n=1443)					Mo (n=982)				
Lithotype	**Stratigraphic Unit**	**n**	**Avg**	**Min**	**Max**	**Med**	**n**	**Avg**	**Min**	**Max**	**Med**	**n**	**Avg**	**Min**	**Max**	**Med**	**n**	**Avg**	**Min**	**Max**	**Med**
ARG	IBU	*22*	11.1	0.50	113	2	*225*	18.8	1	42	19	*225*	399	2	29200	42	*179*	3.59	0.50	50.5	1.50
PLT	FW	*0*					*0*					*2*	106	74	138	106	*2*	10	10	10	10
	HW	*0*					*0*					*0*					*0*				
	IBU	*221*	8.23	0	92	1.30	*358*	14.5	2	48	14.1	*385*	713	0	16900	92	*258*	5.13	0.20	69.5	1
SLT	FW	*1*	6	6	6	6	*6*	13	8	20	12	*6*	118	5	220	130	*2*	1	0.50	1.50	1
	HW	*0*					*0*					*0*					*0*				
	IBU	*258*	8.59	0	68.8	2.20	*371*	14.4	2	35	15	*383*	800	0	12000	102	*265*	7.35	0.10	215	1
SST	FW	*67*	1.50	0	21	1	*129*	7.38	1.70	20	6	*173*	153	1	2280	94	*73*	2.53	0.20	79	0.50
	HW	*23*	2.53	0	10	0.20	*32*	7.56	2	28	6	*37*	99	0	714	20	*16*	0.81	0.30	5	0.50
	IBU	*50*	2.93	0	25	1	*138*	10.3	3	29	10	*128*	439	0	10400	45	*83*	4.61	0.10	90	0.60
MV	MV	*27*	2.04	0.50	23	0.50	*104*	7.92	1	31	6	*104*	1290	24	50000	201	*104*	2.53	0.50	13.5	1.50

		Ni (n=1492)					Pb (n=1300)					Zn (1493)				
Lithology	**Stratigraphic Unit**	**n**	**Avg**	**Min**	**Max**	**Med**	**n**	**Avg**	**Min**	**Max**	**Med**	**n**	**Avg**	**Min**	**Max**	**Med**
ARG	IBU	*225*	36.2	4	84	36	*222*	30.5	1	437	16.5	*224*	112	28	180	116
PLT	FW	*4*	26.5	22	34	25	*2*	235	180	290	235	*4*	90.5	64	134	82
	HW	*0*					*0*					*0*				
	IBU	*388*	30.2	10	62	30	*343*	148	3	3880	40	*388*	137	28	1060	132
SLT	FW	*6*	28.2	20	42	26	*5*	34.8	10	59	35	*6*	109	96.0	140	104
	HW	*0*					*0*					*0*				
	IBU	*399*	27.9	8	106	28	*346*	108	1	3170	20	*399*	130	26	254	118
SST	FW	*181*	16.3	4	128	14	*120*	16.9	1	189	11	*181*	52.7	6	159	46
	HW	*40*	13.9	4	32	12	*22*	12.6	3	50	6.50	*40*	44.0	16	106	35
	IBU	*147*	27.1	3	1030	20	*136*	16.2	1	154	7	*147*	69.6	10	166	66
MV	MV	*102*	11.8	3	65	8.50	*104*	7.32	2	30	6.50	*104*	42.6	2	124	38

Table 15: Summary geochemical information grouped by stratigraphic unit and location for the 18 boreholes sampled by Eiseb. All values are reported in ppm. ARG=argillite, PLT=phyllite, SLT=siltstone, SST=sandstone, MV=metavolcanic, IBU=interbedded unit, FW=footwall, HW=hangingwall, n=number of samples, AVG=average, Min=minimum, Max=maximum, Med=median.

		Ag (n=669)					Co (n=1363)					Cu (n=1443)					Mo (n=982)				
Stratigraphic Unit	**Location**	**n**	**Avg**	**Min**	**Max**	**Med**	**n**	**Avg**	**Min**	**Max**	**Med**	**n**	**Avg**	**Min**	**Max**	**Med**	**n**	**Avg**	**Min**	**Max**	**Med**
FW	CA	*7*	3.79	0.50	10	2	*60*	8.75	2	20	8	*106*	159	1	1830	98	*22*	3.20	0.50	10	1
	EA	*39*	0.80	0	4.10	0.40	*39*	6.45	1.7	17.5	5.5	*39*	110	2	637	46	*39*	0.52	0.20	2.80	0.40
	NEA	*22*	2.23	0.20	21.0	1.50	*36*	7.06	3	16	6	*36*	172	4	2280	115	*16*	7.26	0.40	79	0.50
HW	CA	*8*	6.50	4	10	5	*17*	9.47	2	28	8	*22*	141	4	714	69	*1*	5	5	5	5
	EA	*15*	0.42	0	4.60	0.10	*15*	5.39	2.90	10.5	4.4	*15*	36.9	0	397	8	*15*	0.53	0.30	1.4	0.50
	NEA	*0*					*0*					*0*					*0*				
IBU	CA	*104*	9.94	0.50	113	4	*549*	14.8	1	48	15	*586*	652	1	29200	56	*314*	5.60	0.50	215	1.50
	EA	*281*	5.34	0	62.7	0.50	*281*	14.6	2.80	34.1	14.8	*281*	562	0	6590	57	*281*	3.68	0.10	69.9	0.40
	NEA	*166*	11.4	0	85.5	3.50	*262*	15.1	3	35	15	*254*	736	1	7710	93	*190*	7.92	0.50	111	1.50
MV	MV	*27*	2.04	0.50	23	0.50	*104*	7.92	1	31	6	*104*	1290	24	50000	201	*104*	2.53	0.50	13.5	1.50

		Ni (n=1492)					Pb (n=1300)					Zn (n=1493)				
Stratigraphic Unit	**Location**	**n**	**Avg**	**Min**	**Max**	**Med**	**n**	**Avg**	**Min**	**Max**	**Med**	**n**	**Avg**	**Min**	**Max**	**Med**
FW	CA	*116*	16.4	4	52	14	*52*	30.1	1	290	10	*116*	59.5	16	146	54
	EA	*39*	14	4	39	13	*39*	16	3	189	9	*39*	53.2	11	125	44
	NEA	*36*	21.5	8	128	16	*36*	13.3	7	27	12	*36*	43.8	6	159	35
HW	CA	*25*	15.8	4	32	14	*7*	24.9	4	50	20	*25*	48.2	16	106	42
	EA	*15*	10.5	5	20	11	*15*	6.80	3	20	6	*15*	37	18	75	28
	NEA	*0*					*0*					*0*				
IBU	CA	*616*	29.7	3	84	30	*505*	55.1	1	1670	20	*615*	103	10	180	106
	EA	*281*	26.9	8	51	28	*281*	127	3	3880	15	*281*	144	33	322	142
	NEA	*262*	35	9	1030	30	*261*	129	2	3170	30	*262*	138	16	1060	124
MV	MV	*102*	11.8	3	65	8.50	*104*	7.32	2	30	6.50	*104*	42.6	2	124	38

5.1.2 Geophysical data interpretation

5.2 Geological Mapping

Section 3.2.4 and 4.2.1 describes the geophysical data sets made available for this project. The magnetic image products generated by Greg Symons for Eiseb (2011-2014) and used in this study include AS, RTP, TMI, and various derivatives of these (1vd-RTP, etc). A geological map of the area was produced by Dr Smalley using the rationale illustrated in Figure 5-4 and Figure 5-5.

FORMATION	MAGNETIC CHARACTER	EXAMPLE
MAMUNO FORMATION	Occassional peaks in magnetic response, but generally low and featureless	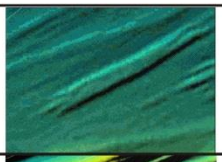
D'KAR FORMATION	Laterally continuous units with strong linear magneric trends. Defines a regional fabric	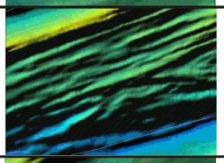
NGWAKO PAN (± Kuke Formation)	Consistently low magnetic response	
KGWEBE FORMATION	Strong magnetic response, erratic texture. Broader linear features than D'Kar Formation	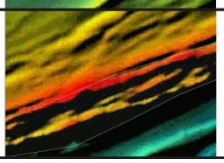

Figure 5-4: Summary table illustrating the rationale used to map the geology of the Eiseb area. The example images are taken from a regional TMI composite of aeromagnetic survey data provided by the Geological Survey of Namibia (www.mme.gov.na) and Department of Geological Survey, Lobatse, Botswana (1994-2008) (www.gov.bw).

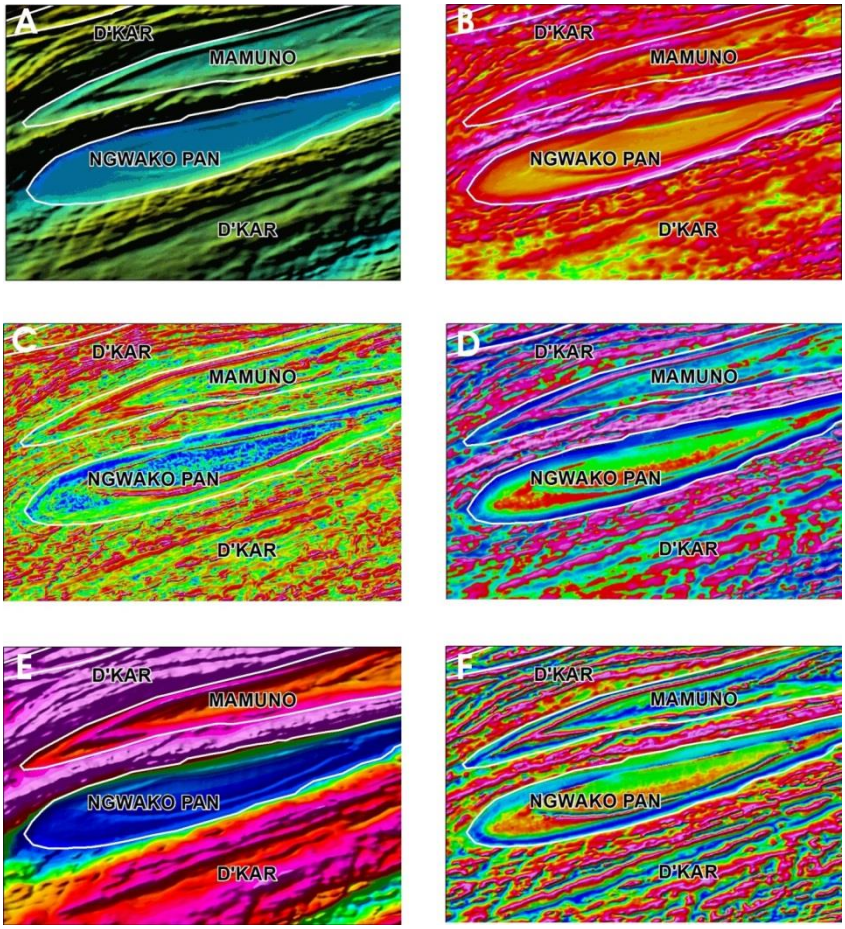

Figure 5-5: Example of geological mapping of the Eiseb area using Namibian government regional aeromagnetic survey data (www.mme.gov.na). (A) Total Magnetic Intensity (TMI); (B) Analytical Signal (AS); (C) RTP total horizontal derivative (RTP-THD); (**D**) RTP first vertical derivative (RTP-1VD); (**E**) Reduced to Pole (RTP); (**F**) Tilt derivative of the RTP (RTP-TDR). The location shown is the fold closure of the east anticline (EA).

Earlier studies which attempted to correlate and map the geology of Namibia and Botswana beneath the Kalahari sediments using regional airborne magnetic maps were consulted for this study, namely Hutchins and Reeves (1980) and Meixner and Peart (1984). More recently, Lehmann et al. (2015) produced a geological map of Namibia and Botswana using mostly the same regional Namibian and Botswanan government airborne magnetic survey data, and in a similar manner to the map created by Dr Smalley. The boundaries defined by Lehman et al. (2015) have been compared against the available borehole data for this study in an attempt to ground-truth the mapping. Limited structural mapping has also been carried out for this study.

5.2.1 Ground-truthing the Lehmann et al. (2015) geological map

In general the portion of geological map presented by Lehman et al. (2015) (Figure 5-6) which covers the Eiseb area is in agreement with the available borehole data, except for the mapping of the Kgwebe Formation.

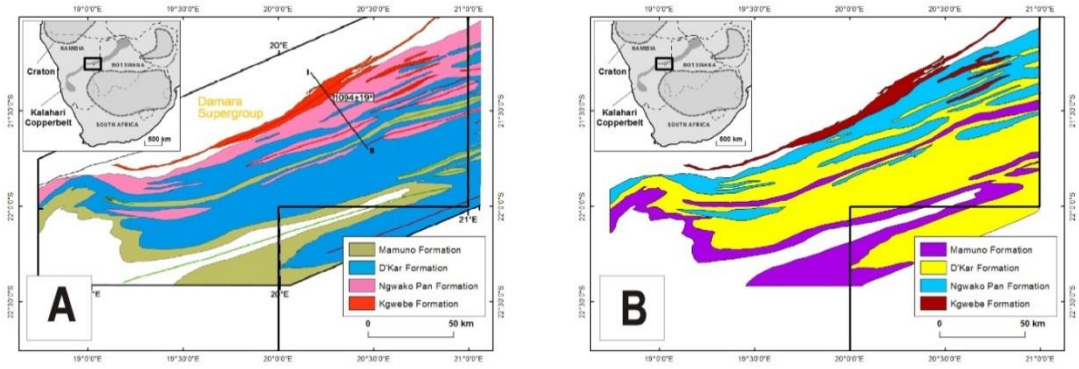

Figure 5-6: Geological map of the Eiseb section of central Eastern Namibia from Lehmann et al. (2015) (**A**) was geo-referenced and redrawn using ArcGIS (**B**) and the colours changed to reflect the convention used for this study.

Drilling in the north of the study area, where Lehmann et al. (2015) mapped the Kgwebe Formation, was in agreement with the results of scattered drilling in the region which confirmed the presence of volcanics, schists and gneisses. Areas of concern are the elongate Kgwebe Formation bodies mapped just to the east of this. Drilling from ten boreholes across one of these features recorded sandstones, phyllites, siltstones and argillites, but nothing to suggest the Kgwebe Formation (Figure 5-7). These intersections are more indicative of the D'Kar Formation, which has been mapped to the north and south of these features. The Kgwebe in this region has therefore been remapped as D'Kar Formation.

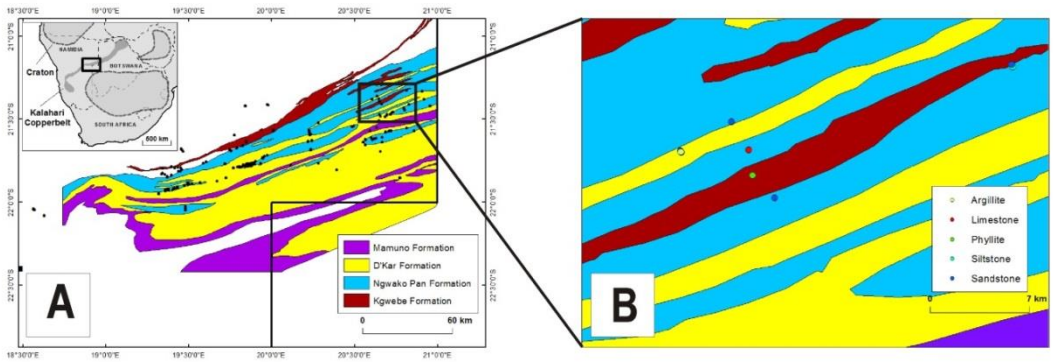

Figure 5-7: Geological map of the Eiseb area (after Lehmann et al., 2015) overlain by the Eiseb borehole locations (black dots). The lithotypes first intersected below the Kalahari Group (B) were used to validate the geological mapping in this area.

The remainder of the geological mapping was compared in the same way to the Eiseb geological database and no other significant differences were noted. Therefore, no further adjustments have been made to the geological map presented by Lehmann at al. (2015) for the Eiseb study area.

5.2.2 Structural Mapping

The various aeromagnetic image products that were used to map structures in the Eiseb area were the AS, RTP, RTP-1VD, TMI and TDR. Figure 5-8 shows an example of how this was done using the RTP magnetic image product.

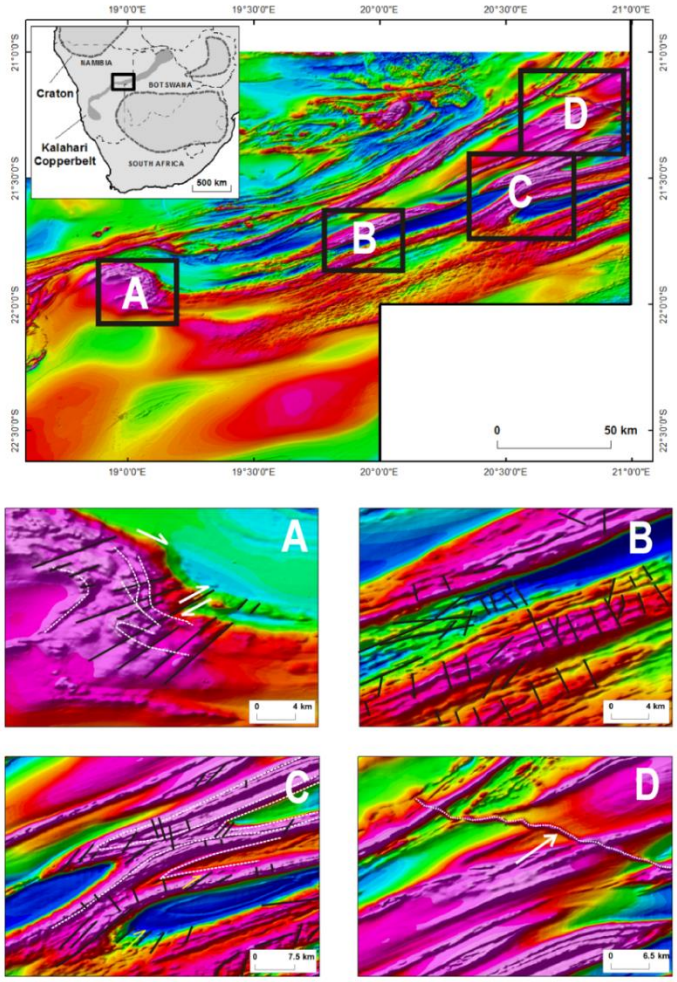

Figure 5-8: Deciphering of the sense of shear on the large rotational feature in the Eiseb area using the RTP magnetic image rendered from the Namibian governments regional aeromagnetic survey data (www.mme.gov.na). In this area NE-SW tending faults also show a dextral sense of movement (**A**). NNW-SSE faults along fold limbs are interpreted as axial planar cleavage on the central anticline (**B**), although the orientation of these shifts to a more NNE-SSW orientation towards the east (**C**). Late stage Karroo dolerite dykes are also easily identified in the magnetic image products as these form distinct NW-SE trending lineations which do not appear to disturb the underlying lithotypes (**D**). Faulting thought to be associated with rheological contrasts is shown as dotted white lines.

The most common structural features mapped during this study were faults perpendicular to fold limbs which trend NNW-SSE in the central study area and rotate to the east in the eastern study area to an almost N-S to NNE-SSW orientation in NEA and EA. In the southern D'Kar Formation units longer, >10 km NNE-SSW trending faults can also be seen in the magnetic image maps (Figure 5-9). There is no obvious sense of the timing of these faults, as neither appears to offset the other, so it is possible that they are coeval. The NW-SE orientation of the Karoo dyke swarms in both Namibia and Botswana is perpendicular to the main rift axis (Figure 5-8D). Bedding parallel thrust faults/shear zones between the D'Kar and Ngwako Pan Formation are evident throughout the study area, particularly on northern fold limbs, with local overthrusting common.

Regardless of the magnetic image produce used to view the Ngwako Pan Formation strata, faults are very rarely observed (Figure 5-5). This does not imply that these rocks are not faulted, an absence of faulting in thick sandstone packages is very unlikely. Rather, there is no observable magnetic signature to the faulting in this formation.

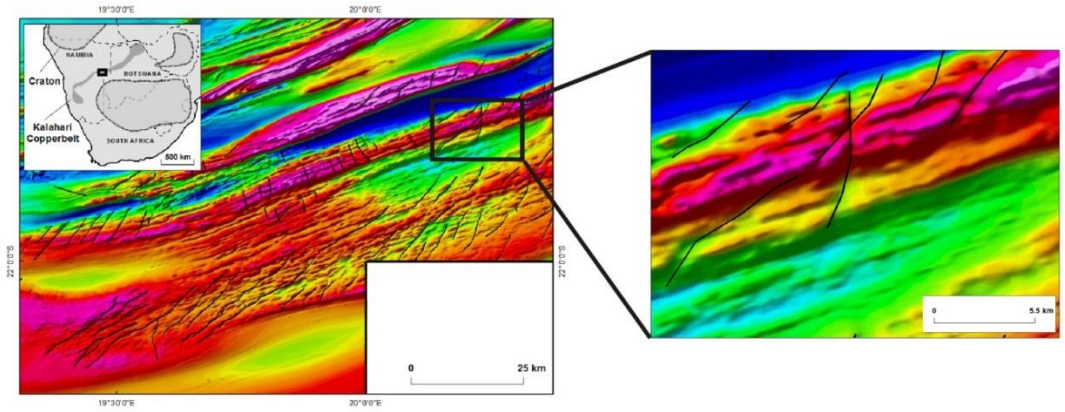

Figure 5-9: RTP image from the Namibian government regional aeromagnetic survey data from the southern portion of the Eiseb (www.mme.gov.na). The long (5-10 km), sinuous NNE-SSW/NE-SW faults contrast the short (2-4 km) axial faulting oriented NNW-SSE.

The overall sense of movement across the Eiseb is dextral, which is seen on a basin-scale (Figure 5-10) as well on the scale of individual faults. The NNE-SSW/NE-SW trending faults illustrate this sense of movement.

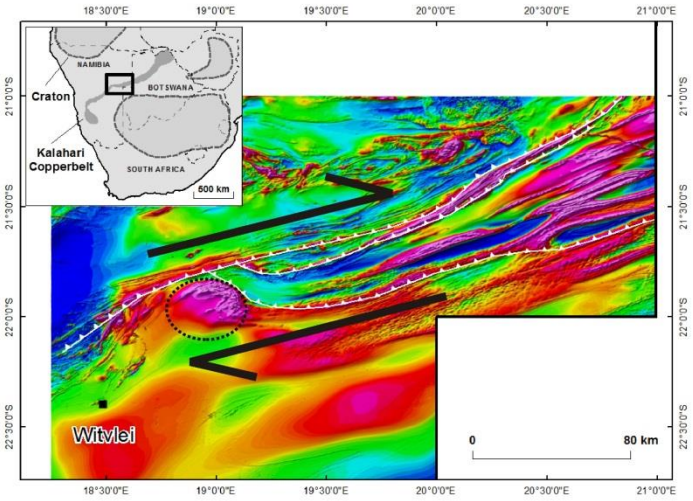

Figure 5-10: RTP magnetic image rendered from the Namibian governments regional aeromagnetic survey data (www.mme.gov.na). This shows the overall sense of movement across the Eiseb (black arrows) in relation to the southern Damara Thrust Zone (*pers comm.* Corner, 2015) shown in white. The dotted black line shows the outline of inferred rotated basement horst.

The western portion of the study area is dominated by a large, magnetically prominent feature interpreted as a basement horst. There is a distinctive rotation of the rocks to the east around this feature where the strata appear to ramp on to the horst and pinch out further west of this block. The geology to the west of the horst shows a distinctly different magnetic signature to those of the east, with the rocks showing much thinner linear trends of a much more magnetically consistent nature. The Witvlei, Dordabis and Klein Aub deposits all occur to the west of the horst. The uplift and dextral rotation of this horst likely occurred during the Pan African Damara Orogeny.

A geological map is presented in Figure 5-11 which illustrates the main structural features of the Eiseb area.

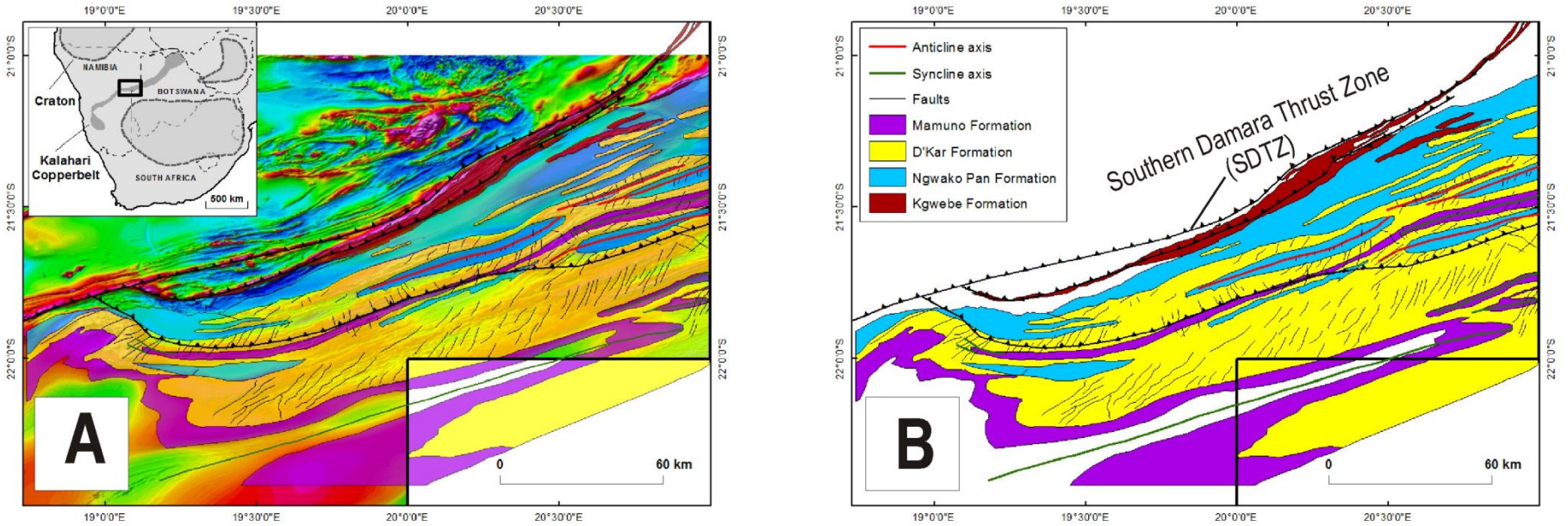

Figure 5-11: Geology and main structural features of the Eiseb, modified after Lehmann et al. (2015). **(A)** is shown with a 30% transparency overlain on the RTP image product of the Namibia government's regional airborne magnetic survey data (www.mme.gov.na). The map is also shown without the magnetic image underlay (**B**).

5.3 Zircon Geochronology

Although an attempt was made to analyse at least 120 zircons from each location, for sample ZR-01 from the metavolcanic rock (WB-1) only 57 zircons were analysed (Figure 5-12); 97 zircons were analysed from sample ZR-02 (CZ-1)(Figure 5-13: U-Pb concordia plots of the detrital zircon grains for ZR-02. The red ellipses represent the analyzed grains, and include an internal 2-sigma error. Plot drawn using Isoplot (ver. 4.1).Figure 5-13) and 125 zircons from sample ZR-03 (NEA-PL-2) were analysed (Figure 5-14). This was due to the fact that in some instances the grains analysed were not zircons, or readings were taken too close to the edge of the zircon grains, making the results unusable. Although less than 60 grains were dated for ZR-01, Vermeesch (2004) showed that there is still 95% confidence that no fraction ≥ 0.085 was missed, but that the maximum probability of having missed at least one fraction > 0.055 is ~64% (Appendix III). The results were analysed using Isoplot (ver. 4.1) (Ludwig, 1991).

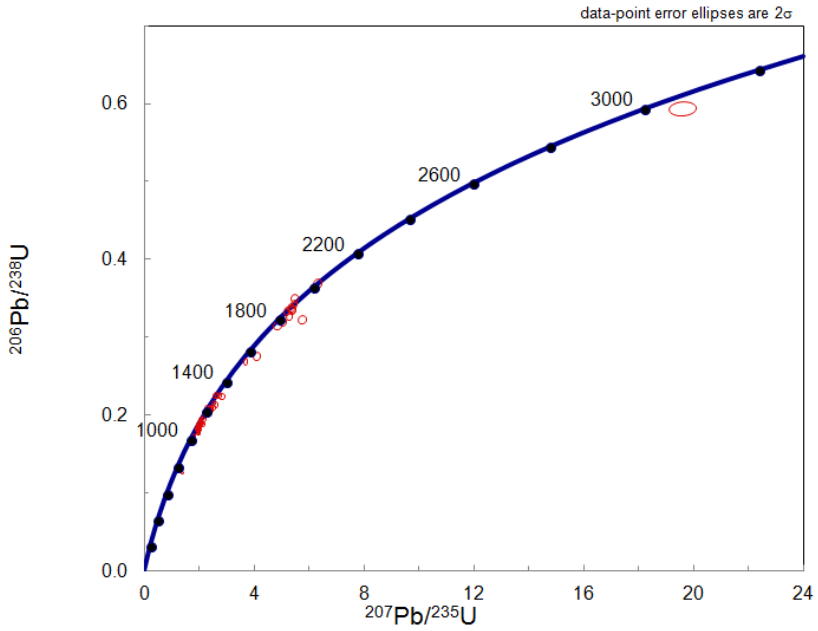

Figure 5-12: U-Pb concordia plots of the detrital zircon grains for ZR-01. The red ellipses represent the analyzed grains, and include an internal 2-sigma error. Plot drawn using Isoplot (ver. 4.1).

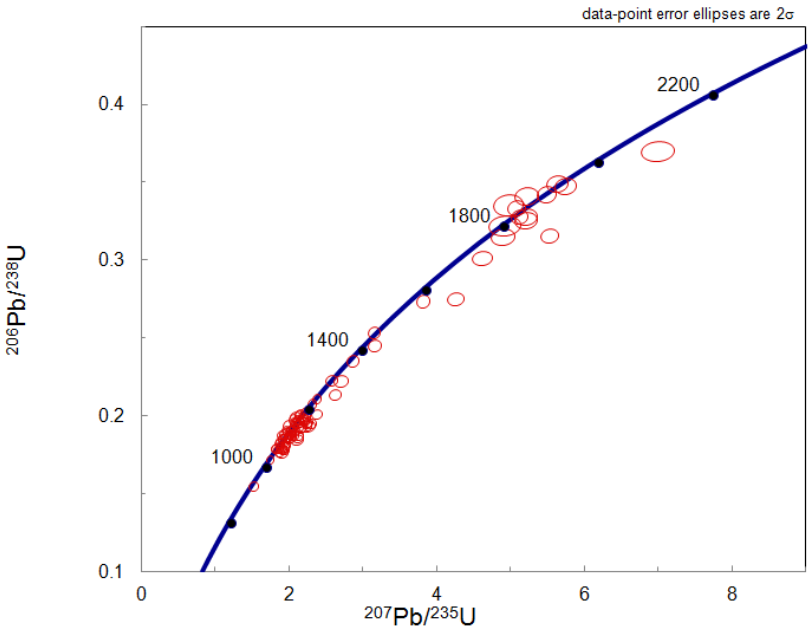

Figure 5-13: U-Pb concordia plots of the detrital zircon grains for ZR-02. The red ellipses represent the analyzed grains, and include an internal 2-sigma error. Plot drawn using Isoplot (ver. 4.1).

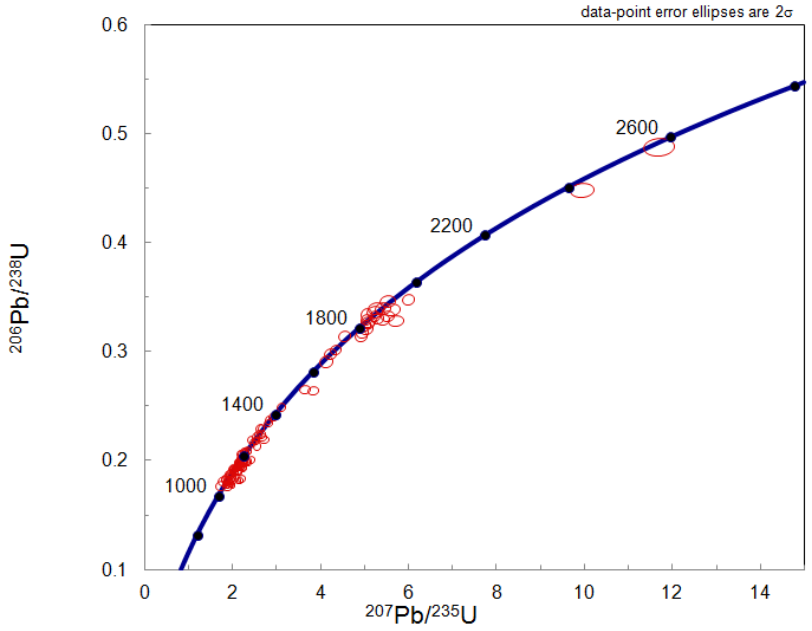

Figure 5-14: U-Pb concordia plots of the detrital zircon grains for ZR-03. The red ellipses represent the analyzed grains, and include an internal 2-sigma error. Plot drawn using Isoplot (ver. 4.1).

The majority of the grains analysed plot on concordia, save for ZR-02, which shows a number of discordant ages (Figure 5-13). Most of the ages cluster in two age ranges, between 1000 Ma and 1400 Ma and between 1800 Ma and 2000 Ma.

Texturally the grains from ZR-02 are slightly smaller than those of ZR-01 and ZR-03, ranging from ~60x35µm and ~100x75µm (Figure 5-15). The zircon grains from sample ZR-01 range

from ~100x60µm to ~150x80µm. The smaller grains are generally subhedral to equant with few prism facets. The large grains, which are the majority, are euhedral to subhedral with prismatic terminations and elongate crystal shapes. On average the euhedral to subhedral grains in ZR-03 are ~80µm in length and 45µm wide. Under cathode luminescence the zircon grains in all of the samples show good compositional zoning, and none are sufficiently rounded to suggest long transport distances from source rocks, although some are clearly only fragments.

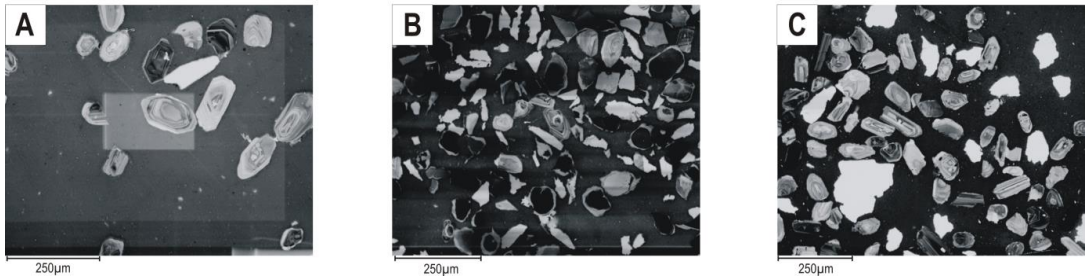

Figure 5-15: Cathode luminescence images of zircon grain mounts. **A:** the metavolcanic sample ZR-01 (WB-1); **B:** ZR-02 from borehole CZ-1; and **C:** Sample ZR-03 from borehole NEA-PL-2.

Figure 5-16 shows density plots of the sample data and the main age peaks. The samples all showed a strong bimodal distribution of ages from the Mesoproterozoic and the Paleoproterozoic with some outliers. The Mesoproterozoic ages for the samples are similar across the sample group, with the oldest grains recorded for the hangingwall sediments of ZR-02 at 1173.9 ± 5.2 Ma. The Palaeoproterozoic ages are similar for the hangingwall and footwall samples ZR-02 and ZR-03 (1876 ± 13 Ma and 1891.2 ± 3.8 Ma respectively), but are significantly older for the metavolcanic rock which indicate an age of ~1939 ± 11 Ma. The significance of these findings is discussed in detail in Section 7.1.1.

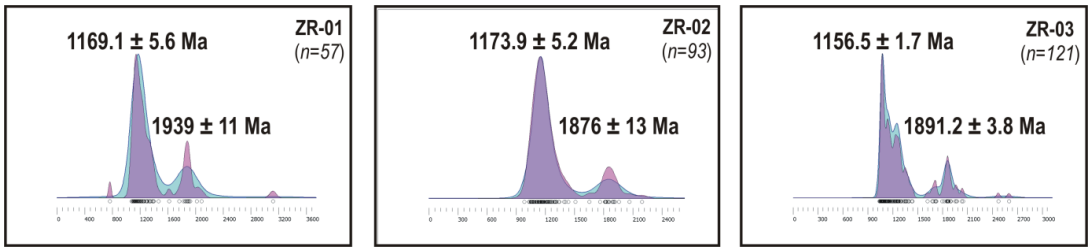

Figure 5-16: U-Pb ages for detrital zircons in the Eiseb study area. The main age peaks were extracted using the normal mixture modelling algorithm of Galbraith (2005) using the Densityplotter (ver.7.0) (Vermeesch, 2012).

5.4 Petrography: Optical and EMPA

The results from transmitted and reflected light work will be reported together with the results of the EMPA and the QEMSCAN®. The samples have been separated out into their respective locations within the basin and will be discussed according to the location of the sample within the stratigraphy, i.e. hangingwall, footwall or mineralised zone. Samples from the EA and NEA boreholes are grouped as the East; and the CA and CZ borehole samples are grouped as Central. The WB borehole samples (West) are taken from metavolcanic rocks, therefore these will be discussed separately. Three samples were taken as representative of basement, two from outcrops of the Oorlogsende Member just north of the study area and one from a quarry where Kgwebe Formation geology is partially exposed. The results are presented in the following section.

5.4.1 Basement volcanics

5.4.1.1 Kgwebe Quarry Sample

The rock has a fine-grained matrix and a porphyritic texture. The dominant phenocrysts are anorthoclase, sanidine and quartz which average ~1mm in length but can be as small as 100µm, and often occur as aggregates. The matrix is composed of fine-grained quartz (Figure 5-17).

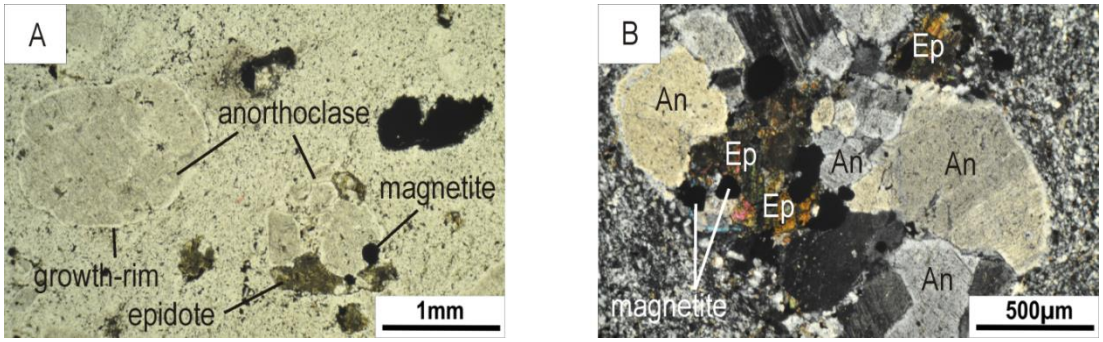

Figure 5-17: Photomicrograohs of sample KG-1 from the Kgwebe Formation quary in Botswana. Under PPL (**A**) the growth rims which surround many anorthoclase phenocrysts are seem as white halos. Magnetite often forms embayments into these phenocrysts and is commonly associated with altered epidote (**A & B**). **B** taken under XPL.

The dominant phenocryst is anorthoclase which occasionally shows late-stage growth rims but these are cryptocrystalline so difficult to identify. Microcline was also observed, and as with the other phenocrysts, contains abundant fine-grained subhedral inclusions of a high relief second order birefringence mineral, possibly epidote. This altered epidote occurs within the groundmass, surrounding anorthoclase phenocrysts, or in an intergranular texture with polycrystallibe phenocrysts (Figure 5-17). Zircon is a common accessory phase.

There is some evidence of deformation in the form of undulose extinction and subgrain formation. Rare calcite was also identified.

Under transmitted light the opaque minerals have a bimodal distribution of equant minerals ranging in size from >250µm to <50µm, and a second population of anhedral opaques which occur disseminated throughout the groundmass and are <10µmin size on average.

The equant opaque minerals were identified using EMP as Ti-bearing magnetite, reaching up to 5.95 wt.% Ti in one magnetite crystal. One magnetite phenocryst was found to contain 1.5 wt. % Zn (Figure 5-18). The anhedral opaque minerals were identified as barite. Magnetite is commonly fractured and the fractures filled by apatite. Apatite is in turn commonly surrounded by barite suggesting a paragenesis of magnetite -> apatite -> barite. Zircon also appears to post-date magnetite.

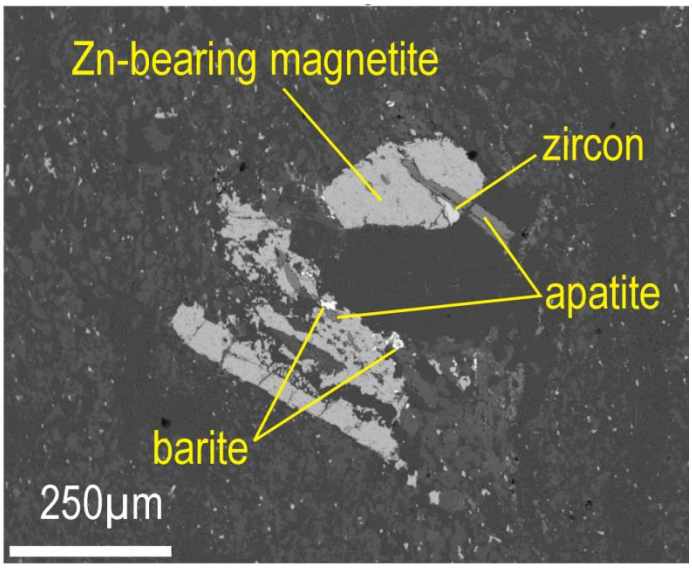

Figure 5-18: Backscatter electron microphotograph of the main opaque phases found in KG-1: magnetite and barite.

5.4.1.2 Oorlogsende Member: OE-1

The rock has a fine-grained matrix and a porphyritic texture. The phenocrysts identified in this rock were anorthoclase and sanidine roughly equal portions. Quartz phenocrysts showing undulose extinction were also identified, as was rare microcline. On average the phenocrysts were ~1.1mm long but they range from ~2mm to ~0.1mm (Figure 5-19) and are often polycrystalline.

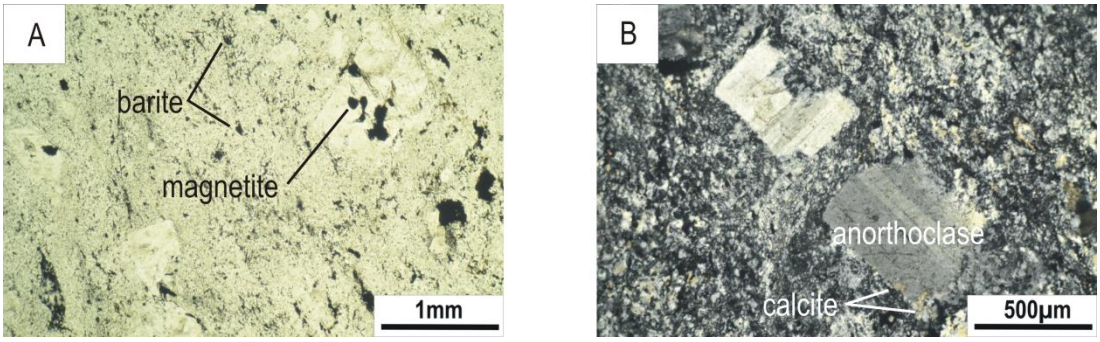

Figure 5-19: Photomicrographs of the Oorlogsende Member sample OE-1 showing, **A:** the common occurrence of the opaque minerals barite and magnetite. The former is present as fine-grained anhedral crystals which are very common in the groundmass and form a weak fabric in the rock by their parallel alignment, and the latter forms euhedral to subhedral crystals commonly associated with the feldspar phenocrysts. **B:** Calcite is common both within the groundmass of the rock, and along the edges of the phenocrysts.

Muscovite laths reaching 100µm long were observed parallel to the edges of some of the phenocrysts. A microfracture was observed cross-cutting an anorthoclase crystal. This microfracture was filled by fine-grained high birefringence platy minerals, most likely secondary micas or calcite. These same minerals were seen as small zones, 100-150µm long, parallel to the long axis of some phenocrysts. Altered epidote is also present in this rock as intergranular crystals associated with polycrystalline feldspar phenocrysts and euhedral opaque minerals.

Calcite is present along the grain boundaries of some of the larger alkali feldspar phenocrysts, but occurs more commonly as fine-grained anhedral crystals within the groundmass. It is often associated with opaque minerals and intergranular to polycrystalline phenocrysts of alkali feldspar. In one example calcite has pseudomorphed a phenocryst of alkali feldspar.

The phenocrysts show occasional deformation twinning and undulose extinction could suggest that these rocks have undergone some deformation.

Under transmitted light the opaque minerals, as with KG-1, have a bimodal distribution of very fine-grained opaques, which account for ~10-15% of the rock, and euhedral to subhedral opaques which range from ~50-300µm long and account for only 1% of the rock. The fine-grained opaques appear elongated parallel to one another, defining a pseudo-fabric in the rock. Zircon is a common accessory phase in this rock.

In reflected light and EMPA the fine-grained anhedral opaque mineral was identified as barite, and the euhedral opaques as Ti-bearing magnetite (Figure 5-20). Magnetite is texturally later than anorthoclase, but pre-dates apatite in this rock.

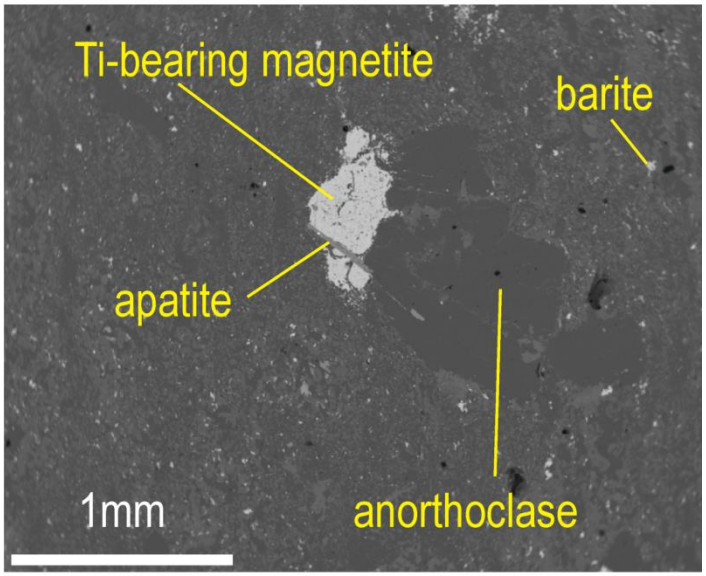

Figure 5-20: Backscatter electron microphotograph of OE-1 during EMPA showing the paragensis of anorthoclase ->magnetite ->apatite in this rock.

5.4.1.3 Oorlogsende Member: OE-2

The rock has a fine-grained matrix and a porphyritic texture. This rock appears highly altered, with a more coarse-grained matrix than the previous two samples, composed mainly of quartz and plagioclase. The groundmass in this rock contains patches of acicular fine-grained plagioclase needles, as well as discernible calcite, altered epidote and very fine-grained cubic opaque minerals (Figure 5-21). The zones of acicular plagioclase can be up to 1mm long and 0.7mm wide. The rock is dominated by alkali feldspar phenocrysts of sanidine and anorthoclase, as well as plagioclase and rare quartz phenocrysts which are sometimes intergrown in micrographitic textures. All of the feldspars show some alteration to sericite, seen as a dusty brown coating on many of the phenocrysts. Many phenocrysts are fractured with cracks filled by fine-grained platy minerals, possibly muscovite, which can also form veinlets across these phenocrysts. Polycrystalline phenocrysts of alkali feldspar, calcite, quartz, opaque minerals and altered epidote are fairly common. Zircon is an accessory phase, but more common in this rock than the previous two samples.

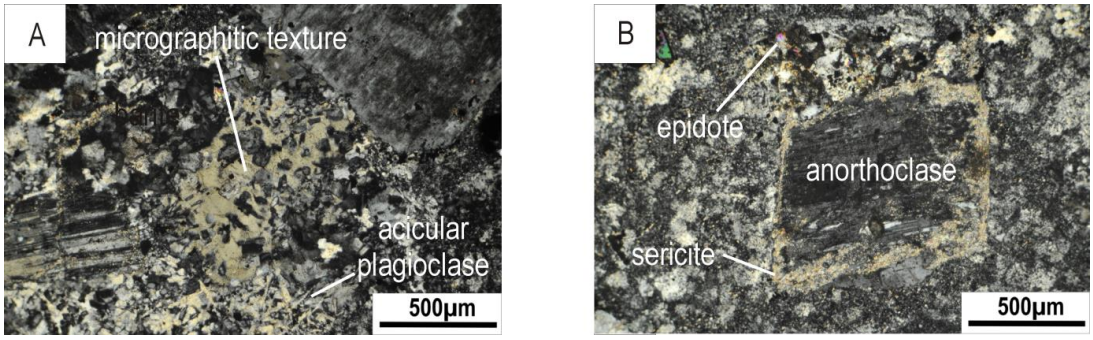

Figure 5-21: Photomicrographs taken under XPL of sample OE-2 from the Oorlogsende Member. Micrographitic textures are commonly developed between quartz and alkali feldspars adjacent to mineral aggregates (**A**). Acicular plagioclase needles are commonly developed in patches throughout the groundmass. Alteration of feldspars to sericite is commonly observed, particularly along grin boundaries and along cleavage planes (**B**). Zones of altered epidote, calcite, feldspars and equant opaque minerals are common. The bright green mineral in B is zircon.

In transmitted light the euhedral opaque minerals, which average 200µm long, are frequently associated with altered epidote, calcite and quartz. Fine-grained opaques are also commonly disseminated throughout the groundmass. Under reflected light a single subhedral lath of covellite ~100µm long was identified by its distinctive red-blue bireflectance.

EMPA was used to investigate the opaque mineralogy of OE-2. Sphalerite was identified, and in one instance was associated with a mineral (S = 25 wt.%, Cu = 49 wt.%, As = 11 wt. % and Sb = 14 wt.%) which has a similar composition to watanabeite ($Cu_4(As,Sb)_2S_5$) (webmineral.com). EMPA also identified another mineral (~60µm long) not seen in the previous two samples, clausthalite (PbSe). This mineral which contains both Pb and Se, and forms a solid solution with galena (Figure 5-22)(Bowles et al., 2011).

A quartz phenocryst with numerous inclusions was also investigated from OE-2. The opaque inclusions included magnetite, zircon and Ce-La-Nd minerals.

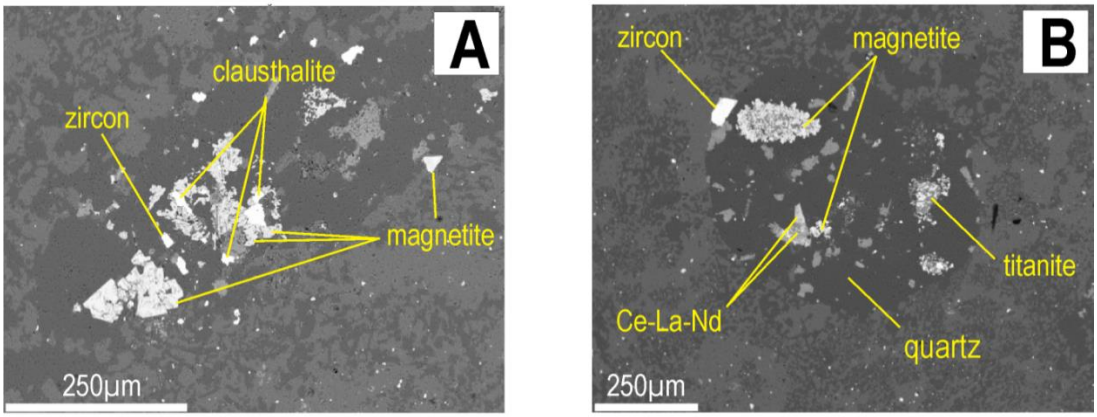

Figure 5-22: Backscatter electron photomicrograph of intergranular opaque minerals in the Oorlogsende Member sample OE-2. There is an apparent association between the Pb-Se mineral chlausthalite and magnetite (**A**). Magnetite forms aggregates within a quartz phenocryst. The aggregate has an ovoid shape. The phenocryst also contains titanite intergrown with magnetite, and an unknown Ce-La-Nd phase (**B**).

5.4.1.4 Basement Classification

The petrography alone is insufficient for classifying the basement rocks, other than to say that they are igneous rocks. Time did not allow for these samples to be subjected to XRF, therefore a new technique was employed. Experimental studies by Beard and Drake (*pers.comm*, 2016) have shown that repeat area scans of polished thin sections by EDS can produce results comparable to those obtained by XRF for classifying igneous rocks (Appendix IV-A). This method was tested using the basaltic glass standard BCR-2 (Wilson, 1997). An area of the BCR-2 standard reference material with an even flat surface measuring ~3mmx3mm was chosen. A total of 43 rectangular area scans of various sizes were taken from the chosen portion of BCR-2 and the oxide weight percentages for Na, Mg, Al, Si, P, K, Ca, Ti and Fe were measured and the results averaged (Figure 5-23). The average was then compared to the published results for the composition of BCR-2. The results show good agreement with for the BCR-2 standard (Stdev <1 wt.% for all oxides) (Table 16).

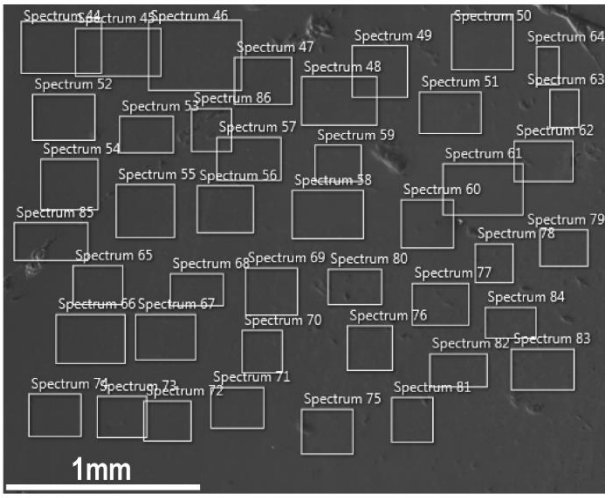

Figure 5-23: Backscattered electron image of the BCR-2 standard area scans, Spectrum 44-86. The area scan calculates the average composition of each block and the average of all of the blocks is taken as the average of the sample (Beard and Drake *pers comm.*, 2016).

Table 16: The published oxide weight % values for the BRC-2 standard and associated standard deviation values (±) compared to the results of the area scans using EMP. The standard deviation between the published results and the area scans show good agreement between the results for all of the oxides analysed.

	Published		Area Scan		Result
	Wt. %	±	Wt. %	±	Stdev
Na_2O	3.16	0.11	3.31	0.07	0.11
MgO	3.59	0.05	3.69	0.08	0.07
Al_2O_3	13.5	0.20	13.9	0.19	0.27
SiO_2	54.1	0.80	54.9	0.85	0.55
P_2O_5	0.35	0.02	0.31	0.06	0.03
K_2O	1.79	0.05	1.82	0.05	0.02
CaO	7.12	0.11	6.95	0.12	0.12
TiO_2	2.26	0.05	2.32	0.08	0.04
FeO	12.4	0.20	12.0	0.28	0.27

In order to obtain representative average compositions for the basement samples in this study two locations were chosen from each polished thin section. At each location an average of 40 overlapping area scans were done to quantify the major oxide contents of Na_2O, MgO, Al_2O_3, SiO_2, P_2O_5, K_2O, CaO, TiO_2, MnO and FeO (Fe^{2+}), as shown in Figure 5-24 for a total of ~80 blocks per slide (Table 17; Appendix IV-B).

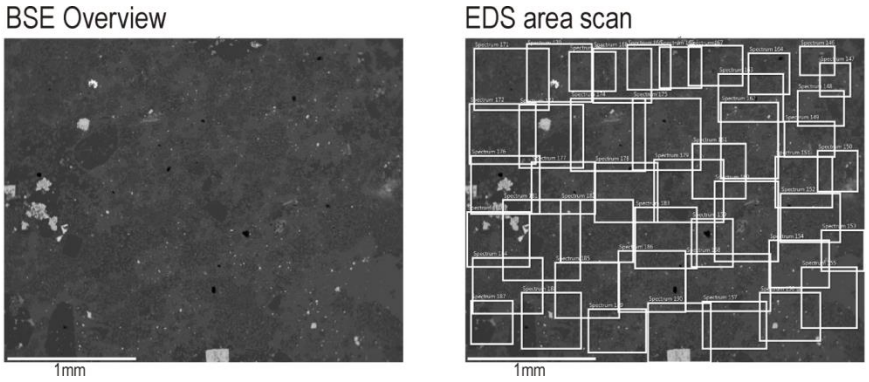

Figure 5-24: Example of a back scatter electron image showing the overlapping area scans used for the EDS major oxide compositional analysis of the basement rocks (OE-2). Two areas of this size were analysed for each of the basement samples and the results averaged to produce the compositional data in **Table 17.**

Table 17: Major element oxide compositions for the three basement samples KG-1, OE-1 and OE-2 as determined by EDS area scans. Values are averages. AI has been determined by Na_2O+K_2O/Al_2O_3 using weight percentages and ASI=Al_2O_3/CaO + Na_2O+K_2O.

	Na_2O	MgO	Al_2O_3	SiO_2	P_2O	K_2O	CaO	TiO_2	MnO	FeO	AI	ASI
KG-1 (*n=94*)	3.73	0.02	12.9	70.7	0.03	5.38	0.83	0.39	0.05	1.74	0.71	1.30
OE-1 (*n=102*)	2.87	0.02	11.6	71.7	0.02	5.67	1.48	0.33	0.07	1.71	0.74	1.16
OE-2 (*n=88*)	0.74	0.08	9.82	64.6	0.02	6.97	0.22	0.26	0.03	1.08	0.78	1.24

The results in Table 17 were plotted on a TAS (total alkali silica) diagram for classifying volcanic rocks by composition (Figure 5-25).

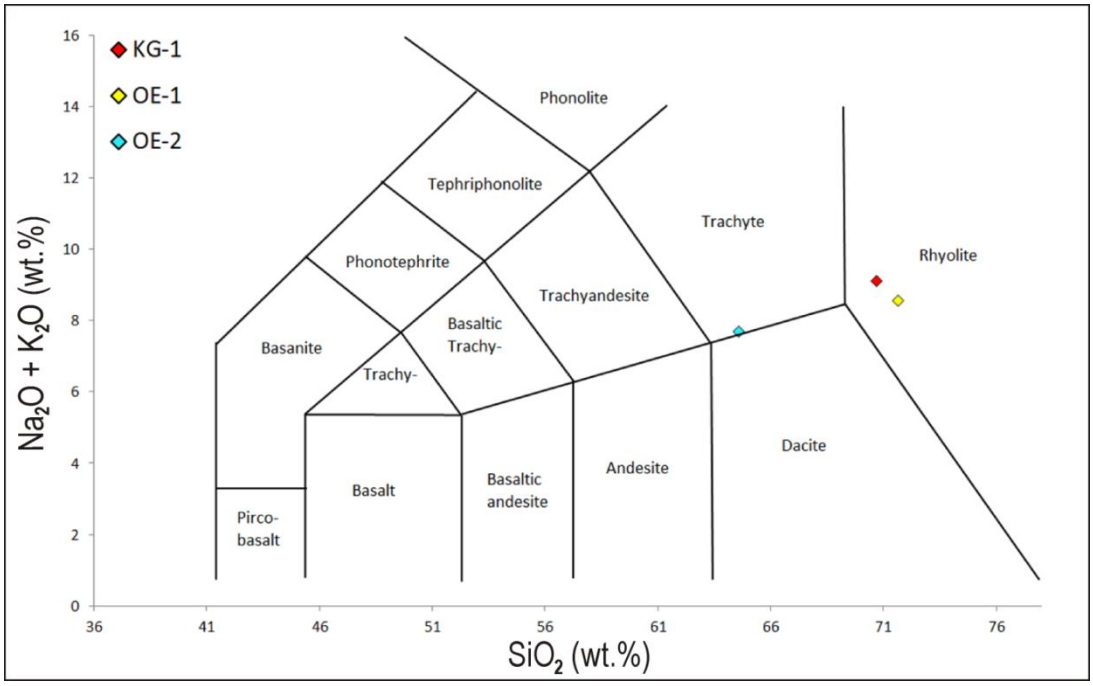

Figure 5-25: The basement samples are plotted on a TAS diagram for the classification of igneous rocks. Each point represents the average composition for a given sample based on ~80 area scans per sample (Table 18)(Appendix IV-B). KG-1 and OE-1 plot within the rhyolite field and OE-2 plots within the trachyte field bordering on the dacite field. The TAS diagram boundaries are redrawn after Le Maitre et al. (2005).

KG-1 and OE-1 plot within the rhyolite field of the TAS diagram and OE-2 plots within the trachyte field on the border with a dacite composition. The agpaitic index (AI) is below 1 (Na_2O+K_2O/Al_2O_3) for all the samples, which indicates that they are not peralkaline (Table 18). The aluminium saturation index ($ASI=Al_2O_3/CaO + Na_2O+K_2O$) for these samples is between 1.1 and 1.2. This indicates that these rocks are peraluminous. These rocks have high K_2O contents, particularly OE-2, which is ~7 wt.% K_2O (Stdev = 1.66 wt.%)

5.4.2 Metavolcanics

Fours samples were taken from the metavolcanic rocks in the west, two from each borehole WB-1 and WB-2 (Figure 5-26).

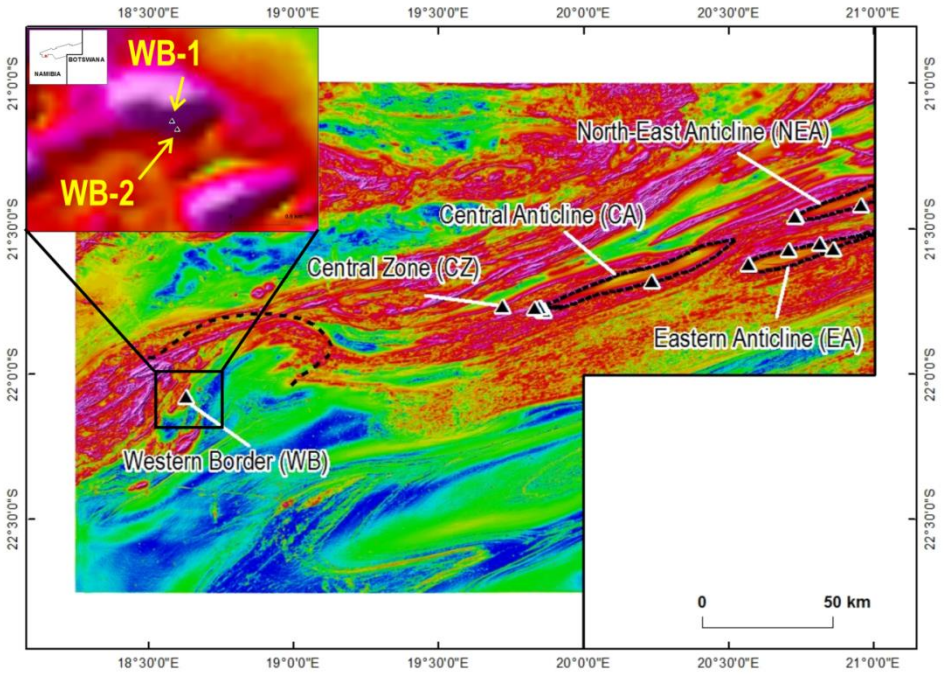

Figure 5-26: Magnetic map of the study area showing the location of boreholes WB-1 and WB-2 (INSERT). Background is the GSN regional airborne magnetic survey Analytical Signal (AS) image.

The samples taken from WB-1 and WB-2 are fairly similar; the rocks are folded and banded with alternating layers of more competent, coarse-grained subhedral quartz > albite > oligoclase (<1mm wide) and phyllosilicates (chlorite, sericite and muscovite) and calcite (Figure 5-27). In thin section the fine-grained minerals define a strong schistose fabric which wraps around coarse felsic minerals, rotating them into the foliation. The samples are cut by numerous veins. The opaque minerals occur primarily within lenses of coarse grained quartz-plagioclase. The overall compositions are summarised as:

Quartz: 50%

Plagioclase: 15% (~10% albite, 5% oligoclase)

Muscovite/chlorite/sericite: 30%

Calcite: 5%

Opaques: 5%

Quartz phenocrysts are subhedral to anhedral and show mild undulose extinction (average grain size ~0.2mm). Along fine-grained layers quartz shows major grain size reduction to

form sutured to polygonal clusters which show strong undulose extinction. Oligoclase shows some deformation twinning. Quartz and plagioclase form rare imbricate structures indicative of prolonged deformation. Plagioclase occurs as subhedral grains which average ~0.2 – 0.4mm long. There is some break down of feldspars to sericite. The fine-grained layers in these rocks are a combination of calcite, chlorite, muscovite and sericite intergrowths. In some instances chlorite has a very strong green colour suggesting it is iron-rich, and occasionally cubic opaque minerals form fine-grained stringers in these units.

These rocks show brittle fracturing in the form of micro-thrusts which off-set coarse felsic minerals and opaques, suggesting movement along fine-grained minerals. Lenses of more competent minerals are commonly stretched out and boudinaged between fine-grained layers. These rocks also show evidence of having undergone ductile deformation. Micro-folding occurs in both the coarse and fine-grained layers. The latter also show some development of crenulation cleavages, and quartz/carbonate veining is common throughout. Coarse-grained euhedral opaque minerals occur in both the fine and coarse layers. Opaques are also present as interstitial cementing phases elongated parallel to the veins. The majority of these irregular bodies, however, occur within the more competent layers as an interstitial phase/cement between quartz and feldspar grains.

The opaque minerals are identified as pyrite, bornite and chalcopyrite. Pyrite commonly occurs as euhedral crystals, up to 0.7mm long (average~0.2mm long), and shows the development of quartz pressure shadows. Quartz in these settings shows undulose extinction. The large bodies of interstitial opaques (up to 3mm long) are copper sulfide minerals.

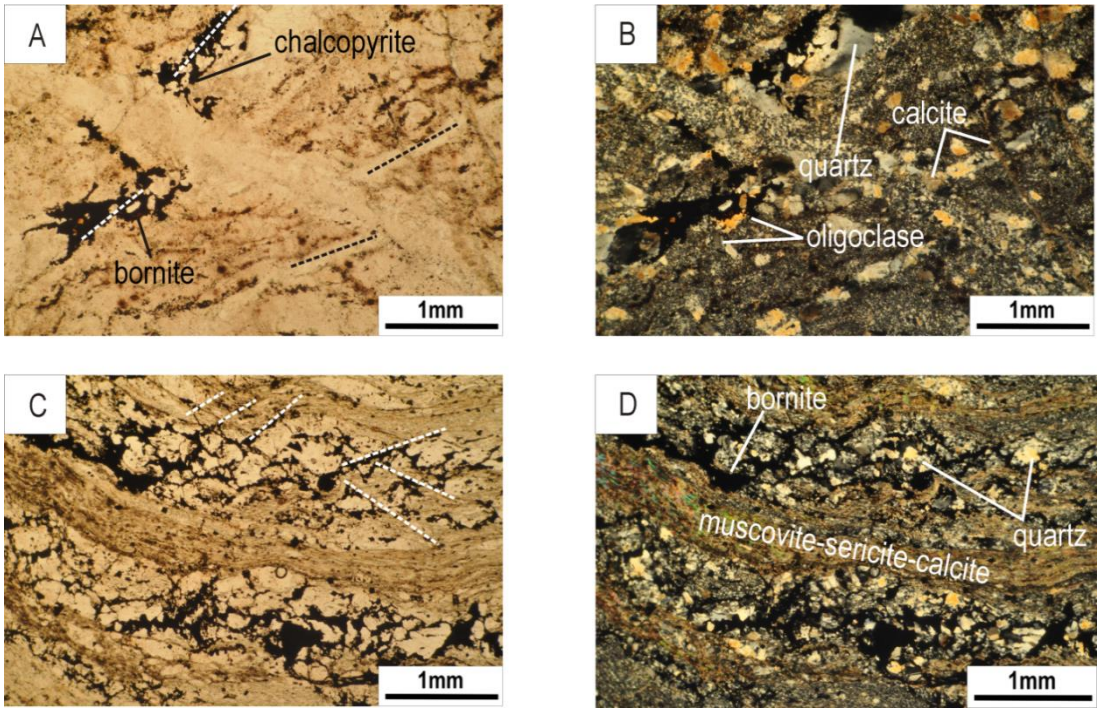

Figure 5-27: Micro-faulting along a zone of fine-grained quartz off-sets copper sulfides (EPS-02: **A:** PPL & **B:** XPL). Alternating bands of coarse silicates and fine-grained phyllosilicates show evidence of micro-folding (EPS-04: **C:** PPL), and micro-faulting (**D:** XPL). The opaque phase (bornite) favours the coarse-grained layers.

Copper sulfides occur in both boreholes WB-1 and WB-2. WB-1 contains minor chalcopyrite > bornite, but copper sulfides are more common WB-2 (sample EPS-04) where bornite >> chalcopyrite (Figure 5-28). Bornite is often spatially associated with magnetite, growing around its edges and in cracks along magnetite grains.

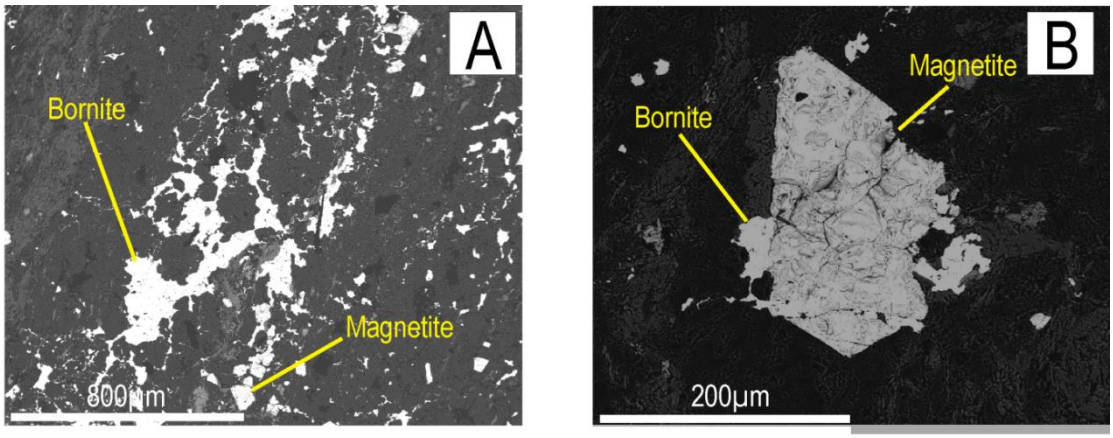

Figure 5-28: Bornite and magnetite micro-textural relationship along zones of increase porosity from EPS-04, WB-2. Photomicrographs taken during EMPA.

EMPA identified phases not distinguished using reflected light. Very fine veins of Ce-Nd-La mineral(s) were seen throughout the metavolcanics. These also form minerals seen on the edges of pyrite grains in WB-1. Subhedral pyrite identified in WB-1 was shown to contain

microscopic bornite and cobaltite along their grain boundaries and between pyrite grains (Figure 5-29). EMPA suggests cobaltite contains minor Ni (~1 wt.%). For WB-2 pyrite is more common away from the mineralised zone, and shows alteration along grain boundaries. Fracturing is common in this pyrite suggesting pre-deformation growth of this phase.

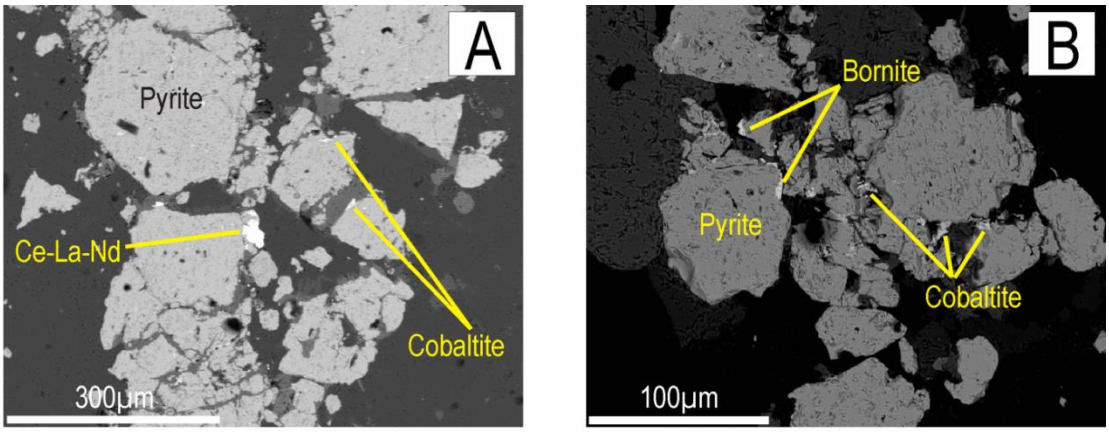

Figure 5-29: Pyrite contains inclusions of quartz and plagioclase (**A**). An alteration halo is developed around this mineral of a fine-grained unidentified iron-oxide, and calcite (EPS-03, WB-2). **B:** Microscopic cobaltite and bornite were identified using EMPA (EPS-02, WB-1).

The veins show pinching at their ends suggesting that these rocks were deformed after veining. Some of the opaques have been off-set by faulting, suggesting pre-deformational growth. Bornite and cobaltite favour the cracks and grain boundaries of pyrite and magnetite so these were most likely precipitated at a later stage, but the coarse interstitial bodies are off-set by fracturing so this suggests syn-deformational growth. The overall distribution of the copper sulfides suggests fluids exploiting porosity within the coarser grained lenses in the rock.

5.4.2.1 Metavolcanic Classification

The same method that was used to classify the basement volcanic samples (described in Section 5.4.1.4) was used to classify the metavolcanic rocks. Two sites were randomly selected from each polished thin section and approximately 80 sites scanned and averaged to calculate the major oxides: Na_2O, MgO, Al_2O_3, SiO_2, P_2O_5, K_2O, CaO, TiO_2, MnO and FeO (Fe^{2+}) (Figure 5-30, Table 18: Major element oxide compositions for the four metavolcanic samples EPS-01 – EPS-04 as determined by EDS area scans. Values are averages. AI has been determined by Na_2O+K_2O/Al_2O_3 using weight percentages and ASI=Al_2O_3/CaO + Na_2O+K_2O.Table 18).

Table 18: Major element oxide compositions for the four metavolcanic samples EPS-01 – EPS-04 as determined by EDS area scans. Values are averages. AI has been determined by Na_2O+K_2O/Al_2O_3 using weight percentages and ASI=Al_2O_3/CaO + Na_2O+K_2O.

	Na_2O	MgO	Al_2O_3	SiO_2	P_2O	K_2O	CaO	TiO_2	MnO	FeO	AI	ASI
EPS-01 (*n=81*)	4.11	0.93	12.1	68.3	0.23	2.87	2.59	0.41	0.08	3.49	0.58	1.27
EPS-02 (*n=93*)	10.3	0.09	17.2	61.7	0.09	0.44	6.57	0.23	0.11	1.54	0.62	1.00
EPS-03 (*n=99*)	4.36	0.87	13.8	70.1	0.06	2.63	3.31	0.59	0.09	3.93	0.51	1.34
EPS-04 (*n=79*)	5.12	0.92	16.4	56.2	0.39	3.39	0.52	0.89	0.04	3.13	0.52	1.81

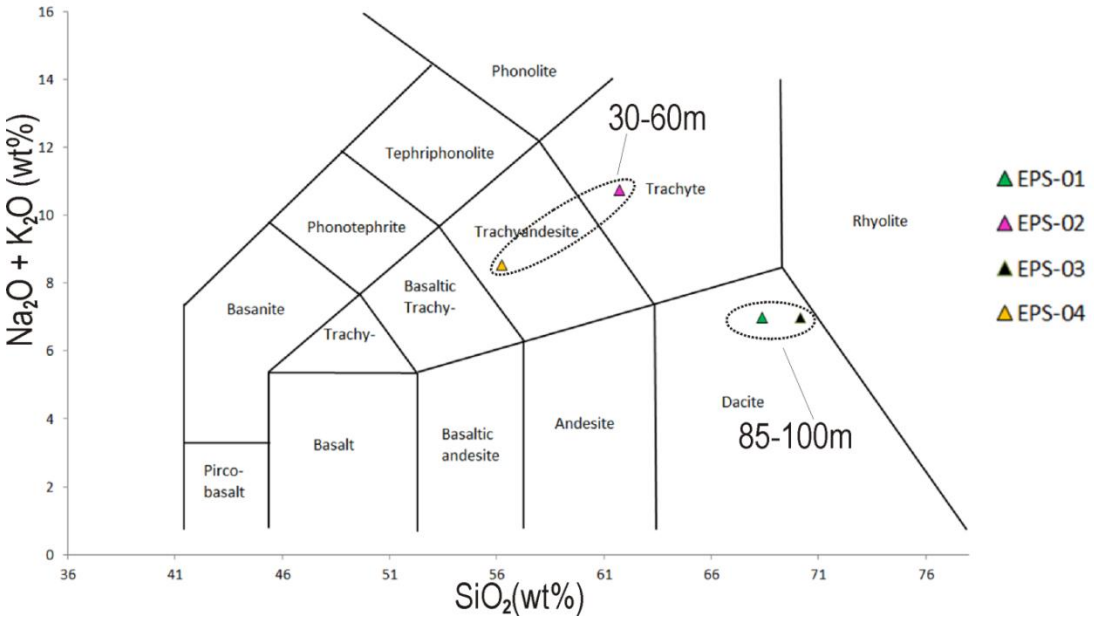

Figure 5-30: The metavolcanic samples are plotted on a TAS diagram for the classification of igneous rocks. EPS-01 and EPS-03 are from similar depths and both plot within the dacite field of the TAS diagram. Samples EPS-02 and EPS-04 are from shallower depths in the boreholes (WB-1 and WB-2) and plot in the Trachyte and Trachyandesite fields respectively. Boundaries redrawn after Le Maitre et al. (2005).

EPS-01 and EPS-03 both plot within the dacite field of the TAS diagram. EPS-02 and EPS-04 plot within the trachyte and trachyandesite fields respectively. The agpaitic index (AI) is below 1 (Na_2O+K_2O/Al_2O_3) for all the samples, which indicates that they are not peralkaline (Table 18). The aluminium saturation index (ASI=Al_2O_3/CaO + Na_2O+K_2O) for these samples is between 1.0 and 1.3 for EPS-01 to EPS-03, but is very high for EPS-04 at 1.8. The ASI suggests that all of these rocks are peraluminous.

5.4.3 Hangingwall

5.4.3.1 Eastern Study Area

Samples: OPS-11 & OPS-14

The hanging wall sandstones are inequigranular and medium-grained with a subarkose composition (average grain size <0.35mm to 0.5mm) (Figure 5-31). The average composition:

Quartz: 40%

Feldspar: 15% (albite >anorthoclase>microcline)

Muscovite/sericite: 35%

Biotite/chlorite: 5%

Opaques: 3%

Zircon and titanite: 2%

Quartz forms equant/polygonal to anhedral grains up to 0.42mm long (average 0.2mm). The larger grains have sutured boundaries with sub-grain formation common. These show strong undulose extinction. There are some triple junctions developed between quartz subgrains, but these show some undulose extinction.

The feldspars are dominantly albite, but anorthoclase and minor microcline were also identified. The feldspars are all largely altered to or replaced by sericite, with no one feldspar being preferentially altered. These grains are about the same size as the quartz grains, averaging about 0.2mm. Undulose extinction and deformation twinning in albite are common.

Muscovite is present both as very fine-grained laths intergrown with sericite and chlorite, and as large laths up to 0.4mm long and up to 35µm wide. The longer laths tend to be bent, suggesting that these were part of the detrital assemblage. Fine-grained aggregates of chlorite are common between grain boundaries, but these are very fine-grained so may include sericite and/or muscovite.

Titanite is a fairly common accessory phase, forming high relief subhedral crystals up to 0.05mm long.

Under transmitted light the opaques account for about 3% of the rock and occur as rounded clusters/aggregates (~0.4mm) of euhedral to cubic grains with occasional

individual grains (<35µm to 0.35mm). In one of the samples (OPS-8) there are a number of coarse bands of opaques associated with blocky biotite, fine-grained muscovite, titanite, and calcite.

Under reflected light the opaques were identified as magnetite.

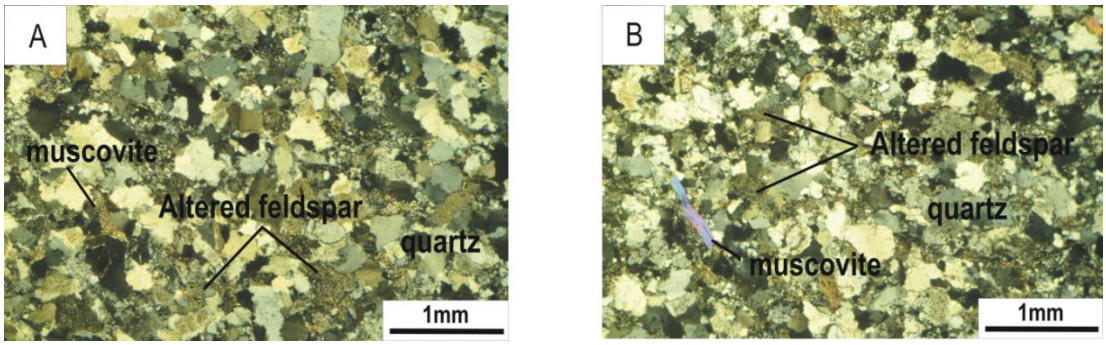

Figure 5-31: Photomicrographs from the hanging wall sandstones in the east of the study area. **A:** Subhedral to anhedral quartz and sericitised feldspar are common in OPS-11 (EA-NL-1). **B:** Muscovite is commonly bent, but forms long laths up to 0.4mm (OPS-14). Photomicrographs taken in XPL.

The sandstones show evidence of deformation by compaction, as suggested by the strong undulose extinction and sub-grain formation in quartz and feldspars, as well as bent muscovite laths. The alteration of feldspars to sericite suggests interaction with a fluid, but there are no obvious indicators of metamorphism beyond lower greenschist facies in these rocks. The triple junctions with undulose extinction suggest equilibrium conditions were reached.

5.4.3.2 Central Study Area

Sample: OPS-6

The hangingwall in the central area is characterised by fine-grained subarkose sandstone (average grain size ~300µm to <50µm) with an incipient foliation (Figure 5-32). This foliation is defined by the preferred orientation of fine-grained muscovite, sericite and chlorite. The average composition is:

Quartz: 50%

Feldspar: 15% (albite>>oligoclase)

Muscovite/sericite: 25%

Carbonate: 5%

Biotite/chlorite: 3%

Opaques: 2%

Quartz and feldspars generally form lenticular aggregates between braided networks of fine-grained micaceous minerals which define a weak fabric in this rock. The plagioclase is generally subhedral and often replaced by sericite. Quartz is commonly elongated parallel to the fabric developed in the rock and shows evidence of grain-size reduction along this fabric. Quartz and feldspar grains show sub-grain formation and some undulose extinction.

Muscovite laths reach 0.2mm and some of them are bent at an angle to the foliation. The majority, however, are extremely fine-grained and occur with sericite and chlorite. Opaque porphyroblasts are common parallel to the incipient fabric. Rare blocky biotite laths (0.3mm) were also observed, most often associated with the opaque minerals. These show some alteration to chlorite.

The opaque minerals account for about 2% of the rock, and are generally euhedral to rounded, reaching up to ~200µm long, as well as occasional fine-grained (<%100µm) stringers. Under reflected light the opaques were identified as magnetite.

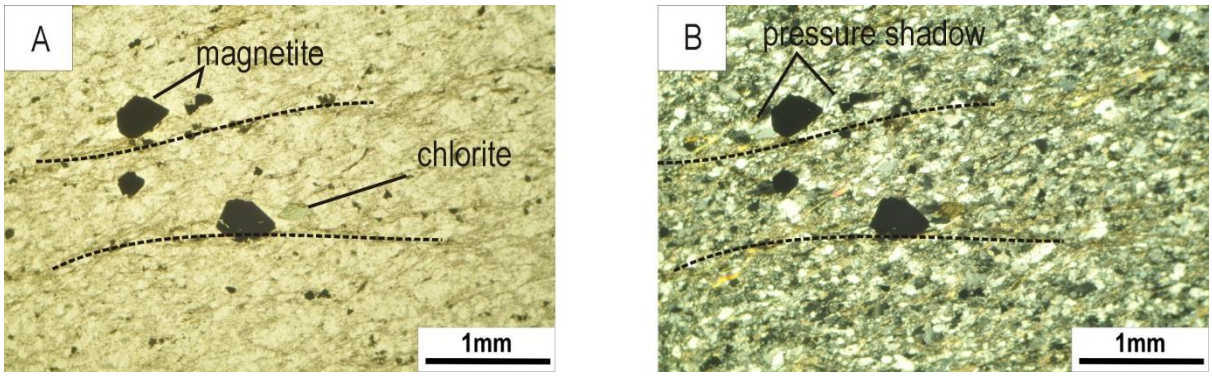

Figure 5-32: Photomicrographs of the subarkose hangingwall sandstone (OPS-6, CA-PL-1) under transmitted light in PPL (**A**) and XPL (**B**). The dashed lines show the development of a very weak foliation.

5.4.4 Interbedded Unit

5.4.4.1 Eastern Study Area

Samples: OPS-8, OPS-9, OPS-10, OPS-13, PST-2D2-1, PST-2D2-2, PST-4D1-1, PST-4D1-2, PST-4D1-3, PST-4D2-1, PST-4D2-2 & PST-4D2-3

Medium-grained subarkose sandstones were identified in samples OPS-8, -9, -10 and PST-4D1-1. Their average composition can be summarised as:

Quartz: 65%

Feldspar: 10% (albite>>oligoclase>anorthoclase)

Muscovite/sericite: 15%

Chlorite: 5%

Opaques: 5%

The sandstones are generally massive with variable amounts of fine-grained muscovite and sericite defining weak fabric in places, which is reinforced by the parallel alignments of chlorite and opaque mineral aggregates (Figure 5-33).

The dominant mineral constituents are quartz and albite. About 2/3 of the subhedral plagioclase has been replaced/altered to sericite, while the remainder show only minor variable alteration. Quartz forms anhedral (up to 0.2mm long) grains which show well developed undulose extinction. Plagioclase also forms similar sized grains. Quartz shows evidence of grain size reduction to form euhedral to polygonal lenses parallel to the weak fabric. The rock also contains coarse muscovite laths (0.3mm long) which are occasionally bent at an angle to the poorly developed fabric. Blocky to anhedral chlorite is also present throughout the rock with laths of up to ~80µm long occurring in bands with opaque mineral phases. The shape suggests that biotite formed part of the detrital assemblage, and has broken down to form chlorite.

Accessory zircon was also observed in this rock. In some of the sandstone samples the amount of phyllosilicates can increase up to ~30% of the rock, forming more a pronounced fabric. Opaques account for about 5% of the subarkose sandstones. Muscovite laths ~400µm long define relict bedding in these rocks which is at an angle to the weakly developed fabric.

Under transmitted light the opaques range from <50µm to ~250µm in diameter, and are disseminated throughout the rock. They commonly occur as fine-grained aggregates of euhedral to subhedral grains which favour the more micaceous parts of the rock.

Under reflected light the opaque are identified as magnetite. Magnetite forms subhedral to anhedral grains which have largely been altered to hematite.

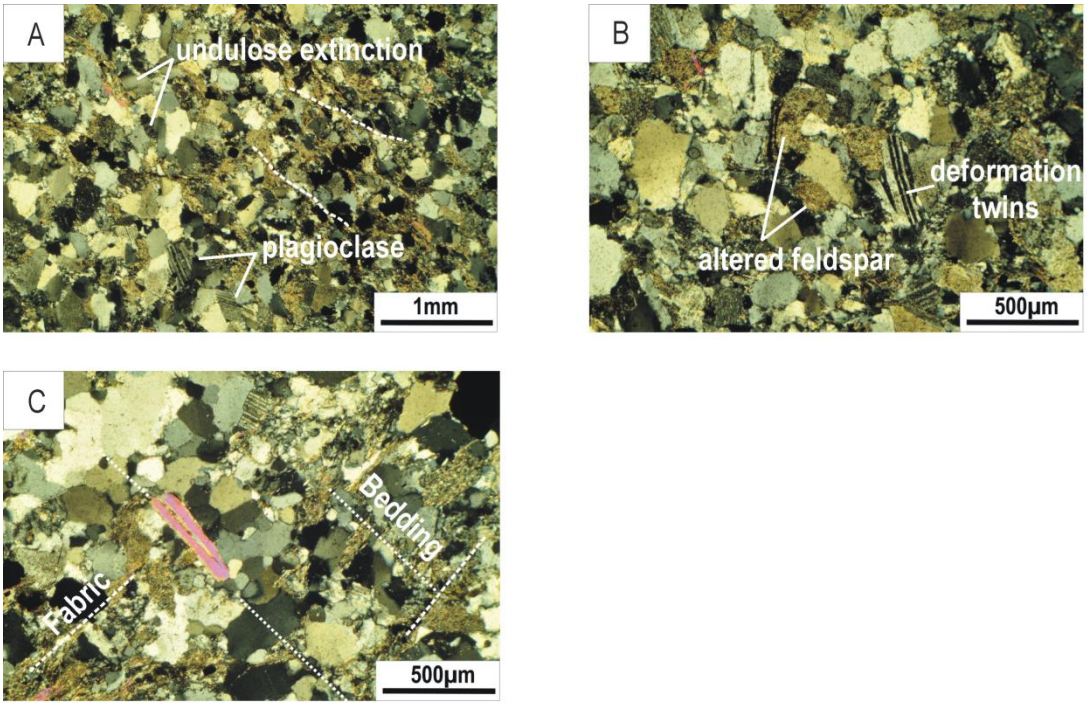

Figure 5-33: Photomicrographs of the IBU sandstones. **A:** A weakly developed foliation is defined by fine-grained platy minerals (white dashed lines). Many of the quartz grains show undulose extinction (OPS-8). **B:** Much of the plagioclase in OPS-8 has been altered to sericite, and those which have not been altered commonly show deformation twinning. **C:** The alignment of detrital muscovite and some of the felsic minerals suggest relict bedding in the rock was at an angle to foliation developed by fine-grained platy minerals in OPS-10.

In sample OPS-10 there are a few magnetite-rich layers which occur parallel to the fabric developed in the rock. Titanite is also common in these layers, and neither magnetite nor titanite show pressure shadow development, suggesting they grew with the fabric.

Samples OPS-13, PST-2D2-1, PST-2D2-2, PST-4D2-1, PST-4D2-2 and PST-4D2-3 are also from the eastern study area, however, these are from siltstones rather than sandstones (Figure 5-34). These rocks have strong fabrics defined by the parallel alignment of fine-grained phyllosilicates such as muscovite and sericite, and possibly other clay minerals too fine to identify. The average composition is:

Quartz: 27%

Plagioclase: 3% (oligoclase>albite)

Muscovite/sericite: 35%

Chlorite: 24%

Biotite: 5%

Opaques: 5%

Carbonate: 1%

These rocks are lepidoblastic. The matrix is comprised of very fine-grained phyllosilicates including muscovite, sericite and chlorite, which define a strong foliation in these rocks. The dominant silicate is quartz which shows strong evidence of rotation into the foliation of rounded clasts (porphyroblasts). Inclusion trails suggest the original bedding was at an angle to foliation. Quartz grains reach up to 0.6mm long (average <0.2mm) and where parallel to the foliation, show elongation in the direction of the fabric and a sigmoidal shape. Undulose extinction is common in elongate quartz, but less common in rotated grains.

Feldspars have largely been replaced by/altered to sericite, and only a few (<0.2mm) subhedral oligoclase, albite and minor anorthoclase were identified. Muscovite laths (up to 0.6mm) are oriented at an angle (~ 90˚) to the defined foliation, commonly in the same orientation as the quartz inclusion trains, suggesting this may be remnant bedding. The muscovite laths often have pressure shadows adjacent to their long axes, and alteration to clays is common along the edges of these large laths. Biotite, in turn, commonly shows alteration to chlorite. Biotite tends to occur as individual blocky laths, or as aggregates with one or two other grains reaching up to 70µm. Rare anhedral carbonate minerals were also observed (reaching, 0.35mm). These occur as stringer-type bodies parallel to the foliation. Fine-grained euhedral to rounded zircon (<35µm to 70µm) and subhedral titanite are accessory phases (70µm).

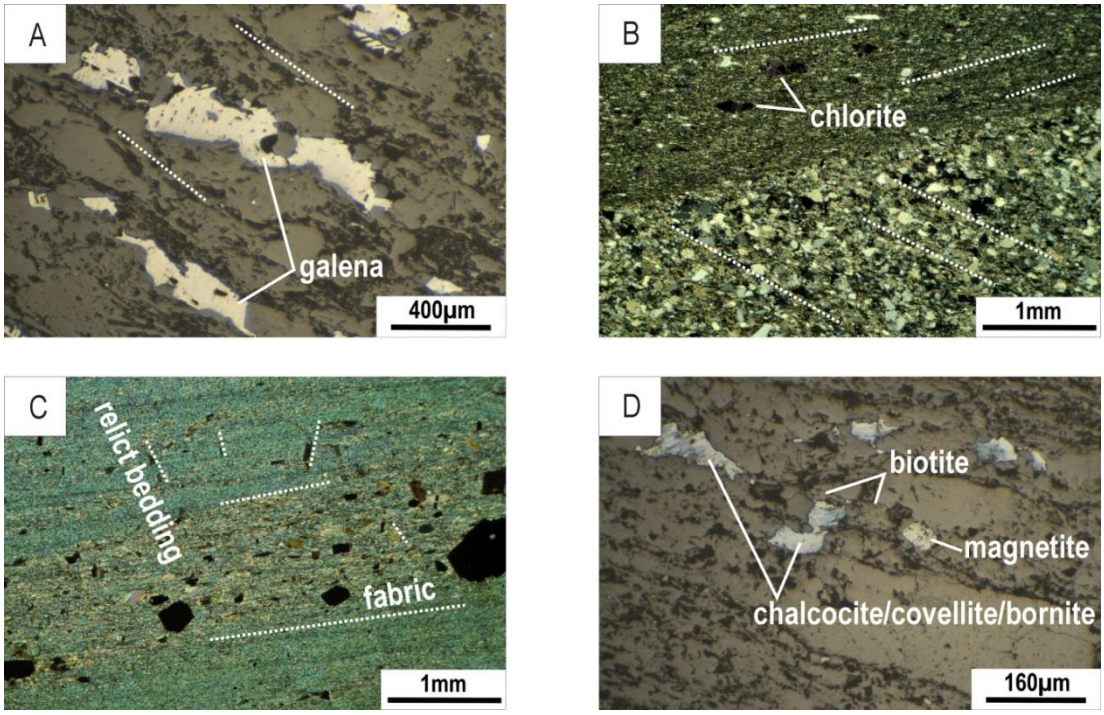

Figure 5-34: Photomicrographs of the IBU siltstones (foliation shown by white dashed lines). **A:** Under reflected light the opaque minerals in the eastern anticline (EA) were identified as galena. Photomicrograph from OPS-13. **B:** Many of the siltstones show interbeds of coarser and finer material. The fabric developed in the fine-grained layer is at an angle to that developed in the sandy unit (PST-2D2-2). **C:** Biotite appears to be detrital in most of the siltstones, demonstrating the orientation of the original bedding at an angle to the foliation (PST-4D2-1). **D:** The opaques in NEA are magnetite and anhedral chalcocite, covellite and bornite intergrowths (PST-4D2-3).

Under transmitted light the opaque minerals show a bimodal distribution. Individual euhedral to cubic minerals averaging 0.35mm in diameter tend to occur with coarse biotite/chlorite laths. Opaques also occur as irregular bodies up to 1mm long which are aligned with the foliation.

Under reflected light the opaque minerals are identified as galena, magnetite, bornite, chalcocite and covellite. Chalcocite herein refers to the chalcocite group minerals. The two samples from EA, PST-2D2-1 and 2 are similar in terms of their opaque mineralogy, which is dominated by galena. In these samples galena is elongated in anhedral bodies parallel to the foliation. Rare chalcocite was also identified. Although no magnetite was identified during reflected light work, EMPA identified magnetite in complex textural intergrowths with both galena and chalcocite (Figure 5-35). The opaque minerals from the NEA samples are dominantly magnetite, but anhedral copper sulfides are also present. Copper sulfides are in the form of bornite, which shows alteration to covellite along its edges, and chalcocite, which shows alteration to bornite and covellite along grain boundaries.

The siltstones all show signs of deformation, but many preserve relict bedding suggesting deformation may have been due to compaction. Both biotite and muscovite appear to have

been detrital phases as they define the relict bedding in most cases, and both show some development of pressure shadows. The sulfides are all aligned to the fabric in the rocks, rather than with relict bedding. This may suggest their growth was syn-deformational. Magnetite, where present, is aligned parallel to the foliation, but often has pressure shadows of quartz and biotite. Their locations suggest a second generation of biotite, one associated with the fabric forming event(s).

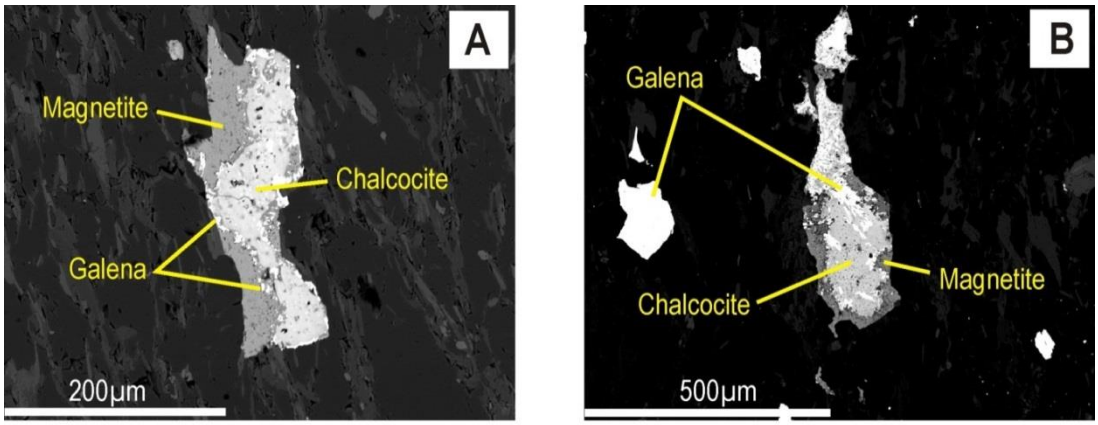

Figure 5-35: EMPA photomicrographs of the complex textural intergrowths between galena (very bright), chalcocite (medium brightness) and magnetite (low brightness) in sample PST-2D2-1 from the IBU.

The IBU commonly contains argillite and phyllite units. Two thin sections were examined to characterise the phyllites of the eastern study area PST-4D1-2 and 3 (Figure 5-36). Compositionally the phyllites examined are similar to the siltstones from NEA, consisting of rounded to angular quartz and plagioclase grains in a matrix of fine grained muscovite-sericite. The main differences are textural. The phyllites have very strongly developed foliation. In PST-4D1-2 magnetite porphyroblasts are common, but show two different orientations, one aligned to the foliation (up to 500µm long), the other at ~45˚(average 150µm long). Pressure shadows, parallel to the fabric, of quartz, biotite and sulfide minerals are common for these rotated porphyroblasts. In PST-4D1-3 magnetite is oriented parallel to the main foliation, but a poorly developed crenulation fabric is developed irregularly in this rock. There are two generation of biotite in this rock, one is blocky (~200µm long) and oriented at an angle of ~-45˚ to the fabric (most likely detrital), the other forms abundant elongate bodies ~200-500µm long oriented with the main fabric of the rock. The biotite aligned with the foliation has no pressure shadows developed, suggesting syn-deformational growth. The large magnetite porphyroblasts (~200µm diameter) which have pressure shadows developed but are at an angle to the fabric are pre-deformation, and are slowly being rotated into the foliation. The fine-grained magnetite has no pressure shadows so it has most likely formed syn-deformation.

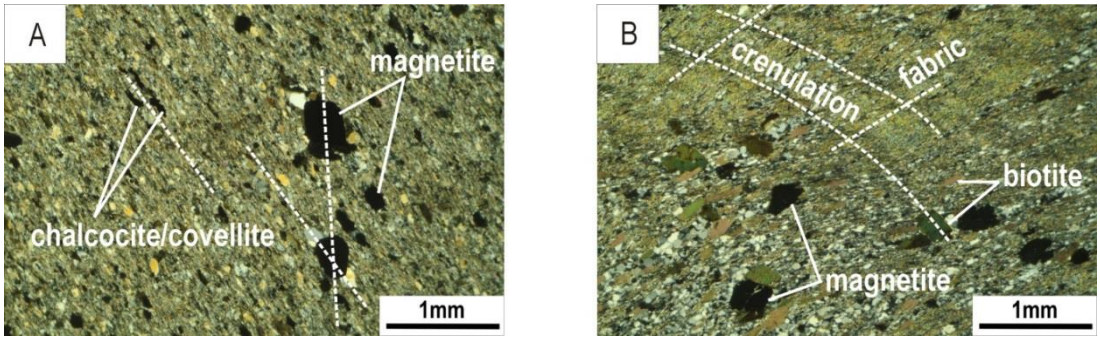

Figure 5-36: Photomicrographs of the phyllite units within the IBU in the eastern study area. **A:** Magnetite growth is elongated parallel to the main foliation developed in the rock, but some large porphyroblasts show an orientation at ~45˚ to this fabric. Sulfide minerals are common parallel to the foliation and in the pressure shadows of magnetite porphyroblasts (PST-4D1-2). **B:** Two generations of biotite are evident, one parallel to the main fabric in the rock, and the second at an angle to it (PST-4D1-3).

These phyllites both contain chalcocite, variably altered to covellite. Chalcocite-covellite occurs as irregular bodies elongated parallel to the foliation, reaching up to 1mm in length. Inclusions of chalcocite-covellite are common within magnetite crystals of either orientation, and vice versa, suggesting that these two phase grew together episodically. These sulfides are also common in the pressure shadows of magnetite grains.

5.4.4.2 Central Study Area

Samples: EPS-06, EPS-07, EPS-09 to EPS-13, EPS-15, EPS-16, EPS-18, EPS-30 to EPS-32 & OPS-1 to OPS-4

Samples were selected from sandstones and siltstones generally within 20m of the mineralised horizons, except for one sample, OPS-1, which is taken 100m above the mineralised zone from borehole CA-PL-3. EPS-11, -12, -18 and EPS-32 are all from argillite units.

The samples are virtually identical, although the samples were taken from different depths and boreholes (EPS-10, OPS-4 & OPS-6). The average composition for the hanging wall subarkose sandstone is:

Quartz: 45%

Feldspar: 10% (albite>>oligoclase)

Muscovite/sericite/chlorite: 35%

Opaques: 7%

Titanite: 3%

The subarkoses in the central study area are fine to very-fine grained with a strongly lepidoblastic texture defined by anastomosing layers of phyllosilicates which show a preferred parallel orientation.

The quartz is anhedral with grains showing undulose extinction, and grain-size reduction by sub-grain formation and recrystallization to fine-grained polygonal quartz with occasional triple junctions developed. The subhedral feldspars, predominantly albite, are an average of <100µm long and show deformation twinning and sutured grain boundaries, with only minor alteration to sericite observed. Quartz and feldspar for lenses ~50µm thick, elongated parallel to the foliation.

The phyllosilicates are dominantly muscovite and chlorite-rich, and also contain sericite. These thin (<20µm thick) fine-grained layers are associated with opaque minerals, and fine-grained titanite (~30µm long) and rare calcite. Individual muscovite laths up 150µm long also occur in these rocks, with only a few slightly bent. Zircons are present as small clusters of up to 5 grains which together form an aggregate about 40µm long.

Under transmitted light the opaque minerals occur in two distinct size classes. Porphyroblasts 70µm long are disseminated throughout the rock. These are generally equant to subhedral, but with mostly straight edges. The second major size-class is <30µm which occur as clusters and lenses of equant minerals aligned parallel to the developed foliation in this rock. These clusters can trail for up to 2mm along the foliation. Single euhedral to subhedral grains in this size class are also scattered throughout the rock. These have no pressure shadows.

Under reflected light the minerals are identified as magnetite. EMPA identified Ce-La-Nd mineral veinlets parallel to the foliation and along the edges of magnetite grains (Figure 5-37). A few microscopic grains of an unknown copper mineral were also detected using EMPA in between the elongate quartz crystals in the pressure shadow of the large magnetite porphyroblast.

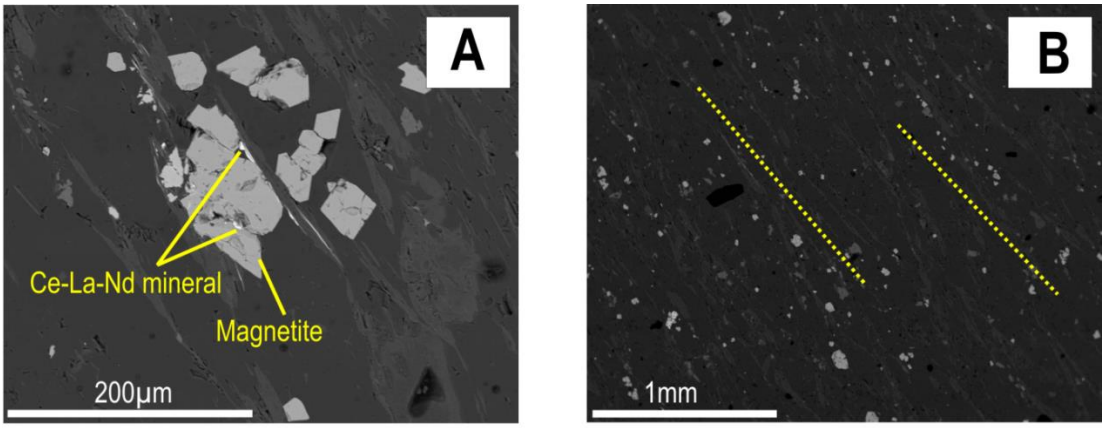

Figure 5-37: Magnetite occurs as euhedral to subhedral crystals (**A**) parallel to the fabric of the rock, and with quartz pressure shadows. (**B**) Ce-La-Nd minerals occur between magnetite grains and as stringers parallel to the fabric. Photomicrographs taken using the EMP, both images are from sample OPS-4.

The limited alteration of feldspar to sericite in these rocks can either suggest that there was little feldspar in these rocks to begin with, or that the alteration of the feldspars to sericite is largely complete, with little of the original feldspars remaining. These rocks have strongly developed foliations suggestive of deformation.

The Ce-la-Nd phase is inferred to be syn-tectonic, because of its common alignment parallel to the foliation.

Samples were also taken from fine-grained siltstones in the IBU of the central study area (EPS-09, OPS-1, OPS-2 & OPS-3). Mineralogically these samples are virtually identical, and composed largely of fine-grained muscovite, chlorite and sericite with lesser felsic minerals and variable calcite contents (Figure 5-39). OPS-3 contains about 5% calcite whereas OPS-1 contains none.

The average composition for the siltstones (excluding calcite) is:

Muscovite/chlorite/sericite: 65%

Quartz: 15%

Biotite: 13%

Opaques: 7%

Fine-grained chlorite, muscovite and sericite define strong fabrics in these siltstones. Quartz is present as elongate subhedral grains about 0.2mm long, and which are aligned parallel to the foliation. These show undulose extinction and sub-grain formation. Rare albite is evident beneath the sericite on a few grains suggesting plagioclase feldspar is also

present. Quartz with undulose extinction also forms elongate aggregates in the pressure shadows of biotite and euhedral opaque minerals.

Biotite forms blocky to subhedral laths elongated parallel to the foliation with quartz pressure shadows. They average 0.4mm long, but reach up to 0.3mm. Biotite shows variable alteration to chlorite. In sample OPS-3 biotite favours the slightly coarser relict beds (~2mm thick), where it occurs with calcite and coarse opaque minerals, as well as minor zircon and rutile. Calcite forms blocky laths elongated parallel to the foliation, reaching a maximum length of 0.4mm.

The opaque minerals have a bimodal distribution. The majority occur as euhedral crystals up to 0.4mm long with pressure shadows commonly developed, and the second occurrence is as anhedral bodies elongated parallel to the foliation with no pressure shadows. The second occurrence is isolated to the coarse layers of OPS-3 and does not occur in OPS-1.

Under reflected light the dominant opaque mineral is identified as subhedral to cubic magnetite grains which have undergone variable amounts of oxidation. The smaller grains rarely show elongation in line with the foliation, and are more generally subhedral to cubic in shape. OPS-2 contains minor anhedral chalcopyrite and bornite inclusions in magnetite (Figure 5-38).

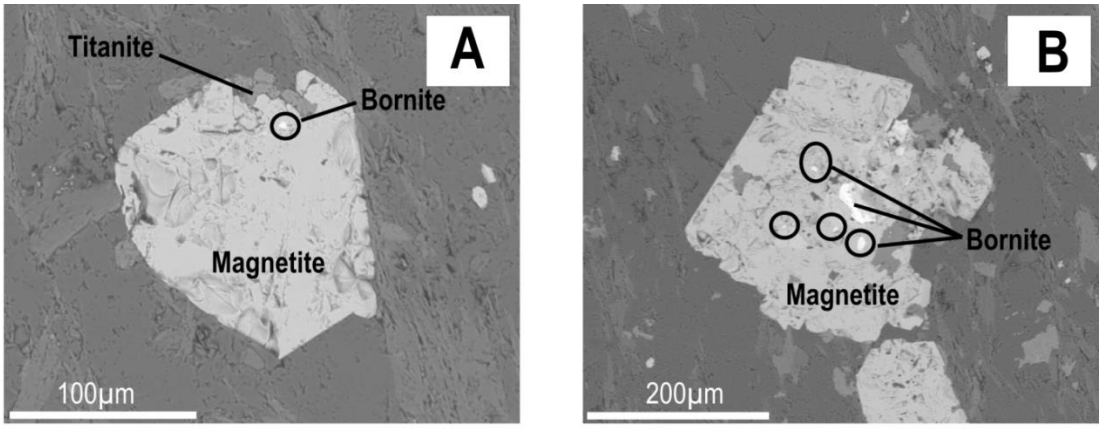

Figure 5-38: Magnetite clearly post-dates bornite in sample OPS-2. Photomicrographs taken during EMPA.

Under reflected light the elongate bodies associated with the coarser layers in OPS-3 are identified as bornite and chalcopyrite.

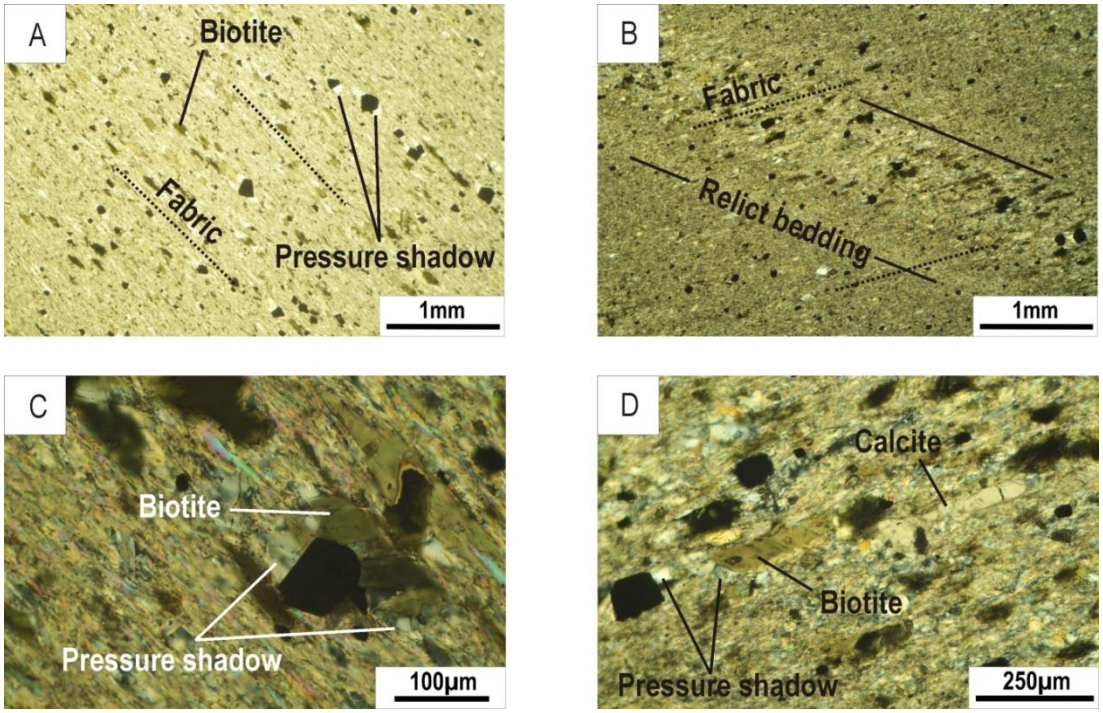

Figure 5-39: Photomicrographs from the hanging wall siltstone in the central study area. **A:** Fine-grained phyllosilicates define a strong fabric with opaques and biotite aligned to this foliation. Photomicrograph taken from OPS-1 under PPL **B:** Compositional layers have preserved relict bedding which is at an angle to the foliation of the rock. Photomicrograph taken from OPS-3 under PPL **C:** Biotite and opaque minerals show the development of pressure shadows parallel to the foliation. Photomicrograph taken from OPS-1 under XPL **D:** Biotite and calcite form elongate subhedral crystals parallel to foliation which have quartz grown in their pressure shadows. Photomicrograph taken from OPS-3 under XPL.

EMPA was carried out on these samples. This confirmed the presence of magnetite, as well as apatite in these rocks. Apatite occurs as subhedral grains which show some elongation and alignment to the foliation (Figure 5-40). A Ce-La bearing vein was also identified in OPS-1 and OPS-3. Galena was also identified in OPS-3 using EMPA.

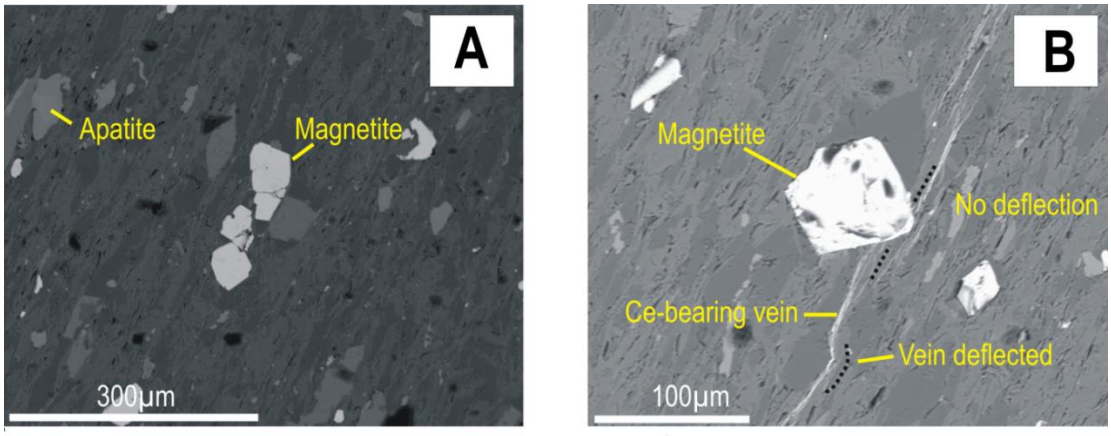

Figure 5-40: EMP Photomicrographs from EMPA of OPS-3 showing apatite (**A**), magnetite, and the Ce-bearing vein (**B**).

The layering in OPS-3 is indicative of the cyclical changes occurring during the deposition of the siltstones in the interbedded unit. This layering appears to have been exploited by mineralising fluids, as suggested by the growth of copper and lead sulfides preferentially in the coarser-grained layers. The elongation of the sulfides in these layers without the development of pressure shadows would suggest that mineralisation in these units was syn-deformational, exploiting secondary permeability associated with quartz ± feldspar. Calcite is also associated with the coarser units and shows elongation with the foliation. Some pressure shadow development is seen, but it is difficult to make statements about the timing of this mineral. Both magnetite and biotite have strongly developed pressure shadows suggesting that these phases were already present when deformation began in these rocks.

As well as using EMPA to confirm mineralogy, EMPA was also used on EPS-09 in order to confirm the findings of Dawborn (2013) that native silver was occurring with chalcocite. This was confirmed, and in the sample analysed native silver was shown to only occur in chalcocite not enclosed by magnetite i.e. chalcocite inclusions in magnetite contained no native silver (Figure 5-41). This suggests a paragenesis of chalcocite –> magnetite –> chalcocite + silver.

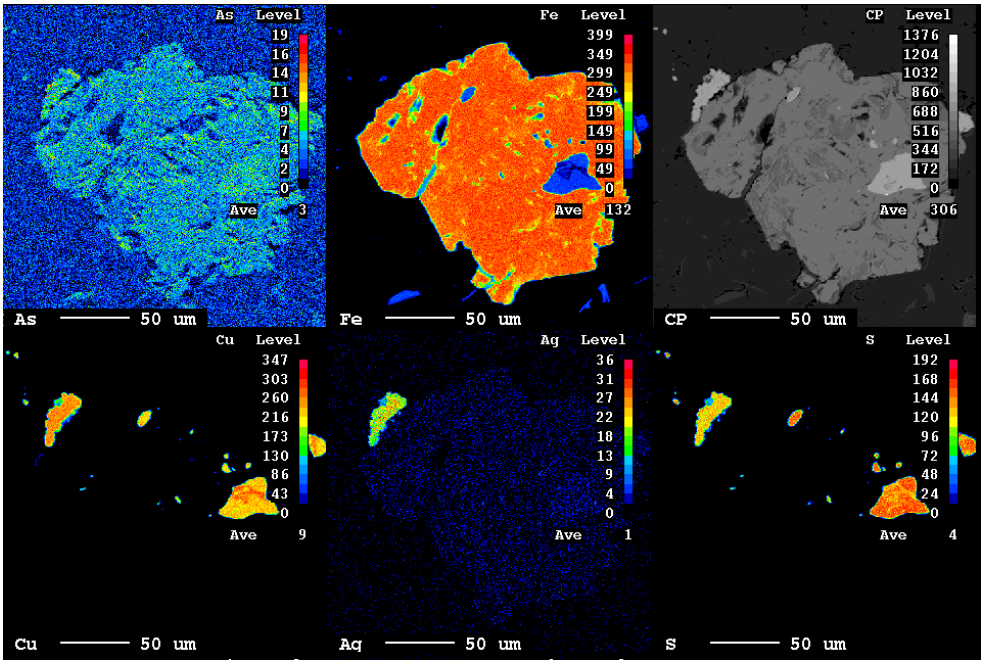

Figure 5-41: Element map of magnetite which is spatially associated with copper sulfide minerals. Native silver does not occur within the chalcocite inclusion, but occurs with the chalcocite on the magnetite grain boundary.

EPS-11 is from an argillite unit in the IBU, but it has a very similar composition to the siltstones described, although it is generally more fine-grained. Biotite defines primary bedding orientations and pre-dates the foliation forming event(s). Fine-veinlets of Ce-La-Nd mineralogy were also observed in this rock, parallel to the foliation.

The other rocks logged as argillites in the central study area are represented by the polished thin sections EPS-12, EPS-18 and EPS-32. EPS-12 and 18 are from intersections above mineralised horizons, and EPS-32 from below.

EPS-12, although primarily comprised of fine-grained quartz and very fine-grained muscovite-sericite, is cut by a thick (0.5cm) folded quartz vein which shows some evidence of fracturing, suggesting it is most likely an early bedding-parallel vein. The quartz in the vein has sutured boundaries, undulose extinction, and shows sub-grain formation. Some calcite is also present along quartz grain boundaries within the vein. The rock can be divided into two main litho-types, one is extremely fine-grained muscovite and sericite/clay minerals associated with opaque minerals, and the other is quartz and plagioclase rich, and associated with chlorite (Figure 5-42).

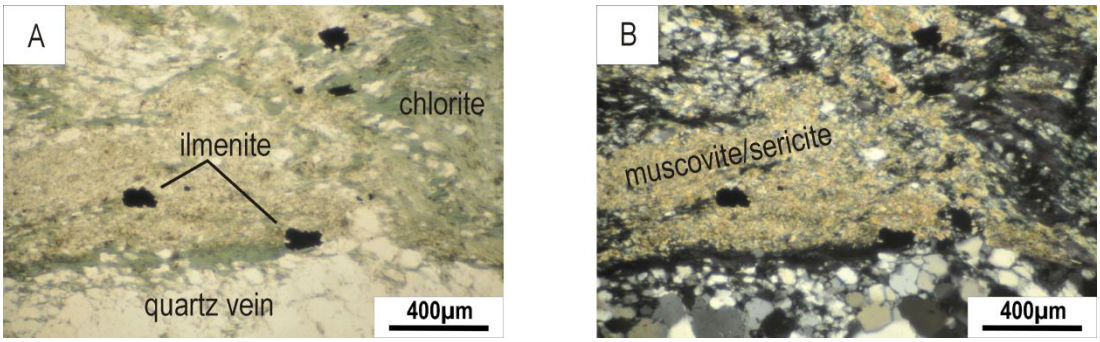

Figure 5-42: Photomicrographs from the interbedded unit argillite EPS-12 in the central study area. **A:** In PPL under transmitted light the two main litho-types are distinguished from each other and the quartz vein on the basis of colour. The vein is clear, the chlorite-rich unit is green and the muscovite-sericite unit is dusty brown. **B:** In XPL the quartz vein is clearly visible as euhedral to subhedral grains which fine towards the edge of the vein to form polygonal quartz with triple junctions.

EPS-18, although argillaceous to silty, contains abundant calcite (>70%). Calcite forms straight edged euhedral to subhedral blocky grains which average 150µm in length (Figure 5-43The rock has a banded appearance in thin section defined by alternating layers of calcite and fine-grained muscovite and sericite, with minor quartz and rare plagioclase grains (<150µm long). The fine-grained minerals define a foliation in the rock visible in the argillaceous bands, and braided networks of muscovite-sericite which run through the calcite-rich layers.

The opaque minerals identified in EPS-12 were primarily ilmenite and minor fine-grained (<20µm) chalcopyrite, galena and pyrite. This was the only sample in which ilmenite was identified using EMPA (O = 33 wt%, Ti = 31 wt% and Fe = 36 wt%). Ilmenite forms ~100µm long subhedral laths within zones of intense alteration to fine-grained platy minerals assumed to be muscovite and sericite associated with quartz veining. EPS-18 contains abundant fine-grained cubic opaques (~25µm long) which form aggregates roughly parallel to the foliation. Under reflected light these were identified as pyrite. These show no particular preference for either the calcite-rich or argillaceous layers in the rock.

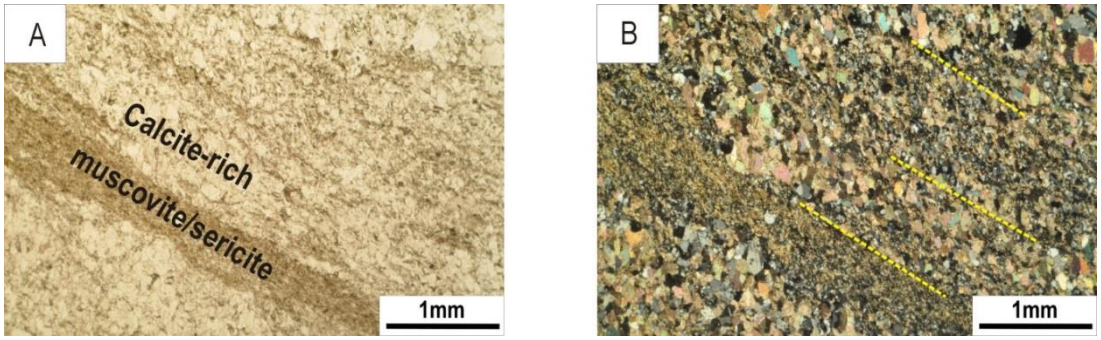

Figure 5-43: Photomicrographs from the interbedded unit argillite EPS-18 in the central study area. **A:** In PPL under transmitted light the calcite-rich bands are distinguished on the basis of their light colour relative to the muscovite-sericite bands which are a dusty brown colour. **B:** In XPL the calcite-rich units are more readily identified due to the high birefringence colours of calcite. In both XPL and PPL it is evident that this rock is strongly foliated.

EPS-32 is similar to EPS-12 and EPS-18 with a strong foliation defined by the preferred orientation of very fine-grained muscovite, sericite and chlorite. EPS-32, however, also contains lenses (<100µm up to 0.5mm thick) of felsic and carbonate minerals, and veinlets of iron oxide. Opaque minerals are disseminated throughout the rock and show no preference for either the fine-grained or coarser-grained lenses. The Fe-oxide phase (orange-red in PPL and XPL) forms common foliation-parallel veinlets throughout the rock, forming dominantly along the boundaries between more felsic and more micaceous mineral bands, and often associated with blocky chlorite (assumed to be a biotite breakdown product).

The felsic bands of the rock are often bordered by iron oxide veins, and bounded between more chlorite-rich units. The felsic bands are generally equigranular with roughly polygonal grain boundaries and some elongation parallel to foliation. The opaque minerals often show chlorite and quartz, and rarely biotite, growth in pressure shadows. They have no obvious preferred orientation relative to the foliation developed in the rock.

Under reflected light the opaque minerals were all identified as magnetite.

5.4.5 Footwall

5.4.5.1 Eastern Study Area

Samples: OPS-12 & OPS-15

The footwall samples were taken 10-20m from the mineralised zone within medium-grained grey sandstone units. The rocks are fine-grained (<35µm up to 0.7mm long) with a

lepidoblastic to granoblastic texture. A foliation is weakly developed and defined by the preferred orientation of very fine-grained muscovite, sericite and chlorite laths, as well as fine-grained (<35µm long) recrystallized polygonal felsic minerals (Figure 5-44).

These Eastern footwall samples have an average composition of:

Quartz: 55%

Plagioclase: 5%

Muscovite/sericite: 18%

Biotite/chlorite: 7%

Opaques: 3%

Calcite: 12%

Quartz grains form elongate and sutured coarser grains (up to 0.7mm long) showing strong undulose extinction, but also form bands of very fine (<35µm long) equant grains which show no undulose extinction. Feldspar grains, reaching up to 0.55mm, are anhedral, with irregular to sutured boundaries and twinning (plagioclase). Most of the feldspar has, however, been replaced by/altered to very fine-grained sericite. The few (~1%) plagioclase crystals which have not been altered show the formation of sub-grains, as well as deformation twinning. Calcite is common, and accounts for about 12% of the rock, reaching similar sizes to the felsic minerals. This mineral, with it distinctive cleavage, and twinning, occurs as anhedral to subhedral (rarely cubic) crystals, often elongated parallel to the fabric in the rocks. In places calcite appears to almost blend into the braided networks of the micaceous minerals which cross-cut these rocks. Fine-grained muscovite, sericite and chlorite braided networks define a lepidoblastic textures which bends around the felsic minerals and give the rocks a greenish colour. Chlorite generally forms fine-grained greenish-brown plates and is confined to aggregates along grain-boundaries between felsic minerals, however, occasional pseudomorphs after biotite are observed where chlorite takes on a browner colour and forms blocky laths. Biotite occurs as subhedral to blocky grains up to 0.35mm long elongated parallel to the foliation. Coarse-grained, bent muscovite (up to 0.4mm long) laths occur sporadically throughout the rock. These laths are commonly bent at an angle to the developed foliation. Titanite and zircon are fairly common accessory minerals in these rocks.

Under transmitted light the opaque minerals appear equant. They occur as cubic to euhedral grains ~0.15mm across. The grains are disseminated throughout the rock, but tend to favour micaceous assemblages. There are occasional lenses where the opaques form bands (up to 0.35mm long). There are also opaque aggregates which form veinlets with a deep red colour (suggesting goethite). These remain dark under transmitted light.

The opaque minerals are all magnetite, occasionally showing evidence of oxidation. Magnetite shows no development of pressure shadows. There are some incredibly fine-grained minerals which may be chalcopyrite, but they are too fine to classify. A <35µm long lath of covellite was observed in sample OPS-12, which is closer to a mineralised horizon than OPS-15.

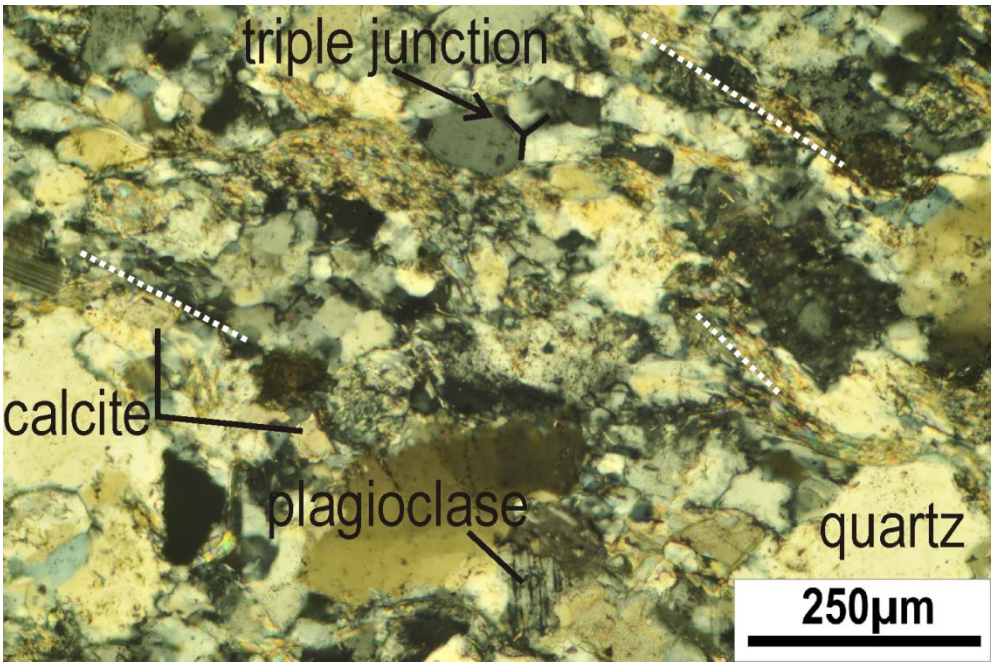

Figure 5-44: Photomicrograph of the main textural and mineralogical features of the footwall in the east of the study area. Image taken from OPS-12.

Undulose extinction and the formation of sub-grains in quartz and plagioclase, as well as the bending of muscovite laths, suggest compaction of the sediment pile, and brittle flexing. The absence of undulose extinction in the quartz grains which share triple junctions suggests that this quartz re-equilibrium during the deformation event which produced the triple junctions. No pressure shadows on the magnetite, and the growth of this mineral parallel to the fabric suggest that the magnetite grew with the fabric. The fine-grained

braided networks of muscovite, chlorite and sericite suggest that a fluid has moved through this rock.

The thinning of the muscovite and biotite grains along their edges also suggests leaching may have occurred, most likely by a fluid phase exploiting the foliation. Hydrothermal fluids exploiting the foliation are also implied by the growth of magnetite during fabric formation. The preferential breakdown of feldspars to sericite is also indicative of fluids.

5.4.5.2 Central Study Area

Samples: OPS-5, OPS-7, EPS-5, EPS-13, EPS-15, EPS-17, EPS-19 & EPS-27

These samples were taken from fine-grained grey sandstone units. Sample OPS-7 includes an interbed of argillite (Figure 5-45). The sandstone units are fine-grained (<0.1 - 2.5µm diameter) with sutured boundaries between the larger grains common. Schistosity is poorly developed in OPS-5 with alignment of the muscovite/sericite laths subordinate to the volume of felsic minerals which show no alignment. In sample OPS-7 the volume of phyllosilicates is higher and the schistocity more strongly developed. Opaque mineral clusters are aligned with the micaceous lenses, particularly along the contact between the sandstone and the finer-grained, argillaceous interbed.

The average composition of the Central footwall sandstones is:

Quartz: 50%

Plagioclase: 15%

Muscovite/sericite/chlorite: 32%

Opaques: 3%

Closer to the argillaceous interbed the volume of quartz and plagioclase declines, and is almost entirely absent in the argillite. The sandstone is dominated by quartz which is largely anhedral to subhedral and averages 2µm in length. Quartz shows undulose extinction, sutured grain boundaries and sub-grain formation. Plagioclase feldspar is identified by its characteristic twinning. All the plagioclase has been altered to sericite to some degree, and in general grain boundaries have sutured edges. Fine-grained (<35µm diameter) polygonal felsic minerals are common aggregates interstitially between coarser minerals. Closer to the argillite interbed the felsic minerals commonly occur as lenses boudinaged between layers of phyllosilicates. In these bands the felsic minerals are more elongate and fine-grained (<35µm length). Pseudomorphs after biotite are common as fine-

grained blocky grains dispersed throughout the sandstone where biotite has retrogressed to chlorite. Chlorite is also common with fine-grained muscovite and sericite as aggregates along grain boundaries. These are more common towards the argillite interbed where these minerals form connected networks and define a strong foliation in the rock. Some coarse-grained bent muscovite (~0.15mm long) laths are also present. Accessory zircon and titanite are also present in the rock, as are minor carbonate minerals (calcite).

The argillite layer is composed primarily of very fine-grained muscovite and sericite and contains lenses/streaks of felsic minerals and thin bands of dark brown material which has strong asymmetric microfolds. EMPA identified this as mineral as titanite. Euhedral felsic minerals are present in the bends of some of these folds, as are opaque minerals, suggesting these grew after folding. There is a vein (0.25mm diameter) roughly parallel to the foliation. Away from the vein are what look like deformed/ folded felsic aggregates between parallel bands of dark fine-grained minerals. These aggregates appear completely recrystallized to form stretched honeycomb textures. The minerals in these clusters are euhedral and elongated parallel to the foliation, and have been extensively replaced by/altered to sericite. One such cluster has a carbonate mineral core.

In transmitted light the contact between the arkose/sandstone and the argillite interbed is marked by aggregates of anhedral opaque minerals with some red (goethite?) staining. These clusters are elongated parallel to the foliation/contact and reach up to 2mm long and 0.01mm thick. In the sandstones the opaques form subhedral grains reaching 0.5µm long but generally are all less than 0.1µm long, with a slight elongation parallel to the foliation, occurring as single grains and aggregates. On average the opaques are less than 0.05mm long, and show a strong association with the micaceous minerals. In the argillite unit the opaques occur as very thin streaks (<0.01mm long) parallel to the foliation. Opaques also occur in the bends of folds as subhedral aggregates.

In reflected light and using EMPA, the opaques in the sandstones are identified as anhedral magnetite. In the sandstone with the interbed of argillite the sandstone also contains covellite, with minor very fine-grained chalcopyrite and bornite. Covellite dominates the assemblage of opaques which mark the contact between the sandstone and the argillite interbed. Occasional inclusions of chalcopyrite occur within these anhedral covellite aggregates. Anhedral and pitted magnetite grains also occur along this boundary, as well as rare bornite. Covellite was identified growing along the edges of magnetite grains,

however, chalcopyrite and bornite tend to occur as isolated grains (<0.01mm long). In the argillite the opaques are dominantly magnetite, covellite, bornite and chalcopyrite.

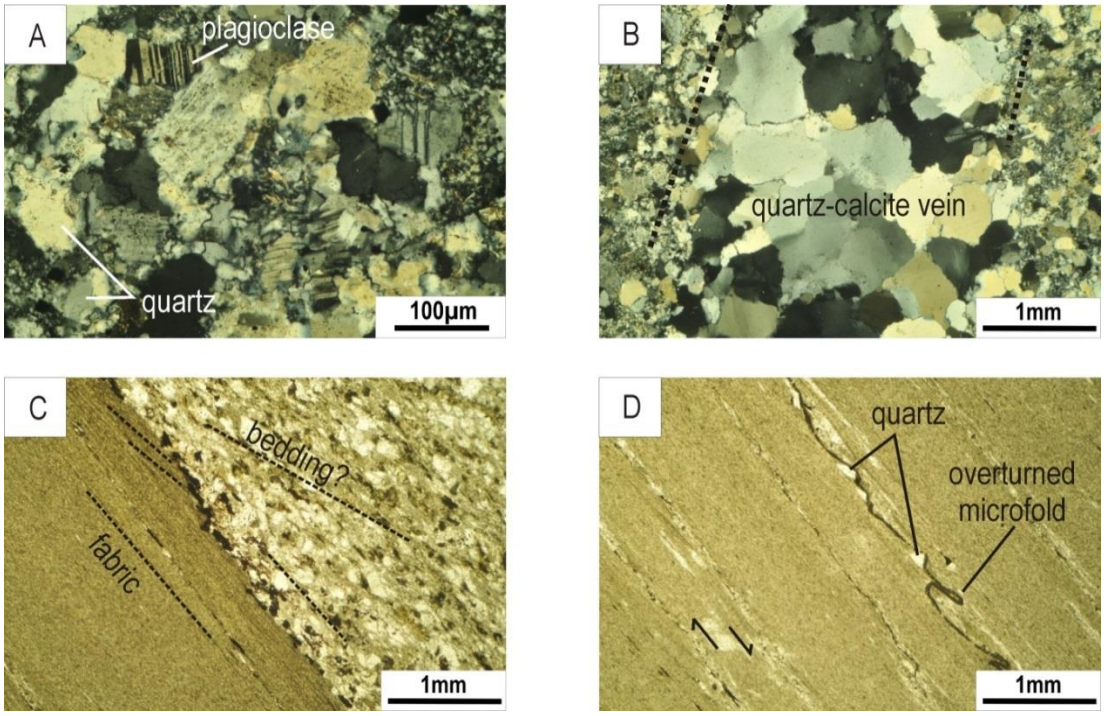

Figure 5-45: Photomicrographs from the footwall sandstone lithotypes in the central study area. **A:** Typical sandstone composition of plagioclase and quartz showing sutured boundaries, sub-grain formation and fine-grained polygonal felsic aggregates along grain boundaries (recrystallization). Photomicrograph from OPS-5 in XPL. **B:** Quartz-calcite vein cross-cutting the footwall sandstone. Photomicrograph from OPS-5 in XPL. **C:** Contact between the sandstone and fine-grained argillite unit from OPS-7. Remnant cross-bedding is visible, as well as a strong schistose fabric in the argillite. Photomicrograph from OPS-7 in PPL. **D:** A thin layer of titanite is micro-folded and deflected around angular quartz grains. Photomicrograph from OPS-7 in PPL.

EMPA showed that the covellite crystals in the sandstone contain inclusions of titanite. Anomalous Zn values, up to 12 wt. %, were also reported for covellite from this layer. Ilmenite was also identified in the sandstone using EMPA. There is a quartz-calcite vein which cuts across the footwall sandstone sample OPS-5 which contains a few opaque minerals. Under reflected light a large subhedral grain was identified as chalcopyrite (~2mm long) with magnetite ~3µm across. Bornite is present along the edges of the chalcopyrite and one edge of the magnetite. Small sporadic crystals of chalcopyrite, bornite and covellite are also identified in the vein. A large anhedral grain of galena and bornite was also identified (~0.4mm long). The two share a relatively straight grain boundary and are relatively equal in size. Covellite shows a strong alignment to the foliation in the argillite layer (Figure 5-46).

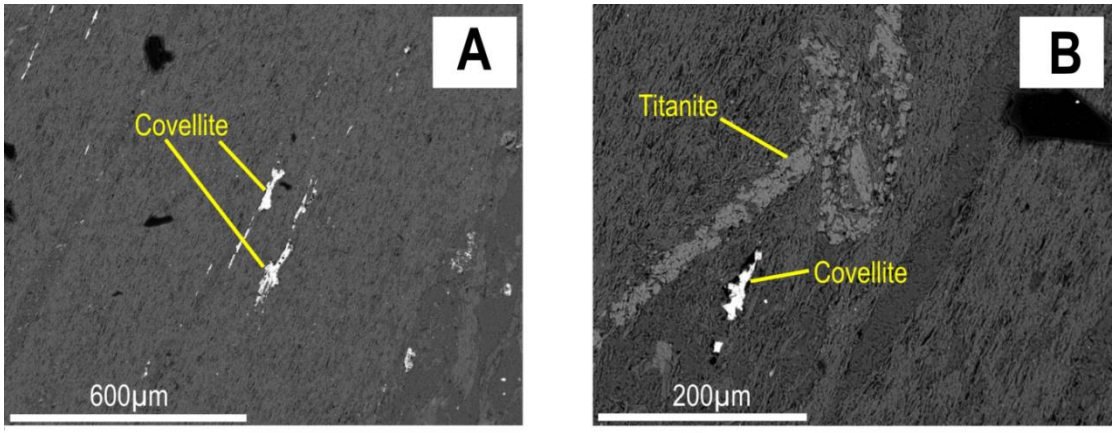

Figure 5-46: Covellite shows a strong alignment to the foliation in the fine-grained sediment layer within sample OPS-7. Photomicrographs taken during EMPA.

The sandstone units show evidence of having undergone compaction. The presence of undulose extinction, sutured boundaries and sub-grain formation suggest this. Bent detrital muscovite laths would also suggest this. The argillite unit, however, suggests more dynamic, ductile deformation. The folding deflects around occasional detrital quartz grains and aggregates, with the fine folded units showing no indication of stretching or shearing. The way these veins have precipitated and deformed suggests that Ti-rich fluids were exploiting zones of increased porosity proximal to the thin layers of coarse quartz, around which they deflect. The presence of the same copper-sulfide minerals and magnetite in the sandstone, vein and the argillite unit suggests that these were mineralised at the same time. The concentration of these phases along the contact between these contrasting lithotypes suggests the contact formed an important fluid conduit. The absence of pressure shadows around these opaques implies that they grew during or after deformation, although their alignment parallel to the foliation could be used to argue for a syn-deformational origin. Magnetite forming with chalcopyrite in the quartz-carbonate vein within the sandstone indicates that magnetite and the copper-sulfides precipitated at the same time.

Overall the mineralogy and textures of the additional samples were similar to those already discussed for the footwall of the central area, however, additional opaque minerals were identified. These findings are summarised in a series of photomicrographs (Figure 5-47, Figure 5-48 & Figure 5-49).

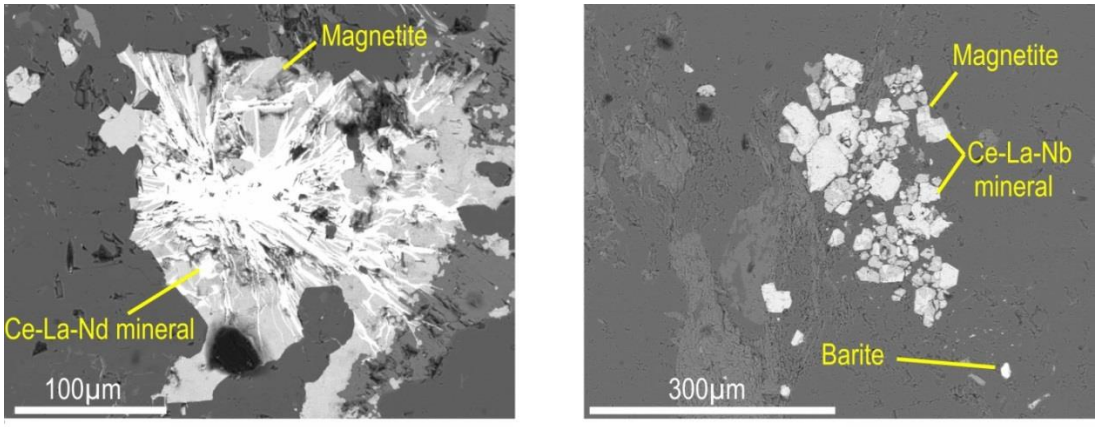

Figure 5-47: Magnetite intergrown with Ce-La-Nd minerals in footwall sample EPS-13, CA-PL-9. Photomicrograph taken during EMPA.

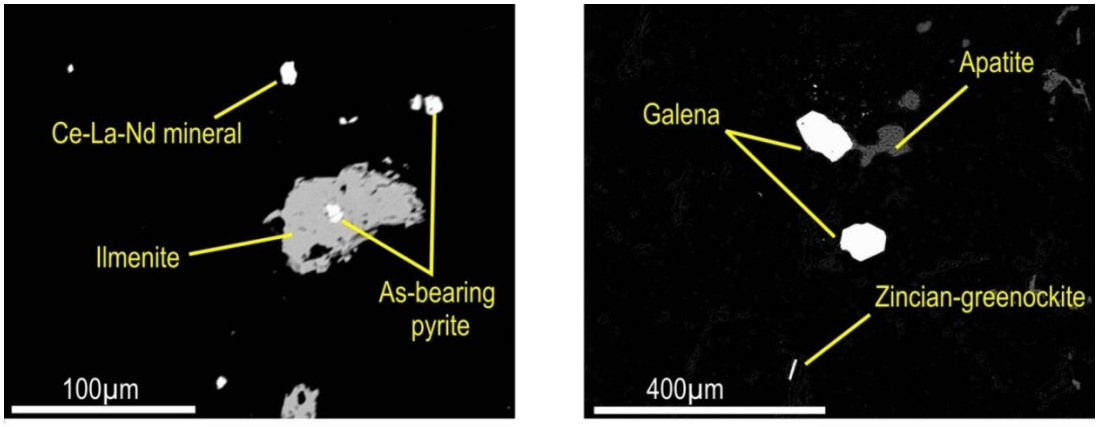

Figure 5-48: Subhedral to anhedral ilmenite was identified in sample EPS-19, CA-PL-6. Apatite, euhedral galena and zincian-greenockite were also identified in this rock. Photomicrograph taken during EMPA.

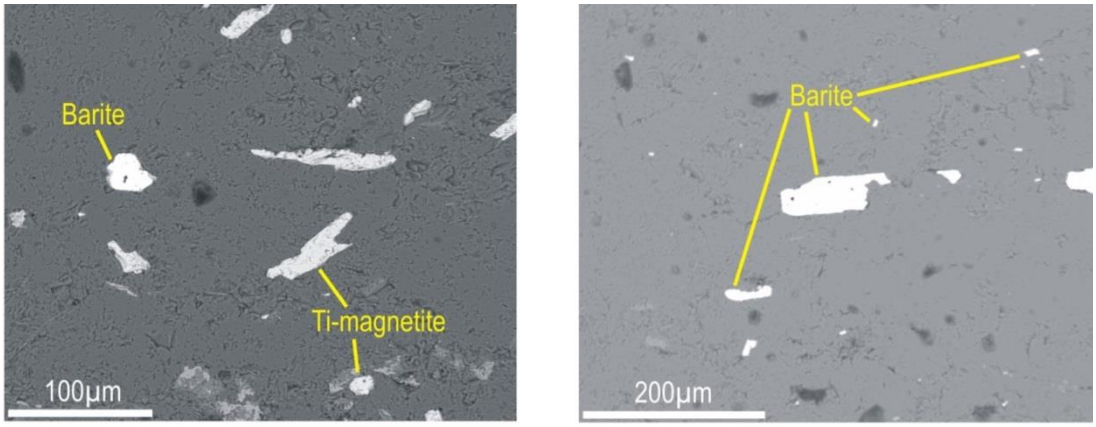

Figure 5-49: Barite is a fairly common opaque mineral in the footwall sample from EPS-05, about 15m below EPS-19, CA-PL-6. Magnetite reports high Ti values which may suggest exsolutions of ilmenite. Photomicrograph taken during EMPA.

5.4.6 Unmineralised Central Zone

Samples were taken from ~166m (EPS-14) and 287m depth (EPS-08) from borehole CZ-1. This borehole forms part of the central area, but is to the WNW of the nose of central anticline (CA) and contains no copper mineralisation (Figure 5-50).

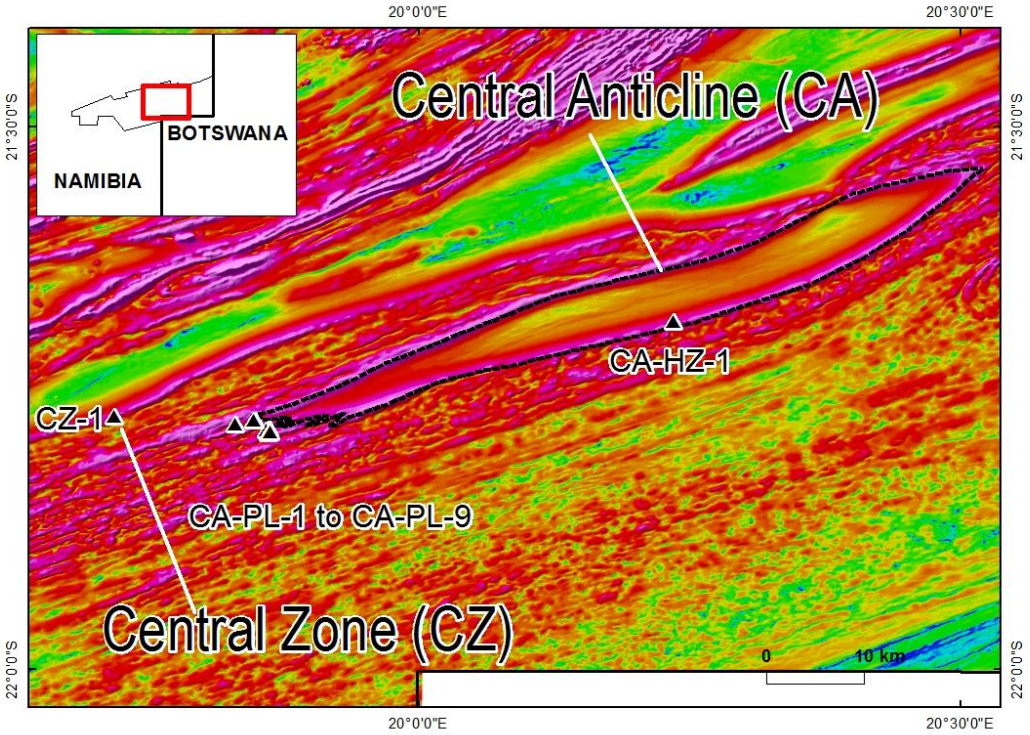

Figure 5-50: Borehole CZ-1 is located to the WNW of the Central Anticline. Background is the GSN regional airborne magnetic survey Analytical Signal (AS) image.

Sample EPS-14 has an average composition of:

Quartz: 65%

Plagioclase: 10%

Muscovite/sericite/chlorite: 15%

Biotite: 7%

Opaques: 3%

In hand specimen the sample is fine-grained and light grey sandstone with bands of reddish brown minerals. The bands appear siliceous and have a sugary appearance. The reddish-brown minerals look like the products of the oxidation of iron-rich minerals. Throughout the rock are coarse-grained dark minerals and medium-grained micaceous aggregates.

In thin section the banding in the rock is defined primarily by the euhedral to subhedral opaque minerals (Figure 5-51). These form the reddish bands seen in hand specimen and as well as opaque minerals (~0.65mm long) are composed predominantly of biotite (<0.35mm long) aggregates, and minor zircon (average grain size ~0.15mm), rutile and chlorite. The opaque minerals are also scattered throughout the sample, with maximum grain sizes reaching about 0.4mm diameter. The bulk of the rock is composed of quartz and plagioclase. Quartz grains are subhedral to angular with sutured boundaries and undulose extinction common. The average grain size is ~0.4mm diameter. Sericitised feldspars are common, and account for approximately 10% of the rock. Euhedral to subhedral grain shapes are suggested by the grain outlines. In about a third of these grains the conversion of these feldspars is incomplete and fine-grained clay minerals are clustered around the core of the feldspars but twinning is preserved, suggesting plagioclase was the dominant feldspar. Plagioclase also shows undulose extinction and sub-grain boundary formation. Along the grain boundaries between quartz and plagioclase is a network of fine-grained sericite, chlorite and muscovite. Occasional fine-grained biotite laths are also present with the phyllosilicates as well as small euhedral hematite crystals. Along grain boundaries polygonal quartz is also common. This recrystallized quartz shows undulose extinction and the development of triple junctions. There is also the suggestion of incomplete recrystallization of plagioclase in the form of grains with abundant deformation twinning, but no polygonisation. Detrital muscovite is identified in the rock (<0.35mm long), and is usually bent.

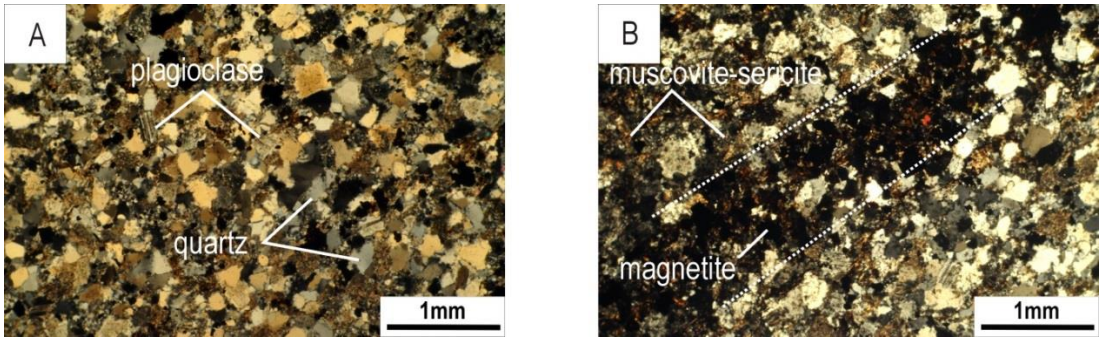

Figure 5-51: Photomicrographs from sample EPS-14 showing the texture of the rock in XPL (**A**) and the magnetite bands associated with muscovite and sercite (**B**).

The opaque phases in this rock were identified using EMPA (Figure 5-52). The dominant phase in the dark bands is magnetite. This magnetite is commonly cracked with a cubic to subhedral shape. Zircons also show brittle fracturing (Figure 5-52D).

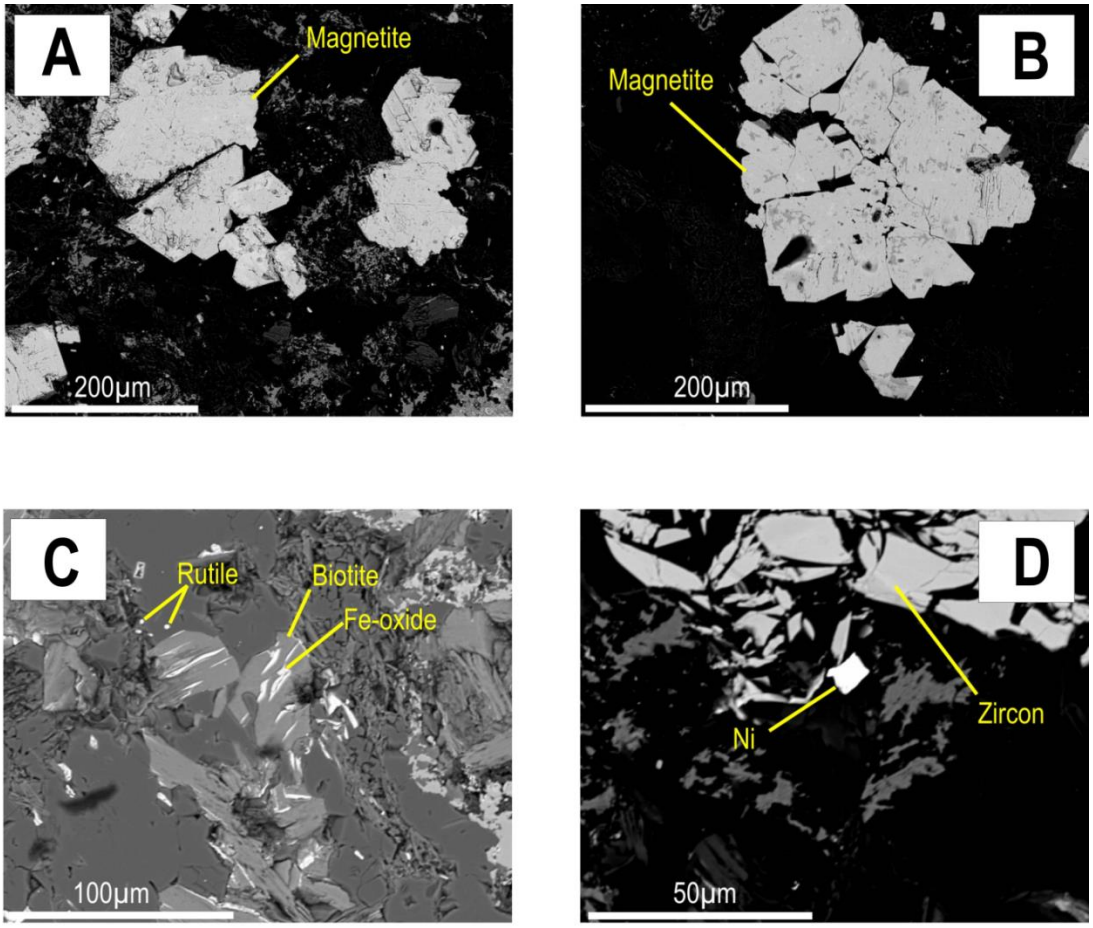

Figure 5-52: Magnetite forms subhedral to cubic aggregates which show brittle fracturing (**A & B**). An Fe-oxide phase has exsolved from biotite along cleavage planes (**C**). Zircon has also undergone brittle fracturing (**D**). In this sample a single grain of almost pure Nickel was also identified. Photomicrographs taken during EMPA on sample EPS-14, CZ-1.

EMPA also identified Fe-oxide exsolutions associated with the biotite along the bands, and an anomalous grain of pure nickel (Ni = 97 wt%, Fe = 1.17 wt%, Ti = 0.51 wt%, Cr = 0.43 wt%). Nickel was not identified anywhere else in the Eiseb.

The rock has undergone compaction and deformation, as shown by the presence of undulose extinction, sub-grain formation and brittle fracturing. Zircons and rutile, suggest sedimentary heavy mineral banding, and the magnetite either concentrated at the same time or grew from a fluid exploiting this banding.

Sample EPS-08 was taken from a carbonate below the banded sandstone of EPS-14. The carbonate has an average composition of:

Calcite: 70%

Muscovite/Chlorite: 10%

Quartz: 20%

Under transmitted light the sample is a fine-grained carbonate with opaque minerals defining a foliation. Individual carbonate grains are generally too fine to distinguish, however, larger carbonate grains of calcite can reach up to 0.35mm, and account for about 50% of all the carbonate present. These grains have rounded ends on their long axis and are largely elongate parallel to foliation. Within the carbonate matrix there are occasional rounded to sub-rounded quartz grains which show undulose extinction, the largest of which is approximately 0.3mm. Finer-grained lenses of angular to sub-rounded silicate minerals (probably quartz) are common throughout. These show undulose extinction and some sub-grain boundary formation. These lenses often contain minor fine-grained muscovite and very fine-grained opaque minerals. There are two fabrics developed in this rock. The first fabric is defined by opaque minerals. The opaque minerals are irregular and appear to blend together to form this foliation of roughly parallel bands (Figure 5-53). There is a second type of opaque minerals which are cubic and also follow the same foliation trend, suggesting they formed at the same time as the elongate opaques. The second fabric is defined by silicate lenses, and very fine grained chlorite and muscovite. This fabric is crenulated and folded in an irregular way which often drags down the first fabric, suggesting it was formed after the first fabric.

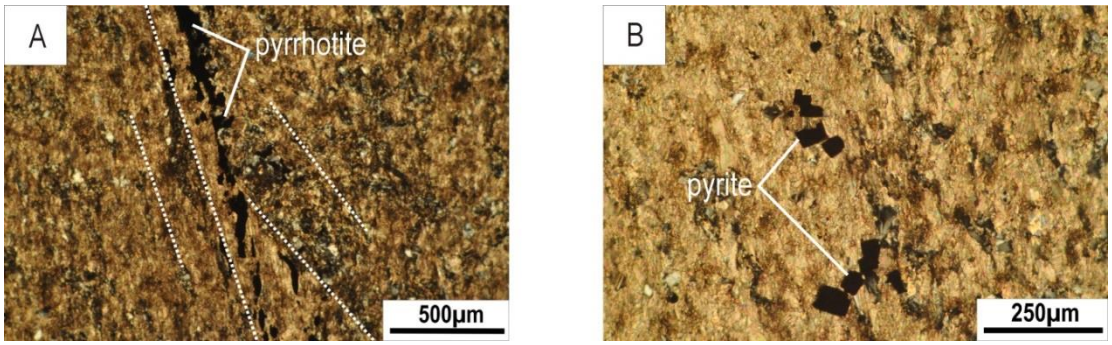

Figure 5-53: Pyrrhotite defines a foliation in the rock which is distorted by a second foliation which deforms the first (**A**). Pyrite occurs in lenses parallel to the foliation (**B**). Both images taken in XPL.

Under reflected light, and using EMPA, the opaque minerals are identified as elongate, anhedral pyrrhotite with occasional inclusions of galena (Figure 5-54: Pyrrhotite forms elongate bodies parallel to the foliation. Photomicrographs taken during EMPA.Figure 5-54). The rare cubic clusters are pyrite.

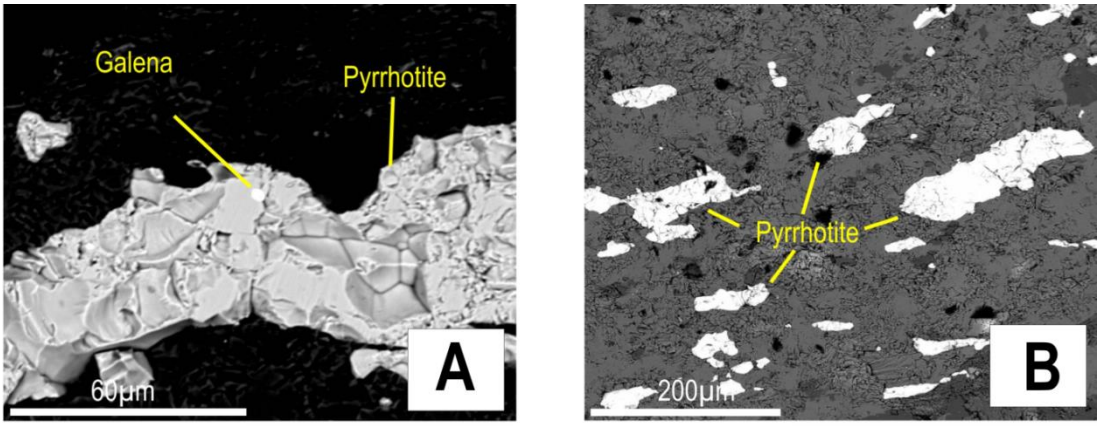

Figure 5-54: Pyrrhotite forms elongate bodies parallel to the foliation. Photomicrographs taken during EMPA.

5.4.7 Mineralised Zone

5.4.7.1 Eastern Study Area

Samples: PB-14, PST-2D2-4, PST-4D1-4, PST-7D1-1, PST-7D1-2

The samples are taken from the mineralised zones of NEA and the EA. These rocks are commonly foliated, fine-grained (siltstones to phyllites) and interbedded with layers of subhedral quartz ± feldspar (>35µm <0.4mm long). Opaque minerals occur as interstitial cements and elongated irregular minerals parallel to the foliation (Figure 5-55). The foliation is largely defined by abundant bright green chlorite, and colourless to brown fine-grained muscovite and sericite.

The average composition of these units is:

Chlorite: 35%

Muscovite/sericite: 27%

Quartz: 20%

Plagioclase: 3%

Biotite: 5% (up to 10%)

Titanite: 5%

Opaques: 5%

Quartz is typically subhedral and shows both undulose extinction and the development of sub-grains. Plagioclase is rarely discernable but twinning is sometimes still preserved however, in most instnaces this mineral has been extensively replaced by sericite.

Muscovite and sericite define the foliation in this rock, together with chlorite. Muscovite also forms coarser bent laths (~35µm long) scattered throughout the rock.

Chlorite has a bimodal occurrence in these rocks, as coarse laths elongated parallel to compositional layering, and fine-grained plates commonly intergrown with muscovite and sericite which define the foliation. Foliation forming chlorite concentrates parallel to opaque minerals, and shows some alteration to/from biotite. Coarse chlorite laths (up to 0.7mm long), elongated parallel to the layering, occur in the finer-grained portions of these rocks intergrown with quartz. A few of these laths are bent suggesting they were pre-deformation. There is some alteration apparent along grain boundaries and cleavage planes. Chlorite commonly shows alteration to/from biotite and rare pressure shadows are sometimes associated with these coarser laths. There is a strong association between chlorite and the opaque minerals.

One of the samples (PST-4D1-4) contains abundant biotite, up to 10%. Biotite forms irregular to blocky laths elongated parallel to layering in the felsic layers of the rock. Biotite appears to be pre-fabric development as pressure shadows are common. Alteration along the grain boundaries and cleavage planes is common. There is a strong association between the opaques and biotite.

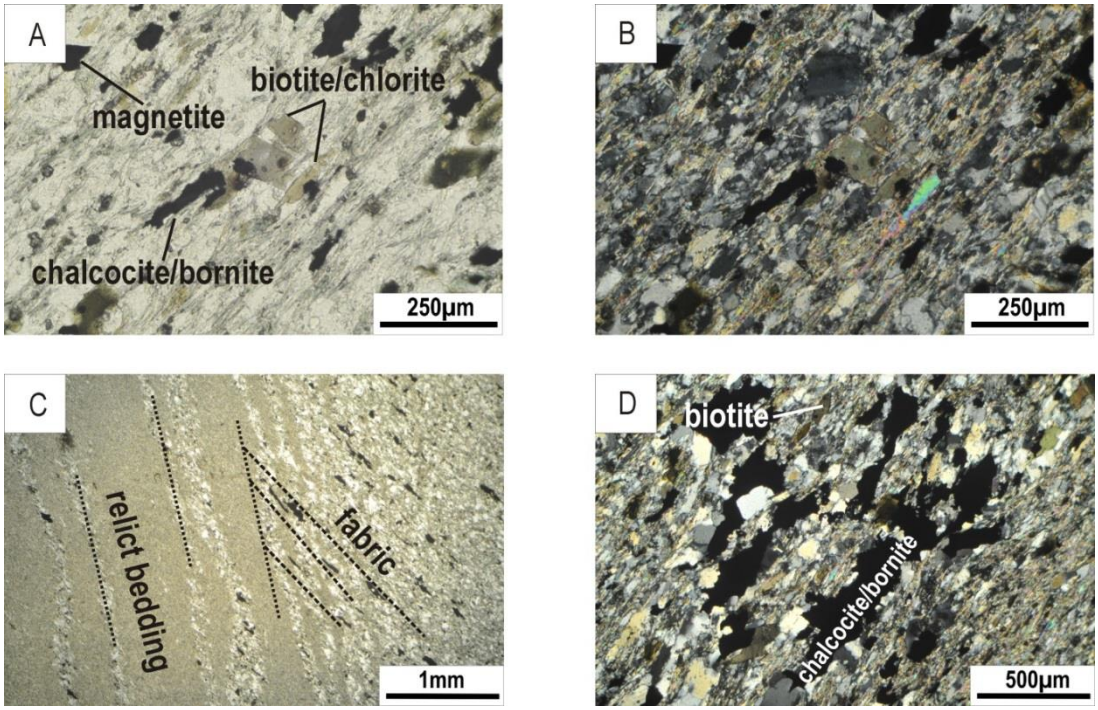

Figure 5-55: Photomicrographs from the mineralised siltstones and phyllites of the eastern study area. **A:** The ore minerals chalcocite and bornite are replacing biotite/chlorite blocky laths parallel to the foliation. Photomicrograph from sample PST-4D1-4, borehole NEA-PL-1, taken in PPL. **B:** Occassional plagioclase grains are preserved and show characteristic twinning. Detrital muscovite grains are rarely aligned to the foliation. Photomicrograph from sample PST-4D1-4, borehole NEA-PL-1, taken in XPL. **C:** Felsic minerals (white) form thin layers which indicate original sedimentary bedding. Opaque minerals favour the coarse felsic band where they form lenses parallel to the foliation. Photomicrograph from sample PST-7D1-1, borehole EA-SL-1, taken in PPL. **D:** Biotite, altering to/from chlorite, shows a strong spatial association with copper mineralisation. Photomicrograph from sample PST-4D1-4, borehole NEA-PL-1, taken in PPL.

Occasional subhedral to euhedral calcite is also observed (~0.1mm diameter) and associated with the coarser felsic units. Euhedral epidote is also observed in these units (<35µm long). Titanite occurs as euhedral to blocky minerals typically <35µm distributed throughout the rock.

The opaques are elongated at an angle to the compositional layering in the rocks suggesting that the layering may be remanent bedding. This implies that the opaques developed with the fabric in these rocks.

Under reflected light the opaque minerals elongated with the foliation are identified as chalcocite with exsolutions of bornite and vice versa. Replacement of bornite by covellite is common in these intergrowths, but less common for pure bornite.

Magnetite is fairly common, forming euhedral porphyroblasts up to 0.4mm diameter which occur spatially near the copper sulfides, and which show an alignment with the foliation. Rare examples show magnetite and Cu(-Fe) sulfides sharing straight grain boundaries,

suggestive of growth under equilibrium conditions (Figure 5-56). Galena is also fairly common and occasionally occurs as inclusions within magnetite and Cu-Ag sulfides.

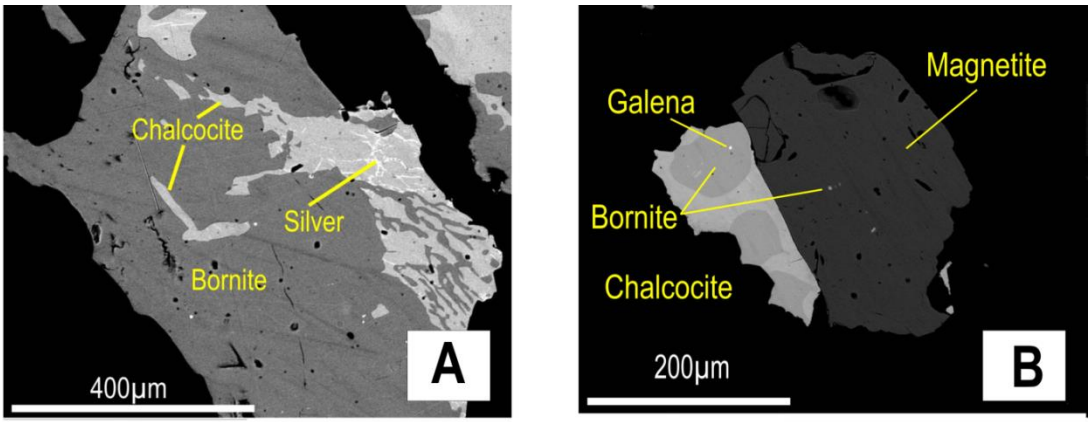

Figure 5-56: A: Bornite and chalcocite commonly form exsolutions textures. Native silver is within chalcocite grains. B: Galena forms inclusions within bornite and magnetite grains. Magnetite and chalcopyrite share a straight boundary. Photomicrographs taken from sample PST-4D1-4 from borehole NEA-PL-1.

PST-2D2-4 shows similar characteristics to those observed in PST-2D2-1, with complex intergrowth textures observed between an iron-oxide phase, assumed to be goethite or lepidochrosite (EMPA Fe: 65wt. %, O: 35wt. %), and Cu(-Fe) sulfide minerals (Figure 5-57).

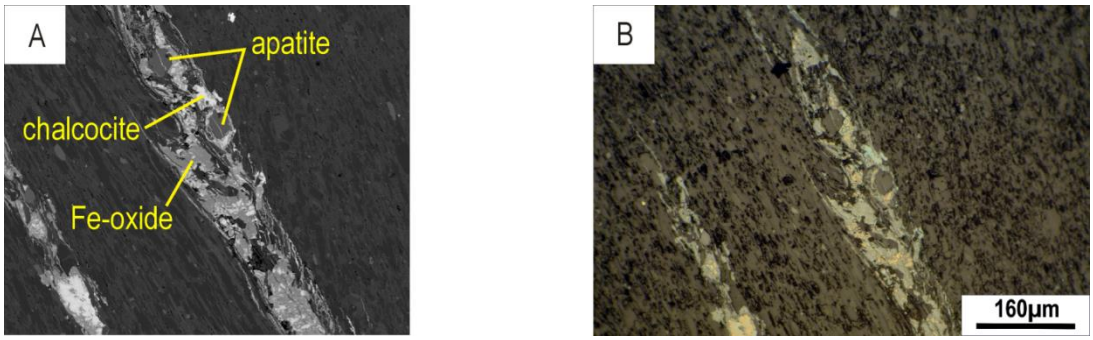

Figure 5-57: EMPA photomicrograph (**A**) of a mineralised layer from PTS-2D2-4 from EA-PL-1. Apatite, goethite/lepidocrocite and chalcocite form the main constituents of the ore assemblage in this rock. **B**: Photomicrograph of the same view taken under reflected light. The iron-oxides appear light grey, and the copper sulfides as blue (chalcocite) to orange (bornite).

In this rock apatite forms part of the ore assemblage, and is assumed to be metamorphic/hydrothermal in origin because it occurs with the Cu-Ag sulfides parallel to the foliation without the development of pressure shadows. Mineralisation occurs in layers parallel to the foliation, forming inclusion within the iron-oxide, but also intergrown with this phase. The apatite crystals have been cut by a layer parallel vein which is assumed to be one of the late stage Ce-La-Nd veins which are commonly observed.

Biotite appears to be detrital in this rock, or formed prior to the main foliation forming event because it is associated with pressure shadows and shows more of an alignment to the remnant bedding than the foliation. Magnetite occurs in the coarser bands of these rocks and shows alignment to the foliation, suggesting that this phase was precipitated during the foliation forming event or in the later stages of it because this phase is not deformed. The straight boundary seen between chalcocite and magnetite in one of the samples (PST-4D1-4) suggests equilibrium conditions existed between these two minerals during their growth. Galena and at least some copper sulfides must have been present prior to the main mineralising event as they form inclusions in magnetite, and in the case of galena, also within the copper sulfides. The copper sulfides formed during the main mineralising event show a strong association with chlorite, the fabric in the rock and magnetite. The elongation of these sulfides parallel to the fabric suggests that mineralisation was related to the formation of the foliation. As with the magnetite, the fact that none of these elongated bodies have been deformed or have pressure shadows suggests a late stage emplacement. The fluids responsible for the mineralisation have preferentially exploited the permeability associated with the coarse-grained portions of these rocks as there are almost no opaques associated with the fine-grained layers.

5.4.7.2 Central Study Area

Samples: PB-6, PB-8 and PB-12

Polished blocks were prepared from mineralised intersections of three different drillholes representing three different lithotypes, a sandstone, siltstone and phyllite. These form the basis of the analysis carried out using the QEMSCAN in the following section, which also included polished thin sections from the mineralised metavolcanic (EPS-04), footwall from the CA (OPS-7), and hangingwall samples from EA (OPS-11) and the CZ (EPS-14). Eight polished grain mount samples were also investigated using the QEMSCAN.

5.5 QEMSCAN Textural and Mineralogical Investigation

Subsequent to recording the spectral measurements and BSE intensities using the QEMSCAN, samples were processed with the iDiscover 5.4 software package from FEI (Table 19). The individual fields within a given sample were stitched together to produce false colour mineral maps (Figure 5-58 to Figure 5-60 & Figure 5-63 to Figure 5-70). The software was then used to analyse the mineralogy, mineral associations and textures.

Table 19: Samples analysed using QEMSCAN. All samples prefixed with 'PB' are polished blocks and the whole rock samples are polished thin sections. Grain mount samples prefixed with 'MG' are thin sections.

Sample No.	Borehole	Lithotype	Location	Representative whole-rock sample
MG-1	WB-1	Metavolcanic	Footwall	/
MG-3	WB-2	Metavolcanic	Mineralised zone	EPS-04
MG-5	NEA-PL-1	Sandstone	Hanging wall	/
MG-6	CA-PL-6	Sandstone	Mineralised zone	PB-6
MG-9	EA-SL-1	Phyllite	Mineralised zone	PB-9
MG-10	NEA-PL-1	Phyllite	Mineralised zone	PB-10
MG-12	CA-PL-1	Phyllite	Mineralised zone	PB-12
MG-13	CA-PL-1	Siltstone	Footwall	OPS-7
PB-08	CA-PL-3	Siltstone	Mineralised zone	/
OPS-11	EA-NL-1	Sandstone	Hangingwall	/
EPS-14	CZ-1	Siltstone	Hangingwall	/

5.5.1 SIP Mineralogy

The primary pixel allocation generates mineral lists with over 350 definitions. The first stage of analysis is therefore grouping minerals into a manageable list which is representative and relevant to the study (Appendix V). Minerals were grouped using (Deer et al., 2013) as a reference guide. For example, dravite, schorl and dravite-schorl were all grouped into ‘Tourmaline’.

Minerals which accounted for <0.0051 % of a given sample were grouped into the category ‘other phases’ to simplify the list further and remove single pixel data. The simplified categories define a secondary SIP (~40 entries) which was used to classify the pixels of both the whole rock and grain mount samples. ‘Unclassified’ pixel data and two trap (T) mineral definitions, ‘Cu-Fe sulfide (T)’ and 'K-Al-Fe-silicate (T)’ were kept in the secondary SIP. The 'Cu-Fe sulfide' trap, for example, is used to define pixels which contain Cu, Fe and S, but for which no specific mineral has been defined within the primary SIP. The compositional boundaries are less strict for 'trap' definitions.

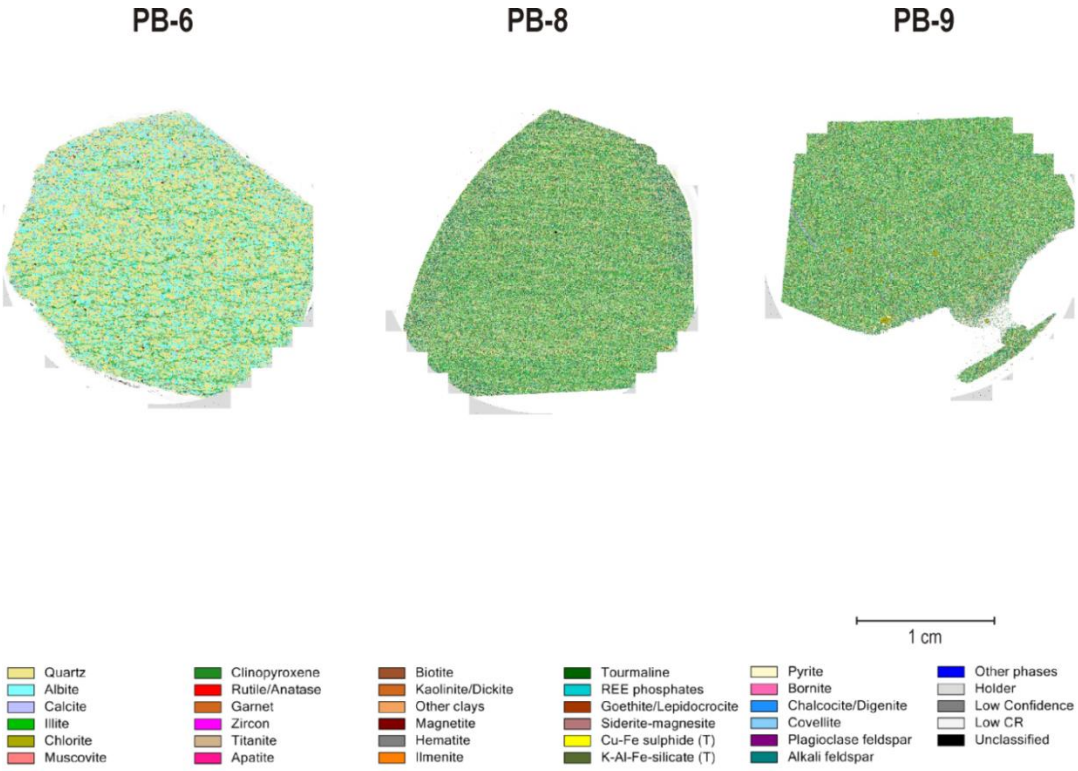

Figure 5-58: False colour mineral maps of PB-6 (sandstone), PB-8 (siltstone) and PB-9 (phyllite).

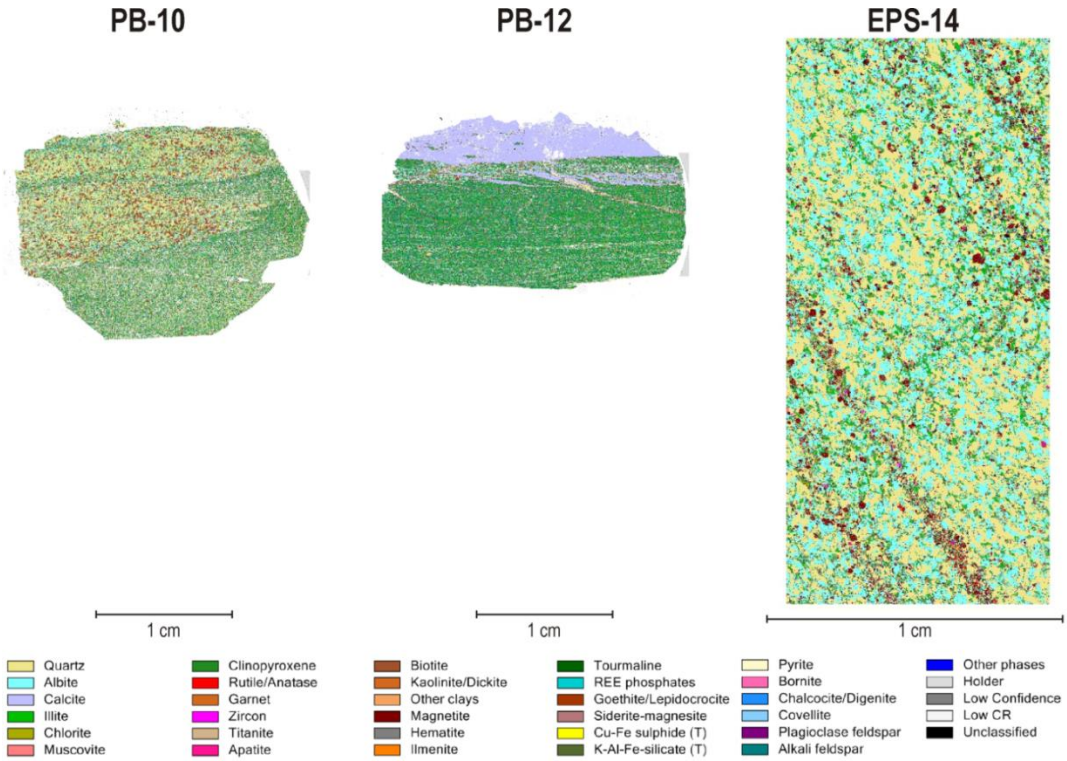

Figure 5-59: False colour mineral maps of PB-10 (phyllite), PB-12 (phyllite) and EPS-14 (siltstone).

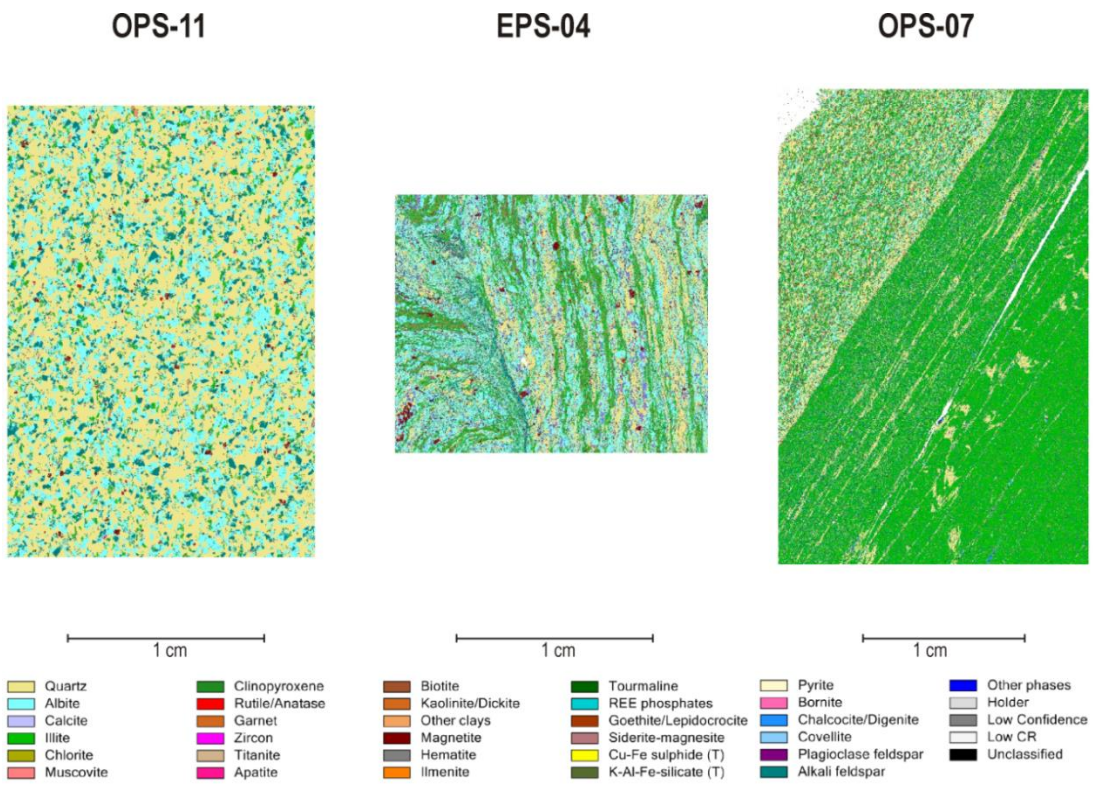

Figure 5-60: False colour mineral maps of OPS-11 (sandstone), EPS-04 (Metavolcanic) and OPS-7 (siltstone).

The modal mineralogy of the whole rock samples from the sandstone units, PB-6 and OPS-11 each contain approximately ~50% quatz, and 20-30% albite as the main mineral constituents. The phyllite samples PB-9 and PB-10 were compositionally similar to the siltstone of PB-8 with approximately 30-35% quartz, 10-15% illite and 15% alkali feldspars. PB-12, although also a phyllite, is cut by a large calcite vein. The modal mineralogy for PB-12 is thus 20% calcite, ~19% illite and 18% alkali feldspars. EPS-14 is dominated by quartz (~44%) and albite (28%), and OPS-7 by illite (~50%), quartz (~17%) and alkali feldspars (16%) (Figure 5-61 & Table 20).

PB-6 is coarse-grained and quartz-albite dominated. Braided networks of illite and chlorite define a weakly developed fabric in the rock (Figure 5-58). PB-8, 9 and 12 are generally fine-grained and dominated by illite, chlorite and quartz. Sample PB-8 is slightly coarser grained than PB-9 and 12 and contains more abundant quartz and has a strongly developed fabric. PB-12 is cut by a calcite vein which runs sub-parallel to the fabric developed in the rock, but also cross-cuts this fabric. PB-10 is largely fine-grained and dominated by illite and chlorite, but contains interbeds of coarser material (Figure 5-59). These interbeds are quartz-, albite- and magnetite-rich. EPS-14 is quartz-albite dominated with a strongly developed mineral banding. The banding is defined by magnetite and zircon, as well as illite-chlorite. The latter two minerals also form narrow bands which cross-cut the banding.

OPS-11 is a coarse-grained quartz-rich rock which contains abundant alkali feldspar and albite, as well as accessory illite-chlorite, muscovite and magnetite (Figure 5-60). EPS-04 has a strongly developed fabric in at least two directions. The main minerals in this sample are quartz, albite, alkali feldspar and illite. The rock is strongly deformed and folded with no one mineral defining the fabric(s). OPS-7 also shows a strong fabric, as well as the contact between a fine-grained illite-rich assemblage and a coarser quartz- albite-illite assemblage. Occasional quartz-rich layers are evident throughout the fine-grained illite-rich portion of the sample, and these show micro-folding with quartz growth in the hinge zones. Summary information on the modal abundance of each mineral per sample is shown in Figure 5-61 andTable 20.

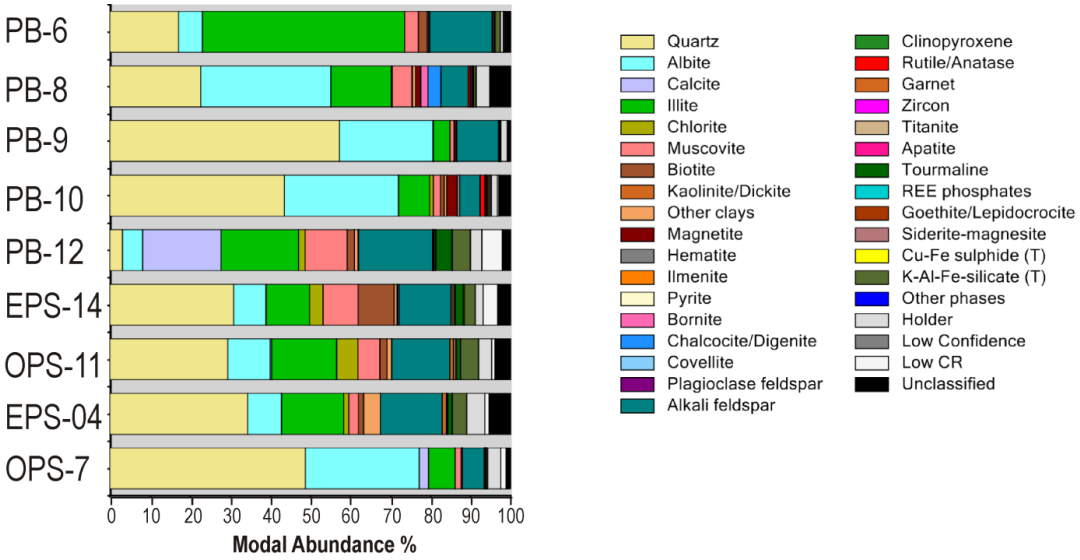

Figure 5-61: Modal abundance (volume per cent) for the whole rock sample set using the secondary SIP groupings.

The magnetic separates (MG samples) were measured using stepping intervals of 50µm, 5µm and 1µm (Figure 5-63 to Figure 5-70). The coarse scan of 50µm compares well to the 5µm and 1µm scans in terms of characterising modal abundances with the standard deviation for each mineral in the secondary SIP reporting values <1 (Table 21).

Table 20: Summary modal mineralogy for the whole rock sample set using the secondary SIP. The table includes only entries >0.0051 %. The suffix (T) denotes trap definitions.

	PB-6	PB-8	PB-9	PB-10	PB-12	EPS-14	OPS-11	EPS-04	OPS-7
Quartz	48.82	34.45	29.47	30.93	3.17	43.61	57.33	22.71	17.18
Albite	28.40	8.43	10.54	8.01	5.05	28.44	23.32	32.49	5.93
Calcite	2.35	0.00	0.38	0.14	19.57	0.05	0.08	0.00	0.09
Illite	6.58	15.52	16.26	10.79	19.35	7.72	4.16	15.05	50.37
Chlorite	0.01	1.24	5.30	3.35	1.60	0.89	0.04	0.22	0.02
Muscovite	1.57	2.38	5.47	8.78	10.49	1.79	0.94	4.88	3.39
Biotite	0.08	1.31	1.77	8.95	1.82	0.91	0.08	0.15	2.21
Kaolinite/Dickite	0.00	0.01	0.00	0.01	0.01	0.06	0.00	0.01	0.00
Other clays	0.08	4.17	1.21	0.69	0.87	0.64	0.11	0.79	0.30
Magnetite	0.08	0.00	0.00	0.08	0.13	2.55	0.44	1.12	0.01
Hematite	0.01	0.00	0.00	0.02	0.01	0.66	0.09	0.18	0.00
Ilmenite	0.00	0.00	0.00	0.00	0.02	0.01	0.00	0.00	0.00
Pyrite	0.00	0.01	0.00	0.00	0.00	0.00	0.00	0.00	0.00
Bornite	0.00	0.00	0.00	0.18	0.00	0.00	0.00	1.80	0.00
Chalcocite/Digenite	0.01	0.00	0.00	0.33	0.01	0.00	0.00	3.24	0.33
Covellite	0.00	0.00	0.00	0.00	0.00	0.00	0.00	0.00	0.02
Plagioclase feldspar	0.00	0.00	0.00	0.01	0.00	0.00	0.00	0.00	0.01
Alkali feldspar	5.44	15.42	14.43	12.87	18.49	5.05	10.44	6.80	15.57
Orthopyroxene	0.00	0.00	0.00	0.00	0.00	0.00	0.01	0.00	0.00
Clinopyroxene	0.01	0.02	0.03	0.03	0.01	0.00	0.02	0.00	0.03
Rutile/Anatase	0.12	0.00	0.05	0.01	0.04	1.17	0.03	0.50	0.02
Garnet	0.00	0.97	0.87	0.38	0.22	0.07	0.00	0.02	0.02
Zircon	0.01	0.01	0.01	0.01	0.01	0.09	0.01	0.01	0.03
Titanite	0.06	0.18	0.49	0.39	0.31	0.01	0.25	0.00	0.35
Apatite	0.12	0.22	0.28	0.26	0.22	0.16	0.07	0.41	0.17
Tourmaline	0.07	1.03	0.92	2.00	3.94	0.18	0.01	0.05	0.06
REE phosphates	0.03	0.11	0.07	0.04	0.07	0.06	0.02	0.13	0.05
Goethite/Lepidocrocite	0.00	0.00	0.00	0.00	0.01	0.29	0.02	0.03	0.00
Siderite-magnesite	0.00	0.00	0.00	0.01	0.08	0.33	0.05	0.10	0.00
Cu-Fe sulfide (T)	0.00	0.00	0.00	0.25	0.00	0.00	0.00	0.09	0.01
K-Al-Fe-silicate (T)	0.33	3.54	4.46	2.66	4.45	0.38	0.07	0.59	1.25
Other phases	0.12	0.05	0.07	0.07	0.09	0.09	0.03	0.07	0.01
Holder	3.26	4.49	3.22	1.95	2.80	1.45	1.53	3.31	0.74
Low Confidence	0.00	0.00	0.00	0.01	0.00	0.00	0.00	0.00	0.00
Low CR	1.34	1.04	0.77	3.62	5.11	0.36	0.03	0.08	0.28
Unclassified	1.09	5.36	3.94	3.21	2.04	2.96	0.81	5.15	1.53

The standard deviation is slightly higher for the categories: holder and low CR (CR = count rate) as these are both more abundant in the 50µm samples. Higher standard deviation values are also reported for some of the major mineral constituents: quartz, albite, illite and magnetite due to the finer stepping intervals picking up minerals otherwise diluted by the 50µm pixel size, as demonstrated by Figure 5-62.

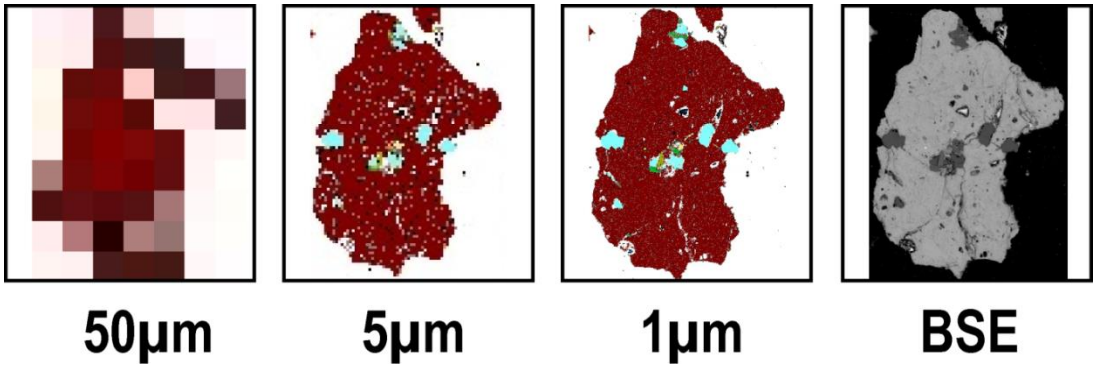

Figure 5-62: Grain mount sample MG-12 showing the same grain at different stepping intervals. Magnetite is shown as the maroon pixels, cyan shows albite inclusions within the grain, and the highly reflective mineral inclusions shown in the BSE image (right) have been mapped by the SIP in black to denote that the pixels are 'unclassified.' Albite inclusions in magnetite are not detected in the 50µm scan, but are clearly seen in both the 5µm and 1µm scans.

All of the MG samples contain some magnetite. Samples MG-5, 10 and 12 contain the most magnetite at all stepping intervals, with each reporting over 40%, while sample MG-9 reported <1%. Samples MG-3 and MG-6 both contain between 20-30% magnetite, and samples MG-1 and MG-13 contain <10% and <3%, respectively. The other minerals from the MG samples are primarily the major constituents of the whole rock samples, i.e. quartz, albite, illite and chlorite. The modal mineralogy for the MG samples is summarised in Figure 5-71.

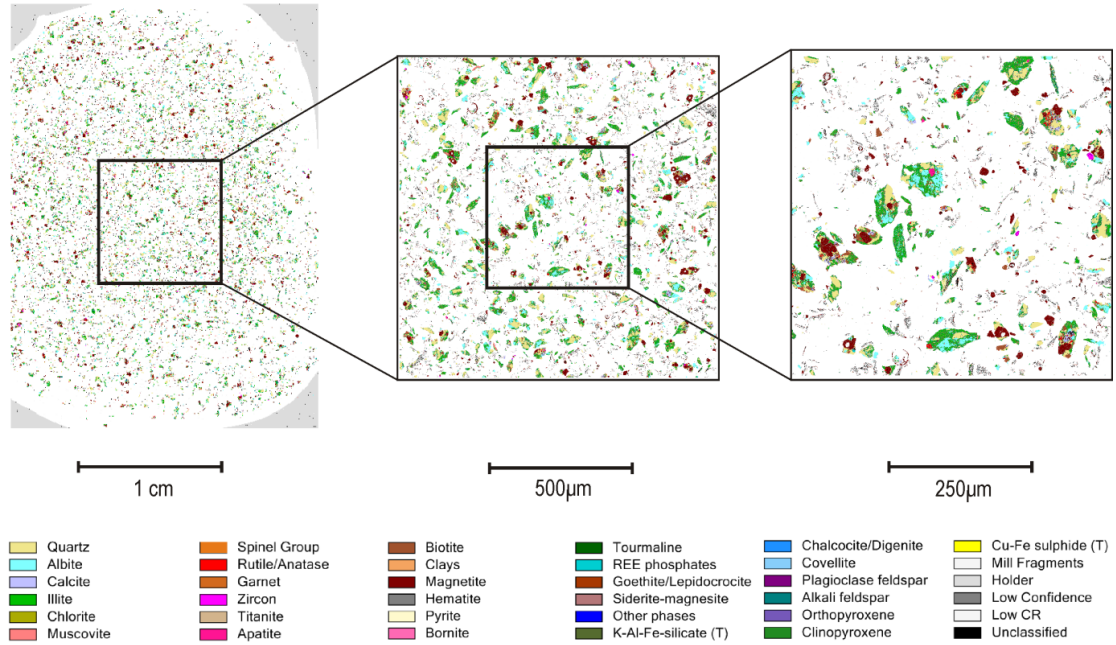

Figure 5-63: False colour mineral maps of MG-1 at a stepping interval of 50µm (LEFT), 5µm (CENTRE) and 1µm (RIGHT).

The average particle sizes for the magnetite in MG-1 range between ~50µm and <5µm. Magnetite grains are generally euhedral in shape, but are poorly liberated from whole rock aggregates (Figure 5-63).

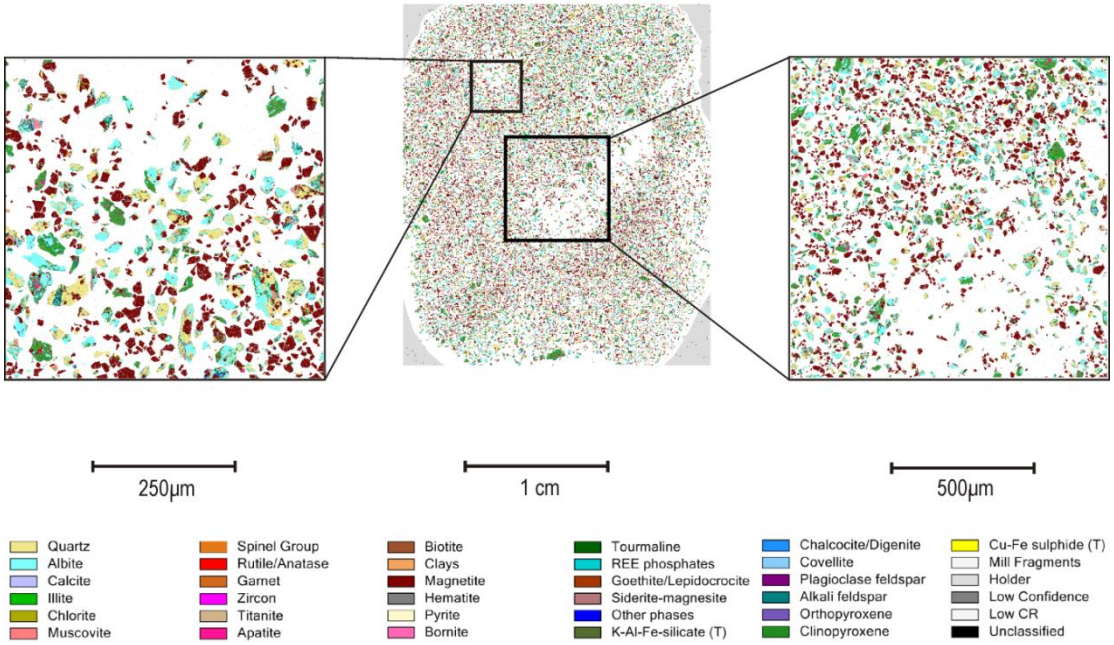

Figure 5-64: False colour mineral maps of MG-3 at a stepping interval of 1µm (LEFT), 50µm (CENTRE), and 5µm (RIGHT).

Sample MG-3 contains abundant magnetite, with an average diameter of ~50µm. The magnetite grains are largely euhedral and well liberated from gangue aggregates (Figure 5-64). The magnetite in MG-5 is slightly larger on average (~70µm diameter) than MG-1 or MG-3 (~50µm diameter). Euhedral to subhedral magnetite shows embayments of minerals such as albite and quartz, but also titanite (Figure 5-65).

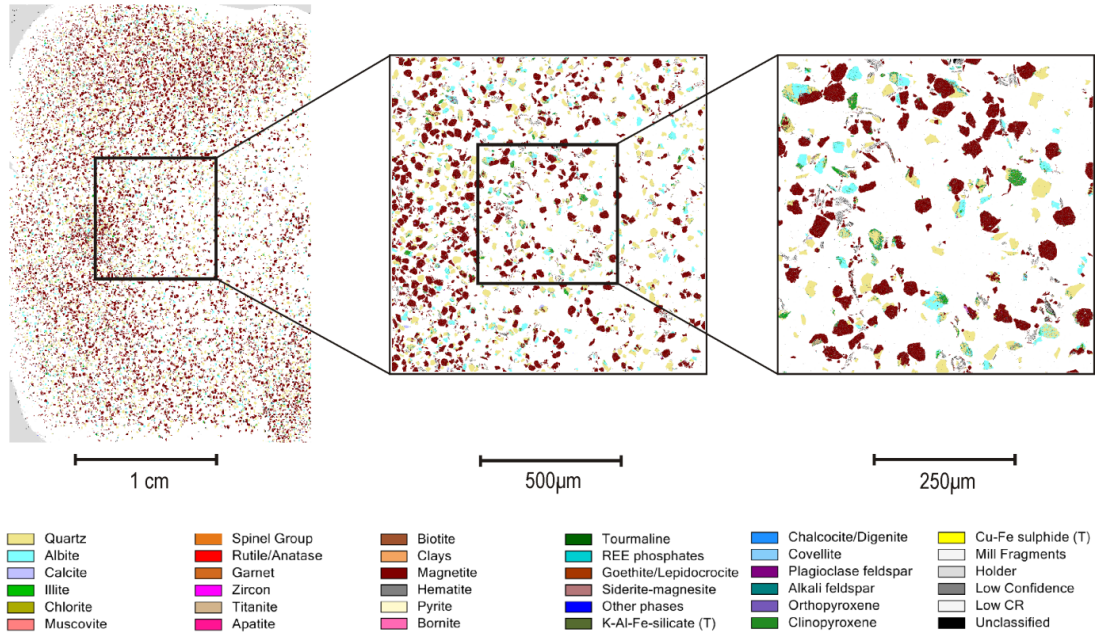

Figure 5-65: False colour mineral maps of MG-5 at a stepping interval of 50µm (LEFT), 5µm (CENTRE) and 1µm (RIGHT).

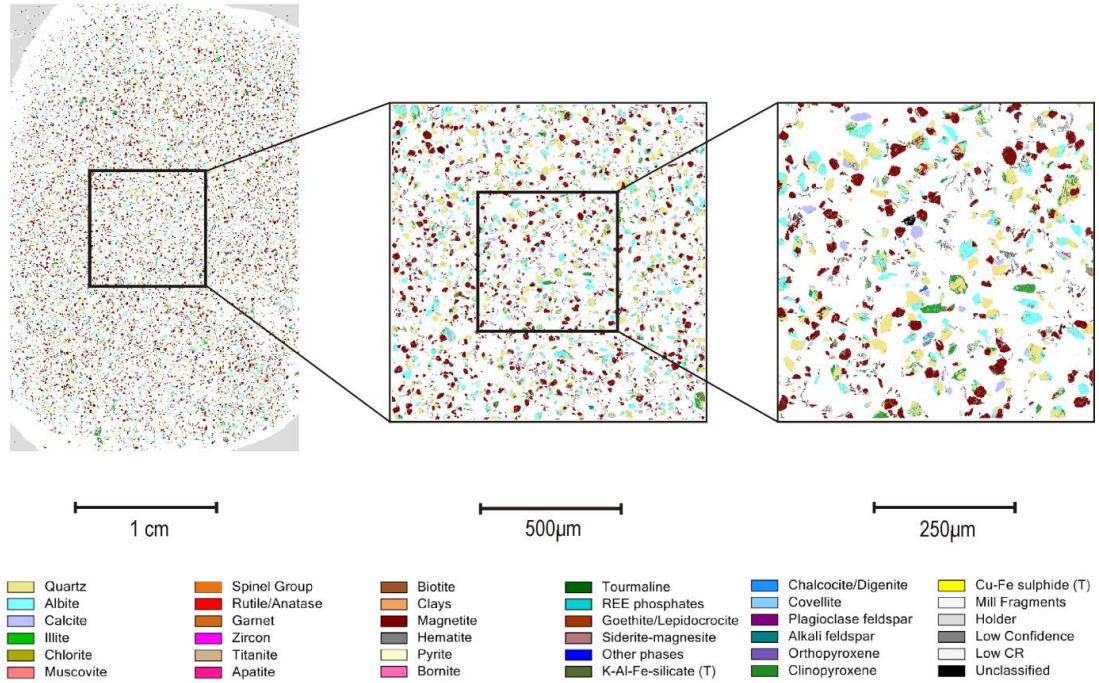

Figure 5-66: False colour mineral maps of MG-6 at a stepping interval of 50µm (LEFT), 5µm (CENTRE) and 1µm (RIGHT).

The subhedral magnetite grains in sample MG-6 are on average ~50µm long. Calcite is a common inclusion in these grains, as is chalcocite/digenite (Figure 5-66).

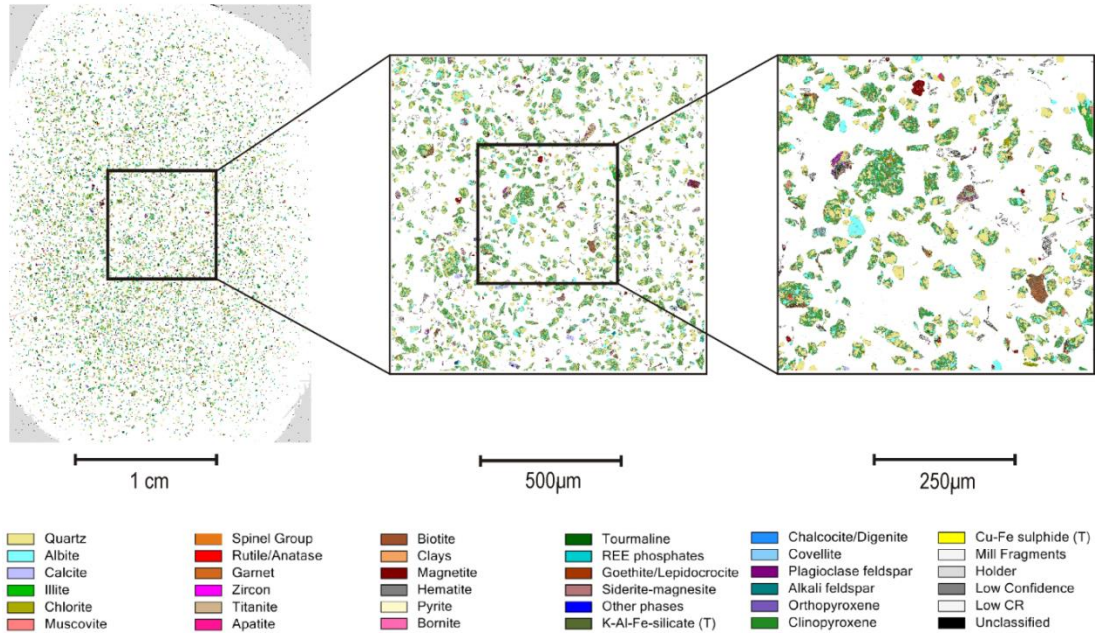

Figure 5-67: False colour mineral maps of MG-9 at a stepping interval of 50µm (LEFT), 5µm (CENTRE) and 1µm (RIGHT).

MG-9 contains almost no magnetite. The few grains present are on average ~<10µm in diameter (Figure 5-67).

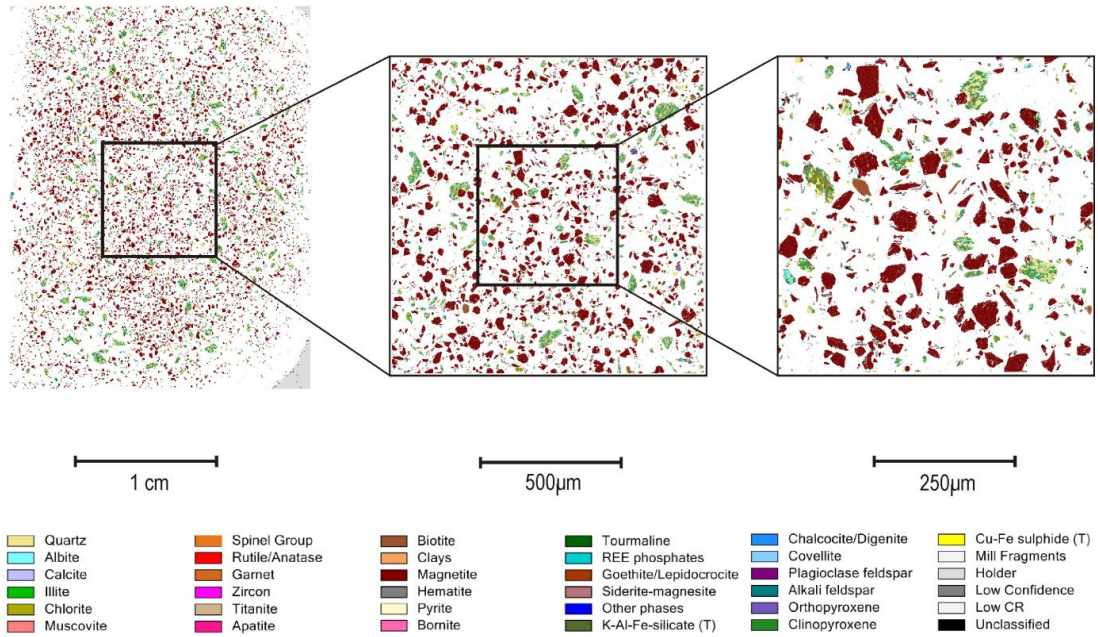

Figure 5-68: False colour mineral maps of MG-10 at a stepping interval of 50µm (LEFT), 5µm (CENTRE) and 1µm (RIGHT).

MG-10 contains abundant euhedral to subhedral magnetite which is on average ~85µm in diameter (Figure 5-68).

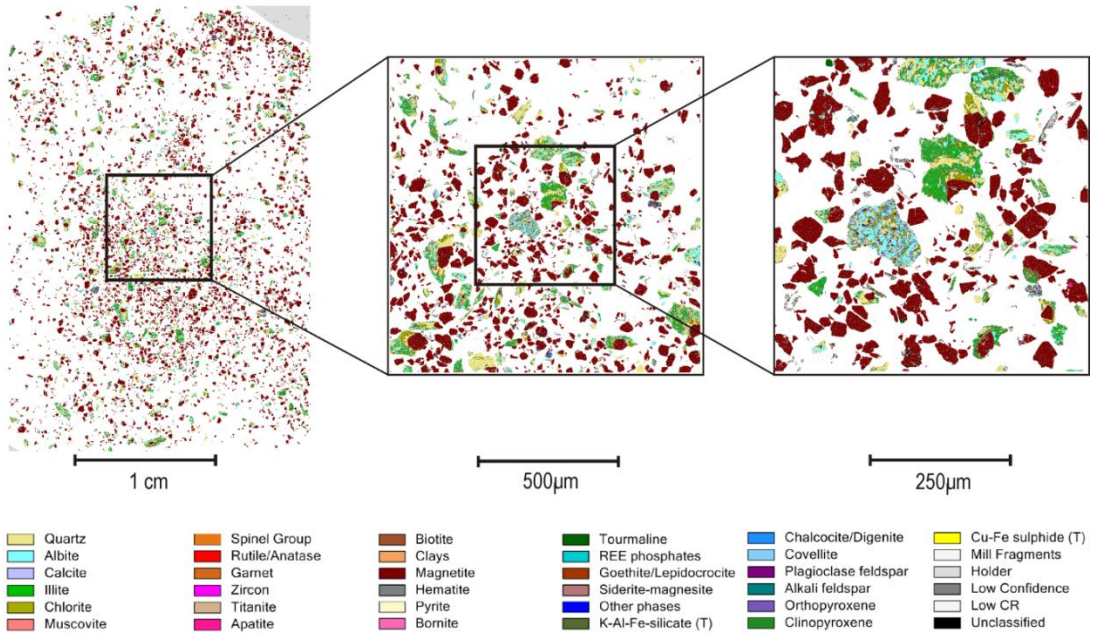

Figure 5-69: False colour mineral maps of MG-12 at a stepping interval of 50µm (LEFT), 5µm (CENTRE) and 1µm (RIGHT).

Euhedral to subhedral magnetite in sample MG-12 contains inclusions of albite, chalcocite/digenite, and an unclassified mineral phase. On average the particles are ~85µm in diameter (Figure 5-69).

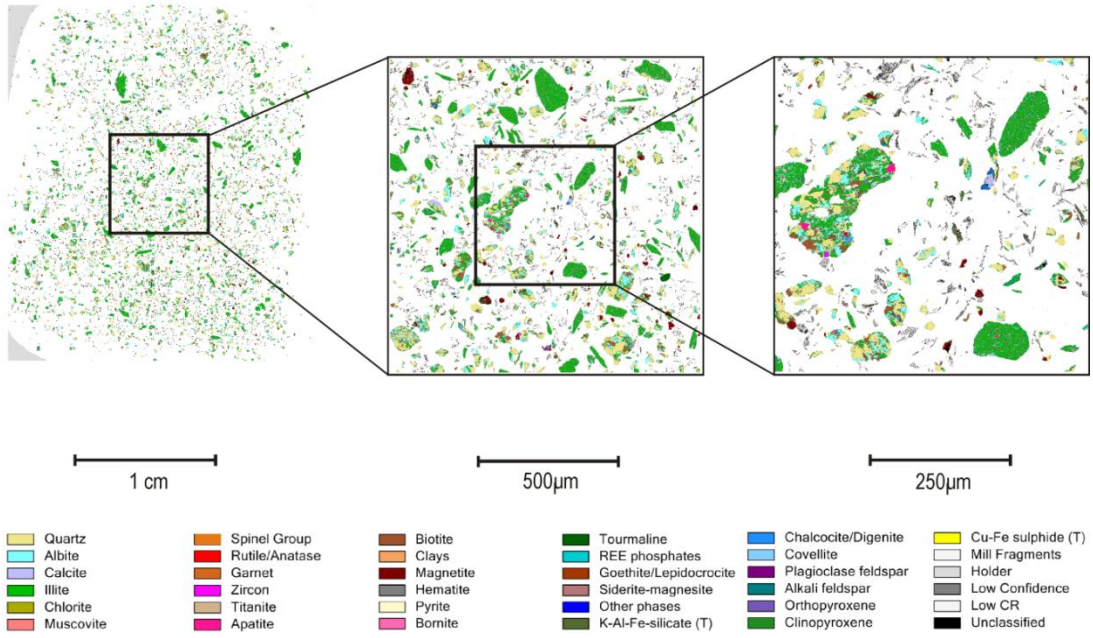

Figure 5-70: False colour mineral maps of MG-13 at a stepping interval of 50µm (LEFT), 5µm (CENTRE) and 1µm (RIGHT).

Very little magnetite is present in MG-13, with average grain sizes below ~40µm. Euhedral grains occur both within gangue aggregates and as isolated grains (Figure 5-70).

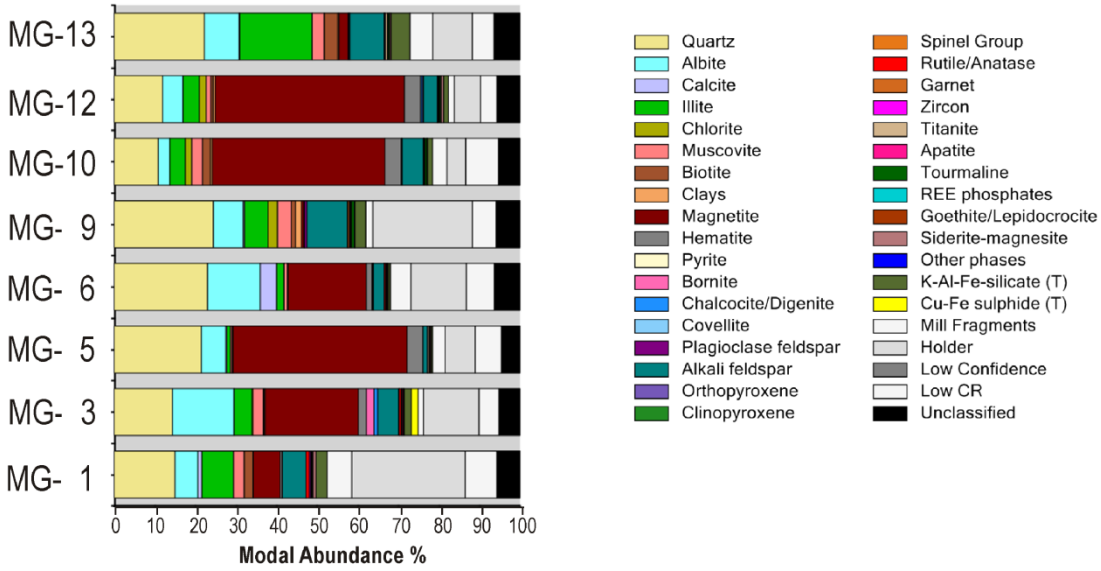

Figure 5-71: Modal abundance (volume per cent) for the grain mount sample set using the secondary SIP groupings.

Table 21: Summary modal mineralogy for the MG sample set using the secondary SIP for stepping interval of 50µm, 5µm, 1µm and the standard deviation between them. Table derived using the iDiscover software from QEMSCAN data.

	Stepping interval : 50µm								Stepping interval : 5µm							
	MG-1	**MG-3**	**MG-5**	**MG-6**	**MG-9**	**MG-10**	**MG-12**	**MG-13**	**MG-1**	**MG-3**	**MG-5**	**MG-6**	**MG-9**	**MG-10**	**MG-12**	**MG-13**
Quartz	15.00	14.33	21.49	22.99	24.45	10.85	11.94	22.19	21.32	15.21	26.17	26.84	34.64	9.14	14.30	22.93
Albite	5.63	15.20	6.00	13.01	7.34	2.85	4.96	8.59	8.31	18.05	8.36	16.31	10.54	2.27	5.43	9.23
Calcite	0.96	0.00	0.28	4.01	0.29	0.03	0.11	0.15	1.32	0.00	0.23	4.08	0.62	0.03	0.29	0.47
Illite	7.83	4.36	0.89	1.80	5.83	3.83	3.96	17.78	14.41	5.32	1.01	2.18	7.33	2.92	5.06	21.25
Chlorite	0.01	0.31	0.00	0.03	2.30	1.56	1.71	0.08	0.02	0.44	0.02	0.07	2.82	1.29	2.40	0.15
Muscovite	2.61	2.50	0.40	0.80	3.43	2.66	1.17	2.95	3.95	2.69	0.42	0.88	4.41	2.20	1.31	3.52
Biotite	2.12	0.19	0.16	0.08	1.06	1.95	0.53	3.36	3.21	0.21	0.24	0.12	1.59	1.51	0.62	3.83
Clays	0.14	0.27	0.09	0.13	1.46	0.44	0.52	0.29	0.28	0.29	0.09	0.18	1.72	0.36	0.52	0.38
Magnetite	6.60	22.96	42.85	19.30	0.59	42.51	46.61	2.24	8.79	28.12	44.00	23.84	0.84	53.17	47.22	2.92
Hematite	0.53	2.00	3.90	1.44	0.03	4.07	4.04	0.12	0.56	2.78	4.24	2.31	0.04	5.28	3.83	0.16
Pyrite	0.01	0.00	0.01	0.02	0.00	0.00	0.00	0.01	0.01	0.00	0.00	0.01	0.00	0.00	0.00	0.01
Bornite	0.00	1.88	0.00	0.06	0.05	0.02	0.00	0.01	0.00	1.92	0.00	0.07	0.03	0.02	0.00	0.01
Chalcocite/Digenite	0.00	0.90	0.00	0.13	0.03	0.04	0.39	0.25	0.00	1.07	0.00	0.23	0.04	0.04	0.39	0.37
Covellite	0.00	0.00	0.00	0.00	0.00	0.00	0.00	0.03	0.00	0.00	0.00	0.01	0.00	0.00	0.00	0.04
Plagioclase feldspar	0.00	0.00	0.02	0.04	0.64	0.15	0.27	0.04	0.00	0.00	0.06	0.04	0.77	0.20	0.33	0.09
Alkali feldspar	5.78	5.23	1.06	2.64	9.95	5.18	3.37	8.43	7.46	6.02	1.33	2.94	13.10	4.59	3.90	9.36
Orthopyroxene	0.01	0.02	0.02	0.01	0.02	0.00	0.02	0.00	0.01	0.02	0.02	0.02	0.01	0.00	0.01	0.01
Clinopyroxene	0.01	0.00	0.03	0.00	0.02	0.02	0.02	0.04	0.00	0.00	0.05	0.01	0.05	0.01	0.02	0.06
Olivine	0.03	0.02	0.02	0.05	0.02	0.01	0.01	0.01	0.04	0.02	0.03	0.06	0.02	0.01	0.01	0.02
Spinel Group	0.00	0.00	0.02	0.03	0.00	0.00	0.01	0.01	0.00	0.00	0.06	0.02	0.00	0.00	0.00	0.02
Rutile/Anatase	0.87	0.50	0.02	0.32	0.05	0.01	0.04	0.06	1.02	0.58	0.04	0.39	0.09	0.01	0.04	0.04
Garnet	0.00	0.13	0.01	0.02	0.44	0.23	0.21	0.07	0.01	0.14	0.04	0.01	0.58	0.17	0.26	0.09
Zircon	0.27	0.00	0.01	0.02	0.01	0.01	0.02	0.08	0.22	0.00	0.00	0.01	0.01	0.01	0.01	0.04
Titanite	0.00	0.01	0.40	0.06	0.24	0.09	0.17	0.56	0.00	0.01	0.48	0.08	0.40	0.10	0.23	0.69
Apatite	0.20	0.29	0.05	0.13	0.17	0.08	0.10	0.17	0.22	0.43	0.04	0.13	0.19	0.05	0.11	0.21

Table 21: *Continued*.

	Stepping interval : 1µm								Stdev							
	MG-1	**MG-3**	**MG-5**	**MG-6**	**MG-9**	**MG-10**	**MG-12**	**MG-13**	**MG-1**	**MG-3**	**MG-5**	**MG-6**	**MG-9**	**MG-10**	**MG-12**	**MG-13**
Quartz	19.38	17.80	21.60	27.14	34.64	8.56	11.29	22.37	3.24	1.80	2.67	2.31	5.88	1.19	1.58	0.39
Albite	9.34	17.14	9.08	15.54	10.54	1.85	7.03	8.69	1.91	1.46	1.61	1.72	1.85	0.50	1.09	0.34
Calcite	1.17	0.00	0.11	4.47	0.62	0.01	0.02	0.46	0.18	0.00	0.09	0.25	0.19	0.01	0.14	0.18
Illite	14.06	4.02	1.80	2.67	7.33	2.19	5.84	19.83	3.70	0.68	0.49	0.44	0.87	0.82	0.95	1.74
Chlorite	0.02	0.31	0.01	0.05	2.82	1.14	2.55	0.05	0.01	0.07	0.01	0.02	0.30	0.21	0.45	0.05
Muscovite	3.61	2.25	0.70	1.17	4.41	1.96	1.26	3.31	0.70	0.22	0.17	0.20	0.57	0.36	0.07	0.29
Biotite	3.50	0.18	0.23	0.13	1.59	1.62	0.74	4.13	0.73	0.02	0.05	0.03	0.31	0.23	0.11	0.39
Clays	0.33	0.28	0.11	0.22	1.72	0.36	0.60	0.40	0.10	0.01	0.01	0.05	0.15	0.05	0.05	0.06
Magnetite	9.43	29.68	43.00	23.20	0.84	54.88	46.38	1.70	1.48	3.51	0.62	2.46	0.15	6.70	0.44	0.61
Hematite	0.66	2.95	4.21	2.22	0.04	5.44	3.78	0.08	0.06	0.50	0.19	0.48	0.01	0.75	0.14	0.04
Pyrite	0.01	0.00	0.01	0.01	0.00	0.00	0.00	0.00	0.00	0.00	0.00	0.01	0.00	0.00	0.00	0.00
Bornite	0.00	1.73	0.00	0.06	0.03	0.02	0.00	0.01	0.00	0.10	0.00	0.01	0.01	0.00	0.00	0.00
Chalcocite/Digenite	0.00	1.01	0.00	0.21	0.04	0.10	0.05	0.57	0.00	0.09	0.00	0.05	0.01	0.03	0.19	0.16
Covellite	0.00	0.00	0.00	0.01	0.00	0.00	0.00	0.05	0.00	0.00	0.00	0.00	0.00	0.00	0.00	0.01
Plagioclase feldspar	0.00	0.00	0.01	0.09	0.77	0.00	0.84	0.00	0.00	0.00	0.02	0.03	0.08	0.10	0.31	0.04
Alkali feldspar	8.42	5.59	2.18	3.26	13.10	3.94	4.40	9.89	1.34	0.39	0.58	0.31	1.82	0.62	0.52	0.74
Orthopyroxene	0.02	0.02	0.02	0.02	0.01	0.00	0.01	0.01	0.00	0.00	0.00	0.01	0.01	0.00	0.00	0.00
Clinopyroxene	0.00	0.00	0.06	0.01	0.05	0.01	0.03	0.06	0.00	0.00	0.02	0.00	0.02	0.01	0.00	0.01
Olivine	0.04	0.03	0.04	0.06	0.02	0.02	0.01	0.03	0.01	0.01	0.01	0.00	0.00	0.00	0.00	0.01
Spinel Group	0.00	0.00	0.07	0.00	0.00	0.00	0.01	0.00	0.00	0.00	0.02	0.02	0.00	0.00	0.00	0.01
Rutile/Anatase	1.09	0.49	0.03	0.39	0.09	0.02	0.03	0.07	0.11	0.05	0.01	0.04	0.02	0.00	0.01	0.01
Garnet	0.01	0.11	0.00	0.00	0.58	0.19	0.29	0.12	0.00	0.02	0.02	0.01	0.08	0.03	0.04	0.02
Zircon	0.28	0.00	0.00	0.01	0.01	0.01	0.01	0.11	0.03	0.00	0.00	0.01	0.00	0.00	0.01	0.03
Titanite	0.00	0.01	0.64	0.05	0.40	0.10	0.25	0.61	0.00	0.00	0.12	0.02	0.10	0.01	0.04	0.07
Apatite	0.29	0.24	0.03	0.10	0.19	0.02	0.13	0.50	0.05	0.10	0.01	0.02	0.01	0.03	0.01	0.18

Table 21: *Continued*.

	Stepping interval : 50µm								Stepping interval : 5µm							
	MG-1	**MG-3**	**MG-5**	**MG-6**	**MG-9**	**MG-10**	**MG-12**	**MG-13**	**MG-1**	**MG-3**	**MG-5**	**MG-6**	**MG-9**	**MG-10**	**MG-12**	**MG-13**
Tourmaline	0.23	0.09	0.02	0.09	0.75	0.43	0.34	0.31	0.32	0.13	0.03	0.06	0.98	0.45	0.42	0.57
REE phosphates	0.05	0.06	0.01	0.03	0.05	0.02	0.02	0.04	0.07	0.08	0.02	0.04	0.06	0.02	0.03	0.04
Goethite/Lepidocrocite	0.12	0.01	0.04	0.03	0.01	0.02	0.05	0.05	0.22	0.02	0.04	0.04	0.02	0.02	0.09	0.07
Siderite-magnesite	0.75	0.13	0.28	0.24	0.10	0.15	0.54	0.32	1.44	0.18	0.38	0.28	0.11	0.20	0.64	0.51
Other phases	0.01	0.03	0.02	0.02	0.03	0.02	0.03	0.02	0.04	0.04	0.02	0.03	0.05	0.02	0.03	0.04
K-Al-Fe-silicate (T)	2.69	1.75	0.38	0.49	2.66	1.14	1.17	4.60	3.34	2.02	0.45	0.55	3.54	0.94	1.36	5.22
Cu-Fe sulfide (T)	0.00	1.72	0.00	0.10	0.03	0.06	0.00	0.02	0.00	1.67	0.00	0.10	0.02	0.03	0.00	0.05
Mill Fragments	6.02	1.28	3.08	5.01	1.67	3.57	1.50	5.63	10.16	1.63	4.05	6.77	2.61	4.41	2.07	6.73
Holder	27.96	13.67	7.38	13.59	24.53	4.50	6.41	9.74	0.84	2.44	0.64	1.28	2.47	0.55	0.97	1.46
Low Confidence	0.05	0.07	0.05	0.09	0.01	0.16	0.03	0.02	0.05	0.08	0.07	0.11	0.01	0.19	0.04	0.01
Low CR	7.77	4.86	6.39	6.86	5.77	7.96	4.04	5.34	3.80	2.32	2.33	2.68	2.22	3.54	2.02	1.84
Unclassified	5.73	5.22	4.63	6.35	5.97	5.38	5.69	6.40	8.55	6.05	5.05	7.24	8.05	6.24	6.01	7.58

Table 21: *Continued*.

	Stepping interval : 1µm								Stdev							
	MG-1	MG-3	MG-5	MG-6	MG-9	MG-10	MG-12	MG-13	MG-1	MG-3	MG-5	MG-6	MG-9	MG-10	MG-12	MG-13
Tourmaline	0.36	0.10	0.05	0.09	0.98	0.48	0.56	0.32	0.06	0.02	0.02	0.02	0.13	0.03	0.11	0.15
REE phosphates	0.11	0.06	0.02	0.04	0.06	0.02	0.03	0.05	0.03	0.01	0.00	0.01	0.00	0.00	0.01	0.01
Goethite/Lepidocrocite	0.19	0.01	0.07	0.04	0.02	0.02	0.08	0.08	0.05	0.01	0.02	0.01	0.00	0.00	0.02	0.02
Siderite-magnesite	1.33	0.16	0.50	0.27	0.11	0.20	0.69	0.52	0.37	0.02	0.11	0.02	0.01	0.03	0.07	0.11
Other phases	0.04	0.04	0.02	0.04	0.05	0.02	0.04	0.04	0.02	0.01	0.00	0.01	0.01	0.00	0.00	0.01
K-Al-Fe-silicate (T)	3.26	1.68	0.73	0.64	3.54	0.82	1.56	4.75	0.36	0.18	0.18	0.07	0.51	0.16	0.20	0.32
Cu-Fe sulfide (T)	0.00	1.63	0.00	0.12	0.02	0.03	0.00	0.12	0.00	0.05	0.00	0.01	0.01	0.02	0.00	0.05
Mill Fragments	9.79	1.67	5.25	6.41	2.61	5.01	2.27	8.30	2.29	0.22	1.09	0.93	0.55	0.72	0.40	1.34
Holder	1.10	2.26	0.82	1.42	2.47	0.43	1.32	1.60	15.58	6.53	3.84	7.07	12.74	2.32	3.05	4.74
Low Confidence	0.04	0.11	0.07	0.11	0.01	0.18	0.04	0.01	0.01	0.02	0.01	0.01	0.00	0.02	0.01	0.01
Low CR	3.59	2.36	2.54	2.52	2.22	3.54	1.90	1.93	2.35	1.46	2.28	2.46	2.05	2.55	1.20	1.99
Unclassified	8.54	6.07	6.03	7.23	8.05	6.84	5.96	9.23	1.62	0.48	0.72	0.51	1.20	0.73	0.17	1.42

5.5.1.1 Characterising Uncertainty

5.5.1.1.1 Trap Definitions and Unclassified Material

Uncertainty can be introduced into the results due to the limitations inherent in any (SIP) spectral database, which is trying to capture the complexities of the natural world. Assessing the contributions of trap definitions to the mineral classifications is one way to characterise this uncertainty (Section 4.5), another is to review the amount of material the SIP was unable to classify. If either of these variables are too large then the results are less reliable.

Trap definitions were identified for all of the samples and the modal proportion of their contribution each sample calculated for both the whole rock (Table 22) and MG samples (Table 23). Pixels allocated to trap definitions have been separated out into those that fall along particle boundaries or rims, and those that are grouped into minerals based on loosely defined spectral criteria (mineral definition traps).

In the whole rock samples trap definitions account for < 1% to over 18% of the overall classifications, but most of these definitions are based on boundary and rim pixels. The actual mineral trap definitions only account for a maximum of ~5% for any given sample, and of those definitions, a K-Al-Fe-silicate trap accounts for over 80% of the volume. The second mineral trap definition is a Cu-Fe-sulfide trap, but this accounts for <0.3% of the modal mineralogy and was only detected in PB-10, EPS-04 and OPS-7 in order of decreasing abundance. PB-8 and EPS-04 have the most unclassified material of the whole rock samples (Figure 5-72).

Table 22: Summary information for the modal abundance of trap definitions and unclassified material for the whole rock polished sections as calculated using the primary SIP.

	PB-6	PB-8	PB-9	PB-10	PB-12	EPS-14	OPS-11	EPS-04	OPS-7
Boundary/Rim Traps	1.43	1.77	2.44	8.43	13.02	0.56	0.20	1.71	1.36
Mineral Definition Traps	0.38	4.46	5.57	3.70	5.16	0.96	0.12	4.15	1.63
Dominant Single Mineral Trap	0.33	3.54	4.46	2.66	4.45	0.38	0.07	0.59	1.25
All Traps combined	1.81	6.22	8.01	12.13	18.17	1.52	0.32	5.86	2.99
Unclassified Pixels	1.09	5.36	3.94	3.21	2.04	2.96	0.81	5.15	1.53

Table 23: Summary information for the modal abundance of trap definitions and unclassified material for the grain mount polished sections as calculated using the primary SIP for the 5µm scans.

	MG-1	MG-3	MG-5	MG-6	MG-9	MG-10	MG-12	MG-13
Boundary/Rim Traps	2.32	1.6	0.87	1.35	3.4	1.53	0.97	2.79
Mineral Definition Traps	4.79	4.91	0.89	1.2	4.53	1.43	2.41	6.16
Dominant Single Mineral Trap	3.34	2.02	0.45	0.55	3.54	0.94	1.36	5.22
All Traps combined	7.11	6.51	1.76	2.55	7.94	2.95	3.37	8.96
Unclassified Pixels	8.55	6.05	5.05	7.24	8.05	6.24	6.01	7.58

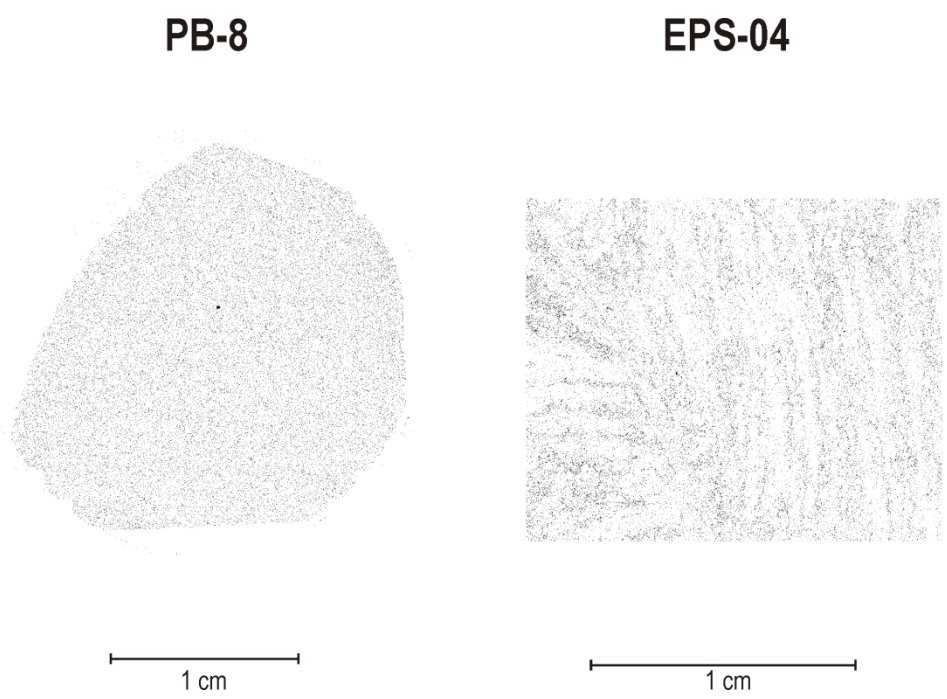

Figure 5-72: False colour mineral maps showing only the unclassified pixels in black for PB-8 and EPS-04.

The trap and unclassified pixel counts are similar for all stepping intervals for the MG samples (Table 23). In total the trap definitions account for ~1.5 - 9% of each sample. MG-1, MG-3 and MG-13 contain more mineral trap definitions than boundary or rim traps, but for the rest of the samples the split between the two trap styles is fairly even. As with the whole rock samples, the main phase contributing to the mineral trap definition is a K-Al-Fe silicate trap, with a minor contribution from a Cu-Fe sulfide trap (up to ~1.7% for MG-3). All of the samples have between ~4 - 9% unclassified material, with the 5µm stepping interval measurements recording the highest volumes of unclassified material in most cases. At a stepping interval of 5µm samples MG-1 and MG-9 contain the most unclassified material (Figure 5-73).

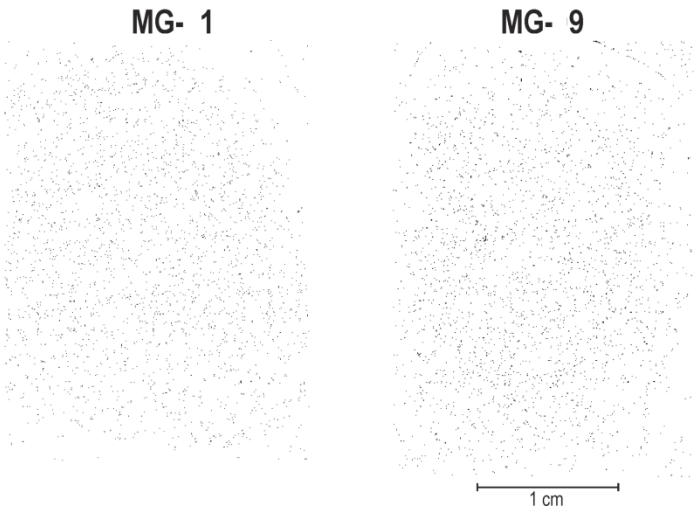

Figure 5-73: False colour mineral maps showing only the unclassified pixels in black for MG-1 and MG-9.

5.5.2 QEMSCAN SIP vs Optical Petrography

The polished thin sections OPS-11, OPS-7, EPS-14 and EPS-04, used for the QEMSCAN analysis, were examined under transmitted and reflected light to determine whether the major minerals mapped by the SIP matched optical observations. The amount of each mineral estimated during optical mineralogy is subjective and is therefore expected to differ from the quantitative proportions reported by the SIP. The identification of the correct mineralogy by the SIP was therefore prioritised for this study.

Under transmitted light sample OPS-11 from the hangingwall of borehole EA-NL-1 was identified as a medium-grained arkosic sandstone (Figure 5-74). The main minerals were identified as quartz, plagioclase feldspar, muscovite/sericite, biotite, chlorite, and magnetite. The SIP identified quartz, feldspar (albite and alkali feldspar), muscovite and magnetite, but only very minor chlorite and biotite. The major fine-grained flakey mineral mapped by the SIP was illite. Interaction with hydrothermal fluids and chemical weathering will alter muscovite and feldspars to illite/smectite and sericite, both of which are too fine-grained to identify under the microscope. The SIP identification of illite coincides with optical identifications of muscovite/sericite.

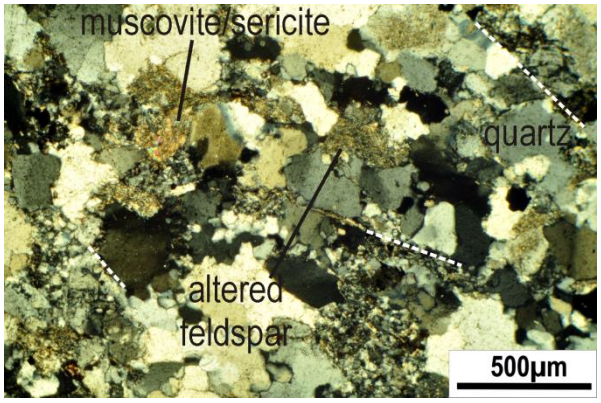

Figure 5-74: Photomicrograph of polished section OPS-11 from a hangingwall arkosic sandstone (borehole EA-NL-1). The rock shows evidence of brittle fracturing (dashed lines), sutured grain boundaries and recrystallization, as well as undulose extinction. This suggests that this rock has undergone deformation by compaction. The image was taken in XPL.

A polished thin section was cut from sample OPS-7 in order to investigate the contact between the sandstone footwall of borehole CA-PL-1 and a thin fine-grained siltstone (Figure 5-75). The coarse-grained portion of the rock was identified as a slightly arkosic micaceous schist containing quartz, plagioclase, muscovite/sericite/chlorite, magnetite and the copper(-Fe) sulfides covellite, bornite and chalcopyrite. The finer-grained interbed was phyllitic and identified as more than 80% muscovite/sericite during optical observations. The opaque phases were concentrated along the boundary between these contrasting lithotypes, but were also dispersed in the pressure shadows of rigid minerals present in the phyllite, and parallel to the foliation in the schist.

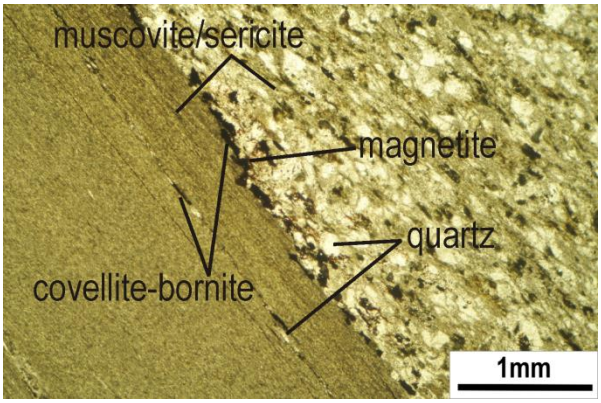

Figure 5-75: Photomicrograph from polished section OPS-7 in the footwall of borehole CA-PL-1 under PPL. The sample marks the contact between a competent quartzitic schist and a very fine-grained micaceous phyllite. Opaque minerals are present parallel to the foliation (yellow dotted lines) of both lithotypes, but within the phyllite preferentially aggregate in the pressure shadows of quartz grains in occasional sandy lenses. The opaque phases are most concentrated along the contact between the two lithotypes.

The SIP identified the same phases as optical work, with the dominant mineral identified as illite, then quartz, alkali feldspar, albite and muscovite in order of decreasing abundance.

The hangingwall polished thin section from borehole CZ-1 was identified under transmitted light as a trongly banded medium-grained sandstone (Figure 5-76). The banding was defined by abundant opaque phases, primarily strongly oxidised magnetite. The dominant mineral phases noted in the groundmass were quartz and strongly sericitised feldspars, as well as unaltered plagioclase grains and fine-grained muscovite/sericite. In the mineral bands an assortment of heavy minerals were identified, such as zircon and rutile, but other phases such as biotite were also present. EMPA on this sample showed strong evidence for brittle deformation within this rock with both magnetite and zircon fractured (Figure 5-52).

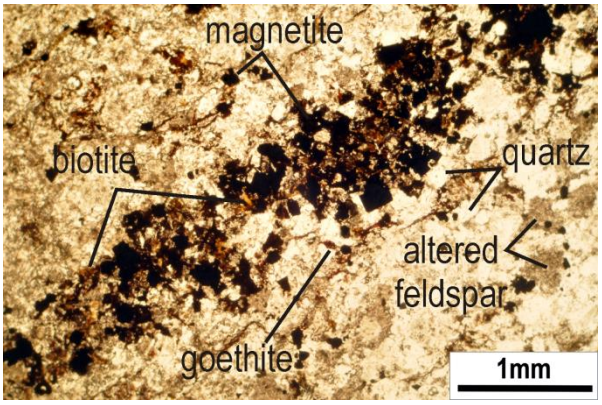

Figure 5-76: Photomicrograph from polished section EPS-14, the hangingwall sandstone from borehole CZ-1. The opaque minerals which define the banding in this rock are black in this PPL image. The strongly sericitised nature of the feldspars in this sample is seen as a dusty coating over many of the grains. Under XPL this was identified as sericite/muscovite.

The SIP had no trouble identifying the main constituents of this rock, quartz, albite and illite (sericite/muscovite). It also identified the oxidation of the magnetite grains with the individual particles showing a mixture between hematite and magnetite pixels allocations.

Polished thin section EPS-04 from the western portion of the study area (borehole WB-2) was prepared from a mineralised intersection of a metavolcanic rock (Figure 5-77). The rock contains roughly equal portions of quartz and feldspar with an intensely strained, folded and boudinaged fabric. The rock is segregated into layers of coarser-grained material and almost mylonitic fine-grained sericite/muscovite. The opaques are generally interstitial to the coarser material, but also occur as veinlets and stringers. The opaques were identified as primarily bornite and magnetite.

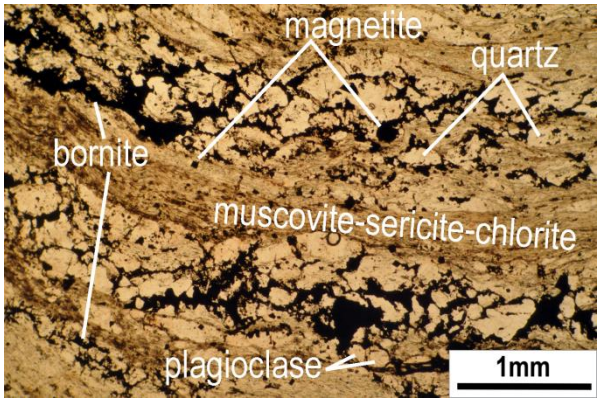

Figure 5-77: Photomicrograph from polished thin section EPS-04 (borehole WB-2). The mineralisation in this sample is strongly segregated to coarser mineral units defined by quartz and feldspar. Fine-grained magnetite is present both proximal to interstitial bornite, and as fine-grained euhedral crystals within the muscovite/sericite/chlorite bands. Image taken in PPL.

The SIP identified the main mineral in this sample as albite, followed by quartz. The fine-grained material was identified primarily as illite, but muscovite was also identified. In thin section under reflected light chalcocite was not readily distinguished, however, this mineral was found to dominate over bornite in the QEMSCAN analysis. This may just be a function of the pixel size, or the complex nature of the textural relationship between these two phases producing mixed spectra.

Overall the SIP mineral identifications compared well against observations made under transmitted and reflected light, especially for the minerals of interest, the copper(-Fe) sulfides, as well as magnetite, and the dominant minerals, quartz, albite, alkali feldspar and illite (sericite/muscovite).

5.6 Magnetite and Cu(-Fe) sulfide mineralisation

The iDiscover software was used to modify the mineral maps for the whole rock and MG samples to display only the minerals of interest, those identified as magnetite and the Cu(-Fe) sulfides. PB-10 showed a strong textural relationship between quartz horizons and the minerals of interest (Figure 5-78). Chalcocite/digenite, Cu-Fe sulfide (T), bornite and magnetite, in order of decreasing abundance, are strongly associated with the coarser grained portion of this rock. Chalcocite/digentite and magnetite are focussed along microfractures in PB-12. The fractures are associated with microfolding of earlier (pre-deformation) calcite-quartz veins. An association with muscovite is also seen for PB-12. EPS-14 contains no sulfides, but magnetite forms in layers parallel to the foliation.

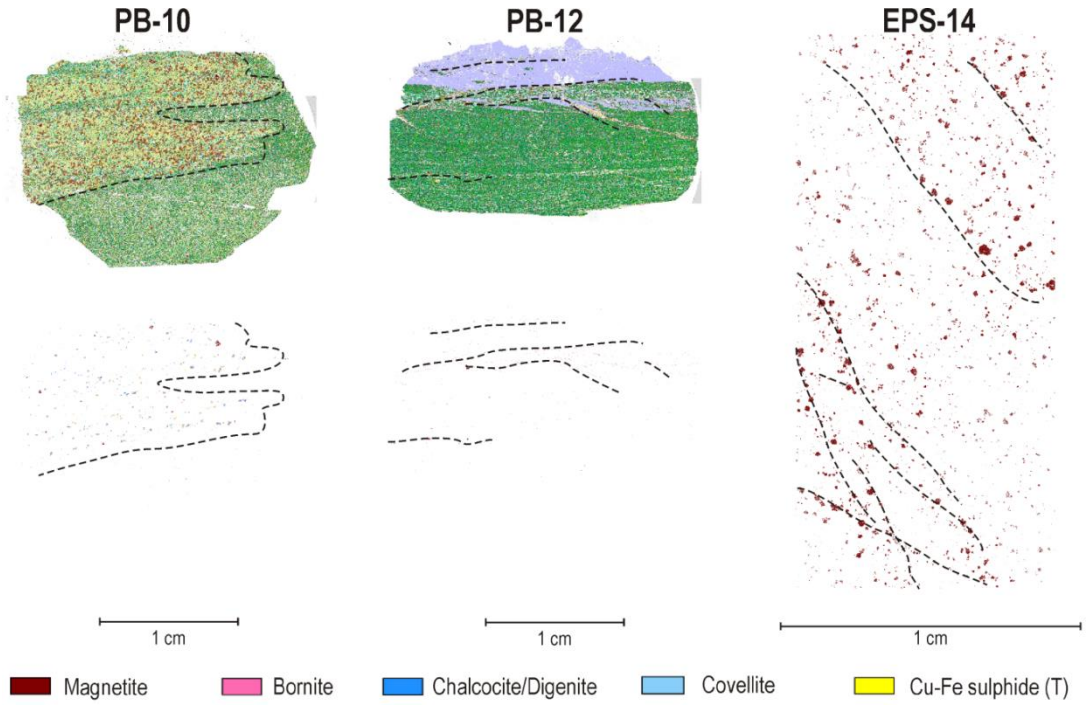

Figure 5-78: False colour mineral maps showing the an overview for PB-10 and PB-12 (TOP-LEFT and TOP-CENTRE), and selective mineral maps for PB-10 (BOTTOM-LEFT), PB-12 (BOTTOM-CENTRE) and EPS-14 (RIGHT) showing only the minerals magnetite, bornite, chalcocite/digenite, covellite and Cu-Fe sulfide (T). Dashed lines indicate the general trends of the minerals shown.

OPS-11 shows no clear trends in the distribution of magnetite, and contains no Cu(-Fe) sulfides (Figure 5-79). EPS-04, however, shows that both magnetite and the Cu(-Fe) sulfides are concentrated with the fabric in the rock. The latter are primarily interstitial to the coarse-grained quartz and feldspar and associated with magnetite. The Cu(-Fe) sulfides also occur as stringers, as does magnetite. OPS-7 shows the clearest evidence of the link between deformation and mineralisation. In this sample the Cu(-Fe) sulfides are clearly seen to occur parallel to foliation, and in the hinge zones of micro-folds.

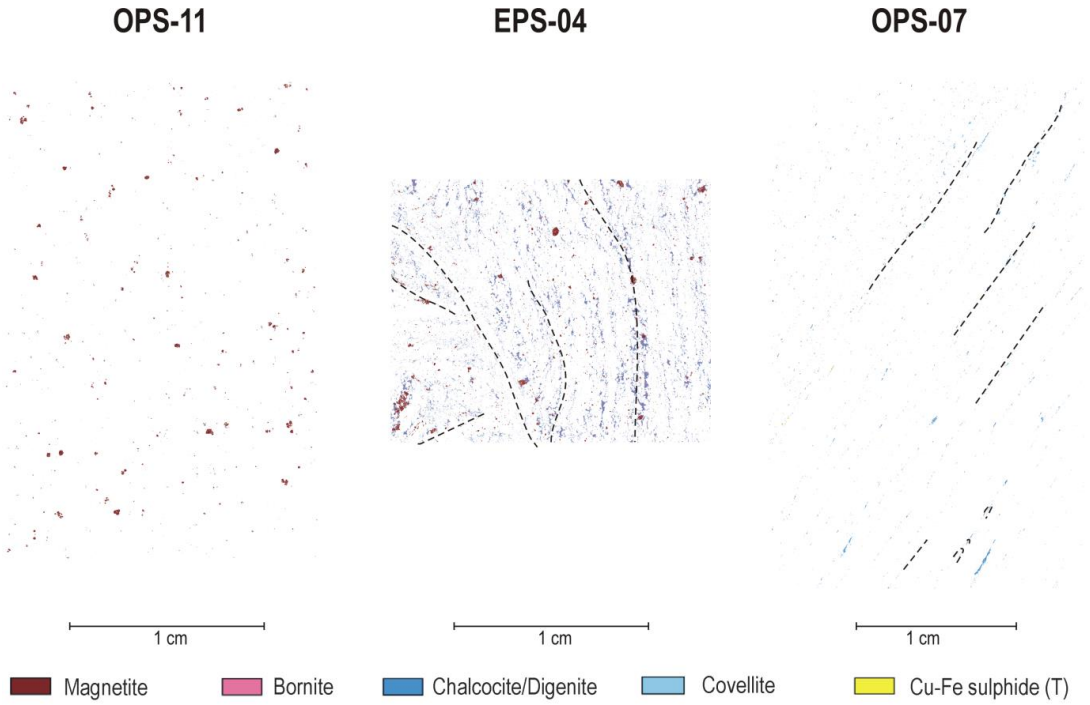

Figure 5-79: False colour mineral maps for three whole rock samples, OPS-11, EPS-04 and OPS-7. The maps show only magnetite and the copper(-Fe) minerals. Dashed lines have been included to indicate the trends of these minerals.

5.6.1 Mineralisation within the metavolcanics

The metavolcanics all contain magnetite, and some degree, Cu(-Fe) sulfides. Small (<30µm diameter) anhedral chalcopyrite is seen in EPS-01 and EPS-03. In these samples sulfides often occur with magnetite, either within bands (~50µm wide) of calcite and fine-grained phyllosilicates parallel to the foliation or associated with chloritisation. There is a marked difference between EPS-01 and 03, and the mineralised area (EPS-02 and EPS-04). In EPS-02 mineralisation is dominantly in the form of chalcopyrite with some alteration to covellite, such as in Figure 5-80, adjacent to quartz, calcite and magnetite foliation parallel layers, or in some cases, fractures. In EPS-02 and EPS-04 alternating bands of quartz/alkali feldspar and fine-grained phyllosilicates are more commonly developed. Mineralisation favours the quartzo-feldspathic layer. Mineralisation EPS-04 is in the form of bornite with some alteration to covellite. This mineralisation exploits the secondary porosity along grain boundaries within the more resistant layers of the rock. These rocks have undergone multiple stages of dynamic deformation and show both brittle and ductile deformation features. EPS-02 would suggest that the brittle fracturing happened after the foliation forming event.

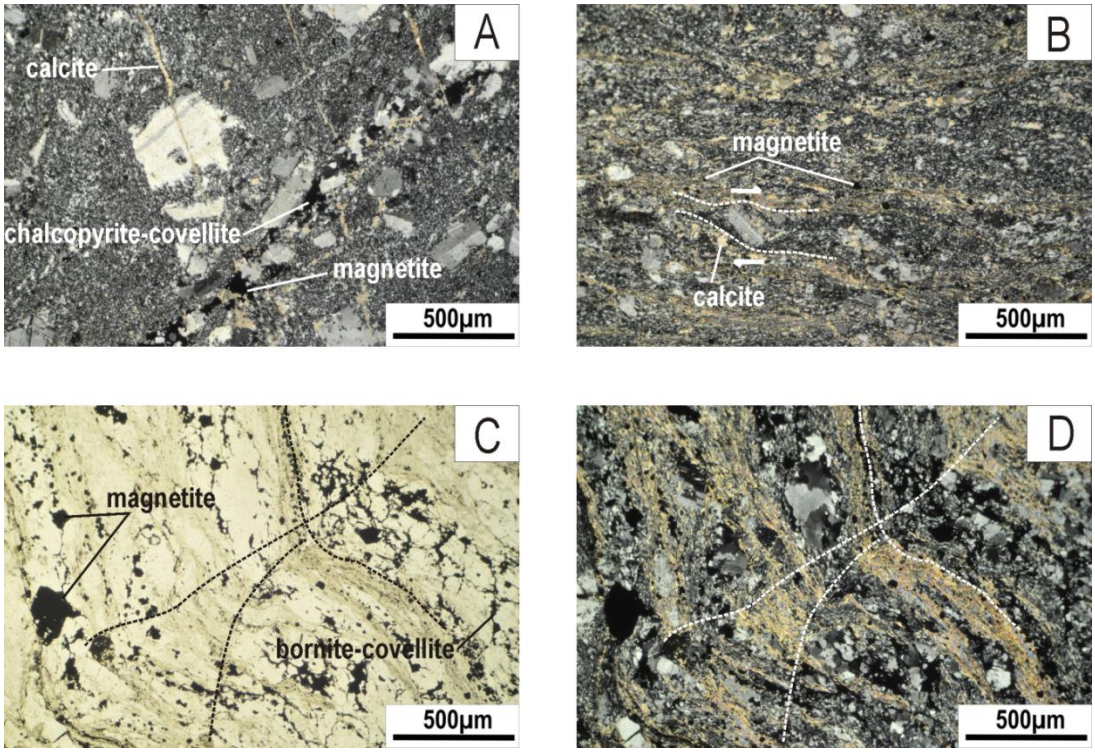

Figure 5-80: Photomicrographs from the metavolcanic sample suite showing opaque minerals. **A**: EPS-02 shows brittle fracturing at an angle to the quartzo-feldspathic layer within the rock. Phenocrysts do not show any displacement along fractures. Magnetite and Cu(-Fe) sulfides occur within the foliation parallel quartz-feldspathic layers. These layers appear to texturally precede brittle fracturing in this rock. Image taken under XPL. **B**: EPS-03 shows the rotation of a sandine phenocryst into the foliation. Magnetite micrporphyroblasts occur in the calcite and phyllosilicates-rich layers of the rock. Image taken under XPL. C & D: EPS-04 under PPL (**C**) and XPL (**D**) showing the preferential concentrations of magnetite and Cu(-Fe) sulfides within the quartzo-feldspathic layers of the rock. The finer units are primary comprised of phyllosilicates and calcite, and chlorite. The dashed lines indicate microfolding in the rock. Dynamic deformation is suggested by the multiple hinge zones developed from the micro-fold.

The 1µm measurements of the MG samples from the QEMSCAN analysis also provided information on the mineral inclusions in magnetite within the metavolcanic rocks, and provide evidence for the timing of mineralisation (Figure 5-81). Magnetite from the sample MG-3, the mineralised metavolcanic, contains abundance Cu(-Fe) sulfides. The mineralisation is primarily bornite and the Cu-Fe sulfide trap definition (T), with lesser chalcocite/digenite. Mineralisation occurs interstitially, as fracture fill, and as inclusions within magnetite grains. Regardless of where the mineralisation occurs, the mineralogy is consistent on a local scale.

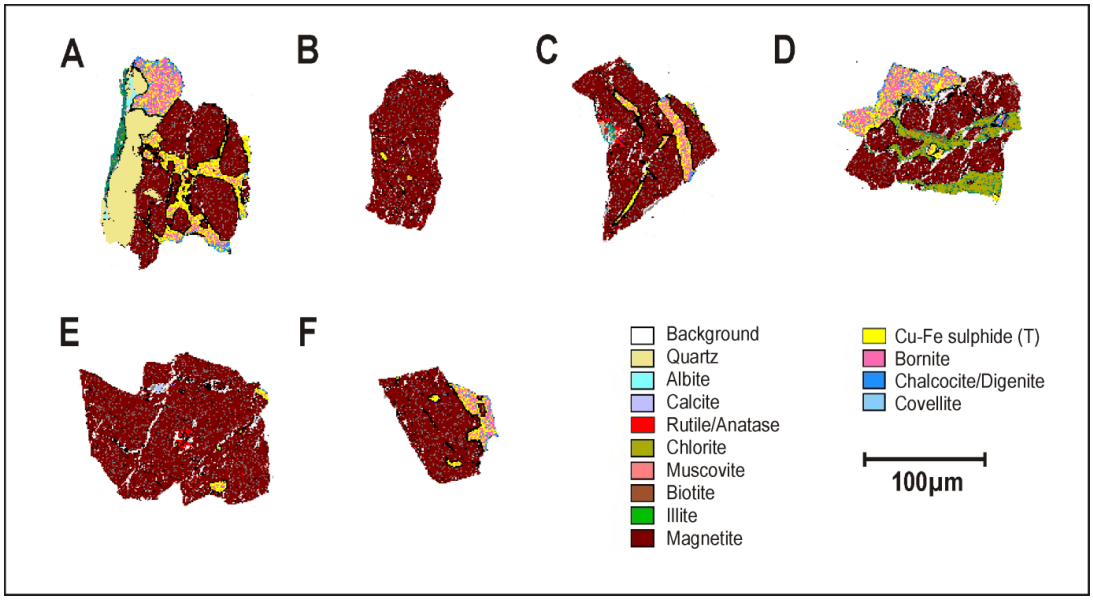

Figure 5-81: False colour mineral maps of magnetite particles from MG-3. Bornite-Cu-Fe sulfide occur interstitially to magnetite (**A**), as inclusions (**B, D, E** and **F**), as fracture-fill (**C**), and as embayments into magnetite grains (**F**).

5.6.2 Mineralisation within the sedimentary rocks

Three main styles of mineralisation were noted in the Eiseb Deposits. Disseminated mineralisation, vein-hosted sulfides, and foliation parallel lenses, layers, and anhedral bodies.

5.6.2.1 Disseminated

Sulfides are often observed within the groundmass of the rock, where they form anhedral bodies, usually associated with either lenses or at least a few grains of quartz in argillaceous rocks (Figure 5-82-**A**). In sandstones and siltstones sulfide disseminations are more commonly associated with phyllosilicates along the grain boundaries of quartz and feldspar detritus. The primary minerals are chalcocite and bornite, which often form exsolutions textures (Figure 5-82-**B**). Fine-grained chalcopyrite is rare.

5.6.2.2 Quartz-(carbonate) veins

Foliation parallel (Figure 5-82-**C**) and discordant quartz veins (Figure 5-82-**D**) are seen in the sandstone and siltstone lithotypes. These veins contain calcite, and often show folding, suggesting many of them formed before deformation. The deformed veins do not contain sulfides as such, but on rare occasions sulfides are present along fractures within the veins, and along the vein boundaries. Undeformed veins, whether discordant or concordant, dominantly contain chalcopyrite and bornite.

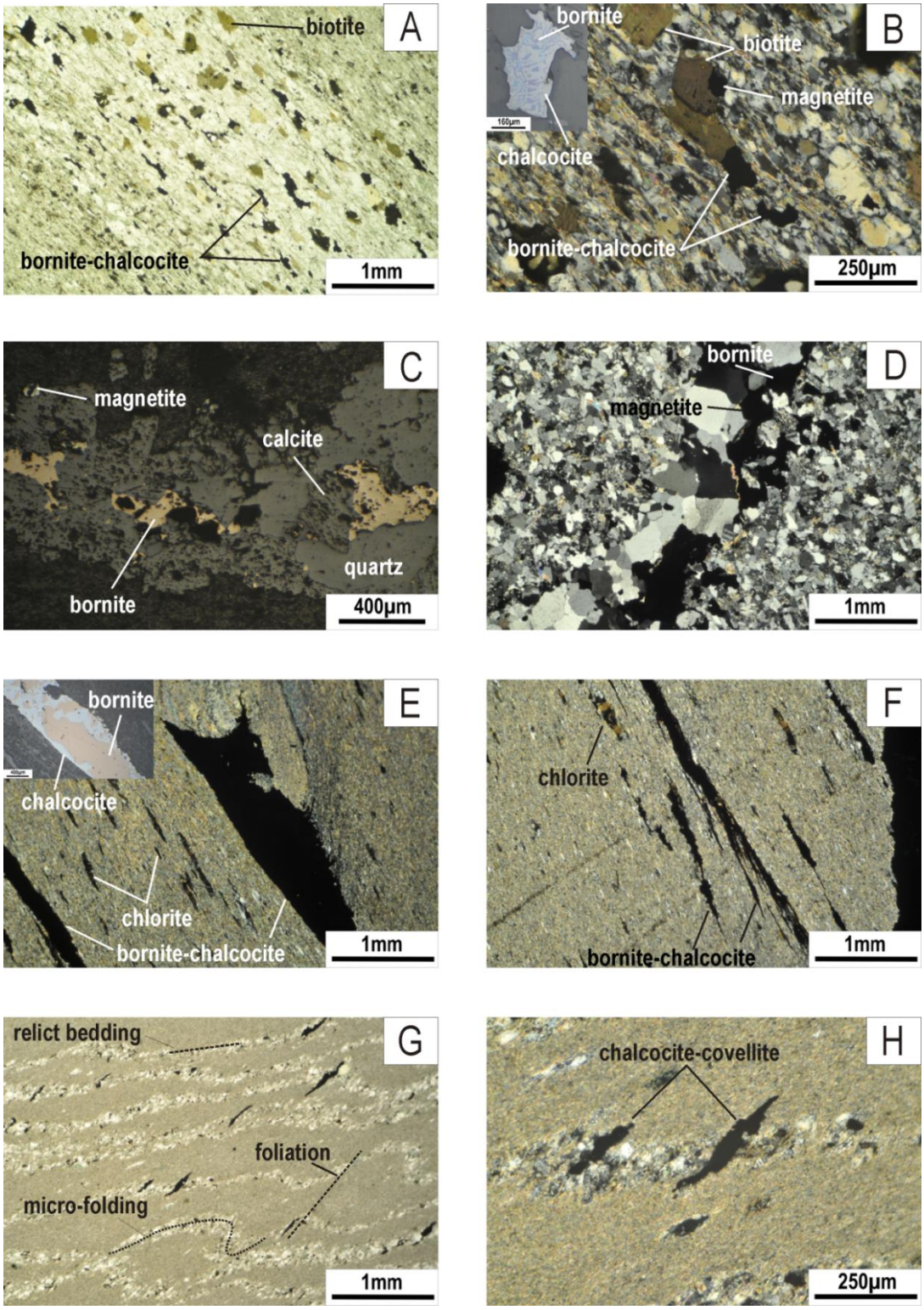

Figure 5-82: Photomicrographs of the main mineralisation styles encountered in the Eiseb (meta-) sedimentary rocks. A&B: Bornite and chalcocite, which form exsolutions textures (insert B), are disseminated within the coarse-grained part of the rock (PST4-D1-4). C: Quartz-calcite veins containing bornite and magnetite (EPS-07). In D bornite and magnetite are concentrated on the edge of a folded and fractured quartz-carbonate vein (EPS-09). E: Bornite and chalcocite, which form exsolutions textures (insert E) occur parallel to the foliation (E & F) and along the hinge zone of a fold (E) (PST2-D2-4). G & H: The foliation forms at an angle to the relict bedding with sulfides elongated parallel to the foliation (PST7-D1-1). Borg (1988a) interpreted similar txtures from the Klein Aub and Lake Ngami deposits as chalcocite pseudomorphs after evaporite minerals such as gypsum.

Where chalcopyrite is the dominant Cu-Fe sulfide, some alteration to digenite is evident along grain boundaries. Where bornite is the dominant Cu-Fe sulfide, chalcopyrite may be present along grain boundaries. Veins which contain bornite commonly contain some magnetite, and veins which contain chalcopyrite often contain galena.

5.6.2.3 Foliation-parallel

Cu(-Fe) sulfides are most commonly present as foliation parallel lenses and irregular elongate bodies of chalcocite and bornite (Figure 5-82-**E** to **-H**). Whether present as continuous layers (Figure 5-82-**E & F**) or S-shaped elongate bodies (Figure 5-82-**G & H**), the sulfides are always associated with quartz (and feldspar) lenses. Neither the S-shaped bodies nor the foliation parallel lenses/layers show development of pressure shadows.

The textures shown in Figure 5-82-**G** and -**H**, from the Eastern Anticline, are similar to those identified by Borg (1988a) at the Klein Aub and Lake Ngami deposits (Figure 5-83). These textures were interpreted as Cu sulfide (e.g. chalcocite) pseudomorphs after evaporite minerals such as gypsum, which typically grow perpendicular to bedding in coarse-grained layers (Borg, 1988a; Borg and Maiden, 1989).

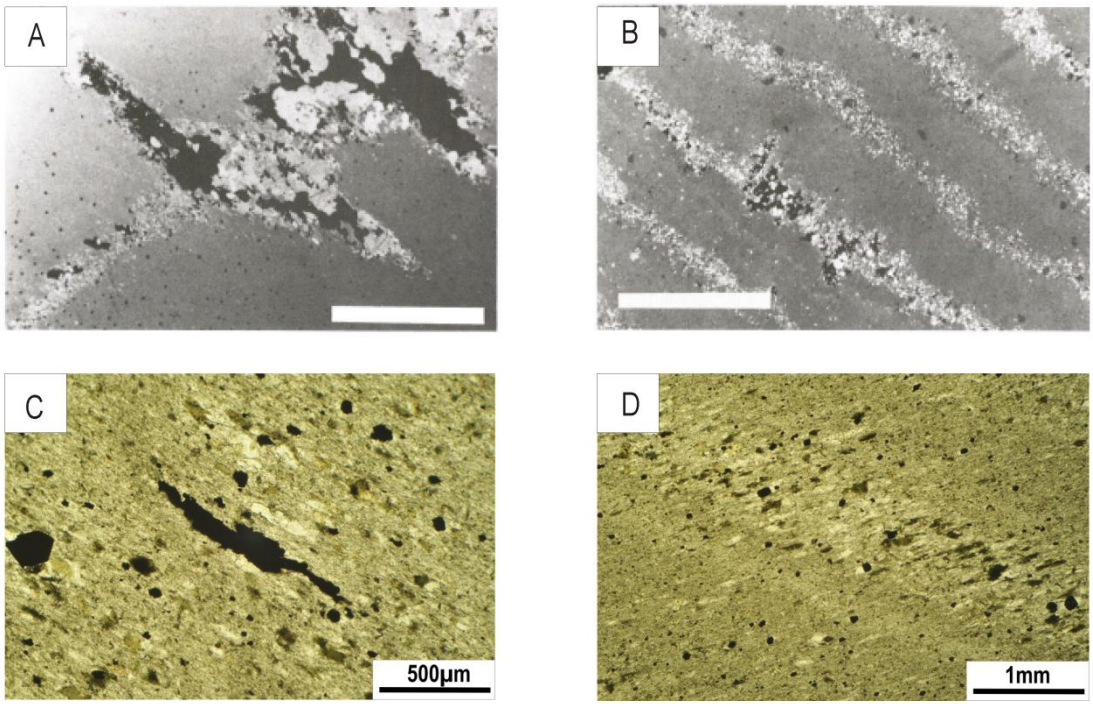

Figure 5-83: Photomicrographs of thin sections from the Lake Ngami area (Botswana) from Borg (1988a) (**A & B**), and from sample OPS-3 from borehole CA-PL-3 (**C & D**) in the Eiseb showing (opaque) Cu sulfides concentrating in the coarser layers of laminated rocks, along with calcite, and in OPS-3 also magnetite. Cu sulfides from both the Lake Ngami area, and from the Eiseb, are interpreted as pseudomorphs after evaporite minerals (e.g. gypsum). In photomicrograph **A** the Cu sulfides have been stretched and pressure shadows are evident, suggesting replacement of evaporite minerals took place prior to deformation in the rock, however, in the Eiseb (**C**) no pressure shadows are developed on the Cu sulfides, suggesting syn-deformation replacement of evaporite minerals. The scale bars in **A & B** are 5mm.

The same Cu-sulfide textures were also identified in sample OPS-3 from the Central Anticline. These also show no development of pressure shadows (Section 5.4.4.2). The absence of pressure shadows and the S-shape of the Cu-sulfides would suggest that replacement took place during the waning stages of deformation. The preservation of these textures in rocks from the Central Anticline and from over 100km away within the Eastern Anticline suggests that this late-stage mineralisating event was basin-wide.

5.6.3 Magnetite Petrography

5.6.3.1 Oxidation of magnetite

Optical microscopy revealed an important feature of magnetite in samples taken from across the Eiseb: oxidation to hematite, known as martitisation. This process has been linked to the waning stages of ore-forming processes under decreasing temperatures. This process is also common in weathering zones and supergene modified ore deposits or oxidative hydrothermal zones (Nadoll et al., 2014). Martitisation refers to the alteration (by oxidation) of magnetite to hematite, while alteration of hematite to magnetite is referred to as mushketovitization (Figure 5-84). The former is caused by oxidizing or acidic fluids, and the latter by reducing fluid-rock reactions (Ohmoto, 2003). Both processes are generally pseudomorphic, and given the right oxygen fugacity and pH conditions, can represent considerable volumetric changes in the rock (Nadoll et al., 2014).

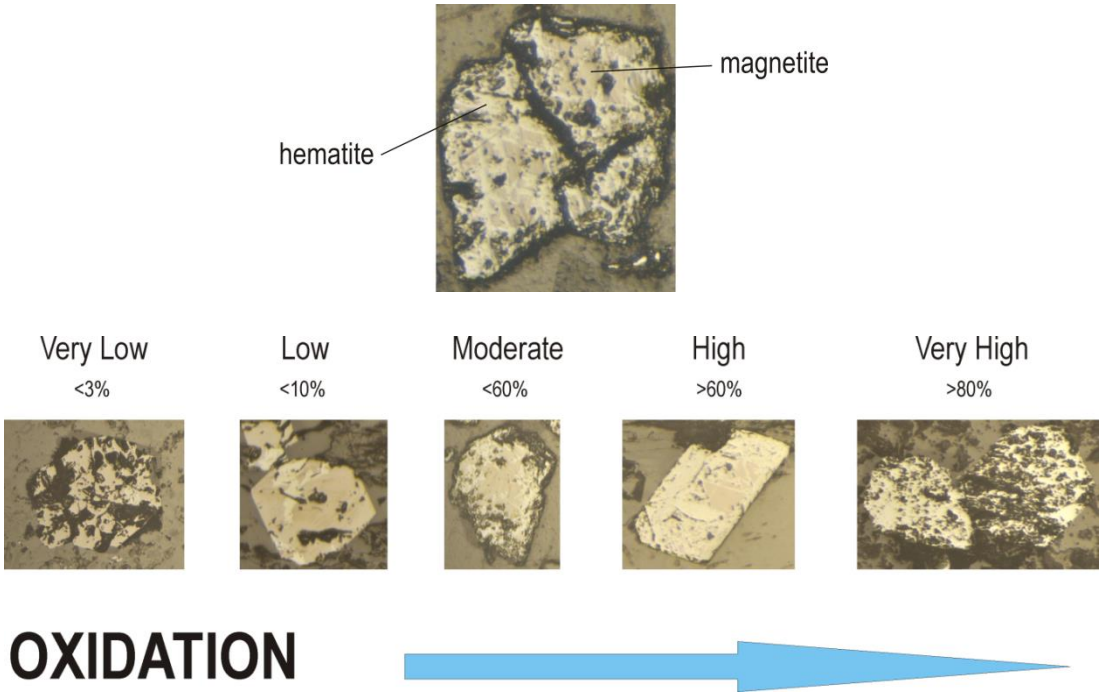

Figure 5-84: Photomicrograph of a magnetite crystal from the grain mount sample MG-5 from borehole NEA-PL-1 showing moderate oxidation of magnetite (pink) to hematite (yellow) along lattice planes (TOP). The level of oxidation for magnetite in every polished thin section was categorised using a scale devised for this study based on the percentage of hematite in any given magnetite grain (BOTTOM).

The metavolcanic samples show moderate to high levels of martitisation in only one sample, EPS-03 from 85m depth (Table 24). The overlying mineralised sample, EPS-04 from the same borehole at a depth of 33m shows almost no martitisation of magnetite (borehole WB-2). The magnetite from borehole WB-1 samples also show very low levels of

martitisation although these were taken at similar depths to EPS-03 suggesting that perhaps martitisation is directly linked to geochemistry of mineralised horizons.

Table 24: Summary table of the petrographic characteristics of magnetite in the polished thin sections from the Eiseb Deposits. BH=borehole; MG=magnetite, MS=magnetite stringer; MP=magnetite porphyroblasts; RF=rock fabric (foliation or lepidoblastic texture); PS-MP=pressure shadows developed on magnetite porphyroblasts; MP-F=magnetite porphyroblasts parallel to the fabric of the rock; CFS=copper-iron sulfides; OX=oxidation level based on the chart presented in **Figure 5-83**. X=magnetite not present; *=magnetite not observed under reflected light, but confirmed using EMPA.

Sample ID	Borehole	Lithotype	Stratigraphy	MG	MS	MP	RF	PS-MP	MP-F	CFS	OX
EPS-01	WB-1	MV	MV	√	√	√	√	√	√		low
EPS-02	WB-1	MV	MV	√	√	√	√		√	√	low
EPS-03	WB-2	MV	MV	√	√	√	√	√	√		mod-high
EPS-04	WB-2	MV	MV	√	√	√	√	√	√	√	low
EPS-05	CA-PL-6	SBX	FW	*							
EPS-06	CA-PL-6	SST	IBU	√	√	√				√	v.low
EPS-07	CA-PL-6	SLT	IBU	√		√	√		√	√	v.low
EPS-08	CZ-1	LST	FW	X			√				
EPS-09	CA-PL-7	SLT	IBU	√		√	√	√		√	v.low
EPS-10	CA-PL-7	SST	IBU	√	√	√		√			mod-high
EPS-11	CA-PL-8	ARG	IBU	X							
EPS-12	CA-PL-8	ARG	IBU	X							
EPS-13	CA-PL-9	SST	IBU	√	√	√	√	√	√		v.low
EPS-14	CZ-1	SLT	HW	√	√	√	√	√	√		mod-high
EPS-15	CA-PL-4	SST	IBU	√	√	√			√		v.low
EPS-16	CA-PL-5	SLT	IBU	√	√	√	√	√	√		high
EPS-17	CA-HZ-1	SST	FW	√	√	√	√	√			high
EPS-18	CA-PL-5	ARG	IBU	X							
EPS-19	CA-PL-6	SLT	FW	X							
EPS-20	CA-PL-6	SST	FW	√	√	√	√	√	√		mod-high
EPS-21	CA-PL-6	SST	FW	√	√	√					mod-high
EPS-22	CA-PL-6	SST	FW	√	√	√	√	√			high
EPS-23	CA-PL-6	SST	FW	√	√	√	√	√			mod-high
EPS-24	CA-PL-6	SST	FW	√	√	√		√			high
EPS-25	CA-PL-6	SLT	FW	√	√	√	√	√	√		high
EPS-26	CA-PL-6	SST	FW	√	√	√		√			high
EPS-27	CA-PL-6	SST	FW	√	√	√	√	√			mod-high
EPS-28	CA-PL-6	SST	FW	√	√	√		√			mod-high
EPS-29	CA-PL-6	SST	FW	√	√	√	√	√			high
EPS-30	CA-PL-7	SLT	IBU	√	√	√	√	√			v.low
EPS-31	CA-PL-7	SLT	IBU	√	√	√	√	√	√		v.low
EPS-32	CA-PL-7	ARG	IBU	√	√	√	√	√			mod-high
EPS-33	CA-PL-7	SST	FW	√	√	√	√	√	√		high
OPS-1	CA-PL-2	SLT	IBU	√		√	√	√	√		low
OPS-2	CA-PL-2	SLT	IBU	√	√	√	√	√	√	√	v.low
OPS-3	CA-PL-3	SLT	IBU	√	√	√	√	√	√	√	v.low-low
OPS-4	CA-PL-3	SST	IBU	√	√	√	√	√			v.low
OPS-5A/B	CA-PL-3	SST	FW	√	√	√		√		√	v.low
OPS-6	CA-PL-1	SST	HW	√	√	√	√	√	√		mod-high
OPS-7	CA-PL-1	SLT	FW	√		√	√	√		√	low
OPS-8	EA-NL-2	SST	IBU	√	√	√		√			mod-high
OPS-9	EA-NL-2	SST	IBU	√	√	√	√				mod
OPS-10	NEA-PL-1	SST	IBU	√	√	√		√			high

Table 24: *Continued.*

Sample ID	Borehole	Lithotype	Stratigraphy	MG	MS	MP	RF	PS-MP	MP-F	CFS	OX
OPS-11	EA-NL-1	SST	HW	√	√	√		√			mod-high
OPS-12	EA-NL-1	SST	FW	√	√	√		√			low
OPS-13	NEA-SL-1	SLT	IBU	√	√	√	√	√	√		mod-high
OPS-14	NEA-SL-1	SST	HW	√	√	√					mod-high
OPS-15	NEA-PL-2	SST	FW	√	√	√	√				mod
PST2D2-1	EA-PL-1	SLT	IBU	*							
PST2D2-2	EA-PL-1	SLT	IBU	*							
PST2D2-4	EA-PL-1	SLT	MZ	*							
PST4D1-1	NEA-PL-1	SST	IBU	√	√	√	√		√		high
PST4D1-2	NEA-PL-1	PLT	IBU	√		√	√		√	√	low
PST4D1-3	NEA-PL-1	PLT	IBU	√		√	√	√	√		mod
PST4D1-4	NEA-PL-1	PLT	MZ	√		√	√	√	√	√	v.low
PST4D2-1	NEA-PL-2	SLT	IBU	√	√	√	√		√		v.low
PST4D2-2	NEA-PL-2	SLT	IBU	√	√	√	√		√	√	low
PST4D2-3	NEA-PL-2	SLT	IBU	√	√	√	√		√	√	mod
PST7D1-1	EA-SL-1	PLT	MZ	x							
PST7D1-2	EA-SL-1	PLT	MZ	x							

The hangingwall samples all show moderate to high levels of magnetite martitisation regardless of geographic location, or proximity to mineralised horizons. The footwall samples are more variable. Where present magnetite from this unit show moderate to high levels of martitisation unless the sample also contains Cu(-Fe) sulfides. Magnetite from sample OPS-12 from the footwall sandstone in EA-NL-1, however, also has low levels of martitisation, but contains no visible sulfides.

The Interbedded Unit is much more variable than the other stratigraphic units with martitisation of magnetite from these units ranging from very low to high, regardless of geographic location. In the east magnetite from EA-2 shows moderate to high levels of martitisation, as do the North East Anticline samples, except for one. PST-4D2-1 shows almost no martitisation of magnetite, but stratigraphically sits within meters of a mineralised horizon. The Central Anticline samples show no relationship to mineralised horizons, with magnetite showing high or low levels of martitisation in samples within meters of each other. None of the samples from the Interbedded Unit show any systematic variations in magnetite martitisation on the basis of lithotype. Magnetite does, however, show a strong association between low levels of martitisation and the presence of Cu(-Fe) sulfides. The only sample which does not follow this observation is PST-4D2-3 from NEA-PL-2. This sample shows moderate levels of martitisation.

None of the samples show any evidence of a hematite precursor phase; all of the magnetite appears to be the primary Fe-oxide phase which has subsequently begun to oxidise. Although it is possible that the hematite cores, which would indicate a precursor, could have been entirely replaced by magnetite under increasing metamorphic temperatures over time, palimpsest textures would have shown this. No such textures have been found in the polished sections reviewed for this study.

5.6.3.2 Petrographic characteristics of magnetite

Optical microscopy identified three main types of magnetite: fine-grained stringers of equant grains (<50µm diameter), large euhedral porphyroblasts up to 250µm in diameter and magnetite intergrown or texturally associated with Cu(-Fe) sulfides (Figure 5-85).

5.6.3.2.1 Type 1: Stringer magnetite

Fine-grained (10-30µm diameter) euhedral magnetite forms stringers, and to a lesser extent aggregates, which are parallel to foliation in foliated rocks (MS in Table 24). Chlorite ± sericite are commonly associated with this type of magnetite. In some samples magnetite can be much coarser (up to ~150µm long) but follows the same textural patterns. martitisation does not exceed 10% of any given magnetite grain, and is usually closer to 5%. This type of magnetite is present in almost all of the samples.

5.6.3.2.2 Type 2: Magnetite (micro-) porphyroblasts

Magnetite forms large subhedral to euhedral grains (~ 200µm long). There are two subtypes within this category (MP in Table 24):

a) Pressure shadows are developed (more common);
b) Pressure shadows are not developed.

Maritisation is more advanced in this type of magnetite, reaching up to 90%. This type of magnetite is present in all of the samples.

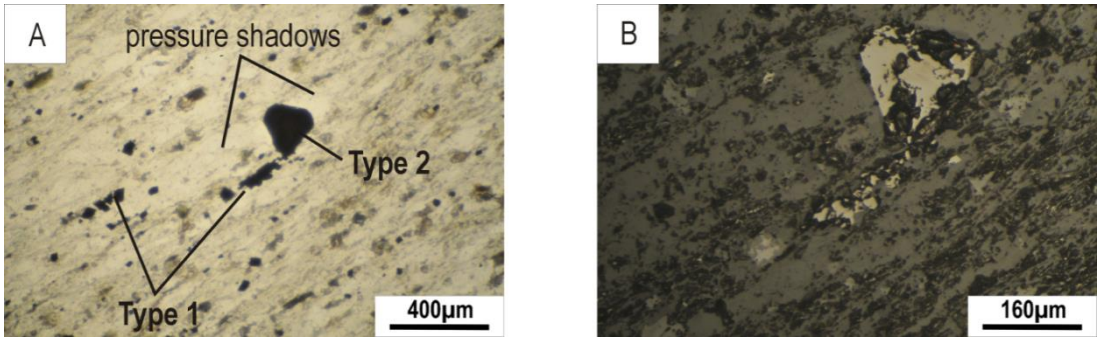

Figure 5-85: Photomicrographs of magnetite from OPS-2 from borehole CA-PL-2 showing fine-grained magnetite stringers parallel to the foliation of the rock (Type 1) and a magnetite porphyroblast (Type 2) with pressure shadows developed parallel to the foliation of the rock. Images taken in PPL (**A**) and under reflected light (**B**).

5.6.3.2.3 Type 3: Magnetite associated with Cu(-Fe) sulfides

Magnetite is intimately associated with copper-(iron) sulfide minerals (CFS in Table 25), including chalcocite, bornite, covellite and chalcopyrite (Figure 5-86). This type of magnetite is euhedral to subhedral and ranges from <20 to >100µm diameter. In foliated rocks this type of magnetite occurs parallel to the foliation, often shows the development of pressure shadows, commonly filled by quartz and Cu(-Fe) sulfides. Inclusions of Cu(-Fe) sulfides may be present in magnetite grains, and magnetite may be present within Cu(-Fe) sulfides. Not all of the mineralised zones contain visible magnetite. Martitisation is low in all the samples which contained Type 3 magnetite.

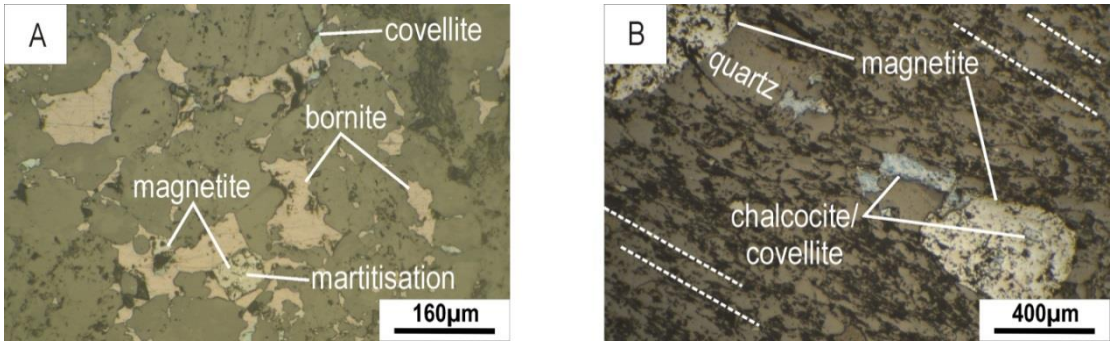

Figure 5-86: Photomicrographs showing the relationship between magnetite and Cu(-Fe) sulfides in Type 3 magnetite under reflected light. **A:** Weakly martitised magnetite shares straight boundaries with bornite which is partly altered to covellite along its edges (EPS-04). **B:** Magnetite and the Cu-sulfides are aligned parallel to the foliation developed in sample PST-4D1-2. Magnetite shows pressure shadow development parallel to the foliation. These pressure shadows are filled by quartz and the chalcocite showing alteration to covellite. Magnetite also contains inclusions of chalcocite altering to covellite. These inclusions are rounded and elongated parallel to the foliation.

Magnetite was not identified in seven of the 60 polished thin sections examined, and in four, magnetite was only discernable using an EMPA (Table 24). In the samples containing visible magnetite (49 thin sections) Type 1 magnetite was observed in all but seven of the samples.

All of the thin sections which contained magnetite contained Type 2 magnetite, and almost three quarters of these showed the development of pressure shadows associated with magnetite. Approximately half of the samples show Type 2 magnetite aligned parallel to the foliation.

Type 3 magnetite was identified in about a quarter of the samples from a range of rock types. Type 2 magnetite with pressure shadow development is commonly associated with Type 3 magnetite, but so is Type 1. An important feature common to most of the samples containing Type 3 magnetite is foliation of the host-rock. Only two samples lack fabric development but they are sandstones so this is to be expected (EPS-06 & OPS-5).

Type 1 magnetite shows no pressure shadow development, and shows a clear association with the deformation, occurring parallel to the foliation in most rocks, this suggests a syn-deformational origin for Type 1 magnetite. Type 2 magnetite appears earlier than Type 1. Type 2 shows rotation into the fabric and pressure shadow development in foliated rocks. This suggests that this type of magnetite is burial metamorphic, i.e. pre-deformation. Type 3 magnetite, magnetite associated with Cu(-Fe) sulfides, is both burial metamorphic (Type 2) magnetite (where pressure shadows are developed) and related to deformation (where pressure shadows are absent and magnetite is aligned with the foliation). An alternative hypothesis is that the pressure shadows were inherited from a precursor Fe-bearing mineral which magnetite replaced.

6 Results 2: Magnetite

6.1 LA-ICP-MS Magnetite Trace Element Geochemistry

In total 579 individual magnetite grains were analysed for their minor and trace element concentrations (Appendix VI-A). The time resolved analytical signals for the spectral results were visually screened to check the background signal, and to check for inclusions which may be affecting the main signal.

6.1.1 Glitter™

The GLITTER ™ software package (Griffin et al., 2008) outputs trace element concentrations in ppm, the sigma 1 error and the minimum detection limits. The following explanation is taken directly from the GLITTER ™ Software Manual (van Achterbergh et al., 2007).

Trace Element Concentrations

Trace element concentrations are calculated using the following equations:

$$conc_{ni} = (cps_{nij} / abundance_{j}) / (yield_{ni}) \quad \underline{1}$$

where:
$conc_{ni}$ = the concentration of element **i** in analysis **n**
cps_{nij} = the mean count rate (background-subtracted) of isotope **j** of **i** in analysis **n**
$abundance_{j}$ = natural abundance of isotope **j**
$yield_{ni}$ = cps per ppm of element **i** in analysis **n**

The yield of element **i** in analysis **n** is determined by:

$$yield_{ni} = yield_{ns} * Int(yield_{ni} / yield_{ns})^{std} \quad \underline{2}$$

where:
$yield_{ns}$ = cps per ppm of the internal standard **s** in analysis **n**
$Int(yield_{ni} / yield_{ns})^{std}$ = the ratio of the yield of element **i** in analysis **n** to the yield of the internal standard **s** in analysis **n**, interpolated over the standard analyses.

One Sigma Error

The one sigma error estimates use √N counting statistics on the signal and background counts, propagated through the equations. An assumed 1%

uncertainty (relative) on the elemental concentrations of the reference material, and a 3% uncertainty (relative) on the values of the internal standard is propagated throughout the calculations.

The Minimum Detection Limit

The detection limit (MDL) at the 99% confidence level is determined by Poisson counting statistics:

MDL = 2.3* √(2B)

where B is the total counts in the background interval.

6.1.2 Data Treatment

Initially over 100 grains were analysed from each of the bulk magnetite samples in order to determine whether there were different populations within a given sample. The data showed little change in the degree of variability when the number of grains analysed was dropped to 35 (MG-5); therefore, the number of grains analysed per sample was reduced to ≤20 for subsequent samples.

The results were scrutinised according to the following criteria:

- trace element concentrations were compared against the minimum detection limits for each measurement. Where trace element concentrations were lower than detection limits the Glitter™ calculated concentration was replaced with '<dl';
- where trace element concentrations for calcium, silica and aluminium were over 10 wt. % (100,000 ppm) the measurement was rejected. These are assumed to be silicate inclusions (Appendix VI-B)
- the standard deviations of the NIST 610 and 612 reference materials were also reviewed (Table 27)(Appendix VI-C).

6.1.3 NIST Standard Reference Material (SRM)

Investigations into magnetite trace element geochemistry by previous authors using LA-ICP-MS have relied on a variety of reference materials (RM), and often multiple RMs, for a single study (e.g. USGS GSE-1G and NIST SRM 2782). Recently, however, Nadoll and Koenig (2011) showed empirically that the NIST 610 glass can be a reliable calibration material for

magnetite LA-ICP-MS data for spot sizes ≥25µm, but also suggested that an internal standard for Fe is required for accurate concentration calculations. The NIST 610 & 612 glasses were therefore used for instrument calibration during this study and EMPA measurements of FeO averaged over ten grains per sample were used for the internal ^{56}Fe standard (Table 25) (Dare et al., 2014; Nadoll and Koenig, 2011).

Table 25: FeO weight percentages obtained during EMPA averaged over ten magnetite grains per sample.

	MG-1	MG-3	MG-4	MG-6	MG-5	MG-10	MG-12	MG-13	MG-14	KG-01	OE-1	OE-2
FeO (wt. %)	98	96	95	98	96	96	96	97	98	56	91	95

The accuracy of the measurements was determined statistically by comparing the results of repeated measurements against the published values for the SRMs used (relative difference) (Table 26). The precision was tested by comparing the standard deviation of the repeat measurements against the average values for the same measurements (relative standard deviation).

The analyses of SRM NIST 610 show that precision and accuracy, measured by the RD and RSD respectively, were good, as both of these are below 10% for all elements, save Th, where precision is not as sharp. The SRM NIST 612 reference material produced similar results for accuracy and precision for most elements, with the exception of Sc, Fe, Mg and Th. Poor precision is to be expected for iron from NIST 612 because of the very low iron values in the SRM versus the ^{56}Fe internal standard used to calibrate the results. Although the RD value for Mg is slightly elevated, the precision is good. The higher RD and RSD for Sc are within acceptable limits (<20%) and are accounted for by the low levels of this element in the grains analysed. The very high RD and RSD values for Th are assumed to also be due to their low levels in the grains analysed.

Table 26: Summary statistics for the standard reference materials analysed during LA-ICP-MS analysis, NIST-610 and NIST-612.

	SRM				This Study				QAQC			
	610		**612**		**610**		**612**		**610**		**612**	
	Avg	*STDev*	*Avg*	*STDev*	*Avg*	*STDev*	*Avg*	*STDev*	*Rdiff*	*RSD*	*Rdiff*	*RSD*
Mg	449	45	68	7	432	6.48	57.2	1.48	-3.78	1.50	-17.2	2.58
Al	10500	318	11000	106	10300	115	10600	285	-1.47	1.12	-3.11	2.69
Si	326000	2800	337000	4670	326000	1880	337000	3680	0.00	0.58	-0.02	1.09
Ca	81500	1430	85100	715	81600	1230	84300	2440	0.08	1.51	-0.83	2.89
Sc	468	22	40	3	455	7.31	45.5	8.42	-2.76	1.60	12.8	18.5
Ti	461	16	43	4	452	8.63	41.9	4.71	-1.87	1.91	-2.54	11.2
V	455	18	39	2	450	6.98	38.9	0.99	-1.01	1.55	-0.19	2.54
Cr	410	20	37	2	408	6.56	36.9	1.22	-0.42	1.61	-0.27	3.32
Mn	450	15	38	2	444	6.88	38.7	1.71	-1.26	1.55	1.88	4.41
Fe	479	19	54	5	459	42.2	120	70.3	-4.20	9.18	75.9	58.5
Co	405	26	35	2	410	5.83	35.1	0.67	1.29	1.42	0.40	1.90
Ni	445	24	39	2	459	4.65	39.2	1.06	3.06	1.01	0.57	2.70
Cu	433	29	38	3	441	6.75	38.1	1.20	1.87	1.53	0.24	3.14
Zn	469	34	40	2	460	6.71	38.9	1.75	-1.89	1.46	-2.78	4.50
Ga	444	15	38	2	433	6.40	36.8	0.87	-2.43	1.48	-3.29	2.36
Ge	424	BDL	37	1	447	6.86	39.8	1.04	5.36	1.53	7.30	2.60
Y	467	27	38	3	463	6.77	37.5	1.48	-0.82	1.46	-1.19	3.93
Zr	449	29	38	3	452	21.4	38.2	1.82	0.70	4.74	0.64	4.76
Nb	462	51	39	3	466	8.35	38.3	1.16	0.77	1.79	-1.75	3.03
Mo	429	28	38	3	418	7.39	36.7	1.09	-2.68	1.77	-3.45	2.98
Ag	252	11	23	3	251	3.93	22.0	0.79	-0.49	1.57	-4.26	3.57
Sn	430	30	39	2	430	6.57	38.4	0.97	0.07	1.53	-1.45	2.52
Hf	439	37	36	3	435	6.49	36.9	1.77	-0.98	1.49	2.49	4.81
Ta	471	23	37	3	447	6.48	36.3	1.22	-5.17	1.45	-1.88	3.36
W	435	16	38	1	444	7.33	38.3	0.73	2.00	1.65	0.84	1.89
Pb	417	36	39	3	426	7.24	38.4	1.28	2.23	1.70	-1.58	3.34
Th	453	131	38	2	443	104	53.7	115	-2.22	23.6	34.2	213.6

*NIST values reported in Jochum et al. (2011).Abbreviations: SRM - standard reference material; Avg - average; STDev - standard deviation; RD - relative difference; RSD - relative standard deviation.

6.1.4 Magnetite Trace Element Geochemistry

Magnetite grains were analysed for the elements ^{24}Mg, ^{27}Al, ^{28}Si, ^{43}Ca, ^{47}Ti, ^{51}V, ^{52}Cr, ^{55}Mn, ^{59}Co, ^{60}Ni, ^{63}Cu, ^{66}Zn, ^{69}Ga, ^{72}Ge, ^{89}Y, ^{93}Nb, ^{95}Mo, ^{107}Ag, ^{118}Sn, ^{182}W, ^{208}Pb and ^{232}Th. Additional elements were added after the first two samples, MG-1 and MG-14, were analysed. ^{45}Sc, ^{90}Zr, ^{178}Hf and ^{181}Ta were added to all subsequent analyses in order to facilitate comparisons of the results with those common in the literature.

Dare et al. (2014) tested ^{40}Ar interference by measuring multiple isotopes of Cr, Mg and Ti known to cause argide or oxide interferences on Zr, Nb and Cu. They found that the only significant interferences where Zr concentrations can be strongly influenced by isotopic

interference from ^{50}Ti and ^{40}Ar are from very high Ti magnetite (5-10 wt.% Ti), but that in general no argide isotopic interferences were significant enough to require calculation corrections on any of the results. Individual analyses from this study reported up to 5 wt.% Ti, but these were rare and therefore no corrections have been made to any of the results presented herein. The magnetite minor and trace element concentrations are summarised in Table 27, and in Table 28 the data are presented as median concentrations (Figure 6-2). The variability in trace element concentrations is shown in Figure 6-1 for select elements. In order to mitigate the effects of outliers the majority of the data analysis herein has been done using the median.

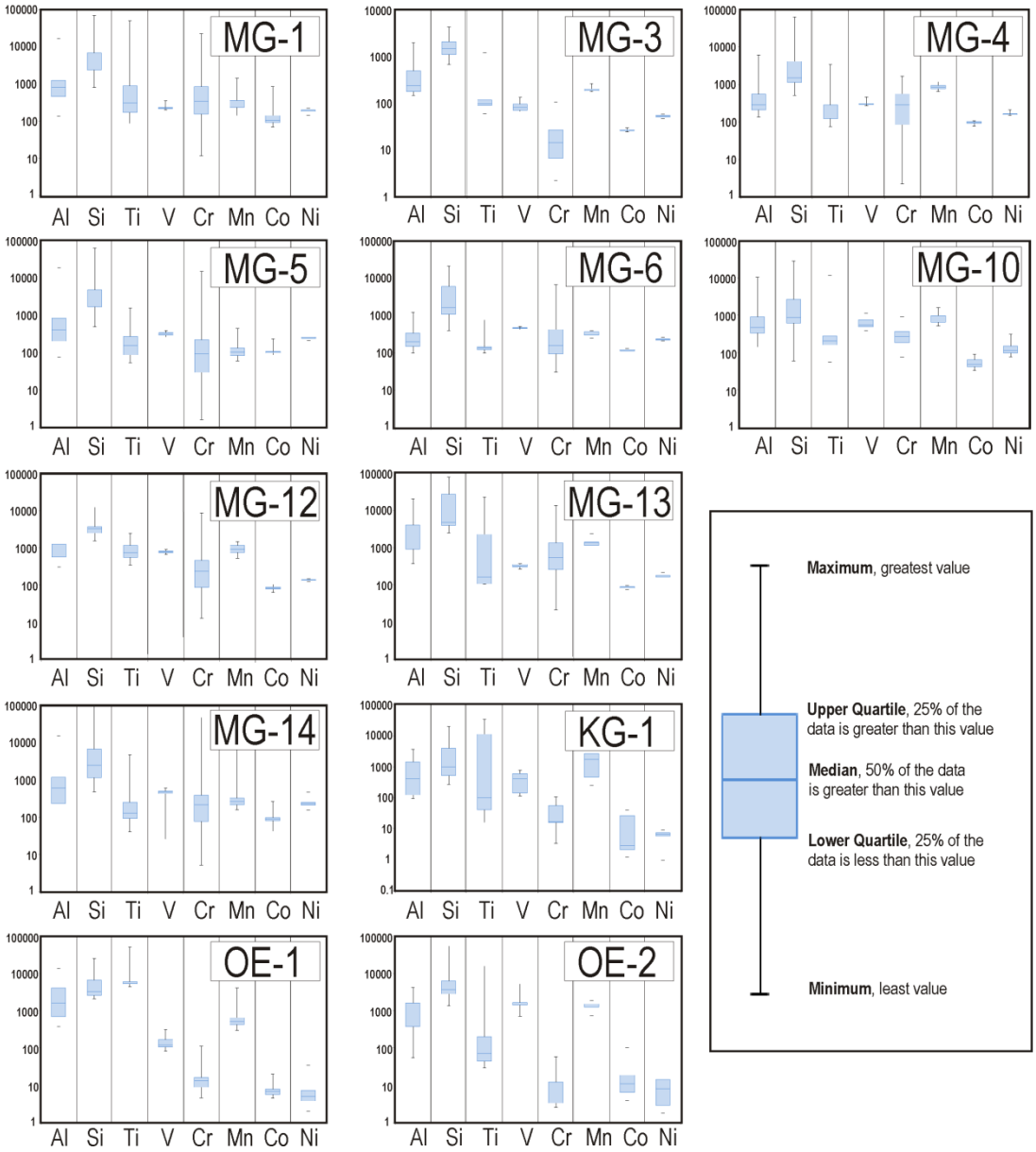

Figure 6-1: Box and whisker plots show the variability in Al, Si, Ti, V, Cr, Mn, Co and Ni concentrations for the magnetite bulk samples.

Table 27: Mean, minimum and maximum minor and trace element compositions for magnetite from each sample location. Samples where no measurement was taken are marked by an '\'. 'dl' refers to the detection limit, reported as a minimum and maximum for the sample suites in the table.

		MG-1			MG-3			MG-4			MG-5			MG-6			MG-10		
		(n=64)			(n=20)			(n=112)			(n=35)			(n=19)			(n=118)		
	DL	Mean	Min	Max	Mean	Min	Max	Mean	Min	Max	Mean	Min	Max	Mean	Min	Max	Mean	Min	Max
Mg	0.07-0.37	593	39.5	6190	33.7	7.61	183	101	18.2	761	192	31.0	1110	70.6	20.9	240	164	19.5	2220
Al	0.32-1.39	1420	136	16700	401	145	1930	863	74.7	19300	640	135	6190	333	100	1240	1070	141	10410
Si	18-94.7	8630	814	69700	1660	670	4240	6360	501	64600	5870	522	63200	5140	398	21900	2900	60.2	28300
Ca	16.4-200	613	151	4640	212	71.5	934	136	14.9	1560	4120	37.3	78000	300	83	699	732	22.4	14300
Sc	0.09-0.33	\	\	\	1	0.32	2.28	0.57	0.09	5.28	0.55	0.10	2.28	0.71	0.48	1.25	1.23	0.13	24.0
Ti	0.35-2.22	3080	87	50700	161	59.1	1180	251	53.8	1570	350	77.1	3470	178	100	780	363	55.9	11500
V	0.04-0.29	232	197	355	86.3	66.2	131	323	261	392	307	273	465	471	426	517	625	391	1150
Cr	0.71-3.79	1180	11.7	22300	22.4	2.17	106	428	1.54	15200	444	2.25	1670	672	30.5	6790	304	75.3	916
Mn	0.24-0.97	345	143	1420	196	175	261	118	59.3	450	878	651	1180	334	249	402	840	513	1580
Co	0.05-0.23	150	69.7	839	26.5	24.0	29.3	105	86.5	234	98.0	77.4	108	121	112	133	53.7	33.4	89.7
Ni	0.39-1.37	191	144	220	52.8	46.5	58.0	253	212	293	163	149	214	236	210	265	127	78.1	313
Cu	0.06-0.41	239	43.8	1940	686	0.39	6240	2.42	0.05	32.9	57.1	0.66	388	7100	0.25	38700	14.2	0.07	284
Zn	0.2-1.29	406	82.3	11200	26.1	15.6	62.7	291	99.1	9860	170	107	221	183	129	474	127	70	249
Ga	0.05-0.13	4.19	2.15	10.9	6.29	4.14	10.7	4.02	2.83	8.60	7.67	3.68	64.9	5.19	3.71	6.88	8.52	3.41	151
Ge	0.52-1.64	4.99	3.19	34.5	6.05	4.05	8.38	5.04	3.03	34.0	6.59	2.69	91.4	9.13	6.34	34.0	7.90	3.25	172
Y	0.01-0.04	12.1	0.02	96.3	8.43	0.04	30.0	3.28	0.01	54.6	15.0	0.04	300	5.39	0.05	64.4	9.6	0.06	169
Zr	0.02-0.15	\	\	\	168	0.09	797	117	0.29	2080	35.6	0.28	178	12.4	0.04	81.5	295	2.59	6310
Nb	0.01-0.14	4.71	0.05	72.8	1.11	0.14	7.22	0.69	0.02	9.85	0.96	0.02	11.3	0.27	0.07	1.38	0.71	0.01	36.6
Mo	0.09-0.61	10.2	1.78	42.0	0.25	0.17	0.33	2.05	0.06	9.41	0.69	0.11	4.44	4.79	0.51	37.8	0.27	0.07	2.01
Ag	0.03-0.5	1.02	0.03	25.1	0.88	0.45	3.10	0.79	0.02	19.7	248	0.05	2090	22.1	0.36	72.9	200	0.05	2012
Sn	0.31-1.28	2.74	0.38	44.2	1.17	0.71	2.51	1.39	0.28	18.5	1.94	0.34	6.31	3.16	3.16	3.16	1.79	0.34	11.1
Hf	0.01-0.04	\	\	\	3.77	0.03	18.8	2.29	0.03	36.5	1.94	0.11	8.35	0.32	0.05	2.17	3.54	0.33	22.0
Ta	0.01	\	\	\	0.03	0.01	0.09	5.05	0.00	235	3.17	0.01	47.0	0.05	0.01	0.10	12.0	0.00	316
W	0.02	2.33	0.56	7.15	0.39	0.03	2.40	2.44	0.01	15.2	1.01	0.02	3.85	1.52	0.05	4.45	0.16	0.02	0.83
Pb	0.07-0.12	614	141	2130	1.05	0.04	7.91	51.0	0.83	269	93.6	1.02	327	24.6	0.13	108	4.22	0.02	101
Th	0.01	57.2	1.08	219	3.04	0.02	6.37	15.0	0.01	470	9.9	0.62	36.0	3.24	0.03	9.33	3.39	0.07	73.4

Table 27: *Continued.*

		MG-12 (n=22)			MG-13 (n=9)			MG-14 (n=121)			KG-1 (n=19)			OE-1 (n=20)			OE-2 (n=20)		
	DL	Mean	Min	Max	Mean	Min	Max	Mean	Min	Max	Mean	Min	Max	Mean	Min	Max	Mean	Min	Max
Mg	0.11-0.51	234	76.4	1000	2300	90.3	13900	332	17.9	9580	40.1	6.63	162	218	13.8	1380	54.4	11.5	192
Al	0.43-1.90	1200	302	6040	4790	367	20600	1432	69.2	15700	918	95.9	3700	2920	379	13700	1190	54.2	4230
Si	23.6-119	3670	1560	12400	19800	2467	76900	8320	487	94900	4430	273	19700	5830	2110	25600	7780	1350	55200
Ca	31.1-139	217	109	608	4680	172	21100	677	124	12000	6490	44.7	24600	3120	127	22700	322	87.9	1600
Sc	0.15-0.62	1.40	0.62	7.42	3.06	0.50	9.41	\	\	\	3.30	0.25	12.4	4.67	1.89	10.2	1.48	0.40	4.01
Ti	0.64-2.61	969	344	2460	4900	102	22200	303	40.4	4750	8290	15.9	34000	10500	4400	51700	952	29.3	16100
V	0.07-0.35	783	675	908	323	260	366	458	25.8	598	399	115	778	139	83.1	320	1690	705	5220
Cr	1.04-4.43	659	13.2	8810	2260	20.8	13400	742	5.10	48000	34.4	3.39	109	23.8	4.64	111	11.9	2.54	59.6
Mn	0.35-1.15	948	524	1470	1400	946	2350	436	156	9940	1620	247	3620	707	300	4050	1360	732	1890
Co	0.07-0.31	83.5	64.6	105	84.7	74.6	95.7	96.8	41.7	267	14.8	1.20	39.6	7.99	4.48	19.8	20.3	3.91	101
Ni	0.67-1.70	138	124	147	172	150	214	236	154	470	6.43	0.97	9.05	7.13	2.01	34.3	17.1	1.75	132
Cu	0.09-0.55	1300	125	3050	1220	20.7	6380	370	0.58	19400	3.25	0.27	10.6	3.63	0.55	14.0	39.2	0.82	197
Zn	0.25-1.52	349	129	3580	193	98.1	331	390	67.3	30200	120	26.7	315	961	100	7750	615	44.1	2230
Ga	0.05-0.36	10.9	6.27	18.0	8.72	4.28	23.3	3.99	2.44	13.4	18.8	7.98	41.5	17.9	10.7	38.9	57.9	17.0	638
Ge	0.74-1.98	13.9	9.43	23.3	20.9	2.81	107	6.25	3.25	22.6	3.12	1.13	8.42	7.35	2.83	12.2	8.08	4.58	16.4
Y	0.01-0.05	7.65	1.83	21.4	49.8	0.96	229	43.4	0.10	2150	44.8	0.01	255	53.6	8.35	155	98.9	0.51	462
Zr	0.04-0.19	97.1	15.7	408	26.7	4.57	141	\	\	\	227	0.03	2310	75.5	1.00	841	142	6.68	717
Nb	0.02-0.17	3.34	0.39	9.74	14.6	0.12	66.6	0.99	0.03	18.3	61.1	0.02	445	67.8	19.8	93.3	75.4	0.38	367
Mo	0.01-0.66	7.94	0.77	24.3	2.23	0.78	3.79	4.45	0.21	59.9	3.71	0.07	13.1	4.41	0.87	28.7	0.59	0.25	1.28
Ag	0.03-0.77	0.80	0.36	3.86	355	0.36	2400	0.31	0.02	11.4	0.27	0.18	0.39	0.95	0.68	2.51	0.73	0.48	1.70
Sn	0.36 -1.5	2.01	1.58	3.21	5.91	1.59	12.1	7.03	0.34	111	21.2	0.44	58.4	46.1	23.1	95.6	8.00	0.83	70.9
Hf	0.01-0.05	2.63	0.71	6.41	1.56	0.16	6.27	\	\	\	54.6	0.05	216	3.37	0.08	26.4	6.63	0.24	26.7
Ta	0.01	0.24	0.03	0.60	1.09	0.01	3.40	\	\	\	21.6	0.05	94.0	2.40	0.32	6.31	0.33	0.03	1.12
W	0.01-0.06	2.54	0.84	4.40	1.88	0.30	5.76	0.84	0.03	7.65	3.38	0.06	24.1	73.1	11.9	126	1.04	0.10	2.94
Pb	0.03-0.19	654	89.8	1340	285	19.3	920	103	4.73	600	24.6	0.10	88.9	102	25.4	286	281	0.36	1220
Th	0.01	31.5	0.96	93.6	7.75	2.96	17.3	10.2	0.21	80.8	0.99	0.03	3.91	30.2	9.7	71.3	10.7	0.45	61.9

Table 28: Median of minor and trace element concentrations (in ppm) for magnetite per polished thin section. The highest value for each element is emphasised in bold. The number of measurements above the detection limit (dl) for each site is shown as a percentage.

		MG-1	MG-3	MG-4	MG-5	MG-6	MG-10	MG-12	MG-13	MG-14	KG-1	OE-1	OE-2
	% >dl	n=64	n=20	n=112	n=35	n=19	n=118	n=22	n=9	n=121	n=19	n=20	n=20
Mg	100	210	15.7	76.9	88.8	49.3	46.6	173	**352**	71.6	23.6	68.8	39.2
Al	100	809	233	409	286	197	364	746	1080	599	406	**1650**	843
Si	100	**3760**	1510	2950	1500	1670	579	3320	4730	2500	994	3310	3720
Ca	71	234	123	62.9	191	197	62.5	175	446	308	**1330**	337	252
Sc	88	\	0.65	0.33	0.25	0.65	0.44	0.86	1.41	\	1.98	**4.59**	1.39
Ti	99	308	96.3	155	157	135	208	730	159	131	101	**5480**	73.5
V	100	226	80.1	323	300	466	486	774	322	463	405	121	**1550**
Cr	98	349	14.1	92.4	286	156	181	235	**545**	217	16.9	13.4	6.13
Mn	100	292	192	104	870	328	639	893	1340	270	**1730**	520	1370
Co	100	**104**	26.6	102	99.1	119	40.1	82.3	85.1	90.1	2.90	6.82	11.1
Ni	98	189	52.9	**254**	163	233	92.5	139	172	234	6.86	5.05	8.23
Cu	93	208	8.18	0.78	24.3	**1560**	0.46	1120	191	27.8	2.37	1.25	25.0
Zn	100	129	21.3	152	177	160	102	199	174	127	103	179	**408**
Ga	100	3.98	6.00	3.84	5.99	5.15	5.92	8.94	5.65	3.60	14.2	14.5	**28.4**
Ge	100	4.35	5.79	4.66	3.96	7.69	3.93	**13.4**	9.40	5.67	2.98	7.26	7.51
Y	74	4.29	6.07	0.33	1.72	0.80	0.86	5.18	7.42	6.35	0.17	35.2	**37.1**
Zr	86	\	**76.9**	21.6	25.6	6.44	33.8	60.2	9.32	\	1.52	7.67	64.9
Nb	86	0.51	0.30	0.30	0.25	0.10	0.04	2.34	0.31	1.18	3.70	**69.2**	26.8
Mo	80	**9.22**	0.26	1.66	0.40	0.68	0.10	6.88	2.07	2.49	1.57	2.11	0.48
Ag	62	0.14	0.52	0.04	0.22	**6.89**	0.08	0.49	1.89	0.05	0.24	0.82	0.65
Sn	88	0.84	0.95	0.79	0.91	3.16	0.60	1.88	4.99	0.89	19.2	**42.8**	2.39
Hf	45	\	1.00	0.90	1.05	0.07	1.00	1.41	0.44	\	0.34	0.44	**3.59**
Ta	38	\	0.01	0.02	0.02	0.05	0.00	0.17	0.48	\	**5.57**	1.23	0.22
W	31	1.90	0.05	1.33	0.48	0.32	0.06	2.17	0.69	0.38	0.58	**69.4**	0.56
Pb	99	535	0.42	36.1	74.7	10.5	0.16	**602**	201	0.42	20.6	96.6	205
Th	37	**42.0**	3.20	1.77	2.57	1.96	0.39	9.56	5.38	6.39	0.49	23.8	3.79

From Table 28 it is evident that all of the sample suites contain Mg, Al, Si, V, Mn, Co, Zn, Ga and Ge above detection limits and Ti, Cr, Ni and Pb above detection for > 98% of the measurements. The elements Sc, Cu, Y, Zr, Nb, Mo and Sn are above detection for >75% of the measurements, and Ag for 62% of the measurements.

The elements whose concentrations are above detection limits least often are Hf, Ta, W and Th. These elements are commonly detected in less than 50% of the measurements, with W detected in only 31%. Hf is most often detected in measurements from suite OE-1 and OE-2 (70%), with W also frequently detected in OE-1 (75%). Ta is most often detected in MG-12 (64%), and Th in KG-1 and MG-6 (53% in each).

The bold values in Table 28 indicate the sample suites which have the highest value for a given element. The basement sample suites show elevated median concentrations for

several elements. OE-1 is characterised by elevated Ti (0.5 wt.%) and Al (0.1 wt.%), as well as elevated Sc, Nb, Sn and W. OE-2 has the highest median V concentrations of all of the sample suites at 0.2 wt. %. OE-2 is characterised by high Zn, Ga, Y and Hf median concentrations relative to the other sample suites. KG-1 shows elevated Ca and Mn, at ~ 0.1 wt.% and ~0.2 wt.%, respectively. KG-1 also has the highest Ta values. The barren metavolcanic sample suite MG-1 has relatively high Si, Co, Mo and Th concentrations. The mineralised metavolcanic suite has high Zr concentrations, which are similar to those reported for OE-2 and MG-12. The only sample suite from a mineralised sandstone, MG-6, has the highest concentrations of both Cu and Ag, which suggests that the ablation encountered copper-sulfide inclusions within magnetite grains. Few of the other sedimentary sample suites have characteristically high elements concentrations. MG-12 has relatively high Ge and Pb concentrations, MG-13 has high Cr and MG-4 elevated Ni. Of note is the relative depletion of the basement samples in the spinel group elements Cr, Co and Ni relative to the sedimentary samples.

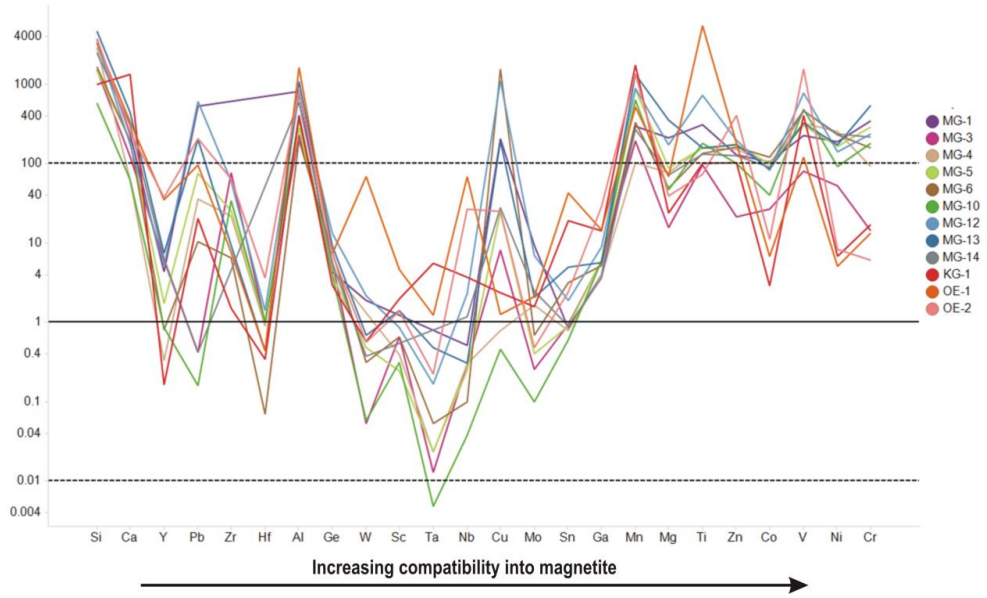

Figure 6-2: Median minor and trace element concentrations in magnetite plotted for each of the sample locations. A solid line is drawn at 1ppm and dashed lines at 0.01 and 100 ppm, an order of magnitude above and below 1 ppm.

The median concentration plot in Figure 6-1 shows that for the majority of the samples the minor and trace element concentrations are above 1 ppm, with sub-ppm values recorded for Y, Pb, Hf, Sc, Ta, Nb and Mo for some samples. Median concentrations for Si, Al and Mn are similar for all of the samples, varying only by an order of magnitude. All of the samples show detectable concentrations of the spinel group elements, Mn, Mg, Ti, Zn, Co, V, Ni and Cr.

In order to highlight some of the differences and similarities between the samples normalisation plots have been used. Dare et al. (2014) recommend normalisation to bulk continental crust, based on the reasoning that whether magnetite is from a magmatic or hydrothermal source, the fluid (or melt) would travel through the crust. The normalisation would therefore approximate the fluid (melt) composition in a continental setting. Nadoll et al. (2012), on the other hand, use the well-studied I-type granite Inner Zone Batholith (IZB) magnetite series from Japan (Spong, 1998) to compare magnetite from different geological settings to igneous magnetite. They also use a burial metamorphic magnetite standard (BMS) as a normalisation tool to further highlight differences and similarities between magnetite from different locations. Here all three normalisations have been used, but only for the elements most compatible into the magnetite structure which were above detection for > 98% of the samples, Mg, Al, Ti, V, Cr, Mn, Co, Ni, Zn and Ga (Table 29).

Table 29: Normalisation values used for this study were from bulk continental crust (BCC) (Rudnick and Gao, 2003), and from magnetite standards. The magnetite standards used were median values from burial metamorphic magnetite (BMS) from the Belt Supergroup (Nadoll et al., 2012), and the Inner Zone Batholith from Japan (IBZ) (Spong, 1998).

	Mg	Al	Ti	V	Cr	Mn	Co	Ni	Zn	Ga
BCC	16369	44511	2238	2238	135	488	27	59	72	16
BMS	51	463	294	287	173	76	33	108	100	10
IBZ	362	1111	174	2449	10	2083	82	60	384	15

Figure 6-3 displays the median sample suite data normalisations in order of increasing compatibility into magnetite, using the method of Dare et al. (2014). Relative to BCC all of the samples show similar depletions in Al and Mg. Ga and Mn values for the samples hover just above and below the BCC value, over an order of magnitude. The same three samples separate out on the basis of Ti concentration (as with the IBZ normalisation), with OE-1 recording the highest concentrations relative to BCC, then MG-12 and MG-1, and the remainder of the samples clustering together. Zn concentrations are similar for all of the samples, with OE-1 slightly higher and MG-3 slightly lower than BCC. The basement samples, KG-1, OE-1 and OE-2, have the lowest relative concentrations of Co. The mineralised MG-3 and MG-10 samples have almost exactly the same amount of Co as BCC, and the remaining samples have similar concentrations relative to BCC. Relative to BCC OE-2 shows the strongest enrichment in V, and MG-3 and OE-1 the lowest. KG-1 clusters with the remaining samples which vary from ~0.4 to ~0.1 relative to BCC. Ni values are relatively similar for the basement samples, with MG-3 almost identical to BCC.

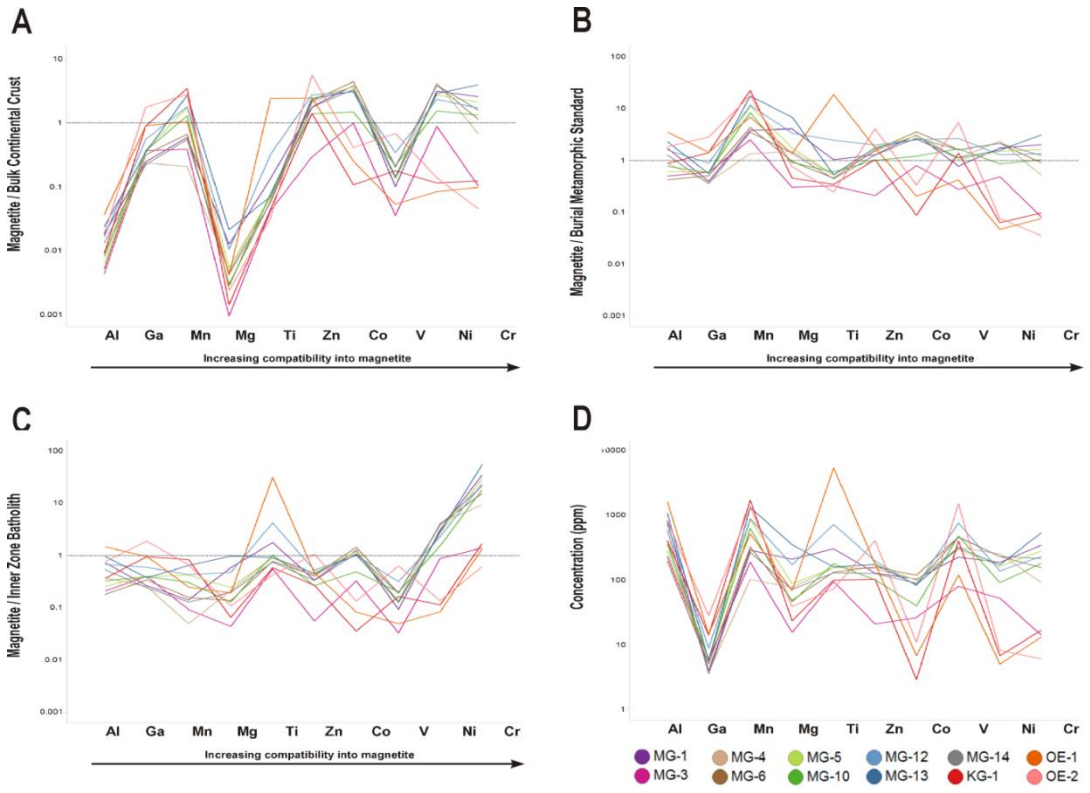

Figure 6-3: Magnetite median results (**D**) normalised to BCC (**A**), BMS (**B**) and IBZ (**C**).

The majority of the samples, however, show a relative enrichment in Ni, as well as Cr, relative to BCC, and the basement samples and MG-3 show depletion in Cr.Normalisation to the burial metamorphic standard separates the basement magnetite samples from the other samples by highlighting the relative depletion of the basement in Cr, Co and Ni relative to the sedimentary samples, and the enrichment in V of OE-1. The BMS normalisation shows similarities between the samples in terms of Mg, Al and Mn concentrations, but these vary by up to two orders of magnitude.

Normalisation to the IBZ shows that the samples are largely depleted in trace elements relative to magnetite from a granitic source rock. OE-1 is slightly enriched in Al and strongly enriched in Ti relative to IBZ. Ti concentrations are also higher for the mineralised sample MG-12, and the barren metavolcanic MG-1, but most samples fall within 0.5 of IBZ magnetite. Ni and Cr normalisations effectively separate out the basements samples and MG-3 from the rest of the sample suites. The Cr values for these samples are very close to the IBZ, as is Ni for MG-3. The basement samples OE-1, OE-2 and KG-1, however, are depleted in Ni relative to IBZ and the rest of the sample suites.

The compositional variations between the magnetite suites sampled are further highlighted in a series of scattergrams presented in Figure 6-4. The Mn-Mg plot does not distinguish between the different sample locations, but the Mn-Co plot distinguishes both the basement samples and the mineralised metavolcanic samples. These all have low Co contents. The V-Cr plot separates out the basement samples into two end member groups based on V content. Samples OE-1 and MG-3 form a low V group (<100 ppm) and OE-2 a high V group (>1000 ppm). The ratio between Ni and Co distinguishes the basement group samples, which have low Ni and Co content (<80 ppm), and the mineralised metavolcanic MG-3, which has a slightly higher Ni content. The Ni-Ti plot also shows this distinction between the basement magnetite grains and those from elsewhere in the Eiseb. The Ti content distinguishes between OE-1 magnetite, which has high Ti (<1000 ppm), and KG-1 and OE-2, which have low Ti contents (<500 ppm). The Ga-Zn ratio for all of the sample suites show a positive correlation between these two elements, with the basement samples reporting slightly higher Ga content.

Although these plots are able to effectively distinguish between the basement samples and the samples from the metavolcanics and the sediment-hosted magnetite, the distinctions between the latter groups of samples are less clear. MG-1 appears to consistently overlap with the sedimentary samples, except for the V vs Cr plot where it shows lower V content compared to the sedimentary samples.

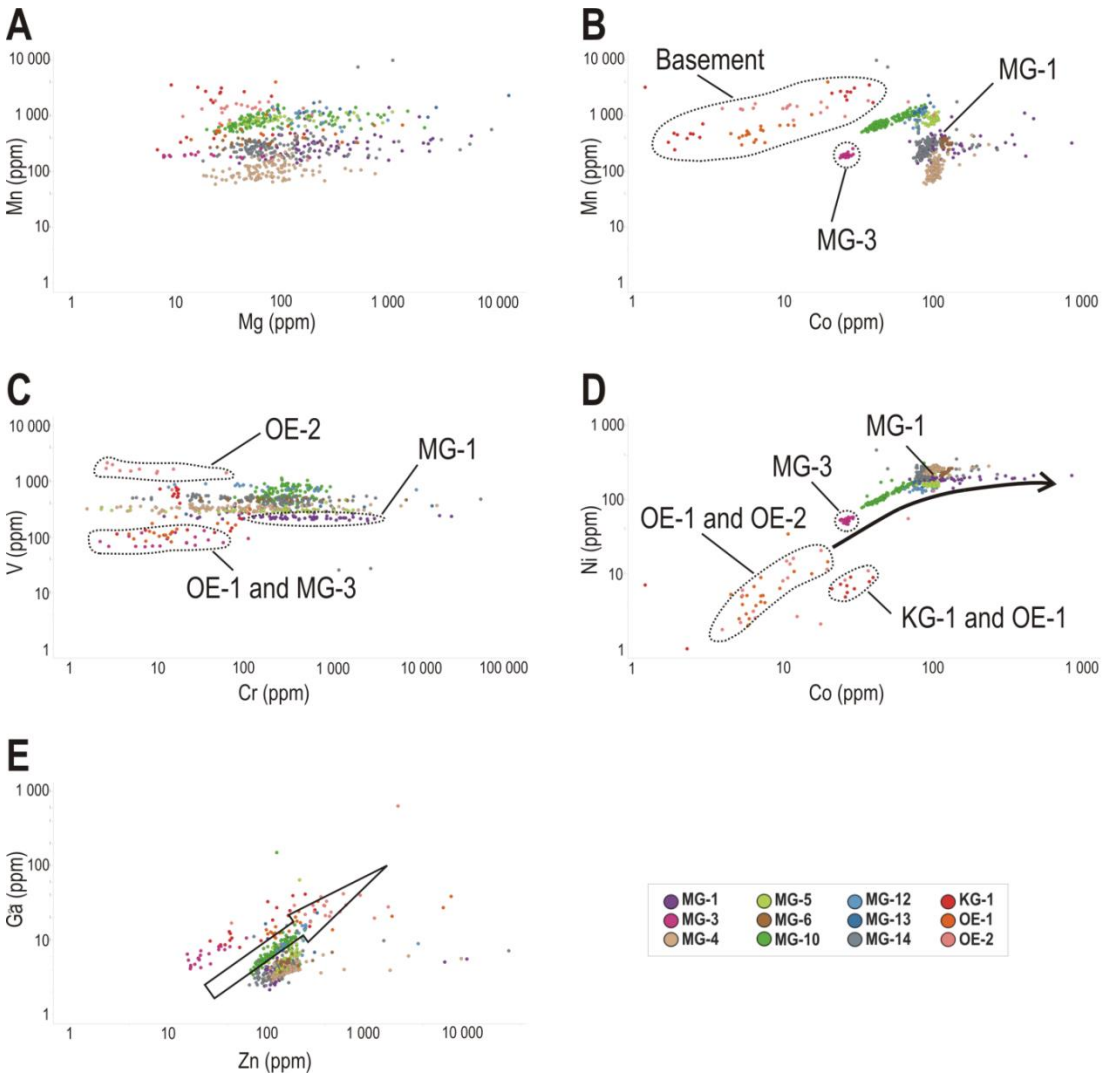

Figure 6-4: Scattergrams of spinel elements from all of the magnetite grains analysed for this study for: Mn-Mg (**A**), Mn-Co (**B**), V-Cr (**C**), Ni-Co (**D**), Ga-Zn (**E**) and Ni-Ti (**F**). The element concentrations are on a log scale. See text for explanation of groupings and arrows.

Lithotype appears to play an important role in the partitioning of certain trace elements into magnetite, as illustrated in Figure 6-5. The V-Co ratio distinguishes between magnetite from different source rocks. Magnetites from phyllites have the highest V concentrations for a range of Co values. Sandstones have the lowest overall V-Co ratios, except for MG-6 from the mineralised sandstone, which has higher V than magnetite from the other sandstones. The siltstone magnetite samples plot between the phyllites and the sandstones. The Mn-Co ratio shows less obvious distinctions based on rock type, with overlap common between different rock types. The V-Cr ratio distinguishes between the sandstones and phyllites, with the latter plotting at higher V concentrations than the former. The phyllites, particularly MG-10, show narrow ranges in Cr content relative to the

sandstones. MG-6 plots away from the other sandstone magnetite samples, overlapping with both the siltstone and phyllites. The Ni-Co ratio shows a strong linear relationship between these elements for MG-10 and MG-6, but does not distinguish between the different lithotypes. The Ti concentration, although not plotted, does not show any obvious relationship to lithotype.

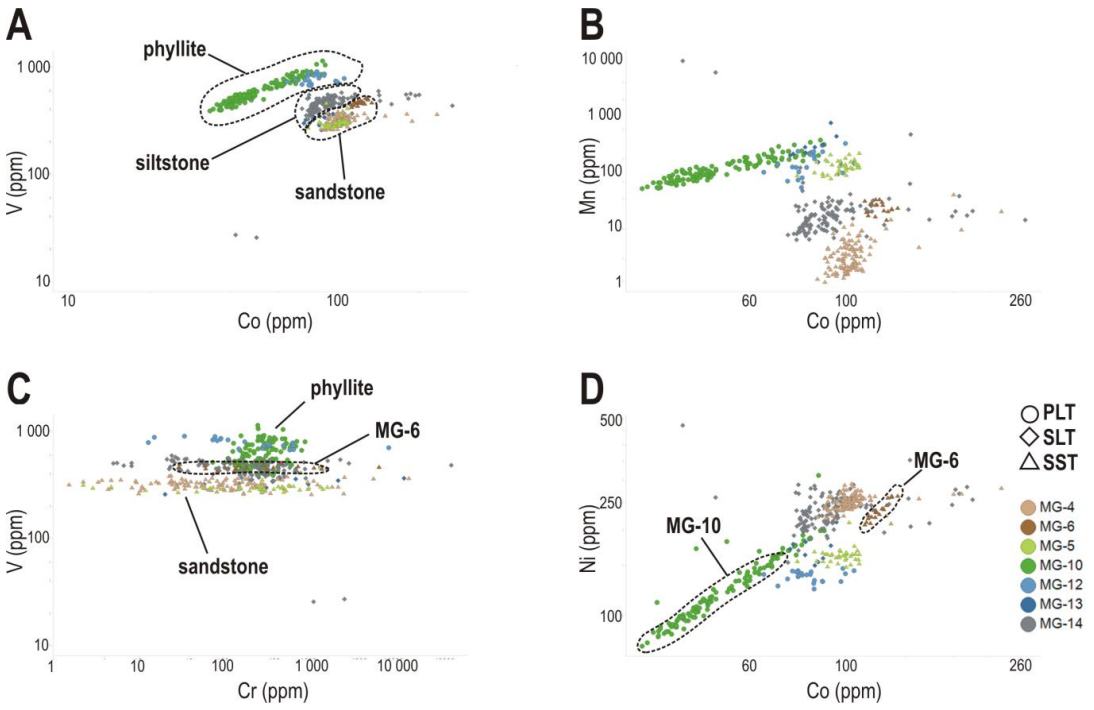

Figure 6-5: Sediment-hosted magnetite measurements are compared and distinguished based on lithotype for the element ratios V-Co (**A**), Mn-Co (**B**), V-Cr (**C**) and Ni-Co (**D**). The abbreviations used are PLT - phyllite, SLT - siltstone, SST - sandstone.

6.2 Palaeomagnetic Investigation

6.2.1 Palaeomagnetic Direction

The results from the both the alternating fields and thermal demagnetisation methods were analysed using the PuffinPlot software (Lurcock and Wilson, 2012). The remanence directions recorded for each step were examined using orthogonal plots. The remanence recorded for most of the specimens was directed fairly steeply upwards towards the north (Figure 6-6). Most of the specimens, however, produced internally scattered directions, suggesting overprinting of the primary remanence directions.

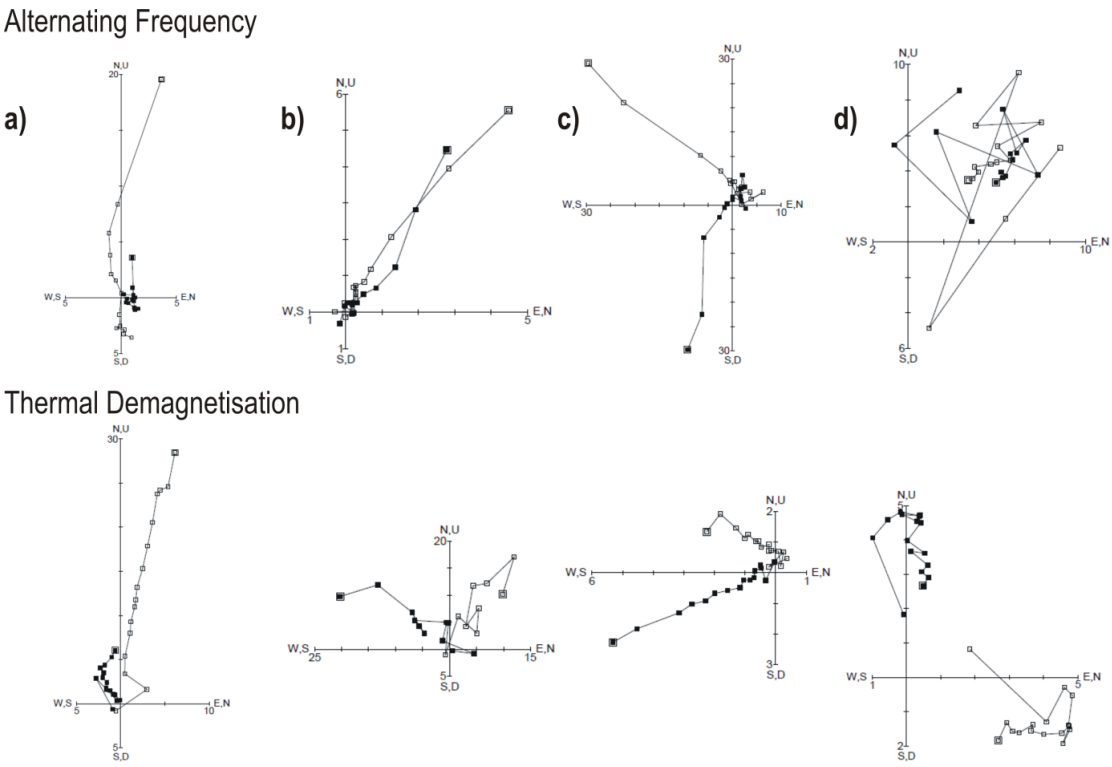

Figure 6-6: Examples of orthogonal plots for AF (top) and thermal demagnetisation (bottom) methods for specimens a) OPS-6; b) OPS-7; c) OPS-8 and d) OPS-15. The solid symbols represent horizontal projections, defined by North (N), East (E), South (S) and West (W); the open symbols represent the vertical projections along North (N), Down (D), South (S) and Up (U) axes. All axes are expressed in mT.

Thermal demagnetisation up to 680˚C was carried out on one specimen from each sample. The sandstone specimens showed shallow linear relationship between remanence intensity and temperature (Figure 6-7). Remanence intensity decreased with increasing temperature in a fairly stable manner up to ~600˚C, which is consistent with magnetite being the dominant remanence carrier.

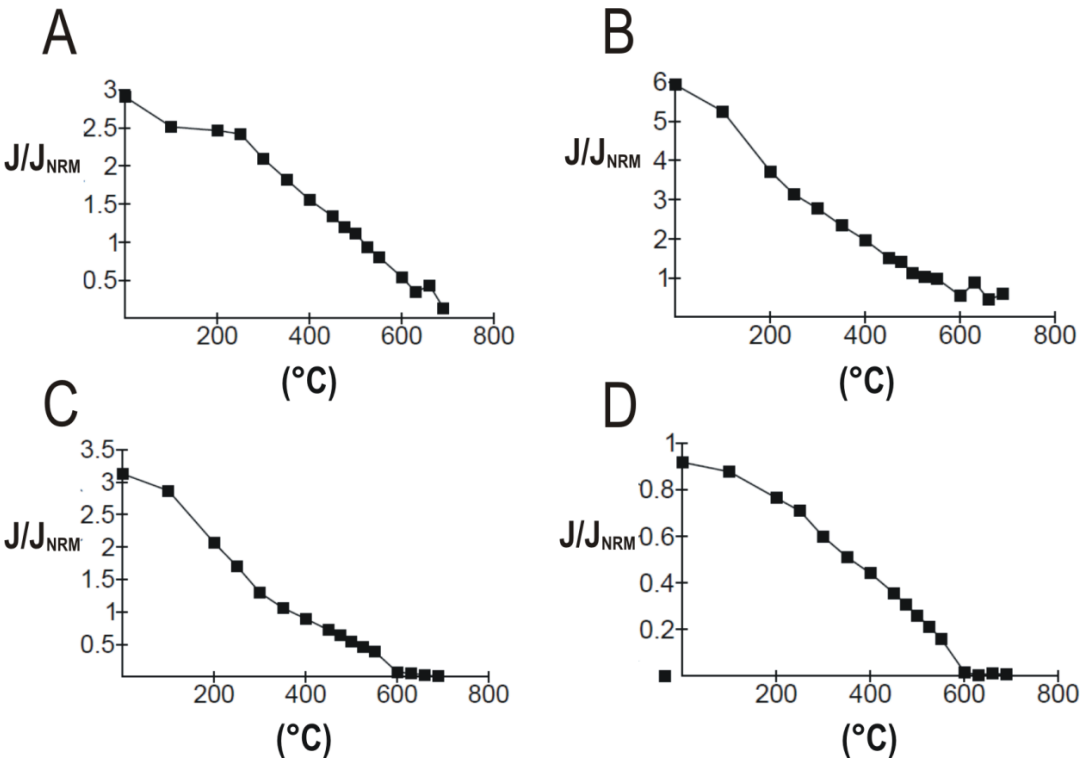

Figure 6-7: Thermal step demagnetisation of sandstone example sub-samples from OPS-6 (**A**), -8 (**B**), -10 (**C**) and -14 (**D**). Each black square represents a step in demagnetisation process. Axial intensity values (J) are expressed as a ratio of the natural remanent magnetisation (NRM) intensity (J_{NRM}).

Thermal demagnetisation of the siltstones, and some of the sandstone samples (OPS-5, -7, -12 and -15) were less stable with intensities increasing erratically. No contribution by minerals such as goethite is suggested by these results, as this would have caused perturbations of the signal within specific temperatures ranges, e.g. between 80-120 ˚C for goethite, which was not seen (Dunlop and Özdemir, 2001).

The site mean characteristic remanent magnetisation (ChRM) directions were calculated using principal component analysis (PCA), and Fisher statistics (Table 30, Figure 6-8) (Fisher, 1953; Lurcock and Wilson, 2012). OPS-4, -5, -9, -12 and OPS-15 failed to give sufficiently coherent mean ChRM directions, however, OPS-2, -6, -7, -8, -10, -11 and OPS-14, recorded fairly stable directions. OPS-14 and OPS-6 produced the most reliable directions with α_{95} for both samples <10˚. The α_{95} is a measure in degrees of the 95% confidence cone about the mean. Fisher's precision parameter ***k*** is a measure of the dispersion of a population about a true mean direction. The larger this value, the more concentrated the direction (Tauxe, 2010). The ***k*** values for OPS-6 and OPS-14 are the highest of the sample set at 87.9 and 63.2 respectively. The site mean ChRM directions were combined to give an overall declination of 350.4˚, and an inclination of -70.8˚ (α_{95} = 21.5˚, *k* = 7.6).

Table 30: Site mean characteristic remanent magnetisation (ChRM) directions. Sites which produced incoherent or aberrant directions are not included. The ***n*** column indicates the number of specimens used to calculate the mean declination (dec) and inclination (inc) for each site. The α_{95} in degrees is the radius of the 95% confidence cone about the mean, while *k* is the precision parameter of Fisher (1953).

Site	*n*	Dec. (˚)	Inc. (˚)	α_{95} (˚)	*k*
OPS-2	3	315.9	-38.9	23.1	29.4
OPS-6	4	278.7	-81.1	9.9	87.9
OPS-7	4	352.9	-62.3	44	5.3
OPS-8	2	28.5	-79.3	36.7	48.5
OPS-10	4	75.1	-55.7	52	4.1
OPS-11	3	307.4	-52.8	61.4	5.1
OPS-14	4	1.6	19.4	11.6	63.2
Mean	24	350.4	-70.8	21.5	7.6

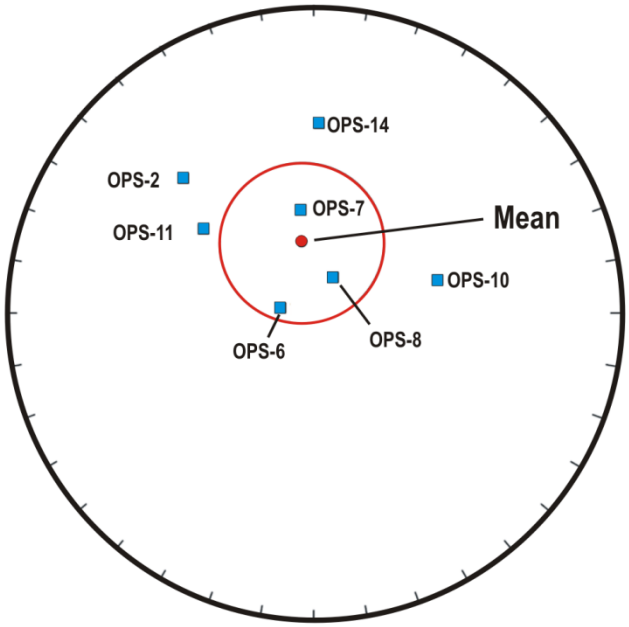

Figure 6-8: Equal area stereonet mean ChRM directions for each sample, as well as the site mean. The error on the mean is illustrated by the 95% confidence cone (red).

A tilt test was carried out to determine whether the remanence measured was coeval with, pre- or post- folding (Graham, 1949; Watson and Enkin, 1993). The test is a measure of whether a bedding correction applied to the ChRM increases or decreases the value of ***k***. If the value decreases then folding predates the ChRM, if not, and the value of ***k*** increases, then strata acquired remanence after folding. The value of ***k*** decreased during the tilt test, suggesting that Eiseb strata acquired their ChRM after deformation, i.e. after the Damara Orogeny. The fold test was negative at the 95% confidence level.

The mean ChRM direction for each sample was used to locate individual virtual geomagnetic poles (VGP), as well as an overall Site VGP (mean of the sample means) and Sample VGP (mean of the individual specimens) as shown in Table 31 and Table 32. The VGP is the physical location of the geomagnetic pole generated by the geocentric dipole responsible for the observed magnetic field direction (ChRM) for a given location on the Earth's surface (sample latitude and longitude) (Tauxe, 2010).

Table 31: Mean VGP for each of the samples. The site latitudes are shown in column λ, the longitudes in column ϕ, and the VGP latitude and longitude as VGP λ and VGP ϕ respectively. The first semi-axis of the VGP confidence ellipse is shown in column **dp** and the second semi-axis of the VGP confidence ellipse in column **dm**.

Site	Λ (˚)	Φ (˚)	VGP λ (˚)	VGP φ (˚)	Dp (˚)	Dm (˚)
OPS-2	-22	20	49.3	281.5	16.4	27.6
OPS-6	-22	20	23.5	218.7	18.4	19
OPS-7	-22	20	67.3	213.7	53.4	68.6
OPS-8	-22	21	39.7	188.3	66.4	69.8
OPS-10	-21	21	23.9	142.5	53.2	74.4
OPS-11	-22	21	42.6	265.3	58.5	84.8
OPS-14	-21	21	88.4	129.6	8.2	13.8

Table 32: Summary VGP results and Fisher statistics (Fisher, 1953). Dec = declination; inc = inclination.

Parameter	*n*	dec/φ (˚)	inc/λ (˚)	α95 (˚)	k
Site direction	8	350.4	-70.8	21.5	7.6
Sample direction	27	352	-69.8	13.4	5.3
Site VGP	8	206.1	51.0	33.1	3.7
Sample VGP	27	207.2	50.3	18.8	3.2

6.2.2 Rock Magnetism

Room-temperature rock magnetic and thermomagnetic data were collected from OPS-2, OPS-7, OPS-8, OPS-10 and OPS-12. Enough data were collected to characterise the mineralogy, size and domain state of the magnetic remanence carrier(s) from all five samples.

Using rock chips from each sample, hysteresis loops were generated (Figure 6-9). The hysteresis loops were similar for all the samples, suggesting similar mineralogy and domain states for all the samples. The hysteresis loops suggest fine-grained (<500 nm) multi-domain (MD) magnetite.

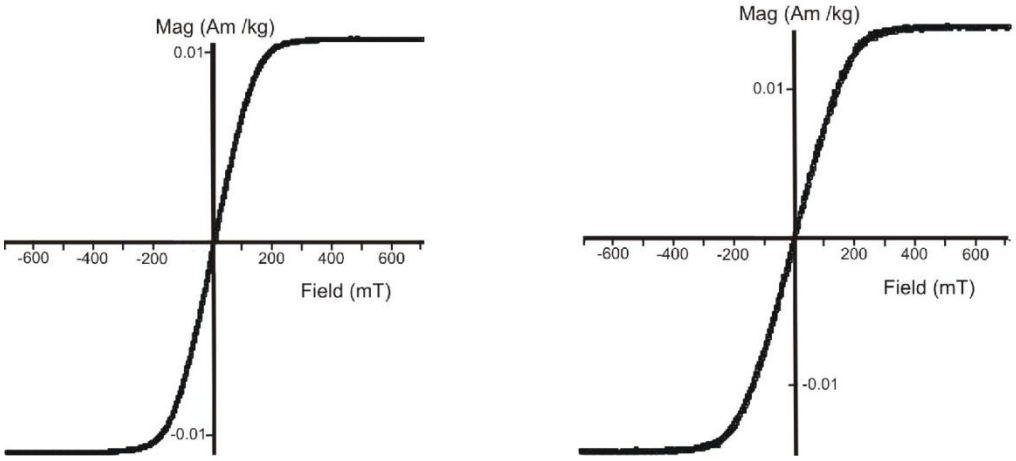

Figure 6-9: Hysteresis plots for two representative samples, OPS-02 and OPS-12. The narrow shape of these plots is suggestive of multi-domain magnetite (MD).

The Curie temperature of the main magnetic mineral(s) for a selection of samples was determined by measuring thermomagnetic curves (Figure 6-10). The second derivative method (Tauxe, 1998), with a running average of 3 was used (Table 33). The estimated error on these values is ± 5˚C.

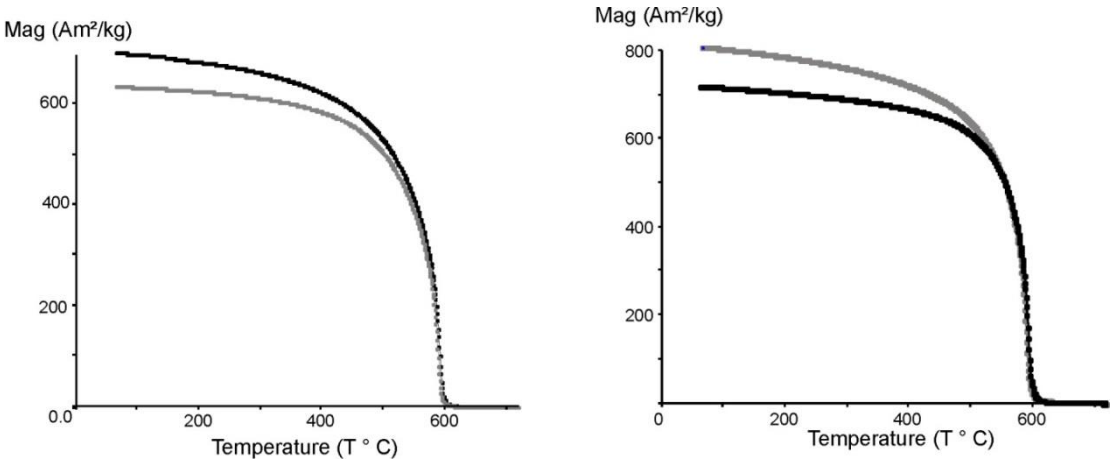

Figure 6-10: Curie temperature plots for two representative samples, OPS-02 (LEFT) and OPS-10 (RIGHT). The plots show a single drop-off and a relatively stable return cooling path.

Table 33: Curie temperatures for each of the five samples were calculated using the second derivative method of Tauxe (1998) and a running average of 3.

Sample No.	Borehole No.	T ˚ C
OPS-2	CA-PL-2	596
OPS-7	CA-PL-1	587
OPS-8	EA-NL-1	606
OPS-10	NEA-PL-1	596
OPS-12	EA-NL-1	587

The samples all showed a single Curie temperature and a sharp drop off during demagnetisation. The Curie temperatures suggest very pure magnetite (~580˚C). The curves are also strongly reversible, suggesting minimal alteration of the magnetic mineral (magnetite) occured during heating.

7 Discussion

7.1 Geology of the Eiseb

7.1.1 Zircon Geochronology

The dominance of Mesoproterozoic ages from the zircons analysed for this study would suggest that the main sediment source rocks for the Eiseb were of this age. The Kgwebe Formation in Botswana, and a lateral equivalent in Namibia (the Oorlogsende Member), have been dated at 1106 ± 2 Ma and 1094 +18/-20 Ma, respectively (Hegenberger and Burger, 1985; Schwartz et al., 1996). Kampunzu et al. (2000) dated zircons within the Ngwako Pan Formation in the north-east of Botswana at a mean age of 1104 ± 16 Ma, and suggested that the Kgwebe Formation was the primary sediment source for the Ghanzi Group sediments in Botswana. The ages obtained in this study, however, are at least 50 Ma older than these rocks for all of the units sampled. The metavolcanics analysed for ZR-01 are favoured as likely sediment sources for the footwall, and possibly even the hangingwall lithotypes, rather than the Oorlogsende Member and Kgwebe Formation equivalents, although the inclusion of the sedimentary units into the Ghanzi Group is not rejected (Figure 7-1).

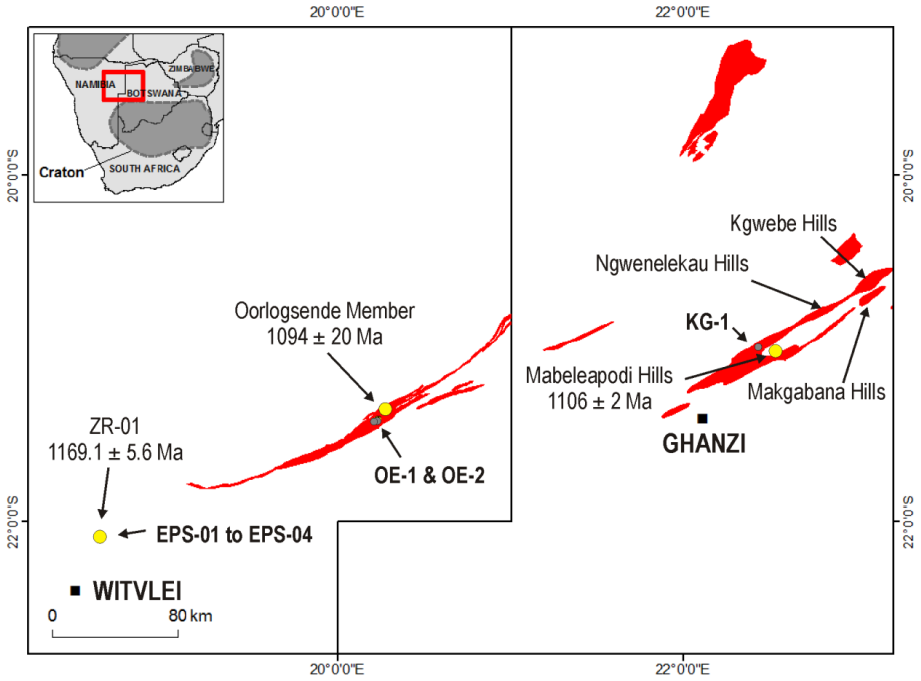

Figure 7-1: Regional distribution of the Kgwebe Formation and published zircon ages for the Oorlogsende Member (Hegenberger and Burger, 1985); the Mabeleapodi Hills outcrop (Schwartz et al., 1996) and the Eiseb metavolcanic, ZR-01 (yellow circles). The samples used in this study for whole rock geochemistry are indicated in bold, KG-1, OE-1 and OE-2, and EPS-01-EPS-04. EPS-01 and ZR-01 were sourced from the same 10cm of drill core.

Miller (2008) makes reference to an isolated outcrop of rhyolite on the farm 'Tsumis Park 421' south of Rehoboth yielding ages of 1130 ± 75 Ma and 1132 ± 75 Ma (Schalk, 1970). These ages fall within the two main periods of volcano-sedimentary deposition in the Nauzerus Group of the Sinclair Supergroup. The first cycle was of felsic volcanism and sedimentation at ~1230 Ma of the interfingering Nückopf and Grauwater Formations, and the second was the Langberg Formation volcanics, which has been dated at 1100 Ma (Miller, 2008). The results of this study agree with the findings of Pfurr et al. (1991) that magmatism was continuous between ~1200 and 1100 Ma. The Kgwebe Formation, which has been correlated to the Oorlogsende Member and the Langberg Formation in central eastern Namibia by Rankin (2015), is too young to correlate the results of this study with, and the Nückopf Formation is too old at ~1200 Ma (Becker and Schalk, 2008). A correlation of these results with the Grauwater Formation is therefore suggested for the metavolcanics, which falls between the Langberg and the Nückopf Formations, but which has no known correlatives in Botswana (Figure 7-2).

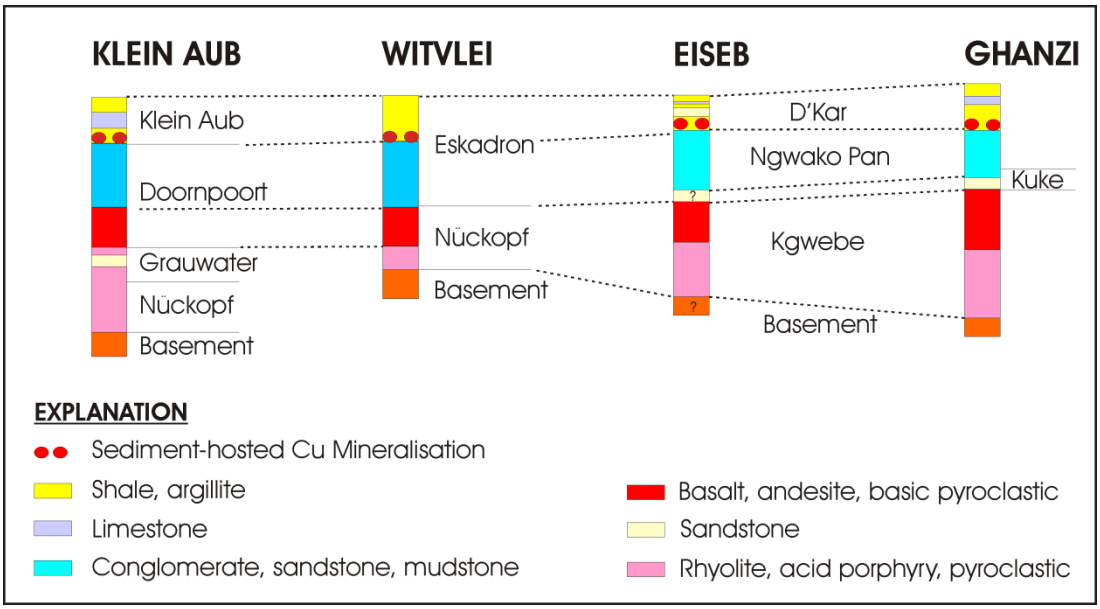

Figure 7-2: Stratigraphic correlation of the Eiseb deposits with the stratigraphy from Ghanzi, Klein Aub and Witvlei (**bold**). The logs show Formation names i.e. Doorpoort Formation, Eskadron Formation etc. The dashed lines show the preferred correlations from the results of the current study. Basement and Kuke Formation correlatives in the Eiseb are not confirmed so denoted by '?.' The correlations are modified after Borg (1987).

Schwartz et al. (1996) argue that the minimum age for the Ghanzi Group equivalents in Namibia can be set by the age of the Blaubeker diamictite which overlies the Mamuno Formation equivalent, the Kamtas Formation. The base of the Kamtas, a regional unconformity, also defines the start of the Damara Supergroup. The age of the Blaubeker diamictite is constrained by K-Ar ages of detrital muscovite in the Kuibis Formation at <635

± 13 Ma and the overlying Schwartzrand Formation at <567 ± 12 Ma (Horstmann et al., 1990). The maximum age constraints set for the Ghanzi Group by dating of the Kgwebe Formation and the Oorlogsende Member are ~1100 Ma, but the results of the current study suggests that this should be extended to at least ~1170 Ma (Section 5.3).

Zircon geochronology has shown that the sediments of the Eiseb were derived from the uplifted Mesoproterozoic basement metavolcanics tentatively correlated with the Grauwater Formation. The magnetically prominent rotated basement horst appears to be a regional kink fold adjacent to the two main branches of the southern Damaran thrust zone (Figure 7-3).

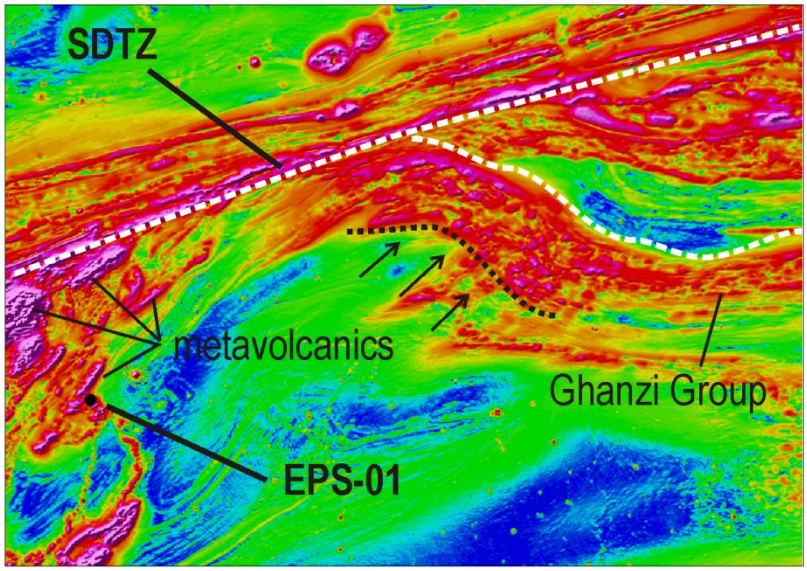

Figure 7-3: The basement horst is bordered to the north and to the east by the southern Damara thrust zone (SDTZ) (white dashed lines), and to the west by metavolcanics which form long NNE trending linear ridges. The arrows indicate the zone of uplift associated with a possible basement inlier at depth. Background map: Namibian Government regional airborne magnetic data (www.mme.gov.na), AS-image product.

Regional gravity data covering the basement horst indicate that this uplifted block is associated with a gravity low (Figure 7-4). A similar gravity low exists in Botswana near Ghanzi. This could indicate the position of the second uplifted basement segment not seen in the airborne magnetic data. Zircon geochronology by Kampunzu et al. (2000) suggests a younger source consistent with the Oorlogsende Member and Kgwebe Formation rhyolites for the Ngwako Pan sediments in Botswana. This supports the findings of Borg (1988) who postulated the KSG rift propagated from South Africa into southern Namibia northward and then east into Botswana, tracing the western edge of the Kalahari Craton. This is shown by the younging of the sediments to the west for Eiseb-Ghanzi Basin.

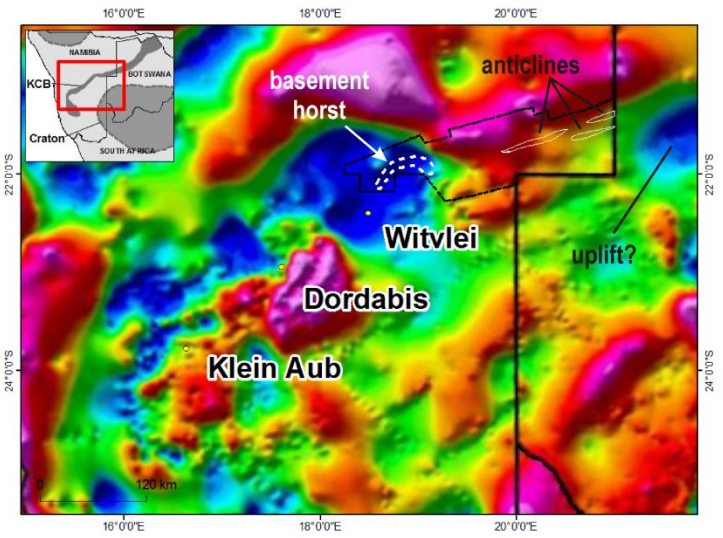

Figure 7-4: Residual Bouguer Gravity map showing the location of the basement horst and a possible basement high in Botswana, near Ghanzi. Gravity data compiled by Corner (2000) and reported in Miller (2008).

Another possible interpretation of the basement horst is that it is an intrusive similar to the Hook batholith in central Zambia - a syn-collisional, shallow crustal pluton associated with the Pan African orogeny (Milani et al., 2015). The kinematics of the Hook granite are similar to the basement horst, as shown inFigure 7-5, occurring between two regional thrusts.

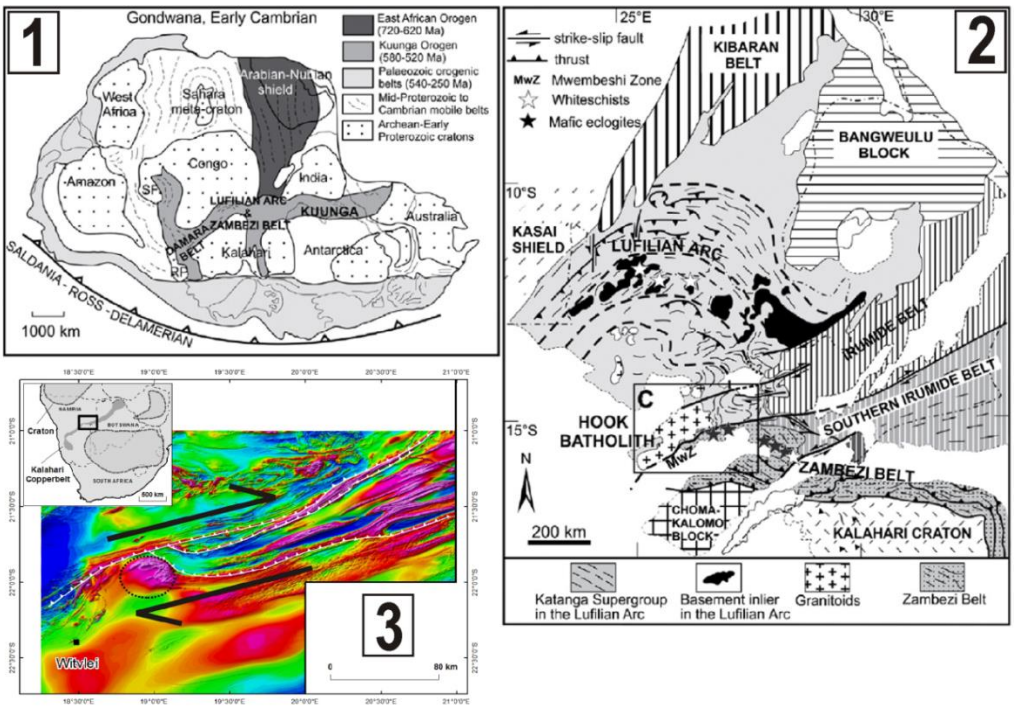

Figure 7-5: The Gondwana supercontinent during the Early Cambrian (**1**); geological map of the Lufilian and Zambezi Belts (**2**); and the location of the Eiseb basement horst (black circle) between two regional Damaran thrusts (white) on the GSN regional aeromagnetic RTP map (**3**). Image 1 and 2 are taken directly from Milani et al. (2015).

Whole rock analyses from the metavolcanics sampled during this study (including EPS-01 which was taken from the same 10cm piece of drillcore crushed to produce ZR-01) and the rhyolites and trachyte volcanic basement samples (OE-1, OE-1 and KG-1), were compared against the published geochemical data from the Kgwebe Formation acid volcanics in Botswana and their lateral equivalents, the Nauzerus Group in Namibia (Table 34).

Geochemically the Eiseb samples OE-1 and OE-2, which plot in the rhyolite and trachyte fields of the TAS diagram, respectively, fit well with the published compositional variations for the acid volcanics of the Nauzerus Group and the Kgwebe Formation (Becker et al., 2005; Kampunzu et al., 1998; Ziegler and Stoessel, 1993) (Table 34,Figure 7-6). KG-1, taken from a quarry in the Mapeleapodi Hills, has an almost identical major oxide geochemistry to the Mapeleapodi Hills data published by Kampunzu et al. (1998), confirming the accuracy of the EMPA area scan method for major oxide analysis.

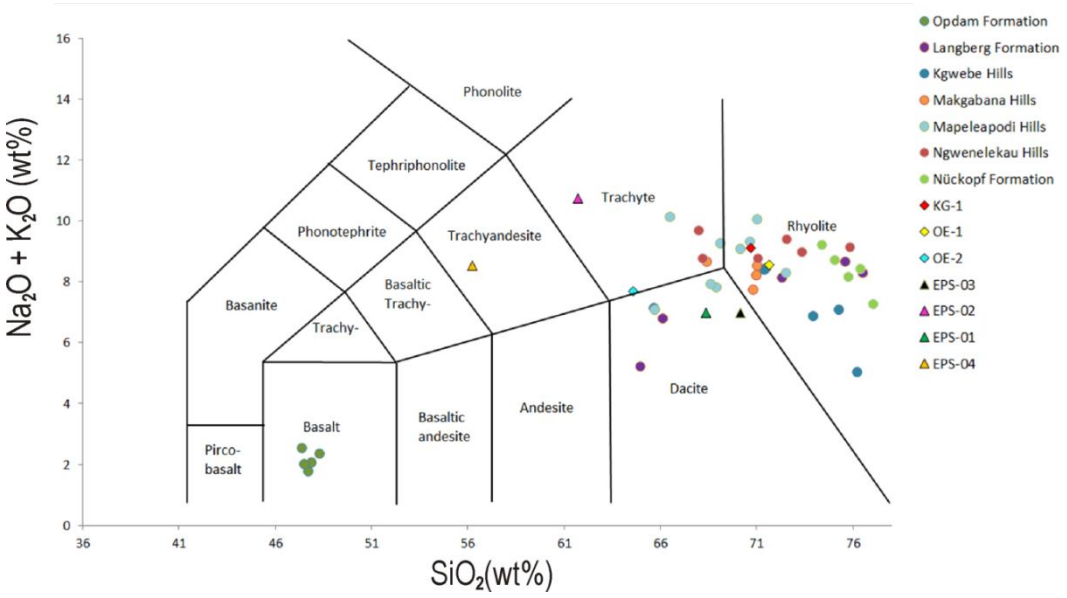

Figure 7-6: TAS diagram comparing the volcanic (OE-1 & OE-2) and metavolcanic (EPS-01 – EPS-04) samples from the Eiseb to published data for the Kgwebe Formation and the Nauzerus Formation using the data presented in **Table 34**: Kgwebe Hill, Mapeleapodi Hills, Makgabana Hills and Ngwenelekau Hills (Kampunzu et al., 1998); and the Nauzurus Group in Namibia: Opdam Formation (Becker at al., 2005), Langberg Formation (Becker et al. 2005) and Nückopf Formation (Ziegler and Stoessel, 1993). The volcanic samples from the Eiseb plot within the rhyolite and trachyte fields, as do those of the Kgwebe. The metavolcanic samples which host mineralisation, EPS-02 and EPS-04, plot in the high alkali trachyte field, and trachyandesite fields, respectively. TAS boundaries redrawn after Le Maitre et al. (2005).

Table 34: Geochemical results for the acid volcanics (KG-1, OE-1 & OE-2) and metavolcanics (EPS-01-EPS-04) from this study and published select major oxide geochemistry for the acid volcanics from the Kgwebe Formation outcrops in Botswana: Kgwebe Hill, Mapeleapodi Hills, Makgabana Hills and Ngwenelekau Hills (Kampunzu et al., 1998); and the Nauzurus Group in Namibia: Opdam Formation (Becker at al., 2005), Langberg Formation (Becker et al. 2005) and Nückopf Formation (Ziegler and Stoessel, 1993).

Source	Sample ID	Location	SiO_2	Na_2O	K_2O
This study	KG-1	*Mapeleapodi Hills	70.7	3.73	5.38
This study	OE-1	*Oorlogsende	71.7	2.87	5.67
This study	OE-2	*Oorlogsende	64.6	0.74	6.97
This study	EPS-01	WB-1 (98m)	68.3	4.11	2.87
This study	EPS-02	WB-1 (64m)	61.7	10.3	0.44
This study	EPS-03	WB-2 (85m)	70.1	4.36	2.63
This study	EPS-04	WB-2 (33m)	56.2	5.12	3.39
Becker et al. (2005)	05.00.37	Langberg Formation	66.1	4.03	2.77
Becker et al. (2005)	140998-1	Opdam Formation	47.4	2.41	0.14
Becker et al. (2005)	140998-2	Opdam Formation	47.7	1.69	0.10
Becker et al. (2005)	210899-1	Opdam Formation	47.9	1.93	0.14
Becker et al. (2005)	210899-2	Opdam Formation	47.5	1.87	0.16
Becker et al. (2005)	210899-3	Opdam Formation	48.3	2.03	0.33
Becker et al. (2005)	M 00-10	Langberg Formation	65.0	3.95	1.28
Becker et al. (2005)	M 00-3	Langberg Formation	76.5	2.90	5.39
Becker et al. (2005)	M 00-8	Langberg Formation	75.6	1.79	6.86
Becker et al. (2005)	M 99-11	Langberg Formation	71.5	2.95	5.51
Becker et al. (2005)	M 99-4	Langberg Formation	72.3	2.70	5.44
Kampunzu et al. (1998)	203	Kgwebe Hills	76.2	2.63	2.41
Kampunzu et al. (1998)	206	Kgwebe Hills	75.3	3.92	3.17
Kampunzu et al. (1998)	226	Kgwebe Hills	74.0	3.24	3.63
Kampunzu et al. (1998)	259	Kgwebe Hills	71.4	3.06	5.33
Kampunzu et al. (1998)	276	Kgwebe Hills	65.7	4.28	2.87
Kampunzu et al. (1998)	008	Mapeleapodi Hills	72.5	3.08	5.21
Kampunzu et al. (1998)	009	Mapeleapodi Hills	70.6	1.36	7.97
Kampunzu et al. (1998)	012	Mapeleapodi Hills	66.5	2.43	7.69
Kampunzu et al. (1998)	013	Mapeleapodi Hills	65.7	2.25	4.84
Kampunzu et al. (1998)	0140	Makgabana Hills	71.0	4.79	3.73
Kampunzu et al. (1998)	0143	Makgabana Hills	70.8	4.51	3.24
Kampunzu et al. (1998)	0146	Makgabana Hills	71.0	3.84	4.38
Kampunzu et al. (1998)	0154	Makgabana Hills	68.4	3.39	5.28
Kampunzu et al. (1998)	0355	Ngwenelekau Hills	68.0	2.72	6.97
Kampunzu et al. (1998)	0357	Ngwenelekau Hills	68.2	4.10	4.68
Kampunzu et al. (1998)	0358	Ngwenelekau Hills	73.3	1.92	7.05
Kampunzu et al. (1998)	064	Mapeleapodi Hills	68.6	3.55	4.37
Kampunzu et al. (1998)	0800	Mapeleapodi Hills	69.1	3.09	6.18
Kampunzu et al. (1998)	094	Ngwenelekau Hills	71.1	1.99	6.78
Kampunzu et al. (1998)	1030	Mapeleapodi Hills	70.1	1.84	7.24
Kampunzu et al. (1998)	129	Mapeleapodi Hills	71.0	2.96	7.09
Kampunzu et al. (1998)	170	Ngwenelekau Hills	72.6	2.29	7.10
Kampunzu et al. (1998)	174	Ngwenelekau Hills	75.8	0.87	8.26
Kampunzu et al. (1998)	63480	Mapeleapodi Hills	68.9	3.97	3.84
Ziegler and Stoessel (1993)	KAW3041	Nückopf Formation	75.1	3.68	5.04
Ziegler and Stoessel (1993)	KAW3164	Nückopf Formation	74.4	3.46	5.75
Ziegler and Stoessel (1993)	KAW3165	Nückopf Formation	78.9	2.79	5.68
Ziegler and Stoessel (1993)	KAW3177	Nückopf Formation	79.3	3.91	4.32
Ziegler and Stoessel (1993)	P07	Nückopf Formation	76.4	2.94	5.48
Ziegler and Stoessel (1993)	P10	Nückopf Formation	75.8	2.78	5.37
Ziegler and Stoessel (1993)	W04	Nückopf Formation	77.1	0.82	6.46

The volcanic and metavolcanic samples show distinct geochemical trends on the TAS diagram which suggests progressive depletion in silica from the unaltered to altered

samples, as shown in Figure 7-7. The alteration of OE-1 to form OE-2 appears to result from a loss of ~8 wt. % SiO_2 from OE-1 with only a minor loss of alkali elements. The alteration index of Ishikawa et al. (1976) can be used to quantify the intensity of chlorite and sericite alteration, and is calculated as: $[(100(K_2O+MgO))/(K_2O+MgO+Na_2O+CaO)]$. Values between 20 and 60 indicate unaltered rocks and between 50 and 100 indicates hydrothermally altered rocks (Large et al., 2001). The alteration indeces are 54 and 56 for samples KG-1 and OE-1, respectively, but 88 for OE-2, suggesting advanced alteration of this rock.

The similarity between the two metavolcanic samples (EPS-01 & EPS-03) at depth (85-100m), which do not contain significant Cu(-Fe) sulfide mineralisation, suggests that these two rocks likely represent the starting composition for samples EPS-02 and EPS-04, taken from the same boreholes at shallower depths of 64m and 33m, respectively (Figure 7-7). The metavolcanics were progressively leached of silica during alteration/deformation (~10-15 wt. %), but mildly enriched in alkali elements (~2-3 wt.%). The mineralising event (EPS-04) resulted in more substantial loss in SiO_2 of ~5.5 wt. %, compared to EPS-02. There is also a depletion in alkali elements between EPS-02 and EPS-04, but as can be seen in Table 35, this is more accurately described as a halving of Na_2O and an almost 10-fold increase in K_2O from EPS-02 (0.4 wt. %) to EPS-04 (3.4 wt. %), although within the same borehole, WB-2, EPS-04 has similar total alkali contents to EPS-03 (6.99 wt.% and 8.51 wt.%, respectively).

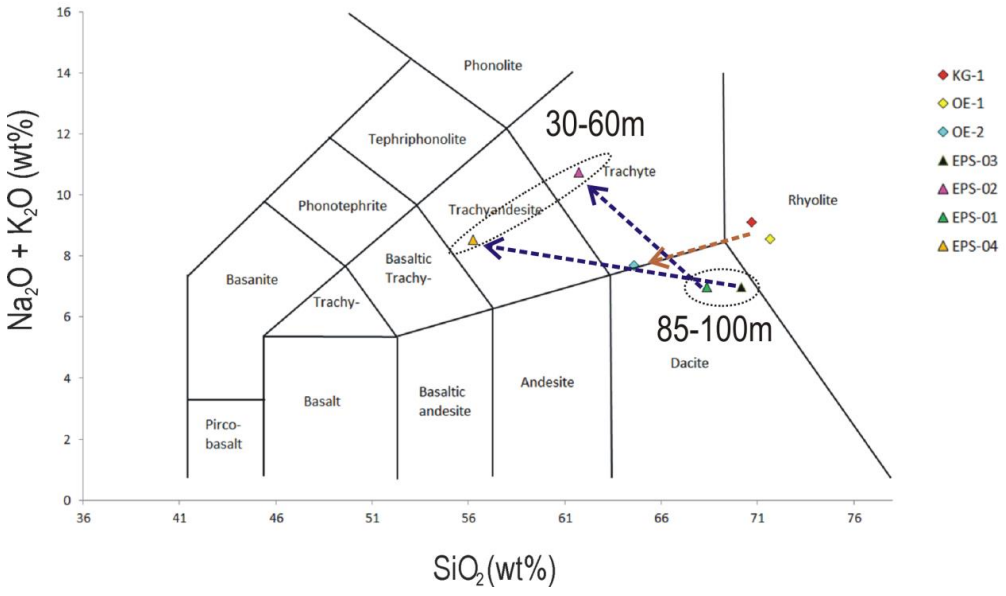

Figure 7-7: TAS diagram showing the changes in SiO_2 and alkali elements for the metavolcanic samples from the same boreholes (blue dashed lines) and the volcanic samples KG-1 and OE-1 during alteration to OE-2 (brown dashed line). TAS boundaries redrawn after Le Maitre et al. (2005).

The Ishikawa et al. (1976) alteration indeces for EPS-01 (36), -03 (31) and -04 (43) suggest alteration primarily in the form of albitisation, especially for EPS-02 which has an index of 3.

7.2 Magnetite and Cu(-Fe) sulfide mineralisation

Mineralisation favours coarse-grained layers/laminae in the rock; there are almost no sulfides associated with the fine-grained portion of any of the rocks investigated. Permeability, whether primary or secondary, exerts a strong control on mineralisation. Even 'disseminated' mineralisation is associated with microscopic lenses of quartz. Mineralisation interstitial to the coarse fraction in a rock has often been used as evidence for the diagenetic origin of Cu(-Fe) sulfide mineralisation in SSC deposits, as the Cu(-Fe) sulfides are seen to be exploiting primary permeability. The metavolcanic samples contain Cu(-Fe) sulfides interstitial to coarse mineral layers, this suggest that these textures can also be syndeformational, where fluids are exploiting secondary permeability.

There is a strong textural relationship between magnetite and the Cu(-Fe) sulfides. Type 2 magnetite often contains Cu(-Fe) sulfide inclusions in mineralised rocks, with the sulfides also often favouring the pressure shadows around magnetite for deposition. In foliated rocks Type 1 magnetite forms stringers parallel to the foliation and sulfides, where present, form along the same lines, often within microns of magnetite stringers. This suggests that both were syn-deformation. Type 3 magnetite appears to form with mineralisation, or the sulfides are preferentially depositing around magnetite. The two share boundaries, which can be straight, suggesting equilibrium conditions, or embayed, suggesting the replacement of magnetite by sulfides. The contrasting redox conditions required to deposit both magnetite and Cu-sulfides favour magnetite forming as a secondary mineral by replacement of sulphides such as pyrite.

The oxidation of magnetite to hematite appears to be linked to mineralisation. In almost all instances magnetite associated with mineralisation shows low levels of oxidation, while magnetite away from the Cu(-Fe) sulfides shows moderate to high levels. This is consistent with what would be expected from the redox conditions conducive to the precipitation/growth of both of these phases, i.e. reducing conditions which become mildly oxidising over time to produce alteration products such as hematite from magnetite and covellite/digenite from bornite and chalcocite.

A close investigation of samples which contained both vein-hosted and disseminated Cu(-Fe) sulfide mineralisation showed that in all instances the mineralogy was identical (Figure 7-8). The sulfide mineralogy showed the same bornite-chalcocite exsolution textures in EPS-09 (Figure 7-8-A&B) regardless of whether the sulfide was hosted in a vein or in the

groundmass of the rock. In sample OPS-5 chalcopyrite was characterised by covellite along its edges, the same was seen in the groundmass (Figure 7-8-C&D). This strongly suggests that the disseminated and vein-hosted mineralisation is coeval.

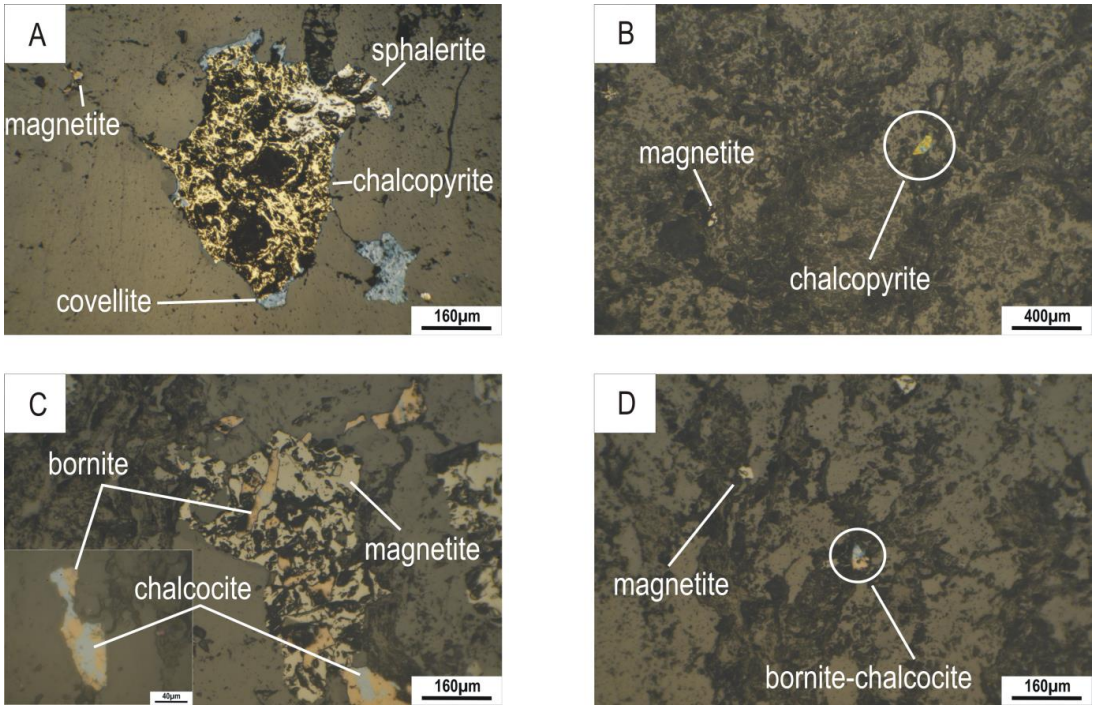

Figure 7-8: Reflected light photomicrographs of sulfide mineralogy within veins (A & C) compared to disseminated mineralisation (B & D) for EPS-09 (A & B) and OPS-5 (C & D). Insert **C** showing the typical exsolution textures between chalcocite and bornite.

7.3 Magnetite trace element geochemistry

Dare et al. (2014) devised a scatterplot to distinguish between magnetite from hydrothermal systems from those in magmatic systems on the basis of the Ni/Cr ratio, which in hydrothermal systems should be greater than 1. Using the method of Dare et al. (2014) the results from this study have been plotted in Figure 7-9.

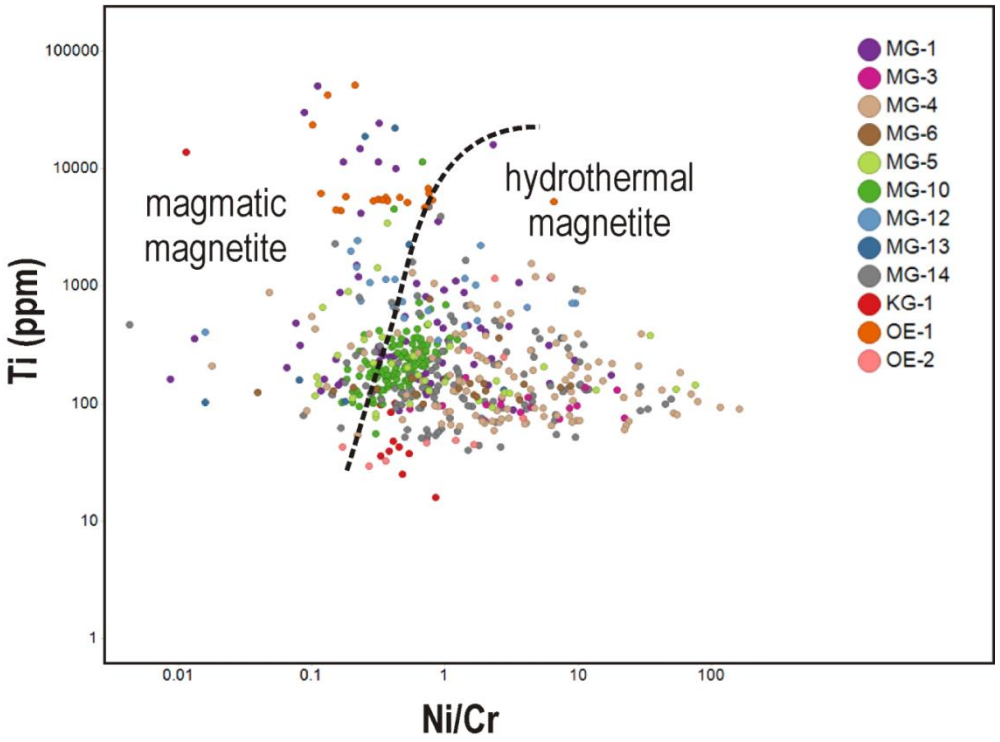

Figure 7-9: Plot of Ti (ppm) versus Ni/Cr ratio in magnetite as determined by LA-ICP-MS. The fields for magmatic and hydrothermal magnetite are drawn after Dare et al. (2014). Cr was not detected in 12 of the magnetite grains analysed and 9 grains contained no detectable Ni.

Figure 7-9 suggests that the majority of the magnetite analysed for this study was hydrothermal in origin. The unaltered basement sample OE-1 plots firmly within the magmatic field, but OE-2 and KG-1 plot within the hydrothermal field. The metavolcanic sample MG-1 appears to be a combination of the two, with many of the results plotting in the magmatic field, as well as overlapping with magnetite from the sedimentary rocks in the hydrothermal field, as does the OE-2 magnetite. There is a fair amount of scatter in the Ni/Cr ratio for the magnetite from the sedimentary samples, but generally all fall within the range of ~100-1000 ppm Ti.

7.3.1 Volcanic and metavolcanic magnetite

TAS diagram plots suggest that the un-mineralised, deformed metavolcanic rocks (EPS-01 and EPS-03) in the western study area have a dacite composition similar to the

Oorlogsende samples (OE-1 and OE-2) and KG-1 from the Kgwebe Formation in Botswana, which plotted in the rhyolite/trachyte field of the TAS diagram. Although zircon geochronology has shown that the meta-dacites are at least 60Ma older than the Oorlogsende Member or Kgwebe Formation, the whole-rock compositional similarities between these locations, coupled with the results of Figure 7-9, are used to compare OE-1 magmatic magnetite to the hydrothermal magnetite produced by alteration (OE-2), deformation (MG-1) and deformation coupled with mineralised (MG-3) (Figure 7-10).

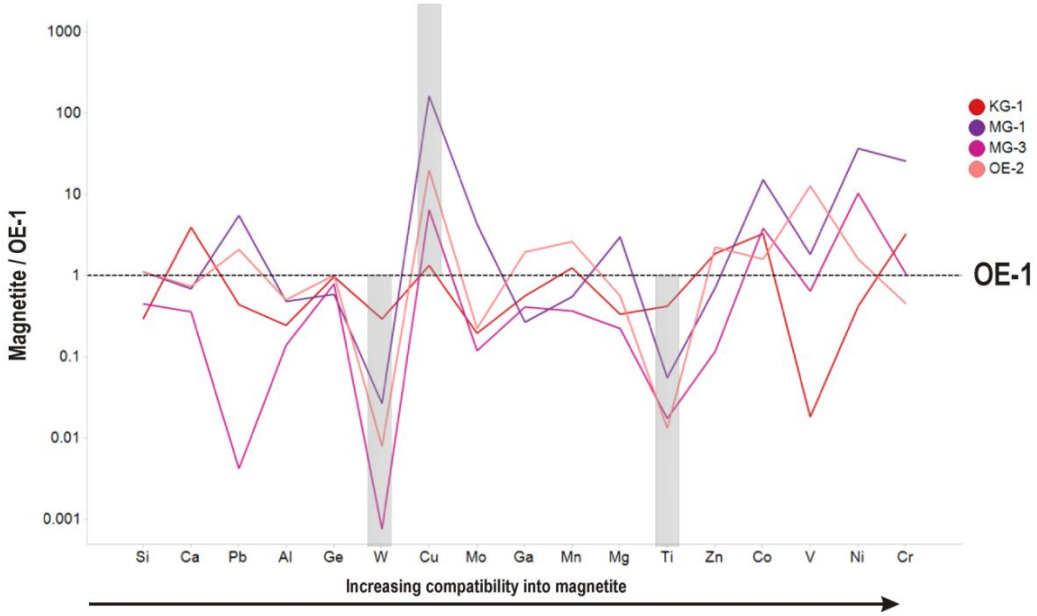

Figure 7-10: Median trace element concentration (ppm) for magnetite from the metavolcanic samples MG-1 and MG-3, and the altered rhyolite OE-2, normalised against OE-1. All of the samples show systematic variations in W, Cu and Ti relative to OE-1, as highlighted by grey bars. With the exception of V there is a general increase in the slope from Ti to Cr reflecting the increased concentration of these elements as a function of their compatibility into magnetite.

In Figure 7-10 the data have been normalised to OE-1 as a baseline for comparison. It is evident from the figure that there are systematic variations in the trace elements W, Cu and Ti for all of the samples, whether altered, deformed or mineralised. This suggests strongly that the factors governing the partitioning of at least those three elements were fairly consistent for all of the hydrothermal magnetite samples.

Unravelling the consequences of deformation and alteration on the composition of magnetite in the different settings then becomes possible, as shown in the schematic diagram Figure 7-11. Magnetite in the volcanic rocks which have undergone deformation, alteration and metamorphism are depleted in W and Ti relative to magmatic magnetite, and show enrichment in Cu. OE-1 records median values for Ti of ~0.6 wt.%, and 69ppm W,

compared to only 96ppm Ti and 0.05ppm W in MG-3. OE-1 contains 1.25ppm Cu, while MG-1 contains almost 100ppm.

Magnetite in host-rocks which have undergone alteration only, with no deformation, are enriched in V relative to magnetite from deformed and undeformed host-rocks. Magnetite in volcanics which have undergone deformation and metamorphism have relatively higher concentrations of Co and Ni than magmatic magnetite, and are particularly enriched in Cr. Magnetite associated with deformed and metamorphosed host rocks shows similar trace element distributions, but shows no change in Cr concentrations relative to magmatic magnetite. The gains in Cu and Co seen in the magnetite chemistry are also seen in thin section where syn/post-deformation cobaltite and bornite occur in the fractures around pre-deformation pyrite (Figure 5-29). Overall the relative concentrations of trace elements in magnetite from the mineralised host-rock are lower for all of the elements measured, with a marked decrease in Pb relative to magnetite from all other settings. Si, Ca, Al and Ge concentrations for magnetite from the altered and the deformed host rocks are almost identical to that of magmatic magnetite.

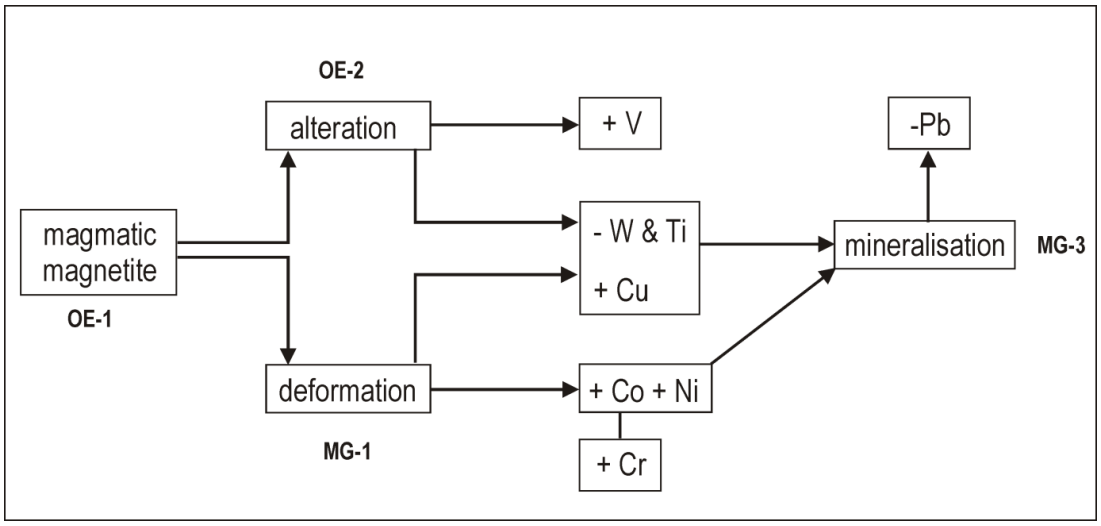

Figure 7-11: Schematic illustration of the effects of alteration and deformation relative to the composition of magmatic magnetite. Alteration and deformation of the host-rock result in a net loss of W and Ti, relative to magmatic magnetite, and the addition of Cu. Alteration alone produces magnetite with higher V concentrations than either magmatic magnetite, or magnetite in the deformed rocks. Where the host-rock has undergone deformation only, magnetite is enriched in Co, Ni and Cr. In the sample which hosts significant Cu concentrations, magnetite is characterised by significantly lower Pb concentrations.

Magnetite from KG-1 is the most similar to OE-1, except for marked increases in Ca, and significantly lower V concentrations. This could reflect local conditions. Extensive carbonate alteration is reported from Zeta and Plutus in the Botswana section of the KCB, coupled with lower V contents, this could indicate that the deposit has been exposed to more

oxidising conditions, and account for the lack of magnetite in these deposits (Hall, 2013). Vanadium is very sensitive to redox conditions due to its 5+ oxidation state, and at high oxygen fugacity it becomes incompatible into the magnetite structure (Bordage et al., 2011). Alteration of the rhyolites (as represented by OE-2 magnetite) therefore appears to produce the most reducing conditions, because V concentrations are the highest here, almost triple that of OE-1 (median = 1550ppm).

The divalent ions Mg, Mn, Ni and Co for example, are thought to partition into magnetite in a magmatic setting independently of the prevailing oxygen fugacity (Nadoll et al., 2014). The enrichment in Ni seen in the deformed samples is particularly diagnostic for distinguishing between the different volcanic and metavolcanic samples, as shown in Figure 7-12. Deformation has little effect on the amount of V incorporated into magnetite relative to magmatic magnetite, but alteration in the absence of deformation has a strong influence on fO_2 as seen by the availability of V.

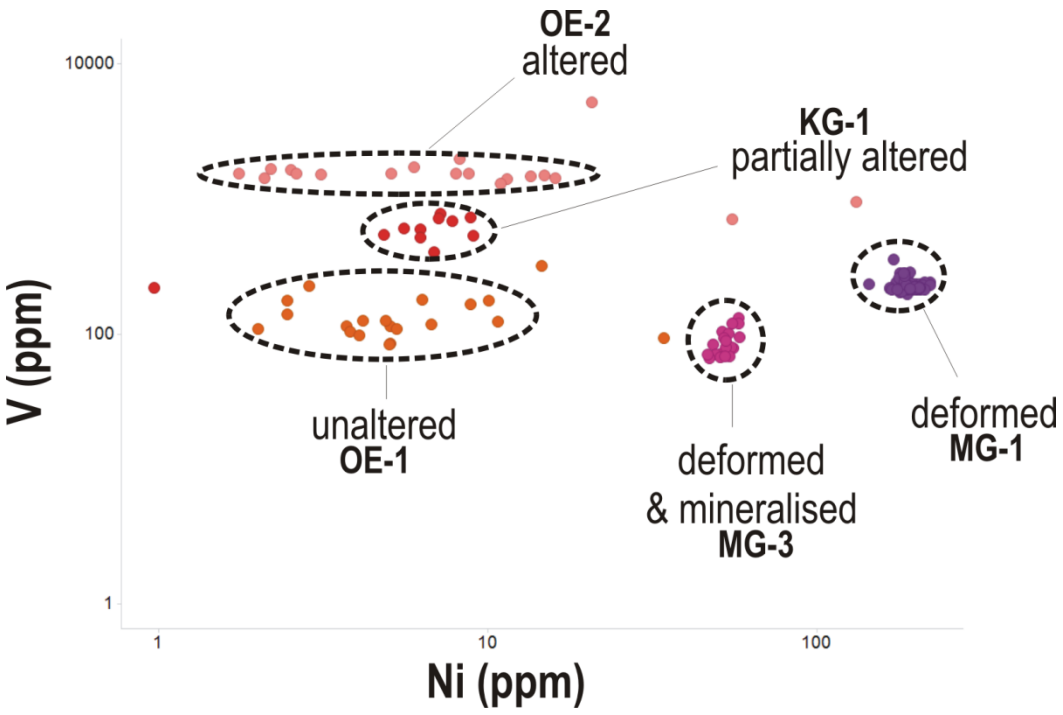

Figure 7-12: Vanadium versus Ni concentrations (ppm) for the magnetite sampled from the metavolcanic rocks (MG-1 & MG-3) and the rhyolite samples (OE-1, OE-2 and KG-1). The V/Ni ratio for each of the environments sampled are clearly illustrated dashed circles enclosing magnetite analyses from each location. The Ni content of the rhyolites which have not undergone deformation/metamorphism, show a fair amount of spread in the data, but have fairly narrow ranges in terms of V concentrations. Magnetite from the metavolcanics which have undergone deformation/metamorphism (MG-1) and contain mineralisation have very narrow ranges for both V and Ni concentrations.

Figure 7-12 clearly identifies mineralisation-associated magnetite as distinct from the other volcanic and metavolcanic magnetite samples. This figure could be interpreted as suggesting that although there is a net gain in Ni for the deformed samples relative to the undeformed rhyolites of the Oorlogsende Member and Kgwebe Formation, there is a loss of Ni associated with the mineralising event at MG-3. As Ni is highly compatible into the magnetite structure, this loss of Ni is most likely related to the changing availability of this element in the fluid, but could also reflect changes in temperature. Co-crystallising phases could also account for the decline in Ni available for magnetite incorporation between MG-1 and MG-3. Nickel was detected in some of the cobaltite measured during EMPA for EPS-02 which could account for this loss.

The composition of the fluid, and therefore element availability, provide a first order control on the minor and trace element concentrations in magnetite from hydrothermal systems (Ilton and Eugster, 1989; Nadoll et al., 2014). Experimental work by Ilton and Eugster (1989) demonstrated that even minor to trace concentrations of Zn, Mn, Cu, and Cd in magnetite can indicate strong enrichment of these base metals in chloride-rich hydrothermal fluids. Zinc concentrations in magnetite almost double between the unaltered and the altered rhyolites with OE-1 reporting 129ppm and OE-2 408ppm Zn. This change is seen in thin section as well, OE-2 contains abundant sphalerite while OE-1 contains none. The metavolcanic MG-1 contains similar levels of Zn to OE-1 (129ppm) but MG-3 contains a fraction of this, ~21ppm. Zinc is a chalcophile element so it is possible that with MG-3 a Zn-bearing phase fractionated from the fluid before or at the same time as magnetite, although in thin section there is no clear evidence of this. Manganese is strongly enriched in the altered rhyolite OE-2 (~1400ppm) relative to the unaltered rhyolite (520ppm), suggesting that this element was also enriched in the fluids associated with alteration in OE-2. However, KG-1 also had >0.1 wt.% Mn but was not as altered as OE-2 so perhaps there is another aspect to this which is unclear. Magnetite from the metavolcanics has 200-300 ppm Mn which suggests that Mn was enriched in the fluid, although not as strongly as in the rhyolites. Similar concentrations in the mineralised and unmineralised samples suggests that availability of this element was not affected by the mineralising event.

Element availability and the composition of the hydrothermal fluid are also strongly influenced by co-crystallising phases. MG-1 has the highest overall Cu concentrations of the samples, followed by OE-2 and then MG-3 (median = 208 ppm, 25 ppm and 8ppm,

respectively). This indicates that the hydrothermal fluids associated with deformation and alteration were enriched in Cu. The lower values in MG-3 are a reflection of the precipitation of Cu-bearing sulfides being concomitant with that of the magnetite, effectively depleting the fluid of Cu. This agrees with petrographic evidence which shows both magnetite and bornite occurring together, exploiting the secondary permeability created by deformation. Silver concentrations for these samples were all in the ppb range and show no direct correlation to Cu. Therefore, it is unlikely that Cu was present as inclusions, although as S was not measured, Cu from inclusions cannot be ruled out. The other chalcophile elements (Pb, Sn, Mo, Zn) have lower concentrations (<10ppm), but show increase in MG-3 as compatibility into the magnetite structure increases towards Co and Ni (>10ppm) (Figure 7-15). Pb in MG-3 magnetite is almost 4-orders of magnitude lower than in MG-1 suggesting Pb was most likely being crystallised out of the fluid around the same time magnetite was. Petrographically there is no evidence of Pb-bearing minerals forming in MG-3, but in a classic precipitation series of sulfides, galena would be deposited further away from the Cu(-Fe) sulfides from cooler fluids, so wouldn't be expected in MG-3. OE-2, which is enriched in Pb relative to KG-1 and OE-1, and contains galena and other Pb-bearing phases, but the paragenesis to magnetite is unclear. Pb is very incompatible into the magnetite structure because of its large ionic radius, therefore its detection in magnetite may be due to microscopic Pb-bearing inclusions in magnetite.

The elements Y, Nb, Sn, W and Th are relatively enriched in magnetite from OE-1 (~35-100ppm). In general these elements are thought to be highly incompatible into the magnetite structure because of their 4+ oxidation state, so their incorporation into magnetite is most likely also a function of their abundance in the fluid/melt. Magnetite from all of the igneous and hydrothermal deposits investigated by Nadoll et al. (2014) show that Sn is rarely above detection limits, except in skarn and Henderson Climax-type Mo deposits. In the rhyolites KG-1 and OE-1 Sn is between 20-40ppm, favouring the latter, but in the altered sample and the metavolcanics is only 1-2ppm. Nadoll et al. (2014) found that Sn and Ga concentrations correlated to temperatures of formation for many hydrothermal ore deposits. Through studying magnetite from a range of deposit types they found higher values (>10ppm) for both of these elements correspond to ore deposits formed at higher temperatures (>300˚C) (Figure 7-13A).

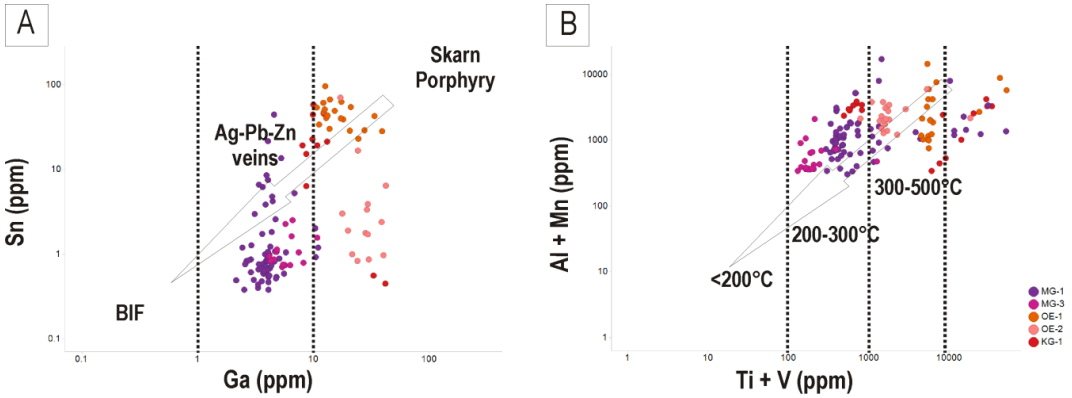

Figure 7-13: A: Sn vs. Ga concentrations for magnetite from the volcanic and metavolcanic samples measured. The fields shown on the diagram were interpreted from the data of Nadoll et al. (2014) which showed magnetite associated with BIF either had low, or below detection limit concentrations of Sn and Ga. The concentration of Sn for both BIF/iron ore and Ag-Pb-Zn hydrothermal vein type magnetite rarely exceeded 10ppm, although higher concentrations of Ga are associated with the veins. Magnetite from the igneous Henderson Climax-type Mo deposit has the highest Sn and Ga concentrations, (generally >100 ppm). Igneous and hydrothermal porphyry magnetite is characterised by high Ga concentrations, but lower Sn contents than the Henderson -type magnetite. **B:** This same relationship has been shown for the Al + Mn vs Ti + V concentrations of known ore-deposits, with higher concentrations in all elements thought to represent higher temperatures of formation. The temperature ranges are based on information published by Nadoll et al. (2014) for the same deposits described in **A**.

There is a general decrease in the concentrations of both of these elements from the unaltered rhyolites of OE-1 and KG-1 to the metavolcanic samples (MG-1 & MG-3). This could be used to suggest that the temperatures associated with the formation of the magnetite at MG-3 were slightly higher than MG-1. In magmatic systems the concentrations of Al and Ti are directly related to the temperature of formation, as these elements are considered immobile at sub-magmatic temperatures (Verlaguet et al., 2006). Nadoll et al. (2014) found the same to be true for hydrothermal magnetite, where on average increased concentrations of these elements was associated with higher temperatures of formation.

Figure 7-13 could therefore be interpreted as a gradual decline in temperature from magmatic magnetite (OE-1) towards hydrothermal magnetite associated with alteration, and later, deformation, in a progressively cooling system. Petrographically there is no evidence to suggest that this is not the case. Although the host-rocks to the magnetite in MG-1 and MG-3 are clearly of a volcanic nature, very little of the magnetite appears to pre-date deformation. The majority of the magnetite in both samples was euhedral and on average <50µm in length. Thin section analysis showed no pressure shadows developed on magnetite of this size, and a clear association of the magnetite with the fabric. The rocks also show no mineralogical evidence of having exceeded greenschist facies metamorphism, so formational temperatures in the range of <300˚C for the MG-1 and MG-3 samples, as

suggested by Figure 7-13, are entirely plausible. Nadoll et al. (2014) have demonstrated that temperature is one of the key controls in the overall concentrations of trace elements in magnetite, with low temperature deposits such as BIF showing the lowest overall concentrations of trace elements, and high temperature skarn and porphyry magnetite showing the highest concentrations.

An attempt has been made to determine whether magmatic magnetite trace elements in the unaltered rhyolite OE-1 could be used to distinguish the tectonic setting of the parent rock using the method of Pearce et al. (1984) who distinguished various acid volcanics on the basis of Nb vs. Y (Figure 7-14). The results could not be compared directly to whole rock data for OE-1 because none was available, however, as the TAS diagram has already shown that there are strong similarities in terms of age and composition between OE-1 and other rhyolites from the Kgwebe Formation in Botswana, these were used as a basis for comparison.

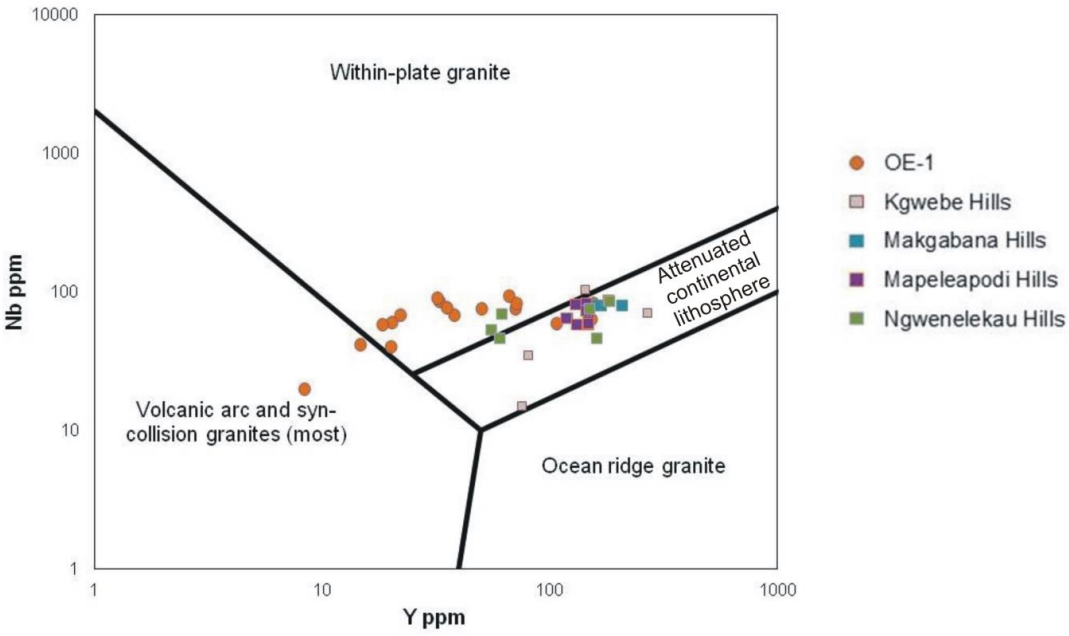

Figure 7-14: Nb vs. Y for magmatic magnetite (OE-1) compared to whole rock data from Kampunzu et al. (1998) for Kgwebe Hills, Makgabana Hills, Mapeleapodi Hills and Ngwenelekau Hills. Diagram boundaries after Pearce et al. (1984).

The Nb vs Y plot for OE-1 magmatic magnetite shows some overlap with whole rock analyses done by Kampunzu et al. (1998), suggesting that the parent rocks to OE-1 are within plate volcanic rocks emplace in an attenuated continental crust, as are the Kgwebe Formation rhyolites.

7.3.2 Sediment-hosted magnetite

The binary plot in Figure 7-9 suggests that all of the magnetite from the sedimentary rocks sampled for this study is hydrothermal in nature, with no obvious magmatic magnetite present. The magnetite from the sediments, when normalised to BCC (bulk continental crust), shows remarkable homogeneity with respect to the distribution of the spinel group elements Al, Ga, Mn, Mg, Ti, Zn, Co, V, Ni and Cr (Figure 7-15A). This distribution pattern is mimicked by magnetite from the metavolcanic samples MG-1 and MG-3, although the MG-3 magnetite contains lower overall trace element contents (Figure 7-15B).

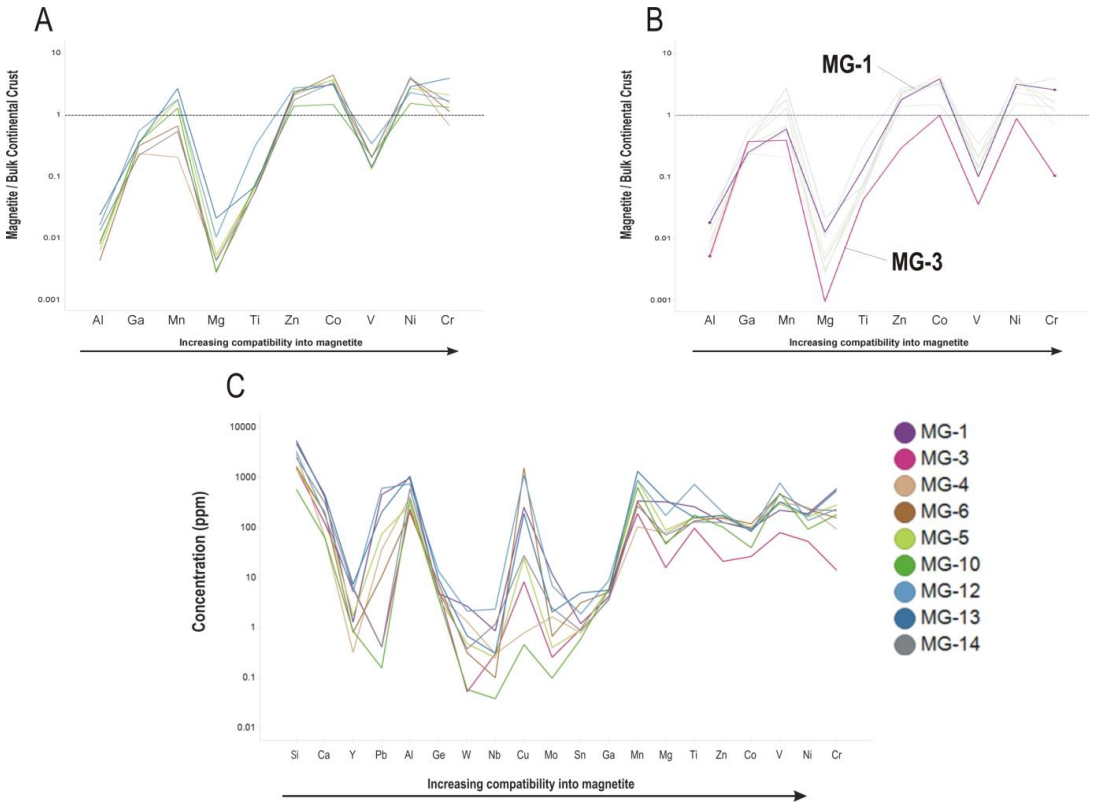

Figure 7-15: Median spinel trace element concentrations for magnetite from the sedimentary samples (A) and the metavolcanic samples (**B**) normalised against BCC (bulk continental crust) using the values from Rudnick and Gao (2003). Magnetite from the sedimentary rocks (MG-4 to -14) shows strong depletions in Al, Mg, Ti and V relative to BCC, and similar enrichments for Zn, Co and Ni. Manganese and Cr show the most variability, although by less than an order of magnitude. The magnetite from MG-3 is depleted in all of the spinel group elements relative to BCC. MG-1 shows depletions for all of the elements relative to BCC, but also enrichments in Ti, Co, V and Cr. **C:** The median values for 20 of the elements measured, with no normalisation, show the overall consistency of the data.

The variation amongst the samples is evident when considering just the median concentrations (Figure 7-15C) but the systematic variations in composition relative to BCC suggests that the assumptions of Dare et al. (2014) are accurate, that hydrothermal fluids likely interacted with crustal rocks, and that differences in abundance of trace elements reflects different abundances of these elements in the liquid and/or differences in their

partition coefficients into magnetite. After Cu, Mo and Pb the elements Y, Nb, Sn and W show the most variability in concentration but these elements are all minor components of the total trace element contents in magnetite (<10ppm/element, usually <1ppm), and are considered largely incompatible in the magnetite structure. Molybdenum is particularly sensitive to oxygen and sulfur fugacities and in all cases is below 10ppm and usually <1ppm (Dare et al., 2012; Nadoll et al., 2014). Variability in the incorporation of this element is most likely reflecting fluctuating fugacity conditions associated with magnetite precipitation. Molybdenum will be preferentially taken up in molybdenite rather than in the magnetite structure.

The apparent compositional similarities in spinel element concentrations suggested by the BCC normalisation between the metavolcanic samples and the magnetite extracted from the sedimentary rocks can be interpreted in two ways. The first interpretation is that the magnetite in the sedimentary rocks was sourced from the metavolcanics, as a detrital component, and the second is that magnetite precipitated from hydrothermal fluids operating on a regional scale across these different rock types.

A scenario in which magnetite forms part of the detrital assemblage is not hard to envision. Magnetite will has been shown to retain its chemical composition through weathering and transportation, preserving the details of its provenance (Dupuis and Beaudoin, 2011; Grigsby, 1990). The results from zircon geochronology have already demonstrated that the metavolcanic suite contributed detritus to the Eiseb. This detritus could easily have included magnetite. Texturally, there is evidence in support of at least some pre-deformation magnetite. Sample EPS-14 provides the most convincing evidence because magnetite occurs in bands with other heavy minerals such as zircon, but this is only seen in one sample, so cannot be used to make assertions about the whole basin. Other evidence for magnetite being pre-deformation is exemplified by Type 2 magnetite. This type often has strongly developed pressure shadows, and in some cases is aligned with relict bedding. Type 2 magnetite, however, is usually in the range of ~150µm, while the magnetite analysed by LA-ICP-MS for MG-1 and MG-3 was an average of ~60µm, making it unlikely that Type 2 magnetite was sourced from MG-1 or MG-3. The average size of magnetite analysed in this study, from any location, was usually <100µm in length. This excludes much of the Type 2 magnetite in favour of Type 1 magnetite, just on the basis of grain size. Type 1 magnetite shows euhedral grain shapes and no pressure shadows so is unlikely to be detrital. The most important feature of Type 1 magnetite in this context, however, is that is

shows a clear relationship to the fabric forming event in both the sedimentary rocks and the metavolcanics. Type 1 magnetite could therefore not have been eroded and transported from MG-1 into the sedimentary pile because deformation occurred after sedimentation of the Eiseb. Stevens (2015) investigated the occurrence of magnetite-bearing metasediments at Broken Hill. Here magnetite occurs as disseminations in a range of sediments, with no clear detrital associations. Texturally this magnetite is aligned to the bedding in the rocks, and is transgressed by later tectonic fabrics. Diagenetic and biogenic origins for magnetite are rejected on the basis of the disseminated nature of the magnetite, with no clear preference for a particular lithological unit, and no clear lithological distinctions between adjacent magnetite-bearing and magnetite barren zones. Stevens (2015) favours the presence of hydrothermal plumes as the mechanism for sporadic precipitations of magnetite, which are then dispersed over a wide area, across a range of rock types. This explanation accounts for a number of observations, but does not resolve, for example, the presence of magnetite disseminations in amphibolites or in the 'Potosi-type' gneiss adjacent to magnetite-bearing metasediments. The same is true for the magnetite within the Eiseb. It is most commonly found associated with fabrics which suggest syn-deformational growth of magnetite, and is found in almost every rock type described for this study, including the metavolcanics and the fine-grained argillaceous rocks. Homogeneity between the samples on the basis of magnetite as part of the detrital assemblage is inconsistent with the evidence.

Metamorphism is known to produce almost pure magnetite with homogeneous compositions and low trace element contents (Frost, 1991a; Hall and Fischer, 1977; Johnson, 1979). During metamorphism the stability of magnetite is controlled by oxide-silicate equilibria, graphite-bearing equilibria, and sulfide equilibria. The rocks in the Eiseb show no indication of having contained significant quantities of carbon. Graphite, for example, would have been detected during the rock magnetic work done as part of the palaeomagnetic investigation.

Equilibria involving the Fe-Si-O-H system were generated by Frost (1991a). He found that reduction followed prograde metamorphism during the production of magnetite because of the limited availability of free oxygen in metamorphic fluids. The creation of magnetite in this setting can dramatically lower the oxygen fugacity of a fluid, but does not necessarily have to result in volumetrically significant quantities of magnetite being created. Magnetite is also not likely to be produced in graphitic rocks, which are more conducive to the

production of FeO because of the strongly reducing environment generated by graphitic rocks during progressive metamorphism. In graphitic rocks the stable iron-bearing minerals would be pyrrhotite or pyrite because of the positive correlation between carbon and sulfur content in pelitic rocks. Magnetite would not be stable in these rocks (Frost, 1991a). In this system then, only oxide-silicate and sulfide equilibria are likely to have controlled magnetite precipitation.

Equilibria involving Fe-oxides and Fe^{2+} in silicates affects the amount of magnetite produced because these equilibria do not require a change in the oxidation of state of iron to produce magnetite (Frost, 1991a). Equilibria involving changes in the oxidation state of Fe will also directly influence the amount of magnetite produced. Particularly relevant to this study is the presence of biotite, which was observed in many of the samples. Biotite incorporates Fe into its structure in either oxidation state, and in metamorphosed rocks, the breakdown of biotite releases this iron which can be taken up to form magnetite. Biotite is often bedding-parallel in the sedimentary rocks of the Eiseb, suggesting it formed prior to deformation. It often shows evidence of alteration along it's edges and evidence of chloritisation, both of which will result the release of iron. The breakdown of biotite could therefore have had a significant effect on the formation of magnetite during the deformation of the Eiseb. If this is the case then it is possible that the pressure shadows observed on Type 2 magnetite are inherited from this early biotite (Figure 7-16). Evidence for Fe-oxide conversion of biotite was presented in Figure 5-52 for EPS-14.

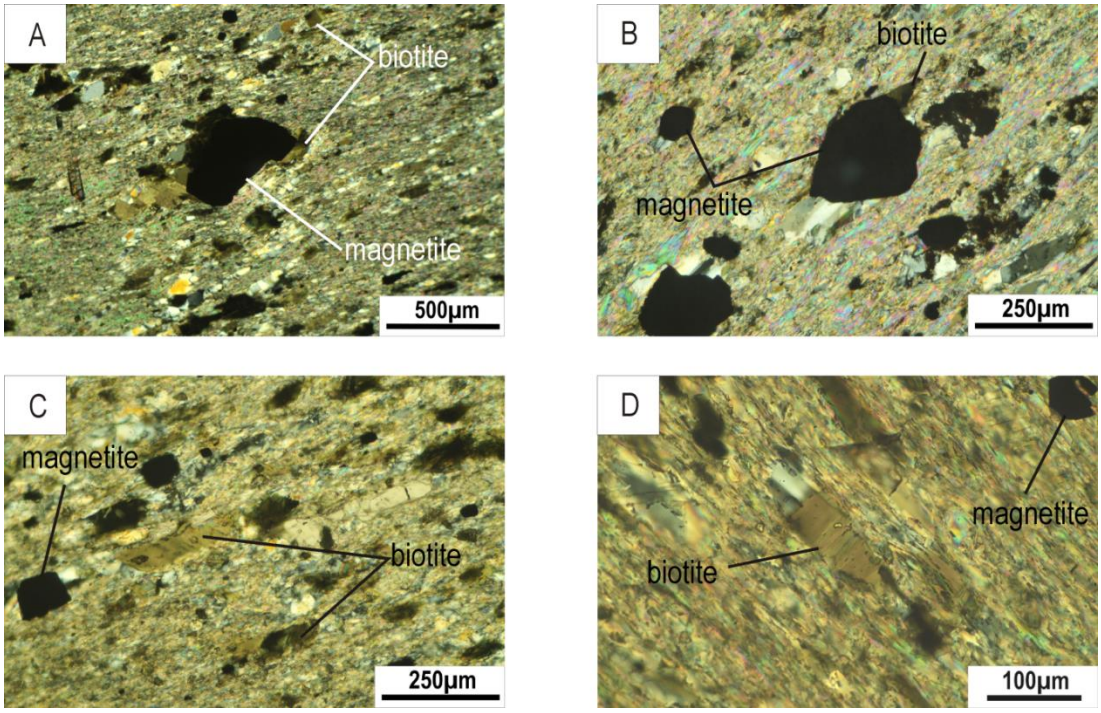

Figure 7-16: Photomicrographs of the textural association between magnetite and pre-deformation biotite from **A:** PST4-D2-2 (NEA-PL-1), **B:** EPS-20 (CA-PL-6), **C:** OPS-3 (CA-PL-3), and **D:** OPS-1 (CA-PL-2). Pressure shadows are commonly associated with biotite when it is oriented parallel to the foliation, Type 2 magnetite shows similar pressure shadows which means that it either formed prior to deformation, as part of a pre-deformation assemblage which included biotite, or magnetite growth replaces biotite during metamorphism and the pressure shadows are inherited. All photomicrographs taken under XPL.

Sulfur fugacity is a function of oxygen fugacity, and in most metamorphic environments H_2S will be the dominant sulfur species (Frost, 1991a). In rocks such as schists metamorphism can dramatically lower the oxygen fugacity of the fluid, and hence the sulfur fugacity, but in graphite-free rocks, conditions are less reducing so sulfur fugacity also increases. The reaction in which magnetite is produced from pyrite is:

$$6\ FeS_2 + 6\ H_2O + O_2 = 2\ Fe_3O_4 + 6\ H_2S$$

Metamorphic growth of magnetite for the Eiseb is feasible by any of the mechanisms discussed, with textural evidence favouring growth during deformation. Goldfarb et al. (2005) have shown that in the case of orogenic lode Au deposits which formed during metamorphism the fluids involved are generally in equilibrium with the surrounding rocks because they were developed under ambient metamorphic temperature and pressure conditions. This would explain the consistency in the magnetite chemistry developed across the Eiseb, and also accounts for the poorly developed alteration haloes associated with mineralisation. Sericite, chlorite, muscovite and recrystallised quartz are all commonly associated with mineralisation, but they are also commonly present away from mineralisation, so their presence or absence cannot be used to vector for Cu-Ag sulfides.

Magnetite, which also forms part of the alteration assemblage, records the subtle geochemical changes in the fluid during sulfide deposition and so can be used to vector for mineralisation.

The trace element distributions for the metavolcanic rocks allowed for the distinction between the mineralised and non-mineralised areas on the basis of the binary plot of V vs Ni, this plot, however, does not distinguish mineralised from non-mineralised in the sediment-hosted magnetite samples (Figure 7-17).

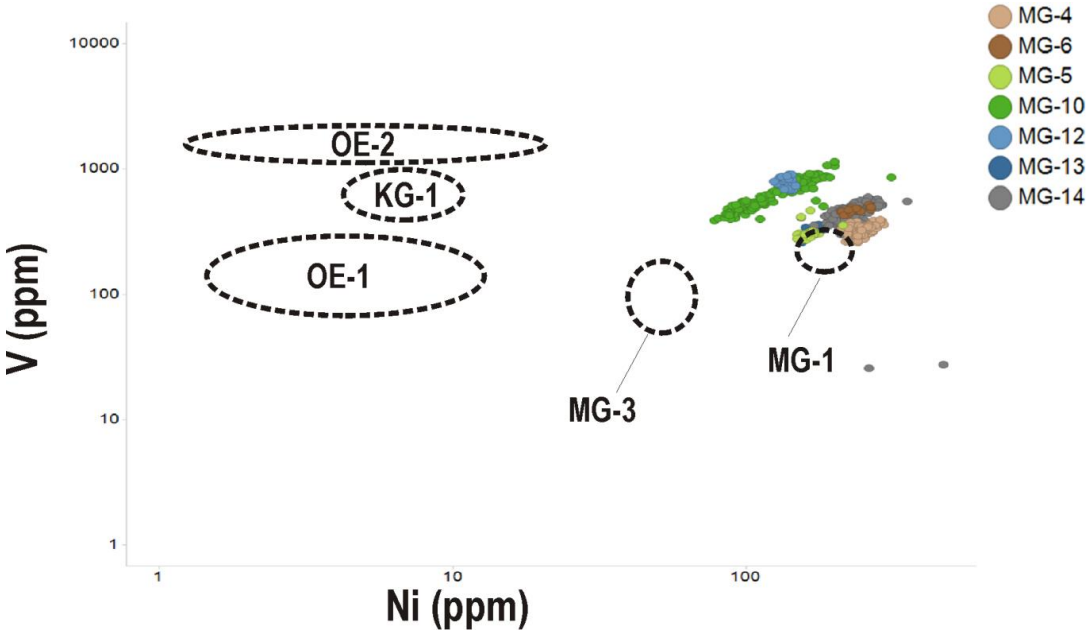

Figure 7-17: Vanadium vs. Ni binary plot for sediment-hosted magnetite samples relative to the volcanic and metavolcanic samples OE-1, OE-2, KG-1, MG-3 and MG-1. The mineralised sediment-hosted magnetite samples MG-6, MG-10 and MG-12 cannot be distinguished from un-mineralised samples on the basis of this diagram.

A V vs Co plot is more effective at distinguishing mineralised and non-mineralised in the sediment-hosted magnetite (Figure 7-18). Vanadium concentrations within the mineralised phyllites are highest, and most likely reflect the more reducing conditions typical of this type of sediment. MG-10 from NEA-PL-1 shows the most variable V contents relative to both Ni and Co, and positive correlations with these elements, possibly indicating variably fO_2, but also the coupled substitution of V with both Ni and Co. This coupled substitution is not restricted to Ni and Co, but includes Mn and Zn (r^2 >0.8 for all elements). This suggests that vanadium is present in the 4+ oxidation state.

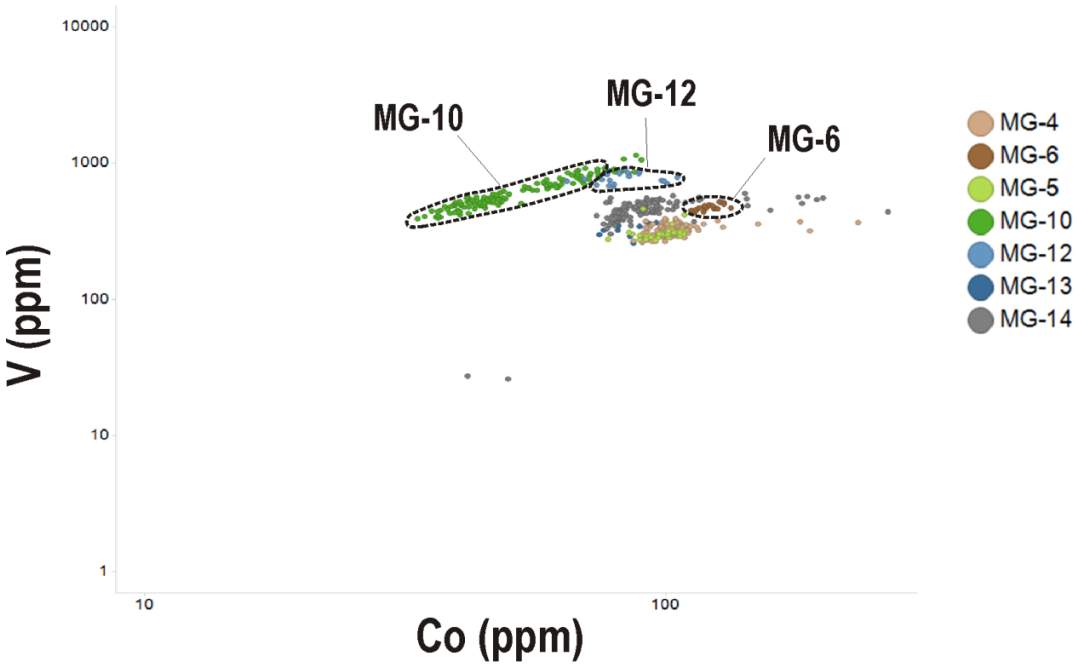

Figure 7-18: Vanadium vs. Co for the sediment-hosted magnetite samples distinguishes mineralised from non-mineralised host-rocks. MG-10 shows a strong linear relationship between Co and V.

MG-6 magnetite from the mineralised sandstone is distinguished from magnetite from the footwall sandstone, MG-4 within the same borehole (CA-PL-6). Relative to the magnetite in MG-4, the MG-6 magnetite has slightly higher Co and V concentrations. The V and Co concentrations from MG-4 overlap with the sandstone from borehole NEA-PL-1, MG-5, which is hangingwall, and the footwall sandstone MG-13 (CA-PL-1), although this sample has slightly less Co. This overlap implies that the V concentrations are a function of rock type, rather than being controlled by where in the stratigraphy the sandstone is deposited, or where the sandstone is situated geographically. Vanadium as a proxy for fO_2 explains the differences in concentrations, sandstones should be more oxidising than argillaceous rocks. The concentration of V in MG-6, which plots away from the other sandstones, suggests that it is more reducing, which is probably why it is mineralised (Stanistreet and Stollhofen, 1999). Alternatively, the rock has been reduced by the mineralising process.

Geochemical data from the specific intersections sampled for the MG grain mounts were available for the mineralised intersections only (MG-3: 33m; MG-6: 222m; MG-10: 280m and MG-12: 186m). When the median results from LA-ICP-MS are compared to the assay data for the same intersections, it is evident that all of the magnetite samples are enriched in Ni and Co relative to the whole rock (Figure 7-19). The LA-ICP-MS data show that for MG-3, MG-6 and MG-10, Pb is more enriched in the whole rock than magnetite. This makes sense from a geochemical perspective because Pb will preferentially partition into sulfides

rather than into magnetite. The high values in MG-12 are likely a function of nano-scale inclusions rather than Pb within the magnetite structure. Silver was reported at >10ppm in assays from all of the mineralised intersections, and in all cases this was higher than the average reported for the stratigraphic horizon within which the mineralised horizons occur. Magnetite analyses all report lower Ag than the assay data. LA-ICP-MS results from MG-6 are the closest to the assay results, however, with almost 7ppm Ag in MG-6 relative to 17.5ppm in the whole-rock. Binary plots of Ag versus Cu show strong linear relationships between these elements for magnetite in MG-6 and MG-13 which suggests that they may be inclusions (Figure 7-20).

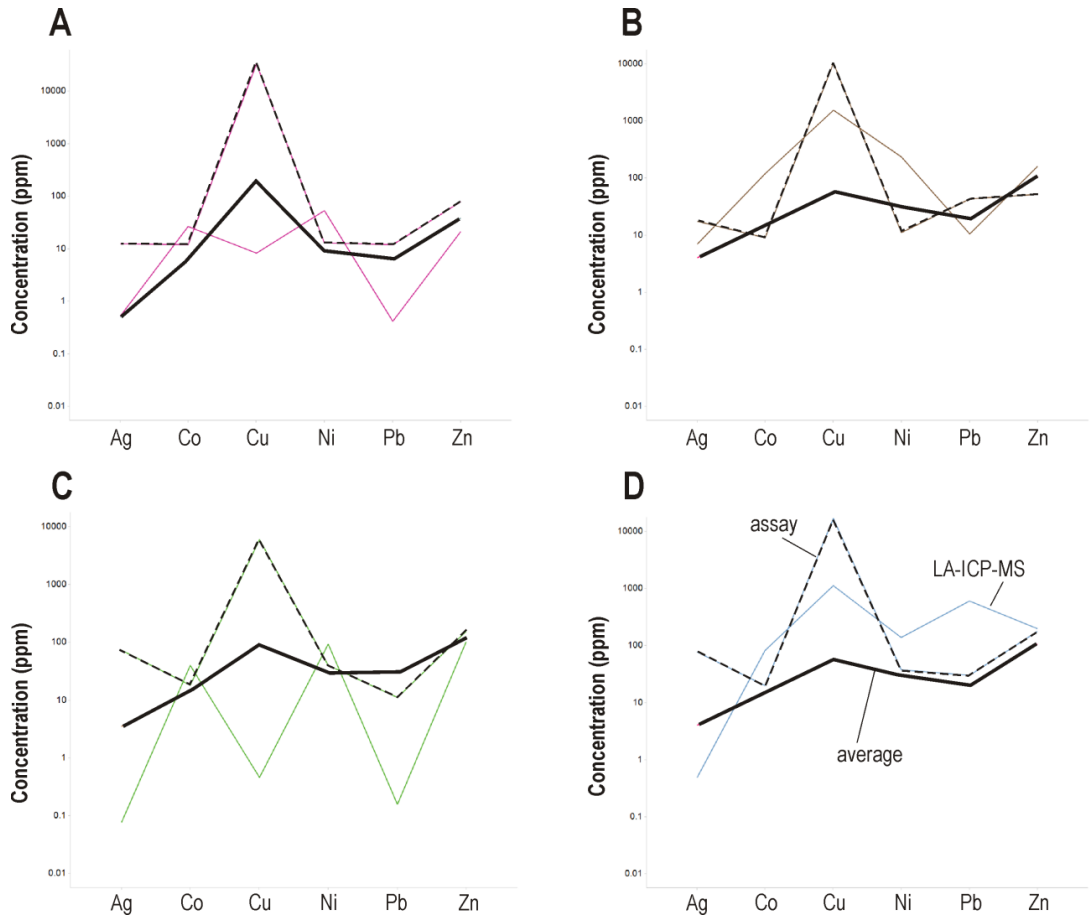

Figure 7-19: Median trace element concentrations from magnetite are compared to whole-rock assay results from the same depth (dashed line), and the average for the specific stratigraphic unit the sample was taken from (solid black line). **A:** MG-3; **B:** MG-6; **C:** MG-10; and **D:** MG-12. The stratigraphic units used for comparison were the median values taken from Table 15 (for the MV MG-3). IBU-CA (MG-6 & MG-12) and IBU-NEA (MG-10).

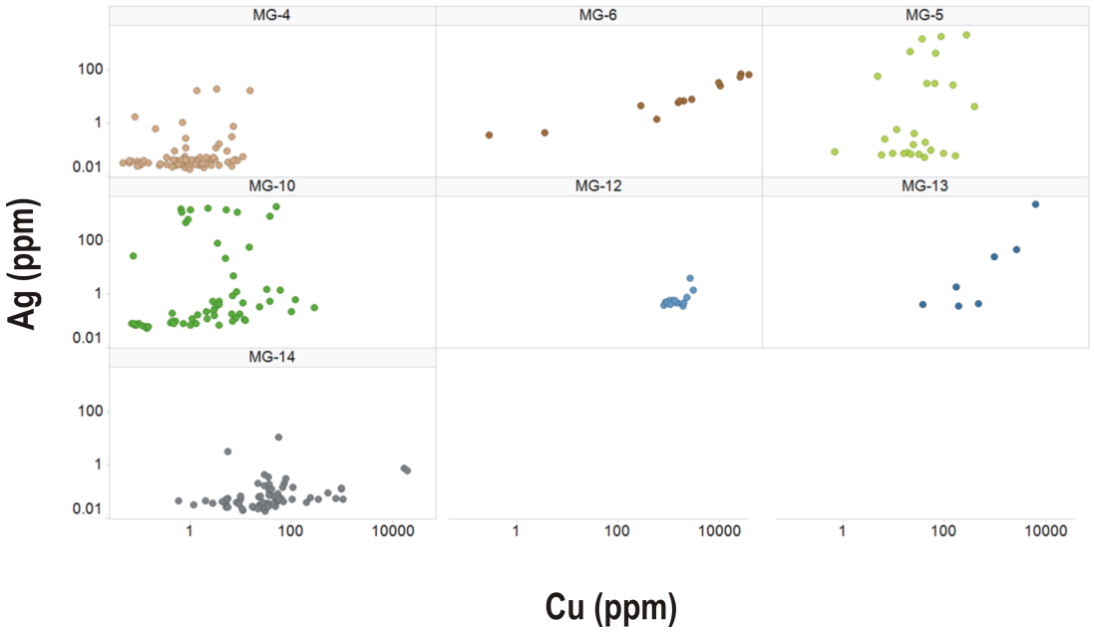

Figure 7-20: Silver vs. Cu plots for all of the magnetite from the sedimentary samples. Most samples shows an erratic relationship between these elements, magnetite from MG-6 and MG-13, however show a linear relationship.

Martitisation is a process which is thought to have an influence on the trace element contents of magnetite in hydrothermal systems. Nadoll et al. (2012, 2014) place a theoretical cut-off on the levels of martitisation below which the LA-ICP-MS analysis will not be adversely affected at <10% surface area. However, Angerer et al. (2012) have suggested that most spinel elements are retained during moderate-temperature martitisation. Cornell and Schwertmann (2003) on the other hand, have suggested that divalent cations are expelled during this process. This was tested on the Eiseb samples by comparing two siltstone samples which had contrasting levels of oxidation (Figure 7-21). MG-14, which reported moderate-high levels of martitisation (~60% of grain area), is from a hangingwall sample and MG-13, which generally has low levels of maritisation (<3% grain area), from a footwall sample. Both fall within the central part of the study area, and show fairly consistent trace element distributions. MG-14 reports marginally higher V and Ni contents, while MG-13 is higher for Mg, Al, Cr, Mn and Zn. Titanium, Co and Ga are very similar for both. If martitsation were expelling any trace elements during martitisation V should be the first because this element is extremely sensitive to changes in redox. Vanadium is present either in the V^{3+} or V^{4+} oxidation state depending on the oxygen fugacity conditions. At high fO_2 it becomes incompatible into the magnetite structure because of its 5+ oxidation state. The changes in abundance of this element in magnetite therefore tracks changes in fO_2. Martitisation involves increasing fO_2, which should have an

effect on the abundance of V. No significant changes in V concentrations in magnetite are evident between the sandstone which has undergone no martitisation, and the one which has, which suggests martitisation has little effect on the trace element chemistry of magnetite within the Eiseb.

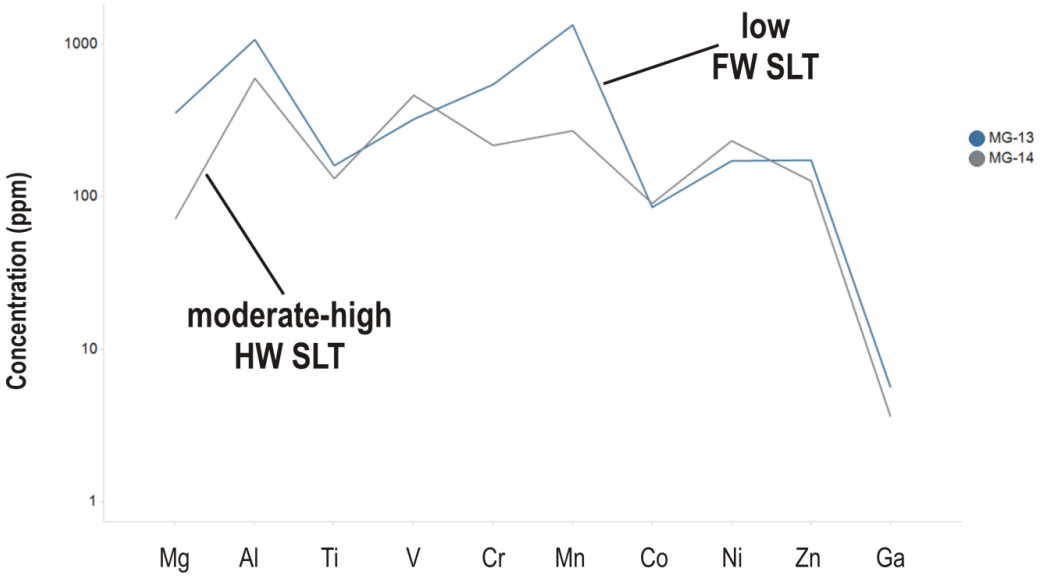

Figure 7-21: Median oncentrations of some spinel elements in magnetite from two siltstone samples with variable levels of martitisation. MG-14 is from a hangingwall (HW) siltstone (SLT) which shows moderate to high levels of martitisation for magnetite (borehole CZ-1). MG-13 is from a footwall (FW) siltstone which shows low levels of martitisation.

Petrographic analysis has suggested that the metamorphic conditions prevalent in this basin were never above 350˚C, never exceeding greenschist facies. These temperature estimates have been supported for the volcanic and metavolcanic samples on the basis of magnetite trace element using Ga vs. Sn, and Ti+V and Al+Mn scatter plots. Figure 7-22 illustrates that magnetite hosted in the sediments falls within restricted ranges on both of these diagrams, between 250-250˚C. These results overlap with the metavolcanic samples MG-1 and MG-3 and fall within the rage of deposits such as the Lucky Friday Ag, Pb-Zn veins from the Coeur d'Arlene mining district in Idaho (Nadoll et al., 2014; Doughty and Chamberlain, 1996). Further information about the geological setting in which magnetite formed can be gained using discriminant plots.

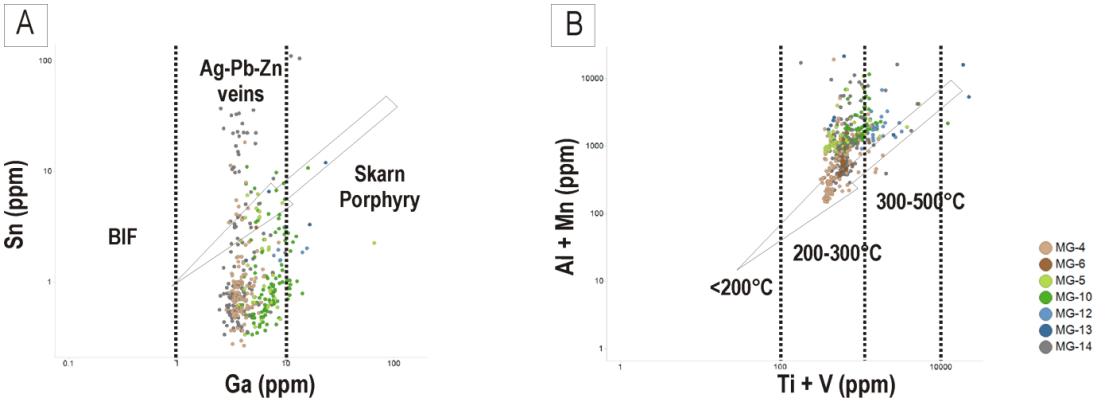

Figure 7-22: Tin vs. Ga (**A**) and Al + Mn versus Ti + V (**B**) for the sediment-hosted magnetite samples indicating restricted formational temperatures for this type of magnetite.

Discriminant plots are designed to highlight elements, element ratios or element combinations which group specific deposit types within distinct fields (Dupuis and Beaudoin, 2011). The discriminant diagrams Dupuis and Beaudoin (2011) developed have formed the bench mark for numerous studies into ore deposit fingerprinting using magnetite trace element geochemistry (Acosta-Góngora et al., 2014; Chen et al., 2015; Dare et al., 2012; Huang et al., 2014, 2016, 2015; Nadoll et al., 2014). These diagrams were constructed using the average composition of magnetite from a range of mineralised deposit types based on EMPA results from magnetite grains where individual analyses did not exceed <2 wt.% trace elements. The first two plots were developed to distinguish:

1. Ni-Cu-PGE deposits from all other deposit types (Ni + Cr vs Si + Mg);
2. VMS deposits from all other deposit types not distinguished in 1 (Al/(Zn + Ca) vs Cu/(Si + Ca)).

Dare et al. (2012) tested the validity of the Ni-Cu-PGE discrimination plot on the massive sulphide Ni-Cu-PGE deposits from the Sudbury Igneous Complex using LA-ICP-MS techniques on magnetite from both the whole-rock, and detrital till samples thought to be associated with these deposits. They found that while most of their data plotted within the field defined for Ni-Cu-PGE deposits, titanomagnetite from the Creighton deposits had unusually high Ni + Cr and low Si + Mg and plotted outside of the field. Boutroy et al. (2014) tested this diagram further with trace element compositions from 13 major Ni-Cu deposits from around the world. They found that the Ni-Cu field defined by Dupuis and Beaudoin (2011) accurately distinguished primary magnetite from these deposit types. Boutroy et al. (2014), however, also found that secondary magnetite from these deposits (associated with serpentinisation of the host rocks, related to replacement or within veins) plotted within the field defined by Dupuis and Beaudoin (2011) for VMS deposits. They attribute

this to the fact that most VMS deposits are characterised by low temperature replacement of sulfides by magnetite, a signature preserved by secondary magnetite in Ni-Cu-PGE deposits. Similar minor and trace element compositions for replacement, disseminated and vein-hosted secondary magnetite from Ni-Cu-PGE deposits were used to infer that they were formed from a similar fluid under similar physiochemical conditions, i.e. that they were contemporaneous.

The Eiseb samples were tested against these fields, using the same criteria (Figure 7-23). No sample with >2 wt. % trace element content was used (89 samples excluded). These plots confirmed that the magnetite from these samples share no characteristics with known Ni-Cu sulfide deposits, nor with VMS deposits. Based on the work of Boutroy et al. (2014) this could also indicate that none of the magnetite in the Eiseb formed from the replacement of sulfides.

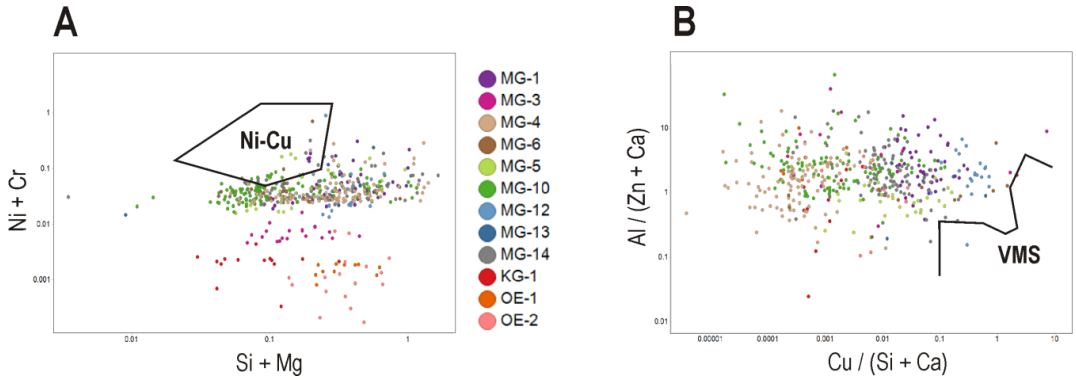

Figure 7-23: Ni + Cr vs. Si + Mg plot (**A**) and Al / (Zn + Ca) vs Cu / (Si + Ca) plot (**B**) of the Eiseb data using the fields defined by Dupuis and Beaudoin (2011) to discriminate between Ni-Cu sulfide deposits, and VMS deopsits. All elements calculated as weight percentages.

The second set of diagrams developed by Dupuis and Beaudoin (2011) are used to distinguish between IOCG, Kiruna, BIF, porphyry Cu, skarn and Fe-Ti-V deposits using Ni/(Cr + Mn) vs Ti + V and Ca + Al + Mn vs Ti + V plots. These diagrams are meant to be used in conjunction with each other to distinguish different deposit types (Figure 7-23 & Figure 7-24). BIF deposits, for example, commonly plot within the skarn field on the Ni/(Cr+Mn) vs. Ti+V diagram, and some Opemiska and Archean porphyry deposits overlap with the BIF field on the Ca+Al+Mn vs Ti+V diagram. Opemiska type deposits, however, can be distinguished using only the Ni/(Cr+Mn) vs Ti+V diagram. Nadoll et al. (2014) and Chung et al. (2015) extended the field for BIF on the Al+Mn vs Ti+V to include formations with lower trace element contents, whereas Huang et al. (2015) extended this field to accommodate slightly higher Ti+V concentrations, such as those found in the Bayan Obo deposit of Mongolia. The Ca+Al+Mn vs Ti+V diagram is most useful for the distinction of skarn, IOCG,

Kiruna-type and porphyry deposits. Figure 7-24 suggests that magnetite from the sediments in the Eiseb has an overwhelmingly IOCG-type signature based on the Ca+Al+Mn vs Ti+V discrimination plot, with the mineralised metavolcanic MG-3, and the footwall sandstone MG-4 suggesting a BIF affinity. The Ni/(Cr+Mn) vs Ti+V plot also suggests this overlap between the BIF and IOCG signature for some of the magnetite, but most of the data fall within the skarn field. The basement samples are not distinguished in the Ni/(Cr+Mn) vs Ti+V diagram because of their low Ni/(Cr+ Mn) ratio, but in the Ca+Al+Mn vs Ti+V diagram they plot within the IOCG field with some scatter into the skarn field for KG-1, and scatter into the porphyry field for OE-2. OE-1, however, plots firmly within the porphyry field on this diagram.

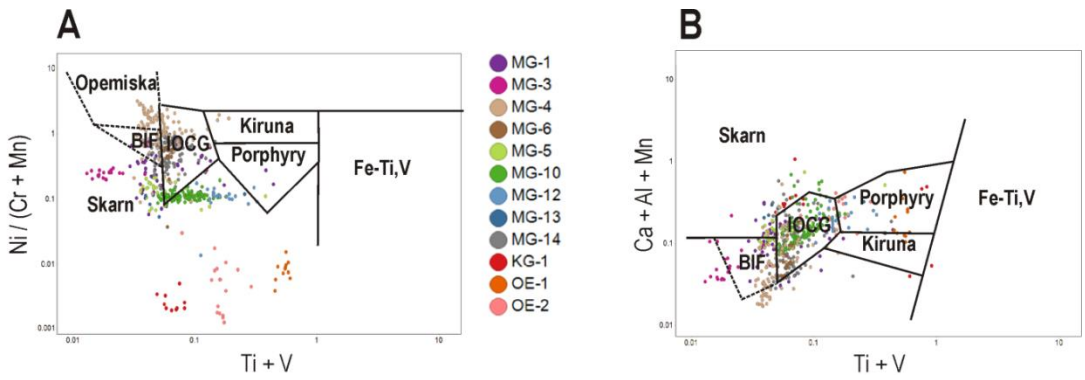

Figure 7-24: Ni/(Cr+Mn) vs Ti+V (**A**) and Ca+Al+Mn vs Ti+V (**B**) discriminant plots to distinguish magnetite from Kiruna, IOCG, porphyry Cu, Fe-Ti-V and BIF deposits. In **A** the Eiseb data plot mostly between the BIF and IOCG fields, with the mineralised metavolcanic sample (MG-3) plotting in the skarn field at low Ti +V, and the basement rhyolites (KG-1, OE-1 and OE-2 plotting in the same field but with higher Ti+V and lower Ni/(Cr+Mn). MG-10 and MG-13 show variable Ti+V and plot within the skarn field. **B** suggests that the Eiseb magnetite has an overwhelmingly IOCG signature, with minor scatter into the skarn and BIF fields. The sandstone of MG-4 and the mineralised metavolcanic MG-3 plot partly inside, but mostly outside, of the BIF field. The basement sample OE-1 plots mostly within the porphyry field, as do some MG-12 grains.

The diagrams of Dupuis and Beaudoin (2011) suggest that the basement to the Eiseb has a signature similar to that of magnetite from porphyry deposits but with lower Ni/(Cr+Mn). Magnetite from within the Eiseb is characterised by a dominantly IOCG type signature, a feature shared by the metavolcanic sample MG-1. MG-3 and MG-4 suggest a second signature, more akin to BIF, or a skarn deposit.

IOCG type mineralisation has been located in the Great Bear magmatic zone in the Northwest Territories in Canada, including the past producing Terra Mine, and Sue-Dianne, NICO, Damp, Fab and Nori/Ra Deposits. Here magnetite trace elements were measured from a range of deposits by LA-ICP-MS (Acosta-Góngora et al., 2014). The results of their study were plotted on the same discrimination diagram by Dupuis and Beaudoin (2011); however, much of the data plotted outside of the defined fields for IOCG deposits, in

similar positions to the bulk of the Eiseb data on the Ni/(Cr+Mn) vs Ti+V diagram. Acosta-Góngora et al. (2014) attribute this 'skarn-like' signature to the characteristically low Ni concentrations of the south-central part of the Great Bear magmatic zone and concluded that the complexity of the IOCG signature was not adequately addressed by the discriminant plots of Dupuis and Beaudoin (2011).

Huang et al. (2014) found that magnetite trace elements from the Fe-Cu deposit of the Eastern Tianshan Orogenic Belt (Hami Region) in NW China overlapped with the skarn field on the Ni/(Cr+Mn) versus Ti+V diagram of Dupuis and Beaudoin (2011). This was interpreted as indicating a hydrothermal source for some of these deposits, whose origin is still contentious. There was also minor overlap of the data with the BIF and IOCG fields. Direct comparisons of the distributions of the spinel elements from this Fe-Cu deposit with the distributions of these elements in BIF and IOCG deposits showed important differences between these deposits, despite their geochemical affinities. A similar method has been employed for the Eiseb data (Figure 7-25).

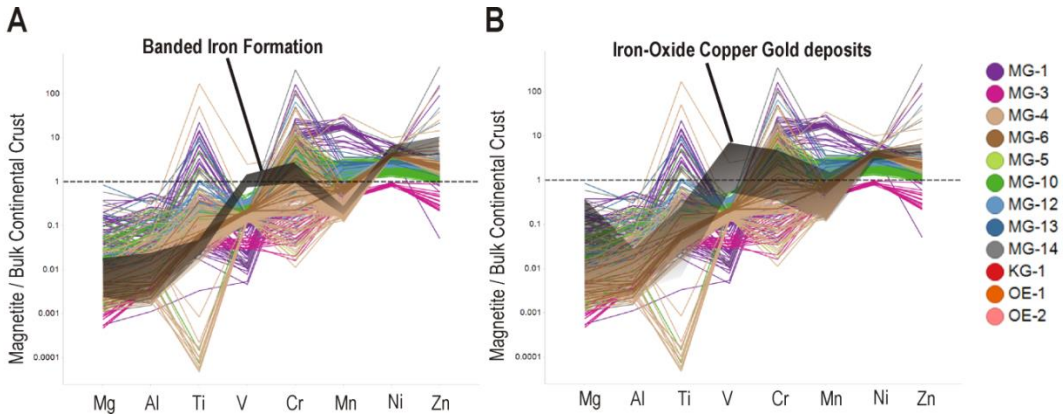

Figure 7-25: Comparison diagrams of the normalised trace element patterns for magnetite from the Eiseb with **A**: Banded Iron Formation (BIF) and **B**: Iron-oxide Copper Gold (IOCG) deposits. The data have been normalised to bulk continental crust using values from Rudnick and Gao (2003), and the compositional fields for BIF and IOCG deposits are after Dupuis and Beaudoin (2011).

Figure 7-25 demonstrates clearly that although some of the Eiseb data plot within both the BIF and IOCG fields in the Dupuis and Beaudoin (2011) discrimination diagrams, the Eiseb data show much more variable trace elements concentrations.

IOCG deposits linked to the SSC mineralisation in the Greater Lufilian Arc is not a new suggestion. In his thesis Lobo-Guerrero Sanz (2005) proposed that there was a genetic link between the sediment-hosted copper mineralisation seen across the KCB and CAB, and granitoid intrusions with an IOCG-type character. Those linked to the SSC deposit at Witvlei in central eastern Namibia are dated between 1108 to 1059 Ma (Okatjepuiko site), which is

within error of the Re-Os date reported by Sillitoe et al. (2015) of 1089 to 1054 Ma for the mineralised pre-Katangan basement of the Domes regions in the Zambian Copperbelt. Sillitoe et al. (2015) propose that this pre-enrichment was critical to the formation of the deposits seen within parts of the Zambian Copperbelt, but while they favour porphyry type enrichment of the pre-Katangan basement, an IOCG-type enrichment of the pre-Ghanzi Group basement, as suggested by Lobo-Guerrero Sanz (2005), is tentatively supported by magnetite trace element analyses herein. Although the Oorlogsende sample, OE-1 plotted within the porphyry field, the zircon geochronology results do not support these younger rocks as a major source of detritus to the Eiseb.

7.3.3 Summary

Alteration in the rhyolites is accompanied by increased concentrations of V in magnetite. This suggests that alteration has a reducing influence on the fO_2. In the already deformed metavolcanics the slight decrease in V between magnetite in MG-1 and MG-3 suggests that mineralisation was accompanied by increases in fO_2. The decrease in Ni contents for magnetite during mineralisation can be attributed to the co-crystallisation of cobaltite, which contains up to 3 wt.% Ni. Zinc concentrations almost double from the unaltered rhyolite to the altered one, a feature which is seen both within the magnetite chemistry, and in the overall mineral assemblage, suggesting the fluids associated with magnetite precipitation were strongly enriched in Zn. This enrichment is seen in the metavolcanic which has undergone deformation, but less so in magnetite from MG-3 which is Cu mineralised. The decrease in Zn in magnetite from MG-3 is taken to imply that a Zn-bearing phase fractionated out of the fluid at the same time as magnetite. The sedimentary rocks all have relatively high Zn contents, varying between 100-200ppm with no clear relationship to mineralisation. This is consistent with petrographic observations which showed no significant Zn-bearing minerals associated with Cu-Ag sulfides in the sedimentary rocks, however, these values still imply that the fluid was enriched in Zn. Manganese, which is strongly enriched in the altered rhyolites and less enriched in the metavolcanics, does not appear to have been affected by the mineralising event, but was mobilised during alteration of the volcanic rocks. The concentration of this element remains relatively consistent between magnetite from mineralised and unmineralised sedimentary rocks. This suggests that Mn was not involved in the precipitation of magnetite or the mineralising event, i.e. there was no co-precipitating Mn-phase. In the

deformed metavolcanic Cu reaches 200pm, while in MG-3 only ~8ppm Cu was reported. This indicates that the fluid was enriched in Cu at MG-1, and that a Cu-phase was co-precipitating with magnetite in MG-3. The same is seen in the Pb values recorded in magnetite. They are very high in MG-1 (>500ppm) and fall considerably in MG-3 (0.42ppm). Lead appears to have also been enriched in the altered sample OE-2, but whether this is a function of nano-scale inclusions or true accommodation of Pb into the magnetite structure is uncertain. The former is more likely, and would suggest galena precipitated prior to magnetite.

The strong overlap in concentration of the spinel elements between magnetite in the metavolcanic and sedimentary rocks suggests a common fluid enriched in base metals (Mn, Ni, Co, Cu and Zn). The Sn vs. Ga and Al+Mn vs. Ti+V diagrams of Nadoll et al. (2014) suggest that the temperatures of formation were in the region of 200-300˚C for the metavolcanic and sedimentary rocks, with slightly higher temperatures associated with MG-3 and up to 350˚C for the basement acid volcanics. The overlap in trace element concentrations between magnetite from the sedimentary rocks and the metavolcanics not only suggests precipitation from a fluid of similar composition, but in order to maintain this composition, there would have to have been a low fluid-rock ratio, or fluids would have to have been in equilibrium with the surrounding rocks, i.e. developed under the ambient pressure and temperature conditions associated with metamorphism. If the fluid-rock ratio were high, or the fluids were not in equilibrium with ambient metamorphic conditions, magnetite would show much more variability in trace element contents as the fluid would have had to equilibrate with a variety of host-rocks. MG-10 marks a transition in the magnetite chemistry. Trace elements in this sample account for a total of 0.3 wt% compared with 0.9 wt.% in MG-12. Low trace element concentrations in magnetite from MG-10 are associated with coupled substitution for V with Mn, Zn, Co and Ni. Overall the trace elements suggest that the fluid did not contain significant quantities of sulfur, as suggested by the dominance of chalcocite and bornite over chalcopyrite (in order of increasing sulfur content). Magnetite contains numerous chalcophile elements which favour sulfides, their presence in magnetite therefore also suggests low sulfur availability in the fluid. The availability of Fe^{3+} is also a limiting factor in precipitation of Cu-sulfides with chalcocite indicating limited availability of Fe^{3+} in the fluid/host-rock (Muchez and Corbella, 2012).

In order to distinguish between mineralised and unmineralised metavolcanics V vs. Ni binary plots can be used. This plot will also identify magnetite from rhyolites which have undergone alteration (OE-2) from truly magmatic magnetite (OE-1). The Nb vs. Y concentrations of magmatic magnetite can also be used to distinguish the tectonic setting of the parent rock, which in this case was a 'within-plate' rhyolite emplaced within an attenuated lithosphere.

In order to identify mineralised horizons in the sedimentary rocks from unmineralised lithotypes, V vs. Co plots can be used. The discrimination plots devised by Dupuis and Beaudoin (2011) demonstrate that there is no VMS or Ni-Cu-PGE signature in the magnetite from the Eiseb, however, an IOCG type affinity is suggested by high Ti+V contents of these rocks relative to Al+Mn.

7.3.4 Palaeomagnetic Investigation

Although the Fisher statistics are not very good for the ChRM, the samples are recording a common direction, as seen in Figure 6-8. The overall mean ChRM direction for the Eiseb samples gives a pole position of 51˚S, 26.1˚E. This position falls on the Triassic portion of the apparent polar wander path (APWP) for the Kalahari craton defined by Torsvik et al. (2012). APWPs are assembled by combining paleomagnetic pole positions from various continental fragments into a coherent dataset (Dunlop and Özdemir, 2001; Tauxe, 2010). The APWP of Torsvik et al. (2012) was defined on the basis of palaeomagnetic data compiled according to the classification system of Van der Voo, where only data with a quality factor Q ≥ 3 was used (Van der Voo, 1990). The quality factor of Van der Voo (1990) measures the accuracy of the paleopole determination used to construct an APWP as a score out of his seven proposed criteria (Van der Voo, 1990):

1. the age of the rock has been reliably determined, and the assumption that magnetisation is the same age as the rock is valid;
2. sufficient number of samples tested (n >24 ; k ≥10, and the α95 ≤16˚);
3. appropriate treatment in a paleomagnetic laboratory, samples should all be adequately demagnetised and the magnetic components effectively isolated using methods such as PCA;
4. field tests should be used that constrain the age of magnetisation;

5. structural controls are known, that the strata which are being tested are part of a craton or tectonic block which has been used to define the APW, and that the orientation of the strata is known, and has been used in a fold test to determine the relative timing of the magnetisation;
6. the presence of reversals;
7. no resemblance to paleopoles of younger age.

Results of Q ≥ 3 were found to be sufficient for Phanerozoic data sets of Europe and North America, and according to Tauxe (2005) most authors use poles with Q > 2. Other criteria have also been proposed, which are modifications to the Van der Voo (1990) quality factor, such as Besse and Courtillot (2002). Their method requires that the poles used to construct an APWP satisfy the first five criteria fully before being included, but do not require the last two. Once 'reliable' poles for uniform time intervals have been selected the results have to be combined into an APAW using a 'curve-fitting' method (Tauxe, 2005). A master path for the APWP of Gondwana produced by Besse and Courtillot (2002) tracks the movement of continental fragments as far as 200 Ma ago. This was extended by Torsvik et al. (2008) as far as 320 Ma, and again to 550Ma (Torsvik et al., 2012; Torsvik and Cocks, 2013).

The results of this study have been plotted according to the most recent APWP for Gondwana of Torsvik et al. (2012), which was constructed using 229 poles, and excluded results from peri-Gondwana elements (e.g. Avalonia) (Figure 7-26). The results suggest and age of ~230 Ma, with a large error margin of ±20 Ma (Figure 7-27).

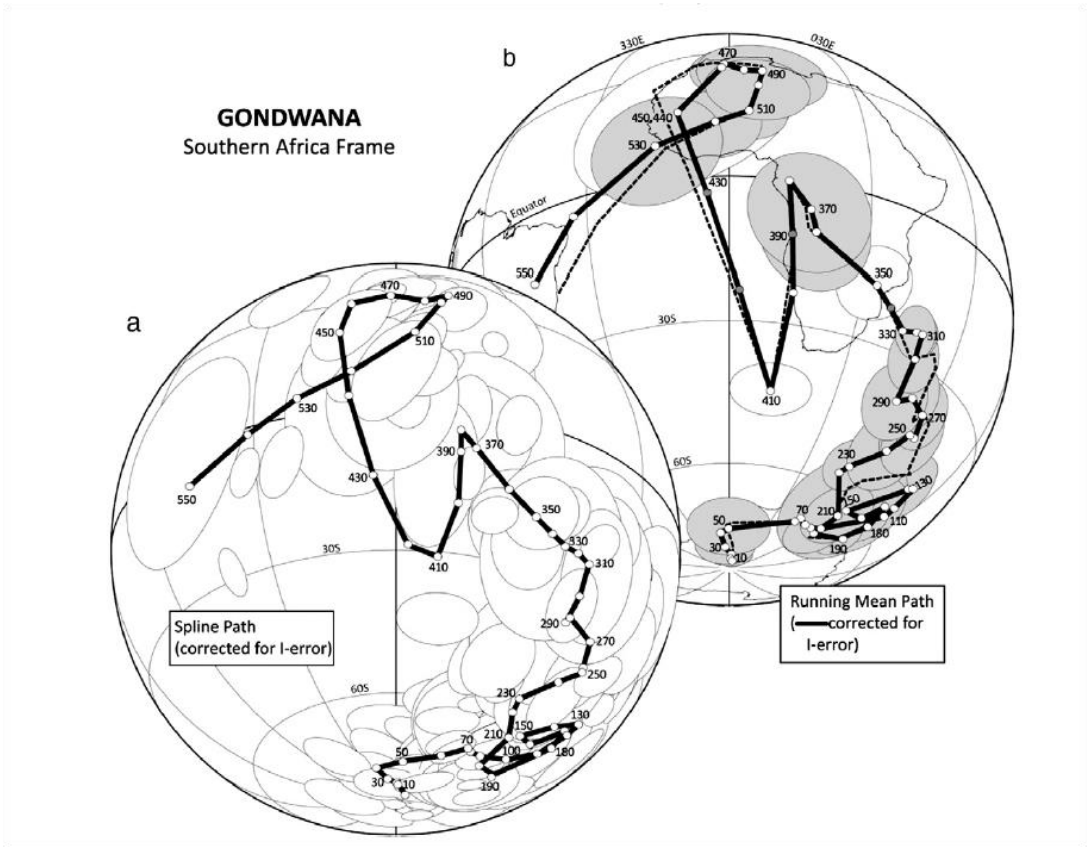

Figure 7-26: The APWPs for Gondwana constructed using the fitted spherical spline path (a) and the Running Mean path (b) methods. The white shading shows the 95% confidence ovals for the input poles and the grey shading shows the α_{95} ovals after a sedimentary inclination correction as been applied. The results of this study were plotted using the APWP spline path in (a). Figures taken from Torsvik et al. (2012).

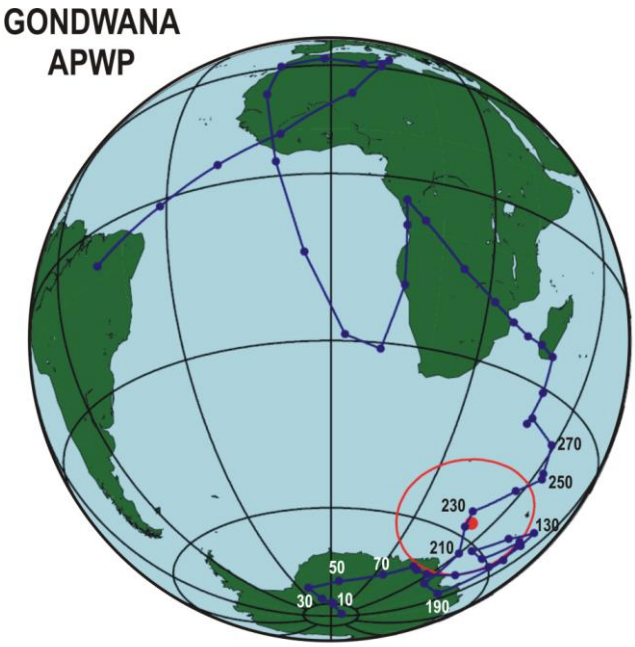

Figure 7-27: Pole position (red dot) from the Eiseb plotted on the APWP (spline path) of Torsvik et al. (2012) (blue line). The α_{95} confidence ellipse is plotted as a red circle around the pole.

The textural evidence presented in the Section 5.6.3 strongly suggests magnetite growth occuring during deformation, i.e. during the Pan-African Damara Orogeny (~530 Ma). This is inconsistent with the Triassic date suggested by the paleomagnetic study. Although magnetite from the Eiseb could be recording a remagnetisation event, for this to have been regional, large-scale tectonic processes would have to have been active during this time. Such large-scale processes include the formation of orogenic belts, deformation and metamorphism, e.g. remagnetisation of the Paraguay, Pampean and Dom Feliciano belts occurred during the closure of the Clymene Ocean during the final stages of assembly of western Godwana (Font et al., 2012; Tohver et al., 2006). During the Triassic the Eiseb would have been in the vicinity of the South Pole and thus part of an extensive Gondwana glaciation. The next major regional event which could have affected the Eiseb was the emplacement of the Central Atlantic Magmatic Province at ~200 Ma (and opening of the Central Atlantic Ocean ~195 Ma), which likely resulted in the break-up of Pangea (Deenen et al., 2010; Labails et al., 2010; Torsvik et al., 2012). Neither of these is likely to have produced the regional-scale ChRM recorded by the Eiseb rock because they are too recent.

Another alternative is that the ChRM is chemical remanent magnetisation (CRM). There is evidence of Permo-Carboniferous remagnetisation associated with both the Hecynian/Alleghenian orogen, and also the stable carbonate platform rocks in the Appalachians which have no spatial relationship to orogensis at that time. A low temperature CRM was found to be carried by authigenic magnetite for the Appalachian limestones (Jackson, 1990). The orientation of most of the magnetite in this study, however, was parallel to the foliation, therefore unlikely to be of an authigenic origin. The trace element study on magnetite suggests that it is metamorphic in origin. CRM can also be imparted through phase transitions, such as the oxidation of magnetite to maghemite (Dunlop, 1995). There was no suggestion however, of the presence of maghemite during the rock magnetism part of this investigation, rather that magnetite was very pure, as would be expected from metamorphic magnetite.

The most likely cause of the Triassic date suggested by the paleomagnetic investigation is that an error was made somewhere. The ChRM sample means cluster fairly well so it is unlikely that the error was introduced during demagnetisation. An error in the sample orientations would have a dramatic impact on the results of the mean ChRM, and although every effort was made to ensure that this data was correct, it seems the most likely source of error.

8 Synthesis

The Ghanzi Group sediments were deposited within an intracontinental rift basin characterised by bimodal volcanism and block faulting. The basement complex to the KSG Rift Zone in the vicinity of the Eiseb shows little evidence of deformation other than minor brittle fracturing of phenocrysts within the rhyodacites of the Oorlogsende Member exposed to the north of the study area. A similar feature has been observed in the Zambian Copperbelt, where the pre-Katangan basement shows no evidence of the fold-thrust event which deformed the Katangan Supergroup. In Zambia this has been interpreted as a local decoupling of the basement from the Katangan Supergroup during Lufilian deformation (Daly et al., 1984; McGowan et al., 2006). A similar scenario is suggested here for most of the pre-Ghanzi Group basement in central eastern Namibia during the Damara Orogeny (Nückopf-Kgwebe Formation). The older basement meta-volcanics, however, dated at ~1180 Ma, were deformed during this orogeny, due to their proximity to the basement horst feature. The immobile elements Nb and Y detected in magnetite from the younger (1100 Ma) Oorlogsende Member unaltered basement rhyolite confirm the findings of Kampunzu et al. (1998), that these volcanics were 'within plate' and injected into an 'attenuated continental lithosphere' as per the classification scheme devised by Pearce et al. (1984). Borg and Maiden (1987) reported similar findings from the basalts of the Nückopf-Kgwebe Formation at Klein Aub. Although not deformed as such, interaction with a fluid is suggested by the secondary micas seen filling the fractures in the altered rhyolite (OE-2), as well as calcite, epidote and sericitisation of feldspars. There is no clear evidence to suggest multiple overprinting alteration events, therefore a single, perhaps prolonged, event is suggested, most likely spanning the length of the Damara Orogeny which peaked ~530 Ma (Ahrendt et al., 1978). Whole-rock geochemistry suggests that alteration has resulted in a loss of SiO_2 and Na_2O and an introduction of K_2O. Magnetite geochemistry and petrography have shown that base metals (Cu, Zn, Co, Ni and Pb) were also introduced into these rocks during alteration, as was V. At Klein Aub the basalts which form part of the pre-Ghanzi basement in Namibia show evidence of Cu, Zn and Co leaching during alteration associated with the Damara Orogeny (Borg and Maiden, 1987; Borg, 1988a). The alteration of the basement rocks, such as those at Klein Aub as a feasible explanation for the Cu endowment of the KCB is supported by the presence of Cu-bearing minerals in the altered rhyolites exposed at Eiseb. The source of the other base metals, particularly Co and Zn, could equally have been these leached basalts. Sweeney et al. (1991) also support a pre-Katangan basement source for the metals of the Zambian Copperbelt.

The basement horst shows evidence of alteration, but also of dynamic deformation. Deformation of this inlier appears to have been coeval with the deformation of the Ghanzi Group in the Eiseb, suggesting deformation during the Pan-African Orogeny (Daly et al., 1984; Miller, 1983; Porada and Berhorst, 2000). The dextral movement on the basement horst drags and stretches the strata around this feature, suggesting that sedimentation occurred after this block was uplifted, and then rotated after lithification of the basin sediments. This is confirmed by zircon geochronology, which has shown the (meta-) volcanics in the vicinity of the basement horst to be the primary protolith contributing detritus to the basin.

Deposition of the Ghanzi Group sediments commenced sometime after 1170 Ma in the Eiseb, and after ~1100 Ma in Botswana, as controlled by the position of basement highs (Schwartz et al., 1996, Kampunzu et al., 1998). The minimum age of deposition for this Group is set by the basal sequence of the Damaran, bracketed by the Blaubeker diamictite at ~635 Ma (Horstmann et al., 1990). Regional uplift during early Ghanzi Group sedimentation is evidenced by the thick sequences of sandstones and conglomerates commonly reported from Botswana and eastern Namibia (Borg and Maiden, 1986; Borg, 1988a; Modie, 1996). The absence of substantial conglomerate beds within the basal sequences of the Eiseb could indicate that movement was restricted in this area, or more likely, that drilling has not accessed these beds yet. Deposition of largely fluvial coarse continental siliciclastic material (Ngwako Pan Formation) into the Eiseb was followed by the deposition of finer marine to lacustrine sediments (D'Kar Formation). At Klein Aub, and within Botswana, lacustrine environments were favoured for the deposition of most of the D'Kar Formation (Borg and Maiden, 1986; Modie, 1996; Ruxton, 1981). These interpretations are not challenged by the data presented for the Eiseb.

The sedimentary successions of the Ghanzi Group underwent deformation and metamorphism to greenschist facies during the Damaran Orogeny (530 ± 10 Ma). This resulted in basin inversion and the creation of secondary permeability, facilitated by competency contrasts, bedding parallel thrusting and the reactivation of pre-existing rift-related structures with roughly E-W and ~N-S orientations.

Cu-Ag mineralisation, primarily bornite and chalcocite, is hosted within coarse laminae in finer-grained host-rocks. This relative grain-size difference can be in the order of a few microns, or tens of microns, and holds true across a range of rock types, including sedimentary rocks such as siltstones or argillites to the metavolcanic rocks in the western

part of the study area. The secondary permeability in the metavolcanics shows a strong relationship to deformation and the development of layering/banding (gneissic texture) within the rock.

There is no evidence of a significant pre-orogenic stage to the Cu-Ag mineralisation seen in the Eiseb. The bulk of the Cu-Ag mineralisation occurs parallel to the foliation, but within laminae of enhanced permeability, and in the pressure shadows of resistant minerals such as magnetite, consistent with growth during deformation. Textural evidence from the Central Anticline and the Eastern Anticline show that at least some of the Cu sulfides were formed by replacement of evaporite minerals during deformation. Inclusions of Cu sulfides within magnetite are most likely the result of magnetite replacing sulfides which contained some copper.

Magnetite chemistry suggests that magnetite grew during metamorphism, most likely from precursor Fe-bearing minerals such as biotite or pyrite. The growth of magnetite from metamorphic/hydrothermal fluids, or from a precursor Fe-bearing phase, would have produced localised, but sharp reductions in the fO_2 of the fluid it was precipitating from, which in turn could have triggered the precipitation of Cu-Ag sulfides. The genesis of magnetite through the conversion of pyrite is thus favoured, as this would also produce the H_2S required for the precipitation of sulfide minerals. Borg and Maiden (1986) report abundant pre-deformation pyrite within the Kagas Member of the Klein Aub Formation (D'Kar Formation equivalent), something not seen in the Eiseb, perhaps because Type 2 magnetite is replacing pyrite. This would then account for the close spatial relationship between the Cu-Ag sulfides and magnetite, in which sulfides are often observed replacing magnetite. The presence of chalcophile elements within magnetite is also thus explained, they were not competing with coeval sulfide precipitation. Silver was not noted within the sulfide inclusions in magnetite mapped during EMPA, suggesting that silver precipitated late in this evolving hydrothermal system, also suggested by its location along lattice planes in Cu-Fe-sulfide minerals. Galena is the only other significant sulfide present. Although sphalerite and barite are known to occur, they are not as common as galena. Galena sometimes forms inclusions within both magnetite and the ore-stage Cu-Ag sulfides, suggesting that this phase formed at least partly pre-deformation. There is a second stage of galena which is present with chalcocite and together they replace magnetite (PST-2D2-1) which implies that galena was part of the main ore assemblage in the eastern study area.

Vein-hosted and disseminated Cu-Ag sulfide mineral assemblages within the host-rock are consistent for any given sample. This was confirmed for the metavolcanic rocks, the central anticline, and samples from the eastern study area. There are no replacement textures between the disseminated sulfides which suggest remobilisation, let alone remobilisation to form veins. Sillitoe et al (2010) conclude that the similarities between disseminated and vein-hosted mineralisation argue for them being contemporaneous. Work done by Dawborn (2012) prior to this project showed that not only was the mineralogy the same between these different mineralisation styles, but so were textures. Magnetite from PST4D-2-2 contained inclusions of Cu-sulfides which preserved the exsolution textures developed between bornite and chalcocite, a feature also observed in foliation parallel sulfides elsewhere in the rock. Remobilisation of these minerals would have affected the exsolution textures if the sulfides had to migrate into the foliation. These inclusions also attest then to the close temporal relationship between sulfide and magnetite precipitation. Sillitoe et al (2010) draw parallels with porphyry copper systems in which fine-grained disseminated and breccia/stockwork mineralisation styles are contemporaneous. Rare igneous intrusions have also been identified within the CAB and KCB which help to constrain the timing of mineralisation, including the Boseto deposit in Botswana. These intrusions contain the same sulfide and gangue assemblages as their host-rocks, implying that the intrusions and sedimentary hosts were mineralised at the same time, which means that the mineralisation cannot therefore be diagenetic. McGowan et al. (2006) support a synorogenic timing for mineralisation at Nchanga, during basin inversion and contractional tectonism during the Lufilian orogeny as a means of fluid mobilisation and expulsion. Brines would necessarily be the complexing agents with which the fluids carried metals either in pulses, such as at Kansanchi and Frontier, which spanned the peak of Lufilian deformation, or as late-stage discrete events, such as Klein Aub.

The fluids responsible for the scavenging, transport and deposition of iron species and base metals probably resulted from metamorphic devolitisation reactions primarily within the Ghanzi Group. This fluid was either in equilibrium with the metamorphic regime, causing only minor alteration of the country rocks and subtle variations in magnetite trace element chemistry, or there was a low fluid-rock ratio. Circulation of this fluid was driven by deformation and the enhanced geothermal gradient associated with orogenesis and concomitant plutonic intrusions. The abundance of base metals in magnetite suggest that there was limited sulfur available in the fluid. Interaction of this fluid with basinal brines is not excluded however. El Desouky et al. (2008) propose a post-orogenic fluid mixing model

for the ore seen at Lufukwe where one of the fluids was Cu-rich, ≥180˚C with salinities ≥7.7 wt.% NaCl equivalent travelling up strike-slip fault systems and intersecting another, colder, low salinity, reducing fluid. Precipitation of sulfides results from reduction, lowering of fluid temperature or lowering of salinity.

El Desouky et al. (2008) also found an association between mineralisation and NE-SW to ENE-WSW faults, indicative of a reactivation of early rift-related structures during orogenesis. Evidence for an association between stratiform copper mineralisation and orogenesis is not restricted to the PAL, a recent paper on the Paleoproterozoic Nussir deposit in Arctic Norway links this deposit directly to a syn-orogenic setting (Perelló et al., 2015). The Nussir deposit is the oldest sediment-hosted copper deposit yet discovered at 1761 ± 8 Ma and 1768 ± 7 Ma (Re-Os geochronology). This age places its genesis syntectonically with the Svecofennian (Svecokarelian) Orogeny during the amalgamation of the Columbia supercontinent. Paleomagnetic investigations into the Michilla district stratabound copper deposits in Brazil found that mineralisation was also largely post-tectonic (Townley et al., 2007). Similar investigations by Symons et al. (2011) for the mineralisation within the Kupferschiefer Deposits at Sangerhausen (Germany) found two ages for the mineralisation there at ~149 Ma and ~53 Ma from host-rocks which are ~255 Ma. Borg at al. (2012) highlight the significance of these dates as correlating with major crustal events, the London-Bohemia Swell (~150 Ma) and the opening of the Middle Atlantic in the easly Eocene (~53 Ma). Major crustal events, whether thermal, magmatic or tectonic, are easily capable of providing, mobilising and channelizing the huge volumes of metalliferous fluids required to form such large scale deposits as the Kupferschiefer.

A point of contention in the literature has long been how to reconcile the timing of vein-hosted and disseminated mineralisation present in SSC deposits. The disseminations have long been regarded as evidence of early diagenetic/syngenetic mineralisation. The onset of deformation during basin inversion is thought to then 'mobilise' the disseminations into veins. In this way the two occurrences are assigned to different events, and as such the definition of SSC deposits is stretched to cover the whole, from early diagenesis through to basin inversion in mineralising systems which are active over millions of years (Blundell et al., 2003; Cailteux et al., 2005; El Desouky et al., 2010; Hitzman et al., 2005, 2012, 2010). This type of blanket inclusion in ore deposit terminology hampers exploration efforts because of plethora of aspects inherent in the definition, all underpinned by a diagenetic origin at the start of these deposits. Groves et al. (2010) presented a similar argument with

reference to IOCG deposits where, "a too-embracing definition which includes associated deposits and potential end members and analogs" has had negative impacts on exploration because of a failure to produce robust models. In the context of SSC deposits, Maiden and Borg (2011) discuss how this failure has resulted in exploration models driven by 'favourable horizons' where regional redox boundaries ultimately control the location of mineralisation (Maiden and Borg, 2011). Herein a new definition is proposed, which includes the current geological, geochemical and tectonic characteristics of some SSC deposits within the KCB, the Zambian Copperbelt and elsewhere, 'orogenic-sediment-hosted-stratiform-copper' (O-SSC). This distinguishes these emerging deposits from those described by authors such as Alex Brown of low-temperature, long-lived, diagenetic to syngenetic sediment-hosted stratiform copper deposits with no temporal association to an orogeny (Brown, 2014).

9 O-SSC Deposits

O-SSC deposits show geochemical, textural and structural evidence of ore-genesis either during early, syn- or late-deformation due to orogenesis, and without the requirement of a pre-ore diagenetic/syngenetic SSC component which can be 'upgraded'. The primary controls on Cu sulfide deposition for this type of deposit are (Figure 9-1):

- **structural controls** - e.g. bedding-parallel faulting and areas of structural complexity. Where strata are pinched or appear thinned, these are likely to have focussed ore-bearing fluids. Syn-rift structures, both parallel to the main rift and perpendicular to it, are likely to be reactivated during deformation and will form deep-seated fault networks which can mobilised and channelize metalifferous fluids. Sites of dilation such as fold hinges and thrust/fault intersection. These features can be recognised using geophysical techniques such as gravity or magnetic surveys for strata under cover (overburden or forested), and from careful geological mapping of field relationships if the strata are exposed;
- **gravity anomalies** - these may correspond to uplifted basement fragments or indicate syn-deformation intrusions, both of which would focus fluid flow and reactivate deep-seated syn-rift faults which can channel hydrothermal fluids, or which may contain important pre-enrichments of ore minerals/metals;

- **magnetic anomalies** - these may indicate basement fragments or intrusions, but will also highlight faulting and contrasting magnetic responses in the underlying geology;
- **stratigraphic boundaries** - rheological contrasts and redox boundaries could play an important role in focussing fluid flow and forcing precipitation of ore. These may be difficult to distinguish on a local scale;
- **permeability** - structural sources of secondary permeability: brecciation in competent rocks and foliation/cleavage in fine-grained lithotypes; fine-grained layers with sandy interbeds or metamorphic segregation/gneissic-texture development, can also result in increased secondary permeability.

A schematic model for O-SSC deposits is presented in Figure 9-1. This model highlights the different features which may be important in locating this type of mineralisation, and as such, is in fact a number of models presented together. Deciding which are the most important is an ongoing challenge for exploration geologists.

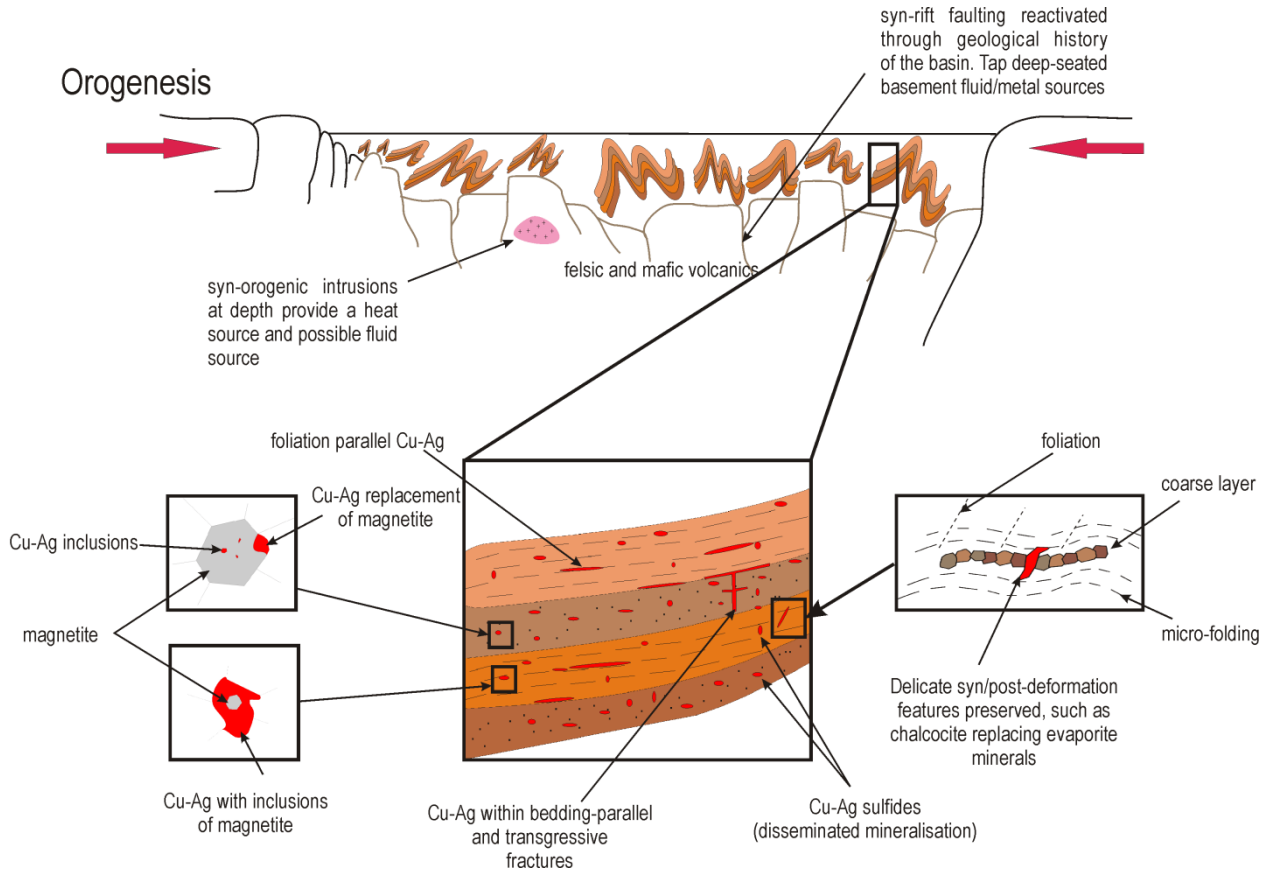

Figure 9-1: Schematic diagram of O-SSC deposits showing the main features which should be tested for exploration purposes. The rift basin is exposed to regional compression (red arrows) during orogenesis which causes folding of the basin sedimentary rocks, as well as associated thrusting and faulting (dashed lines), potentially reactivating deep-seated syn-rift faults which tap the bimodal basement and focus fluid flow (blue lines). Uplifted basement fragments also contain fault networks which may channel fluid flow to the overlying rift sediments. The basement may contain a pre-enrichment of ore minerals (red crosses) from a previous mineralising event which may have been leached by hydrothermal fluids, and transported via seismic pumping to the overlying sedimentary sequences. Syn-deformational intrusions may have provided important heat sources to drive hydrothermal fluids, as well as the uplift of basement segments. Within the folded sedimentary sequences rheological contrasts and redox boundaries play a role in metal precipitation (red lines), particularly where brecciation, faulting, thrusting and fold closures have contributed to secondary permeability development.

10 Recommendations

The objectives of this work were to characterise the geology of the Eiseb, to investigate the applicability of magnetite trace element analysis as a petrogenetic indicator for ore deposits of this type, and to address the inclusion of the Eiseb into an SSC mineralisation model. The work herein has addressed these key areas, but is not exhaustive. Further research into the Eiseb, (O-)SSC deposits, and the use of magnetite for mineral deposit fingerprinting will contribute greatly to our understanding of the KCB and the CAB and metallogenesis in the region.

Future academic research which would advance the findings of this study could include:

- additional zircon geochronology from different stratigraphic units both within Namibia and Botswana could resolve changes in source areas on a regional scale;
- investigate the ChRM results of the paleomagnetic investigation more fully in order to isolate and mitigate the source of error, or confirm the age of 230 Ma suggested by the data;
- drilling in the vicinity of the basement horst to confirm the geology and place it within a regional context;
- more widespread zircon geochronology across the Eiseb to map out the distribution of source areas, and possibly also isolate potential basement highs beneath the Ghanzi Group sediments;
- a detailed study of the alteration assemblages associated with mineralisation on a regional scale, within the volcanic and sedimentary rocks;
- undertake whole-rock geochemical analyses in order to correlate stratigraphy on a local and regional scale and monitor the influence of hydrothermal/metamorphic fluids on the host-rocks;
- sampling of basic volcanic rocks within the KCB to compare: 1) whole-rock geochemistry of the host-rocks; and 2) LA-ICP-MS trace element geochemical analyses of magnetite; with the results of this study;
- analysis the OE-1 whole-rock Nb and Y concentrations which can be compared with Nb and Y measured by LA-ICP-MS in magnetite from OE-1. Comparing the ratios of these elements in magnetite and the whole rock will test the efficacy of using magnetite chemistry as an indicator for tectonic setting in igneous rocks. This could also be extended to other trace elements used to distinguish tectonic setting for

igneous rocks such as Rb and Zr, and tested on igneous rocks known to contain magnetite;

- including LA-ICP-MS trace element analyses for the sulfides found in the Eiseb will also provide useful information on the partitioning of elements in O-SSC type deposits, and help to confirm or disprove the findings of this study;
- using the findings from the QEMSCAN analysis on the bulk magnetite samples which showed that magnetite from mineralised areas was texturally associated with Cu-Ag mineralisation could be tested in other locations as an means to distinguish barren and mineralised lithotypes.

11 References

Acosta-Góngora, P., Gleeson, S.A., Samson, I.M., Ootes, L., Corriveau, L., 2014. Trace Element Geochemistry of Magnetite and Its Relationship to Cu-Bi-Co-Au-Ag-U-W Mineralization in the Great Bear Magmatic Zone, NWT, Canada. Economic Geology 109, 1901–1928.

Ahrendt, H., Hunziker, J.C., Weber, K., 1978. Age and degree of metamorphism and time of nappe emplacement along the southern margin of the Damara Orogen/Namibia (SW-Africa). Geologische Rundschau 67, 719–742.

Angerer, T., Hagemann, S.G., Danyushevsky, L.V., 2012. Geochemical evolution of the banded iron formation-hosted high-grade iron ore system in the Koolyanobbing greenstone belt, Western Australia. Economic Geology 107, 599–644.

Becker, T., Garoeb, H., Ledru, P., Milesi, J.-P., 2005. The Mesoproterozoic event within the Rehoboth Basement Inlier of Namibia: review and new aspects of stratigraphy, geochemistry, structure and plate tectonic setting. South African Journal of Geology 108, 465–492.

Becker, T., Schalk, K.E.L., 2008. The Sinclair Supergroup of the Rehoboth volcanic arc from the Sossusvlei-Gamsberg area to the Gobabis region. R. McG. Miller, The Geology of Namibia. Geological Survey, Windhoek 1, 8–68.

Besse, J., Courtillot, V., 2002. Apparent and true polar wander and the geometry of the geomagnetic field over the last 200 Myr. Journal of Geophysical Research (Solid Earth) 107, p.2300.

Blundell, D.J., Karnkowski, P.H., Alderton, D.H.M., Oszczepalski, S., Kucha, H., 2003. Copper mineralization of the Polish Kupferschiefer: a proposed basement fault-fracture system of fluid flow. Economic Geology 98, 1487–1495.

Bordage, A., Balan, E., De Villiers, J.P., Cromarty, R., Juhin, A., Carvallo, C., Calas, G., Raju, P.S., Glatzel, P., 2011. V oxidation state in Fe–Ti oxides by high-energy resolution fluorescence-detected X-ray absorption spectroscopy. Physics and Chemistry of Minerals 38, 449–458.

Borg, G., 1988a. Controls on stratabound copper mineralization at Klein Aub Mine and similar deposits within the Kalahari Copperbelts of South West Africa/Namibia and Botswana (PhD Thesis). University of Witwatersrand, Johannesburg.

Borg, G., 1988b. The Koras—Sinclair—Ghanzi rift in southern Africa. Volcanism, sedimentation, age relationships and geophysical signature of a late-middle Proterozoic rift system. Precambrian research 38, 75–90.

Borg, G., Maiden, K.J., 1986. A preliminary appraisal of the tectonic and sedimentological environment of the Sinclair Sequence in the Klein Aub area. Communications of the Geological Survey of Namibia 2, 65–73.

Borg, G. Maiden, K.J. 1987. Alteration of late Middle Proterozoic volcanics and its relation to stratabound copper-silver-gold mineralisation along the margin of the Kalahari Craton in SWA/Namibia and Botswana. In: Pharaoh, T.C., Beckinsale, R.D. & Rickards, D.T. (Eds.), Geochemistry and Mineralization of Proterozoic Volcanic Suites, Geological Society Special Publication, 33, 347-354.

Borg, G., Maiden, K.J., 1989. The Middle Proterozoic Kalahari Copperbelt of Namibia and Botswana. Sediment-hosted stratiform copper deposits, Geological Association of Canada, Special Paper 36, 525–540.

Borg, G., Graf, N. & Maiden, K.J. 1987a. The Klein Aub Fault Zone. A Wrench Fault System in Middle Proterozoic Metasediments in Central SWA/Namibia. Communications of the Geological Survey of SWA/Namibia, 3, 91-98.

Borg, G., Tredoux, M., Maiden, K.J., Sellschop, J.P.F., Wayward, O.F.D. 1987b. PGE- and Au-Distribution in Rift-related Volcanics, Sediments and Stratabound Cu/Ag Ores of Middle Proterozoic Age in CentralSWA/Namibia. In: Prichard, H.M., Potts, P.J., Bowles, J.F.W. & Cribb, S.J. (Eds.), Geo-Platinum '87, 303-318, Elsevier.

Borg, G., Piestrzyñski, A., Bachmann, G., Püttmann, W., Walther, S., Fiedler, M., 2012. An overview of the European Kupferschiefer deposits. In: Hedenquist, J.W., Harris, M., Camus, F. (Eds.), Geology and Genesis of Major Copper Deposits and Districts of the World: A Tribute to Richard H. Sillitoe, Economic Geology Special Publication, 16, 455–486.

Boutroy, E., Dare, S.A., Beaudoin, G., Barnes, S.-J., Lightfoot, P.C., 2014. Magnetite composition in Ni-Cu-PGE deposits worldwide: application to mineral exploration. Journal of Geochemical Exploration 145, 64–81.

Bowles, J.F., Howie, R., Vaughan, D., Zussman, J., 2011. Rock-forming Minerals: Non-silicates: Oxides, Hydroxides and Sulphides. V. 5A. Geological Society.

Brown, A.C., 1997. World-class sediment-hosted stratiform copper deposits: Characteristics, genetic concepts and metallotects. Australian Journal of Earth Sciences 44, 317–328.

Brown, A.C., 2014. Low-temperature sediment-hosted copper deposits. Reference Module in Earth Systems and Environmental Sciences, from Treatise on Geochemistry (Second Edition).(13) 251–271.

Butler, R.F., 1992. Paleomagnetism: magnetic domains to geologic terranes. Blackwell Scientific Publications Boston. 319p.

Cahen, L., François, A., Ledent, D., 1971. Sur l'age des uraninites de Kambove Ouest et de Kamoto Principal et révision des connaissances relatives aux minéralisations uranifères du Katanga et du Copperbelt de Zambia. Annales de la Société géologique de Belgique 94, 185–198.

Cailteux, J.L.H., Kampunzu, A.B., Lerouge, C., Kaputo, A.K., Milesi, J.P., 2005. Genesis of sediment-hosted stratiform copper–cobalt deposits, Central African Copperbelt. Journal of African Earth Sciences 42, 134–158.

Carew, M.J., 2004. Controls on Cu-Au mineralisation and Fe oxide metasomatism in the Eastern Fold Belt, NW Queensland, Australia. (PhD) James Cook University, Townsville.

Catterall, D., 2014. Eiseb Project Stratigraphy, Structure and Mineralisation. Prepared by Blue Clay Agencies (Pty) Ltd (Unpublished Company Report).

Chen, W.T., Zhou, M.-F., Li, X., Gao, J.-F., Hou, K., 2015. In-situ LA-ICP-MS trace elemental analyses of magnetite: Cu-(Au, Fe) deposits in the Khetri copper belt in Rajasthan Province, NW India. Ore Geology Reviews 65, 929–939.

Chung, D., Zhou, M.-F., Gao, J.-F., Chen, W.T., 2015. In-situ LA–ICP-MS trace elemental analyses of magnetite: The late Palaeoproterozoic Sokoman Iron Formation in the Labrador Trough, Canada. Ore Geology Reviews 65, 917–928.

Cornell, R.M., Schwertmann, U., 2003. The iron oxides: structure, properties, reactions, occurrences and uses. John Wiley & Sons.

Corner, B., 1983. An interpretation of the aeromagnetic data covering the western portion of the Damara Orogen in South West Africa/Namibia. Special Publication of the Geological Society of South Africa 11, 339-354.

Corner, B., 2000. Crustal framework of Namibia derived from magnetic and gravity data. Communications of the geological survey of Namibia 12, 13–19.

Cox, D., Lindsey, D., Singer, D., Diggles, M., 2003. Sediment-Hosted Copper Deposits of the World: Deposit Models and Database (No. 03–107). U.S. Geological Survey.

Daly, M.C., Chakraborty, S.K., Kasolo, P., Musiwa, M., Mumba, P., Naidu, B., Namateba, C., Ngambi, O., Coward, M.P., 1984. The Lufilian arc and Irumide belt of Zambia: results of a geotraverse across their intersection. Journal of African Earth Sciences 2, 311–318.

Dare, S.A., Barnes, S.-J., Beaudoin, G., 2012. Variation in trace element content of magnetite crystallized from a fractionating sulfide liquid, Sudbury, Canada: implications for provenance discrimination. Geochimica et Cosmochimica Acta 88, 27–50.

Dare, S.A.S., Barnes, S.-J., Beaudoin, G., Méric, J., Boutroy, E., Potvin-Doucet, C., 2014. Trace elements in magnetite as petrogenetic indicators. Minerium Deposita 49, 785–796.

Dawborn, T., 2012. Antofagasta Minerals: Africa Region: Notes on the field visit, Talismanis JV, Namibia (Unpublished Company Report).

Dawborn, T., 2013. Talismanis Prospecting: SEM and Microprobe Results. Kalahari Copperbelt Geoforum, Maun, Botswana, 25-27 July 2013.

Dawborn, T., 2014. Summary of Exploration Activities and Results (Unpublished Company Report).

Dean, J., 2013. Talismanis Project Area, Namibia: Structural Results from Oriented Drill Core. Kalahari Copperbelt Geoforum, Maun, Botswana, 25-27 July 2013.

Deenen, M.H.L., Langereis, C., Krijgsman, W., El Hachimi, H., El Hassane, C., 2010. Paleomagnetic research in the Argana basin, Morocco: Trans-Atlantic correlation of CAMP volcanism and implications for the late Triassic geomagnetic polarity time scale. Deenen MHL New Chronol. Late Triassic Early Jurassic Geology Ultraiectina 323, 43–64.

Deer, W.A., Howie, R.A., Zussman, J., 1992. An introduction to the rock-forming minerals. Longman London.

Deer, W.A., Howie, R.A., Zussman, J., 2013. An Introduction to the Rock-Forming Minerals, 3rd ed. Mineralogical Society of Great Britain and Ireland.

Dentith, M., Mudge, S.T., 2014. Geophysics for the mineral exploration geoscientist. Cambridge University Press.

Doughty, P.T., Chamberlain, K.R., 1996. Salmon River Arch revisited: new evidence for 1370 Ma rifting near the end of deposition in the Middle Proterozoic Belt basin. Canadian Journal of Earth Sciences 33, 1037–1052.

Dunlop, D.J., 1990. Developments in rock magnetism. Reports on Progress in Physics 53, 707.

Dupuis, C., Beaudoin, G., 2011. Discriminant diagrams for iron oxide trace element fingerprinting of mineral deposit types. Miner Deposita 46, 319–335.

El Desouky, H.A., Muchez, P., Dewaele, S., Boutwood, A., Tyler, R., 2008. Postorogenic origin of the stratiform Cu mineralization at Lufukwe, Lufilian foreland, Democratic Republic of Congo. Economic Geology 103, 555–582.

El Desouky, H.A., Muchez, P., Boyce, A.J., Schneider, J., Cailteux, J.L., Dewaele, S., von Quadt, A., 2010. Genesis of sediment-hosted stratiform copper–cobalt mineralization at Luiswishi and Kamoto, Katanga Copperbelt (Democratic Republic of Congo). Mineralium Deposita 45, 735–763.

Fisher, R., 1953. Dispersion on a sphere, in: Proceedings of the Royal Society of London A: Mathematical, Physical and Engineering Sciences. The Royal Society, pp. 295–305.

Frimmel, H.E., Basei, M.S., Gaucher, C., 2011. Neoproterozoic geodynamic evolution of SW-Gondwana: a southern African perspective. International Journal of Earth Science 100, 323–354.

Font, E., Rapalini, A.E., Tomezzoli, R.N., Trindade, R.I.F., Tohver, E., 2012. Episodic Remagnetizations related to tectonic events and their consequences for the South America Polar Wander Path. Geological Society of London Special Publication 371, 55–87.

Frost, B.R., 1991a. Magnetic Petrology: Factors that control the occurrence of magnetite in crustal rocks, in: Reviews in Mineralogy and Geochemistry 25. pp. 489–509.

Frost, B.R., 1991b. Introduction to oxygen fugacity and its petrologic importance, in: Reviews in Mineralogy and Geochemistry 25. pp. 469–488.

Galbraith, R.F., 2005. Statistics for fission track analysis. CRC Press.

Garlick, W.G., 1961. The syngenetic theory. The geology of the northern Rhodesian Copperbelt: London, MacDonald 146–165.

Goldfarb, R.J., Baker, T., Dube, B., Groves, D.I., Hart, C.J., Gosselin, P., 2005. Distribution, character, and genesis of gold deposits in metamorphic terranes. Economic Geology 100th anniversary volume 40.

Gorman, A., Jenkin, G.R., Catterall, D., Morgan, K., 2013. Constraining a genetic model for copper-silver mineralisation in the Kalahari Copperbelt, Botswana: Mineralogy, geochemistry and structure. Kalahari Copperbelt Geoforum, Maun, Botswana, 25-27 July 2013.

Graham, J.W., 1949. The stability and significance of magnetism in sedimentary rocks. Journal of Geophysical Research 54, 131–167.

Griffin, W.L., Powell, W.J., Pearson, N.J., O'Reilly, S.Y., 2008. GLITTER: data reduction software for laser ablation ICP-MS. Laser Ablation-ICP-MS in the earth sciences. Mineralogical association of Canada short course series 40, 204–207.

Grigsby, J.D., 1990. Detrital magnetite as a provenance indicator. Journal of Sedimentary Research 60 (6), 940-951.

Groves, D.I., Bierlein, F.P., Meinert, L.D., Hitzman, M.W., 2010. Iron oxide copper-gold (IOCG) deposits through earth history: implications for origin, lithospheric setting, and distinction from other epigenetic iron oxide deposits. Economic Geology 105, 641–654.

Hall, J.M., Fischer, J.F., 1977. Opaque mineralogy of basement rocks, Leg 37. Initial Report Deep Sea Drill Project 37, 857–873.

Hall, W.S., 2013. Geology and paragenesis of the Boseto Copper Deposits, Kalahari Copperbelt, Northwest Botswana (MSc. Thesis). Colorado School of Mines, Golden.

Hanor, J.S., 1979. Sedimentary genesis of hydrothermal fluids, in: Barnes, H.L. (Ed.), Geochemistry of Hydrothermal Ore Deposits. John Wiley & Sons, pp. 137–172.

Harrison, A.G., Thode, H.G., 1958. Mechanism of the bacterial reduction of sulphate from isotope fractionation studies. Trans. Faraday Soc. 54, 84–92.

Haynes, D.W., 1986a. Stratiform copper deposits hosted by low-energy sediments; I, Timing of sulfide precipitation, an hypothesis. Economic Geology 81, 250–265.

Haynes, D.W., 1986b. Stratiform copper deposits hosted by low-energy sediments; II, Nature of source rocks and composition of metal-transporting water. Economic Geology 81, 266–280.

Haynes, D.W., Bloom, M.S., 1987a. Stratiform copper deposits hosted by low-energy sediments; III, Aspects of metal transport. Economic Geology 82, 635–648.

Haynes, D.W., Bloom, M.S., 1987b. Stratiform copper deposits hosted by low-energy sediments; IV, Aspects of sulfide precipitation. Economic Geology 82, 875–893.

Hegenberger, W., Burger, A.J., 1985. The Oorlogsende porphyry member, South West Africa/Namibia: its age and regional setting. Communications of the Geological Survey of Namibia 1, 23–29.

Hendjala, F., 2010. Petrography and chemostratigraphy of the Ghanzi-Chobe Supergroup, Kalahari Copperbelt (BSc. Thesis). University of Witwatersrand, Johannesburg.

Hitzman, M., Kirkham, R., Broughton, D., Thorson, J., Selley, D., 2005. The Sediment-Hosted Stratiform Copper Ore System, in: Economic Geology 100th Anniversary Volume. pp. 609–642.

Hitzman, M.W., Selley, D., Bull, S., 2010. Formation of sedimentary rock-hosted stratiform copper deposits through Earth history. Economic Geology 105, 627–639.

Hitzman, M.W., Broughton, D., Selley, D., Woodhead, J., Wood, D., Bull, S., 2012. The Central African Copperbelt: Diverse stratigraphic, structural, and temporal settings the world's largest sedimentary copper district. Society of Economic Geologists Special Publication 16, pp.487–514.

Horstmann, U.E., Ahrendt, H., Clauer, N., Porada, H., 1990. The metamorphic history of the Damara Orogen based on K/Ar data of detrital white micas from the Nama Group, Namibia. Precambrian Research 48, 41–61.

Huang, X., Qi, L., Meng, Y., 2014. Trace Element Geochemistry of Magnetite from the Fe(-Cu) Deposits in the Hami Region, Eastern Tianshan Orogenic Belt, NW China. Acta Geologica Sinica - English Edition 88, 176–195.

Huang, X.-W., Zhou, M.-F., Qiu, Y.-Z., Qi, L., 2015. In-situ LA-ICP-MS trace elemental analyses of magnetite: the Bayan Obo Fe-REE-Nb deposit, North China. Ore Geology Reviews 65, 884–899.

Huang, X.-W., Gao, J.-F., Qi, L., Meng, Y.-M., Wang, Y.-C., Dai, Z.-H., 2016. In-situ LA–ICP–MS trace elements analysis of magnetite: The Fenghuangshan Cu–Fe–Au deposit, Tongling, Eastern China. Ore Geology Reviews 72, 746–759.

Hutchins, D.G., Reeves, C.V., 1980. Regional geophysical exploration of the Kalahari in Botswana. Tectonophysics 69, 201–220.

Ilton, E.S., Eugster, H.P., 1989. Base metal exchange between magnetite and a chloride-rich hydrothermal fluid. Geochimica et Cosmochimica Acta 53, 291–301.

Ishikawa, Y., Sawaguchi, T., Iwaya, S.–., Horiuchi, M., 1976. Delineation of prospecting targets for Kuroko deposits based on modes of volcanism of underlying dacite and alteration halos. Min. Geol. 26, 105–117.

Jackson, M., 1990. Diagenetic sources of stable remanence in remagnetized Paleozoic cratonic carbonates: A rock magnetic study. Journal of Geophysical Research (Solid Earth) 95, 2753–2761.

Jochum, K.P., Weis, U., Stoll, B., Kuzmin, D., Yang, Q., Raczek, I., Jacob, D.E., Stracke, A., Birbaum, K., Frick, D.A., 2011. Determination of reference values for NIST SRM 610–617 glasses following ISO guidelines. Geostandards and Geoanalytical Research 35, 397–429.

John, T., Schenk, V., Mezger, K., Tembo, F., 2004. Timing and PT Evolution of Whiteschist Metamorphism in the Lufilian Arc–Zambezi Belt Orogen (Zambia): Implications for the Assembly of Gondwana. The Journal of Geology 112, 71–90.

Johnson, H.P., 1979. 17. Opaque mineralogy of the igneous rock samples from the Deep Sea Drilling Program Hole 395A. pp. 407-420.

Jowett, E.C., 1991. The evolution of Ideas about the genesis of Stratiform Copper-Silver Deposits, in: Hutchins, R.W., Grauch, R.I. (Eds.), Historical Perspectives of Genetic Concepts and Case Histories of Famous Discoveries Papers Arising from SEG Symposia, October 30 and 31, 1988, Denver, Colorado, Economic Geology Monograph 8. The Economic Geology Publishing Company, pp. 171–132.

Kahle, B., 2013. Regional geophysical interpretation of the Botswana portion of the Kalahari Copperbelt. Kalahari Copperbelt Geoforum, Maun, Botswana, 25-27 July 2013.

Kaplan, I.R., Rittenberg, S.C., 1964. Microbiological fractionation of sulphur isotopes. Microbiology 34, 195–212.

Kampunzu, A.B., Akanyang, P., Mapeo, R.B.M., Modie, B.N., Wendorff, M., 1998. Geochemistry and tectonic significance of the Mesoproterozoic Kgwebe metavolcanic rocks in northwest Botswana: implications for the evolution of the Kibaran Namaqua-Natal belt. Geological Magazine 135, 669–683.

Kampunzu, A.B., Armstrong, R.A., Modis, M.P., Mapeo, R.B.M., 2000. Ion microprobe U-Pb ages on detrital zircon grains from the Ghanzi Group: implications for the identification of a Kibaran-age crust in northwest Botswana. Journal of African Earth Sciences 30, 579–587.

Labails, C., Olivet, J.-L., Aslanian, D., Roest, W.R., 2010. An alternative early opening scenario for the Central Atlantic Ocean. Earth Planetary Science Letters 297, 355–368.

Large, R.R., Gemmell, J.B., Paulick, H., Huston, D.L., 2001. The alteration box plot: A simple approach to understanding the relationship between alteration mineralogy and lithogeochemistry associated with volcanic-hosted massive sulfide deposits. Econ. Geol. 96, 957–971.

Le Maitre, R.W., Streckeisen, A., Zanettin, B., Le Bas, M.J., Bonin, B., Bateman, P., 2005. Igneous rocks: a classification and glossary of terms: recommendations of the International Union of Geological Sciences Subcommission on the Systematics of Igneous Rocks. Cambridge University Press.

Lehmann, J., Master, S., Rankin, W., Milani, L., Kinnaird, J.A., Naydenov, K.V., Saalmann, K., Kumar, M., 2015. Regional aeromagnetic and stratigraphic correlations of the Kalahari Copperbelt in Namibia and Botswana. Ore Geology Reviews 71, 169–190.

Lobo-Guerrero Sanz, A., 2005. Pre- and post-Katangan granitoids of the Greater Lufilian Arc - geology, geochemistry, geochronology and metallogenic significance (PhD thesis). University of the Witwaterand, Johannesburg.

Ludwig, K.R., 1991. ISOPLOT: a plotting and regression program for radiogenic-isotope data; version 2.53. US Geological Survey.

Lurcock, P.C., Wilson, G.S., 2012. PuffinPlot: A versatile, user-friendly program for paleomagnetic analysis. Geochemistry, Geophysics, Geosystems 13, p.6.

Maiden, K.J., Borg, G., 2011. The Kalahari Copperbelt in Central Namibia: Controls on Copper Mineralisation. SEG Newsletter 7, p.6.

Mapeo, R.B.M., Kampunzu, A.B., Armstrong, R.A., 2000. Ages of detrital zircon grains from Neoproterozoic siliciclastic rocks in t... S.Afr.J.Geol. 103, 156–161.

McGowan, R.R., Roberts, S., Boyce, A.J., 2006. Origin of the Nchanga copper–cobalt deposits of the Zambian Copperbelt. Miner Deposita 40, 617–638.

Meixner, H.M., Peart, R.J., 1984. The Kalahari drilling project: a report on the geophysical and geological results of follow-up drilling to the aeromagnetic survey of Botswana. Geological Survey Department.

Milani, L., Lehmann, J., Naydenov, K.V., Saalmann, K., Kinnaird, J.A., Daly, J.S., Frei, D., Sanz, A.L.-G., 2015. A-type magmatism in a syn-collisional setting: The case of the Pan-African Hook Batholith in Central Zambia. Lithos 216, 48–72.

Miller, R.M., 1983. Evolution of the Damara Orogen of South West Africa/Namibia. Geological Society of South Africa Special Publication 11, 115–138.

Miller, R.M., 2008. The Geology of Namibia, Volume 1 - Archaean to Mesoproterozoic. Ministry of Mines and Energy Geological Survey, Windhoek, pp. 309.

Modie, B.N., 1996. Depositional environments of the Meso-to Neoproterozoic Ghanzi-Chobe belt, northwest Botswana. Journal of African Earth Sciences 22, 255–268.

Modie, B.N., 2000. Geology and mineralisation in the Meso-to Neoproterozoic Ghanzi-Chobe Belt of northwest Botswana. Journal of African Earth Sciences 30, 467–474.

Morgan, K., Jenkin, G.R., Catterall, D., Boyce, A.J., Gorman, A., 2013. Developing genetic models for copper-silver mineralisation in the Kalahari Copperbelt, Botswana: Source and evolution of fluids. Kalahari Copperbelt Geoforum, Maun, Botswana, 25-27 July 2013.

Muchez, P., Corbella, M., 2012. Factors controlling the precipitation of copper and cobalt minerals in sediment-hosted ore deposits: Advances and restrictions. Journal of Geochemical Exploration 118, 38–46.

Nadoll, P., Koenig, A.E., 2011. LA-ICP-MS of magnetite: methods and reference materials. J. Anal. At. Spectrom. 26, 1872–1877

Nadoll, P., Mauk, J.L., Hayes, T.S., Koenig, A.E., Box, S.E., 2012. Geochemistry of magnetite from hydrothermal ore deposits and host rocks of the Mesoproterozoic Belt Supergroup, United States. Economic Geology 107, 1275–1292.

Nadoll, P., Angerer, T., Mauk, J.L., French, D., Walshe, J., 2014. The chemistry of hydrothermal magnetite: A review. Ore Geology Reviews 61, 1–32. .

Ohmoto, H., Kaiser, C.J., Geer, K.A., 1990. Systematics of sulphur isotopes in recent marine sediments and ancient sediment-hosted base metal deposits. Stable Isot. Fluid Process. Miner. 23, 70–120.

Ohmoto, H., 2003. Nonredox Transformations of Magnetite-Hematite in Hydrothermal Systems. Economic Geology 98, 157–161.

Özdemir, Ö., Dunlop, D.J., 1997. Effect of crystal defects and internal stress on the domain structure and magnetic properties of magnetite. Journal of Geophysical Research 102, p14

Pearce, J.A., Harris, N.B., Tindle, A.G., 1984. Trace element discrimination diagrams for the tectonic interpretation of granitic rocks. Journal of petrology 25, 956–983.

Pearce, N.J.G., Perkins, W.T., Westgate, J.A., Gorton, M.P., Jackson, S.E., Neal, C.R., Chenery, S.P., 1997. A Compilation of New and Published Major and Trace Element Data for NIST SRM 610 and NIST SRM 612 Glass Reference Materials. Geostandards Newsletter 21, 115–144.

Perelló, J., Clifford, J.A., Creaser, R.A., Valencia, V.A., 2015. An Example of Synorogenic Sediment-Hosted Copper Mineralization: Geologic and Geochronologic Evidence from the Paleoproterozoic Nussir Deposit, Finnmark, Arctic Norway. Economic Geology 110, 677–689.

Pfurr, N., Ahrendt, H., Hansen, B.T., Weber, K., 1991. U–Pb and Rb–Sr isotopic study of granitic gneisses and associated metavolcanic rocks from the Rostock massifs, southern margin of the Damara Orogen: implications for lithostratigraphy of this crustal segment. Communications of the Geological Survey of Namibia 7, 35–48.

Porada, H., Berhorst, V., 2000. Towards a new understanding of the Neoproterozoic-early palæozoic Lufilian and northern Zambezi belts in Zambia and the Democratic Republic of Congo. J. Afr. Earth Sci. 30, 727–771

Rankin, W., 2015. Cross-border correlation of the Damara Belt in Namibia and equivalent lithologies in northwestern Botswana from potential field and magnetotelluric interpretations (PhD thesis). University of the Witwaterand, Johannesburg.

Richards, J.P., Krogh, T.E., Spooner, E.T.C., 1988. Fluid inclusion characteristics and U-Pb rutile age of late hydrothermal alteration and veining at the Musoshi stratiform copper deposit, Central African copper belt, Zaire. Economic Geology 83, 118–139.

Robb, L., 2009. Introduction to Ore-Forming Processes. John Wiley & Sons.

Robb, V., Boshoff, F., 1993. Petrographic and mineralographic examination of 72 borehole core samples from the Maun Copper Venture (No. M/92/5248). Anglo American Research Laboratories (Pty) Ltd. (Unpublished Company Report)

Rudnick, R.L., Gao, S., 2003. Composition of the continental crust. Treatise on geochemistry 3, 1–64.

Ruxton, P.A., 1981. The sedimentology and diagenesis of copper-bearing rocks of the southern margin of the Damaran Orogenic Belt, Namibia and Botswana (PhD thesis). University of Leeds, Leeds.

Schalk, K.E.L., 1970. Some late Precambrian formations in central south west Africa. Annals of the Geological Survey of South Africa 8, 29–47.

Schneider, G.I., Seeger, K., 1992. Chapter 2.3 Copper, in: Mineral Resources of Namibia. Geological Survey of Namibia, p. 118.

Schwartz, M.O., Akanyang, P., Trippler, K., Ngwisanyi, T.H., 1995. The sediment-hosted Ngwako Pan copper deposit, Botswana. Economic Geology 90, 1118–1147.

Schwartz, M., Kwok, Y.Y., Davis, D., Akanyang, P., 1996. Geology, geochronology and regional correlation of the Ghanzi Ridge, Botswana. South African Journal of Geology 99, 245.

Selley, D., Broughton, D., Scott, R.J., Hitzman, M., Bull, S.W., Large, R.R., McGoldrick, P.J., Croaker, M., Pollington, N., 2005. A New Look at the Geology of the Zambian Copperbelt, in: Economic Geology 100th Anniversary Volume. pp. 965–1000.

Sillitoe, R.H., Perelló, J., García, A., 2010. Sulfide-Bearing Veinlets Throughout the Stratiform Mineralization of the Central African Copperbelt: Temporal and Genetic Implications. Economic Geology 105, 1361–1368.

Sillitoe, R.H., Perelló, J., Creaser, R.A., Wilton, J., Dawborn, T., 2015. Two Ages of Copper Mineralization in the Mwombezhi Dome, Northwestern Zambia: Metallogenic Implications for the Central African Copperbelt. Economic Geology 110, 1917–1923.

Simmonds, J., 1998. The Central African Copperbelt: tectonic overview, metallogeny and analysis of current research, in: Geological Society of Australia Abstracts. Geological Society of Australia, pp. 57–59.

Singer, D.A., 1995. World class base and precious metal deposits; a quantitative analysis. Economic Geology 90, 88–104.

Singoyi, B., Danyushevsky, L., Davidson, G.J., Large, R., Zaw, K., 2006. Determination of trace elements in magnetites from hydrothermal deposits using the LA ICP-MS technique, in: SEG Keystone Conference, Denver, USA: CD-ROM.

Sláma, J., Košler, J., Condon, D.J., Crowley, J.L., Gerdes, A., Hanchar, J.M., Horstwood, M.S., Morris, G.A., Nasdala, L., Norberg, N., 2008. Plešovice zircon—a new natural reference material for U–Pb and Hf isotopic microanalysis. Chemical Geology 249, 1–35.

Smalley, T.J., 1998. A preliminary investigation of selected sections of diamond drill core from the Ngamiland Copper Prospect, Botswana (Unpublished Company Report).

Smalley, T.J., 2011. Preliminary Exploration Target Outlines in EPLs, 3907, 3910, 3911, 3915, 3921, 3922, 3924 and 3925 (Unpublished Company Report).

Smalley, T.J., 2012. Comments on aspects of the exploration within the Eiseb Tenements (Unpublished Company Report).

Smalley, T.J., 2013. Magnetic Interpretation (Unpublished Company Report).

Smalley, T.J., 2014. Comments on the Eiseb Report Compiled by D. Catterall (Unpublished Company Report).

Smalley, T.J., Simmonds, A.L.E., Veldsman, H.E., 2012. Comments on Aspects of the Exploration within the Eiseb Tenements (Unpublished Company Report).

Spong, P.L., 1998. Geochemistry of magnetite from convergent-margin plutonic rocks of Australia, Japan and New Zealand (MSc. Thesis). University of Auckland, Auckland.

Stanistreet, I.G., Stollhofen, H., 1999. Onshore equivalents of the main Kudu gas reservoir in Namibia. Geological Society, London, Special Publications 153, 345–365.

Stevens, B.P.J., 2015. Magnetite-bearing zones in metasediments at Broken Hill, Australia: signatures of black smokers? Australian Journal of Earth Sciences 62, 605–624.

Sweeney, M.A., Binda, P.L., Vaughan, D.J., 1991. Genesis of the ores of the Zambian Copperbelt. Ore Geology Reviews 6, 51–76.

Symons, D.T.A., Kawasaki, K., Walther, S., Borg, G., 2011. Paleomagnetism of the Cu–Zn–Pb-bearing Kupferschiefer black shale (Upper Permian) at Sangerhausen, Germany. Miner. Deposita 46, 137–152.

Tauxe, L., 1998. Paleomagnetic Principles and Practice. Springer Science & Business Media.

Tauxe, L., 2010. Essentials of paleomagnetism. University of California Press, London.

Toens, D.P.D., 1975. The geology of part of the Southern foreland of the Damara orogenic belt in South West Africa and Botswana. Geologische Rundschau 64, 175–192.

Tohver, E., D'Agrella-Filho, M.S., Trindade, R.I.F., 2006. Paleomagnetic record of Africa and South America for the 1200–500 Ma interval, and evaluation of Rodinia and Gondwana assemblies. Precambrian Res., Endings and Beginnings: Paleogeography of the Neoproterozoic-Cambrian Transition AGU 2004 Joint Assembly 147, 193–222.

Torsvik, T.H., Müller, R.D., Van der Voo, R., Steinberger, B., Gaina, C., 2008. Global plate motion frames: toward a unified model. Reviews of Geophysics 46, p.44.

Torsvik, T.H., Van der Voo, R., Preeden, U., Mac Niocaill, C., Steinberger, B., Doubrovine, P.V., van Hinsbergen, D.J., Domeier, M., Gaina, C., Tohver, E., 2012. Phanerozoic polar wander, palaeogeography and dynamics. Earth-Science Reviews 114, 325–368.

Torsvik, T.H., Cocks, L.R.M., 2013. Gondwana from top to base in space and time. Gondwana Research 24, 999–1030.

Townley, B., Roperch, P., Oliveros, V., Tassara, A., Arriagada, C., 2007. Hydrothermal alteration and magnetic properties of rocks in the Carolina de Michilla stratabound copper district, northern Chile. Mineralium Deposita 42, 771–789.

Van Achterbergh, E., RAYAN, C., Griffin, W.L., 2007. Glitter User's manual. On line interactive data reduction for the LA-ICPMS microprobe 4.

Van der Voo, R., 1990. The reliability of paleomagnetic data. Tectonophysics 184, 1–9.

Veldsman, H.G., Simmonds, A.L.E., Smalley, T.J., 2010. Eiseb Prospecting and Mining (Pty) Ltd Technical Report (Unpublished Company Report).

Verlaguet, A., Brunet, F., Goffé, B., Murphy, W.M., 2006. Experimental study and modeling of fluid reaction paths in the quartz–kyanite±muscovite–water system at 0.7 GPa in the 350–550 C range: implications for Al selective transfer during metamorphism. Geochimica et cosmochimica acta 70, 1772–1788.

Vermeesch, P., 2004. How many grains are needed for a provenance study? Earth and Planetary Science Letters 224, 441–451.

Vermeesch, P., 2012. On the visualisation of detrital age distributions. Chemical Geology 312, 190–194.

Wanhainen, C., Nigatu, W., Selby, D., Mcleod, C.L., Nordin, R., Bolin, N.-J., 2014. The Distribution, Character, and Rhenium Content of Molybdenite in the Aitik Cu-Au-Ag-(Mo) Deposit and Its Southern Extension in the Northern Norrbotten Ore District, Northern Sweden. Minerals 4, 788.

Watson, G.S., Enkin, R.J., 1993. The fold test in paleomagnetism as a parameter estimation problem. Geophysical Research Letter 20, 2135–2137.

Watters, B.R., 1977. The Sinclair Group: definition and regional correlation. Transactions of the Geological Society of South Africa 80, 9–16.

Waychunas, G.A., 1991. Crystal Chemistry of Oxides and Oxyhydroxides, in: Reviews in Mineralogy and Geochemistry 25. pp. 11–68.

Wilson, S.A., 1997. The collection, preparation and testing of USGS reference material BCR-2, Columbia River Basalt: US Geol. Survey Open-File Report.

Ziegler, U.R.F., Stoessel, G.F.U., 1993. Age determinations in the Rehoboth basement inlier, Namibia. Geological Survey of Namibia, Ministry of Mines and Energy.

12 Appendices

Appendix I: BCR-2 EDS Measurements

No.	Na2O	MgO	Al2O3	SiO2	P2O5	K2O	CaO	TiO2	FeO	Total
1	3.29	3.61	13.7	55.4	0.43	1.75	6.86	2.45	11.6	99.1
2	3.36	3.75	13.8	55.2	0.42	1.76	6.89	2.32	12.1	99.6
3	3.39	3.61	13.9	54.6	0.32	1.87	6.99	2.28	12.0	99.0
4	3.48	3.68	13.9	54.1	0.34	1.79	6.86	2.32	11.8	98.3
5	3.54	3.79	13.7	55.2	0.30	1.75	6.96	2.44	12.1	99.8
6	3.58	3.67	13.7	54.9	0.26	1.85	6.95	2.27	12.1	99.3
7	3.52	3.68	13.8	54.7	0.33	1.81	6.77	2.23	11.9	98.8
8	3.53	3.64	13.8	54.4	0.26	1.81	6.77	2.22	11.9	98.4
9	3.46	3.67	13.8	55.3	0.26	1.88	7.09	2.39	12.4	100
10	3.23	3.75	14.2	54.9	0.41	1.88	6.91	2.23	12.6	100
11	3.34	3.69	14.0	55.2	0.21	1.81	6.93	2.42	12.2	99.7
12	3.32	3.75	13.9	55.2	0.40	1.77	6.83	2.38	11.9	99.4
13	3.49	3.81	13.8	55.0	0.36	1.76	7.07	2.42	12.1	99.9
14	3.33	3.65	13.9	54.8	0.34	1.78	7.09	2.32	12.2	99.4
15	3.38	3.74	14.0	55.3	0.28	1.77	7.04	2.17	11.9	99.6
16	3.39	3.73	13.9	54.9	0.37	1.89	6.95	2.29	12.0	99.3
17	3.43	3.72	13.8	55.3	0.34	1.91	7.06	2.37	12.0	99.9
18	3.43	3.73	13.9	55.2	0.34	1.80	6.96	2.36	12.0	99.7
19	3.46	3.73	13.8	54.6	0.26	1.84	6.91	2.28	12.1	99.0
20	3.48	3.51	13.9	54.6	0.26	1.81	6.92	2.28	11.9	98.6
21	3.51	3.60	13.6	54.6	0.30	1.86	6.82	2.34	11.7	98.3
22	3.48	3.65	13.9	55.7	0.24	1.80	6.94	2.31	12.0	100
23	3.41	3.71	14.0	55.5	0.32	1.92	7.10	2.25	12.1	100
24	3.63	3.71	13.8	55.6	0.24	1.90	7.05	2.21	12.5	101
25	3.49	3.74	13.9	55.3	0.31	1.77	6.87	2.18	12.2	99.8
26	3.55	3.81	13.9	55.3	0.24	1.72	6.93	2.59	12.1	100
27	3.49	3.68	13.7	55.0	0.32	1.87	7.09	2.25	12.1	99.5
28	3.51	3.81	14.0	55.6	0.32	1.84	7.06	2.25	12.3	101
29	3.44	3.71	13.8	55.6	0.31	1.86	7.02	2.31	12.1	100
30	3.59	3.74	13.9	55.6	0.48	1.86	7.01	2.38	12.4	101
31	3.57	3.77	13.6	55.7	0.35	1.84	6.91	2.45	12.2	100
32	3.55	3.59	13.8	54.5	0.23	1.82	6.91	2.33	11.9	98.6
33	3.46	3.69	13.8	55.1	0.38	1.83	7.01	2.25	12.2	99.8
34	3.55	3.70	14.0	55.1	0.38	1.82	6.94	2.33	12.2	100
35	3.40	3.75	13.9	55.1	0.31	1.86	7.08	2.41	12.1	99.9
36	3.48	3.70	13.6	54.7	0.34	1.74	6.98	2.36	11.9	98.7
37	3.53	3.68	14.1	54.5	0.29	1.80	6.91	2.34	11.9	99.1
38	3.47	3.68	14.2	55.2	0.28	1.85	6.90	2.34	12.0	99.9
39	3.58	3.76	14.0	55.3	0.26	1.80	7.05	2.33	12.1	100
40	3.47	3.83	13.9	55.1	0.27	1.77	7.07	2.40	12.5	100

Appendix II: Borehole Summary Data

- WB-1
- WB-2
- CA-PL-1
- CA-PL-2
- CA-PL-3
- CA-PL-4
- CA-PL-5
- CA-PL-6
- CA-PL-7
- CA-PL-8
- CA-PL-9
- EA-PL-1
- EA-NL-1
- EA-NL-2
- EA-SL-1
- NEA-PL-1
- NEA-PL-2
- NEA-SL-1

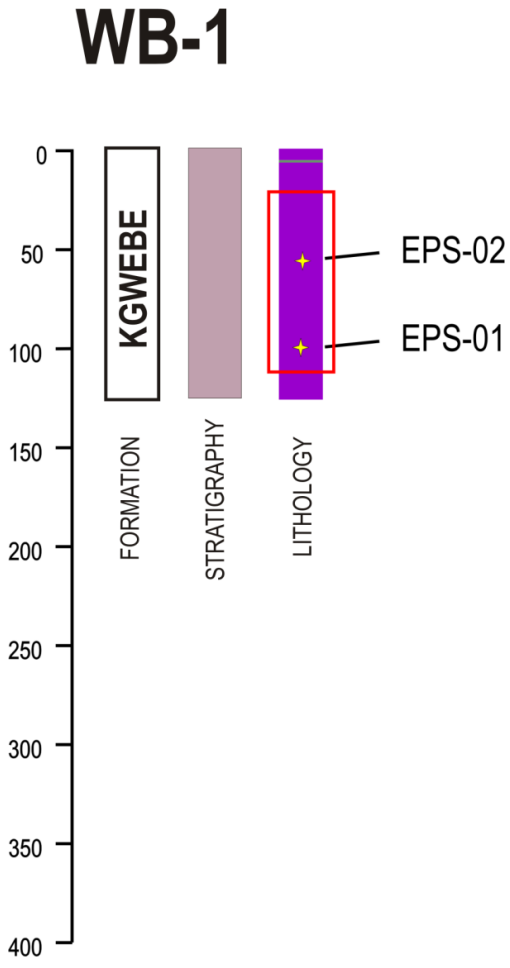
WB-1
0
50
100
150
200
250
300
350
400
KGWEBE
FORMATION
STRATIGRAPHY
LITHOLOGY
EPS-02
EPS-01

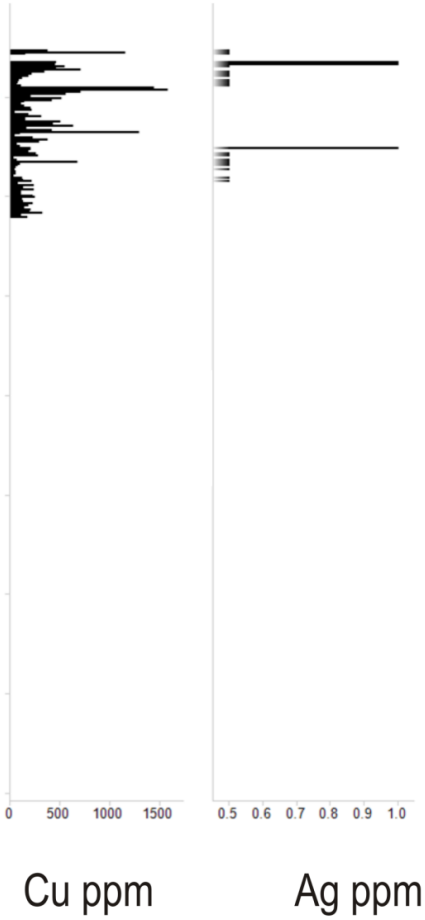
0
500
1000
1500
0.5
0.6
0.7
0.8
0.9
1.0
Cu ppm
Ag ppm

Kalahari Sand
Calcrete
Silcrete
Conglomerate
Gravel
Siltstone
Sandstone
Argillite
Phyllite
Metavolcanic
Limestone
Mineralisation
Sample

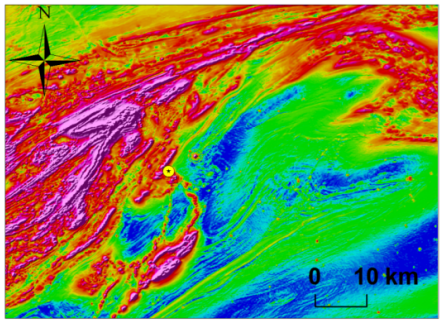
N
0
10 km

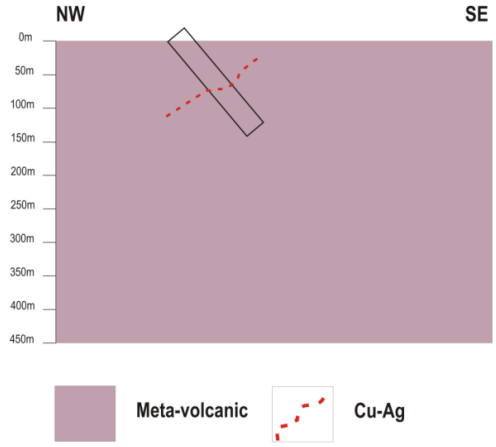
NW
SE
0m
50m
100m
150m
200m
250m
300m
350m
400m
450m
Meta-volcanic
Cu-Ag

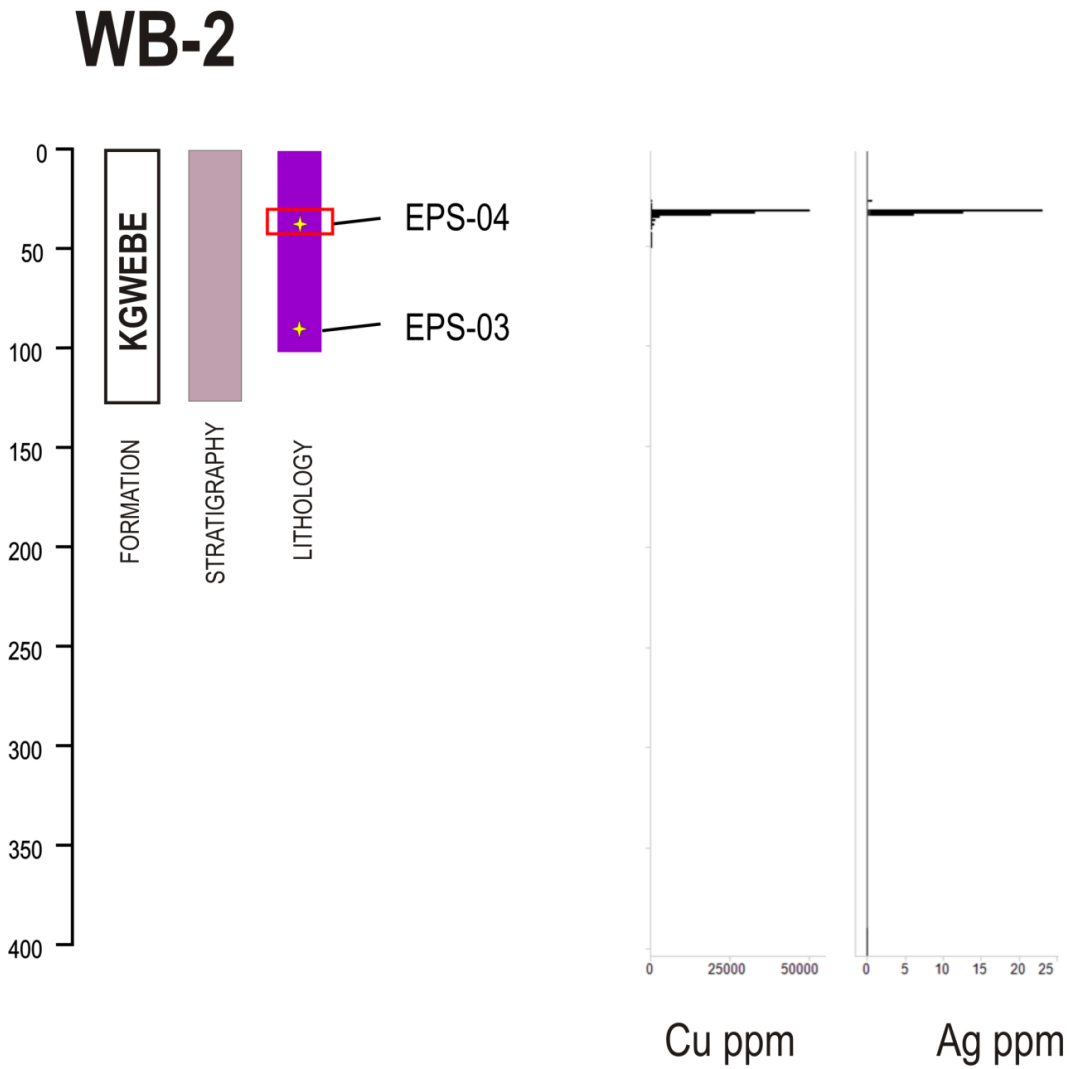
WB-2
0
50
100
150
200
250
300
350
400
KGWEBE
FORMATION
STRATIGRAPHY
LITHOLOGY
EPS-04
EPS-03
0
25000
50000
Cu ppm
0
5
10
15
20
25
Ag ppm

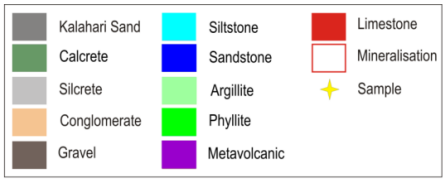
Kalahari Sand
Calcrete
Silcrete
Conglomerate
Gravel
Siltstone
Sandstone
Argillite
Phyllite
Metavolcanic
Limestone
Mineralisation
Sample

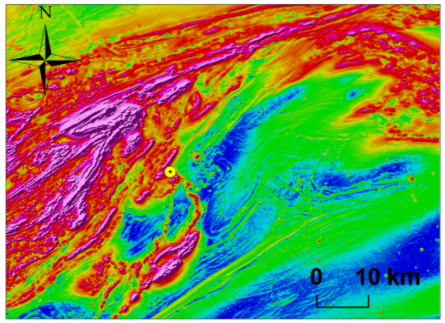
N
0
10 km

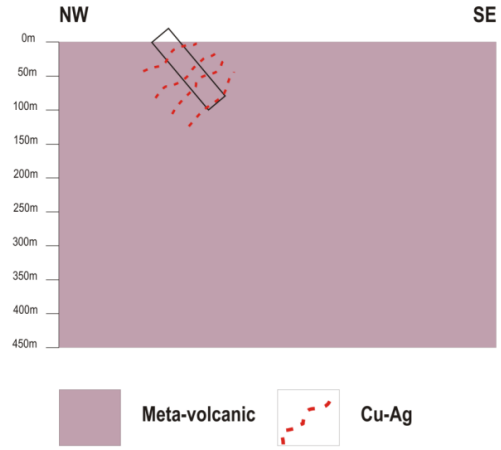
NW
SE
0m
50m
100m
150m
200m
250m
300m
350m
400m
450m
Meta-volcanic
Cu-Ag

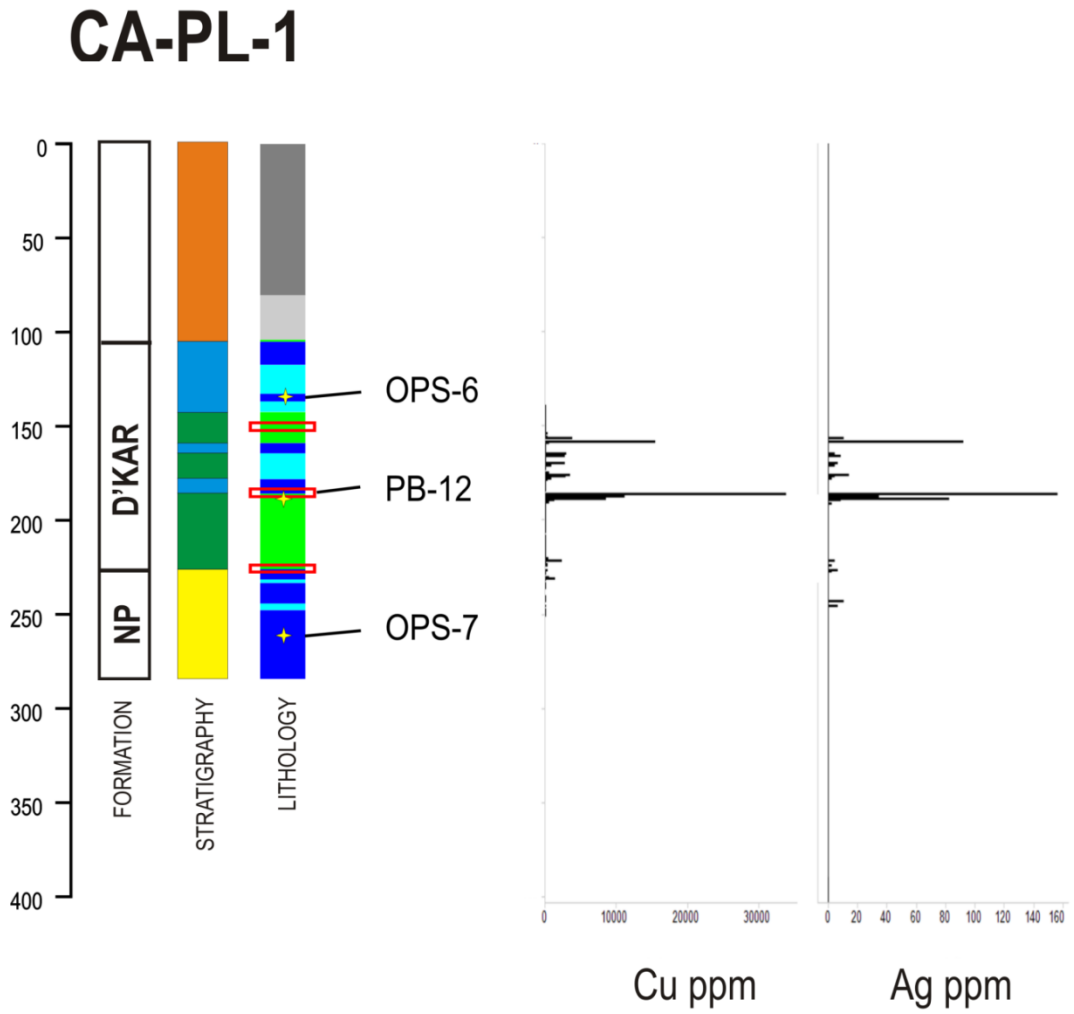
CA-PL-1
0
50
100
150
200
250
300
350
400
D'KAR
NP
FORMATION
STRATIGRAPHY
LITHOLOGY
OPS-6
PB-12
OPS-7
0
10000
20000
30000
Cu ppm
0
20
40
60
80
100
120
140
160
Ag ppm

Kalahari Sand
Calcrete
Silcrete
Conglomerate
Gravel
Siltstone
Sandstone
Argillite
Phyllite
Metavolcanic
Limestone
Mineralisation
Sample

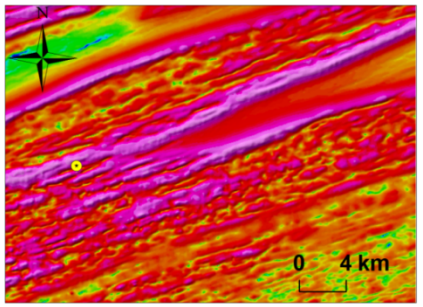
N
0
4 km

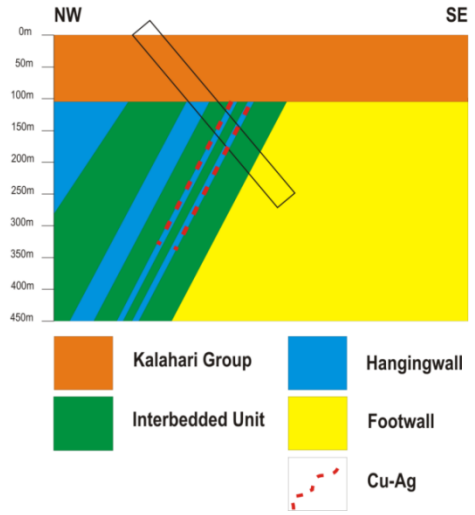
NW
SE
0m
50m
100m
150m
200m
250m
300m
350m
400m
450m
Kalahari Group
Interbedded Unit
Hangingwall
Footwall
Cu-Ag

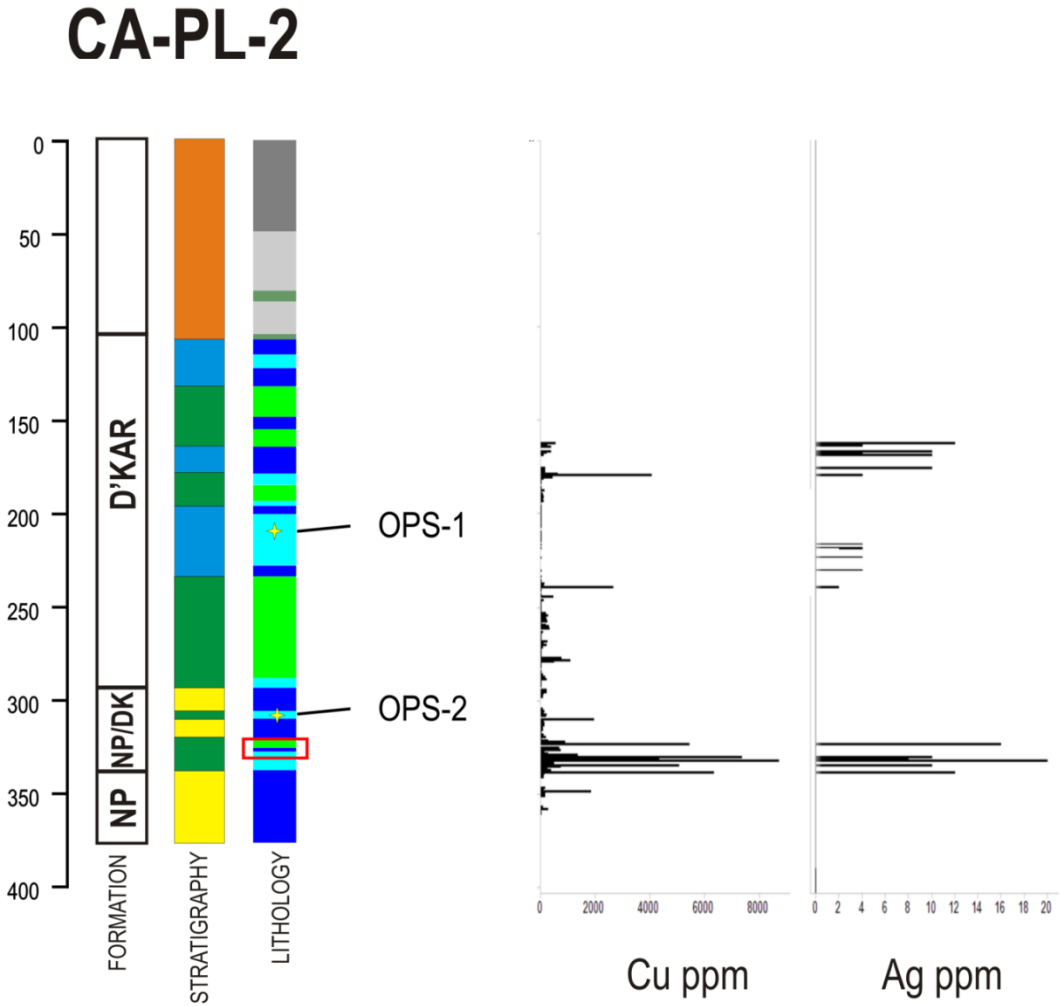
CA-PL-2
0
50
100
150
200
250
300
350
400
D'KAR
NP/DK
NP
FORMATION
STRATIGRAPHY
LITHOLOGY
OPS-1
OPS-2
0
2000
4000
6000
8000
Cu ppm
0
2
4
6
8
10
12
14
16
18
20
Ag ppm

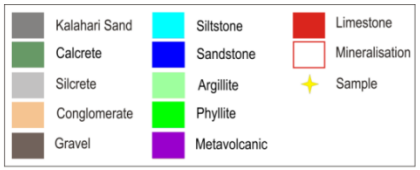
Kalahari Sand
Calcrete
Silcrete
Conglomerate
Gravel
Siltstone
Sandstone
Argillite
Phyllite
Metavolcanic
Limestone
Mineralisation
Sample

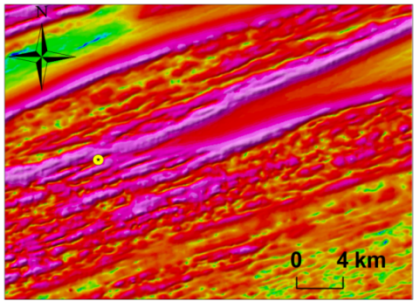
N
0
4 km

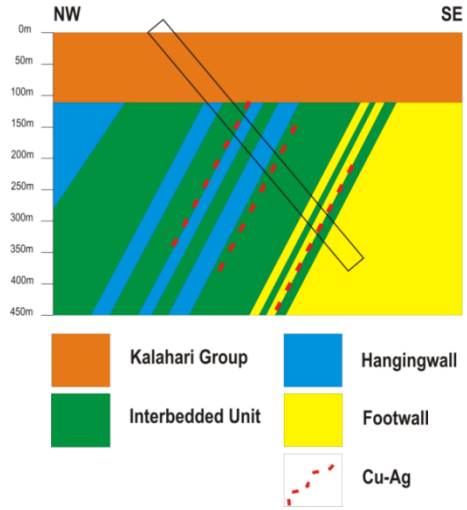
NW
SE
0m
50m
100m
150m
200m
250m
300m
350m
400m
450m
Kalahari Group
Interbedded Unit
Hangingwall
Footwall
Cu-Ag

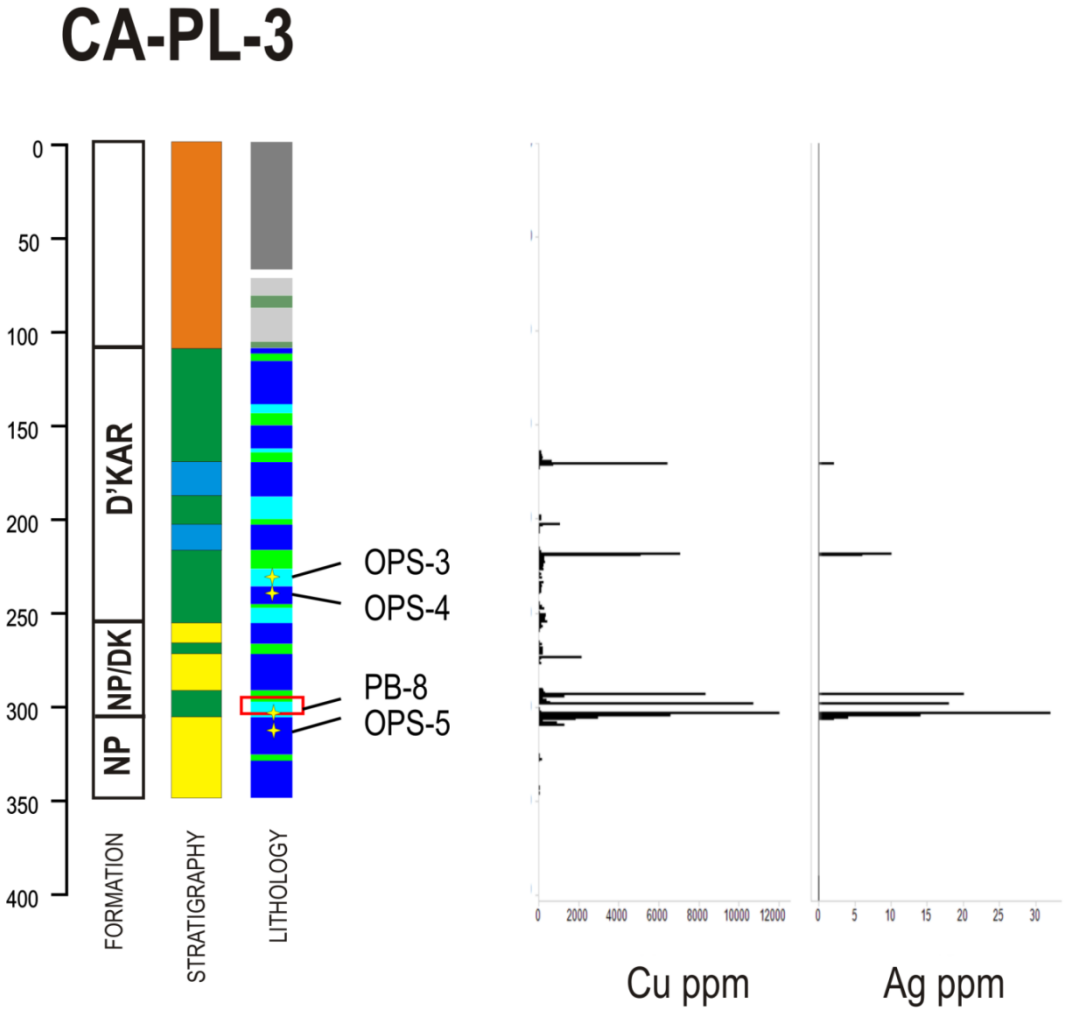
CA-PL-3
0
50
100
150
200
250
300
350
400
D'KAR
NP/DK
NP
FORMATION
STRATIGRAPHY
LITHOLOGY
OPS-3
OPS-4
PB-8
OPS-5
0
2000
4000
6000
8000
10000
12000
Cu ppm
0
5
10
15
20
25
30
Ag ppm

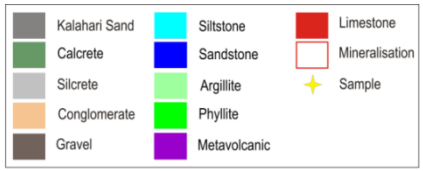
Kalahari Sand
Calcrete
Silcrete
Conglomerate
Gravel
Siltstone
Sandstone
Argillite
Phyllite
Metavolcanic
Limestone
Mineralisation
Sample

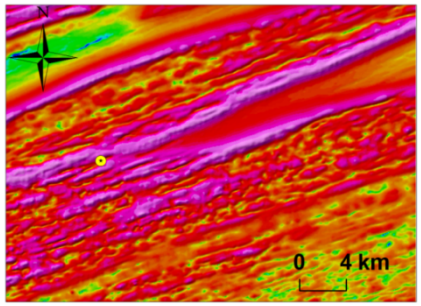
N
0
4 km

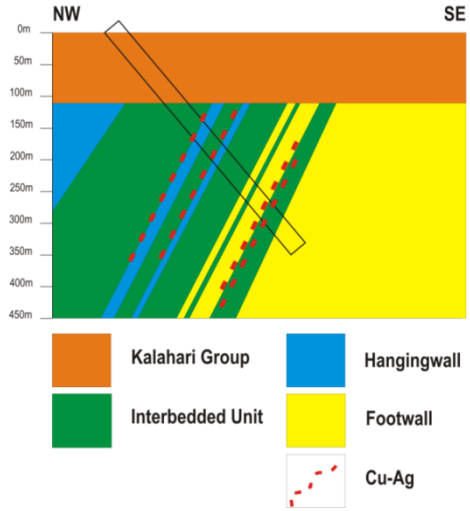
NW
SE
0m
50m
100m
150m
200m
250m
300m
350m
400m
450m
Kalahari Group
Interbedded Unit
Hangingwall
Footwall
Cu-Ag

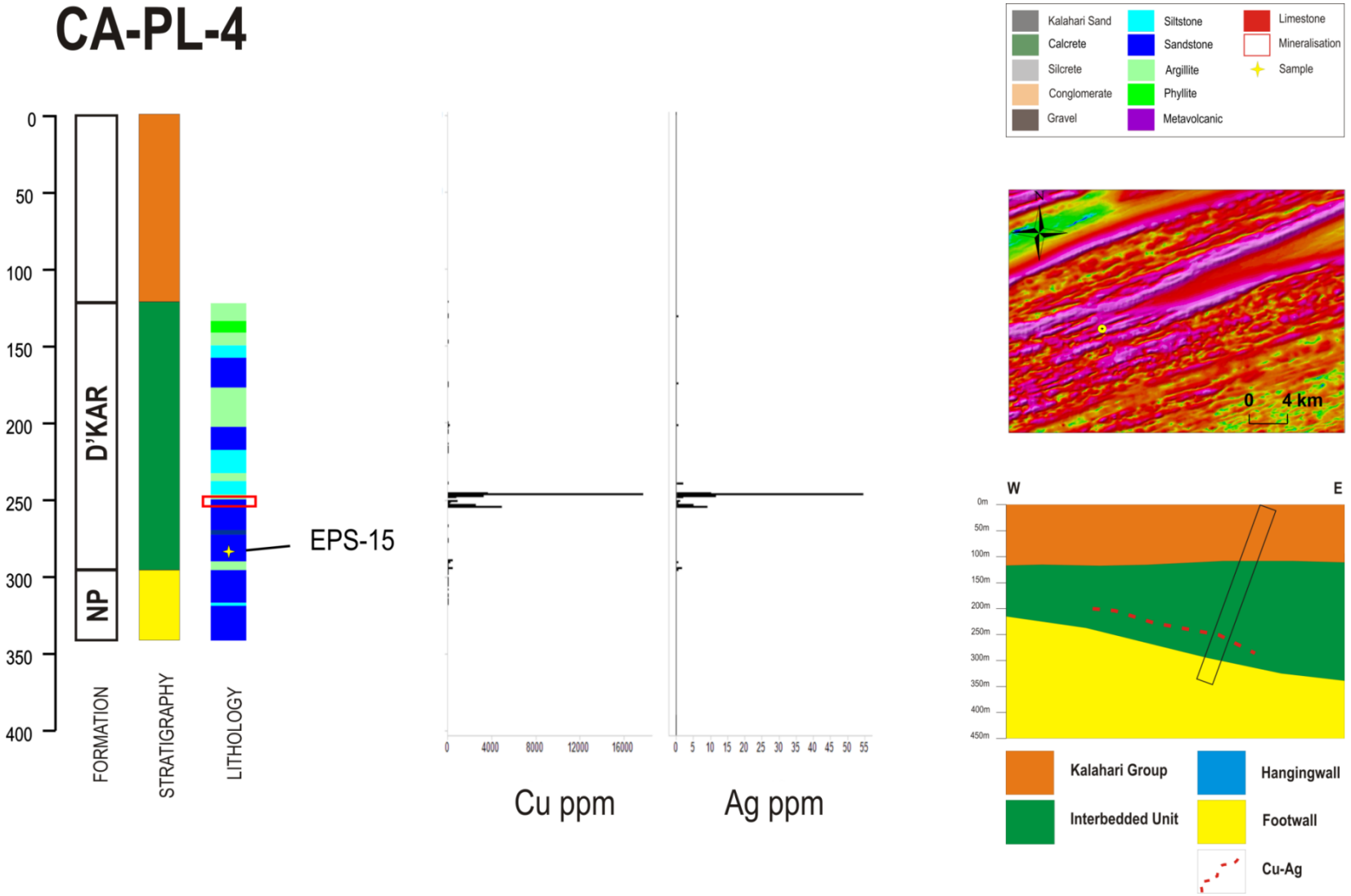
CA-PL-4
0
50
100
150
200
250
300
350
400
D'KAR
NP
FORMATION
STRATIGRAPHY
LITHOLOGY
EPS-15
0
4000
8000
12000
16000
Cu ppm
0
5
10
15
20
25
30
35
40
45
50
55
Ag ppm
Kalahari Sand
Calcrete
Silcrete
Conglomerate
Gravel
Siltstone
Sandstone
Argillite
Phyllite
Metavolcanic
Limestone
Mineralisation
Sample
N
0
4 km
W
E
0m
50m
100m
150m
200m
250m
300m
350m
400m
450m
Kalahari Group
Interbedded Unit
Hangingwall
Footwall
Cu-Ag

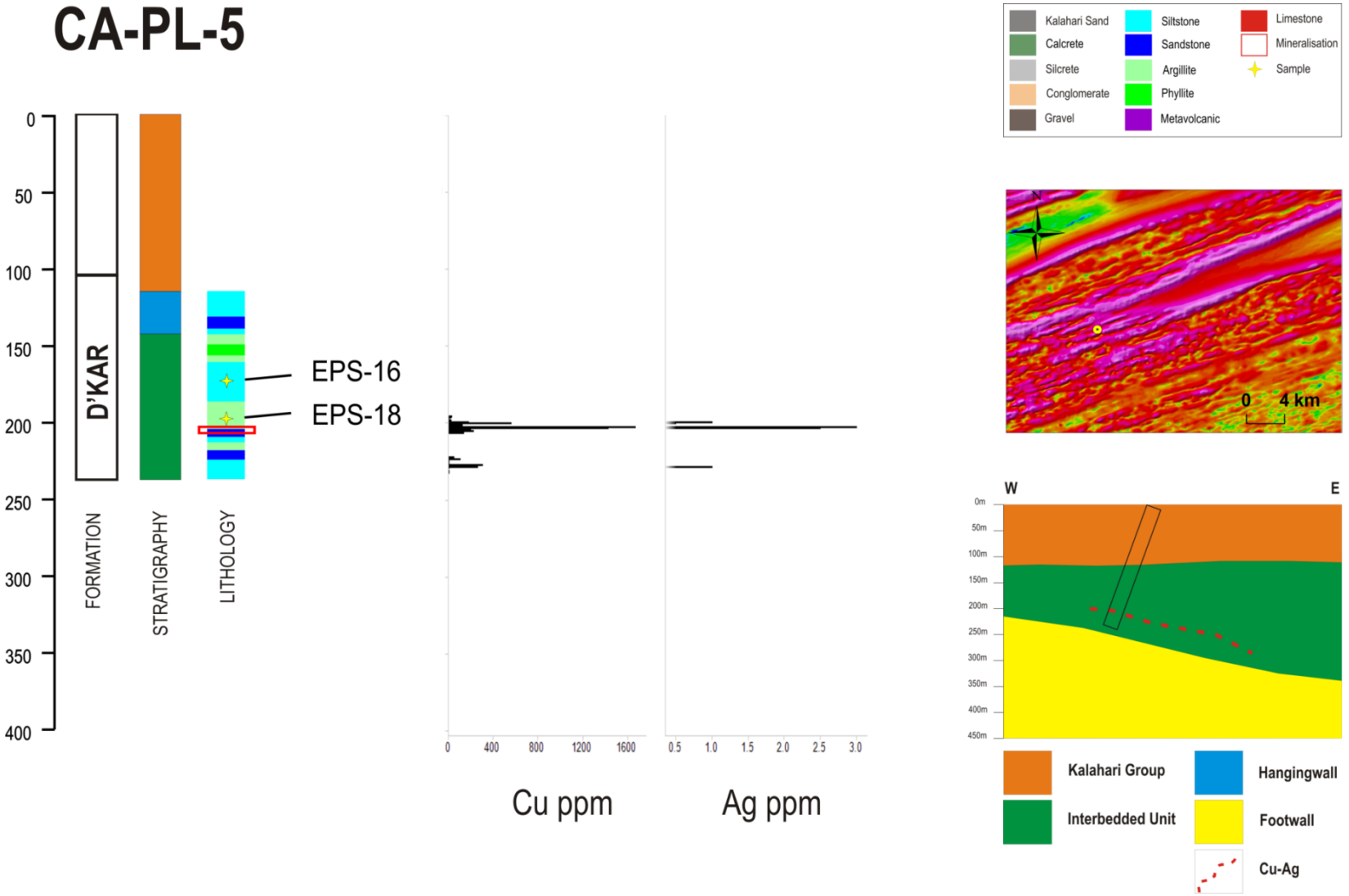
CA-PL-5
0
50
100
150
200
250
300
350
400
D'KAR
FORMATION
STRATIGRAPHY
LITHOLOGY
EPS-16
EPS-18
0
400
800
1200
1600
Cu ppm
0.5
1.0
1.5
2.0
2.5
3.0
Ag ppm
Kalahari Sand
Calcrete
Silcrete
Conglomerate
Gravel
Siltstone
Sandstone
Argillite
Phyllite
Metavolcanic
Limestone
Mineralisation
Sample
N
0
4 km
W
E
0m
50m
100m
150m
200m
250m
300m
350m
400m
450m
Kalahari Group
Interbedded Unit
Hangingwall
Footwall
Cu-Ag

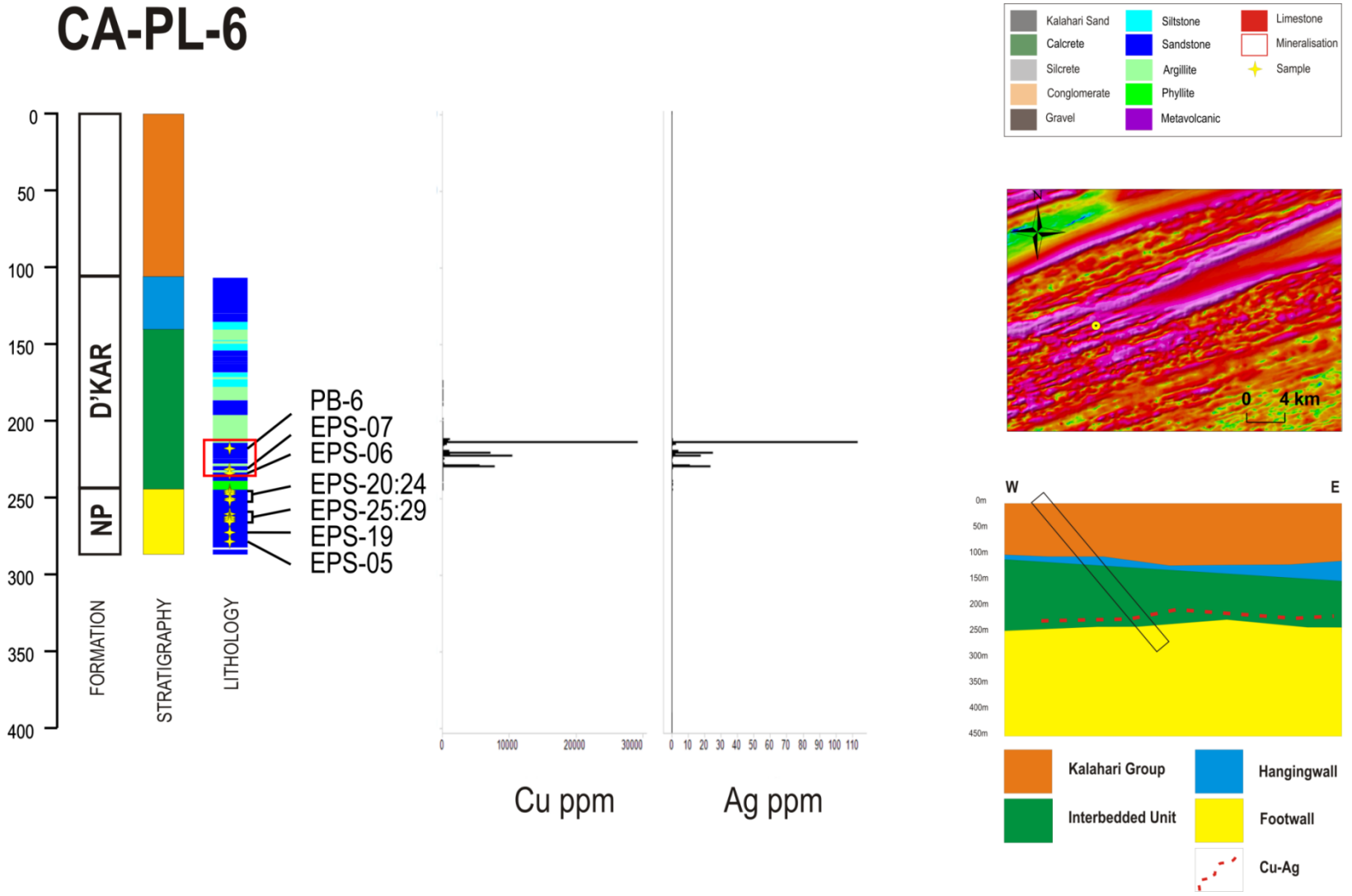
CA-PL-6
0
50
100
150
200
250
300
350
400
D'KAR
NP
FORMATION
STRATIGRAPHY
LITHOLOGY
PB-6
EPS-07
EPS-06
EPS-20:24
EPS-25:29
EPS-19
EPS-05
0
10000
20000
30000
Cu ppm
0 10 20 30 40 50 60 70 80 90 100 110
Ag ppm
Kalahari Sand
Calcrete
Silcrete
Conglomerate
Gravel
Siltstone
Sandstone
Argillite
Phyllite
Metavolcanic
Limestone
Mineralisation
Sample
N
0
4 km
W
E
0m
50m
100m
150m
200m
250m
300m
350m
400m
450m
Kalahari Group
Interbedded Unit
Hangingwall
Footwall
Cu-Ag

CA-PL-7

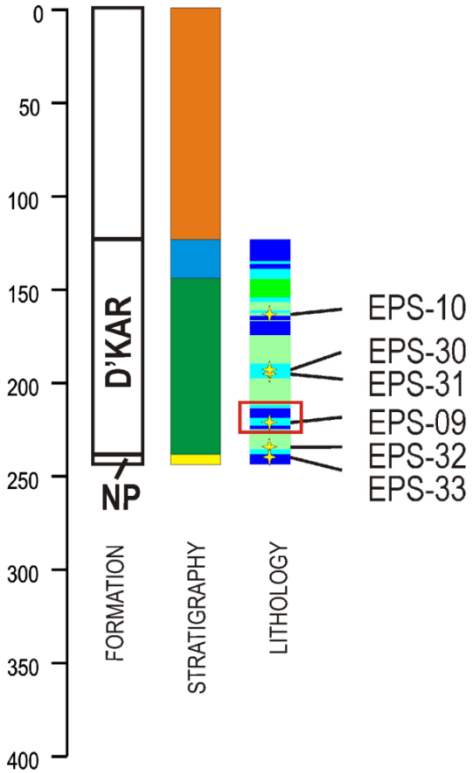
0
50
100
150
200
250
300
350
400
D'KAR
NP
FORMATION
STRATIGRAPHY
LITHOLOGY
EPS-10
EPS-30
EPS-31
EPS-09
EPS-32
EPS-33

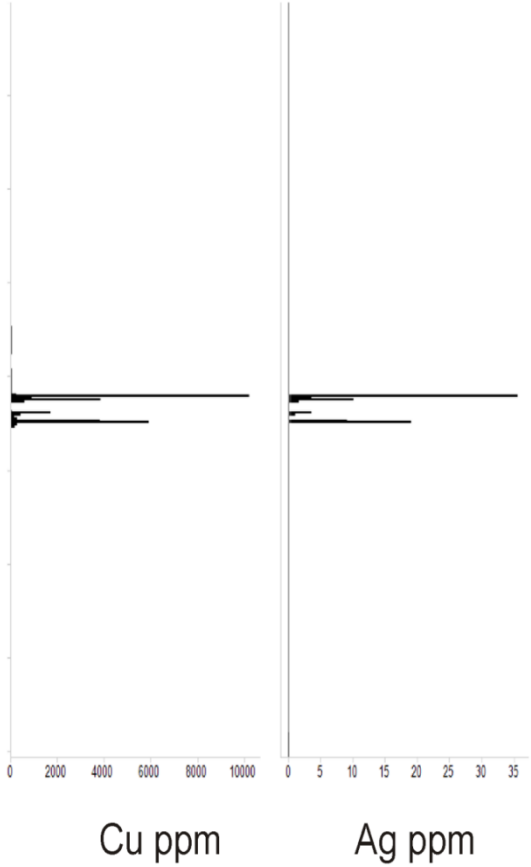
0
2000
4000
6000
8000
10000
0
5
10
15
20
25
30
35
Cu ppm
Ag ppm

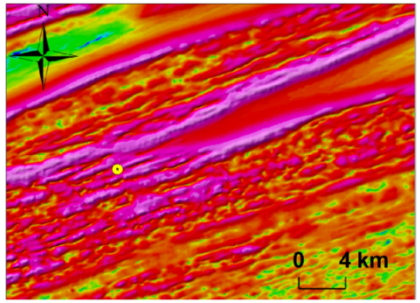
N
0
4 km

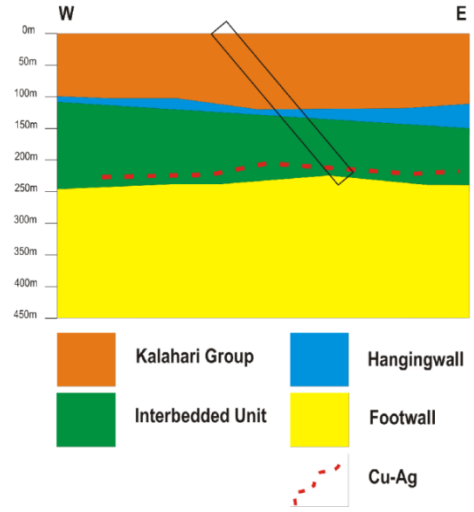
W
E
0m
50m
100m
150m
200m
250m
300m
350m
400m
450m
Kalahari Group
Interbedded Unit
Hangingwall
Footwall
Cu-Ag

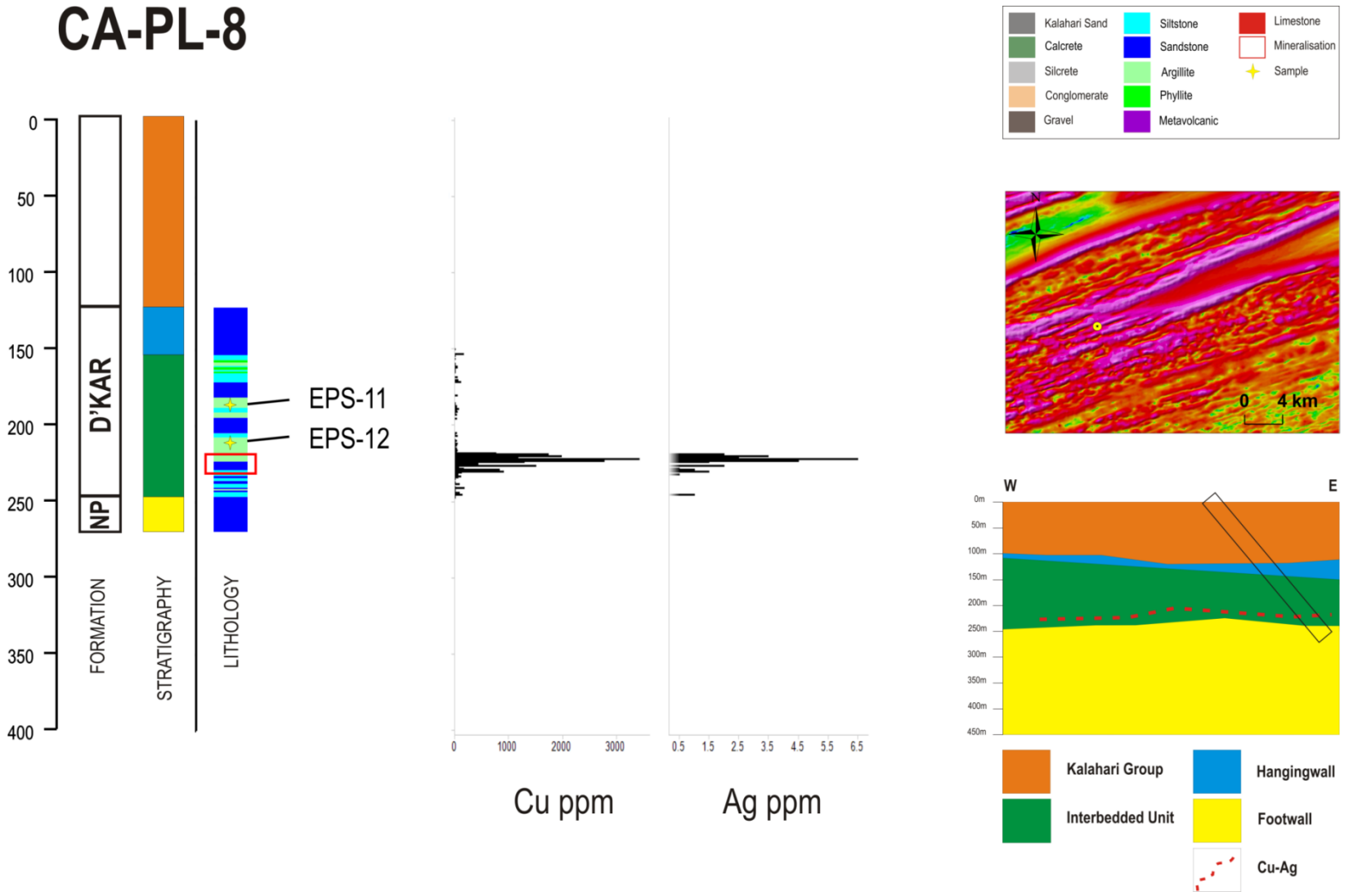
CA-PL-8
0
50
100
150
200
250
300
350
400
D'KAR
NP
FORMATION
STRATIGRAPHY
LITHOLOGY
EPS-11
EPS-12
0
1000
2000
3000
Cu ppm
0.5
1.5
2.5
3.5
4.5
5.5
6.5
Ag ppm
Kalahari Sand
Calcrete
Silcrete
Conglomerate
Gravel
Siltstone
Sandstone
Argillite
Phyllite
Metavolcanic
Limestone
Mineralisation
Sample
N
0
4 km
W
E
0m
50m
100m
150m
200m
250m
300m
350m
400m
450m
Kalahari Group
Interbedded Unit
Hangingwall
Footwall
Cu-Ag

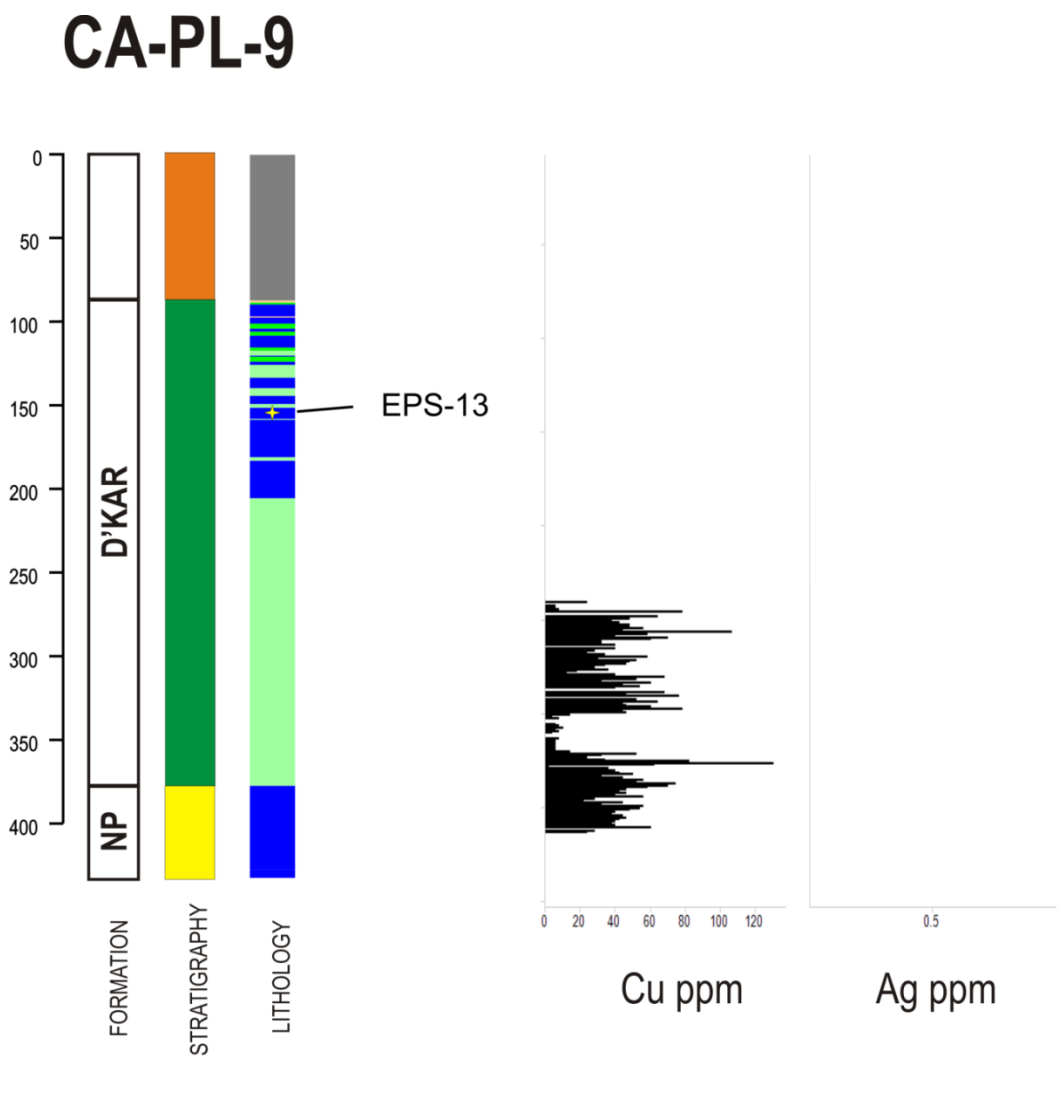
CA-PL-9
0
50
100
150
200
250
300
350
400
D'KAR
NP
EPS-13
FORMATION
STRATIGRAPHY
LITHOLOGY
0 20 40 60 80 100 120
Cu ppm
0.5
Ag ppm

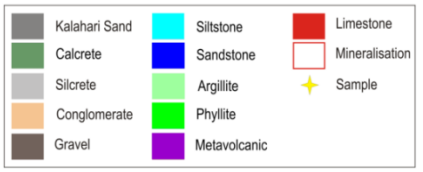
Kalahari Sand
Calcrete
Silcrete
Conglomerate
Gravel
Siltstone
Sandstone
Argillite
Phyllite
Metavolcanic
Limestone
Mineralisation
Sample

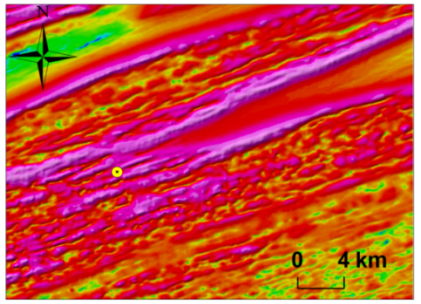
N
0
4 km

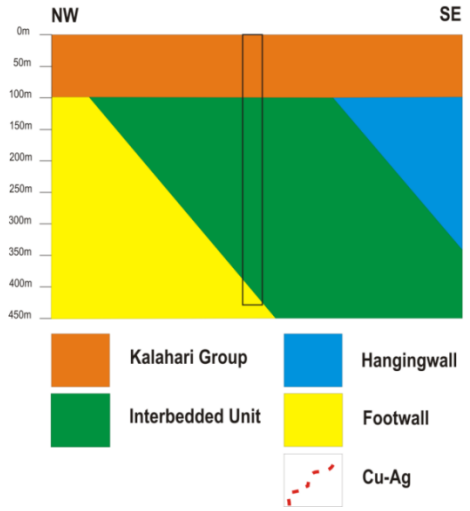
NW
SE
0m
50m
100m
150m
200m
250m
300m
350m
400m
450m
Kalahari Group
Interbedded Unit
Hangingwall
Footwall
Cu-Ag

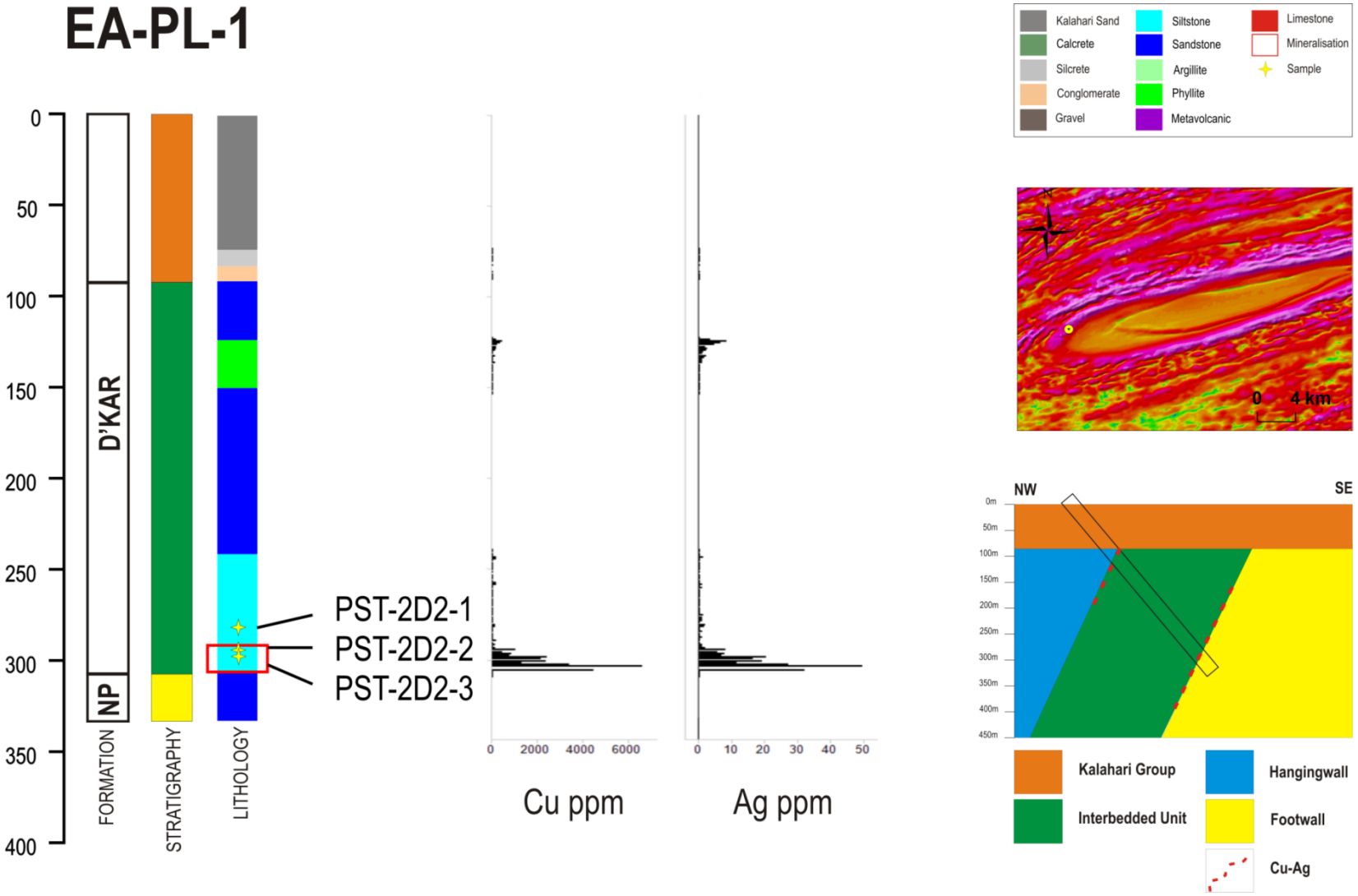
EA-PL-1
0
50
100
150
200
250
300
350
400
D'KAR
NP
FORMATION
STRATIGRAPHY
LITHOLOGY
PST-2D2-1
PST-2D2-2
PST-2D2-3
0
2000
4000
6000
Cu ppm
0
10
20
30
40
50
Ag ppm
Kalahari Sand
Calcrete
Silcrete
Conglomerate
Gravel
Siltstone
Sandstone
Argillite
Phyllite
Metavolcanic
Limestone
Mineralisation
Sample
0
4 km
NW
SE
0m
50m
100m
150m
200m
250m
300m
350m
400m
450m
Kalahari Group
Interbedded Unit
Hangingwall
Footwall
Cu-Ag

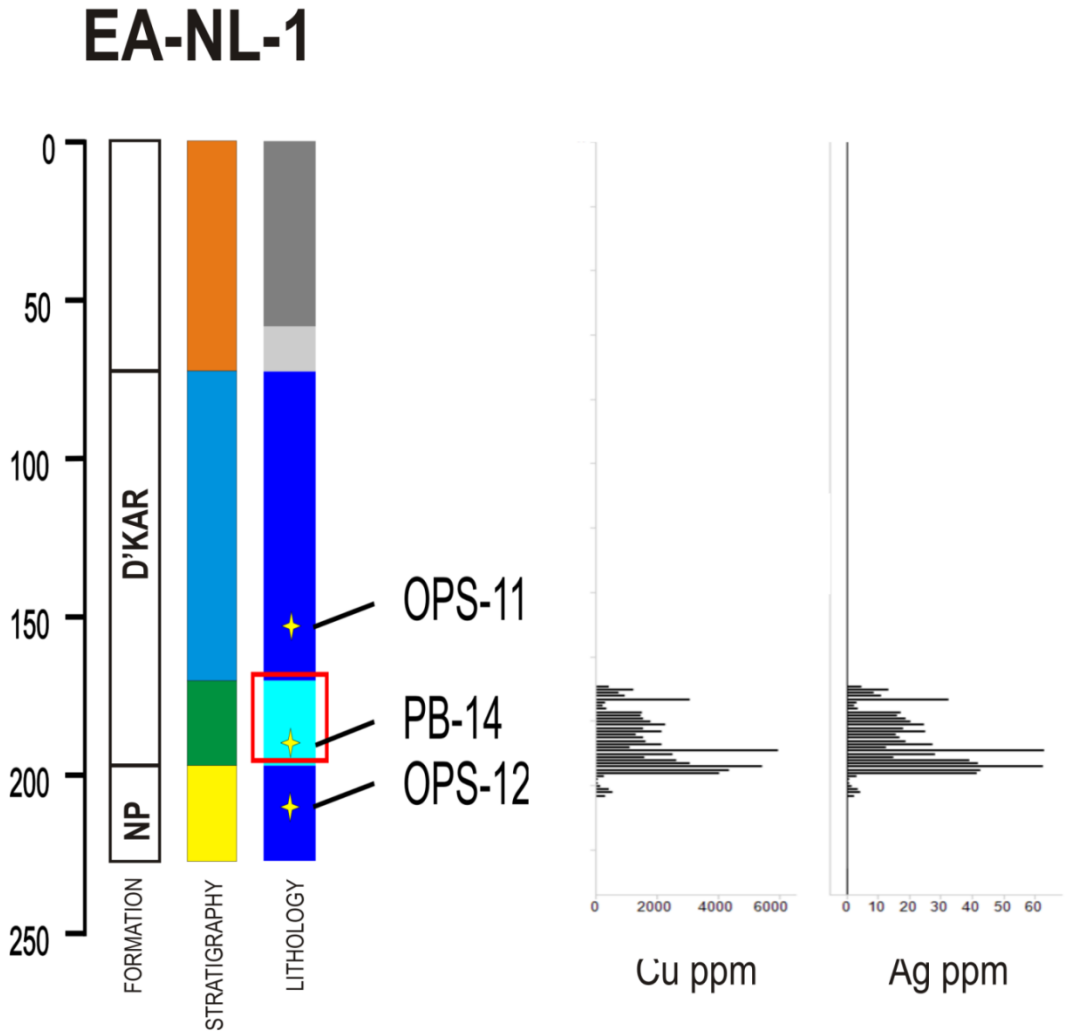
EA-NL-1
0
50
100
150
200
250
D'KAR
NP
FORMATION
STRATIGRAPHY
LITHOLOGY
OPS-11
PB-14
OPS-12
0
2000
4000
6000
Cu ppm
0
10
20
30
40
50
60
Ag ppm

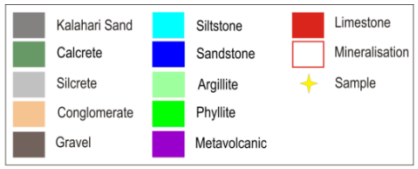
Kalahari Sand
Calcrete
Silcrete
Conglomerate
Gravel
Siltstone
Sandstone
Argillite
Phyllite
Metavolcanic
Limestone
Mineralisation
Sample

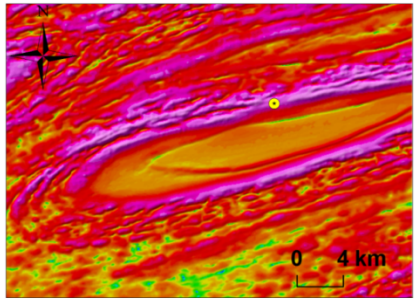
N
0
4 km

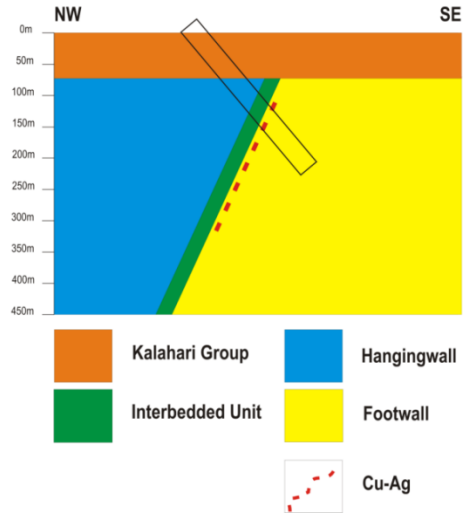
NW
SE
0m
50m
100m
150m
200m
250m
300m
350m
400m
450m
Kalahari Group
Interbedded Unit
Hangingwall
Footwall
Cu-Ag

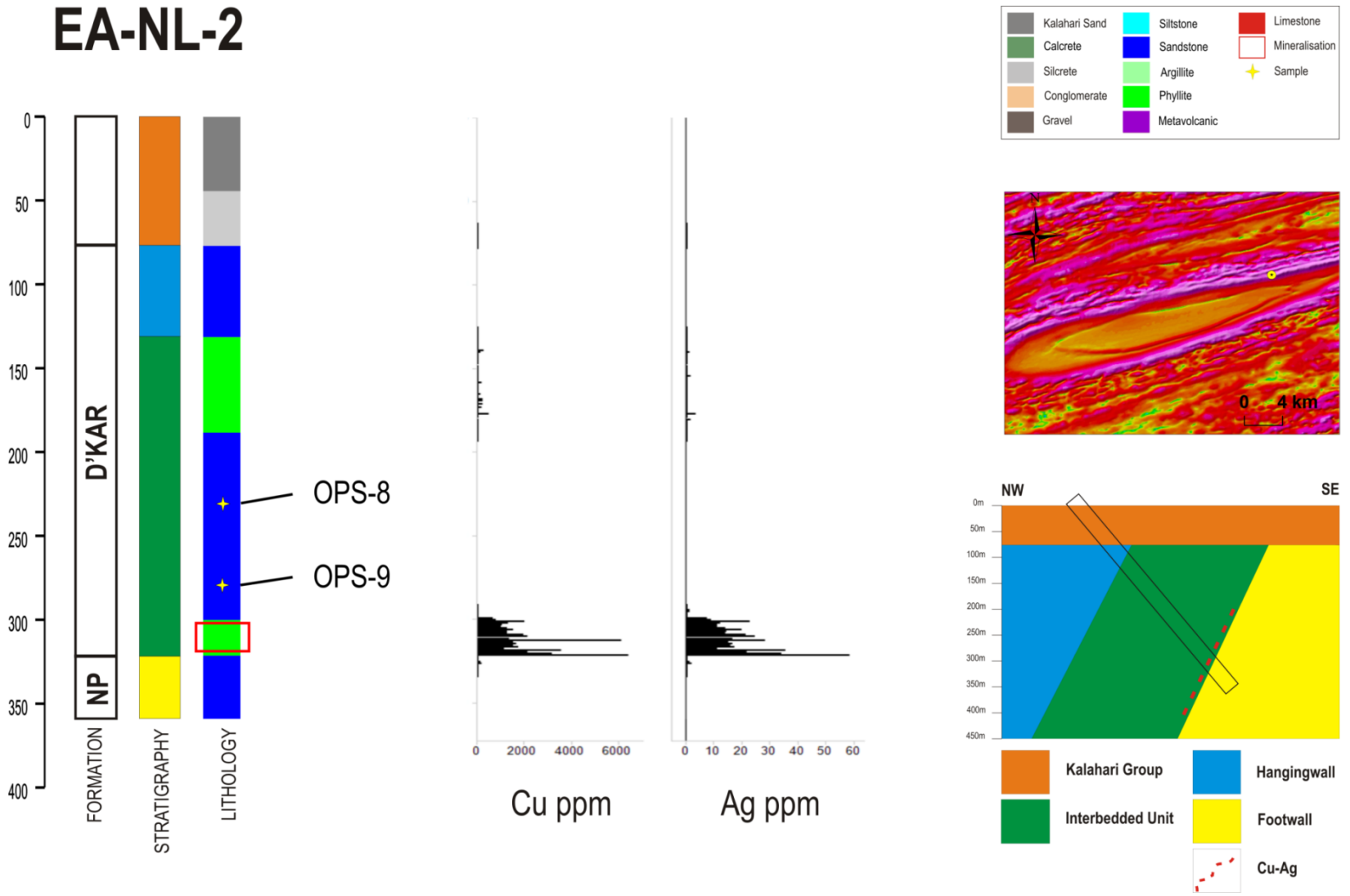
EA-NL-2
0
50
100
150
200
250
300
350
400
D'KAR
NP
FORMATION
STRATIGRAPHY
LITHOLOGY
OPS-8
OPS-9
0
2000
4000
6000
Cu ppm
0
10
20
30
40
50
60
Ag ppm
Kalahari Sand
Calcrete
Silcrete
Conglomerate
Gravel
Siltstone
Sandstone
Argillite
Phyllite
Metavolcanic
Limestone
Mineralisation
Sample
N
0
4 km
NW
SE
0m
50m
100m
150m
200m
250m
300m
350m
400m
450m
Kalahari Group
Interbedded Unit
Hangingwall
Footwall
Cu-Ag

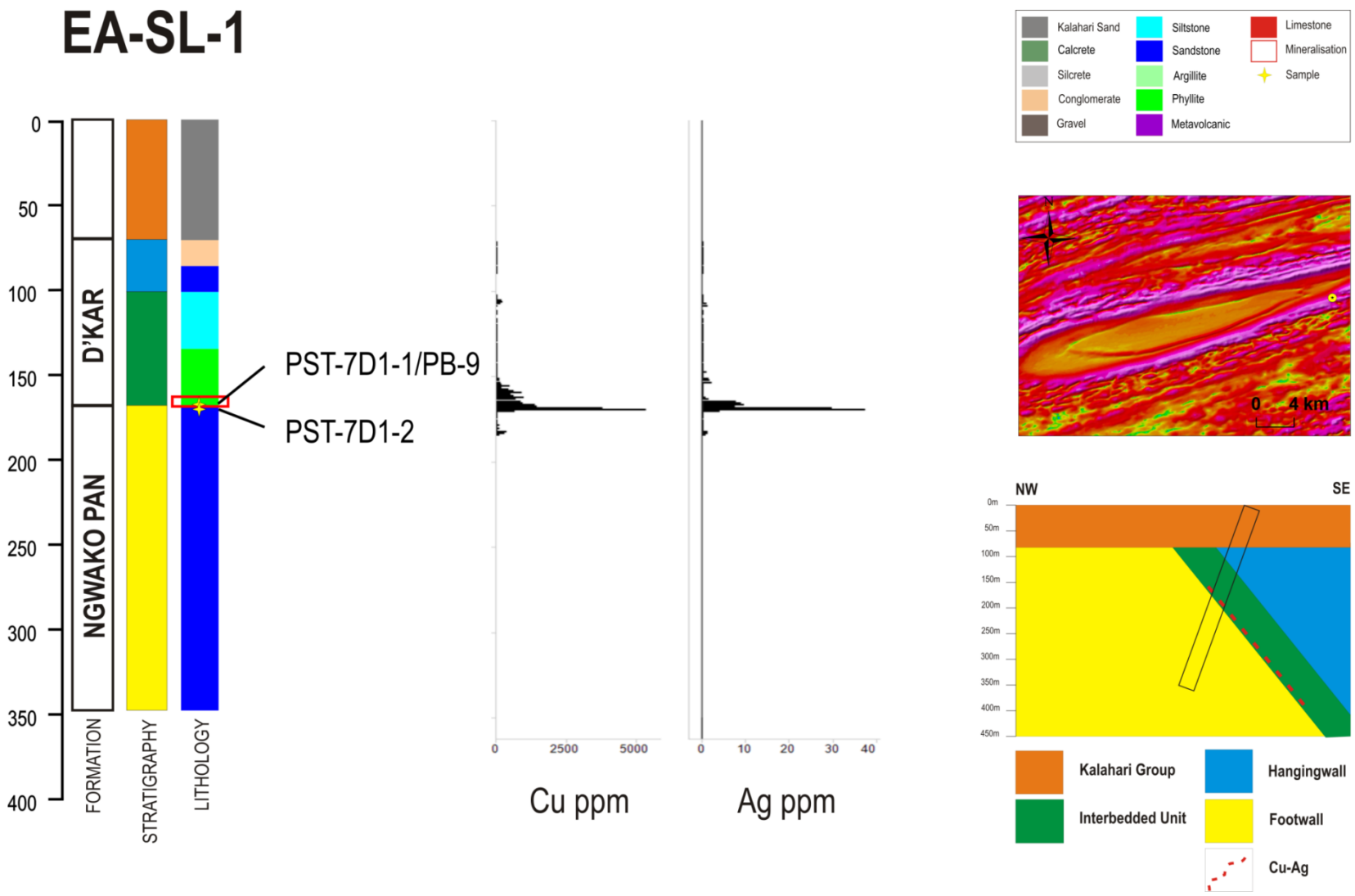
EA-SL-1
0
50
100
150
200
250
300
350
400
D'KAR
NGWAKO PAN
FORMATION
STRATIGRAPHY
LITHOLOGY
PST-7D1-1/PB-9
PST-7D1-2
0
2500
5000
Cu ppm
0
10
20
30
40
Ag ppm
Kalahari Sand
Calcrete
Silcrete
Conglomerate
Gravel
Siltstone
Sandstone
Argillite
Phyllite
Metavolcanic
Limestone
Mineralisation
Sample
N
0 4 km
NW
SE
0m
50m
100m
150m
200m
250m
300m
350m
400m
450m
Kalahari Group
Interbedded Unit
Hangingwall
Footwall
Cu-Ag

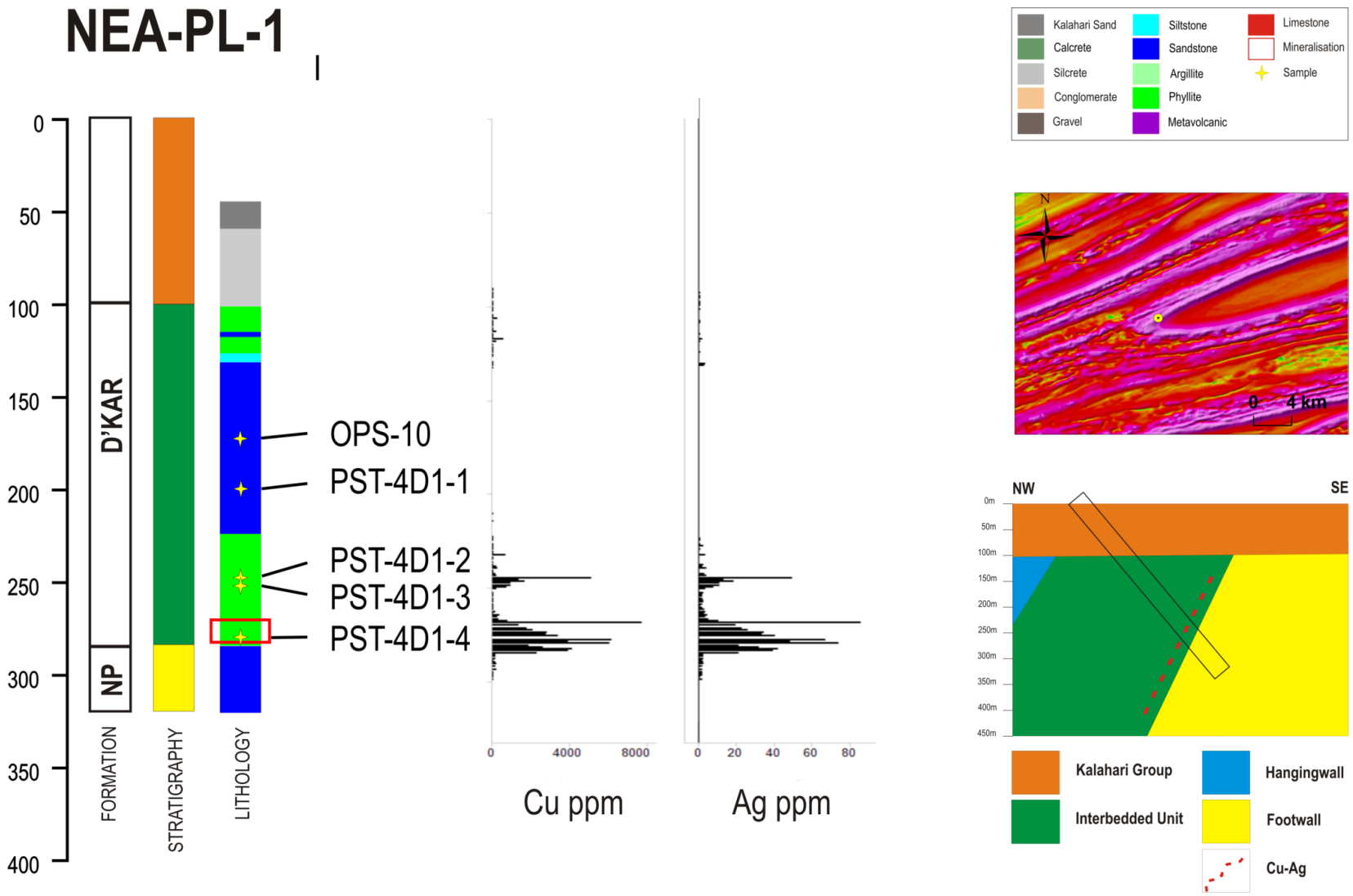
NEA-PL-1
0
50
100
150
200
250
300
350
400
D'KAR
NP
FORMATION
STRATIGRAPHY
LITHOLOGY
OPS-10
PST-4D1-1
PST-4D1-2
PST-4D1-3
PST-4D1-4
0
4000
8000
Cu ppm
0
20
40
60
80
Ag ppm
Kalahari Sand
Calcrete
Silcrete
Conglomerate
Gravel
Siltstone
Sandstone
Argillite
Phyllite
Metavolcanic
Limestone
Mineralisation
Sample
N
0
4 km
NW
SE
0m
50m
100m
150m
200m
250m
300m
350m
400m
450m
Kalahari Group
Interbedded Unit
Hangingwall
Footwall
Cu-Ag

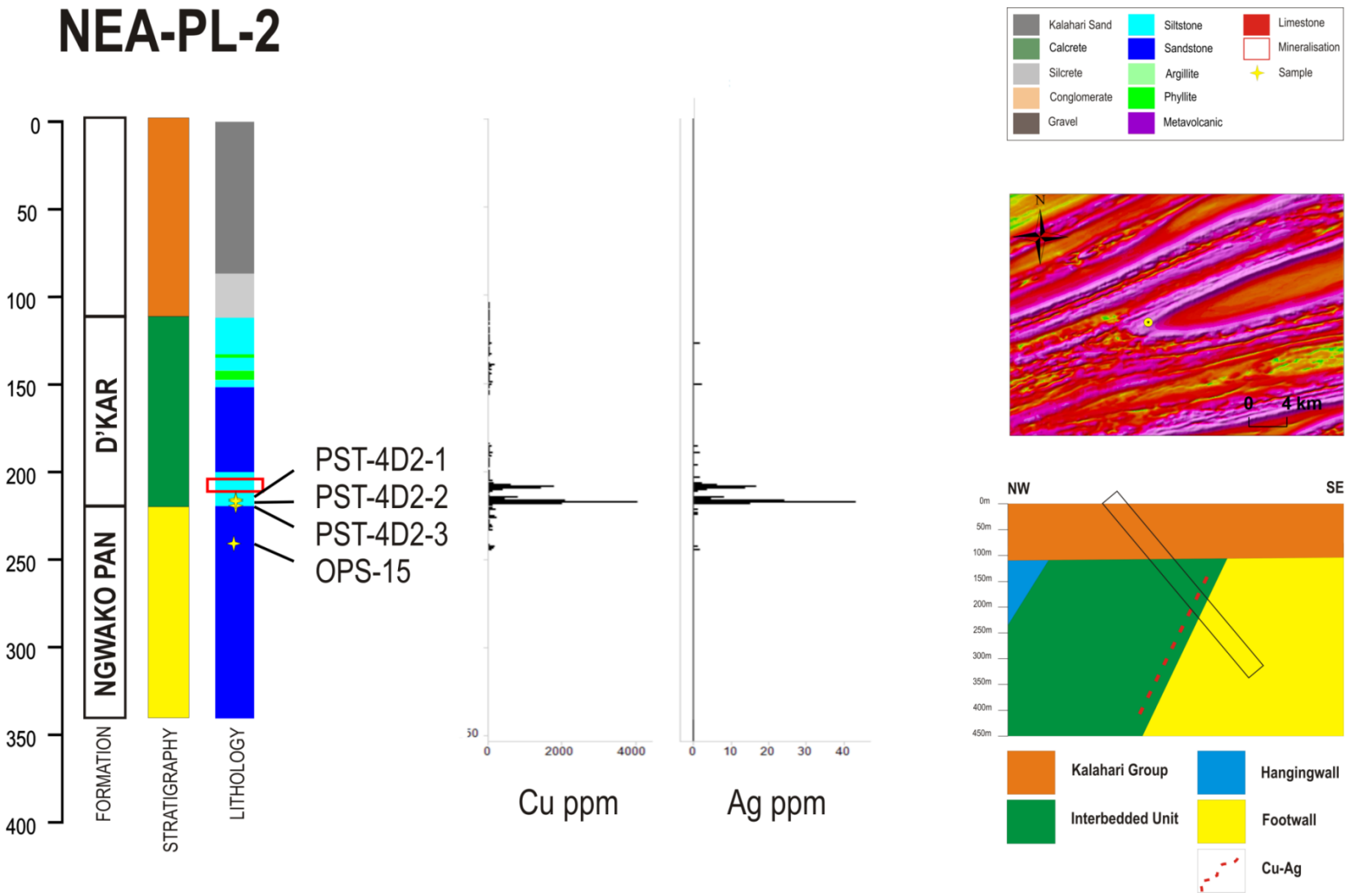
NEA-PL-2
0
50
100
150
200
250
300
350
400
FORMATION
NGWAKO PAN
D'KAR
STRATIGRAPHY
LITHOLOGY
PST-4D2-1
PST-4D2-2
PST-4D2-3
OPS-15
0
2000
4000
Cu ppm
0
10
20
30
40
Ag ppm
Kalahari Sand
Calcrete
Silcrete
Conglomerate
Gravel
Siltstone
Sandstone
Argillite
Phyllite
Metavolcanic
Limestone
Mineralisation
Sample
N
0
4 km
NW
SE
0m
50m
100m
150m
200m
250m
300m
350m
400m
450m
Kalahari Group
Interbedded Unit
Hangingwall
Footwall
Cu-Ag

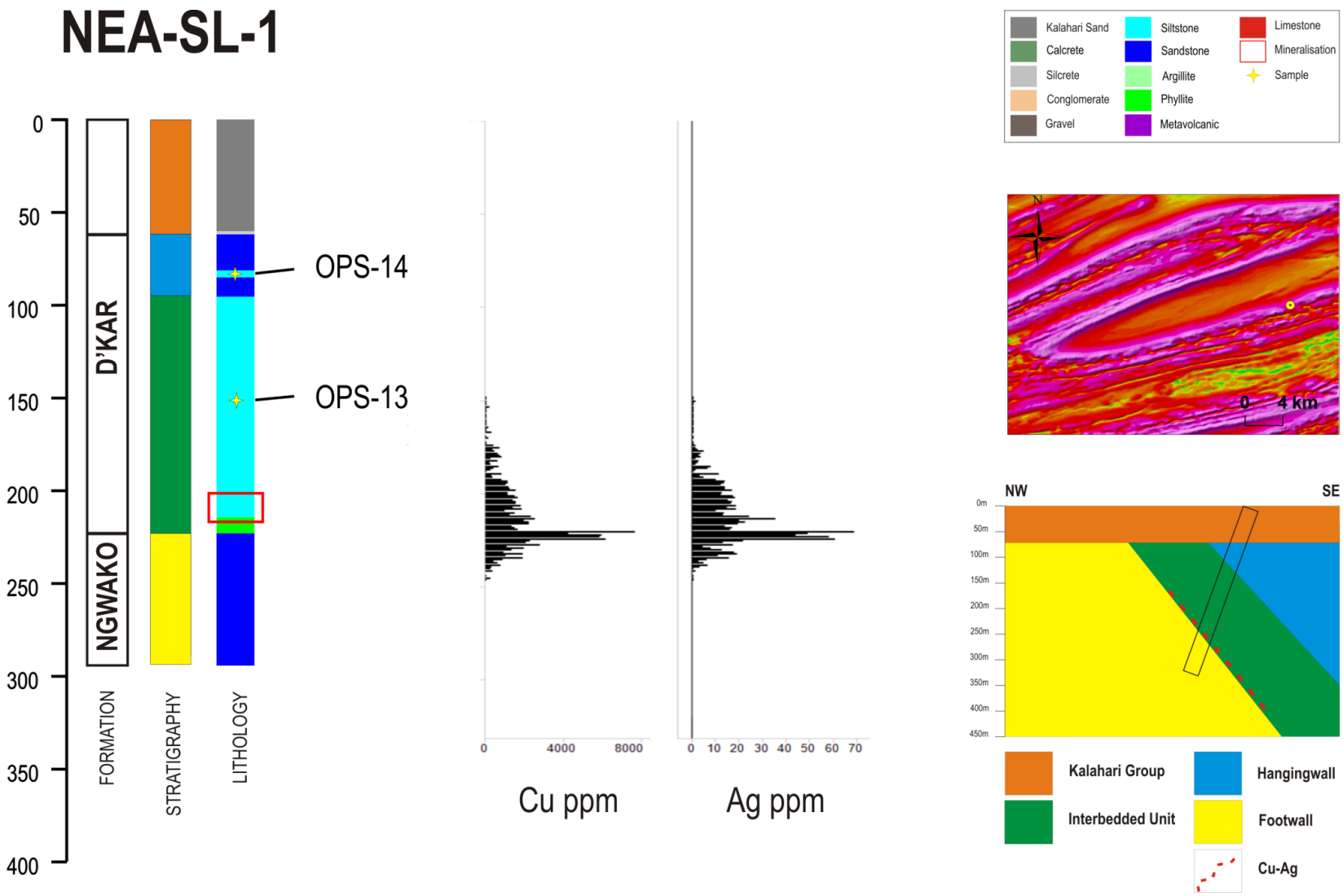
NEA-SL-1
0
50
100
150
200
250
300
350
400
D'KAR
NGWAKO
FORMATION
STRATIGRAPHY
LITHOLOGY
OPS-14
OPS-13
0
4000
8000
Cu ppm
0 10 20 30 40 50 60 70
Ag ppm
Kalahari Sand
Calcrete
Silcrete
Conglomerate
Gravel
Siltstone
Sandstone
Argillite
Phyllite
Metavolcanic
Limestone
Mineralisation
Sample
N
0 4 km
NW
SE
0m
50m
100m
150m
200m
250m
300m
350m
400m
450m
Kalahari Group
Interbedded Unit
Hangingwall
Footwall
Cu-Ag

Appendix III: Zircon Geochronology Results

					Ratios						Ages (Ma)						% discord. (206/238207/235)	% discord. (206/238 207/206)	Best Age	±2s
Sample	Grain No.	Pb (ppm)	U (ppm)	Atomic Th/U	206/238	± s.e.	207/235	± s.e.	207/206	± s.e.	206/238	± 2s	207/235	± 2s	207/206	± 2s				
ZR-01	G001	32.9	139	1.24	0.18	0.002	1.92	0.04	0.08	0.002	1080	25.8	1087	34.7	1103	30.3	0.65	2.07	1103	30
ZR-01	G002	59.3	273	0.36	0.21	0.003	2.28	0.05	0.08	0.002	1223	29.4	1206	38.4	1176	40.4	-1.44	-3.97	1176	40
ZR-01	G003	20.6	82.1	0.59	0.22	0.003	2.60	0.08	0.08	0.002	1306	33.8	1300	48.3	1291	50.6	-0.50	-1.22	1291	51
ZR-01	G004	55.4	284	0.26	0.19	0.002	3.26	0.07	0.13	0.003	1102	27.1	1470	39.5	2053	45.4	25.0	46.3		
ZR-01	G005	101	484	0.59	0.19	0.002	2.03	0.04	0.08	0.001	1123	25.2	1125	28.0	1131	29.9	0.20	0.73	1131	30
ZR-01	G006	97.6	413	1.13	0.19	0.002	6.61	0.11	0.25	0.004	1138	25.6	2061	34.3	3175	36.6	44.8	64.1		
ZR-01	G007	148	476	0.71	0.27	0.003	3.69	0.07	0.10	0.002	1533	34.0	1569	34.3	1618	35.5	2.25	5.23	1618	36
ZR-01	G008	37.0	184	0.55	0.18	0.002	1.95	0.05	0.08	0.002	1077	27.2	1099	40.9	1144	44.6	1.97	5.80	1144	45
ZR-01	G009	38.4	155	0.56	0.22	0.003	2.73	0.06	0.09	0.002	1308	31.5	1338	40.1	1388	42.8	2.26	5.79	1388	43
ZR-01	G010	79.3	388	0.21	0.20	0.003	3.20	0.07	0.12	0.002	1154	27.7	1458	37.9	1934	43.0	20.8	40.3		
ZR-01	G011	60.3	295	0.35	0.19	0.002	2.33	0.05	0.09	0.002	1148	26.6	1220	33.1	1351	36.5	5.90	15.03		
ZR-01	G012	74.0	327	0.88	0.19	0.002	2.13	0.04	0.08	0.002	1107	25.5	1159	31.3	1260	34.5	4.54	12.19	1260	35
ZR-01	G013	0	689	0.81	0.25	0.003	15.0	0.23	0.43	0.006	1462	31.8	2812	35.7	4004	35.7	48.0	63.5		
ZR-01	G014	76.6	241	0.66	0.28	0.004	4.09	0.10	0.11	0.003	1567	37.8	1651	44.0	1762	46.2	5.13	11.1	1762	46
ZR-01	G015	101	462	0.38	0.21	0.003	2.36	0.04	0.08	0.001	1226	27.3	1232	29.3	1244	30.9	0.51	1.49	1244	31
ZR-01	G016	73.5	388	0.31	0.19	0.002	1.93	0.04	0.08	0.001	1097	24.9	1091	28.6	1082	30.6	-0.48	-1.31	1082	31
ZR-01	G017	44.3	213	0.46	0.19	0.002	2.07	0.04	0.08	0.002	1138	26.3	1140	31.8	1146	34.1	0.19	0.67	1146	34
ZR-01	G018	21.5	90.1	0.98	0.19	0.003	2.07	0.05	0.08	0.002	1142	28.2	1139	39.9	1133	42.5	-0.32	-0.80	1133	43
ZR-01	G019	123	507	0.71	0.20	0.003	4.17	0.07	0.15	0.002	1189	27.0	1667	34.0	2337	37.7	28.7	49.1		
ZR-01	G020	98.9	279	0.41	0.33	0.004	5.29	0.09	0.12	0.002	1819	38.9	1867	34.4	1922	34.8	2.58	5.38	1922	35
ZR-01	G021	74.8	373	0.41	0.19	0.002	2.07	0.04	0.08	0.002	1118	25.8	1140	31.5	1183	34.2	1.90	5.44	1183	34
ZR-01	G022	111	265	0.90	0.34	0.004	5.46	0.09	0.12	0.002	1897	40.4	1894	34.7	1891	34.9	-0.19	-0.33	1891	35
ZR-01	G023	98.1	212	1.41	0.33	0.004	5.19	0.09	0.11	0.002	1853	39.9	1851	35.3	1849	35.6	-0.13	-0.21	1849	36

					Ratios						Ages (Ma)						% discord. (206/238207/235)	% discord. (206/238 207/206)	Best Age	±2s
Sample	Grain No.	Pb (ppm)	U (ppm)	Atomic Th/U	206/238	± s.e.	207/235	± s.e.	207/206	± s.e.	206/238	± 2s	207/235	± 2s	207/206	± 2s				
ZR-01	G024	88.0	226	0.71	0.33	0.004	5.38	0.10	0.12	0.002	1862	40.8	1881	37.2	1904	37.7	1.02	2.19	1904	38
ZR-01	G025	169	705	0.38	0.21	0.003	7.24	0.11	0.25	0.004	1219	27.1	2141	34.4	3200	36.2	43.1	61.9		
ZR-01	G026	127	607	0.39	0.19	0.002	2.85	0.05	0.11	0.002	1139	25.8	1368	31.3	1748	35.2	16.8	34.9		
ZR-01	G044	158	642	0.16	0.22	0.003	10.6	0.17	0.34	0.005	1302	28.9	2490	36.1	3681	37.2	47.7	64.6		
ZR-01	G045	57.8	304	0.38	0.18	0.002	2.01	0.04	0.08	0.002	1071	24.7	1120	30.8	1216	34.1	4.33	11.9	1216	34
ZR-01	G046	13.8	76.4	0.50	0.17	0.002	1.82	0.05	0.08	0.002	994	25.9	1051	42.6	1172	48.1	5.40	15.2		
ZR-01	G047	37.4	171	0.84	0.18	0.002	1.96	0.04	0.08	0.002	1087	25.8	1102	34.2	1134	37.3	1.41	4.19	1134	37
ZR-01	G048	97.6	461	0.58	0.18	0.002	3.11	0.06	0.12	0.002	1078	24.8	1435	32.8	2014	37.7	24.9	46.5		
ZR-01	G049	75.8	397	0.20	0.19	0.002	2.30	0.04	0.09	0.002	1118	25.4	1213	30.5	1387	34.0	7.84	19.4		
ZR-01	G050	84.7	408	0.12	0.21	0.003	2.60	0.05	0.09	0.002	1245	28.3	1300	32.6	1394	35.2	4.26	10.7	1394	35
ZR-01	G051	41.8	251	1.21	0.13	0.002	1.39	0.03	0.08	0.002	763	19.0	886	30.9	1207	39.1	13.8	36.7	763	19
ZR-01	G052	0	1179	0.73	0.20	0.002	15.9	0.26	0.57	0.009	1199	26.7	2873	37.2	4423	37.7	58.3	72.9		
ZR-01	G053	106	443	0.73	0.20	0.003	4.88	0.09	0.18	0.003	1179	26.8	1799	35.1	2620	38.7	34.5	55.0		
ZR-01	G054	54.8	392	0.69	0.15	0.002	9.83	0.17	0.47	0.008	918	21.5	2419	37.6	4136	39.4	62.0	77.8		
ZR-01	G055	50.5	276	0.84	0.16	0.002	7.86	0.14	0.35	0.006	962	22.8	2215	38.0	3726	40.6	56.6	74.2		
ZR-01	G056	77.3	310	1.34	0.19	0.002	4.47	0.08	0.17	0.003	1105	25.6	1726	35.9	2592	40.2	36.0	57.4		
ZR-01	G057	152	529	0.37	0.33	0.004	21.4	0.35	0.47	0.007	1845	39.3	3156	38.3	4144	38.2	41.5	55.5		
ZR-01	G058	68.9	154	0.81	0.37	0.005	6.30	0.12	0.12	0.002	2021	44.1	2019	39.4	2017	39.7	-0.11	-0.18	2017	40
ZR-01	G059	105	319	1.13	0.25	0.003	5.91	0.11	0.17	0.003	1423	32.1	1963	37.2	2593	39.8	27.5	45.1		
ZR-01	G060	111	250	1.62	0.33	0.004	7.59	0.14	0.17	0.003	1815	39.6	2183	38.0	2551	39.1	16.9	28.9		
ZR-01	G061	85.2	331	0.69	0.22	0.003	2.67	0.05	0.09	0.002	1303	29.5	1321	33.3	1350	35.3	1.31	3.45	1350	35
ZR-01	G062	91.9	365	0.93	0.20	0.002	5.21	0.09	0.19	0.003	1167	26.6	1854	35.8	2745	39.3	37.0	57.5		
ZR-01	G063	26.6	117	1.03	0.18	0.002	1.93	0.05	0.08	0.002	1080	26.6	1093	38.4	1119	41.7	1.16	3.49	1119	42
ZR-01	G064	0	272	1.24	0.21	0.003	11.8	0.20	0.41	0.007	1228	28.2	2588	39.1	3937	40.4	52.5	68.8		
ZR-01	G065	0	453	0.71	0.31	0.004	17.5	0.29	0.41	0.006	1747	37.7	2964	38.6	3941	38.9	41.1	55.7		
ZR-01	G066	124	433	0.46	0.25	0.003	5.77	0.10	0.17	0.003	1417	31.4	1942	35.8	2561	38.3	27.0	44.7		

					Ratios						Ages (Ma)						% discord. (206/238207/235)	% discord. (206/238 207/206)	Best Age	±2s
Sample	Grain No.	Pb (ppm)	U (ppm)	Atomic Th/U	206/238	± s.e.	207/235	± s.e.	207/206	± s.e.	206/238	± 2s	207/235	± 2s	207/206	± 2s				
ZR-01	G067	0	564	1.24	0.23	0.003	11.3	0.19	0.35	0.006	1356	30.1	2550	37.8	3712	39.1	46.8	63.5		
ZR-01	G068	181	767	0.49	0.20	0.002	7.62	0.13	0.28	0.005	1155	26.0	2187	36.3	3373	38.7	47.2	65.8		
ZR-01	G069	66.9	143	1.29	0.35	0.004	5.47	0.11	0.11	0.002	1933	42.5	1895	39.3	1855	39.7	-2.01	-4.24	1855	40
ZR-01	G070	136	579	0.68	0.20	0.002	6.14	0.11	0.23	0.004	1153	26.1	1996	36.0	3034	39.1	42.2	62.0		
ZR-01	G071	0	201	0.47	0.48	0.006	36.4	0.62	0.55	0.009	2532	52.1	3678	40.4	4380	39.8	31.2	42.2		
ZR-01	G072	55	215	0.77	0.21	0.003	3.36	0.07	0.11	0.002	1243	28.8	1496	36.6	1876	40.8	16.9	33.7		
ZR-01	G074	39.3	218	0.28	0.16	0.002	4.23	0.08	0.19	0.004	949	22.8	1681	37.9	2773	43.6	43.5	65.8		
ZR-01	G075	55.2	268	0.35	0.20	0.003	2.13	0.05	0.08	0.002	1161	26.9	1160	33.5	1159	35.8	-0.11	-0.24	1159	36
ZR-01	G076	29.1	131	0.76	0.19	0.003	2.09	0.06	0.08	0.002	1115	28.6	1147	43.9	1209	47.9	2.79	7.76	1209	48
ZR-01	G077	0	429	1.02	0.16	0.002	6.95	0.12	0.33	0.006	929	21.7	2105	37.6	3596	40.9	55.9	74.2		
ZR-01	G078	33.4	175	0.30	0.19	0.002	2.01	0.05	0.08	0.002	1096	26.4	1118	36.8	1163	40.2	1.99	5.73	1163	40
ZR-01	G079	57.0	125	1.32	0.34	0.004	5.36	0.11	0.12	0.002	1869	41.7	1879	40.5	1891	41.4	0.54	1.18	1891	41
ZR-01	G080	211	827	0.46	0.21	0.003	6.06	0.11	0.21	0.003	1240	27.8	1985	36.2	2885	39.3	37.5	57.0		
ZR-01	G081	88.3	307	1.43	0.21	0.003	2.53	0.05	0.09	0.002	1226	28.1	1282	34.1	1377	37.0	4.32	10.9	1377	37
ZR-01	G082	71.9	309	0.88	0.19	0.002	2.88	0.06	0.11	0.002	1126	26.1	1376	34.9	1789	39.9	18.1	37.0		
ZR-01	G083	0	1089	0.86	0.20	0.002	11.8	0.21	0.42	0.007	1185	26.6	2587	38.6	3995	40.2	54.2	70.3		
ZR-01	G084	85.9	465	0.24	0.18	0.002	2.50	0.05	0.10	0.002	1054	24.3	1271	32.6	1661	37.9	17.1	36.6		
ZR-01	G085	0	460	1.40	0.20	0.002	11.9	0.21	0.44	0.007	1163	26.5	2597	39.5	4041	41.2	55.2	71.2		
ZR-01	G086	91.0	491	0.27	0.18	0.002	1.98	0.04	0.08	0.002	1084	25.2	1109	32.1	1159	35.1	2.27	6.54	1159	35
ZR-01	G087	100	438	0.43	0.21	0.003	3.01	0.06	0.10	0.002	1228	27.9	1411	34.1	1701	37.8	13.0	27.8		
ZR-01	G088	78.6	380	0.89	0.18	0.002	2.78	0.06	0.11	0.002	1052	24.5	1351	34.4	1861	40.1	22.1	43.5		
ZR-01	G089	89.9	428	0.11	0.22	0.003	2.53	0.05	0.09	0.002	1257	28.5	1282	33.2	1324	35.5	1.95	5.11	1324	36
ZR-01	G090	112	610	0.35	0.18	0.002	1.97	0.04	0.08	0.002	1049	24.5	1107	32.8	1223	36.8	5.21	14.2	1223	37
ZR-01	G091	80.7	296	2.45	0.18	0.002	5.17	0.10	0.20	0.004	1084	25.5	1847	38.8	2864	43.4	41.3	62.1		
ZR-01	G092	170	597	0.26	0.25	0.003	11.0	0.20	0.32	0.006	1426	31.8	2526	39.7	3585	41.4	43.5	60.2		
ZR-01	G093	70.5	357	0.38	0.19	0.002	2.01	0.04	0.08	0.002	1115	25.9	1117	32.7	1122	35.1	0.19	0.64	1122	35
ZR-01	G094	0	940	1.54	0.21	0.003	11.0	0.20	0.38	0.007	1218	27.4	2524	39.4	3848	41.4	51.7	68.3		
ZR-01	G095	0	114	0.69	0.13	0.002	9.25	0.19	0.52	0.011	785	21.2	2363	46.5	4293	49.1	66.8	81.7		

					Ratios						Ages (Ma)						% discord. (206/238207/235)	% discord. (206/238 207/206)	Best Age	±2s
Sample	Grain No.	Pb (ppm)	U (ppm)	Atomic Th/U	206/238	± s.e.	207/235	± s.e.	207/206	± s.e.	206/238	± 2s	207/235	± 2s	207/206	± 2s				
ZR-01	G096	78.7	443	0.25	0.18	0.002	1.97	0.04	0.08	0.002	1047	24.3	1105	31.8	1224	35.7	5.30	14.4	1224	36
ZR-01	G097	49.9	112	1.44	0.32	0.004	5.74	0.13	0.13	0.003	1802	42.8	1938	46.6	2087	48.4	7.01	13.7	2087	48
ZR-01	G098	114	526	0.90	0.19	0.002	2.53	0.05	0.10	0.002	1094	25.3	1281	33.8	1611	38.8	14.6	32.1		
ZR-01	G099	188	784	0.37	0.21	0.003	9.67	0.18	0.34	0.006	1220	27.5	2404	39.7	3649	42.2	49.3	66.6		
ZR-01	G100	0	487	2.74	0.19	0.002	13.0	0.24	0.50	0.009	1121	26.0	2677	41.5	4227	43.3	58.1	73.5		
ZR-01	G101	32.0	117	1.18	0.21	0.003	4.74	0.11	0.16	0.004	1244	30.6	1774	44.0	2472	48.9	29.9	49.7		
ZR-01	G102	27.3	133	0.44	0.19	0.003	2.04	0.05	0.08	0.002	1137	28.0	1128	40.2	1110	42.7	-0.84	-2.43	1110	43
ZR-01	G103	28.2	136	0.44	0.19	0.003	2.14	0.07	0.08	0.003	1145	30.7	1161	49.2	1194	52.8	1.45	4.12	1194	53
ZR-01	G104	0	216	2.05	0.21	0.003	5.06	0.11	0.18	0.004	1227	29.1	1829	41.3	2607	45.8	32.9	52.9		
ZR-01	G105	50.9	241	0.34	0.20	0.003	2.61	0.06	0.09	0.002	1180	27.7	1302	36.6	1510	40.9	9.36	21.8		
ZR-01	G106	48.6	204	0.74	0.21	0.003	2.38	0.05	0.08	0.002	1208	28.4	1237	37.0	1288	40.0	2.33	6.20	1288	40
ZR-01	G107	43.7	166	1.26	0.20	0.003	2.27	0.05	0.08	0.002	1184	28.3	1203	38.2	1237	41.3	1.54	4.26	1237	41
ZR-01	G108	121	325	0.47	0.34	0.004	5.34	0.11	0.11	0.002	1877	40.9	1876	39.2	1875	40.1	-0.05	-0.08	1875	40
ZR-01	G109	60.4	148	2.53	0.27	0.004	8.22	0.17	0.22	0.004	1537	35.6	2256	43.3	2992	45.8	31.9	48.6		
ZR-01	G110	46.5	196	0.67	0.21	0.003	2.41	0.06	0.08	0.002	1219	28.9	1247	38.2	1296	41.2	2.22	5.90	1296	41
ZR-01	G111	0	132	1.67	0.21	0.003	11.0	0.22	0.37	0.007	1255	30.4	2520	44.9	3792	47.2	50.2	66.9		
ZR-01	G112	226	833	0.69	0.22	0.003	8.19	0.16	0.27	0.005	1270	28.6	2252	40.1	3323	43.2	43.6	61.8		
ZR-01	G113	70.2	359	0.45	0.18	0.002	2.16	0.05	0.09	0.002	1069	25.0	1167	34.2	1355	38.8	8.44	21.1		
ZR-01	G114	75.8	372	0.46	0.19	0.002	2.36	0.05	0.09	0.002	1105	25.9	1230	35.0	1457	39.8	10.2	24.2		
ZR-01	G115	134	537	2.12	0.17	0.002	3.76	0.08	0.16	0.003	1023	23.9	1583	37.3	2440	43.3	35.4	58.1		
ZR-01	G117	42.9	122	1.04	0.27	0.004	8.38	0.18	0.23	0.005	1519	35.9	2273	45.1	3043	47.9	33.2	50.1		
ZR-01	G118	0	411	1.79	0.22	0.003	19.1	0.37	0.62	0.012	1296	29.6	3046	43.7	4559	45.1	57.4	71.6		
ZR-01	G119	0	601	1.12	0.18	0.002	8.58	0.17	0.35	0.007	1054	24.4	2294	41.4	3709	44.8	54.1	71.6		
ZR-01	G120	80.3	476	0.15	0.17	0.002	1.79	0.04	0.08	0.002	1027	24.3	1043	33.4	1076	36.7	1.50	4.56	1076	37
ZR-01	G121	45.2	299	0.79	0.12	0.002	4.67	0.10	0.28	0.006	739	18.2	1761	40.6	3354	47.4	58.0	78.0		
ZR-01	G122	89.4	128	0.43	0.59	0.008	19.6	0.40	0.24	0.005	3003	61.5	3072	45.5	3118	45.5	2.25	3.69	3118	46
ZR-01	G123	72.0	334	0.39	0.21	0.003	2.40	0.06	0.08	0.002	1208	28.4	1243	37.3	1304	40.5	2.81	7.39	1304	40
ZR-01	G125	0	520	1.56	0.15	0.002	11.3	0.23	0.54	0.011	907	21.4	2551	43.1	4367	46.0	64.5	79.2		

					Ratios						Ages (Ma)						% discord. (206/238207/235)	% discord. (206/238 207/206)	Best Age	±2s
Sample	Grain No.	Pb (ppm)	U (ppm)	Atomic Th/U	206/238	± s.e.	207/235	± s.e.	207/206	± s.e.	206/238	± 2s	207/235	± 2s	207/206	± 2s				
ZR-01	G126	0	341	0.89	0.16	0.002	12.5	0.25	0.55	0.011	982	23.4	2640	44.1	4380	46.7	62.8	77.6		
ZR-01	G127	110	202	4.93	0.32	0.004	18.1	0.37	0.41	0.008	1773	39.8	2993	45.3	3960	46.6	40.8	55.2		
ZR-01	G128	100	200	5.66	0.20	0.003	9.89	0.21	0.37	0.008	1153	27.7	2424	45.0	3776	48.1	52.5	69.5		
ZR-01	G129	38.5	150	1.16	0.20	0.003	2.20	0.06	0.08	0.002	1186	29.0	1182	40.6	1176	43.2	-0.31	-0.83	1176	43
ZR-01	G130	0	172	0.97	0.18	0.002	8.51	0.18	0.34	0.007	1062	26.0	2287	45.4	3683	49.2	53.5	71.2		
ZR-01	G131	52.4	248	0.67	0.19	0.002	1.98	0.05	0.08	0.002	1109	26.8	1108	37.8	1106	40.6	-0.09	-0.23	1106	41
ZR-01	G132	49.4	251	0.48	0.18	0.002	1.97	0.05	0.08	0.002	1087	26.1	1104	36.9	1138	40.2	1.52	4.45	1138	40
ZR-01	G133	19.5	86	1.06	0.18	0.003	1.93	0.06	0.08	0.002	1087	28.1	1092	44.8	1101	48.2	0.40	1.22	1101	48
ZR-01	G134	122	579	0.32	0.19	0.002	3.41	0.07	0.13	0.003	1129	26.3	1506	38.2	2086	44.0	25.0	45.9		
ZR-01	G136	171	1310	0.46	0.19	0.002	13.2	0.27	0.52	0.010	1096	25.2	2694	44.1	4288	46.7	59.3	74.4		
ZR-01	G137	61.7	177	0.52	0.31	0.004	4.84	0.12	0.11	0.003	1763	40.8	1792	45.4	1825	47.1	1.60	3.42	1825	47
ZR-01	G138	61.0	298	0.57	0.18	0.002	3.07	0.07	0.12	0.003	1062	25.3	1425	39.1	2017	45.9	25.4	47.3		
ZR-01	G139	79.5	360	0.68	0.19	0.002	4.56	0.10	0.18	0.004	1106	26.1	1742	41.4	2622	47.2	36.5	57.8		
ZR-01	G140	53.6	222	0.41	0.22	0.003	2.83	0.08	0.09	0.003	1301	32.7	1363	46.7	1463	50.5	4.58	11.1	1463	51
ZR-01	G141	125	289	1.52	0.32	0.004	7.09	0.15	0.16	0.003	1782	39.7	2122	43.8	2471	46.3	16.0	27.9		
ZR-01	G142	0	265	0.46	0.38	0.005	24.6	0.52	0.47	0.010	2079	45.3	3292	46.9	4145	48.0	36.8	49.8		
ZR-01	G143	0	1040	0.55	0.20	0.002	14.1	0.29	0.52	0.010	1163	26.8	2757	45.2	4292	47.8	57.8	72.9		
ZR-01	G144	75.9	314	0.93	0.20	0.003	2.72	0.06	0.10	0.002	1167	27.5	1333	38.8	1612	44.0	12.5	27.6		
ZR-01	G145	74.0	342	0.51	0.18	0.002	4.45	0.10	0.17	0.004	1091	25.9	1721	41.9	2605	48.0	36.6	58.1		
ZR-01	G146	0	338	1.66	0.36	0.005	21.2	0.45	0.42	0.009	2005	43.8	3150	47.0	3992	48.4	36.4	49.8		
ZR-01	G147	204	538	3.86	0.25	0.003	13.7	0.29	0.40	0.008	1420	32.4	2728	45.9	3919	48.4	47.9	63.8		
ZR-01	G148	79.5	446	0.15	0.18	0.002	2.14	0.05	0.09	0.002	1070	25.7	1162	37.6	1340	42.7	7.99	20.2		
ZR-02	G001	21.7	115	0.43	0.18	0.002	1.86	0.05	0.08	0.002	1057	25.9	1066	40.2	1086	36.5	0.83	2.65	1086	36
ZR-02	G002	31.5	164	0.81	0.17	0.002	2.30	0.07	0.10	0.003	994	26.4	1212	47.1	1627	61.6	18.0	38.9		
ZR-02	G003	126	520	1.05	0.20	0.002	2.06	0.04	0.08	0.001	1150	25.1	1135	29.3	1108	36.9	-1.32	-3.76	1108	37
ZR-02	G004	54.0	249	0.31	0.21	0.003	2.38	0.05	0.08	0.002	1232	27.5	1236	33.4	1246	41.4	0.34	1.08	1246	41

					Ratios						Ages (Ma)						% discord. (206/238207/235)	% discord. (206/238 207/206)	Best Age	±2s
Sample	Grain No.	Pb (ppm)	U (ppm)	Atomic Th/U	206/238	± s.e.	207/235	± s.e.	207/206	± s.e.	206/238	± 2s	207/235	± 2s	207/206	± 2s				
ZR-02	G005	50.7	289	0.08	0.18	0.002	1.88	0.04	0.07	0.002	1086	25.5	1073	35.7	1047	43.9	-1.26	-3.72	1047	44
ZR-02	G006	185	498	1.01	0.32	0.004	5.53	0.10	0.13	0.002	1766	37.2	1906	35.6	2063	42.7	7.34	14.4	2063	43
ZR-02	G007	76.3	421	0.32	0.18	0.002	1.92	0.04	0.08	0.002	1053	23.9	1088	31.8	1163	41.1	3.30	9.49	1163	41
ZR-02	G008	30.9	79.6	0.67	0.34	0.005	4.97	0.17	0.11	0.004	1864	51.7	1815	63.8	1761	70.0	-2.68	-5.82	1761	70
ZR-02	G009	52.7	295	0.21	0.18	0.002	1.88	0.04	0.08	0.002	1070	24.6	1074	33.2	1086	41.8	0.42	1.44	1086	42
ZR-02	G010	23.0	111	0.50	0.19	0.003	2.07	0.06	0.08	0.002	1134	27.9	1138	41.9	1148	50.8	0.38	1.26	1148	51
ZR-02	G011	50.2	260	0.53	0.18	0.002	1.95	0.04	0.08	0.002	1053	24.1	1097	32.8	1189	42.4	4.07	11.5	1189	42
ZR-02	G012	58.7	252	0.87	0.20	0.002	2.20	0.05	0.08	0.002	1159	26.3	1181	33.6	1223	42.2	1.85	5.22	1223	42
ZR-02	G013	71.5	327	0.40	0.21	0.003	2.31	0.05	0.08	0.002	1214	27.2	1216	33.3	1221	41.3	0.14	0.55	1221	41
ZR-02	G014	73.9	257	0.67	0.25	0.003	3.15	0.06	0.09	0.002	1454	32.2	1446	36.0	1435	43.3	-0.59	-1.35	1435	43
ZR-02	G015	63.7	378	0.18	0.17	0.002	1.74	0.04	0.07	0.002	1020	23.2	1025	30.8	1037	39.5	0.47	1.63	1037	39
ZR-02	G016	128	313	1.00	0.33	0.004	5.12	0.09	0.11	0.002	1826	38.4	1840	35.5	1857	42.0	0.74	1.66	1857	42
ZR-02	G017	145	311	1.46	0.34	0.004	5.49	0.11	0.12	0.002	1896	41.0	1900	39.4	1905	45.9	0.18	0.47	1905	46
ZR-02	G018	98.1	284	0.73	0.28	0.003	7.78	0.13	0.20	0.003	1613	34.7	2206	37.1	2816	44.5	26.9	42.7		
ZR-02	G019	84.7	443	0.71	0.17	0.002	2.21	0.04	0.09	0.002	1030	23.2	1184	31.1	1480	41.8	13.0	30.4		
ZR-02	G020	102	433	1.02	0.19	0.002	2.26	0.04	0.08	0.002	1139	25.5	1200	31.9	1314	41.0	5.10	13.3	1314	41
ZR-02	G021	28.8	142	0.55	0.18	0.002	2.30	0.06	0.09	0.002	1089	27.0	1214	41.9	1445	53.4	10.3	24.6		
ZR-02	G022	77.9	412	0.26	0.19	0.002	2.04	0.04	0.08	0.002	1113	25.0	1127	31.3	1158	39.8	1.30	3.89	1158	40
ZR-02	G023	66.9	350	0.38	0.18	0.002	1.95	0.04	0.08	0.002	1084	24.6	1099	32.2	1130	40.9	1.32	4.01	1130	41
ZR-02	G024	119	739	0.20	0.16	0.002	2.01	0.04	0.09	0.002	976	21.8	1120	29.4	1414	40.4	12.9	31.0		
ZR-02	G025	52.8	242	0.64	0.19	0.002	2.12	0.05	0.08	0.002	1148	26.4	1155	35.0	1169	43.5	0.58	1.81	1169	44
ZR-02	G026	49.0	236	0.55	0.19	0.002	2.14	0.05	0.08	0.002	1133	26.5	1162	36.4	1218	45.5	2.49	6.98	1218	46
ZR-02	G027	110	482	0.69	0.20	0.003	2.38	0.05	0.09	0.002	1180	27.6	1236	37.2	1337	46.6	4.55	11.78	1337	47
ZR-02	G028	151	279	2.30	0.33	0.004	5.08	0.09	0.11	0.002	1853	39.4	1833	36.9	1812	43.3	-1.10	-2.29	1812	43
ZR-02	G029	30.7	143	0.48	0.20	0.003	2.16	0.06	0.08	0.002	1178	28.4	1167	40.3	1149	48.5	-0.94	-2.57	1149	48
ZR-02	G030	101	614	0.15	0.17	0.002	2.06	0.04	0.09	0.002	1000	22.3	1135	29.3	1406	39.9	11.9	28.9		
ZR-02	G031	106	360	0.45	0.27	0.003	3.82	0.07	0.10	0.002	1558	33.5	1597	34.5	1650	41.7	2.42	5.55	1650	42

					Ratios						Ages (Ma)						% discord. (206/238207/235)	% discord. (206/238 207/206)	Best Age	±2s
Sample	Grain No.	Pb (ppm)	U (ppm)	Atomic Th/U	206/238	± s.e.	207/235	± s.e.	207/206	± s.e.	206/238	± 2s	207/235	± 2s	207/206	± 2s				
ZR-02	G032	78.2	437	0.59	0.16	0.002	3.03	0.06	0.14	0.003	965	22.2	1416	34.1	2182	46.2	31.9	55.8		
ZR-02	G033	24.5	138	0.25	0.18	0.002	1.87	0.05	0.08	0.002	1048	26.0	1071	40.7	1118	50.5	2.09	6.25	1118	50
ZR-02	G034	60.8	293	0.63	0.19	0.002	1.92	0.04	0.08	0.002	1096	25.3	1087	34.0	1070	42.2	-0.84	-2.39	1070	42
ZR-02	G035	65.7	356	0.12	0.19	0.002	2.03	0.04	0.08	0.002	1124	25.7	1126	33.1	1131	41.5	0.14	0.59	1131	41
ZR-02	G036	83.7	467	0.28	0.18	0.002	1.88	0.04	0.08	0.001	1056	23.7	1073	30.1	1111	38.8	1.62	4.92	1111	39
ZR-02	G037	66.1	308	0.54	0.20	0.002	2.21	0.05	0.08	0.002	1153	26.3	1184	34.0	1244	42.8	2.66	7.34	1244	43
ZR-02	G038	41.9	210	0.41	0.19	0.003	2.03	0.06	0.08	0.002	1121	28.2	1124	43.2	1132	52.0	0.27	0.96	1132	52
ZR-02	G039	48.9	233	0.48	0.20	0.002	2.16	0.05	0.08	0.002	1151	26.5	1168	34.8	1202	43.5	1.47	4.23	1202	43
ZR-02	G040	58.4	119	1.61	0.35	0.004	5.74	0.12	0.12	0.002	1922	42.7	1938	42.1	1956	48.8	0.81	1.75	1956	49
ZR-02	G042	42.4	209	0.32	0.20	0.003	2.06	0.05	0.08	0.002	1161	27.2	1134	36.6	1085	44.3	-2.37	-7.03	1085	44
ZR-02	G043	78.4	417	0.30	0.19	0.002	1.98	0.04	0.08	0.002	1099	24.8	1110	31.4	1135	39.9	1.05	3.20	1135	40
ZR-02	G014	73.9	257	0.67	0.25	0.003	3.15	0.06	0.09	0.002	1454	32.2	1446	36.0	1435	43.3	-0.59	-1.35	1435	43
ZR-02	G015	63.7	378	0.18	0.17	0.002	1.74	0.04	0.07	0.002	1020	23.2	1025	30.8	1037	39.5	0.47	1.63	1037	39
ZR-02	G016	128	313	1.00	0.33	0.004	5.12	0.09	0.11	0.002	1826	38.4	1840	35.5	1857	42.0	0.74	1.66	1857	42
ZR-02	G017	145	311	1.46	0.34	0.004	5.49	0.11	0.12	0.002	1896	41.0	1900	39.4	1905	45.9	0.18	0.47	1905	46
ZR-02	G018	98.1	284	0.73	0.28	0.003	7.78	0.13	0.20	0.003	1613	34.7	2206	37.1	2816	44.5	26.9	42.7		
ZR-02	G019	84.7	443	0.71	0.17	0.002	2.21	0.04	0.09	0.002	1030	23.2	1184	31.1	1480	41.8	13.0	30.4		
ZR-02	G020	102	433	1.02	0.19	0.002	2.26	0.04	0.08	0.002	1139	25.5	1200	31.9	1314	41.0	5.10	13.3	1314	41
ZR-02	G021	28.8	142	0.55	0.18	0.002	2.30	0.06	0.09	0.002	1089	27.0	1214	41.9	1445	53.4	10.3	24.6		
ZR-02	G022	77.9	412	0.26	0.19	0.002	2.04	0.04	0.08	0.002	1113	25.0	1127	31.3	1158	39.8	1.30	3.89	1158	40
ZR-02	G023	66.9	350	0.38	0.18	0.002	1.95	0.04	0.08	0.002	1084	24.6	1099	32.2	1130	40.9	1.32	4.01	1130	41
ZR-02	G024	119	739	0.20	0.16	0.002	2.01	0.04	0.09	0.002	976	21.8	1120	29.4	1414	40.4	12.9	31.0		
ZR-02	G025	52.8	242	0.64	0.19	0.002	2.12	0.05	0.08	0.002	1148	26.4	1155	35.0	1169	43.5	0.58	1.81	1169	44
ZR-02	G026	49.0	236	0.55	0.19	0.002	2.14	0.05	0.08	0.002	1133	26.5	1162	36.4	1218	45.5	2.49	6.98	1218	46
ZR-02	G027	110	482	0.69	0.20	0.003	2.38	0.05	0.09	0.002	1180	27.6	1236	37.2	1337	46.6	4.55	11.78	1337	47
ZR-02	G028	151	279	2.30	0.33	0.004	5.08	0.09	0.11	0.002	1853	39.4	1833	36.9	1812	43.3	-1.10	-2.29	1812	43

					Ratios						Ages (Ma)						% discord.	% discord.		
Sample	Grain No.	Pb (ppm)	U (ppm)	Atomic Th/U	206/238	± s.e.	207/235	± s.e.	207/206	± s.e.	206/238	± 2s	207/235	± 2s	207/206	± 2s	(206/238207/ 235)	(206/238 207/206)	Best Age	±2s
ZR-02	G029	30.7	143	0.48	0.20	0.003	2.16	0.06	0.08	0.002	1178	28.4	1167	40.3	1149	48.5	-0.94	-2.57	1149	48
ZR-02	G030	101	614	0.15	0.17	0.002	2.06	0.04	0.09	0.002	1000	22.3	1135	29.3	1406	39.9	11.9	28.9		
ZR-02	G031	106	360	0.45	0.27	0.003	3.82	0.07	0.10	0.002	1558	33.5	1597	34.5	1650	41.7	2.42	5.55	1650	42
ZR-02	G032	78.2	437	0.59	0.16	0.002	3.03	0.06	0.14	0.003	965	22.2	1416	34.1	2182	46.2	31.9	55.8		
ZR-02	G033	24.5	138	0.25	0.18	0.002	1.87	0.05	0.08	0.002	1048	26.0	1071	40.7	1118	50.5	2.09	6.25	1118	50
ZR-02	G034	60.8	293	0.63	0.19	0.002	1.92	0.04	0.08	0.002	1096	25.3	1087	34.0	1070	42.2	-0.84	-2.39	1070	42
ZR-02	G035	65.7	356	0.12	0.19	0.002	2.03	0.04	0.08	0.002	1124	25.7	1126	33.1	1131	41.5	0.14	0.59	1131	41
ZR-02	G036	83.7	467	0.28	0.18	0.002	1.88	0.04	0.08	0.001	1056	23.7	1073	30.1	1111	38.8	1.62	4.92	1111	39
ZR-02	G037	66.1	308	0.54	0.20	0.002	2.21	0.05	0.08	0.002	1153	26.3	1184	34.0	1244	42.8	2.66	7.34	1244	43
ZR-02	G038	41.9	210	0.41	0.19	0.003	2.03	0.06	0.08	0.002	1121	28.2	1124	43.2	1132	52.0	0.27	0.96	1132	52
ZR-02	G039	48.9	233	0.48	0.20	0.002	2.16	0.05	0.08	0.002	1151	26.5	1168	34.8	1202	43.5	1.47	4.23	1202	43
ZR-02	G040	58.4	119	1.61	0.35	0.004	5.74	0.12	0.12	0.002	1922	42.7	1938	42.1	1956	48.8	0.81	1.75	1956	49
ZR-02	G042	42.4	209	0.32	0.20	0.003	2.06	0.05	0.08	0.002	1161	27.2	1134	36.6	1085	44.3	-2.37	-7.03	1085	44
ZR-02	G043	78.4	417	0.30	0.19	0.002	1.98	0.04	0.08	0.002	1099	24.8	1110	31.4	1135	39.9	1.05	3.20	1135	40
ZR-02	G044	29.8	154	0.36	0.18	0.003	2.48	0.07	0.10	0.003	1077	27.4	1265	44.0	1602	56.6	14.9	32.8		
ZR-02	G045	51.3	271	0.38	0.18	0.002	1.87	0.04	0.07	0.002	1079	25.3	1070	34.9	1053	43.2	-0.86	-2.49	1053	43
ZR-02	G046	44.3	102	1.13	0.34	0.005	5.22	0.13	0.11	0.003	1890	44.5	1856	47.6	1819	54.1	-1.87	-3.94	1819	54
ZR-02	G047	36.4	162	0.98	0.19	0.002	1.96	0.05	0.08	0.002	1095	27.0	1101	41.0	1114	49.9	0.51	1.66	1114	50
ZR-02	G048	50.0	258	0.41	0.18	0.002	1.92	0.05	0.08	0.002	1094	25.7	1087	35.4	1074	43.7	-0.66	-1.82	1074	44
ZR-02	G049	49.5	241	0.47	0.19	0.003	2.31	0.05	0.09	0.002	1147	27.1	1215	37.7	1340	47.5	5.60	14.4	1340	47
ZR-02	G050	40.2	190	0.49	0.20	0.003	2.11	0.05	0.08	0.002	1157	27.4	1151	37.6	1140	45.9	-0.56	-1.47	1140	46
ZR-02	G051	69.7	279	0.67	0.22	0.003	2.58	0.06	0.08	0.002	1293	30.2	1294	38.8	1298	46.8	0.11	0.41	1298	47
ZR-02	G052	64.4	350	0.30	0.18	0.002	1.97	0.04	0.08	0.002	1070	24.7	1107	33.2	1181	42.5	3.30	9.37	1181	42
ZR-02	G053	0.0	0	4.08	2.00	1.299	286	178	1.04	0.607	7082	5582	5747	1769	5290	1194	-23.2	-33.9		
ZR-02	G054	45.5	205	0.78	0.19	0.002	2.16	0.05	0.08	0.002	1130	26.8	1167	37.5	1239	46.9	3.19	8.79	1239	47
ZR-02	G056	44.4	209	0.41	0.20	0.003	2.63	0.06	0.09	0.002	1200	28.4	1310	39.0	1497	49.1	8.42	19.9		

					Ratios						Ages (Ma)						% discord. (206/238207/235)	% discord. (206/238 207/206)	Best Age	±2s
Sample	Grain No.	Pb (ppm)	U (ppm)	Atomic Th/U	206/238	± s.e.	207/235	± s.e.	207/206	± s.e.	206/238	± 2s	207/235	± 2s	207/206	± 2s				
ZR-02	G057	72.7	364	0.52	0.18	0.002	1.99	0.04	0.08	0.002	1091	25.0	1113	32.8	1156	41.6	1.92	5.61	1156	42
ZR-02	G058	42.0	261	0.65	0.15	0.002	1.89	0.05	0.09	0.003	889	22.6	1077	40.1	1483	54.9	17.5	40.1		
ZR-02	G059	96.6	447	0.73	0.19	0.002	1.98	0.04	0.08	0.002	1120	25.6	1109	32.8	1089	40.8	-0.98	-2.80	1089	41
ZR-02	G060	16.7	89.9	0.37	0.18	0.003	1.85	0.07	0.08	0.003	1060	29.0	1062	51.0	1070	60.1	0.26	0.96	1070	60
ZR-02	G061	50.8	226	0.35	0.22	0.003	2.30	0.05	0.08	0.002	1263	29.3	1213	37.1	1127	44.1	-4.11	-12.0		
ZR-02	G062	50.6	250	0.27	0.20	0.003	2.14	0.05	0.08	0.002	1174	27.3	1161	36.0	1137	43.9	-1.17	-3.27	1137	44
ZR-02	G063	69.0	167	0.79	0.35	0.004	5.64	0.12	0.12	0.002	1928	42.3	1922	41.0	1916	47.6	-0.35	-0.65	1916	48
ZR-02	G064	44.8	253	0.22	0.18	0.002	1.95	0.05	0.08	0.002	1064	25.1	1100	35.7	1174	45.3	3.29	9.38	1174	45
ZR-02	G065	56.4	245	0.73	0.20	0.003	2.24	0.06	0.08	0.002	1186	28.5	1193	40.0	1206	48.6	0.53	1.60	1206	49
ZR-02	G066	29.4	135	0.55	0.20	0.003	2.10	0.06	0.08	0.002	1171	29.5	1147	44.4	1104	52.2	-2.10	-6.12	1104	52
ZR-02	G067	52.5	200	0.64	0.23	0.003	2.86	0.07	0.09	0.002	1360	31.9	1372	40.6	1392	48.7	0.84	2.24	1392	49
ZR-02	G068	26.6	114	0.98	0.19	0.003	2.00	0.06	0.07	0.002	1142	29.7	1114	47.2	1062	54.8	-2.50	-7.54	1062	55
ZR-02	G069	102	494	0.56	0.19	0.002	2.07	0.04	0.08	0.002	1115	25.5	1140	33.1	1188	41.9	2.13	6.10	1188	42
ZR-02	G070	44.4	216	0.42	0.20	0.003	2.10	0.05	0.08	0.002	1150	27.6	1149	39.1	1149	47.6	-0.09	-0.11	1149	48
ZR-02	G071	22.0	103	0.50	0.20	0.003	2.21	0.07	0.08	0.003	1162	30.5	1184	48.7	1226	58.1	1.85	5.21	1226	58
ZR-02	G072	87.5	440	0.50	0.19	0.002	1.90	0.04	0.07	0.002	1095	25.1	1082	32.9	1058	40.9	-1.21	-3.56	1058	41
ZR-02	G073	49.7	222	0.74	0.20	0.003	2.26	0.06	0.08	0.002	1150	27.6	1200	39.2	1293	48.8	4.17	11.1	1293	49
ZR-02	G074	121	546	0.90	0.19	0.002	2.08	0.04	0.08	0.002	1105	25.2	1141	32.8	1210	41.9	3.11	8.69	1210	42
ZR-02	G075	48.0	93.1	2.16	0.33	0.004	5.21	0.13	0.12	0.003	1826	43.3	1854	47.8	1887	54.9	1.49	3.20	1887	55
ZR-02	G076	35.5	195	0.58	0.17	0.002	1.91	0.05	0.08	0.002	1017	25.2	1085	40.0	1225	51.1	6.27	17.0		
ZR-02	G077	104	718	0.93	0.13	0.002	2.22	0.04	0.13	0.002	766	18.0	1189	32.3	2071	47.1	35.6	63.0		
ZR-02	G078	38.8	34.7	6.95	0.32	0.005	4.92	0.17	0.11	0.004	1798	51.6	1806	66.7	1816	73.7	0.41	0.95	1816	74
ZR-02	G079	70.3	351	0.42	0.19	0.002	1.96	0.05	0.07	0.002	1124	26.2	1100	35.1	1056	42.8	-2.13	-6.45	1056	43
ZR-02	G080	26.1	120	0.53	0.20	0.003	2.21	0.07	0.08	0.002	1172	30.2	1185	47.1	1211	56.1	1.10	3.18	1211	56
ZR-02	G081	54.2	268	0.32	0.20	0.003	2.13	0.05	0.08	0.002	1160	27.4	1158	37.2	1157	45.5	-0.15	-0.29	1157	45
ZR-02	G082	29.1	116	1.13	0.20	0.003	2.53	0.07	0.09	0.003	1171	30.3	1280	47.8	1469	58.9	8.50	20.3		

					Ratios						Ages (Ma)						% discord. (206/238207/235)	% discord. (206/238 207/206)	Best Age	±2s
Sample	Grain No.	Pb (ppm)	U (ppm)	Atomic Th/U	206/238	± s.e.	207/235	± s.e.	207/206	± s.e.	206/238	± 2s	207/235	± 2s	207/206	± 2s				
ZR-02	G083	70.9	278	1.46	0.19	0.002	2.03	0.05	0.08	0.002	1121	26.4	1124	36.6	1132	45.2	0.30	1.00	1132	45
ZR-02	G084	25.8	163	0.60	0.15	0.002	1.81	0.07	0.09	0.003	883	25.9	1050	52.9	1417	69.9	15.9	37.7		
ZR-02	G085	37.0	212	0.51	0.16	0.002	2.37	0.06	0.11	0.003	957	23.8	1234	40.1	1756	54.1	22.4	45.5		
ZR-02	G086	92.5	334	0.26	0.27	0.003	4.25	0.09	0.11	0.002	1565	35.1	1685	39.5	1838	47.7	7.10	14.9	1838	48
ZR-02	G088	80.3	432	0.25	0.19	0.002	1.98	0.04	0.08	0.002	1096	25.2	1109	33.3	1137	42.0	1.21	3.64	1137	42
ZR-02	G089	7.17	54.6	1.50	0.10	0.002	1.73	0.09	0.12	0.007	626	26.3	1020	78.2	2002	111.9	38.6	68.7		
ZR-02	G090	385	184	4.63	0.69	0.042	65.6	4.54	0.69	0.052	3395	318	4264	193	4704	164.2	20.4	27.8		
ZR-02	G091	52.4	139	1.05	0.30	0.004	4.62	0.11	0.11	0.003	1696	38.8	1753	43.3	1822	50.9	3.24	6.94	1822	51
ZR-02	G092	66.0	332	0.45	0.19	0.002	1.90	0.04	0.07	0.002	1108	25.8	1081	34.6	1031	42.3	-2.42	-7.46	1031	42
ZR-02	G093	29.6	155	0.35	0.18	0.003	2.10	0.07	0.08	0.003	1089	30.4	1150	53.2	1267	64.4	5.27	14.1	1267	64
ZR-02	G094	17.5	73.2	1.17	0.19	0.003	1.96	0.07	0.08	0.003	1112	30.4	1102	51.9	1082	60.3	-0.97	-2.77	1082	60
ZR-02	G095	45.7	186	1.35	0.19	0.002	2.03	0.05	0.08	0.002	1109	27.0	1125	39.7	1160	48.8	1.50	4.42	1160	49
ZR-02	G096	23.9	116	0.46	0.19	0.003	2.24	0.09	0.08	0.003	1137	33.8	1194	60.9	1302	71.8	4.82	12.7	1302	72
ZR-02	G097	43.5	213	0.76	0.18	0.002	1.91	0.05	0.08	0.002	1060	25.7	1084	38.0	1134	47.4	2.24	6.58	1134	47
ZR-02	G098	37.2	300	0.46	0.11	0.002	2.11	0.05	0.14	0.003	686	17.4	1153	37.8	2184	55.9	40.5	68.6		
ZR-02	G099	11.5	62.3	0.70	0.16	0.003	2.09	0.09	0.09	0.004	975	30.6	1145	62.7	1483	79.0	14.8	34.2		
ZR-02	G100	94.1	506	0.92	0.16	0.002	2.19	0.05	0.10	0.002	977	23.3	1179	36.2	1573	48.9	17.1	37.9		
ZR-02	G101	31.9	190	0.31	0.16	0.003	1.97	0.08	0.09	0.004	980	29.6	1104	58.4	1360	73.2	11.3	28.0		
ZR-02	G102	25.0	153	0.44	0.15	0.002	1.53	0.05	0.07	0.003	925	25.2	941	46.7	980	57.0	1.71	5.64	980	57
ZR-02	G103	43.8	198	0.76	0.20	0.003	2.60	0.07	0.10	0.003	1156	28.9	1301	44.1	1549	55.4	11.1	25.4		
ZR-02	G104	4.06	32.7	0.43	0.11	0.002	1.50	0.08	0.10	0.005	696	26.6	930	73.7	1539	103.3	25.2	54.8		
ZR-02	G105	56.1	250	0.42	0.21	0.003	2.62	0.06	0.09	0.002	1248	29.7	1306	40.5	1406	49.8	4.50	11.2	1406	50
ZR-02	G106	52.3	235	0.79	0.19	0.002	2.18	0.05	0.08	0.002	1133	26.9	1176	37.9	1256	47.3	3.60	9.75	1256	47
ZR-02	G107	33.9	177	0.66	0.18	0.002	2.24	0.06	0.09	0.003	1059	27.0	1193	44.0	1447	56.3	11.3	26.8		
ZR-02	G108	120	458	0.46	0.24	0.003	3.16	0.07	0.09	0.002	1410	31.8	1448	37.7	1506	45.8	2.63	6.36	1506	46
ZR-02	G109	58.2	137	1.26	0.33	0.004	5.21	0.12	0.12	0.003	1816	41.6	1853	45.3	1897	52.5	2.04	4.30	1897	53
ZR-02	G110	76.7	471	0.69	0.15	0.002	2.14	0.05	0.10	0.003	912	22.6	1160	39.3	1661	53.9	21.4	45.1		
ZR-02	G111	0	336	0.54	0.80	0.010	77.6	1.55	0.70	0.014	3785	72.2	4431	46.1	4740	51.6	14.6	20.1		

					Ratios						Ages (Ma)						% discord. (206/238207/235)	% discord. (206/238 207/206)	Best Age	±2s
Sample	Grain No.	Pb (ppm)	U (ppm)	Atomic Th/U	206/238	± s.e.	207/235	± s.e.	207/206	± s.e.	206/238	± 2s	207/235	± 2s	207/206	± 2s				
ZR-02	G112	40.2	205	0.57	0.18	0.003	2.11	0.07	0.09	0.003	1066	28.1	1152	47.1	1319	58.7	7.44	19.1		
ZR-02	G113	112	635	0.24	0.18	0.002	2.08	0.05	0.09	0.002	1050	24.5	1142	34.7	1323	45.3	8.05	20.6		
ZR-02	G114	6.58	30.8	1.69	0.16	0.003	2.67	0.12	0.12	0.006	934	33.1	1320	74.0	2020	94.1	29.3	53.8		
ZR-02	G115	30.2	156	0.55	0.18	0.002	1.83	0.05	0.07	0.002	1060	27.0	1056	43.2	1050	52.0	-0.33	-0.89	1050	52
ZR-02	G116	68.7	394	0.72	0.16	0.002	1.91	0.05	0.09	0.002	975	23.8	1085	37.9	1316	50.0	10.2	26.0		
ZR-02	G117	41.2	223	0.22	0.19	0.003	2.03	0.06	0.08	0.002	1098	28.2	1125	44.7	1179	54.4	2.42	6.92	1179	54
ZR-02	G118	27.1	162	1.04	0.15	0.002	1.99	0.07	0.10	0.004	875	25.4	1110	52.4	1606	70.2	21.2	45.5		
ZR-02	G120	45.0	247	0.35	0.18	0.002	1.92	0.05	0.08	0.002	1053	25.8	1089	39.1	1161	49.0	3.24	9.29	1161	49
ZR-02	G121	100	565	0.42	0.17	0.002	2.08	0.05	0.09	0.002	1034	24.3	1144	35.1	1358	46.2	9.55	23.8		
ZR-02	G122	1.78	0.64	6.67	1.03	0.089	96.3	9.39	0.68	0.068	4576	563	4649	266	4682	214.8	1.57	2.26		
ZR-02	G123	48.4	249	0.63	0.18	0.002	2.39	0.06	0.10	0.002	1048	25.6	1239	40.3	1589	52.8	15.4	34.1		
ZR-02	G124	35.6	189	0.83	0.17	0.002	1.89	0.05	0.08	0.002	992	25.0	1078	40.9	1257	52.8	7.94	21.0		
ZR-02	G125	39.8	239	0.40	0.16	0.002	2.08	0.06	0.09	0.002	957	24.0	1143	40.7	1516	54.4	16.3	36.9		
ZR-02	G126	21.5	109	0.66	0.18	0.003	1.91	0.06	0.08	0.003	1045	28.3	1084	49.4	1164	60.1	3.57	10.2	1164	60
ZR-02	G127	84.7	406	0.43	0.20	0.003	2.19	0.05	0.08	0.002	1165	27.8	1179	38.4	1205	47.1	1.15	3.32	1205	47
ZR-02	G128	92.2	248	1.31	0.30	0.004	5.04	0.12	0.12	0.003	1674	38.3	1826	44.2	2004	52.5	8.29	16.5		
ZR-02	G129	36.3	155	0.40	0.22	0.003	2.71	0.07	0.09	0.002	1292	31.9	1330	44.9	1392	53.8	2.85	7.21	1392	54
ZR-02	G130	122	704	0.44	0.16	0.002	2.75	0.07	0.12	0.003	966	23.4	1341	39.6	2005	53.5	28.0	51.8		
ZR-02	G131	36.2	180	0.52	0.19	0.003	2.12	0.06	0.08	0.002	1099	27.8	1155	44.0	1263	54.5	4.85	13.0	1263	54
ZR-02	G132	28.8	147	0.87	0.17	0.003	2.42	0.08	0.10	0.003	1015	27.8	1248	50.7	1678	65.5	18.7	39.5		
ZR-02	G133	86.0	395	0.69	0.19	0.003	2.24	0.05	0.08	0.002	1145	27.1	1195	38.0	1287	47.6	4.17	11.0	1287	48
ZR-02	G134	83.7	442	0.28	0.19	0.002	2.13	0.05	0.08	0.002	1107	26.3	1157	37.2	1255	47.0	4.40	11.9	1255	47
ZR-02	G135	59.6	308	0.45	0.18	0.002	2.22	0.06	0.09	0.002	1070	26.3	1186	40.8	1406	52.4	9.81	23.9		
ZR-02	G136	38.0	236	0.44	0.16	0.003	2.23	0.08	0.10	0.004	930	28.0	1189	57.6	1698	75.2	21.8	45.3		
ZR-02	G137	57.3	156	0.74	0.31	0.004	4.90	0.13	0.11	0.003	1764	43.0	1802	51.2	1848	58.8	2.11	4.52	1848	59
ZR-02	G138	23.1	126	0.88	0.16	0.002	1.92	0.06	0.08	0.003	984	26.9	1089	49.3	1307	62.6	9.64	24.7		
ZR-02	G139	62.3	334	0.42	0.18	0.002	2.03	0.05	0.08	0.002	1056	25.9	1126	39.9	1265	50.6	6.22	16.5		

					Ratios						Ages (Ma)						% discord. (206/238207/235)	% discord. (206/238 207/206)	Best Age	±2s
Sample	Grain No.	Pb (ppm)	U (ppm)	Atomic Th/U	206/238	± s.e.	207/235	± s.e.	207/206	± s.e.	206/238	± 2s	207/235	± 2s	207/206	± 2s				
ZR-02	G140	69.5	377	0.16	0.19	0.003	2.02	0.05	0.08	0.002	1111	27.1	1122	39.7	1144	48.7	0.96	2.88	1144	49
ZR-02	G141	45.0	116	1.47	0.29	0.004	4.98	0.14	0.12	0.003	1652	41.2	1817	52.5	2012	61.3	9.07	17.9		
ZR-02	G142	92.6	213	0.78	0.37	0.005	6.99	0.18	0.14	0.003	2028	47.3	2111	50.6	2193	57.8	3.91	7.52	2193	58
ZR-02	G143	63.9	265	1.39	0.20	0.003	2.84	0.09	0.10	0.003	1159	30.5	1365	50.1	1706	62.7	15.1	32.1		
ZR-02	G144	47.4	247	0.35	0.19	0.003	2.04	0.06	0.08	0.002	1105	27.5	1128	42.0	1173	51.4	2.02	5.79	1173	51
ZR-02	G145	48.8	252	0.52	0.18	0.003	2.37	0.07	0.10	0.003	1073	27.5	1234	45.6	1528	58.3	13.0	29.8		
ZR-02	G146	18.7	105	0.41	0.17	0.003	1.93	0.07	0.08	0.003	993	27.9	1090	52.2	1290	65.5	8.89	23.0		
ZR-02	G147	44.0	243	0.94	0.16	0.002	2.17	0.07	0.10	0.003	976	27.4	1172	52.1	1554	67.4	16.7	37.2		
ZR-02	G148	0	0.64	1.67	1.73	0.184	208	23.1	0.87	0.088	6471	869	5427	296	5049	216.4	-19.3	-28.2		
ZR-03	G01	392	103	0.63	0.14	0.002	4.51	0.08	0.23	0.003	1319	14.0	1732	17.4	2277	15.7	-23.8	-42.1		
ZR-03	G02	102	23.6	0.86	0.07	0.002	2.00	0.05	0.20	0.003	1152	13.5	1114	19.1	1043	16.4	3.40	10.4		
ZR-03	G03	26.1	5.60	0.53	0.07	0.003	1.88	0.09	0.20	0.003	1158	17.6	1074	34.1	910	29.3	7.80	27.2		
ZR-03	G04	72.6	16.7	0.89	0.08	0.002	1.99	0.06	0.19	0.003	1134	13.8	1111	20.9	1070	18.5	2.00	6.00	1070	19
ZR-03	G05	64.7	13.8	0.33	0.08	0.002	2.20	0.07	0.21	0.003	1207	15.2	1181	23.2	1136	20.7	2.20	6.30	1136	21
ZR-03	G06	161	37.3	0.73	0.08	0.002	2.17	0.05	0.20	0.003	1188	13.4	1173	17.6	1147	15.2	1.30	3.60	1147	15
ZR-03	G07	195	40.2	0.37	0.08	0.002	2.25	0.05	0.20	0.002	1160	13.4	1197	18.6	1267	16.9	-3.10	-8.50	1267	17
ZR-03	G08	262	56.5	0.64	0.07	0.002	1.99	0.04	0.19	0.002	1137	12.8	1112	16.8	1066	14.3	2.20	6.70	1066	14
ZR-03	G09	112	37.9	0.58	0.10	0.002	4.34	0.09	0.30	0.004	1698	18.8	1702	20.7	1708	17.9	-0.20	-0.60	1708	18
ZR-03	G10	67.5	27.0	1.12	0.11	0.002	4.55	0.11	0.31	0.004	1761	20.0	1740	22.1	1716	19.2	1.20	2.60	1716	19
ZR-03	G11	314	61.8	0.20	0.08	0.002	2.12	0.04	0.20	0.002	1166	12.9	1157	16.3	1140	13.9	0.80	2.30	1140	14
ZR-03	G12	263	0	1.05	0.38	0.007	15.3	0.26	0.29	0.003	1645	17.3	2837	19.8	3844	16.9	-42.0	-57.2		
ZR-03	G13	101	21.3	0.27	0.08	0.002	2.29	0.07	0.21	0.003	1217	15.3	1210	23.2	1201	21.0	0.50	1.30	1201	21
ZR-03	G14	138	28.7	0.78	0.07	0.002	1.84	0.05	0.18	0.002	1060	12.6	1060	19.0	1062	17.0	0.00	-0.20	1060	13
ZR-03	G15	307	77.8	0.44	0.09	0.002	2.81	0.06	0.24	0.003	1370	14.9	1358	17.3	1340	14.7	0.90	2.20	1340	15
ZR-03	G16	168	35.8	0.46	0.08	0.002	2.27	0.06	0.20	0.003	1167	13.9	1203	20.4	1271	18.7	-3.00	-8.20	1271	19
ZR-03	G17	80	19.4	0.43	0.08	0.002	2.62	0.07	0.23	0.003	1328	16.3	1305	23.1	1270	20.6	1.70	4.50	1270	21
ZR-03	G18	89	18.8	0.59	0.08	0.002	2.00	0.05	0.19	0.003	1131	13.7	1114	20.6	1085	18.3	1.40	4.20	1085	18
ZR-03	G19	162	36.6	0.34	0.08	0.002	2.41	0.06	0.22	0.003	1275	14.5	1246	18.8	1200	16.2	2.30	6.30	1200	16

					Ratios						Ages (Ma)						% discord. (206/238207/235)	% discord. (206/238 207/206)	Best Age	±2s
Sample	Grain No.	Pb (ppm)	U (ppm)	Atomic Th/U	206/238	± s.e.	207/235	± s.e.	207/206	± s.e.	206/238	± 2s	207/235	± 2s	207/206	± 2s				
ZR-03	G20	148	60.9	1.04	0.11	0.002	5.04	0.10	0.33	0.004	1836	19.7	1826	20.2	1817	17.2	0.50	1.10	1817	17
ZR-03	G21	119	28.6	0.80	0.08	0.002	2.16	0.05	0.21	0.003	1205	14.1	1167	19.7	1100	17.0	3.20	9.50	1100	17
ZR-03	G22	329	0	1.44	0.64	0.011	285	4.84	3.24	0.038	9316	57.6	5742	20.5	4596	16.6	62.2	103		
ZR-03	G23	221	53.6	0.80	0.08	0.002	2.25	0.05	0.21	0.003	1220	13.7	1197	17.9	1157	15.3	2.00	5.50	1157	15
ZR-03	G24	364	76.9	0.38	0.08	0.002	2.14	0.04	0.20	0.002	1187	13.0	1163	16.2	1122	13.7	2.00	5.80	1122	14
ZR-03	G25	114	24.9	0.59	0.08	0.002	2.11	0.06	0.20	0.003	1165	13.9	1152	20.4	1129	18.1	1.10	3.20	1129	18
ZR-03	G27	147	33.5	0.39	0.08	0.002	2.46	0.06	0.22	0.003	1262	14.5	1261	19.6	1261	17.3	0.10	0.00	1261	17
ZR-03	G28	156	29.0	0.33	0.08	0.002	1.87	0.05	0.18	0.002	1067	12.9	1069	19.9	1075	18.0	-0.20	-0.70	1067	13
ZR-03	G29	270	54.4	0.43	0.08	0.002	2.14	0.05	0.19	0.002	1118	13.1	1161	19.2	1243	17.7	-3.70	-10.0	1243	18
ZR-03	G30	34.0	20.4	0.84	0.17	0.004	11.7	0.28	0.49	0.007	2559	29.9	2580	26.2	2599	22.6	-0.80	-1.50	2599	23
ZR-03	G31	258	54.2	0.81	0.09	0.002	2.12	0.05	0.18	0.002	1073	12.3	1156	18.0	1316	16.8	-7.10	-18.4	1073	12
ZR-03	G32	51.7	11.4	0.84	0.07	0.003	1.91	0.07	0.19	0.003	1109	15.1	1085	26.6	1039	24.1	2.20	6.70	1039	24
ZR-03	G33	260	56.8	0.22	0.08	0.002	2.51	0.05	0.22	0.003	1270	14.1	1276	17.9	1286	15.6	-0.40	-1.30	1286	16
ZR-03	G34	231	46.4	0.44	0.08	0.002	2.06	0.05	0.19	0.002	1120	12.8	1137	17.8	1170	15.9	-1.50	-4.30	1170	16
ZR-03	G35	226	48.2	0.59	0.08	0.002	2.06	0.05	0.19	0.002	1136	12.8	1136	17.4	1138	15.2	0.00	-0.20	1138	15
ZR-03	G36	136	53.4	0.73	0.11	0.002	5.05	0.11	0.33	0.004	1858	20.1	1827	20.7	1793	17.7	1.70	3.60	1793	18
ZR-03	G37	388	72.6	0.43	0.08	0.002	1.99	0.04	0.18	0.002	1049	11.8	1112	16.8	1239	15.5	-5.70	-15.3	1049	12
ZR-03	G38	15.4	3.00	0.51	0.07	0.005	1.80	0.12	0.18	0.004	1072	20.7	1047	46.2	998	42.9	2.30	7.30	1072	21
ZR-03	G39	264	97.8	0.53	0.11	0.002	5.23	0.10	0.33	0.004	1848	19.2	1858	19.0	1870	16.1	-0.50	-1.20	1870	16
ZR-03	G40	120	26.8	0.87	0.07	0.002	1.93	0.05	0.19	0.002	1111	13.3	1093	20.1	1058	17.8	1.70	5.10	1058	18
ZR-03	G43	83.3	19.3	1.22	0.08	0.002	1.93	0.05	0.18	0.002	1068	13.2	1093	21.1	1145	19.6	-2.30	-6.70	1068	13
ZR-03	G44	64.7	15.9	0.58	0.08	0.002	2.53	0.07	0.22	0.003	1293	15.8	1282	22.9	1266	20.6	0.80	2.10	1266	21
ZR-03	G45	388	77.5	0.37	0.08	0.002	2.01	0.04	0.19	0.002	1129	12.4	1119	16.1	1100	13.8	0.90	2.60	1100	14
ZR-03	G46	329	65.7	0.28	0.08	0.002	2.19	0.05	0.20	0.002	1153	12.8	1179	17.0	1228	15.1	-2.20	-6.10	1228	15
ZR-03	G47	291	62.1	0.49	0.09	0.002	2.36	0.05	0.20	0.002	1163	12.8	1231	17.0	1353	15.4	-5.50	-14.0	1353	15
ZR-03	G48	85.2	31.4	0.72	0.11	0.003	4.95	0.11	0.32	0.004	1774	19.8	1811	22.0	1854	19.4	-2.00	-4.30	1854	19
ZR-03	G49	34.0	8.70	0.81	0.09	0.003	2.54	0.09	0.20	0.003	1201	17.0	1285	29.5	1430	28.7	-6.50	-16.0		
ZR-03	G50	344	124	0.24	0.13	0.002	5.99	0.12	0.35	0.004	1923	19.9	1975	19.7	2031	16.9	-2.60	-5.30	2031	17

					Ratios						Ages (Ma)						% discord. (206/238207/235)	% discord. (206/238 207/206)	Best Age	±2s
Sample	Grain No.	Pb (ppm)	U (ppm)	Atomic Th/U	206/238	± s.e.	207/235	± s.e.	207/206	± s.e.	206/238	± 2s	207/235	± 2s	207/206	± 2s				
ZR-03	G51	622	170	0.49	0.24	0.004	7.99	0.15	0.24	0.003	1380	14.7	2230	19.7	3140	17.7	-38.1	-56.1		
ZR-03	G52	72.2	17.4	1.25	0.08	0.002	1.96	0.06	0.19	0.003	1098	13.8	1102	22.4	1112	20.5	-0.40	-1.30	1098	14
ZR-03	G53	74.5	17.5	0.09	0.12	0.003	3.92	0.10	0.23	0.003	1343	16.3	1619	23.5	2000	22.5	-17.1	-32.9		
ZR-03	G54	189	73.3	0.88	0.11	0.002	5.10	0.10	0.33	0.004	1815	19.2	1836	19.9	1861	17.2	-1.10	-2.40	1861	17
ZR-03	G55	255	53.5	0.27	0.08	0.002	2.32	0.05	0.21	0.003	1211	13.4	1218	17.4	1231	15.2	-0.50	-1.60	1231	15
ZR-03	G56	110	22.9	0.64	0.08	0.002	1.98	0.05	0.19	0.002	1098	13.0	1107	19.7	1127	17.9	-0.80	-2.60	1098	13
ZR-03	G57	335	73.5	0.43	0.08	0.002	2.30	0.05	0.21	0.003	1208	13.4	1213	17.3	1223	15.1	-0.40	-1.20	1223	15
ZR-03	G58	238	53.7	0.15	0.08	0.002	2.66	0.06	0.23	0.003	1331	14.7	1316	18.4	1295	15.9	1.10	2.70	1295	16
ZR-03	G59	198	79.1	0.82	0.12	0.002	5.29	0.11	0.33	0.004	1841	19.3	1868	20.1	1899	17.4	-1.40	-3.10	1899	17
ZR-03	G60	251	47.1	0.32	0.07	0.002	1.87	0.04	0.18	0.002	1082	12.3	1070	17.4	1048	15.1	1.10	3.20	1082	12
ZR-03	G61	80	18.0	0.80	0.08	0.003	2.12	0.07	0.19	0.003	1128	14.3	1155	23.6	1208	22.0	-2.30	-6.60	1208	22
ZR-03	G62	292	58.9	0.43	0.08	0.002	2.02	0.04	0.19	0.002	1123	12.5	1124	16.9	1125	14.7	0.00	-0.20	1125	15
ZR-03	G63	248	53.4	0.42	0.08	0.002	2.23	0.05	0.20	0.002	1186	13.2	1190	17.6	1197	15.5	-0.30	-0.90	1197	16
ZR-03	G64	15.8	3.40	0.89	0.07	0.004	1.73	0.10	0.18	0.003	1048	18.4	1020	40.4	961	37.2	2.80	9.00	1048	18
ZR-03	G65	236	49.6	0.36	0.08	0.002	2.19	0.05	0.20	0.002	1183	13.2	1176	17.7	1167	15.5	0.50	1.40	1167	16
ZR-03	G66	234	48.2	0.46	0.08	0.002	2.10	0.05	0.19	0.002	1135	12.7	1149	17.5	1178	15.6	-1.30	-3.70	1178	16
ZR-03	G68	33.5	0	1.88	0.10	0.003	4.13	0.13	0.29	0.004	1644	21.3	1661	28.7	1683	26.2	-1.00	-2.30	1683	26
ZR-03	G69	270	50.5	0.36	0.08	0.002	1.98	0.05	0.18	0.002	1060	12.1	1109	17.8	1208	16.4	-4.40	-12.2	1060	12
ZR-03	G70	197	38.8	0.18	0.08	0.002	2.14	0.05	0.20	0.002	1171	13.3	1163	18.4	1149	16.2	0.70	1.90	1149	16
ZR-03	G71	39.1	8.50	1.00	0.08	0.004	1.89	0.09	0.18	0.003	1044	17.4	1078	36.0	1150	35.1	-3.20	-9.30	1044	17
ZR-03	G72	62.9	14.5	0.56	0.08	0.003	2.33	0.07	0.21	0.003	1222	15.3	1222	24.0	1224	21.9	0.00	-0.20	1224	22
ZR-03	G73	72.2	16.0	0.77	0.09	0.003	2.35	0.07	0.19	0.003	1111	13.8	1227	22.9	1440	22.4	-9.50	-22.8		
ZR-03	G74	62.4	15.8	0.85	0.09	0.003	2.56	0.07	0.21	0.003	1243	15.4	1288	23.6	1365	22.0	-3.50	-8.90	1365	22
ZR-03	G75	56.3	24.1	1.28	0.11	0.003	5.04	0.13	0.32	0.004	1793	20.8	1827	24.5	1866	21.9	-1.80	-3.90	1866	22
ZR-03	G76	40.5	0	1.70	0.08	0.003	1.88	0.07	0.18	0.003	1053	14.5	1073	26.8	1116	25.5	-1.90	-5.60	1053	15
ZR-03	G77	162	32.1	0.48	0.08	0.002	2.02	0.05	0.18	0.002	1090	12.6	1123	19.0	1189	17.5	-2.90	-8.30	1090	13

					Ratios						Ages (Ma)						% discord. (206/238207/235)	% discord. (206/238 207/206)	Best Age	±2s
Sample	Grain No.	Pb (ppm)	U (ppm)	Atomic Th/U	206/238	± s.e.	207/235	± s.e.	207/206	± s.e.	206/238	± 2s	207/235	± 2s	207/206	± 2s				
ZR-03	G78	290	109	0.67	0.11	0.002	5.02	0.10	0.32	0.004	1806	19.0	1823	20.3	1843	17.7	-0.90	-2.00	1843	18
ZR-03	G79	56.3	11.8	0.76	0.08	0.003	1.95	0.06	0.18	0.003	1070	13.9	1099	24.1	1160	22.8	-2.70	-7.80	1070	14
ZR-03	G80	92.6	53.7	1.08	0.16	0.004	9.96	0.22	0.45	0.006	2386	24.9	2431	23.1	2469	20.1	-1.80	-3.40	2469	20
ZR-03	G81	404	109	0.72	0.34	0.007	11.3	0.23	0.24	0.003	1383	15.0	2552	21.9	3681	19.9	-45.8	-62.4		
ZR-03	G82	718	0	1.58	0.44	0.009	18.0	0.36	0.30	0.004	1689	18.0	2991	22.6	4039	20.0	-43.5	-58.2		
ZR-03	G83	171	36.7	0.45	0.08	0.002	2.16	0.05	0.20	0.003	1175	13.4	1167	19.1	1154	16.9	0.70	1.80	1154	17
ZR-03	G84	84	16.7	0.28	0.08	0.002	2.19	0.06	0.19	0.003	1143	14.0	1177	22.2	1242	20.7	-2.90	-7.90	1242	21
ZR-03	G85	144	32.6	0.39	0.10	0.002	2.77	0.07	0.21	0.003	1236	14.2	1348	20.6	1531	19.4	-8.30	-19.3		
ZR-03	G86	82	21.8	0.81	0.09	0.002	2.65	0.07	0.22	0.003	1300	15.6	1316	22.8	1342	20.8	-1.20	-3.10	1342	21
ZR-03	G87	190	69.6	0.45	0.12	0.003	5.53	0.12	0.33	0.004	1850	19.6	1906	21.5	1968	19.0	-2.90	-6.00	1968	19
ZR-03	G88	190	41.4	0.34	0.10	0.002	2.74	0.07	0.21	0.003	1225	14.0	1340	20.1	1529	19.0	-8.60	-19.9		
ZR-03	G89	197	41.5	0.35	0.09	0.002	2.35	0.07	0.20	0.003	1175	14.2	1229	22.2	1326	20.9	-4.40	-11.4	1326	21
ZR-03	G90	129	27.7	0.65	0.08	0.002	2.03	0.06	0.19	0.002	1126	13.4	1125	20.8	1124	18.9	0.10	0.20	1124	19
ZR-03	G91	239	53.1	0.69	0.08	0.002	2.22	0.06	0.20	0.002	1150	13.4	1186	20.2	1255	18.7	-3.10	-8.40	1255	19
ZR-03	G92	81.0	19.0	0.41	0.09	0.003	2.72	0.08	0.22	0.003	1277	15.6	1334	23.7	1428	22.2	-4.30	-10.6	1428	22
ZR-03	G93	139	36.2	0.34	0.09	0.002	3.10	0.08	0.25	0.003	1431	16.3	1432	21.5	1434	19.2	0.00	-0.20	1434	19
ZR-03	G94	469	82.9	0.10	0.08	0.002	1.98	0.04	0.18	0.002	1083	12.1	1109	17.3	1160	15.6	-2.30	-6.60	1083	12
ZR-03	G95	295	100	0.23	0.12	0.003	5.42	0.12	0.33	0.004	1836	19.5	1889	21.8	1948	19.4	-2.80	-5.80	1948	19
ZR-03	G96	251	50.2	0.22	0.09	0.002	2.43	0.06	0.20	0.003	1178	13.7	1252	20.6	1382	19.3	-5.90	-14.8	1382	19
ZR-03	G97	170	32.6	0.39	0.08	0.002	1.90	0.05	0.18	0.002	1080	12.9	1081	20.3	1085	18.4	-0.10	-0.40	1080	13
ZR-03	G98	189	38.7	0.36	0.08	0.002	2.13	0.05	0.20	0.002	1154	13.4	1158	19.8	1166	17.9	-0.40	-1.10	1166	18
ZR-03	G99	97.8	20.9	0.52	0.08	0.002	2.14	0.06	0.20	0.003	1154	14.2	1163	22.9	1180	21.0	-0.70	-2.20	1180	21
ZR-03	G100	207	50.7	0.80	0.24	0.006	6.58	0.15	0.20	0.003	1185	14.0	2056	23.7	3097	22.9	-42.4	-61.7		
ZR-03	G101	245	46.2	0.21	0.08	0.002	2.01	0.05	0.19	0.002	1115	13.0	1120	19.9	1131	18.0	-0.50	-1.40	1131	18
ZR-03	G102	360	125	0.31	0.15	0.003	6.64	0.15	0.33	0.004	1825	19.6	2065	22.9	2314	20.9	-11.6	-21.2		
ZR-03	G103	162	52.9	0.89	0.13	0.003	4.63	0.12	0.26	0.003	1515	17.4	1754	23.7	2053	22.3	-13.6	-26.2		
ZR-03	G104	163	34.5	0.43	0.09	0.002	2.44	0.06	0.20	0.003	1158	13.6	1255	21.3	1426	20.4	-7.70	-18.8		
ZR-03	G105	190	36.9	0.47	0.08	0.002	1.88	0.05	0.18	0.002	1064	12.7	1075	20.3	1097	18.6	-1.00	-3.00	1064	13

					Ratios						Ages (Ma)						% discord. (206/238207/235)	% discord. (206/238 207/206)	Best Age	±2s
Sample	Grain No.	Pb (ppm)	U (ppm)	Atomic Th/U	206/238	± s.e.	207/235	± s.e.	207/206	± s.e.	206/238	± 2s	207/235	± 2s	207/206	± 2s				
ZR-03	G106	192	42.9	0.22	0.09	0.002	2.68	0.07	0.22	0.003	1286	14.8	1324	21.4	1385	19.6	-2.80	-7.10	1385	20
ZR-03	G107	59.6	12.9	0.90	0.08	0.003	1.94	0.07	0.18	0.003	1063	14.8	1094	27.7	1157	26.6	-2.80	-8.10	1063	15
ZR-03	G108	292	91.2	0.12	0.11	0.003	4.93	0.11	0.31	0.004	1758	18.9	1807	22.3	1864	19.9	-2.70	-5.70	1864	20
ZR-03	G109	86.6	37.0	1.00	0.12	0.003	5.42	0.14	0.34	0.004	1885	21.2	1887	24.8	1891	22.2	-0.10	-0.30	1891	22
ZR-03	G110	238	51.7	0.55	0.08	0.002	2.21	0.06	0.20	0.002	1160	13.2	1183	19.7	1225	18.0	-1.90	-5.30	1225	18
ZR-03	G111	393	0	1.34	0.27	0.006	13.7	0.31	0.37	0.005	2028	21.2	2729	24.3	3299	22.0	-25.7	-38.5		
ZR-03	G112	249	48.9	0.27	0.08	0.002	2.05	0.05	0.19	0.002	1140	13.1	1133	19.5	1121	17.5	0.60	1.70	1121	18
ZR-03	G113	207	80.7	0.75	0.13	0.003	5.71	0.14	0.33	0.004	1829	20.2	1933	24.1	2046	21.9	-5.40	-10.6	2046	22
ZR-03	G114	39.1	9.70	1.25	0.08	0.004	2.21	0.09	0.19	0.003	1116	16.4	1185	31.2	1314	30.7	-5.80	-15.0		
ZR-03	G115	67.5	15.4	0.52	0.08	0.003	2.34	0.08	0.21	0.003	1219	15.6	1225	25.7	1236	23.8	-0.50	-1.30	1236	24
ZR-03	G116	134	55.9	1.09	0.11	0.003	5.08	0.13	0.33	0.004	1823	20.6	1832	25.1	1843	22.6	-0.50	-1.10	1843	23
ZR-03	G117	132	58.5	1.06	0.12	0.003	5.52	0.14	0.35	0.004	1917	21.1	1904	24.4	1891	21.7	0.70	1.40	1891	22
ZR-03	G118	126	32.3	0.68	0.08	0.002	2.59	0.07	0.22	0.003	1303	15.4	1297	22.8	1287	20.6	0.50	1.30	1287	21
ZR-03	G119	56.8	11.9	0.71	0.07	0.003	1.83	0.07	0.18	0.003	1077	14.6	1057	26.8	1018	24.4	1.90	5.80	1077	15
ZR-03	G120	136	32.1	1.16	0.09	0.003	2.17	0.06	0.18	0.002	1076	13.1	1171	22.2	1351	21.7	-8.10	-20.4	1076	13
ZR-03	G121	182	35.2	0.45	0.08	0.002	1.88	0.05	0.18	0.002	1076	12.9	1074	21.1	1072	19.2	0.10	0.30	1076	13
ZR-03	G122	327	63.8	0.30	0.08	0.002	2.14	0.06	0.19	0.002	1118	12.8	1162	20.0	1246	18.6	-3.80	-10.3	1246	19
ZR-03	G123	9.30	2.10	0.99	0.08	0.006	1.93	0.16	0.18	0.005	1084	24.7	1093	58.2	1110	56.2	-0.80	-2.30	1084	25
ZR-03	G124	90.8	19.5	0.48	0.08	0.003	2.15	0.07	0.20	0.003	1168	14.9	1164	25.2	1156	23.2	0.40	1.10	1156	23
ZR-03	G125	268	52.9	0.35	0.08	0.002	2.01	0.05	0.19	0.002	1122	13.2	1118	20.6	1112	18.6	0.30	0.90	1112	19
ZR-03	G126	109	24.7	0.95	0.08	0.002	1.94	0.06	0.19	0.003	1102	13.7	1094	23.2	1077	21.2	0.80	2.40	1077	21
ZR-03	G127	120	41.0	0.66	0.10	0.003	4.22	0.11	0.30	0.004	1681	19.1	1678	24.7	1675	22.3	0.20	0.40	1675	22
ZR-03	G128	305	0	2.09	0.41	0.010	15.8	0.38	0.28	0.004	1588	18.0	2863	26.4	3944	24.4	-44.5	-59.7		
ZR-03	G129	182	41.5	0.64	0.08	0.002	2.30	0.06	0.20	0.003	1188	13.9	1213	21.6	1258	19.9	-2.00	-5.60	1258	20
ZR-03	G130	141	30.6	0.55	0.08	0.002	2.15	0.06	0.20	0.003	1165	13.9	1164	22.3	1165	20.3	0.00	0.00	1165	20
ZR-03	G131	224	63.7	0.40	0.10	0.003	3.64	0.09	0.27	0.003	1517	17.0	1559	23.0	1617	21.0	-2.70	-6.20	1617	21
ZR-03	G132	390	112	0.45	0.11	0.003	3.84	0.10	0.26	0.003	1510	16.8	1601	23.1	1723	21.4	-5.70	-12.4	1723	21

					Ratios						Ages (Ma)						% discord. (206/238207/235)	% discord. (206/238 207/206)	Best Age	±2s
Sample	Grain No.	Pb (ppm)	U (ppm)	Atomic Th/U	206/238	± s.e.	207/235	± s.e.	207/206	± s.e.	206/238	± 2s	207/235	± 2s	207/206	± 2s				
ZR-03	G133	208	41.0	0.26	0.08	0.002	2.16	0.06	0.19	0.003	1146	13.6	1169	21.9	1213	20.4	-2.00	-5.60	1213	20
ZR-03	G134	351	90.6	1.31	0.08	0.002	2.13	0.06	0.19	0.002	1142	13.2	1157	20.6	1185	18.9	-1.30	-3.60	1185	19
ZR-03	G135	169	35.0	0.43	0.08	0.002	2.08	0.06	0.19	0.003	1148	13.6	1143	21.7	1134	19.7	0.40	1.20	1134	20
ZR-03	G136	165	37.1	0.30	0.08	0.002	2.53	0.07	0.22	0.003	1271	15.1	1280	23.4	1295	21.5	-0.70	-1.90	1295	22
ZR-03	G137	161	33.6	0.45	0.08	0.003	2.25	0.07	0.19	0.003	1143	13.9	1196	23.1	1292	22.0	-4.40	-11.5	1292	22
ZR-03	G138	249	60.7	0.37	0.14	0.004	4.20	0.12	0.22	0.003	1308	15.6	1674	25.3	2171	25.0	-21.9	-39.8		
ZR-03	G139	81.5	23.0	0.78	0.09	0.003	2.93	0.09	0.24	0.003	1386	17.1	1389	26.2	1393	24.1	-0.20	-0.50	1393	24
ZR-03	G140	160	41.2	0.51	0.09	0.002	2.80	0.08	0.23	0.003	1356	15.8	1357	23.3	1358	21.2	0.00	-0.20	1358	21
ZR-03	G141	106	48.2	1.27	0.12	0.003	5.63	0.15	0.34	0.004	1880	21.1	1921	26.3	1965	24.0	-2.10	-4.30	1965	24
ZR-03	G142	244	60.7	0.98	0.12	0.003	3.50	0.10	0.20	0.003	1194	14.1	1527	24.1	2024	24.2	-21.8	-41.0		
ZR-03	G143	0.50	0	1.97	0.86	0.037	703	46.4	5.91	0.364	12459	340	6658	76.2	5030	43.5	87.1	148		
ZR-03	G144	94.5	45.7	1.57	0.11	0.003	5.27	0.15	0.34	0.005	1882	21.9	1864	27.6	1844	25.0	1.00	2.10	1844	25
ZR-03	G145	103	22.6	0.54	0.08	0.003	2.29	0.08	0.20	0.003	1167	14.8	1210	25.7	1288	24.5	-3.50	-9.40	1288	25
ZR-03	G146	177	39.7	0.62	0.09	0.003	2.51	0.07	0.20	0.003	1167	13.9	1274	23.0	1461	22.4	-8.40	-20.1		
ZR-03	G147	91.3	0	1.91	0.11	0.003	5.23	0.15	0.34	0.004	1869	21.4	1857	26.9	1844	24.4	0.70	1.40	1844	24
ZR-03	G148	256	51.4	0.34	0.08	0.002	2.25	0.06	0.19	0.002	1137	13.4	1195	22.1	1303	21.1	-4.90	-12.7	1303	21
ZR-03	G149	246	54.4	0.88	0.09	0.003	2.20	0.07	0.18	0.002	1084	13.3	1181	23.6	1364	23.3	-8.20	-20.5	1084	13
ZR-03	G150	470	109	0.37	0.15	0.004	4.44	0.12	0.21	0.003	1246	14.3	1720	24.7	2357	24.7	-27.5	-47.1		

Appendix IV-A: BCR-2 EMPA Area Scan Results

No.	Na_2O	MgO	Al_2O_3	SiO_2	P_2O_5	K_2O	CaO	TiO_2	FeO	Total
1	3.29	3.61	13.7	55.4	0.43	1.75	6.86	2.45	11.6	99.1
2	3.29	3.75	13.8	55.2	0.42	1.76	6.89	2.32	12.1	99.6
3	3.22	3.61	13.9	54.6	0.32	1.87	6.99	2.28	12.0	98.8
4	3.22	3.67	13.9	54.1	0.34	1.79	6.86	2.32	11.8	98.0
5	3.39	3.79	13.7	55.2	0.30	1.75	6.96	2.44	12.1	99.6
6	3.33	3.67	13.7	54.9	0.26	1.85	6.95	2.28	12.1	99.0
7	3.33	3.68	13.8	54.7	0.33	1.81	6.78	2.24	12.0	98.7
8	3.35	3.64	13.8	54.4	0.26	1.81	6.77	2.22	11.9	98.2
9	3.36	3.66	13.7	55.3	0.26	1.88	7.09	2.39	12.4	100
10	3.34	3.74	14.2	54.9	0.41	1.88	6.91	2.24	12.6	100
11	3.46	3.69	14.0	55.1	0.21	1.81	6.94	2.42	12.2	99.8
12	3.28	3.75	13.9	55.2	0.40	1.77	6.84	2.38	11.9	99.4
13	3.23	3.81	13.8	55.0	0.36	1.76	7.07	2.42	12.1	99.6
14	3.19	3.65	13.9	54.8	0.34	1.78	7.09	2.32	12.2	99.2
15	3.33	3.74	14.0	55.3	0.28	1.77	7.04	2.17	11.9	99.5
16	3.38	3.72	13.9	54.9	0.37	1.89	6.95	2.29	12.0	99.3
17	3.24	3.72	13.8	55.3	0.34	1.91	7.06	2.38	12.0	99.7
18	3.32	3.72	13.9	55.2	0.34	1.80	6.96	2.36	12.0	99.6
19	3.22	3.72	13.8	54.6	0.26	1.84	6.91	2.28	12.1	98.7
20	3.29	3.51	13.8	54.6	0.26	1.81	6.92	2.28	11.9	98.4
21	3.25	3.60	13.6	54.6	0.30	1.86	6.82	2.35	11.7	98.0
22	3.26	3.64	13.9	55.7	0.24	1.80	6.94	2.32	12.0	99.7
23	3.31	3.71	14.0	55.5	0.32	1.92	7.10	2.25	12.1	100
24	3.28	3.71	13.8	55.6	0.24	1.90	7.05	2.21	12.5	100
25	3.40	3.74	13.9	55.3	0.31	1.77	6.87	2.18	12.2	99.7
26	3.35	3.80	13.9	55.3	0.24	1.72	6.94	2.59	12.1	99.9
27	3.31	3.68	13.7	55.0	0.32	1.87	7.10	2.25	12.1	99.4
28	3.28	3.80	14.0	55.6	0.32	1.84	7.07	2.25	12.4	100
29	3.30	3.71	13.8	55.6	0.31	1.86	7.02	2.31	12.1	100
30	3.39	3.74	13.9	55.6	0.48	1.86	7.01	2.38	12.4	101
31	3.34	3.77	13.6	55.7	0.35	1.84	6.91	2.45	12.2	100
32	3.35	3.59	13.8	54.5	0.23	1.82	6.91	2.33	11.9	98.4
33	3.46	3.69	13.8	55.1	0.38	1.83	7.01	2.25	12.2	99.8
34	3.30	3.70	14.0	55.1	0.38	1.82	6.95	2.33	12.2	99.8
35	3.36	3.75	13.8	55.1	0.31	1.86	7.08	2.41	12.1	99.8
36	3.35	3.69	13.6	54.7	0.34	1.74	6.98	2.36	11.9	98.6
37	3.29	3.67	14.1	54.5	0.29	1.81	6.91	2.34	11.9	98.8
38	3.40	3.68	14.2	55.2	0.28	1.85	6.91	2.34	12.0	99.8
39	3.31	3.76	14.0	55.3	0.26	1.80	7.05	2.34	12.1	99.9
40	3.23	3.82	13.9	55.1	0.27	1.77	7.08	2.40	12.5	100
41	3.23	3.71	13.6	54.8	0.24	1.82	7.03	2.29	12.1	98.8
42	3.31	3.39	14.4	51.5	0.28	1.85	6.60	2.24	11.1	94.6
43	3.07	3.51	14.5	51.5	0.33	1.94	6.58	2.20	11.4	95.1

Appendix IV-B: Volcanic and Metavolcanic EMPA Area Scan Results (sort applied on total)

Sample	Na_2O	MgO	Al_2O_3	SiO_2	P_2O	K_2O	CaO	TiO_2	MnO	FeO	Total
OE-1	1.48	0	7.63	66.1	0	4.74	1.01	0.23	0	1.21	82.4
OE-1	4.86	0.01	12.1	61.5	0	2.90	6.55	0.05	0.28	1.20	89.5
OE-1	1.22	0.02	11.3	60.6	0	8.09	7.20	0.18	0.22	0.75	89.5
OE-1	0.96	0	8.79	64.4	0.01	6.45	7.17	0.10	0.28	1.46	89.6
OE-1	2.78	0	12.3	63.2	0.01	6.42	4.38	0.46	0.07	1.56	91.3
OE-1	2.10	0	11.9	61.9	0.05	6.96	6.53	0.51	0.35	1.83	92.1
OE-1	3.36	0	12.9	65.6	0	6.03	3.10	0.25	0.09	1.00	92.3
OE-1	6.07	0	15.7	64.2	0.02	3.48	1.75	0.32	0	0.89	92.4
OE-1	1.88	0.04	11.9	65.3	0	7.55	4.63	0.24	0.10	0.77	92.5
OE-1	4.55	0	13.8	68.8	0	4.44	0.55	0.42	0	0	92.6
OE-1	1.18	0.06	7.78	71.4	0	5.36	4.76	0.16	0.04	1.97	92.7
OE-1	2.74	0	11.7	65.1	0.04	5.82	4.61	0.54	0.16	2.07	92.8
OE-1	8.83	0.03	18.8	63.2	0	0.69	1.06	0	0.15	0.16	92.9
OE-1	3.20	0	10.4	72.5	0	4.11	1.27	0.15	0.06	1.38	93.1
OE-1	6.52	0.08	14.7	67.2	0.14	2.02	1.74	0.15	0.07	0.65	93.2
OE-1	1.42	0.01	10.3	67.0	0	6.81	3.91	0.40	0.11	3.38	93.3
OE-1	2.38	0	10.8	65.5	0.17	5.92	6.38	0.36	0.14	1.78	93.3
OE-1	1.57	0.05	10.0	68.3	0	6.14	4.03	0.48	0.28	2.57	93.4
OE-1	1.84	0.05	8.78	75.2	0.07	5.12	1.69	0.13	0.08	1.08	94.0
OE-1	4.26	0.05	11.9	72.7	0	3.32	0.78	0.08	0.06	0.93	94.0
OE-1	3.30	0	11.3	71.9	0.13	4.79	0.33	0.92	0	1.39	94.1
OE-1	0.86	0	7.74	73.9	0.13	5.67	3.81	0.19	0.15	1.74	94.2
OE-1	3.69	0	12.6	70.3	0	5.30	0.38	0.28	0.11	1.69	94.4
OE-1	3.29	0.04	14.7	65.8	0	7.67	0.55	0.58	0.03	1.71	94.4
OE-1	5.39	0.05	17.4	62.7	0	6.74	0.24	0.18	0	1.67	94.4
OE-1	4.83	0.02	12.6	70.9	0	3.31	1.43	0.34	0	0.93	94.4
OE-1	4.70	0.02	13.7	69.7	0	4.47	0.27	0.27	0	1.35	94.5
OE-1	1.83	0	8.65	77.7	0	4.82	0.18	0.47	0.06	1.02	94.7
OE-1	6.36	0	17.8	64.1	0.02	4.91	0.26	0.08	0	1.31	94.8
OE-1	4.56	0.04	12.3	70.1	0	3.50	1.29	0.42	0	2.64	94.9
OE-1	2.03	0	11.0	71.9	0.05	6.28	1.50	0.37	0.05	1.75	94.9
OE-1	1.62	0.03	9.82	71.1	0	6.06	1.20	0.42	0	4.74	95.0
OE-1	1.26	0	10.5	69.9	0	7.00	3.98	0.40	0.23	1.73	95.0
OE-1	3.17	0.03	11.4	72.8	0	4.96	0.73	0.17	0	1.83	95.1
OE-1	1.66	0.02	9.78	72.7	0	6.09	1.36	0.58	0.12	2.93	95.2
OE-1	3.35	0	12.9	71.6	0	6.13	0.52	0.12	0	0.74	95.3
OE-1	1.36	0.01	8.49	75.7	0	5.55	0.98	0.35	0.15	2.87	95.4
OE-1	1.33	0	8.88	76.3	0	5.91	0.90	0.26	0.04	1.79	95.4
OE-1	2.73	0	13.1	68.7	0	7.29	1.40	0.47	0	1.79	95.5
OE-1	3.74	0	12.0	67.3	0.05	4.85	2.85	0.25	0.19	4.19	95.5
OE-1	3.45	0.02	11.5	74.0	0	4.51	0.34	0.12	0	1.57	95.5
OE-1	2.89	0	12.5	70.4	0.04	6.49	1.55	0.31	0.16	1.26	95.6
OE-1	2.83	0	16.6	60.9	0	9.88	2.57	1.23	0.11	1.54	95.6
OE-1	1.85	0.05	10.3	70.1	0.05	6.14	4.03	0.64	0.24	2.32	95.6

Sample	Na_2O	MgO	Al_2O_3	SiO_2	P_2O	K_2O	CaO	TiO_2	MnO	FeO	Total
OE-1	1.44	0.04	8.48	78.5	0	5.46	0.83	0.20	0	0.69	95.7
OE-1	3.13	0.01	10.9	75.5	0.05	4.65	0.50	0.20	0.15	0.63	95.7
OE-1	2.26	0	9.38	74.0	0	4.95	0.64	0.13	0	4.36	95.8
OE-1	4.68	0	12.6	73.4	0	3.51	0.49	0.12	0.07	0.85	95.8
OE-1	3.68	0	12.7	72.4	0.03	5.39	0.18	0	0.03	1.38	95.8
OE-1	1.27	0.03	8.59	75.9	0	5.86	0.63	0.45	0	3.03	95.8
OE-1	1.99	0	9.90	75.2	0	5.86	1.04	0.30	0	1.51	95.8
OE-1	2.41	0.05	12.1	71.7	0	7.08	0.37	0.39	0	1.72	95.9
OE-1	3.01	0	10.8	76.4	0.02	4.50	0.34	0.09	0.04	0.67	95.9
OE-1	1.39	0.02	7.93	79.2	0	4.92	0.37	0.24	0.09	1.74	95.9
OE-1	2.35	0.04	11.0	74.0	0	6.19	0.43	0.41	0	1.59	96.0
OE-1	1.68	0	9.64	73.9	0	5.82	2.26	0.50	0.11	2.07	96.0
OE-1	1.81	0.01	11.0	72.5	0	6.70	1.64	0.44	0.13	1.76	96.0
OE-1	2.53	0.07	12.4	70.9	0	6.67	0.92	0.77	0	1.80	96.0
OE-1	6.36	0	17.6	65.2	0.05	5.07	0.16	0.17	0	1.42	96.0
OE-1	4.92	0.03	14.4	70.3	0.03	4.39	0.21	0.19	0.03	1.60	96.1
OE-1	5.08	0.03	15.0	69.6	0.02	5.03	0.21	0.03	0	1.21	96.2
OE-1	2.26	0	11.3	73.1	0	6.55	0.95	0.38	0	1.67	96.2
OE-1	2.23	0	11.3	73.2	0	6.52	0.40	0.27	0	2.27	96.2
OE-1	1.28	0	7.32	80.5	0.03	4.84	0.34	0.07	0.17	1.67	96.2
OE-1	1.87	0.02	12.4	68.7	0	7.87	1.82	0.96	0.10	2.57	96.3
OE-1	1.86	0	11.1	73.7	0	7.14	0.83	0.30	0	1.39	96.3
OE-1	1.80	0	11.8	71.8	0	7.65	1.27	0.31	0.06	1.70	96.3
OE-1	5.28	0	16.3	67.1	0.02	5.94	0.14	0.11	0.13	1.46	96.5
OE-1	2.35	0.05	12.6	68.9	0	7.28	2.28	0.70	0.16	2.40	96.7
OE-1	3.09	0.06	11.2	73.4	0	5.16	1.44	0.47	0.05	1.83	96.7
OE-1	2.46	0.07	12.5	71.1	0.04	7.13	1.65	0.40	0.05	1.31	96.7
OE-1	3.65	0.09	12.4	70.5	0	4.95	0.71	0.10	0	4.38	96.7
OE-1	1.33	0.02	10.0	76.3	0	6.98	0.36	0.20	0.04	1.47	96.7
OE-1	2.87	0.07	11.8	72.9	0	6.02	0.93	0.49	0.01	1.69	96.8
OE-1	1.70	0.01	9.90	74.2	0.02	6.29	1.64	0.76	0.13	2.12	96.8
OE-1	1.47	0.04	9.28	77.8	0.06	5.99	0.53	0.11	0.17	1.38	96.9
OE-1	3.62	0.01	11.8	74.9	0	4.79	0.16	0.13	0	1.49	96.9
OE-1	3.48	0	11.9	73.8	0	4.86	0.57	0.50	0.09	1.67	96.9
OE-1	1.70	0.03	10.1	76.9	0	6.38	0.30	0.28	0.01	1.29	96.9
OE-1	1.47	0.05	9.37	78.1	0	6.29	0.26	0.13	0	1.27	96.9
OE-1	2.41	0	12.5	70.5	0	7.14	1.47	0.64	0	2.25	96.9
OE-1	2.04	0	10.0	76.5	0	5.85	0.41	0.33	0.07	1.69	96.9
OE-1	2.17	0.02	12.7	70.6	0.01	7.77	0.91	0.59	0	2.33	97.0
OE-1	1.68	0.03	10.5	75.0	0	6.80	0.57	0.43	0	2.13	97.1
OE-1	1.72	0.02	10.8	72.1	0	7.06	2.32	0.77	0.05	2.27	97.1
OE-1	2.06	0.05	10.7	75.6	0	6.54	0.43	0.37	0.07	1.50	97.4
OE-1	2.41	0	10.3	77.1	0	5.18	0.22	0.22	0	1.99	97.4
OE-1	3.41	0	12.1	74.9	0.07	5.27	0.39	0.04	0.03	1.32	97.5
OE-1	2.75	0.03	11.2	76.1	0.01	5.66	0.58	0.07	0	1.28	97.6
OE-1	1.16	0.01	10.5	72.7	0.01	7.70	2.51	0.45	0.03	2.67	97.7
OE-1	2.80	0.01	10.9	76.9	0	5.29	0.38	0.20	0	1.30	97.8
OE-1	1.27	0	9.99	77.0	0	6.96	1.16	0.16	0	1.30	97.8

Sample	Na2O	MgO	Al2O3	SiO2	P2O	K2O	CaO	TiO2	MnO	FeO	Total
OE-1	1.96	0	10.7	75.2	0	6.58	0.81	0.29	0.13	2.15	97.9
OE-1	2.08	0.01	10.8	75.1	0.03	6.30	1.15	0.40	0.03	2.02	97.9
OE-1	4.64	0.03	13.4	74.2	0	4.16	0.20	0.16	0.08	1.07	98.0
OE-1	3.94	0	12.7	74.3	0.03	4.79	0.50	0.10	0.09	1.58	98.0
OE-1	4.45	0	13.5	73.1	0	4.66	0.41	0.59	0	1.44	98.2
OE-1	3.66	0	11.8	76.3	0	4.54	0.28	0.17	0.10	1.40	98.2
OE-1	3.37	0	11.9	75.0	0.01	5.08	0.45	0.50	0.01	1.97	98.3
OE-1	4.03	0	12.8	74.1	0	4.90	0.89	0.24	0.06	1.49	98.5
OE-1	3.88	0.01	11.9	75.9	0.11	4.35	0.71	0.23	0.01	1.58	98.7
OE-1	3.98	0	12.3	75.7	0.04	4.77	0.37	0.39	0.07	1.35	99.0
OE-2	6.43	0.04	12.4	43.1	0.02	0.54	0.09	0.06	0.03	0.46	63.1
OE-2	0.25	0.12	8.11	59.5	0	5.84	1.97	0.55	0.10	0.90	77.4
OE-2	2.06	0	7.08	65.8	0	3.05	0.04	0.17	0.11	0.21	78.5
OE-2	3.17	0.10	10.8	60.2	0	4.09	0.04	0.26	0	0.58	79.2
OE-2	5.31	0.58	15.7	52.6	0	3.53	0.24	0.23	0.11	1.22	79.6
OE-2	0.98	0.13	10.9	57.8	0	7.35	0.78	1.16	0	0.75	79.8
OE-2	0.14	0.02	8.09	64.3	0.27	6.39	0.09	0.10	0	0.43	79.8
OE-2	3.36	0.38	15.0	54.1	0	6.12	0.12	0	0	1.20	80.3
OE-2	1.32	0.19	10.6	59.8	0	6.34	0.64	0.80	0.05	0.77	80.5
OE-2	0.20	0.03	8.78	63.9	0.10	7.09	0.12	0.12	0.09	0.49	81.0
OE-2	0.10	0.02	7.99	66.1	0	6.41	0.10	0.27	0.03	0.20	81.2
OE-2	0.30	0.10	10.7	61.2	0	7.85	0.24	0.22	0	0.71	81.3
OE-2	0.06	0.05	7.70	66.8	0	6.27	0.13	0.05	0	0.32	81.4
OE-2	0.12	0.01	8.62	64.9	0	6.98	0.09	0.29	0	0.50	81.5
OE-2	0.18	0.06	9.39	63.8	0.06	7.16	0.13	0.29	0	0.47	81.6
OE-2	4.07	0.03	13.7	57.7	0.07	4.97	0.22	0.08	0	0.93	81.8
OE-2	0.10	0	8.51	65.5	0	6.96	0.11	0.22	0.02	0.54	82.0
OE-2	0.16	0.03	9.14	64.4	0	7.53	0.19	0.17	0	0.39	82.0
OE-2	0.15	0.05	9.02	65.6	0	7.31	0.11	0.06	0.02	0.41	82.7
OE-2	0.12	0.12	8.37	66.4	0	6.95	0.08	0.11	0.02	0.58	82.7
OE-2	0.33	0.02	8.38	67.0	0	6.53	0.15	0.13	0	0.45	83.0
OE-2	0.25	0.02	8.89	66.2	0	7.08	0	0.05	0	0.56	83.0
OE-2	0.28	0.04	10.5	62.8	0	8.12	0.10	0.19	0.01	1.07	83.1
OE-2	0.26	0.06	8.31	67.2	0	6.77	0.10	0.14	0.01	0.37	83.2
OE-2	0.32	0.09	10.4	62.6	0	8.03	0.52	0.83	0.03	0.51	83.3
OE-2	0.38	0.08	9.45	64.7	0	7.35	0.29	0.33	0.06	0.63	83.3
OE-2	2.08	0.08	11.5	62.3	0	6.40	0.09	0.10	0.05	0.70	83.3
OE-2	0.19	0	8.72	66.6	0.13	6.83	0.16	0.17	0.17	0.48	83.4
OE-2	0.24	0.04	9.21	65.5	0	7.31	0.08	0.26	0.09	0.70	83.4
OE-2	0.72	0.14	10.7	62.4	0	7.84	0.14	0.28	0	1.28	83.4
OE-2	0.20	0.03	7.67	69.1	0	5.94	0.13	0.11	0	0.27	83.5
OE-2	0.22	0.04	11.0	62.7	0	8.80	0.09	0.13	0	0.63	83.6
OE-2	0.18	0	6.98	69.8	0	5.46	0.40	0.39	0.03	0.41	83.6
OE-2	0.24	0.08	10.8	63.1	0	8.31	0.13	0.26	0.01	0.82	83.7
OE-2	0.32	0.04	10.7	63.6	0	8.09	0.08	0.23	0	0.72	83.7
OE-2	0.22	0.09	7.23	69.1	0	5.80	0.16	0.25	0	0.98	83.9
OE-2	0.46	0.08	8.54	67.5	0	6.24	0.20	0.17	0	0.67	83.9
OE-2	0.56	0.03	10.2	64.4	0	7.55	0.18	0.15	0.06	0.79	83.9

Sample	Na2O	MgO	Al2O3	SiO2	P2O	K2O	CaO	TiO2	MnO	FeO	Total
OE-2	0.50	0.04	10.2	64.4	0	7.91	0.07	0.09	0	0.74	83.9
OE-2	0.98	0.17	13.5	57.6	0	9.58	0.17	0.24	0.01	1.78	84.0
OE-2	0.11	0.13	5.66	64.4	0.23	3.87	0.92	0.88	0.03	7.86	84.1
OE-2	0.65	0.26	11.9	60.0	0.22	8.55	0.54	0.67	0	1.24	84.1
OE-2	0.43	0.06	9.49	65.5	0	7.63	0.09	0.16	0	0.79	84.2
OE-2	0.38	0.06	10.2	64.8	0	7.75	0.12	0.16	0	0.75	84.2
OE-2	0.51	0.08	14.3	57.2	0	10.8	0.16	0.09	0	1.18	84.2
OE-2	0.10	0.13	5.70	70.9	0.10	4.53	0.55	0.56	0.06	1.65	84.2
OE-2	0.09	0.12	7.78	69.0	0	6.01	0.18	0.21	0	0.88	84.3
OE-2	0.15	0.05	6.93	71.1	0	5.69	0.11	0.06	0	0.19	84.3
OE-2	0.24	0.11	10.2	64.8	0	8.15	0.17	0.17	0	0.66	84.4
OE-2	0.86	0.29	14.4	56.2	0	10.2	0.06	0.17	0	2.60	84.7
OE-2	2.33	0.08	13.5	59.7	0	7.76	0.09	0.16	0	0.98	84.7
OE-2	0.32	0.02	13.0	59.9	0	10.6	0.06	0.03	0	0.82	84.7
OE-2	0.60	0.07	10.9	63.8	0	8.24	0.07	0.20	0	0.80	84.7
OE-2	0.53	0.06	11.3	62.9	0	8.56	0.14	0.35	0.06	0.82	84.7
OE-2	0.40	0.03	9.98	65.6	0	7.81	0.10	0.09	0.01	0.73	84.7
OE-2	0.19	0.17	4.66	69.0	0.06	2.99	0.57	0.74	0	6.42	84.8
OE-2	3.21	0.24	12.2	61.0	0.08	4.68	0.22	0.21	0	2.98	84.8
OE-2	0.62	0.14	11.5	62.6	0	8.43	0.19	0.28	0.01	1.12	84.8
OE-2	0.26	0.02	8.35	68.5	0	6.78	0.15	0.17	0.12	0.55	84.9
OE-2	0.21	0.03	8.95	67.9	0	7.00	0.11	0.08	0.07	0.52	84.9
OE-2	0.26	0.08	9.93	65.6	0.04	7.77	0.15	0.23	0.08	0.75	84.9
OE-2	0.34	0.12	10.7	64.4	0	8.37	0.15	0.12	0	0.73	85.0
OE-2	0.45	0.03	10.7	65.0	0	8.25	0.07	0.09	0.01	0.54	85.1
OE-2	0.53	0.06	10.6	64.7	0	8.19	0.12	0.17	0.10	0.74	85.2
OE-2	0.15	0.11	8.10	68.0	0	6.25	0.54	0.69	0	1.32	85.2
OE-2	0.89	0.11	11.4	62.6	0	8.03	0.39	0.62	0.06	1.10	85.2
OE-2	0.52	0.02	6.90	72.0	0	5.27	0.09	0.04	0.05	0.40	85.3
OE-2	0.43	0.06	10.3	65.5	0	7.97	0.06	0.08	0	0.97	85.3
OE-2	0.22	0.03	9.57	67.3	0	7.62	0.06	0.18	0	0.42	85.4
OE-2	0.24	0.12	7.50	65.3	0.29	5.63	0.40	0.47	0.10	5.80	85.9
OE-2	1.06	0.16	12.8	61.3	0.01	8.96	0.20	0.19	0	1.29	86.0
OE-2	0.68	0.18	11.9	62.9	0	8.70	0.19	0.42	0.04	1.06	86.0
OE-2	0.45	0	8.89	69.0	0	7.05	0.06	0.08	0	0.59	86.1
OE-2	0.49	0.06	7.56	71.5	0	5.54	0.16	0.26	0.05	0.56	86.2
OE-2	0.90	0.12	10.6	66.0	0	7.49	0.15	0.11	0	0.93	86.3
OE-2	0.66	0.16	11.5	64.4	0	8.48	0.11	0.13	0.03	0.80	86.3
OE-2	0.25	0.09	7.24	70.2	0.22	5.71	0.18	0.11	0	2.46	86.4
OE-2	0.13	0.05	7.42	72.3	0	6.03	0.12	0.19	0	0.31	86.5
OE-2	0.45	0.07	9.73	67.6	0	7.46	0.12	0.10	0.12	0.86	86.6
OE-2	0.25	0.03	9.13	68.8	0	7.31	0.19	0.28	0.02	0.67	86.6
OE-2	0.18	0.01	6.01	74.2	0	4.91	0.14	0.15	0.15	0.90	86.7
OE-2	0.41	0.05	9.88	67.5	0	7.65	0.08	0.14	0.03	0.93	86.7
OE-2	0.30	0.05	9.49	63.6	0	7.27	0.19	0.15	0.02	6.18	87.2
OE-2	0.45	0.12	11.3	65.1	0	8.92	0.06	0.18	0.13	1.03	87.3
OE-2	0.37	0.02	9.40	69.3	0	7.49	0.07	0.24	0	0.75	87.6
OE-2	0.66	0.05	10.5	67.1	0	7.83	0.46	0.71	0.09	0.73	88.1

Sample	Na2O	MgO	Al2O3	SiO2	P2O	K2O	CaO	TiO2	MnO	FeO	Total
OE-2	2.50	0.05	12.9	64.2	0	7.07	0.17	0.21	0	1.34	88.4
OE-2	0.77	0.08	7.74	71.0	0	5.14	1.15	1.75	0.11	0.88	88.6
KG-1	2.14	0.07	9.74	64.4	0	5.14	0.50	0.32	0.04	1.55	83.9
KG-1	1.76	0.03	10.7	62.4	0	6.56	4.56	0.52	0.18	1.57	88.2
KG-1	2.45	0	10.1	61.5	0	5.10	8.12	0.35	0.37	1.37	89.3
KG-1	3.61	0	12.1	64.6	0	4.52	2.70	0.58	0.01	1.41	89.5
KG-1	2.80	0.04	10.9	68.3	0.10	5.32	3.72	0.16	0.22	1.14	92.8
KG-1	7.08	0	16.3	64.2	0	2.67	1.88	0.21	0.11	0.36	92.8
KG-1	2.01	0.04	10.3	72.0	0.02	5.65	0.82	0.48	0.02	1.78	93.1
KG-1	3.05	0	11.3	71.3	0	5.17	0.76	0.28	0.10	1.47	93.4
KG-1	2.32	0.03	11.1	71.5	0	6.30	0.61	0.31	0.04	1.39	93.6
KG-1	3.88	0	12.3	70.4	0.03	4.62	0.64	0.46	0.05	1.36	93.8
KG-1	2.82	0.02	12.0	69.9	0	6.33	0.43	0.33	0.05	2.08	93.9
KG-1	6.12	0.05	15.9	62.1	0.25	3.66	1.38	2.93	0.01	1.49	93.9
KG-1	2.49	0.06	10.1	68.7	0.53	4.85	4.35	0.26	0.12	2.57	94.0
KG-1	3.56	0	11.2	73.4	0	4.34	0.35	0.22	0.02	1.30	94.4
KG-1	3.86	0	11.9	72.7	0	4.47	0.19	0.29	0	1.13	94.6
KG-1	5.66	0.07	15.1	66.5	0.16	3.69	0.51	1.09	0.13	1.78	94.6
KG-1	3.06	0.10	11.0	73.3	0	4.96	0.80	0.17	0.10	1.20	94.7
KG-1	3.24	0.03	11.7	71.8	0	5.41	0.86	0.50	0.09	1.09	94.7
KG-1	6.65	0.01	16.1	64.1	0.13	2.91	1.06	1.98	0.04	1.80	94.8
KG-1	3.16	0	12.9	68.3	0.05	6.30	1.65	0.36	0	2.04	94.8
KG-1	4.02	0.03	14.1	65.8	0	5.71	1.54	0.63	0.07	2.91	94.8
KG-1	4.53	0	13.1	70.5	0.23	4.30	0.55	0.44	0.03	1.27	94.9
KG-1	2.61	0.02	10.2	75.1	0	4.88	0.37	0.45	0	1.27	94.9
KG-1	6.14	0.09	17.0	66.7	0	4.19	0.29	0.15	0.06	0.48	95.0
KG-1	3.77	0	12.5	72.4	0	5.17	0.17	0.09	0	0.91	95.1
KG-1	5.45	0.08	15.8	64.2	0.06	4.68	0.71	0.77	0	3.45	95.1
KG-1	6.85	0	16.4	66.9	0	3.33	0.59	0.24	0.06	0.82	95.2
KG-1	2.40	0.02	11.4	72.0	0	6.10	0.84	0.54	0	1.90	95.2
KG-1	3.55	0	11.9	72.3	0	4.91	0.30	0.27	0	2.13	95.3
KG-1	2.50	0	8.95	78.4	0	3.92	0.23	0.12	0	1.23	95.3
KG-1	3.27	0	12.9	69.9	0.05	6.00	0.84	0.50	0	1.96	95.4
KG-1	1.43	0	9.92	72.9	0	6.56	0.95	0.65	0	2.97	95.4
KG-1	4.92	0	15.3	67.3	0	5.52	0.48	0.36	0	1.51	95.4
KG-1	3.08	0	11.5	72.2	0	5.17	0.54	0.31	0	2.57	95.4
KG-1	3.28	0.06	11.0	74.9	0	4.47	0.15	0.07	0	1.52	95.5
KG-1	3.11	0	11.4	73.9	0	5.06	0.35	0.19	0	1.48	95.5
KG-1	1.73	0	10.6	72.0	0	6.55	1.25	0.38	0	3.14	95.6
KG-1	3.87	0.03	12.4	73.1	0	4.83	0.19	0.12	0.07	1.07	95.6
KG-1	2.31	0	10.6	71.2	0	5.90	0.87	0.43	0.04	4.37	95.7
KG-1	5.39	0.02	15.1	68.8	0	4.61	0.41	0.33	0	1.13	95.8
KG-1	3.76	0	13.3	69.9	0	5.79	0.48	0.28	0	2.32	95.8
KG-1	2.97	0.01	12.2	73.0	0	5.73	0.25	0.16	0.19	1.29	95.8
KG-1	2.98	0	12.3	71.2	0	5.97	0.49	0.41	0.13	2.39	95.9
KG-1	5.31	0.05	14.0	71.8	0.02	3.30	0.21	0.07	0	1.14	95.9
KG-1	1.57	0.02	11.3	70.8	0	7.62	1.34	0.63	0.06	2.57	95.9

Sample	Na_2O	MgO	Al_2O_3	SiO_2	P_2O	K_2O	CaO	TiO_2	MnO	FeO	Total
KG-1	5.35	0	15.6	67.9	0.08	4.74	0.82	0.30	0.02	1.17	96.0
KG-1	3.11	0	12.3	71.4	0	6.00	1.55	0.32	0	1.40	96.0
KG-1	1.51	0	9.19	76.8	0.01	6.06	0.35	0.32	0	1.88	96.2
KG-1	6.29	0	16.0	68.7	0.01	3.77	0.30	0.04	0.15	0.96	96.2
KG-1	5.18	0.02	15.0	62.4	0.17	4.43	0.87	0.71	0.08	7.33	96.2
KG-1	1.31	0	9.60	76.6	0	6.79	0.18	0.28	0	1.59	96.3
KG-1	5.71	0.01	16.2	66.3	0.15	5.17	1.15	0.42	0.15	1.00	96.3
KG-1	2.15	0.01	10.1	76.1	0	5.76	0.51	0.28	0.05	1.40	96.4
KG-1	7.03	0	17.5	65.7	0.30	3.84	0.37	0.23	0	1.37	96.4
KG-1	3.96	0.02	15.6	65.3	0	7.05	1.41	1.04	0.17	1.94	96.4
KG-1	4.76	0	14.0	70.8	0	4.51	0.50	0.29	0	1.56	96.4
KG-1	4.79	0	14.1	71.5	0	4.81	0.18	0.01	0.08	1.00	96.5
KG-1	1.73	0.01	9.80	75.9	0	6.28	0.38	0.37	0	2.10	96.6
KG-1	5.30	0	15.3	69.3	0	5.25	0.17	0.18	0.06	0.99	96.6
KG-1	4.41	0	14.9	68.1	0	6.01	1.51	0.43	0.05	1.28	96.7
KG-1	3.10	0	13.3	70.5	0	6.63	1.07	0.28	0	1.78	96.7
KG-1	3.02	0.01	12.8	70.8	0	6.45	0.97	0.78	0	1.87	96.7
KG-1	4.77	0	14.1	72.1	0	4.69	0.17	0.07	0	1.00	96.9
KG-1	3.81	0.03	14.5	65.2	0	6.59	0.41	0.34	0.11	5.88	96.9
KG-1	3.38	0	13.3	71.0	0.03	6.36	0.76	0.74	0	1.30	96.9
KG-1	4.37	0.04	14.2	70.2	0	5.59	0.56	0.36	0	1.58	96.9
KG-1	1.54	0	9.10	78.3	0	5.82	0.33	0.30	0.09	1.55	97.0
KG-1	4.10	0	12.7	74.5	0	4.56	0.16	0.06	0	0.98	97.0
KG-1	3.61	0	13.6	70.8	0	6.25	1.03	0.32	0	1.45	97.0
KG-1	5.14	0.04	13.9	69.9	0.07	3.51	0.50	0.37	0.04	3.66	97.2
KG-1	3.07	0	11.5	75.3	0	5.21	0.44	0.42	0	1.28	97.2
KG-1	4.32	0.06	13.4	73.1	0	5.11	0.17	0.15	0.04	0.88	97.3
KG-1	7.21	0.05	17.6	67.4	0	3.46	0.29	0.09	0	1.16	97.3
KG-1	5.17	0	15.5	69.7	0	5.34	0.14	0.17	0	1.31	97.3
KG-1	5.37	0.04	15.1	70.2	0.05	4.75	0.26	0.15	0	1.41	97.4
KG-1	1.63	0	12.7	69.6	0	8.82	1.72	0.46	0.07	2.43	97.4
KG-1	4.59	0	14.7	71.2	0.02	5.52	0.15	0.18	0.06	1.08	97.5
KG-1	1.74	0	10.6	75.7	0	6.71	0.51	0.20	0.04	2.02	97.5
KG-1	3.45	0.02	11.5	76.6	0	4.80	0.15	0.15	0	0.83	97.6
KG-1	4.10	0.01	13.6	72.3	0.16	5.49	0.30	0.23	0	1.49	97.7
KG-1	5.51	0	16.4	68.2	0	5.90	0.23	0.17	0	1.40	97.8
KG-1	1.76	0.06	9.83	77.5	0.01	6.02	0.52	0.31	0	1.73	97.8
KG-1	2.07	0	13.2	69.5	0	8.57	0.97	0.50	0.01	2.93	97.8
KG-1	1.67	0.04	10.0	77.3	0	6.29	0.34	0.20	0	1.99	97.8
KG-1	3.35	0.01	12.4	74.5	0	5.75	0.43	0.38	0.14	1.07	98.0
KG-1	6.20	0.02	17.5	67.0	0	5.32	0.27	0.11	0.06	1.57	98.0
KG-1	3.25	0.04	12.2	74.8	0	5.41	0.33	0.35	0	1.79	98.1
KG-1	3.35	0	13.7	71.4	0.07	6.58	0.61	0.42	0.13	1.81	98.1
KG-1	4.25	0.08	14.3	72.1	0	5.53	0.45	0.25	0	1.20	98.1

Sample	Na_2O	MgO	Al_2O_3	SiO_2	P_2O	K_2O	CaO	TiO_2	MnO	FeO	Total
KG-1	2.53	0.02	11.0	74.6	0	5.52	0.73	0.76	0	3.00	98.2
KG-1	3.26	0	14.5	69.6	0.08	7.83	1.55	0.33	0.22	0.97	98.3
KG-1	3.10	0	11.5	76.0	0	5.42	0.27	0.30	0	1.72	98.3
KG-1	3.45	0.02	12.1	75.7	0	5.38	0.15	0.13	0	1.41	98.4
KG-1	3.96	0.02	13.6	72.2	0	5.53	0.72	0.67	0.10	1.84	98.6
EPS-04	5.19	0.64	14.1	48.7	0.27	2.83	0.37	1.16	0.11	1.83	75.2
EPS-04	3.86	0.86	16.3	48.4	0.10	4.57	0.35	0.88	0.08	2.47	77.8
EPS-04	5.10	0.65	14.5	53.2	0.14	1.39	0.43	0.34	0	2.76	78.5
EPS-04	4.51	0.98	15.4	50.6	0.19	3.08	0.35	0.53	0.05	3.50	79.1
EPS-04	5.25	0.75	16.5	48.4	0.29	3.82	0.50	1.11	0	2.90	79.5
EPS-04	3.32	1.35	17.0	49.5	0.32	4.36	0.49	0.57	0	2.87	79.8
EPS-04	5.15	1.02	17.6	47.9	0.62	3.17	0.61	0.75	0.08	2.95	79.8
EPS-04	6.13	0.64	16.1	54.6	0.04	1.66	0.25	0.34	0.06	1.49	81.3
EPS-04	5.20	0.48	12.2	58.8	0.04	0.93	0.23	0.17	0	3.49	81.6
EPS-04	4.88	0.79	16.3	51.3	0.24	3.87	0.36	0.88	0	3.01	81.6
EPS-04	3.83	0.81	15.5	53.2	0.13	4.27	0.31	0.70	0.01	2.84	81.7
EPS-04	5.66	0.79	17.0	50.7	0.43	3.09	0.72	0.51	0.05	2.92	81.9
EPS-04	3.08	1.38	18.3	47.4	0.68	5.61	0.78	1.51	0.09	3.39	82.2
EPS-04	4.41	0.74	14.4	55.6	0.07	3.53	0.24	0.60	0.01	2.71	82.3
EPS-04	5.25	0.89	16.6	52.3	0.20	3.66	0.25	0.51	0.07	2.62	82.3
EPS-04	5.43	0.69	15.7	52.9	0.29	3.25	0.42	1.19	0.09	2.52	82.5
EPS-04	4.00	1.04	16.0	53.1	0.27	4.28	0.55	0.87	0	2.56	82.6
EPS-04	5.46	1.04	18.5	49.7	0.30	3.90	0.52	0.80	0.15	2.44	82.8
EPS-04	5.25	0.89	16.9	49.5	0.35	3.78	0.53	1.13	0.04	4.62	83.0
EPS-04	3.82	1.30	18.3	49.3	0.64	4.69	0.70	0.51	0.04	3.71	83.0
EPS-04	5.27	0.83	17.0	51.6	0.42	4.33	0.45	0.79	0.06	2.27	83.0
EPS-04	4.15	0.87	14.1	55.8	0.41	3.53	0.64	1.01	0	2.62	83.1
EPS-04	5.07	0.79	15.9	53.8	0.31	3.78	0.32	0.75	0.08	2.86	83.6
EPS-04	4.46	0.83	15.6	53.8	0.49	4.62	0.54	0.66	0	3.01	84.0
EPS-04	3.72	1.50	17.7	48.2	1.39	4.79	1.53	1.63	0	3.66	84.1
EPS-04	5.28	0.72	15.5	55.3	0.23	3.95	0.33	0.52	0.07	2.29	84.2
EPS-04	3.86	1.39	20.6	48.0	0.13	5.33	0.26	0.78	0	3.94	84.3
EPS-04	5.81	0.56	13.5	58.7	0.59	1.34	0.59	0.65	0	2.75	84.5
EPS-04	4.66	0.87	16.2	53.9	0.53	4.47	0.67	0.80	0.04	2.41	84.6
EPS-04	4.63	0.88	16.1	54.0	0.41	4.64	0.43	0.89	0.07	2.97	85.1
EPS-04	5.66	0.95	16.7	54.8	0.28	3.07	0.47	0.82	0.01	2.39	85.1
EPS-04	4.45	0.90	15.8	54.9	0.19	4.68	0.34	0.86	0	3.11	85.3
EPS-04	1.97	1.88	21.7	46.2	0.36	7.03	0.44	2.42	0	3.71	85.6
EPS-04	4.97	0.87	16.3	52.6	0.94	4.22	1.02	0.58	0	4.15	85.6
EPS-04	6.94	0.52	16.7	52.8	0.52	3.65	0.77	0.59	0.18	3.08	85.7
EPS-04	3.96	1.36	20.0	50.9	0.05	5.24	0.21	1.08	0.02	3.31	86.2
EPS-04	5.75	0.69	16.5	55.2	0.61	3.43	0.68	0.69	0.11	2.67	86.3
EPS-04	4.72	1.25	19.7	50.8	0.67	4.77	0.81	0.78	0.02	3.10	86.6
EPS-04	5.80	0.85	17.0	53.7	1.09	2.91	1.13	2.07	0.05	2.13	86.7

Sample	Na_2O	MgO	Al_2O_3	SiO_2	P_2O	K_2O	CaO	TiO_2	MnO	FeO	Total
EPS-04	4.88	0.59	12.2	63.9	0.10	1.05	0.23	0.18	0.07	3.49	86.7
EPS-04	6.91	0.95	19.6	53.8	0	3.63	0.13	0.03	0	1.95	86.9
EPS-04	6.43	0.70	16.4	53.0	0.45	2.79	0.59	0.85	0	5.83	87.0
EPS-04	6.31	0.50	16.9	55.0	0.70	4.06	0.82	0.57	0	2.30	87.1
EPS-04	6.46	0.43	13.2	62.1	0.63	0.93	0.85	0.90	0.03	1.73	87.2
EPS-04	1.83	1.81	19.5	46.0	1.82	6.40	2.12	2.62	0	5.23	87.4
EPS-04	1.70	1.94	22.4	45.6	0.67	7.31	0.79	1.24	0.04	5.95	87.6
EPS-04	5.98	1.08	15.7	58.0	0.18	2.24	0.35	1.24	0	3.06	87.8
EPS-04	7.39	0.74	17.3	57.4	0.30	2.19	0.48	0.95	0.03	1.93	88.6
EPS-04	2.98	1.68	21.6	50.1	0.05	6.27	0.19	1.71	0.07	4.23	88.9
EPS-04	6.94	0.61	14.8	61.4	0.22	1.67	0.35	0.77	0	2.33	89.2
EPS-04	4.07	1.42	20.2	53.6	0.01	5.39	0.18	0.79	0.06	3.64	89.4
EPS-04	2.78	1.06	13.4	61.2	1.09	3.19	1.17	0.40	0	5.36	89.6
EPS-04	2.45	1.67	19.2	55.1	0	5.80	0.16	1.25	0.11	4.06	89.8
EPS-04	2.10	1.38	15.3	60.6	0.70	4.50	0.76	0.66	0	4.09	90.1
EPS-04	3.56	1.02	14.2	59.6	0.53	3.26	0.60	1.27	0.04	6.68	90.7
EPS-04	6.62	0.64	16.4	59.9	0.24	2.46	0.38	0.51	0	3.70	90.9
EPS-04	8.69	0.35	14.9	63.9	0.06	0.60	0.16	0.74	0.15	1.51	91.1
EPS-04	4.32	1.37	19.4	52.8	0.80	4.76	0.81	1.94	0.15	4.85	91.2
EPS-04	3.37	1.09	14.0	62.1	0.41	3.25	0.52	1.95	0.13	4.31	91.2
EPS-04	2.61	0.79	9.55	70.2	0.82	1.90	0.90	1.41	0.05	3.11	91.3
EPS-04	2.65	1.17	13.9	63.1	0	3.63	0.08	0.95	0.13	5.80	91.4
EPS-04	5.19	1.07	17.2	61.3	0	3.34	0.16	0.28	0	3.23	91.7
EPS-04	5.32	1.05	18.3	59.1	0	3.88	0.17	1.35	0.03	2.55	91.7
EPS-04	8.49	0.17	14.7	65.7	0.15	0.59	0.35	0.50	0	1.13	91.8
EPS-04	4.34	1.03	14.8	63.8	0.36	3.16	0.49	0.82	0	3.00	91.8
EPS-04	5.72	1.10	17.1	60.2	0.31	3.04	0.38	1.53	0.01	2.90	92.3
EPS-04	6.43	0.64	14.7	63.6	0.33	1.88	0.61	2.27	0	2.03	92.5
EPS-04	5.22	0.92	14.3	64.3	0.40	2.35	0.30	2.06	0.02	2.72	92.6
EPS-04	9.25	0.34	15.3	65.5	0	0.39	0.12	0.70	0	1.19	92.8
EPS-04	7.34	0.66	16.3	62.9	0.55	1.91	0.69	0.50	0	1.98	92.8
EPS-04	4.08	1.10	15.1	61.8	0.60	3.34	0.70	0.81	0.01	5.34	92.9
EPS-04	7.52	0.35	15.4	64.1	0.47	1.57	0.75	0.50	0.07	2.23	92.9
EPS-04	4.71	1.12	16.4	62.5	0.96	3.62	1.09	0.33	0	2.94	93.7
EPS-04	5.17	0.42	11.0	68.8	0.52	1.31	0.53	0.40	0	5.64	93.8
EPS-04	10.7	0.19	18.8	63.6	0	0.66	0.13	0	0	0.96	95.0
EPS-04	5.53	1.03	17.5	61.5	0.15	3.63	0.41	0.76	0.02	4.45	95.0
EPS-04	7.76	0.63	17.8	64.1	0.59	2.26	0.70	0.18	0	1.76	95.7
EPS-04	7.39	0.79	17.1	65.9	0.29	2.43	0.33	0.37	0	1.82	96.4
EPS-04	7.72	0.73	16.8	66.7	0.13	1.96	0.27	0.39	0.06	2.14	96.9
EPS-03	3.27	0.23	6.59	61.2	0	0.73	15.4	0.04	0.28	1.04	88.7
EPS-03	5.59	0.31	11.2	58.4	0	1.13	13.5	0.15	0.22	1.32	91.8
EPS-03	7.53	0.07	12.6	57.7	0	0.25	13.5	0.13	0.22	0.86	92.8
EPS-03	4.41	0.77	7.86	61.3	0.06	1.35	12.2	0.09	1.76	3.19	93.0
EPS-03	3.69	0.51	10.1	70.4	0.19	1.92	5.05	0.09	0.18	1.95	94.0
EPS-03	4.84	0.19	9.49	65.0	0	0.88	11.3	0.70	0.26	1.44	94.1
EPS-03	4.61	0.45	10.7	63.3	0	1.42	11.1	0.43	0.22	1.93	94.2

Sample	Na_2O	MgO	Al_2O_3	SiO_2	P_2O	K_2O	CaO	TiO_2	MnO	FeO	Total
EPS-03	6.74	0.10	11.6	63.8	0	0.35	10.6	0	0.24	1.16	94.6
EPS-03	2.26	1.05	13.0	64.3	0	3.69	5.32	0.75	0.09	4.18	94.7
EPS-03	4.25	0.57	12.5	64.9	0	2.31	8.24	0.08	0.20	1.88	94.9
EPS-03	7.10	0.27	13.5	63.4	0	0.89	8.45	0.08	0.10	1.73	95.5
EPS-03	5.30	0.20	10.3	67.6	0	0.83	9.06	0	0.18	2.09	95.5
EPS-03	2.54	0.91	18.3	61.8	0	4.69	0.92	1.37	0	5.33	95.9
EPS-03	5.22	0.42	12.4	65.0	0	1.73	8.36	0.03	0.22	2.83	96.2
EPS-03	3.91	0.41	11.0	69.4	0	2.12	6.72	0.27	0.12	2.76	96.7
EPS-03	6.67	0.18	12.4	67.8	0	0.75	7.10	0.07	0.19	1.63	96.8
EPS-03	6.11	0.24	11.9	67.1	0	1.03	8.79	0.09	0.05	1.55	96.8
EPS-03	4.89	0.88	15.4	67.7	0.03	2.84	1.50	0.60	0	3.11	97.0
EPS-03	0.35	2.57	26.2	50.2	0	9.86	0	0.67	0	7.15	97.0
EPS-03	4.32	0.52	10.8	69.0	0	1.74	8.43	0.31	0.17	2.20	97.5
EPS-03	3.14	0.77	12.0	68.8	0	2.82	6.01	0.37	0	3.71	97.6
EPS-03	2.96	0.74	7.95	77.6	0	1.05	4.29	0.16	0.07	2.95	97.8
EPS-03	3.93	0.52	12.7	72.7	0	2.65	2.76	0.14	0.03	2.49	97.9
EPS-03	5.94	0.36	13.5	68.3	0	1.73	5.56	0.10	0.15	2.31	97.9
EPS-03	5.17	0.40	12.0	71.1	0.05	1.66	6.16	0.12	0.06	1.25	98.0
EPS-03	0.74	2.15	26.0	50.8	0.06	10.0	0.38	1.15	0	7.16	98.3
EPS-03	5.29	0.55	13.6	69.0	0	2.31	4.22	0.34	0.01	3.14	98.4
EPS-03	5.26	1.07	17.6	65.6	0	3.61	0.69	0.99	0	3.67	98.6
EPS-03	3.88	0.09	9.26	68.8	0	2.28	9.96	0.48	0.47	3.39	98.6
EPS-03	3.05	0.55	8.98	76.7	0	1.66	5.46	0.21	0	2.28	98.9
EPS-03	4.35	0.74	14.2	68.3	0	3.04	3.27	0.84	0	4.30	99.0
EPS-03	2.96	0.49	7.30	79.4	0	0.86	5.01	0.24	0	2.83	99.1
EPS-03	3.05	0.81	12.0	74.8	0	2.95	2.49	0.15	0.02	2.91	99.2
EPS-03	4.57	1.38	18.0	62.5	0.71	4.05	1.44	0.68	0.09	5.97	99.4
EPS-03	3.73	0.93	14.4	70.5	0	3.46	1.78	0.60	0	3.96	99.4
EPS-03	5.50	1.05	14.9	70.8	0.02	2.14	0.67	0.59	0	3.92	99.6
EPS-03	4.18	0.82	11.2	73.3	0	1.65	4.34	0.33	0.06	3.78	99.6
EPS-03	6.61	0.07	15.5	71.1	0.17	1.46	3.91	0.01	0	0.83	99.6
EPS-03	4.04	1.21	13.3	66.6	0.05	2.45	5.12	0.62	0.06	6.26	99.7
EPS-03	4.98	1.22	18.1	65.6	0.03	3.89	0.52	0.76	0	4.60	99.7
EPS-03	6.17	0.86	15.4	69.7	0.05	2.05	1.14	0.27	0	4.07	99.8
EPS-03	3.10	0.89	13.5	71.0	0	3.55	1.69	0.16	0	5.92	99.9
EPS-03	4.31	0.47	11.1	75.5	0	1.81	4.62	0.21	0.10	1.81	99.9
EPS-03	5.60	0.69	13.4	72.1	0.15	1.79	2.16	0.60	0.03	3.41	100
EPS-03	4.32	1.51	18.0	64.4	0.27	4.25	0.64	0.95	0.05	5.63	100
EPS-03	5.13	1.01	17.1	67.4	0.34	3.42	0.73	1.16	0.04	3.74	100
EPS-03	3.99	0.73	13.4	71.1	0.17	2.90	4.42	0.17	0	3.30	100
EPS-03	3.98	1.09	14.0	73.2	0.03	2.79	0.41	0.59	0.06	4.18	100
EPS-03	4.55	1.72	19.4	60.9	0.02	4.37	0.87	1.69	0.10	6.70	100
EPS-03	5.92	0.94	16.9	66.5	0.17	2.92	1.05	2.35	0	3.58	100
EPS-03	3.58	0.81	10.5	75.7	0	1.63	3.93	0.38	0.09	3.64	100
EPS-03	3.75	0.93	11.7	73.9	0.29	2.03	2.49	0.77	0.11	4.43	100
EPS-03	3.75	1.41	22.0	60.0	0	6.46	1.52	0.35	0.05	4.91	100
EPS-03	4.30	0.93	12.9	75.1	0	2.15	0.99	0.43	0.08	3.52	100

Sample	Na_2O	MgO	Al_2O_3	SiO_2	P_2O	K_2O	CaO	TiO_2	MnO	FeO	Total
EPS-03	4.61	0.88	15.3	70.3	0.61	3.07	0.98	1.40	0	3.33	100
EPS-03	5.06	0.77	14.1	72.8	0.44	2.41	0.98	0.69	0.05	3.22	100
EPS-03	2.78	0.44	15.1	72.3	0	4.22	1.31	0.56	0	3.85	101
EPS-03	3.74	0.94	11.3	76.5	0.09	1.84	1.71	0.52	0	3.98	101
EPS-03	5.77	0.75	16.7	70.3	0.12	2.77	0.41	0.85	0.06	2.84	101
EPS-03	6.32	0.51	14.0	71.9	0	1.59	3.70	0.10	0	2.56	101
EPS-03	5.95	0.79	15.1	71.8	0.13	2.09	0.63	0.62	0	3.60	101
EPS-03	4.19	1.29	14.6	70.5	0.07	2.70	0.73	1.06	0.02	5.56	101
EPS-03	3.48	0.66	12.2	75.7	0.03	2.75	2.34	0.28	0.03	3.30	101
EPS-03	5.58	1.00	15.7	68.7	0.47	2.50	1.22	0.97	0.08	4.60	101
EPS-03	3.59	1.16	13.0	72.8	0.73	2.54	2.01	0.69	0.03	4.44	101
EPS-03	3.60	1.02	11.9	74.8	0.18	2.26	1.79	1.07	0	4.42	101
EPS-03	2.38	0.78	12.0	77.5	0	3.55	1.51	0.04	0.02	3.32	101
EPS-03	3.22	0.72	8.07	82.8	0	0.81	1.66	0.51	0.17	3.12	101
EPS-03	3.15	1.38	19.5	64.6	0	6.05	1.35	0.44	0	4.72	101
EPS-03	4.63	0.91	13.3	74.3	0.34	2.19	1.18	0.69	0.11	3.61	101
EPS-03	3.96	0.81	11.1	74.8	0	1.79	2.56	0.39	0.12	5.66	101
EPS-03	4.63	1.11	15.5	70.3	0.48	3.04	0.97	1.08	0.04	4.23	101
EPS-03	5.18	1.09	13.5	71.5	0	1.53	0.99	1.94	0	5.69	101
EPS-03	2.70	1.23	12.3	73.8	0	2.98	1.57	2.30	0.08	4.53	101
EPS-03	4.56	1.15	14.8	69.9	0.26	2.83	0.55	0.70	0	6.65	101
EPS-03	2.77	1.15	21.7	62.3	0	7.58	0	0.37	0	5.67	102
EPS-03	5.55	0.08	10.9	79.1	0	0.42	3.15	0	0	2.62	102
EPS-03	2.69	0.76	11.1	80.0	0	2.86	1.56	0.20	0.07	2.59	102
EPS-03	6.28	1.20	17.2	66.9	0	2.39	0.59	1.52	0.07	5.70	102
EPS-03	5.20	1.56	14.9	71.0	0.17	1.79	0.43	0.56	0.07	6.17	102
EPS-03	5.80	1.33	15.9	69.1	0.08	1.90	0.62	1.43	0.17	5.85	102
EPS-03	5.87	1.82	21.7	60.2	0.05	4.43	0.58	0.87	0.14	6.70	102
EPS-03	2.85	1.92	13.4	72.8	0.14	2.62	0.57	0.73	0.07	7.49	103
EPS-03	3.40	0.99	9.56	79.3	0	2.13	3.03	1.59	0	2.59	103
EPS-03	4.34	1.13	13.0	74.9	0.02	2.05	0.49	0.41	0	6.49	103
EPS-03	5.96	1.06	14.6	71.9	0	1.65	1.17	0.69	0.04	5.77	103
EPS-03	5.84	1.09	14.2	72.6	0	1.49	1.45	0.73	0	5.62	103
EPS-03	5.71	0.61	14.9	76.5	0	2.57	0.33	0	0	2.54	103
EPS-03	1.74	1.78	12.1	75.6	0	3.02	0.57	1.01	0	7.43	103
EPS-03	3.04	1.56	12.7	74.5	0.02	2.65	1.30	0.56	0	7.13	103
EPS-03	3.75	1.49	23.7	62.6	0	7.23	0	0	0	5.09	104
EPS-03	3.60	1.76	14.6	69.8	0.01	2.78	0.74	1.28	0.11	9.25	104
EPS-03	6.55	1.13	15.9	71.0	0	1.85	1.33	0.51	0.08	6.08	104
EPS-03	4.98	1.24	15.3	73.7	0.05	2.54	0.81	0.79	0.18	4.94	105
EPS-03	0.77	0.89	7.79	89.1	0	3.22	0.60	0.82	0	1.90	105
EPS-03	4.93	0.87	10.4	81.1	0	0.63	1.79	0.97	0.21	4.40	105
EPS-03	1.44	0.18	10.7	86.0	0	1.61	2.71	0.01	0	2.97	106
EPS-03	7.09	0.37	15.2	72.2	0	2.22	6.99	0.18	0	2.32	107
EPS-03	3.17	0.48	16.5	75.3	0	5.03	0.61	0.89	0.36	5.04	107
EPS-02	6.67	0.04	10.6	34.1	0	0.16	27.1	0.15	0.33	0.43	79.6
EPS-02	7.30	0	11.1	36.5	0	0.10	24.3	0.13	0.32	4.10	83.9

Sample	Na_2O	MgO	Al_2O_3	SiO_2	P_2O	K_2O	CaO	TiO_2	MnO	FeO	Total
EPS-02	7.69	0.03	11.8	41.1	0.06	0.13	22.0	0.17	0.37	1.65	85.0
EPS-02	8.27	0.03	12.9	47.5	0.15	0.16	18.7	0	0.43	0.60	88.8
EPS-02	8.55	0.05	13.7	50.2	0	0.18	14.6	0.13	0.32	2.98	90.7
EPS-02	8.88	0	14.1	50.0	0	0.18	16.0	0.47	0.25	1.40	91.3
EPS-02	9.35	0	15.4	50.4	0.05	0.09	15.1	0.76	0.30	1.10	92.6
EPS-02	9.04	0.02	15.0	50.7	0.70	0.16	15.4	0.60	0.12	0.98	92.6
EPS-02	8.82	0.11	13.8	56.4	0	0.14	13.2	0.37	0.20	0.33	93.3
EPS-02	9.75	0	15.6	53.5	0	0.20	13.6	0.02	0.31	0.33	93.4
EPS-02	10.1	0	16.6	55.8	0	0.32	10.3	0	0.15	0.28	93.6
EPS-02	9.84	0	15.3	53.8	0.30	0.22	12.3	0.53	0.16	1.43	93.9
EPS-02	10.6	0.10	18.7	61.9	0.01	0.70	1.05	0.24	0.06	1.01	94.4
EPS-02	9.91	0.06	16.2	54.8	0	0.40	12.5	0.19	0.24	0.57	94.8
EPS-02	10.3	0.01	16.9	56.9	0.02	0.28	9.86	0	0.11	0.43	94.8
EPS-02	10.2	0.05	16.6	56.1	0	0.42	9.33	0.05	0	2.50	95.2
EPS-02	10.3	0	16.9	57.6	0.01	0.29	9.08	0.05	0.31	0.63	95.2
EPS-02	10.3	0	16.8	58.1	0.09	0.28	8.78	0.54	0.06	1.10	96.1
EPS-02	7.60	1.48	19.8	54.1	0.11	2.44	2.21	0.77	0.07	8.07	96.7
EPS-02	9.58	0.48	18.8	60.5	0.12	1.40	2.59	0.57	0.04	2.58	96.7
EPS-02	10.5	0.08	17.5	59.4	0	0.49	7.27	0.04	0.11	1.22	96.7
EPS-02	8.70	0	14.1	65.2	0.30	0.23	6.31	0.01	0.10	1.71	96.7
EPS-02	10.7	0.24	18.2	58.9	0	0.11	7.68	0	0	0.97	96.8
EPS-02	10.5	0.06	17.0	60.5	0.30	0.32	5.97	0.47	0	1.78	96.9
EPS-02	10.8	0	17.7	60.1	0.01	0.23	6.99	0.07	0.10	1.18	97.1
EPS-02	10.6	0	17.9	59.6	0	0.41	7.89	0.12	0.13	0.67	97.3
EPS-02	10.4	0.09	17.6	61.5	0	0.52	5.28	0.14	0.04	1.93	97.5
EPS-02	10.5	0.07	17.5	58.9	0	0.37	6.88	0.04	0.06	3.16	97.5
EPS-02	10.9	0	18.1	61.5	0	0.58	6.07	0	0.14	0.38	97.6
EPS-02	10.6	0.05	17.8	59.7	0	0.59	6.32	0.28	0.16	2.11	97.6
EPS-02	7.92	0	12.5	65.5	0.04	0.27	9.53	0.23	0.24	1.46	97.7
EPS-02	10.6	0	17.7	59.2	0	0.46	8.78	0.07	0.18	0.85	97.9
EPS-02	10.6	0.01	18.0	60.7	0.14	0.47	7.37	0.01	0	0.70	98.0
EPS-02	10.5	0.26	18.3	62.2	0	0.72	4.12	0.07	0	2.02	98.1
EPS-02	9.90	0.06	16.7	63.0	0	0.47	6.14	0.11	0.08	1.72	98.2
EPS-02	11.0	0	18.1	61.9	0.03	0.38	5.83	0	0.08	0.94	98.3
EPS-02	10.7	0	18.1	61.9	0	0.60	6.00	0.10	0.11	0.95	98.5
EPS-02	11.0	0.14	18.8	63.0	0	0.54	3.93	0.03	0.03	1.10	98.5
EPS-02	10.8	0.02	17.9	61.4	0	0.51	7.20	0.06	0.14	0.52	98.6
EPS-02	11.0	0	18.6	62.5	0.03	0.47	5.19	0.10	0.12	0.66	98.7
EPS-02	10.8	0.03	18.2	61.5	0	0.53	6.46	0.07	0	1.23	98.8
EPS-02	11.2	0.03	18.3	63.4	0.05	0.28	4.66	0	0.09	0.91	98.9
EPS-02	10.9	0	18.2	61.8	0.04	0.45	6.40	0.28	0.13	0.81	99.1
EPS-02	11.3	0	18.5	62.8	0	0.26	4.95	0.10	0.06	1.12	99.1
EPS-02	9.99	0	16.5	66.2	0	0.26	5.37	0	0.08	0.81	99.2
EPS-02	11.1	0	18.4	62.8	0	0.40	5.20	0.07	0.17	1.10	99.3
EPS-02	10.7	0.05	18.2	60.2	0	0.57	8.33	0	0.15	1.11	99.3
EPS-02	10.3	0.20	18.1	63.6	0	0.99	3.36	0.27	0.02	2.38	99.3
EPS-02	11.1	0	18.1	61.3	0.02	0.29	8.00	0.10	0.08	0.62	99.6

Sample	Na_2O	MgO	Al_2O_3	SiO_2	P_2O	K_2O	CaO	TiO_2	MnO	FeO	Total
EPS-02	11.1	0	18.2	61.8	0.02	0.48	4.65	0.40	0.03	2.87	99.6
EPS-02	11.3	0	18.9	63.5	0.06	0.47	4.99	0	0.03	0.44	99.6
EPS-02	10.8	0	17.5	63.2	0	0.47	5.22	0.52	0.07	2.09	99.9
EPS-02	10.1	0	16.5	64.7	0.08	0.17	7.80	0	0.12	0.42	99.9
EPS-02	11.1	0.01	18.5	64.4	0.04	0.46	4.26	0.21	0.05	0.83	99.9
EPS-02	9.39	1.01	18.9	56.8	0	1.20	2.41	0.70	0.20	9.34	99.9
EPS-02	7.77	0.18	13.2	72.4	0	0.36	3.92	0.03	0.08	2.04	100
EPS-02	11.1	0	18.7	64.1	0	0.59	4.65	0.21	0.16	0.47	100
EPS-02	11.1	0.01	18.4	63.1	0	0.57	5.92	0	0.07	0.83	100
EPS-02	11.0	0.07	18.3	62.0	0	0.38	7.12	0	0.11	1.16	100
EPS-02	11.1	0.03	18.5	65.1	0.09	0.36	3.91	0.16	0.12	0.82	100
EPS-02	11.1	0.06	19.0	63.7	0.03	0.65	4.52	0.29	0.08	0.79	100
EPS-02	10.2	0	18.2	63.9	0	0.93	5.32	0.01	0.55	1.17	100
EPS-02	11.2	0	18.9	63.9	0.03	0.50	4.93	0.02	0.11	0.71	100
EPS-02	11.0	0.01	18.4	63.1	0.03	0.58	5.91	0.28	0.03	0.95	100
EPS-02	9.48	0.87	18.9	64.2	0	1.04	0.50	0.39	0.05	4.88	100
EPS-02	11.0	0.02	18.8	64.0	0.04	0.71	5.08	0.05	0.10	0.64	100
EPS-02	11.2	0	18.7	64.4	0	0.44	4.97	0.11	0	0.66	100
EPS-02	6.70	0.66	12.3	72.2	0	0.37	3.55	0.49	0.05	4.24	101
EPS-02	8.89	0.73	17.2	66.1	0	1.00	0.82	0.64	0.14	5.19	101
EPS-02	11.5	0.04	19.1	65.2	0.06	0.35	3.56	0.22	0.05	0.71	101
EPS-02	11.2	0.03	17.9	64.2	0	0.16	5.58	0.08	0	2.00	101
EPS-02	11.3	0	18.6	65.2	0.05	0.17	5.08	0.36	0.10	0.42	101
EPS-02	6.50	0.15	11.5	78.2	0	0.54	2.98	0.39	0	1.06	101
EPS-02	11.3	0.02	18.9	64.8	0	0.63	3.83	0.46	0.10	1.43	101
EPS-02	9.50	0.08	15.3	69.8	1.46	0.19	4.04	0.24	0.02	0.84	101
EPS-02	11.3	0	18.5	64.8	0.28	0.26	2.36	0.26	0	3.99	102
EPS-02	11.1	0.04	18.2	65.7	0.57	0.22	4.71	0.55	0.10	1.27	102
EPS-02	11.5	0	19.6	66.0	0.11	0.32	3.94	0.31	0.06	0.90	103
EPS-02	11.9	0.07	17.6	64.8	0.32	0.58	5.64	0.28	0	1.52	103
EPS-02	10.5	0.07	16.8	71.2	0.88	0.04	2.07	0.23	0	0.92	103
EPS-02	11.8	0	19.4	65.7	0.61	0.21	1.61	0.56	0.05	2.95	103
EPS-02	7.40	0.03	11.7	79.9	0	0.20	2.55	0.01	0	1.28	103
EPS-02	11.6	0	18.8	68.0	0	0.17	3.12	0.10	0	1.32	103
EPS-02	11.6	0	19.1	67.5	0	0.40	3.03	0.19	0.02	1.39	103
EPS-02	11.9	0	19.7	69.1	0.13	0.17	1.07	0.50	0	0.96	104
EPS-02	11.2	0	18.6	69.2	0.08	0.49	3.91	0.02	0	0.49	104
EPS-02	12.1	0	20.1	68.1	0.11	0.34	2.40	0.25	0.07	0.56	104
EPS-02	10.4	0	17.3	71.4	0	0.38	3.43	0.07	0	1.23	104
EPS-02	11.8	0	19.1	67.3	0.13	0.20	2.93	1.19	0	1.77	104
EPS-02	12.1	0	19.4	71.4	0.02	0.16	0.52	0.54	0.14	0.56	105
EPS-02	12.3	0	20.0	68.8	0	0.18	2.11	0.31	0	1.33	105
EPS-02	11.8	0	20.4	65.4	0.62	0.53	3.09	0.73	0.49	3.08	106
EPS-01	1.21	0.58	11.9	42.9	0.01	6.86	8.47	0.23	0.12	2.84	75.1
EPS-01	0.87	0.25	11.9	41.9	0.02	8.22	15.9	0.23	0.21	2.15	81.7
EPS-01	3.12	0.93	10.6	61.7	0.04	2.29	0.60	0.47	0.02	3.02	82.7
EPS-01	4.09	0.83	9.00	65.4	0.02	1.11	0.46	0.26	0.03	2.08	83.3

Sample	Na_2O	MgO	Al_2O_3	SiO_2	P_2O	K_2O	CaO	TiO_2	MnO	FeO	Total
EPS-01	4.69	0.74	12.0	59.4	0.12	2.49	2.19	0.49	0.02	2.25	84.4
EPS-01	2.38	0.44	13.0	51.4	0	6.99	10.4	0.18	0.10	1.98	86.8
EPS-01	2.25	0.46	13.4	57.1	0	7.18	5.31	0.12	0.12	2.38	88.4
EPS-01	1.02	0.37	15.1	54.0	0	10.8	4.96	0.17	0.07	2.08	88.6
EPS-01	1.74	0.73	8.03	74.3	0.01	2.12	0.27	0.13	0.04	2.26	89.7
EPS-01	0.97	0.42	15.1	55.3	0.25	10.7	3.72	0.68	0.07	2.47	89.7
EPS-01	5.58	0.95	12.4	64.4	0.46	1.49	1.18	0.77	0.03	3.26	90.5
EPS-01	3.33	1.14	10.7	69.1	0	2.08	0.98	0.59	0.07	2.84	90.9
EPS-01	2.67	1.01	9.18	68.3	0.18	1.89	1.46	1.21	0.05	4.91	90.9
EPS-01	1.94	0.57	10.6	67.7	0	5.02	3.22	0.11	0.09	2.03	91.3
EPS-01	4.20	1.27	11.8	66.7	0.38	1.95	1.40	0.38	0	3.87	91.9
EPS-01	5.53	0.90	14.7	63.2	0.10	2.92	0.72	0.55	0	3.40	92.1
EPS-01	0.80	0.36	11.4	65.0	0	7.80	5.17	0.13	0.05	1.75	92.5
EPS-01	4.62	1.07	11.8	68.5	0	1.80	1.39	0.42	0.11	2.90	92.6
EPS-01	4.41	1.23	12.0	62.5	0.56	1.91	3.95	1.00	0.15	5.21	92.9
EPS-01	5.46	1.21	14.4	62.2	0.04	2.30	2.36	0.64	0.09	4.19	93.0
EPS-01	2.40	0.56	7.90	77.8	0	1.72	0.30	0.13	0.04	2.13	93.0
EPS-01	3.37	1.54	12.5	63.3	1.02	2.56	2.82	1.22	0.05	5.16	93.5
EPS-01	5.51	0.76	11.7	69.1	0	1.44	2.04	0.15	0.11	2.94	93.7
EPS-01	3.21	1.07	10.3	67.1	0.06	2.02	5.78	0.93	0.15	3.45	94.0
EPS-01	2.80	0.73	12.3	67.9	0.06	5.08	1.88	0.25	0	3.13	94.2
EPS-01	3.95	0.87	12.8	65.1	0	4.18	3.30	0.52	0.18	3.55	94.4
EPS-01	3.44	0.72	14.1	65.2	0.08	5.21	1.84	0.57	0.04	3.24	94.5
EPS-01	4.33	1.09	11.6	67.5	0.68	1.90	3.82	0.43	0.14	3.12	94.6
EPS-01	3.35	1.31	10.6	69.9	0.06	2.17	2.12	0.37	0.10	4.71	94.7
EPS-01	3.38	0.85	9.48	74.0	0.41	1.33	1.02	0.75	0.05	3.56	94.9
EPS-01	1.12	0.25	12.2	67.5	0	8.20	3.79	0	0	1.98	95.0
EPS-01	2.88	1.73	15.3	61.0	0.09	3.97	1.24	1.82	0.23	6.88	95.2
EPS-01	4.18	0.94	10.8	73.1	0.09	1.57	0.74	0.83	0	2.96	95.2
EPS-01	5.66	0.97	14.0	67.3	0.12	2.30	0.62	0.53	0.14	3.69	95.4
EPS-01	3.65	1.32	11.2	71.0	0.01	2.30	1.17	0.10	0.10	4.60	95.4
EPS-01	4.83	0.81	12.2	69.9	0.07	1.93	2.28	0.42	0.08	2.92	95.5
EPS-01	4.19	1.17	11.6	68.4	0.75	1.91	2.27	0.81	0.11	4.43	95.6
EPS-01	3.62	0.92	9.32	71.0	0.47	1.38	5.56	0.31	0.21	3.05	95.8
EPS-01	3.93	0.84	9.01	73.7	0.18	1.22	3.49	0.18	0.18	3.13	95.8
EPS-01	3.69	0.77	9.94	72.8	0.12	1.55	2.95	1.11	0.05	3.15	96.1
EPS-01	2.91	0.69	9.22	78.6	0.05	1.87	0.42	0.21	0	2.26	96.2
EPS-01	2.55	0.50	13.8	66.4	0.05	6.96	2.38	0.31	0	3.44	96.4
EPS-01	5.75	0.94	12.7	71.3	0.57	1.37	0.83	0.28	0.03	3.02	96.8
EPS-01	2.97	0.61	8.34	77.1	0.02	1.60	3.24	0.16	0.02	2.77	96.9
EPS-01	5.29	1.14	13.7	66.8	0.61	2.02	1.96	0.61	0.08	4.81	97.0
EPS-01	5.20	1.07	11.7	71.0	0.07	1.31	1.82	0.05	0	4.85	97.1
EPS-01	4.31	1.22	11.9	68.8	0	2.16	2.84	0.34	0.04	5.57	97.1
EPS-01	2.82	0.75	8.76	78.7	0	1.60	1.64	0.27	0.02	2.67	97.2
EPS-01	4.26	0.71	12.6	69.2	0.07	3.50	2.21	0.45	0.13	4.04	97.2
EPS-01	6.13	0.96	13.4	68.3	0.34	1.53	3.28	0.09	0.03	3.28	97.4
EPS-01	4.47	0.92	12.1	73.6	0.45	1.99	0.94	0.32	0	2.71	97.5

Sample	Na_2O	MgO	Al_2O_3	SiO_2	P_2O	K_2O	CaO	TiO_2	MnO	FeO	Total
EPS-01	1.61	0.72	6.36	85.0	0.10	1.56	0.16	0.02	0.03	2.04	97.6
EPS-01	6.59	0.65	13.3	66.0	0.82	1.22	6.33	0.20	0.12	2.46	97.7
EPS-01	5.01	0.89	10.7	73.0	0.23	1.15	2.69	0.57	0.17	3.69	98.1
EPS-01	4.77	0.74	10.5	70.4	0.21	1.45	4.66	0.11	0.13	5.25	98.3
EPS-01	4.42	0.81	11.2	73.0	0.13	1.92	2.37	1.12	0	3.33	98.3
EPS-01	5.25	1.01	14.6	66.5	0	3.40	4.06	0.35	0.23	2.95	98.4
EPS-01	4.53	1.15	13.4	70.7	0.29	2.73	1.88	0.29	0.03	3.49	98.4
EPS-01	4.62	1.34	13.9	67.8	0.06	2.50	0.95	1.09	0.20	6.00	98.4
EPS-01	6.45	0.74	14.2	70.4	0.17	2.12	1.23	0.19	0.04	3.01	98.5
EPS-01	4.28	0.99	10.8	74.0	0.81	1.43	2.59	1.01	0.16	2.46	98.6
EPS-01	4.13	0.97	10.2	75.3	0	1.32	1.20	0.09	0.12	5.28	98.6
EPS-01	3.36	0.45	9.00	81.8	0	1.71	0.58	0	0.13	1.61	98.6
EPS-01	6.46	0.64	13.9	69.7	0.48	1.53	3.60	0.25	0.07	2.06	98.7
EPS-01	6.97	1.27	17.1	65.0	0.22	2.27	2.26	0.14	0.01	3.85	99.0
EPS-01	4.94	1.16	12.5	73.9	0.04	1.97	0.96	0.05	0.08	3.62	99.2
EPS-01	3.76	1.58	12.1	73.2	0	2.57	1.61	0.02	0.09	4.33	99.2
EPS-01	3.94	1.66	13.5	71.1	0.28	3.24	0.84	0	0	4.81	99.3
EPS-01	5.27	0.93	11.3	71.5	0.65	1.13	2.89	0.16	0.05	5.46	99.3
EPS-01	4.52	1.09	11.4	74.7	0	1.68	1.52	0.17	0.12	4.39	99.5
EPS-01	4.27	1.23	11.2	75.3	0	1.65	2.37	0	0.15	3.40	99.6
EPS-01	8.66	0.66	17.6	64.9	0	1.56	3.42	0.17	0.03	2.92	99.9
EPS-01	4.16	1.35	11.9	71.6	0.71	1.96	1.78	0.11	0.07	6.41	100
EPS-01	4.93	1.03	13.0	68.1	3.17	2.02	4.00	0.58	0.03	3.46	100
EPS-01	5.28	0.84	12.1	76.3	0	1.81	0.71	0.30	0.06	2.95	100
EPS-01	5.90	1.28	14.6	70.9	0	1.89	2.10	0.14	0.06	3.57	100
EPS-01	3.59	1.65	13.6	70.4	0.45	4.27	1.23	0.17	0.16	4.92	100
EPS-01	7.07	1.44	17.0	63.0	0.08	2.67	2.83	1.17	0.13	5.43	101
EPS-01	4.38	1.17	13.2	73.3	0	3.39	1.03	0.85	0.07	3.74	101
EPS-01	6.45	1.04	15.9	68.8	0.70	3.01	2.06	0.29	0.02	3.17	101
EPS-01	6.64	0.92	17.3	67.5	0.52	3.55	1.65	0.44	0.18	3.90	103

Appendix V: Primary and Secondary Mineral Groupings

Quartz	Quartz	**Muscovite**	Muscovite	**K-Al-Fe-silicate (T)**	K-Al-Fe-silicate (T)
	Quartz-boundary		Muscovite-(Fe)	**Orthopyroxene**	Enstatite
	Quartz low Al		Paragonite		OPX En90
	Quartz rim (T)		Muscovite-boundary		OPX En80
	Quartz low CR	**Biotite**	Phlogopite		OPX En70
Albite	Albite		Biotite-(Mg)		OPX En60
	Albite-boundary		Biotite-(Fe)		OPX En50
Chlorite	Clinochlore-(Mg)		Annite		OPX En40
	Clinochlore	**Hematite**	Hematite		OPX En30
	Chlorite	**Ilmenite**	Ilmenite		OPX En20
	Chamosite		Ilmenite-(Mn)		OPX En10
	Clinochlore-(Si)		Ilmenite-(Mg)		OPX En0
	Chloritoid		Ilmenite-boundary	**Clinopyroxene**	Augite
	Corrensite	**Pyrite**	Pyrite		Diopside
	Chamosite-boundary		Pyrite-boundary		Diopside-Hedenbergite
	Clinochlore-boundary		Pyrite rim (T)		Hedenbergite
Rutile/ Anatase	Rutile/Anatase	**Tourmaline**	Dravite		Aegirine
	Rutile-boundary		Dravite-Schorl	**Kaolinite/Dickite**	Kaolinite/Dickite
Garnet	Almandine		Schorl		Kaolinite-boundary
	Spessartine		Elbaite		Kaolinite/Dickite rim (T)
	Pyrope		Dravite rim (T)	**Siderite-magnesite**	Rhodochrosite
	Grossular		Dravite-Schorl rim (T)		Magnesite
	Andradite		Schorl rim (T)		Siderite
	Uvarovite	**Calcite**	Calcite low CR	**Apatite**	Apatite
Alkali feldspar	Anorthoclase		Calcite-boundary		Chlorapatite
	Sanidine		Calcite rim (T)		Fluorapatite
	Microcline/Orthoclase		Dolomite		Apatite-boundary
	K-Al Silicate-boundary		Dolomite-boundary		Apatite rim (T)
	K-Al-silicate (T)	**goethite/ lepidocrocite**	Goethite/ Lepidocrocite	**Cu-Fe sulfide (T)**	Cu-Fe sulfide (T)

Other clays	Berthierine	**Other Phases**	Chalcopyrite	**Bornite**	Bornite
	Glauconite		Sphalerite	**Chalcocite/ Digenite**	Chalcocite/Digenite
	Vermiculite		Galena		Copper
	Montmorillonite		Ni-sulfides		Cu sulfide (T)
	Nontronite		Anthophyllite	**Covellite**	Covellite
	Saponite		Jadeite	**Plagioclase feldspar**	Oligoclase
	Beidellite		Glaucophane		Andesine
	Stevensite		Baddeleyite		Labradorite
	Palygorskite		Cassiterite		Bytownite
	Sepiolite		Sillimanite/Kyanite/ Andalusite		Anorthite
Olivine	Forsterite		Staurolite	**REE phosphates**	Monazite-(Ce)
	Olivine Fo90		Opal		Monazite-(La)
	Olivine Fo80		Cordierite		Monazite-(Nd)
	Olivine Fo70		Talc		Xenotime-(Y)
	Olivine Fo60		Hornblendes		Xenotime-(Y-Yb)
	Olivine Fo50		Amphiboles		Xenotime-(Yb)
	Olivine Fo40		Epidote		Florencite-(Ce)
	Olivine Fo30		Spinel Group		Florencite-(La)
	Olivine Fo20		Allanite		Florencite-(Nd)
	Olivine Fo10		Zoisite		Monazite-boundary
	Fayalite		Serpentine		Monazite-rim (T)
Zircon	Zircon		Oxy-hydroxides	**Magnetite**	Magnetite
	Zircon-boundary		Anhydrite/Gypsum		Fe-Oxide
	Zircon rim (T)		Barite		Fe-Oxide-boundary
	Zircon (T)		Celestine	**Mill fragments**	
Titanite	Titanite		Halite	**Holder**	
	Titanite-boundary		Fluorite	**Low Confidence**	
Illite	Illite		Perovskite	**Low CR**	
	Illite-boundary		Piemontite	**Unclassified**	

Appendix VI-A: LA-ICP-MS Results for Magnetite

Sample	Measurement	Mg	Al	Si	Ca	Sc	Ti	V	Cr	Mn	Co	Ni	Cu	Zn	Ga	Ge
MG-1	1_G051	341	420	1727	192	\	150	222	248	267	264	192	82.7	127	3.70	3.93
MG-1	1_G052	6186	16661	38632	311	\	1209	240	838	441	206	187	549	199	10.3	7.07
MG-1	1_G053	152	919	2579	<dl	\	145	271	90.3	158	82.2	189	109	117	2.65	3.29
MG-1	1_G054	109	572	2438	<dl	\	150	230	29.8	214	139	181	73.4	137	2.87	4.61
MG-1	1_G055	240	1281	9930	<dl	\	315	216	2046	304	150	167	223	82.3	4.02	5.59
MG-1	1_G056	1018	1083	58579	<dl	\	24335	209	568	159	93.7	182	283	98.1	4.02	3.90
MG-1	1_G057	1023	6591	45315	4163	\	1054	280	295	1422	87.7	179	1938	164	10.9	34.5
MG-1	1_G058	49.1	364	2129	232	\	343	243	346	250	86.5	174	197	118	3.67	5.80
MG-1	1_G059	199	859	5431	275	\	11344	233	599	346	69.7	188	210	118	3.36	5.29
MG-1	1_G060	859	975	20305	1125	\	11426	203	1074	427	115	185	303	84.0	3.63	5.67
MG-1	1_G061	138	262	5894	<dl	\	466	234	123	144	97.0	181	115	96.2	2.42	3.25
MG-1	1_G062	139	386	6536	<dl	\	891	228	149	313	101	205	156	138	4.09	3.44
MG-1	1_G063	89.9	373	3190	276	\	553	231	369	269	81.3	184	220	104	10.5	5.66
MG-1	1_G064	136	576	1789	151	\	239	221	1375	255	93.3	208	99.2	124	3.89	4.41
MG-1	1_G065	639	922	21519	225	\	155	233	282	259	175	200	198	132	4.20	3.62
MG-1	1_G066	2484	2572	5911	228	\	181	212	290	234	86.7	206	109	153	4.07	4.66
MG-1	1_G067	273	1231	3869	<dl	\	811	250	255	251	117	182	97.0	132	3.30	4.30
MG-1	1_G068	98.8	402	1359	<dl	\	235	243	23.7	453	98.2	220	408	173	4.79	4.31
MG-1	1_G069	2531	7684	34028	<dl	\	10008	220	472	368	98.3	200	301	130	6.85	5.42
MG-1	1_G070	139	538	3120	155	\	126	228	645	436	119	184	244	148	4.62	4.66
MG-1	1_G071	224	470	2750	170	\	128	203	1523	180	83.5	179	118	96.3	3.03	4.08
MG-1	1_G072	68.0	179	1250	168	\	223	218	199	194	91.2	189	47.9	115	2.87	3.45
MG-1	1_G073	439	1255	4100	235	\	230	208	593	252	135	190	139	125	3.91	4.54
MG-1	1_G074	504	1477	4371	<dl	\	347	236	186	403	102	196	267	141	4.75	4.97

Sample	Measurement	Mg	Al	Si	Ca	Sc	Ti	V	Cr	Mn	Co	Ni	Cu	Zn	Ga	Ge
MG-1	1_G075	63.1	219	1014	<dl	\	176	235	11.7	296	203	205	219	130	4.01	4.52
MG-1	1_G076	1369	1550	3839	153	\	125	211	261	236	92.0	186	43.8	149	3.96	3.85
MG-1	1_G077	2416	4910	19283	<dl	\	487	197	2462	315	153	188	230	129	5.75	4.34
MG-1	1_G078	320	664	1600	<dl	\	153	221	1175	237	161	198	217	120	3.74	4.44
MG-1	1_G080	147	1803	3682	157	\	161	237	22248	1121	407	192	118	11215	5.56	4.08
MG-1	1_G081	141	587	2342	241	\	1102	233	155	331	103	187	267	128	4.24	4.02
MG-1	1_G082	151	260	5479	<dl	\	930	212	192	211	147	188	95.8	100	3.60	4.04
MG-1	1_G083	1986	1301	10930	4635	\	14794	287	833	967	132	192	682	150	4.44	9.81
MG-1	1_G084	69.6	175	981	<dl	\	408	216	94.7	165	83.6	189	70.1	122	2.51	3.53
MG-1	1_G085	479	722	4494	185	\	160	225	207	337	106	199	214	152	4.00	4.31
MG-1	1_G086	88.4	231	1134	<dl	\	119	223	279	286	98.3	201	206	128	3.88	3.56
MG-1	1_G087	649	5076	11339	434	\	439	234	148	180	136	144	302	114	4.35	5.57
MG-1	1_G088	216	577	1741	156	\	162	228	1680	333	303	209	102	145	4.31	3.86
MG-1	1_G089	227	1373	3870	<dl	\	1066	260	49.7	235	97.0	177	79.6	140	3.34	4.62
MG-1	1_G090	327	473	2782	399	\	1514	214	930	284	99.6	201	104	128	3.58	4.28
MG-1	1_G091	1141	1446	3870	188	\	492	228	220	340	92.4	192	279	146	4.15	3.52
MG-1	1_G092	291	1079	7307	<dl	\	50695	264	1665	289	154	185	286	125	4.57	5.28
MG-1	1_G093	164	915	3493	197	\	358	242	16182	899	467	213	149	6725	5.06	4.66
MG-1	1_G094	101	476	1915	<dl	\	244	246	83.4	187	87.1	185	72.1	111	2.49	4.23
MG-1	1_G095	178	756	9736	408	\	4181	214	835	305	348	195	221	103	4.39	4.87
MG-1	1_G096	333	748	3468	196	\	250	231	542	347	98.5	209	242	136	4.00	3.86
MG-1	1_G097	2664	2762	5039	<dl	\	161	232	352	392	114	220	404	203	4.68	5.20
MG-1	1_G098	147	570	4233	343	\	86.9	206	401	165	113	181	93.2	100	3.68	4.35
MG-1	1_G099	39.5	165	1007	<dl	\	314	220	28.1	143	78.7	167	88.8	108	2.15	3.37
MG-1	1_G100	173	1017	3606	186	\	302	229	588	549	111	186	346	138	4.63	6.27
MG-1	1_G101	646	775	2535	<dl	\	258	218	587	340	82.5	202	349	134	3.81	3.57

Sample	Measurement	Mg	Al	Si	Ca	Sc	Ti	V	Cr	Mn	Co	Ni	Cu	Zn	Ga	Ge
MG-1	1_G102	756	867	8934	<dl	\	174	217	298	456	336	194	159	137	3.58	4.29
MG-1	1_G103	2179	3069	28767	224	\	30279	211	2426	326	839	212	368	178	5.25	4.68
MG-1	1_G104	387	662	3243	<dl	\	254	213	408	189	412	168	75.7	136	2.90	3.37
MG-1	1_G105	229	368	1651	<dl	\	145	221	1308	354	115	206	426	139	4.07	3.41
MG-1	1_G106	163	885	2604	310	\	216	224	123	285	99.2	204	148	124	4.11	4.12
MG-1	1_G107	419	835	3584	877	\	879	224	1209	306	132	197	110	126	2.75	3.97
MG-1	1_G109	96.5	136	814	<dl	\	88.8	213	54.2	209	85.4	175	51.9	123	2.58	3.19
MG-1	1_G110	184	1179	9707	1200	\	15939	355	74.7	258	99.8	171	363	134	3.11	6.69
MG-1	1_G111	93.4	929	4209	275	\	440	283	100	458	113	184	371	140	4.15	5.06
MG-1	1_G112	144	340	1586	764	\	178	270	600	244	88.3	185	127	108	3.37	4.63
MG-1	1_G113	193	396	4068	<dl	\	201	216	2945	330	115	192	172	149	3.73	3.27
MG-1	1_G114	135	782	3079	156	\	269	218	636	433	114	205	388	103	4.03	4.64
MG-1	1_G115	204	945	69683	2471	\	454	281	61.2	235	102	184	257	114	3.30	5.07
MG-1	1_G116	133	858	3046	<dl	\	3585	217	215	478	96.4	192	307	111	3.86	4.73

Sample	Measurement	Y	Zr	Nb	Mo	Ag	Sn	Hf	Ta	W	Pb	Th
MG-1	1_G051	0.23	\	0.18	1.78	0.11	0.59	\	\	<dl	178	<dl
MG-1	1_G052	<dl	\	1.45	42.0	0.17	2.02	\	\	<dl	1188	<dl
MG-1	1_G053	<dl	\	0.27	10.7	<dl	0.84	\	\	<dl	427	1.08
MG-1	1_G054	<dl	\	2.42	6.16	0.12	0.61	\	\	<dl	312	<dl
MG-1	1_G055	<dl	\	0.63	17.2	0.21	7.55	\	\	<dl	861	<dl
MG-1	1_G056	10.2	\	72.8	5.71	25.1	21.5	\	\	<dl	298	<dl
MG-1	1_G057	<dl	\	2.85	20.8	10.7	1.20	\	\	4.03	2132	<dl
MG-1	1_G058	22.1	\	0.48	9.26	1.38	0.77	\	\	<dl	524	<dl
MG-1	1_G059	4.35	\	28.4	9.35	0.38	6.65	\	\	<dl	667	<dl
MG-1	1_G060	4.29	\	26.3	14.4	<dl	6.20	\	\	<dl	686	<dl
MG-1	1_G061	2.22	\	0.75	8.75	0.20	1.20	\	\	<dl	706	<dl
MG-1	1_G062	<dl	\	0.67	7.12	<dl	0.54	\	\	<dl	444	<dl
MG-1	1_G063	92.3	\	1.42	15.1	0.36	0.92	\	\	3.12	642	219
MG-1	1_G064	4.82	\	0.26	9.18	<dl	0.84	\	\	1.76	470	46.4
MG-1	1_G065	<dl	\	0.29	4.93	0.15	0.68	\	\	<dl	399	32.7
MG-1	1_G066	36.7	\	0.39	5.63	0.36	0.38	\	\	1.59	330	28.1
MG-1	1_G067	<dl	\	1.79	9.77	0.05	0.40	\	\	<dl	738	<dl
MG-1	1_G068	0.67	\	0.46	17.9	0.14	0.54	\	\	<dl	1208	82.3
MG-1	1_G069	<dl	\	<dl	12.9	0.12	5.27	\	\	<dl	524	<dl
MG-1	1_G070	<dl	\	0.14	<dl	0.21	0.82	\	\	<dl	681	28.9
MG-1	1_G071	<dl	\	0.17	3.07	<dl	0.50	\	\	<dl	202	<dl
MG-1	1_G072	<dl	\	0.37	5.66	0.15	0.87	\	\	<dl	376	<dl
MG-1	1_G073	9.23	\	0.46	3.92	0.20	8.58	\	\	0.92	338	84.5
MG-1	1_G074	2.25	\	0.37	13.7	0.06	0.52	\	\	<dl	680	<dl

Sample	Measurement	Y	Zr	Nb	Mo	Ag	Sn	Hf	Ta	W	Pb	Th
MG-1	1_G075	0.10	\	0.22	6.62	0.11	0.89	\	\	<dl	450	<dl
MG-1	1_G076	<dl	\	0.05	4.76	0.05	0.59	\	\	<dl	193	<dl
MG-1	1_G077	1.48	\	0.59	<dl	0.12	1.05	\	\	<dl	533	<dl
MG-1	1_G078	<dl	\	0.21	2.87	0.08	0.64	\	\	<dl	309	<dl
MG-1	1_G080	9.71	\	0.21	<dl	0.14	0.59	\	\	<dl	307	<dl
MG-1	1_G081	0.40	\	<dl	15.1	0.10	1.23	\	\	<dl	822	<dl
MG-1	1_G082	0.18	\	<dl	4.08	0.04	1.74	\	\	<dl	219	<dl
MG-1	1_G083	<dl	\	25.3	19.4	0.91	4.22	\	\	<dl	1244	<dl
MG-1	1_G084	0.50	\	0.39	4.55	0.59	0.38	\	\	0.56	458	<dl
MG-1	1_G085	<dl	\	0.34	7.85	0.06	0.84	\	\	<dl	557	<dl
MG-1	1_G086	<dl	\	0.38	9.07	0.34	0.72	\	\	2.04	790	50.4
MG-1	1_G087	0.34	\	<dl	24.6	0.12	1.83	\	\	2.48	1137	<dl
MG-1	1_G088	0.29	\	0.17	3.22	<dl	0.73	\	\	1.73	315	<dl
MG-1	1_G089	<dl	\	0.64	9.62	<dl	0.66	\	\	<dl	537	<dl
MG-1	1_G090	<dl	\	3.14	9.32	<dl	0.67	\	\	2.31	513	<dl
MG-1	1_G091	0.49	\	1.50	11.4	0.09	0.56	\	\	<dl	881	<dl
MG-1	1_G092	<dl	\	<dl	11.2	0.35	44.2	\	\	<dl	741	<dl
MG-1	1_G093	14.7	\	0.78	3.76	0.27	0.89	\	\	<dl	509	<dl
MG-1	1_G094	7.17	\	0.30	7.86	<dl	<dl	\	\	<dl	571	<dl
MG-1	1_G095	44.0	\	13.2	6.06	0.28	4.81	\	\	7.15	446	<dl
MG-1	1_G096	<dl	\	0.57	12.3	<dl	0.66	\	\	<dl	751	<dl
MG-1	1_G097	0.14	\	0.51	7.46	0.09	2.59	\	\	<dl	1191	<dl
MG-1	1_G098	<dl	\	0.07	2.39	0.12	0.60	\	\	<dl	192	<dl
MG-1	1_G099	<dl	\	0.19	11.9	<dl	0.49	\	\	<dl	442	<dl
MG-1	1_G100	<dl	\	0.67	13.8	<dl	1.08	\	\	<dl	719	<dl
MG-1	1_G101	<dl	\	0.81	11.9	<dl	1.00	\	\	1.03	623	<dl

Sample	Measurement	Y	Zr	Nb	Mo	Ag	Sn	Hf	Ta	W	Pb	Th
MG-1	1_G102	0.26	\	0.22	3.31	0.28	0.48	\	\	<dl	301	20.7
MG-1	1_G103	<dl	\	63.2	4.90	1.16	13.6	\	\	<dl	809	55.0
MG-1	1_G104	4.86	\	0.40	4.33	0.08	1.28	\	\	0.61	396	<dl
MG-1	1_G105	<dl	\	0.51	11.9	<dl	0.47	\	\	<dl	1021	<dl
MG-1	1_G106	<dl	\	0.43	7.24	0.11	0.84	\	\	<dl	406	<dl
MG-1	1_G107	6.66	\	1.80	3.62	0.05	0.85	\	\	<dl	586	<dl
MG-1	1_G109	0.02	\	0.07	<dl	0.03	0.76	\	\	<dl	141	<dl
MG-1	1_G110	<dl	\	4.26	24.0	0.72	2.97	\	\	<dl	1141	37.7
MG-1	1_G111	12.7	\	0.99	20.9	<dl	0.99	\	\	3.89	958	<dl
MG-1	1_G112	8.08	\	0.51	9.36	0.09	0.76	\	\	3.16	523	<dl
MG-1	1_G113	0.93	\	0.25	<dl	<dl	0.64	\	\	0.84	389	<dl
MG-1	1_G114	<dl	\	0.59	11.5	<dl	1.07	\	\	<dl	536	<dl
MG-1	1_G115	96.3	\	0.62	<dl	1.54	0.44	\	\	<dl	1011	<dl
MG-1	1_G116	<dl	\	10.5	13.4	0.10	3.86	\	\	<dl	640	<dl

Sample	Measurement	Mg	Al	Si	Ca	Sc	Ti	V	Cr	Mn	Co	Ni	Cu	Zn	Ga	Ge
MG-3	SJ3_001	12.1	231	1215	86.1	0.32	138	103	4.62	198	27.5	51.7	2164	25.9	6.58	6.24
MG-3	SJ3_002	63.5	377	1650	<dl	<dl	109	78.6	21.0	261	29.0	55.7	0.73	62.7	10.7	8.38
MG-3	SJ3_003	21.4	521	2091	230	1.27	257	131	33.4	206	29.3	57.8	41.5	16.9	4.34	5.27
MG-3	SJ3_004	13.9	276	1159	<dl	0.39	75.9	83.7	2.17	207	25.2	48.3	0.42	34.4	8.23	5.25
MG-3	SJ3_005	16.1	167	1366	<dl	0.36	71.6	71.4	26.3	224	27.0	51.2	<dl	42.5	8.18	7.99
MG-3	SJ3_006	32.7	476	1680	<dl	0.61	97.7	100	26.4	184	24.9	53.9	<dl	18.6	4.76	5.69
MG-3	SJ3_007	40.5	292	1776	934	0.33	1183	69.9	8.64	181	27.1	53.5	22.5	15.6	6.46	6.17
MG-3	SJ3_008	22.6	236	713	98.8	0.96	113	92.9	12.6	192	26.9	52.3	1754	26.9	4.82	4.05
MG-3	SJ3_009	7.71	182	935	<dl	<dl	97.5	80.4	21.1	191	27.4	54.8	<dl	16.1	5.37	5.70
MG-3	SJ3_010	12.1	175	2678	123	0.49	84.1	120	15.7	192	28.4	57.6	2.4	16.9	4.56	6.80
MG-3	SJ3_011	7.61	180	1690	<dl	2.28	90.5	94.3	106	182	27.1	58.0	<dl	16.8	4.14	4.84
MG-3	SJ3_012	8.8	179	869	<dl	<dl	95.6	68.2	5.54	188	24.4	54.2	6243	20.1	5.68	6.17
MG-3	SJ3_013	15.2	145	1113	<dl	0.59	59.1	70.1	<dl	198	26.3	49.3	24.8	32.6	7.46	5.86
MG-3	SJ3_014	7.62	166	988	<dl	0.69	96.2	79.9	55.3	195	25.9	52.9	0.80	20.8	5.43	5.46
MG-3	SJ3_015	183	1932	4243	88.4	1.61	92.3	120	6.48	177	26.1	55.4	8.2	20.3	5.70	4.91
MG-3	SJ3_016	79.3	724	2295	153	0.76	74.2	67.5	7.05	179	26.0	50.9	23.0	32.6	8.21	7.33
MG-3	SJ3_017	13.8	174	670	<dl	<dl	96.4	66.2	<dl	208	26.2	47.0	<dl	37.6	7.48	5.66
MG-3	SJ3_018	64.8	878	2761	<dl	1.34	93.0	69.9	10.5	185	26.9	46.5	3.4	21.5	7.21	7.50
MG-3	SJ3_019	42.2	528	2070	123	1.84	166	89.5	37.2	175	24.0	52.9	0.48	21.4	4.26	5.98
MG-3	SJ3_020	8.63	178	1325	71.5	0.46	131	68.2	2.73	196	24.4	52.6	0.39	21.2	6.29	5.72

Sample	Measurement	Y	Zr	Nb	Mo	Ag	Sn	Hf	Ta	W	Pb	Th
MG-3	SJ3_001	0.56	5.43	<dl	<dl	3.10	2.51	0.28	0.01	0.06	7.91	<dl
MG-3	SJ3_002	0.14	2.70	<dl	<dl	0.58	1.56	0.07	<dl	0.05	0.16	<dl
MG-3	SJ3_003	17.6	280	0.48	0.28	0.52	<dl	<dl	0.05	0.07	0.94	6.37
MG-3	SJ3_004	6.99	131	<dl	0.23	<dl	<dl	<dl	0.01	<dl	0.16	<dl
MG-3	SJ3_005	<dl	0.52	<dl	<dl	<dl	0.79	<dl	<dl	<dl	0.07	<dl
MG-3	SJ3_006	2.93	67.2	0.21	<dl	0.49	1.06	1.77	<dl	<dl	0.19	1.75
MG-3	SJ3_007	5.87	0.93	7.22	0.30	<dl	1.62	<dl	<dl	<dl	0.21	0.02
MG-3	SJ3_008	18.0	271	0.64	<dl	1.02	1.13	<dl	<dl	2.40	3.36	5.25
MG-3	SJ3_009	0.05	0.56	<dl	0.28	0.45	0.71	<dl	<dl	<dl	0.04	<dl
MG-3	SJ3_010	1.09	53.9	<dl	<dl	<dl	0.87	1.73	<dl	<dl	0.13	<dl
MG-3	SJ3_011	30.0	797	0.29	0.22	0.49	0.95	18.8	0.09	0.03	1.25	<dl
MG-3	SJ3_012	0.04	0.09	0.14	0.25	1.84	0.74	<dl	<dl	<dl	0.75	<dl
MG-3	SJ3_013	6.26	130	<dl	<dl	0.51	1.05	<dl	0.02	<dl	0.39	4.38
MG-3	SJ3_014	10.3	278	0.21	<dl	<dl	0.75	<dl	0.01	<dl	0.44	4.40
MG-3	SJ3_015	13.6	308	0.30	<dl	<dl	2.28	<dl	<dl	<dl	1.33	<dl
MG-3	SJ3_016	0.36	5.87	<dl	0.26	<dl	<dl	<dl	<dl	0.05	<dl	0.16
MG-3	SJ3_017	<dl	<dl	<dl	0.33	0.46	<dl	0.03	0.01	0.04	<dl	<dl
MG-3	SJ3_018	21.3	403	<dl	0.17	0.60	<dl	<dl	<dl	<dl	0.87	<dl
MG-3	SJ3_019	13.2	380	0.47	0.21	<dl	0.83	<dl	<dl	<dl	0.57	<dl
MG-3	SJ3_020	3.34	76.9	<dl	<dl	0.45	0.74	<dl	<dl	<dl	0.20	2.01

Sample	Measurement	Mg	Al	Si	Ca	Sc	Ti	V	Cr	Mn	Co	Ni	Cu	Zn	Ga	Ge
MG-4	SJ4_G001	68.9	523	1717	88.9	0.35	184	354	4.80	134	109	277	0.81	191	4.46	5.24
MG-4	SJ4_G002	73.6	497	1663	129	0.12	191	349	84.7	154	108	254	1.6	217	5.18	5.89
MG-4	SJ4_G003	71.2	199	1335	28.3	0.21	91.7	309	48.4	82.9	91.9	264	0.46	134	3.62	4.97
MG-4	SJ4_G004	48.5	19265	56392	128	1.10	129	331	232	107	109	267	0.60	121	4.83	5.16
MG-4	SJ4_G007	80.1	170	1028	18.5	0.15	365	319	35.1	95.0	106	270	0.26	138	3.85	4.81
MG-4	SJ4_G008	23.8	144	43531	39.4	0.70	402	313	611	79.0	109	267	0.54	127	3.55	5.41
MG-4	SJ4_G009	133	1035	2329	20.1	0.53	159	339	32.9	115	101	261	1.0	159	4.53	3.77
MG-4	SJ4_G010	67.7	674	1996	482	0.15	118	386	567	149	100	290	0.87	215	4.38	5.53
MG-4	SJ4_G011	98.2	225	1250	616	<dl	124	301	8.49	126	104	238	1.3	160	3.60	4.96
MG-4	SJ4_G012	32.0	120	734	44.7	0.20	104	341	3.39	112	115	265	0.06	174	3.86	5.25
MG-4	SJ4_G013	44.9	234	909	50.7	0.23	163	327	140	126	103	251	0.70	168	3.72	4.21
MG-4	SJ4_G014	196	373	4662	313	0.42	1207	362	62.2	88.3	104	293	3.6	1855	3.93	6.80
MG-4	SJ4_G015	51.2	338	6394	101	0.12	646	290	147	75.9	102	254	0.98	127	3.18	4.11
MG-4	SJ4_G016	75.8	501	6088	786	0.31	246	370	148	145	106	275	11.0	205	5.94	34.0
MG-4	SJ4_G017	21.6	96.2	3134	77.7	<dl	77.7	307	47.4	82.1	103	260	0.57	141	3.44	4.80
MG-4	SJ4_G018	53.9	133	800	32.6	0.12	176	368	32.6	121	105	287	0.43	185	3.74	5.23
MG-4	SJ4_G020	173	2161	6104	508	0.39	194	323	56.6	161	115	257	7.1	256	5.13	10.3
MG-4	SJ4_G021	346	2673	6105	117	0.84	881	366	5873	305	234	283	3.1	2846	6.12	5.51
MG-4	SJ4_G022	94.2	108	928	16.7	93.7	<dl	345	2.26	99.3	111	260	0.06	165	3.90	4.61
MG-4	SJ4_G023	49.8	199	1675	84.6	2.32	201	339	26.9	126	107	254	0.49	177	4.33	4.84
MG-4	SJ4_G024	78.0	447	1798	62.0	0.32	130	359	6.27	154	118	264	0.73	193	4.29	4.85
MG-4	SJ4_G025	94.9	565	2730	125	0.35	210	349	9.33	196	110	263	2.6	196	4.33	7.10
MG-4	SJ4_G026	761	7797	30137	151	2.47	692	370	109	91.7	99.6	267	2.0	135	8.60	5.35
MG-4	SJ4_G027	105	433	1831	16.2	0.30	114	309	11.2	127	105	242	0.19	164	4.19	4.55
MG-4	SJ4_G028	149	1150	36640	41.5	1.03	1303	357	495	132	99.6	280	8.8	144	3.98	4.44
MG-4	SJ4_G029	136	1679	4117	190	0.23	210	371	15170	450	181	269	2.8	9858	5.61	5.50

Sample	Measurement	Mg	Al	Si	Ca	Sc	Ti	V	Cr	Mn	Co	Ni	Cu	Zn	Ga	Ge
MG-4	SJ4_G030	108	1358	12757	383	1.62	555	380	2670	226	104	267	3.3	383	6.36	6.78
MG-4	SJ4_G031	59.0	309	64621	106	0.99	86.6	305	233	73.2	101	252	0.80	132	3.35	4.79
MG-4	SJ4_G032	18.2	83.8	1389	15.3	67.8	<dl	343	68.8	84.8	97.8	272	0.24	137	3.41	4.99
MG-4	SJ4_G033	39.1	139	1495	14.9	0.34	74.1	335	99.1	92.8	106	262	0.10	142	3.67	3.86
MG-4	SJ4_G034	168	958	3229	15.7	1.91	128	363	183	107	107	265	0.51	163	4.27	3.97
MG-4	SJ4_G035	47.8	360	2149	55.5	0.62	115	345	41.7	114	106	275	0.78	180	4.04	5.10
MG-4	SJ4_G036	51.4	847	3464	115	0.52	395	356	24.5	181	102	242	5.7	206	4.84	7.42
MG-4	SJ4_G037	54.5	389	1970	40.0	0.14	72.1	336	23.3	94.7	91.4	223	0.82	139	3.65	4.79
MG-4	SJ4_G038	23.4	266	4835	295	0.12	53.8	261	1088	59.3	89.9	241	1.2	121	3.49	4.75
MG-4	SJ4_G039	446	1149	10554	441	5.28	308	323	1293	103	104	254	0.80	624	4.03	5.38
MG-4	SJ4_G040	59.6	428	2437	66.5	0.28	395	338	9.50	172	107	278	0.82	205	4.89	5.49
MG-4	SJ4_G041	78.3	258	2088	43.3	0.13	154	332	197	81.8	105	265	0.49	144	3.39	4.50
MG-4	SJ4_G042	226	2259	5235	29.5	0.69	157	344	16.3	99.1	97.8	247	0.40	151	4.81	5.08
MG-4	SJ4_G043	99.7	678	4737	195	1.37	689	295	159	96.2	99.4	249	32.9	99.1	3.10	4.43
MG-4	SJ4_G044	33.3	252	4079	50.7	0.20	171	286	72.8	82.7	98.6	239	6.9	132	3.51	4.73
MG-4	SJ4_G045	116	1312	4233	174	0.50	87.7	296	99.6	104	90.2	245	17.5	129	3.50	4.10
MG-4	SJ4_G046	122	2429	13815	150	0.63	246	282	311	176	109	247	2.5	157	4.05	5.74
MG-4	SJ4_G048	104	768	3675	49.7	0.26	79.6	316	154	75.9	111	261	0.06	128	3.98	4.14
MG-4	SJ4_G049	49.3	190	3938	21.2	0.34	94.0	328	294	85.3	107	258	0.08	139	3.77	5.40
MG-4	SJ4_G050	71.0	485	3210	63.0	0.32	176	316	249	199	189	270	0.34	361	3.62	5.19
MG-4	SJ4_G051	51.0	144	37462	40.6	0.52	79.2	296	35.5	91.3	99.7	245	0.69	124	3.12	4.55
MG-4	SJ4_G052	53.5	645	5237	1562	0.47	1568	323	58.3	91.5	106	259	1.6	146	3.60	3.80
MG-4	SJ4_G053	51.2	78.1	12169	29.2	0.23	59.7	297	11.4	74.5	101	251	0.05	133	3.25	4.36
MG-4	SJ4_G054	80.7	624	2641	112	0.48	350	321	312	129	102	238	1.9	173	4.65	3.81
MG-4	SJ4_G055	19.2	75.3	501	16.2	70.2	<dl	312	112	83.3	104	251	0.52	146	3.45	4.12
MG-4	SJ4_G056	45.8	91.4	1114	18.4	0.10	59.5	285	104	75.6	101	238	0.12	127	3.35	3.80

Sample	Measurement	Mg	Al	Si	Ca	Sc	Ti	V	Cr	Mn	Co	Ni	Cu	Zn	Ga	Ge
MG-4	SJ4_G057	80.7	557	3347	57.9	0.10	73.1	294	523	78.2	103	250	0.18	130	3.36	4.90
MG-4	SJ4_G058	107	973	2762	72.8	0.47	199	351	1153	155	104	267	1.3	203	4.40	4.66
MG-4	SJ4_G059	92.0	108	1320	18.0	0.18	69.4	311	28.4	78.5	107	254	<dl	132	3.34	4.82
MG-4	SJ4_G060	60.1	131	635	17.2	0.23	67.5	330	276	87.4	105	260	0.15	141	3.60	4.58
MG-4	SJ4_G061	65.6	230	1405	18.2	91.3	<dl	337	54.1	91.8	108	255	1.3	164	4.31	4.39
MG-4	SJ4_G062	60.7	385	1907	48.7	0.37	139	308	1913	129	108	249	0.77	181	3.83	5.17
MG-4	SJ4_G063	61.6	231	1815	260	0.12	106	322	28.4	122	110	258	0.50	162	4.14	3.71
MG-4	SJ4_G064	116	1243	5117	261	1.97	518	323	96.4	134	115	256	2.8	196	3.90	8.11
MG-4	SJ4_G065	58.0	370	1911	50.3	0.13	126	377	199	130	91.4	238	0.52	175	3.93	4.24
MG-4	SJ4_G066	155	1148	3943	211	3.61	155	264	173	84.9	95.5	219	5.2	122	3.69	4.47
MG-4	SJ4_G068	59.2	211	5547	32.9	0.14	96.9	285	282	80.8	99.7	239	0.10	132	3.24	3.50
MG-4	SJ4_G069	105	376	2290	80.5	0.44	206	392	24.3	134	104	286	0.07	180	4.11	4.14
MG-4	SJ4_G070	43.8	271	3367	20.8	0.18	64.8	284	10.6	73.4	95.3	238	0.28	133	3.38	3.89
MG-4	SJ4_G071	63.0	74.7	535	21.2	<dl	65.0	316	39.7	76.3	100	248	0.25	123	3.21	4.04
MG-4	SJ4_G072	128	617	2665	159	0.34	269	365	437	131	98.0	274	0.81	208	4.26	4.97
MG-4	SJ4_G073	56.1	123	749	16.9	0.12	116	321	95.3	70.6	100	254	0.11	124	3.20	4.27
MG-4	SJ4_G074	49.6	103	807	29.6	<dl	90.6	325	89.4	95.6	105	259	0.12	144	3.60	0.95
MG-4	SJ4_G075	27.2	193	8485	22.4	0.17	85.1	306	235	71.7	96.3	238	0.39	118	3.39	4.27
MG-4	SJ4_G076	194	1089	3549	90.9	0.67	155	268	358	103	90.0	239	7.6	140	3.74	4.35
MG-4	SJ4_G077	92.8	632	3301	75.3	0.33	916	348	24.6	195	110	261	3.7	175	5.29	4.69
MG-4	SJ4_G078	105	114	1972	698	0.13	68.1	297	61.4	101	99.0	248	29.9	122	2.99	3.28
MG-4	SJ4_G079	106	707	2819	118	0.29	231	352	137	142	101	279	1.5	192	4.11	4.71
MG-4	SJ4_G081	99.0	730	3431	100	2.30	379	299	125	116	94.2	251	3.2	154	3.62	4.87
MG-4	SJ4_G082	252	1958	11554	112	0.84	1050	274	286	68.2	91.7	236	6.7	110	4.24	4.07
MG-4	SJ4_G083	56.7	302	2961	1061	0.26	1209	318	38.8	112	106	244	0.25	167	4.41	3.69
MG-4	SJ4_G084	117	687	3071	96.3	0.80	70.5	290	126	72.4	101	239	0.09	125	3.59	3.87

Sample	Measurement	Mg	Al	Si	Ca	Sc	Ti	V	Cr	Mn	Co	Ni	Cu	Zn	Ga	Ge
MG-4	SJ4_G085	82.4	1346	4380	223	0.28	286	311	55.8	141	103	243	8.4	207	6.23	5.43
MG-4	SJ4_G086	162	890	10723	62.9	0.97	395	341	979	107	93.2	264	0.56	154	3.69	4.55
MG-4	SJ4_G087	92.5	1116	3957	204	0.26	226	334	17.5	160	98.6	247	6.7	210	5.08	5.21
MG-4	SJ4_G088	29.8	105	31267	17.9	0.37	68.3	285	123	71.1	102	245	0.65	114	3.20	4.10
MG-4	SJ4_G089	39.4	218	2966	43.5	<dl	95.9	295	298	80.0	103	248	0.76	129	3.31	4.18
MG-4	SJ4_G090	556	5065	12132	131	2.11	259	289	134	108	92.6	235	2.1	143	5.42	4.11
MG-4	SJ4_G091	91.1	451	2436	47.6	0.30	391	333	212	112	103	255	0.65	173	3.90	3.83
MG-4	SJ4_G092	22.5	102	579	34.7	0.09	90.1	323	1.54	107	100	247	0.29	163	4.10	3.34
MG-4	SJ4_G093	71.1	82.4	694	16.0	0.19	80.1	294	4.44	84.6	102	240	0.20	137	3.19	4.23
MG-4	SJ4_G094	74.0	600	5878	35.6	0.45	165	334	143	99.9	97.4	259	2.0	147	3.44	4.67
MG-4	SJ4_G095	102	1720	28553	17.2	0.49	75.3	278	84.3	68.1	95.9	253	1.4	110	3.52	3.03
MG-4	SJ4_G096	47.0	275	1791	222	0.42	332	336	37.4	127	91.4	254	0.71	177	3.81	4.50
MG-4	SJ4_G097	86.3	499	2450	62.7	0.26	211	355	105	133	150	260	0.63	211	5.08	5.59
MG-4	SJ4_G099	99.5	1314	4416	292	0.55	426	357	36.1	182	94.2	226	15.1	213	4.47	5.56
MG-4	SJ4_G100	103	358	2164	44.9	0.14	121	356	3.75	132	100	263	0.39	183	4.41	3.75
MG-4	SJ4_G101	230	1186	6474	361	0.62	272	292	996	126	105	246	1.5	191	3.94	5.16
MG-4	SJ4_G102	86.7	1029	3882	138	0.67	588	374	73.5	205	125	226	4.6	221	4.03	6.94
MG-4	SJ4_G103	37.9	122	701	15.8	0.11	83.6	301	4.78	93.5	106	246	<dl	154	3.90	4.32
MG-4	SJ4_G104	79.8	492	2439	208	0.33	219	331	14.2	156	103	254	1.0	180	4.19	5.04
MG-4	SJ4_G105	118	589	3003	83.2	0.29	133	338	48.9	251	129	212	5.5	211	3.92	6.27
MG-4	SJ4_G106	70.8	849	3397	171	0.39	286	322	192	122	96.3	239	2.1	170	3.63	5.23
MG-4	SJ4_G107	81.7	271	2948	17.6	0.13	70.5	266	10.1	65.2	99.6	240	0.82	118	2.83	4.23
MG-4	SJ4_G108	109	581	2765	14.9	0.23	87.8	266	2611	70.3	93.9	239	0.73	150	3.36	4.10
MG-4	SJ4_G109	57.9	226	1284	22.7	0.17	78.8	304	29.2	80.3	110	248	0.66	128	3.23	5.08
MG-4	SJ4_G110	58.2	203	1266	19.4	0.15	72.2	323	25.1	101	99.5	254	0.09	148	3.36	4.25
MG-4	SJ4_G111	124	566	2840	93.9	0.24	164	389	23.1	211	99.8	271	1.3	209	4.59	5.67

MG-4	SJ4_G112	27.5	344	2684	68.7	0.10	118	289	66.8	100	96.5	236	1.7	126	3.55	4.40
MG-4	SJ4_G113	34.6	105	12926	37.2	0.13	66.6	305	217	85.0	101	240	0.63	140	3.50	4.11
MG-4	SJ4_G115	395	2457	23460	59.7	1.09	430	307	2235	114	99.1	237	1.2	123	4.58	3.89
MG-4	SJ4_G116	33.9	137	1184	185	0.42	260	331	30.5	79.1	92.7	263	0.58	130	3.35	3.16
MG-4	SJ4_G117	81.8	730	2947	89.4	0.63	391	342	167	162	99.6	226	0.78	200	5.24	5.21
MG-4	SJ4_G118	36.4	222	884	22.7	0.13	64.5	269	174	63.6	86.5	224	0.88	119	3.29	4.22
MG-4	SJ4_G119	82.6	212	1136	72.1	0.23	126	294	26.6	81.6	99.0	236	0.11	135	3.41	3.61
MG-4	SJ4_G120	56.5	357	1228	29.5	0.14	69.1	305	86.5	72.9	90.4	221	0.34	122	3.00	4.26

Sample	Measurement	Y	Zr	Nb	Mo	Ag	Sn	Hf	Ta	W	Pb	Th
MG-4	SJ4_G001	0.17	20.2	0.27	2.42	0.04	0.59	<dl	<dl	<dl	96.2	<dl
MG-4	SJ4_G002	0.14	14.2	0.26	2.06	0.03	0.74	<dl	0.02	<dl	58.2	<dl
MG-4	SJ4_G003	<dl	9.14	0.14	0.97	0.04	0.91	<dl	<dl	<dl	31.6	<dl
MG-4	SJ4_G004	0.19	9.71	0.30	4.42	<dl	0.79	<dl	<dl	<dl	64.7	3.01
MG-4	SJ4_G007	0.22	<dl	0.15	<dl	<dl	0.57	0.26	<dl	0.09	1.76	<dl
MG-4	SJ4_G008	0.33	<dl	0.42	0.67	0.04	0.58	<dl	<dl	<dl	25.1	<dl
MG-4	SJ4_G009	2.03	43.8	1.48	0.26	0.03	0.58	<dl	0.01	<dl	35.0	2.69
MG-4	SJ4_G010	0.12	<dl	0.14	2.34	<dl	0.49	0.60	0.01	<dl	76.7	<dl
MG-4	SJ4_G011	0.12	5.84	0.16	1.68	0.03	0.39	1.95	<dl	1.72	41.1	0.77
MG-4	SJ4_G012	0.01	2.50	0.12	0.63	0.04	0.30	0.25	<dl	0.92	14.2	<dl
MG-4	SJ4_G013	1.45	42.1	0.28	1.92	0.04	0.79	<dl	0.03	3.18	31.7	2.17
MG-4	SJ4_G014	1.58	5.41	9.85	7.80	0.16	3.71	<dl	<dl	1.40	19.0	<dl
MG-4	SJ4_G015	<dl	13.0	1.60	0.97	0.02	1.21	<dl	0.15	<dl	38.7	<dl
MG-4	SJ4_G016	11.3	27.7	0.51	3.43	0.06	0.66	<dl	0.05	2.31	108	<dl
MG-4	SJ4_G017	0.03	<dl	0.09	0.09	<dl	0.78	<dl	0.00	0.09	1.47	<dl
MG-4	SJ4_G018	0.04	13.6	0.33	2.88	0.02	0.99	<dl	0.04	<dl	53.1	<dl
MG-4	SJ4_G020	<dl	52.1	0.65	7.51	0.04	1.02	<dl	0.02	6.39	143	6.45
MG-4	SJ4_G021	0.31	58.0	0.62	2.62	0.04	1.32	<dl	<dl	2.44	269	<dl
MG-4	SJ4_G022	0.01	0.29	<dl	0.06	<dl	0.54	<dl	<dl	<dl	0.83	0.01
MG-4	SJ4_G023	50.7	1067	3.77	0.68	0.09	0.70	<dl	<dl	<dl	40.2	12.6
MG-4	SJ4_G024	<dl	19.4	0.28	2.42	<dl	0.48	0.80	<dl	<dl	50.3	<dl
MG-4	SJ4_G025	0.86	35.7	0.43	7.30	0.03	0.58	1.66	0.03	5.27	125	<dl
MG-4	SJ4_G026	1.52	<dl	1.96	2.12	0.03	2.31	4.35	0.14	<dl	87.8	15.9
MG-4	SJ4_G027	<dl	<dl	0.25	0.32	<dl	0.34	0.53	<dl	<dl	19.8	0.47
MG-4	SJ4_G028	0.40	26.8	4.15	1.52	<dl	1.00	<dl	0.35	<dl	34.6	<dl
MG-4	SJ4_G029	0.20	<dl	0.38	2.91	0.04	0.53	1.12	0.01	<dl	98.4	<dl

Sample	Measurement	Y	Zr	Nb	Mo	Ag	Sn	Hf	Ta	W	Pb	Th
MG-4	SJ4_G030	20.7	459	0.99	3.02	19.7	1.16	<dl	0.19	<dl	181	<dl
MG-4	SJ4_G031	2.25	48.0	0.18	1.40	<dl	0.67	<dl	<dl	0.51	34.4	<dl
MG-4	SJ4_G032	0.02	7.24	0.05	0.20	0.03	0.50	<dl	<dl	<dl	7.88	<dl
MG-4	SJ4_G033	3.43	113	0.02	0.10	0.03	0.55	3.74	<dl	<dl	2.14	1.38
MG-4	SJ4_G034	<dl	910	0.30	2.19	0.04	0.68	17.6	<dl	<dl	22.4	6.60
MG-4	SJ4_G035	0.14	9.09	0.12	1.84	<dl	0.52	<dl	0.01	<dl	67.4	0.53
MG-4	SJ4_G036	1.14	54.0	1.41	5.76	<dl	0.91	<dl	0.06	<dl	133	<dl
MG-4	SJ4_G037	0.07	5.49	0.08	1.09	<dl	1.71	<dl	<dl	<dl	28.9	<dl
MG-4	SJ4_G038	<dl	5.42	0.05	<dl	<dl	4.11	0.13	235	<dl	5.90	<dl
MG-4	SJ4_G039	<dl	2075	0.46	2.03	0.26	1.17	36.5	<dl	<dl	41.7	<dl
MG-4	SJ4_G040	<dl	18.1	0.64	1.64	0.04	0.61	3.91	<dl	<dl	142	<dl
MG-4	SJ4_G041	0.38	15.7	0.26	0.99	0.03	0.70	<dl	0.04	<dl	20.9	<dl
MG-4	SJ4_G042	0.09	9.00	0.24	1.92	<dl	1.07	<dl	0.01	7.15	19.4	<dl
MG-4	SJ4_G043	16.3	285	1.87	1.38	<dl	11.4	<dl	0.13	<dl	49.4	<dl
MG-4	SJ4_G044	0.32	20.8	0.33	0.69	0.77	1.01	1.13	<dl	<dl	47.5	5.82
MG-4	SJ4_G045	0.20	<dl	0.31	2.64	<dl	5.57	1.79	<dl	<dl	75.5	<dl
MG-4	SJ4_G046	<dl	78.3	0.81	5.01	<dl	1.54	3.24	0.02	7.02	136	<dl
MG-4	SJ4_G048	1.41	32.3	0.06	0.07	0.03	0.37	<dl	<dl	<dl	2.33	0.40
MG-4	SJ4_G049	0.28	15.2	0.95	<dl	1.68	0.74	<dl	<dl	0.23	14.4	2.24
MG-4	SJ4_G050	0.27	22.5	0.35	2.29	0.05	0.62	0.99	<dl	<dl	82.1	2.42
MG-4	SJ4_G051	<dl	<dl	0.09	1.66	1.03	0.37	<dl	0.01	<dl	43.7	1.15
MG-4	SJ4_G052	4.65	<dl	0.94	<dl	<dl	0.70	0.82	<dl	<dl	4.08	0.33
MG-4	SJ4_G053	0.01	<dl	<dl	<dl	0.03	0.50	<dl	0.01	0.01	0.88	<dl
MG-4	SJ4_G054	2.87	160	0.46	2.19	0.02	0.92	<dl	<dl	2.55	127	<dl
MG-4	SJ4_G055	0.05	<dl	<dl	0.11	<dl	0.53	<dl	<dl	0.06	4.05	<dl
MG-4	SJ4_G056	0.07	0.62	<dl	0.23	<dl	0.49	0.06	<dl	0.86	3.10	<dl

Sample	Measurement	Y	Zr	Nb	Mo	Ag	Sn	Hf	Ta	W	Pb	Th
MG-4	SJ4_G057	0.06	4.06	0.12	0.14	<dl	0.48	0.16	0.00	0.27	19.9	<dl
MG-4	SJ4_G058	<dl	74.8	0.25	1.38	0.04	0.80	<dl	0.04	<dl	71.5	<dl
MG-4	SJ4_G059	5.60	154	0.09	<dl	<dl	0.37	<dl	0.01	<dl	2.29	2.05
MG-4	SJ4_G060	0.16	31.3	0.05	<dl	0.03	0.50	<dl	<dl	<dl	1.07	<dl
MG-4	SJ4_G061	0.12	<dl	<dl	<dl	<dl	8.01	0.06	0.00	<dl	2.95	<dl
MG-4	SJ4_G062	0.08	6.93	0.19	2.45	0.02	1.04	0.91	<dl	<dl	74.0	<dl
MG-4	SJ4_G063	0.31	9.54	0.08	0.57	<dl	0.42	0.40	0.01	<dl	27.2	<dl
MG-4	SJ4_G064	<dl	<dl	1.90	5.97	0.05	1.71	<dl	<dl	3.55	154	470
MG-4	SJ4_G065	<dl	<dl	0.15	1.20	0.03	0.96	<dl	0.01	<dl	31.1	1.36
MG-4	SJ4_G066	54.6	872	0.77	3.12	0.09	4.85	<dl	<dl	3.80	40.9	<dl
MG-4	SJ4_G068	0.10	0.98	0.10	0.20	0.03	0.28	<dl	<dl	<dl	11.8	0.26
MG-4	SJ4_G069	<dl	5.43	0.21	1.73	0.04	0.27	0.36	<dl	<dl	65.2	0.53
MG-4	SJ4_G070	0.03	1.15	0.03	<dl	<dl	0.59	0.05	<dl	0.05	3.36	<dl
MG-4	SJ4_G071	<dl	<0.27	<dl	0.12	<dl	1.16	<dl	<dl	<dl	3.43	<dl
MG-4	SJ4_G072	0.43	<dl	0.54	2.55	0.12	1.19	2.30	<dl	<dl	91.8	<dl
MG-4	SJ4_G073	0.06	7.28	0.11	0.31	0.03	0.56	<dl	0.02	<dl	11.0	<dl
MG-4	SJ4_G074	0.11	2.32	0.05	0.24	0.04	0.82	<dl	<dl	<dl	8.94	<dl
MG-4	SJ4_G075	0.32	10.8	0.11	0.39	<dl	0.66	0.54	0.00	<dl	24.6	<dl
MG-4	SJ4_G076	<dl	<dl	0.27	1.23	0.04	4.01	2.54	0.04	<dl	57.4	2.93
MG-4	SJ4_G077	<dl	<dl	0.80	4.35	0.03	1.10	1.09	0.00	2.73	64.0	3.46
MG-4	SJ4_G078	0.33	10.1	0.06	0.27	<dl	3.49	<dl	<dl	0.23	8.50	0.97
MG-4	SJ4_G079	0.25	<dl	0.55	2.98	0.03	0.86	<dl	<dl	1.37	103	<dl
MG-4	SJ4_G081	37.0	948	1.26	1.79	0.12	1.01	<dl	0.17	<dl	100	<dl
MG-4	SJ4_G082	4.49	<dl	3.43	0.34	0.02	2.19	<dl	<dl	<dl	7.91	2.15
MG-4	SJ4_G083	8.42	9.63	5.76	0.14	0.03	0.94	<dl	<dl	<dl	3.28	<dl
MG-4	SJ4_G084	9.34	22.5	0.07	0.21	0.04	0.57	0.87	0.02	<dl	4.35	<dl

Sample	Measurement	Y	Zr	Nb	Mo	Ag	Sn	Hf	Ta	W	Pb	Th
MG-4	SJ4_G085	0.33	<dl	0.99	3.42	0.04	1.13	<dl	0.07	2.28	100	<dl
MG-4	SJ4_G086	6.93	170	1.06	3.16	0.03	1.40	<dl	<dl	<dl	72.8	<dl
MG-4	SJ4_G087	4.18	135	0.65	4.04	0.30	0.94	3.24	0.05	2.78	108	<dl
MG-4	SJ4_G088	0.58	13.8	0.07	0.26	0.03	0.84	<dl	<dl	<dl	12.0	<dl
MG-4	SJ4_G089	<dl	19.0	0.14	1.02	0.03	0.75	0.89	<dl	<dl	10.9	0.56
MG-4	SJ4_G090	4.47	205	0.41	2.19	0.05	1.93	<dl	<dl	<dl	79.7	<dl
MG-4	SJ4_G091	1.66	<dl	0.88	1.65	0.04	1.12	<dl	<dl	1.28	61.0	7.74
MG-4	SJ4_G092	0.45	<dl	0.05	0.55	<dl	0.70	0.66	<dl	<dl	19.6	<dl
MG-4	SJ4_G093	<dl	1.16	0.05	0.76	0.62	0.54	0.12	0.01	0.54	15.2	<dl
MG-4	SJ4_G094	2.43	219	0.50	2.47	0.05	0.93	<dl	<dl	9.37	43.5	<dl
MG-4	SJ4_G095	0.15	5.14	0.08	0.55	0.04	1.68	0.32	<dl	<dl	12.2	0.31
MG-4	SJ4_G096	<dl	25.7	0.65	2.09	0.04	0.98	1.42	<dl	<dl	81.7	<dl
MG-4	SJ4_G097	0.73	39.4	0.45	2.26	<dl	0.65	<dl	<dl	<dl	58.2	1.51
MG-4	SJ4_G099	0.30	41.5	0.61	6.18	16.6	4.70	<dl	0.04	<dl	114	<dl
MG-4	SJ4_G100	<dl	<dl	0.10	1.92	<dl	0.62	<dl	<dl	<dl	66.5	0.12
MG-4	SJ4_G101	0.76	29.6	0.58	4.29	0.05	0.99	<dl	<dl	<dl	121	<dl
MG-4	SJ4_G102	1.42	<dl	2.04	9.41	<dl	1.49	<dl	0.13	<dl	181	<dl
MG-4	SJ4_G103	0.04	1.51	0.14	0.77	<dl	0.71	0.03	0.00	<dl	19.7	<dl
MG-4	SJ4_G104	1.69	101	0.70	2.83	0.04	18.5	2.39	0.04	<dl	85.5	<dl
MG-4	SJ4_G105	<dl	<dl	0.34	6.90	0.03	0.60	1.64	0.01	15.2	112	2.03
MG-4	SJ4_G106	0.51	94.0	0.87	2.52	0.03	1.54	3.02	0.07	<dl	83.7	<dl
MG-4	SJ4_G107	<dl	<dl	0.04	0.34	<dl	0.57	0.28	<dl	<dl	10.9	<dl
MG-4	SJ4_G108	0.07	4.94	0.14	0.48	0.03	0.90	<dl	<dl	0.49	18.4	<dl
MG-4	SJ4_G109	0.31	<dl	0.12	0.59	0.04	0.70	0.24	<dl	0.15	18.8	0.29
MG-4	SJ4_G110	0.11	6.32	0.03	1.61	0.02	0.73	0.32	<dl	<dl	20.2	<dl
MG-4	SJ4_G111	<dl	<dl	0.25	6.43	16.8	0.59	<dl	<dl	<dl	103	3.06

MG-4	SJ4_G112	0.18	3.89	0.33	1.02	0.03	0.61	0.08	<dl	<dl	37.1	0.24
MG-4	SJ4_G113	0.04	<dl	<dl	<dl	0.03	0.72	<dl	<dl	<dl	1.09	<dl
MG-4	SJ4_G115	0.27	<dl	1.34	2.55	0.04	2.32	0.94	0.06	<dl	58.2	<dl
MG-4	SJ4_G116	3.44	92.2	0.30	0.28	0.03	0.98	<dl	<dl	0.59	5.93	0.53
MG-4	SJ4_G117	0.84	49.6	1.98	5.29	0.05	0.64	2.47	0.04	<dl	96.4	4.52
MG-4	SJ4_G118	0.33	22.4	0.08	0.25	0.03	1.03	<dl	<dl	<dl	9.15	<dl
MG-4	SJ4_G119	2.38	30.1	0.28	0.25	<dl	0.81	0.92	<dl	0.48	9.03	<dl
MG-4	SJ4_G120	2.54	54.6	0.09	0.42	0.03	0.81	<dl	0.00	0.52	10.9	<dl

Sample	Measurement	Mg	Al	Si	Ca	Sc	Ti	V	Cr	Mn	Co	Ni	Cu	Zn	Ga	Ge
MG-5	SJ05_G003	233	891	6189	3238	0.92	3468	311	444	1051	101	165	9.4	198	6.89	5.56
MG-5	SJ05_G004	58.8	225	1122	65.6	<dl	156	299	233	878	99.1	163	17.5	178	5.20	3.21
MG-5	SJ05_G005	169	434	2962	139	0.35	258	302	1012	967	86.2	157	18.6	160	5.69	4.33
MG-5	SJ05_G006	32.3	144	564	50.4	<dl	106	292	93.5	730	89.0	168	25.3	142	4.41	3.41
MG-5	SJ05_G008	44.2	292	1386	251	0.19	308	292	152	706	91.4	165	2.8	142	4.16	3.73
MG-5	SJ05_G010	61.8	176	618	48.4	<dl	131	286	12.2	904	93.5	165	10.0	168	5.51	3.87
MG-5	SJ05_G011	166	281	1534	147	0.15	77.1	283	547	651	92.9	164	268	133	3.83	4.23
MG-5	SJ05_G012	123	270	1504	417	0.39	222	317	590	843	107	170	21.0	187	9.28	3.82
MG-5	SJ05_G014	96.4	493	6308	176	0.26	255	311	282	966	104	163	30.9	205	7.23	3.70
MG-5	SJ05_G015	513	552	4760	234	1.52	665	465	1378	1008	90.4	166	41.4	150	4.43	5.19
MG-5	SJ05_G016	43.4	145	522	37.3	<dl	133	300	2.94	907	101	158	2.3	153	5.73	2.73
MG-5	SJ05_G017	405	2862	21398	34257	0.96	220	293	391	1141	92.7	156	4.7	162	6.97	5.73
MG-5	SJ05_G018	892	6193	44741	78022	2.15	367	309	497	749	85.0	169	94.8	116	7.87	5.42
MG-5	SJ05_G019	84.7	266	1327	103	0.12	117	305	1668	1018	105	177	85.3	221	6.80	5.17
MG-5	SJ05_G022	45.6	178	677	115	<dl	125	300	58.4	870	97.1	163	15.8	177	5.72	4.26
MG-5	SJ05_G023	199	411	2657	171	0.66	349	312	669	818	105	165	388	177	6.02	5.26
MG-5	SJ05_G024	53.8	150	1363	462	0.11	118	292	268	802	97.1	161	5.7	151	4.23	3.14
MG-5	SJ05_G026	81.4	218	1138	53.2	0.11	147	293	1482	830	101	166	11.4	182	6.86	3.57
MG-5	SJ05_G027	38.5	135	949	65.4	<dl	82.1	275	516	691	89.1	156	35.3	130	4.19	2.69

Sample	Measurement	Mg	Al	Si	Ca	Sc	Ti	V	Cr	Mn	Co	Ni	Cu	Zn	Ga	Ge
MG-5	SJ05_G028	47.9	286	2228	38.0	0.14	98.8	274	289	699	77.4	156	2.7	131	3.68	3.55
MG-5	SJ05_G029	113	281	1417	350	0.22	169	307	1399	844	103	152	66.1	205	8.87	3.96
MG-5	SJ05_G030	106	483	2959	18300	0.33	129	284	204	982	96.5	153	0.89	183	6.36	4.76
MG-5	SJ05_G031	91.5	330	1282	259	0.25	174	311	263	838	108	166	147	182	7.36	4.54
MG-5	SJ05_G032	524	968	4598	57.5	0.30	201	292	305	951	106	159	10.8	182	8.36	3.01
MG-5	SJ05_G033	88.8	637	1339	51.7	0.20	122	277	48.9	973	91.3	150	0.66	192	5.99	3.40
MG-5	SJ05_G034	69.0	368	3774	191	0.18	157	300	70.3	987	98.0	169	6.6	200	6.39	4.10
MG-5	SJ05_G035	31.0	167	762	206	<dl	207	273	29.5	717	95.6	161	44.4	134	5.08	3.07
MG-5	SJ05_G036	73.7	202	1182	202	0.17	144	319	2.25	793	101	168	64.5	170	5.10	4.74
MG-5	SJ05_G037	180	769	2150	249	0.19	154	303	160	896	108	158	197	207	7.61	5.56
MG-5	SJ05_G038	59.4	259	1139	246	0.25	93.3	305	75.7	742	97.5	171	164	171	5.33	4.38
MG-5	SJ05_G039	479	1101	5577	5191	1.39	477	357	286	1146	103	214	66.7	219	64.9	91.4
MG-5	SJ05_G040	1107	1240	8327	175	2.28	898	416	821	1178	108	153	53.7	214	6.31	4.41
MG-5	SJ05_G041	324	553	63159	265	1.31	1433	299	481	846	101	149	21.4	107	4.94	3.52
MG-5	SJ05_G042	45.7	175	2592	81.6	0.10	112	288	792	708	101	160	24.3	162	4.10	3.78
MG-5	SJ05_G043	56.6	247	1098	379	0.10	381	308	4.81	904	106	166	39.4	177	7.13	3.28

Sample	Measurement	Y	Zr	Nb	Mo	Ag	Sn	Hf	Ta	W	Pb	Th
MG-5	SJ05_G003	41.3	27.2	11.3	0.54	0.07	1.97	<dl	<dl	1.10	142	<dl
MG-5	SJ05_G004	0.42	10.8	0.21	<dl	<dl	0.40	<dl	0.02	<dl	35.1	<dl
MG-5	SJ05_G005	0.79	46.6	0.58	0.80	0.08	3.83	<dl	<dl	1.79	232	<dl
MG-5	SJ05_G006	<dl	4.24	0.14	<dl	0.41	6.12	<dl	<dl	<dl	31.3	<dl
MG-5	SJ05_G008	9.17	36.0	0.97	<dl	<dl	0.88	<dl	<dl	<dl	34.7	<dl
MG-5	SJ05_G010	0.05	0.34	<dl	0.11	<dl	6.31	<dl	<dl	<dl	24.9	<dl
MG-5	SJ05_G011	0.68	11.5	0.02	0.37	2087	2.40	<dl	0.01	0.13	131	0.76
MG-5	SJ05_G012	1.78	31.0	0.51	0.46	488	5.23	<dl	<dl	<dl	112	<dl
MG-5	SJ05_G014	3.51	30.4	0.55	0.17	0.07	0.86	0.78	0.09	<dl	39.4	<dl
MG-5	SJ05_G015	4.62	<dl	2.69	2.15	0.19	1.43	<dl	0.01	2.30	327	36.0
MG-5	SJ05_G016	0.04	0.46	0.06	0.11	<dl	3.91	<dl	47.0	0.02	12.6	<dl
MG-5	SJ05_G017	300	35.8	0.62	0.42	58.8	2.08	0.98	0.02	3.85	38.5	<dl
MG-5	SJ05_G018	44.5	123	1.28	0.26	0.07	0.72	3.73	0.04	2.35	140	10.3
MG-5	SJ05_G019	0.49	1.67	0.03	0.40	1859	0.60	<dl	<dl	<dl	94.7	<dl
MG-5	SJ05_G022	1.76	21.5	0.09	<dl	0.07	4.38	0.61	<dl	<dl	35.6	0.62
MG-5	SJ05_G023	2.77	79.7	1.09	0.85	4.16	2.02	3.01	0.05	1.44	93.3	<dl
MG-5	SJ05_G024	5.10	4.54	0.11	0.22	0.06	3.84	0.11	<dl	0.17	74.7	2.67
MG-5	SJ05_G026	0.63	14.7	0.08	4.44	0.57	0.62	<dl	<dl	0.36	27.3	<dl
MG-5	SJ05_G027	1.41	<dl	<dl	0.16	1444	0.34	<dl	<dl	0.05	21.7	0.92

Sample	Measurement	Y	Zr	Nb	Mo	Ag	Sn	Hf	Ta	W	Pb	Th
MG-5	SJ05_G028	0.62	40.9	0.16	0.18	<dl	0.63	<dl	<dl	0.27	44.6	2.47
MG-5	SJ05_G029	0.99	35.3	0.16	0.47	417	0.47	1.12	<dl	<dl	120	<dl
MG-5	SJ05_G030	39.4	0.28	0.08	<dl	<dl	<dl	<dl	<dl	<dl	10.6	8.39
MG-5	SJ05_G031	1.81	60.4	0.31	1.40	27.0	0.66	<dl	<dl	<dl	134	<dl
MG-5	SJ05_G032	<dl	8.08	0.03	0.54	<dl	0.60	<dl	0.01	<dl	4.25	<dl
MG-5	SJ05_G033	0.36	5.12	0.02	<dl	0.08	0.46	<dl	0.01	<dl	1.02	<dl
MG-5	SJ05_G034	1.66	4.70	0.19	0.24	0.25	2.45	<dl	0.01	0.48	45.5	<dl
MG-5	SJ05_G035	3.04	39.4	0.42	0.13	31.3	0.74	1.47	0.08	0.10	10.3	<dl
MG-5	SJ05_G036	0.35	12.7	0.25	0.34	30.1	0.66	0.58	<dl	<dl	105	2.46
MG-5	SJ05_G037	1.68	31.9	0.10	0.60	<dl	1.17	<dl	<dl	<dl	297	<dl
MG-5	SJ05_G038	0.45	<dl	0.03	0.57	0.06	4.67	<dl	<dl	<dl	128	<dl
MG-5	SJ05_G039	6.28	128	2.63	1.36	<dl	2.28	<dl	0.03	<dl	248	<dl
MG-5	SJ05_G040	<dl	178	3.69	1.60	0.10	0.93	8.35	0.10	<dl	214	34.2
MG-5	SJ05_G041	1.97	75.1	1.81	0.37	0.07	0.66	<dl	<dl	0.75	111	<dl
MG-5	SJ05_G042	0.99	16.4	0.93	0.24	0.16	0.87	2.18	0.01	<dl	73.1	<dl
MG-5	SJ05_G043	2.03	24.1	0.65	0.39	0.05	0.83	0.32	<dl	<dl	80.3	<dl

Sample	Measurement	Mg	Al	Si	Ca	Sc	Ti	V	Cr	Mn	Co	Ni	Cu	Zn	Ga	Ge
MG-6	SJ6_G001	73.3	316	12368	<dl	0.95	137	463	1165	311	124	238	10484	166	5.43	7.69
MG-6	SJ6_G002	60.7	213	3846	111	<dl	120	466	387	357	119	232	25558	155	4.32	6.34
MG-6	SJ6_G003	132	897	1767	<dl	0.67	138	470	30.5	367	116	224	1650	152	5.15	8.20
MG-6	SJ6_G004	20.9	99.8	878	<dl	0.65	119	437	136	269	118	223	16.4	129	5.34	7.00
MG-6	SJ6_G005	49.3	206	1191	<dl	<dl	150	486	156	379	123	239	57.1	171	5.07	8.17
MG-6	SJ6_G006	240	1240	21308	282	0.66	164	514	474	319	129	263	27117	474	6.87	9.32
MG-6	SJ6_G007	33.3	142	1276	523	<dl	149	517	134	305	127	261	11.6	160	6.88	34.0
MG-6	SJ6_G008	24.5	122	1247	<dl	0.60	100	445	325	276	114	221	281	139	3.71	7.14
MG-6	SJ6_G009	166	737	12765	699	<dl	780	494	297	402	121	228	9933	184	6.57	8.79
MG-6	SJ6_G010	42.5	197	21876	<dl	1.25	128	453	1446	389	112	210	2009	158	5.03	9.47
MG-6	SJ6_G011	27.7	157	415	<dl	<dl	115	460	143	249	126	246	3.6	141	3.74	7.57
MG-6	SJ6_G012	27.6	132	398	<dl	<dl	128	462	106	363	115	213	<dl	142	4.56	6.39
MG-6	SJ6_G013	88.1	232	3117	<dl	<dl	362	426	84.5	299	113	215	38667	212	4.50	8.23
MG-6	SJ6_G014	48.1	151	683	<dl	<dl	135	466	188	353	123	240	575	141	5.04	7.10
MG-6	SJ6_G015	77.9	380	1943	<dl	0.56	124	469	6785	328	133	265	2849	298	5.32	8.37
MG-6	SJ6_G016	38.6	150	1216	<dl	0.58	134	476	760	402	118	233	0.28	165	5.05	6.66
MG-6	SJ6_G017	81.0	607	1665	<dl	0.77	146	486	60.4	352	119	236	<dl	165	5.31	8.71
MG-6	SJ6_G018	76.3	189	8639	103	0.63	107	457	62.5	304	114	227	1561	143	5.18	6.87
MG-6	SJ6_G019	33.4	152	976	82.7	0.48	143	501	30.7	325	129	265	0.25	172	5.55	7.45

Sample	Measurement	Y	Zr	Nb	Mo	Ag	Sn	Hf	Ta	W	Pb	Th
MG-6	SJ6_G001	2.46	6.98	<dl	<dl	25.7	<dl	<dl	<dl	<dl	63.1	<dl
MG-6	SJ6_G002	1.82	0.61	<dl	0.76	54.8	<dl	0.07	<dl	1.42	108	<dl
MG-6	SJ6_G003	0.15	1.22	<dl	<dl	6.73	<dl	0.07	<dl	0.11	10.9	0.08
MG-6	SJ6_G004	<dl	1.19	<dl	<dl	<dl	3.16	0.06	<dl	<dl	2.19	<dl
MG-6	SJ6_G005	0.39	6.99	0.10	<dl	<dl	<dl	0.47	<dl	0.32	1.02	0.31
MG-6	SJ6_G006	3.07	22.7	0.27	0.66	72.9	<dl	0.46	<dl	<dl	52.2	<dl
MG-6	SJ6_G007	64.4	5.90	<dl	0.71	<dl	<dl	0.08	<dl	<dl	0.24	9.33
MG-6	SJ6_G008	0.05	0.40	<dl	<dl	4.38	<dl	0.05	<dl	<dl	3.73	<dl
MG-6	SJ6_G009	10.9	20.6	1.38	37.8	32.5	<dl	<dl	0.10	4.45	48.4	7.32
MG-6	SJ6_G010	0.13	<dl	0.10	0.61	6.89	<dl	0.05	<dl	<dl	10.1	<dl
MG-6	SJ6_G011	0.05	<dl	0.09	0.78	0.43	<dl	0.05	<dl	<dl	0.32	0.03
MG-6	SJ6_G012	0.07	0.17	<dl	<dl	<dl	<dl	<dl	<dl	0.07	<dl	<dl
MG-6	SJ6_G013	2.06	<dl	0.09	<dl	68.1	<dl	0.30	<dl	4.23	60.7	8.65
MG-6	SJ6_G014	3.63	81.5	0.08	0.68	1.35	<dl	2.17	<dl	<dl	4.11	2.60
MG-6	SJ6_G015	0.81	8.07	<dl	0.51	7.87	<dl	<dl	<dl	<dl	16.3	2.17
MG-6	SJ6_G016	<dl	7.21	0.07	<dl	0.36	<dl	<dl	<dl	<dl	<dl	<dl
MG-6	SJ6_G017	0.63	31.7	0.23	0.60	<dl	<dl	<dl	0.01	<dl	0.13	0.18
MG-6	SJ6_G018	0.80	2.57	<dl	<dl	5.76	<dl	0.05	<dl	<dl	12.4	1.74
MG-6	SJ6_G019	0.30	0.04	<dl	<dl	<dl	<dl	<dl	<dl	0.05	<dl	<dl

Sample	Measurement	Mg	Al	Si	Ca	Sc	Ti	V	Cr	Mn	Co	Ni	Cu	Zn	Ga	Ge
MG-10	SJ10_G001	80.8	637	2883	<dl	0.63	359	1051	505	1426	89.7	199	0.55	229	10.8	14.8
MG-10	SJ10_G002	91.1	731	11343	<dl	0.48	640	1146	255	1583	87.8	200	0.21	249	14.2	12.6
MG-10	SJ10_G003	288	2737	5931	<dl	0.90	251	877	398	1163	82.6	187	9.9	162	10.4	13.4
MG-10	SJ10_G004	66.4	703	2688	1874	0.43	734	860	494	1109	86.9	313	45.8	165	9.28	14.0
MG-10	SJ10_G005	178	800	3827	14338	3.55	195	803	916	1009	74.1	170	3.7	129	151	172
MG-10	SJ10_G006	94.2	1078	11001	11859	3.27	11461	864	272	1120	80.2	184	95.9	159	9.74	12.6
MG-10	SJ10_G007	189	1611	4640	317	1.39	283	858	270	976	79.9	193	5.1	143	10.1	12.3
MG-10	SJ10_G008	91.3	724	992	<dl	0.48	472	1066	258	1507	83.1	188	0.21	248	13.7	12.5
MG-10	SJ10_G009	920	9964	17014	78.7	3.34	278	809	732	1041	71.3	166	64.9	148	12.7	12.4
MG-10	SJ10_G010	92.0	781	1918	83.5	0.79	291	909	292	1228	79.4	178	2.0	177	10.8	11.5
MG-10	SJ10_G011	653	4448	9326	178	2.36	304	851	413	1095	77.0	164	31.9	160	11.6	10.4
MG-10	SJ10_G012	41.3	306	984	<dl	<dl	232	759	639	981	68.3	160	<dl	128	6.82	10.6
MG-10	SJ10_G013	40.9	307	1059	156	0.50	173	731	710	871	69.3	160	3.1	112	6.92	10.0
MG-10	SJ10_G014	426	2697	4593	780	0.79	272	832	356	1066	76.8	177	2.1	155	10.2	10.1
MG-10	SJ10_G015	1539	10406	26536	1361	24.0	423	860	532	1216	73.8	170	60.3	196	16.0	16.4
MG-10	SJ10_G016	497	3637	8369	3750	1.15	362	919	301	1414	76.3	176	284	201	12.4	9.30
MG-10	SJ10_G017	68.2	447	1159	<dl	0.24	191	759	535	1012	71.2	166	49.9	142	8.75	9.40
MG-10	SJ10_G018	276	3247	9130	4357	3.35	4508	802	386	1012	68.5	159	0.66	141	9.88	9.91
MG-10	SJ10_G019	858	4299	5868	233	0.67	386	712	612	945	66.3	151	0.20	133	7.26	10.0
MG-10	SJ10_G020	202	2288	4953	181	1.75	356	904	260	1224	74.0	170	0.44	197	11.1	9.37
MG-10	SJ10_G021	57.1	446	1053	157	0.38	189	700	379	915	69.6	159	2.8	125	8.72	8.72
MG-10	SJ10_G022	72.9	564	831	351	0.36	367	835	280	1198	71.5	173	0.52	188	11.1	4.81
MG-10	SJ10_G023	85.8	468	4434	283	7.55	160	667	834	875	62.1	153	5.2	115	6.00	9.21
MG-10	SJ10_G024	50.5	397	945	181	0.44	210	778	555	1038	68.8	162	<dl	143	7.58	8.57
MG-10	SJ10_G025	59.6	539	863	<dl	<dl	270	817	342	1071	66.0	150	<dl	162	8.86	7.75
MG-10	SJ10_G026	47.5	370	747	<dl	<dl	252	787	301	1051	67.3	156	76.6	155	8.63	7.87

Sample	Measurement	Mg	Al	Si	Ca	Sc	Ti	V	Cr	Mn	Co	Ni	Cu	Zn	Ga	Ge
MG-10	SJ10_G027	168	941	4308	163	3.01	318	876	352	1201	67.7	161	32.2	200	10.5	9.56
MG-10	SJ10_G028	74.9	545	836	57.5	0.53	412	875	294	1260	67.4	151	<dl	199	10.9	8.47
MG-10	SJ10_G029	59.9	463	720	87.6	0.45	324	851	262	1139	64.7	148	0.90	181	9.99	6.55
MG-10	SJ10_G030	104	806	1358	197	0.56	694	914	163	1370	70.0	165	0.98	222	4.76	7.46
MG-10	SJ10_G031	58.4	456	752	<dl	0.35	278	823	255	1084	67.5	149	<dl	166	9.31	8.29
MG-10	SJ10_G032	39.9	362	809	222	0.34	356	697	313	874	61.4	147	1.2	121	6.49	7.66
MG-10	SJ10_G033	77.7	513	2393	112	0.44	55.9	649	476	821	59.2	143	0.90	115	6.29	7.71
MG-10	SJ10_G034	53.4	435	787	296	0.46	318	753	200	973	63.4	147	0.50	149	8.76	6.95
MG-10	SJ10_G035	71.0	576	1530	132	0.74	216	674	418	914	59.9	133	21.9	132	7.61	7.67
MG-10	SJ10_G036	49.6	363	685	<dl	<dl	218	711	519	961	58.3	135	<dl	135	7.04	6.16
MG-10	SJ10_G037	50.3	325	808	<dl	0.70	191	680	373	869	59.1	127	0.32	125	7.32	7.29
MG-10	SJ10_G038	145	921	2137	632	3.14	245	695	323	933	63.1	169	37.0	139	8.12	6.87
MG-10	SJ10_G039	49.1	222	617	<dl	<dl	163	631	230	802	56.6	133	19.7	108	6.19	6.79
MG-10	SJ10_G040	49.1	434	746	280	<dl	210	667	205	858	61.5	142	6.6	128	7.67	6.81
MG-10	SJ10_G041	803	4093	5106	239	1.21	347	753	218	1036	63.0	141	6.7	173	9.66	7.19
MG-10	SJ10_G042	67.6	443	863	<dl	0.25	235	701	183	917	59.9	137	<dl	147	7.72	7.22
MG-10	SJ10_G043	77.3	655	1187	33.7	0.38	234	691	258	948	59.0	140	<dl	149	7.79	8.53
MG-10	SJ10_G044	66.0	565	693	33.7	0.43	364	778	133	1103	62.6	143	37.9	184	10.5	6.05
MG-10	SJ10_G045	230	1623	2641	<dl	0.51	316	753	191	1049	58.9	132	36.6	167	9.15	6.57
MG-10	SJ10_G046	438	2040	5705	626	18.4	227	630	341	845	55.5	132	8.1	119	8.13	13.3
MG-10	SJ10_G047	282	878	2678	214	2.02	312	725	316	1064	58.3	130	7.8	165	9.69	6.83
MG-10	SJ10_G048	143	544	1333	261	0.55	274	712	289	977	56.6	142	3.4	205	8.57	5.35
MG-10	SJ10_G049	303	1882	4726	123	0.67	243	653	229	962	54.7	123	118	145	8.64	6.10
MG-10	SJ10_G050	299	806	4702	577	3.98	127	521	571	681	48.3	116	9.4	89.3	5.28	6.78
MG-10	SJ10_G051	50.5	233	906	30.2	0.45	103	489	638	614	44.2	107	8.4	78.7	4.10	5.49
MG-10	SJ10_G052	316	1332	3475	1615	1.79	167	503	598	713	52.8	183	23.5	95.1	5.59	6.11

Sample	Measurement	Mg	Al	Si	Ca	Sc	Ti	V	Cr	Mn	Co	Ni	Cu	Zn	Ga	Ge
MG-10	SJ10_G053	40.6	296	777	211	0.61	128	544	570	718	49.1	124	1.2	96.5	5.05	5.69
MG-10	SJ10_G054	45.2	361	622	<dl	0.31	242	670	158	902	53.6	125	0.51	127	7.97	5.98
MG-10	SJ10_G055	43.4	365	646	<dl	0.24	170	592	317	785	49.9	121	0.41	119	6.45	5.83
MG-10	SJ10_G056	31.4	211	500	<dl	<dl	143	539	263	680	47.7	109	0.13	98.8	5.77	6.10
MG-10	SJ10_G057	115	965	1602	184	1.33	135	527	368	670	48.4	114	2.9	95.1	5.18	5.51
MG-10	SJ10_G058	64.2	401	738	53.9	0.24	169	557	416	744	48.6	112	7.0	113	6.61	5.52
MG-10	SJ10_G060	337	765	5103	779	0.33	279	653	129	931	54.3	127	3.7	156	9.50	6.71
MG-10	SJ10_G061	260	1878	10121	400	3.49	182	548	383	794	45.6	106	99.8	111	6.30	6.55
MG-10	SJ10_G062	66.3	431	881	32.7	0.73	273	630	170	918	53.1	121	6.9	154	8.07	5.14
MG-10	SJ10_G063	233	1143	2039	27.6	0.33	181	536	262	714	46.6	114	0.43	101	5.73	5.23
MG-10	SJ10_G064	34.9	393	831	336	1.09	161	557	376	716	47.4	112	0.51	107	5.98	5.60
MG-10	SJ10_G065	68.0	507	1175	247	1.02	230	594	199	807	49.9	115	2.9	125	7.05	4.91
MG-10	SJ10_G066	33.1	252	1359	186	<dl	148	548	296	708	47.8	111	0.75	100	5.53	5.59
MG-10	SJ10_G067	2223	1219	28344	6174	1.11	175	467	281	616	45.0	104	11.0	79.4	5.13	4.88
MG-10	SJ10_G068	211	500	2684	341	0.29	132	486	296	634	44.5	98.7	0.40	89.8	5.14	4.94
MG-10	SJ10_G069	83.3	573	60.2	61.9	0.32	281	619	187	861	48.8	117	14.7	169	8.02	5.21
MG-10	SJ10_G070	36.0	267	505	113	<dl	179	562	271	737	46.3	113	0.74	113	5.95	6.40
MG-10	SJ10_G071	25.3	197	475	39.1	0.23	134	494	142	624	47.6	105	0.09	84.4	5.44	4.97
MG-10	SJ10_G072	41.7	271	576	39.5	0.39	160	514	279	705	46.6	99.9	3.7	96.9	6.39	5.22
MG-10	SJ10_G073	19.5	141	426	23.1	0.20	94.3	429	441	570	41.8	99.3	0.64	69.7	3.98	4.91
MG-10	SJ10_G074	62.1	399	1392	164	1.63	171	522	317	668	45.8	111	4.9	102	5.22	5.32
MG-10	SJ10_G075	45.6	360	673	40.3	<dl	155	494	217	617	44.9	108	0.46	90.2	5.71	5.16
MG-10	SJ10_G076	46.5	377	531	212	0.23	250	583	168	800	47.3	112	0.72	135	7.89	4.70
MG-10	SJ10_G077	121	1098	1945	37.8	0.31	162	530	239	716	45.3	103	36.8	103	6.05	5.29
MG-10	SJ10_G078	36.3	285	665	<dl	0.16	118	471	440	620	41.0	99.6	0.57	83.6	4.36	4.77
MG-10	SJ10_G079	294	2359	3955	250	0.56	430	592	184	822	46.5	114	1.3	126	8.39	4.70

Sample	Measurement	Mg	Al	Si	Ca	Sc	Ti	V	Cr	Mn	Co	Ni	Cu	Zn	Ga	Ge
MG-10	SJ10_G080	57.1	495	741	<dl	0.30	210	608	188	774	48.1	111	0.08	122	7.14	4.12
MG-10	SJ10_G081	91.6	450	749	<dl	0.19	131	464	293	633	42.9	102	0.17	92.0	4.89	5.17
MG-10	SJ10_G082	41.7	339	795	95.3	0.46	104	417	336	555	40.3	91.3	11.5	75.1	4.30	4.01
MG-10	SJ10_G083	<dl	270	560	<dl	0.35	139	492	256	631	42.9	96.0	<dl	94.3	4.91	4.36
MG-10	SJ10_G084	31.2	258	579	37.3	0.15	192	489	332	632	44.0	99.0	<dl	90.8	4.28	3.84
MG-10	SJ10_G085	720	6539	10805	351	1.83	560	538	158	717	44.7	103	0.46	121	9.13	4.70
MG-10	SJ10_G086	36.1	307	73.6	63.1	0.17	171	511	103	667	44.7	107	1.1	103	6.47	3.75
MG-10	SJ10_G087	48.7	326	558	<dl	0.30	188	514	186	682	43.9	104	1.4	106	5.92	4.18
MG-10	SJ10_G088	31.5	288	536	97.5	0.47	174	476	290	639	41.8	101	2.2	91.5	4.88	4.01
MG-10	SJ10_G089	46.0	391	498	<dl	0.22	267	559	113	803	43.3	100	1.0	138	7.64	4.60
MG-10	SJ10_G090	99.5	1009	1480	<dl	0.38	209	530	152	729	43.3	100	0.11	113	6.73	4.76
MG-10	SJ10_G091	33.6	228	499	<dl	0.14	109	441	322	572	40.2	91.7	0.17	80.2	4.04	3.56
MG-10	SJ10_G092	40.3	358	810	22.4	0.29	129	451	284	592	39.8	92.5	<dl	85.8	4.67	4.29
MG-10	SJ10_G093	35.8	269	391	<dl	0.21	197	553	271	733	41.9	97.2	0.07	119	6.38	4.09
MG-10	SJ10_G094	52.8	488	724	<dl	0.28	208	531	137	730	42.4	95.9	<dl	117	6.68	4.33
MG-10	SJ10_G095	58.5	558	886	<dl	0.37	179	499	182	674	40.6	97.1	<dl	107	6.10	3.82
MG-10	SJ10_G096	67.9	778	1182	172	0.77	165	493	181	633	40.3	95.8	0.08	99.6	5.96	4.39
MG-10	SJ10_G097	82.2	808	1314	49.7	0.98	139	438	196	584	40.1	91.1	1.4	87.9	6.18	3.90
MG-10	SJ10_G098	57.3	933	574	350	0.42	312	560	257	846	44.8	172	14.2	134	7.37	3.35
MG-10	SJ10_G099	59.7	515	613	<dl	0.44	277	550	116	795	41.5	98.6	0.08	137	7.44	3.78
MG-10	SJ10_G100	40.5	494	818	259	0.70	119	428	141	584	38.5	87.9	0.20	79.9	4.68	4.72
MG-10	SJ10_G101	22.8	198	464	109	0.18	101	402	320	526	36.9	91.8	0.79	73.6	3.41	4.22
MG-10	SJ10_G102	42.4	301	608	<dl	0.24	99.9	397	261	516	36.5	88.2	0.13	69.9	3.62	3.70
MG-10	SJ10_G103	46.6	361	804	56.3	0.43	195	455	180	595	38.1	88.0	0.07	87.4	4.95	3.93
MG-10	SJ10_G104	385	4404	7045	27.8	1.28	202	487	161	638	39.2	91.4	0.12	104	8.14	3.86
MG-10	SJ10_G105	54.6	386	579	<dl	0.80	233	517	151	757	41.6	97.8	12.3	122	7.71	4.45

Sample	Measurement	Mg	Al	Si	Ca	Sc	Ti	V	Cr	Mn	Co	Ni	Cu	Zn	Ga	Ge
MG-10	SJ10_G106	32.4	223	387	33.8	0.15	140	432	160	575	39.2	86.1	0.32	84.5	5.12	3.82
MG-10	SJ10_G107	66.7	436	482	76.6	0.22	354	517	75.3	767	40.3	92.3	0.15	171	7.40	3.94
MG-10	SJ10_G108	33.3	273	395	<dl	0.22	179	486	151	647	39.0	92.5	<dl	103	5.47	3.68
MG-10	SJ10_G109	34.2	408	26369	94.5	0.18	112	400	339	528	36.2	111	3.6	76.7	3.95	4.11
MG-10	SJ10_G110	48.7	364	445	60.8	0.29	325	509	103	757	41.9	89.8	0.13	128	7.66	3.92
MG-10	SJ10_G111	557	6384	10119	<dl	1.62	201	448	211	588	36.9	90.0	14.5	94.4	7.74	4.08
MG-10	SJ10_G112	47.7	324	419	<dl	<dl	208	513	184	707	39.4	93.0	<dl	117	5.79	3.63
MG-10	SJ10_G113	123	960	1830	84.8	0.32	155	446	164	591	35.5	87.4	0.09	90.5	5.16	3.96
MG-10	SJ10_G114	34.2	255	440	<dl	0.25	174	480	227	653	37.7	86.5	0.10	102	5.43	3.81
MG-10	SJ10_G115	32.2	263	498	<dl	0.39	120	406	292	535	34.4	80.3	40.1	83.9	4.43	3.38
MG-10	SJ10_G116	48.6	401	630	<dl	0.33	219	480	137	682	38.7	94.1	5.2	114	6.46	3.34
MG-10	SJ10_G117	25.7	220	492	<dl	0.13	103	391	385	513	33.4	78.1	0.09	70.4	3.77	3.65
MG-10	SJ10_G118	37.6	345	682	50.5	0.24	120	412	178	522	36.4	84.2	20.2	77.9	4.91	4.28
MG-10	SJ10_G119	29.1	237	341	23.1	0.25	158	438	164	589	36.5	85.0	1.8	91.1	5.07	3.25

Sample	Measurement	Y	Zr	Nb	Mo	Ag	Sn	Hf	Ta	W	Pb	Th
MG-10	SJ10_G001	<dl	144	0.06	<dl	<dl	1.05	5.06	<dl	<dl	0.19	<dl
MG-10	SJ10_G002	0.73	35.9	<dl	0.16	<dl	0.80	<dl	0.01	<dl	0.05	0.10
MG-10	SJ10_G003	0.20	<dl	0.07	<dl	<dl	0.71	<dl	<dl	<dl	0.32	<dl
MG-10	SJ10_G004	3.26	25.6	1.07	0.97	<dl	1.29	1.12	0.09	0.22	3.24	0.70
MG-10	SJ10_G005	36.2	1252	0.08	0.32	0.53	5.10	22.0	<dl	0.07	1.77	11.0
MG-10	SJ10_G006	134	149	36.6	0.28	<dl	5.66	<dl	<dl	0.42	3.24	<dl
MG-10	SJ10_G007	5.39	213	0.09	0.23	<dl	2.89	4.93	<dl	0.08	5.07	<dl
MG-10	SJ10_G008	0.72	30.5	0.03	0.20	<dl	<dl	<dl	<dl	<dl	0.21	0.44
MG-10	SJ10_G009	6.77	288	0.42	0.17	<dl	1.03	7.74	0.03	<dl	2.06	<dl
MG-10	SJ10_G010	10.0	<dl	0.07	0.35	0.22	0.88	<dl	<dl	0.06	5.32	2.53
MG-10	SJ10_G011	9.70	1392	0.31	0.37	<dl	2.32	<dl	<dl	<dl	1.38	3.84
MG-10	SJ10_G012	<dl	36.6	<dl	<dl	<dl	1.09	2.21	0.01	<dl	0.07	0.36
MG-10	SJ10_G013	2.32	81.3	0.04	0.30	0.31	4.16	<dl	<dl	0.05	9.89	0.83
MG-10	SJ10_G014	1.50	74.1	0.08	0.39	0.11	1.05	<dl	<dl	0.09	0.67	0.49
MG-10	SJ10_G015	120	3685	0.78	0.50	1.35	10.9	<dl	0.03	0.77	35.3	73.4
MG-10	SJ10_G016	<dl	42.6	1.17	0.76	0.31	2.62	1.29	<dl	<dl	0.72	0.65
MG-10	SJ10_G017	0.92	39.0	0.03	0.19	2012	4.08	<dl	<dl	<dl	0.27	0.54
MG-10	SJ10_G018	39.4	669	14.4	0.30	1216	2.39	<dl	<dl	<dl	3.32	4.62
MG-10	SJ10_G019	1.50	24.8	0.47	<dl	<dl	0.83	<dl	<dl	<dl	1.08	<dl
MG-10	SJ10_G020	11.7	<dl	0.12	<dl	0.19	1.92	<dl	<dl	<dl	1.15	<dl
MG-10	SJ10_G021	2.64	87.2	0.02	0.15	0.52	1.15	2.39	<dl	<dl	1.21	<dl
MG-10	SJ10_G022	3.10	137	0.09	0.15	<dl	0.96	3.41	0.01	<dl	0.15	<dl
MG-10	SJ10_G023	81.1	6068	0.39	0.46	1519	1.87	<dl	<dl	<dl	49.7	<dl
MG-10	SJ10_G024	<dl	92.9	0.03	<dl	42.8	1.22	2.86	<dl	<dl	0.73	<dl
MG-10	SJ10_G025	<dl	104	0.02	<dl	523	<dl	<dl	<dl	<dl	<dl	0.47
MG-10	SJ10_G026	0.62	35.9	<dl	0.16	<dl	0.48	<dl	<dl	0.03	0.07	0.16

Sample	Measurement	Y	Zr	Nb	Mo	Ag	Sn	Hf	Ta	W	Pb	Th
MG-10	SJ10_G027	14.5	393	0.09	<dl	1.46	2.79	<dl	0.01	<dl	34.0	<dl
MG-10	SJ10_G028	1.43	85.4	0.02	0.12	<dl	0.77	1.78	<dl	<dl	0.25	0.17
MG-10	SJ10_G029	2.07	122	0.02	<dl	669	<dl	<dl	<dl	<dl	0.10	<dl
MG-10	SJ10_G030	2.96	<dl	0.52	<dl	1457	2.43	0.94	<dl	<dl	0.23	0.37
MG-10	SJ10_G031	1.90	<dl	0.03	0.34	0.09	1.01	<dl	<dl	<dl	0.06	<dl
MG-10	SJ10_G032	2.92	54.9	0.47	<dl	<dl	0.59	<dl	0.06	<dl	0.14	<dl
MG-10	SJ10_G033	2.15	81.1	<dl	<dl	<dl	0.56	<dl	<dl	0.02	3.56	1.55
MG-10	SJ10_G034	<dl	94.2	<dl	<dl	<dl	0.99	<dl	<dl	0.05	0.21	<dl
MG-10	SJ10_G035	<dl	71.8	0.12	0.17	<dl	0.92	1.55	<dl	<dl	2.93	2.59
MG-10	SJ10_G036	0.96	38.8	0.03	0.17	<dl	0.70	0.79	0.00	<dl	0.04	0.09
MG-10	SJ10_G037	5.09	349	0.44	<dl	<dl	0.80	<dl	<dl	<dl	0.24	<dl
MG-10	SJ10_G038	<dl	614	0.20	0.55	0.53	9.89	<dl	0.02	<dl	6.04	<dl
MG-10	SJ10_G039	1.04	4.13	0.03	<dl	<dl	0.49	<dl	<dl	<dl	0.04	<dl
MG-10	SJ10_G040	0.31	14.3	<dl	<dl	0.17	0.69	<dl	0.01	0.03	0.09	0.09
MG-10	SJ10_G041	<dl	75.1	0.04	<dl	0.87	2.73	<dl	<dl	<dl	0.71	0.78
MG-10	SJ10_G042	0.64	26.7	0.03	<dl	<dl	0.71	<dl	<dl	<dl	0.04	0.08
MG-10	SJ10_G043	3.33	79.8	0.03	0.15	<dl	0.65	<dl	<dl	<dl	2.19	2.77
MG-10	SJ10_G044	<dl	28.0	<dl	<dl	<dl	0.90	<dl	<dl	<dl	0.10	0.19
MG-10	SJ10_G045	1.85	102	0.08	<dl	<dl	<dl	1.92	<dl	<dl	12.6	0.25
MG-10	SJ10_G046	169	6308	0.78	0.42	1.20	6.79	<dl	<dl	<dl	101	39.4
MG-10	SJ10_G047	18.6	646	0.11	<dl	0.13	3.14	10.6	0.01	<dl	14.0	<dl
MG-10	SJ10_G048	2.15	68.2	<dl	<dl	83.1	3.79	1.19	<dl	<dl	1.41	0.64
MG-10	SJ10_G049	0.46	<dl	0.10	0.40	0.61	3.08	<dl	<dl	0.12	0.45	<dl
MG-10	SJ10_G050	<dl	851	0.11	<dl	0.17	3.51	<dl	<dl	<dl	63.8	<dl
MG-10	SJ10_G051	2.60	113	0.02	<dl	1175	1.13	<dl	<dl	0.02	2.44	<dl
MG-10	SJ10_G052	7.94	220	0.07	2.01	0.32	4.46	13.1	<dl	<dl	22.2	<dl

Sample	Measurement	Y	Zr	Nb	Mo	Ag	Sn	Hf	Ta	W	Pb	Th
MG-10	SJ10_G053	<dl	213	0.03	<dl	<dl	0.52	7.52	<dl	<dl	0.15	<dl
MG-10	SJ10_G054	0.42	23.4	<dl	0.61	<dl	0.86	0.76	<dl	<dl	0.08	<dl
MG-10	SJ10_G055	0.62	32.6	<dl	<dl	0.09	0.51	0.82	0.00	<dl	0.06	<dl
MG-10	SJ10_G056	0.84	59.0	0.02	<dl	<dl	0.42	1.80	<dl	<dl	3.24	<dl
MG-10	SJ10_G057	<dl	490	0.04	<dl	0.24	1.22	14.2	<dl	<dl	6.20	<dl
MG-10	SJ10_G058	<dl	147	0.04	0.11	4.68	1.14	<dl	<dl	<dl	1.13	<dl
MG-10	SJ10_G060	2.55	60.6	<dl	0.26	0.40	7.86	<dl	<dl	<dl	0.43	0.44
MG-10	SJ10_G061	21.9	<dl	0.13	<dl	0.22	2.45	<dl	<dl	<dl	5.72	8.83
MG-10	SJ10_G062	6.01	374	0.10	<dl	0.09	1.09	11.8	<dl	<dl	0.30	2.45
MG-10	SJ10_G063	<dl	47.6	0.09	<dl	0.09	0.40	0.79	<dl	0.03	0.14	<dl
MG-10	SJ10_G064	7.09	239	0.05	<dl	0.10	0.78	8.31	<dl	<dl	8.40	<dl
MG-10	SJ10_G065	7.98	257	0.09	0.12	0.15	0.90	<dl	<dl	<dl	3.58	3.53
MG-10	SJ10_G066	<dl	24.9	<dl	<dl	<dl	3.64	0.36	<dl	<dl	0.09	<dl
MG-10	SJ10_G067	5.39	194	0.10	<dl	0.47	7.08	<dl	<dl	<dl	1.69	<dl
MG-10	SJ10_G068	0.99	54.0	0.03	<dl	<dl	1.70	<dl	<dl	<dl	0.57	0.35
MG-10	SJ10_G069	<dl	29.2	0.02	0.25	58.7	2.84	0.91	<dl	<dl	0.80	<dl
MG-10	SJ10_G070	0.47	41.2	<dl	0.12	<dl	<dl	<dl	0.00	<dl	0.08	0.09
MG-10	SJ10_G071	0.47	32.0	<dl	0.21	0.07	0.35	<dl	<dl	<dl	11.7	<dl
MG-10	SJ10_G072	3.04	141	0.02	<dl	<dl	0.63	4.45	<dl	<dl	0.20	<dl
MG-10	SJ10_G073	0.50	28.9	<dl	0.13	1633	0.63	0.89	<dl	<dl	0.19	<dl
MG-10	SJ10_G074	7.07	241	0.15	<dl	22.7	1.41	6.42	<dl	0.05	3.68	<dl
MG-10	SJ10_G075	<dl	20.9	0.05	0.18	0.08	0.73	<dl	0.00	0.83	0.07	<dl
MG-10	SJ10_G076	0.48	40.4	<dl	<dl	0.08	0.84	1.14	<dl	<dl	0.12	<dl
MG-10	SJ10_G077	<dl	429	0.04	<dl	872	1.95	1.52	0.00	<dl	0.15	<dl
MG-10	SJ10_G078	0.72	34.7	<dl	<dl	<dl	11.1	<dl	<dl	<dl	0.08	<dl
MG-10	SJ10_G079	<dl	<dl	0.44	0.12	0.08	0.68	3.68	<dl	<dl	0.27	0.57

Sample	Measurement	Y	Zr	Nb	Mo	Ag	Sn	Hf	Ta	W	Pb	Th
MG-10	SJ10_G080	0.08	2.59	<dl	<dl	0.07	0.67	<dl	<dl	<dl	0.09	<dl
MG-10	SJ10_G081	0.23	14.1	<dl	0.19	<dl	0.34	<dl	0.00	<dl	0.10	<dl
MG-10	SJ10_G082	<dl	104	0.04	0.19	0.11	7.76	<dl	0.00	<dl	0.99	<dl
MG-10	SJ10_G083	1.90	98.5	0.03	<dl	0.07	0.49	2.83	<dl	<dl	0.07	0.85
MG-10	SJ10_G084	0.96	21.1	0.20	<dl	0.09	0.51	<dl	<dl	<dl	0.17	0.10
MG-10	SJ10_G085	2.71	12.8	1.35	<dl	<dl	1.45	0.33	0.14	<dl	0.52	<dl
MG-10	SJ10_G086	<dl	7.29	<dl	<dl	0.12	0.37	<dl	<dl	<dl	0.18	0.07
MG-10	SJ10_G087	0.73	<dl	0.02	0.21	<dl	0.49	<dl	<dl	<dl	0.13	0.13
MG-10	SJ10_G088	<dl	149	0.08	0.10	1757	0.48	<dl	<dl	<dl	0.16	<dl
MG-10	SJ10_G089	0.54	<dl	0.02	<dl	0.07	0.95	0.46	316	<dl	12.6	<dl
MG-10	SJ10_G090	0.25	11.6	0.04	0.09	0.06	0.55	<dl	<dl	<dl	17.2	<dl
MG-10	SJ10_G091	0.51	40.5	<dl	0.12	<dl	<dl	<dl	30.0	<dl	0.08	0.44
MG-10	SJ10_G092	<dl	105	0.06	0.10	<dl	<dl	1.97	<dl	<dl	0.03	<dl
MG-10	SJ10_G093	<dl	24.5	<dl	0.15	27.1	0.58	<dl	<dl	<dl	0.02	<dl
MG-10	SJ10_G094	<dl	14.5	0.02	0.13	<dl	0.42	0.56	<dl	<dl	0.07	<dl
MG-10	SJ10_G095	<dl	62.3	0.03	<dl	0.07	0.44	<dl	<dl	<dl	0.11	<dl
MG-10	SJ10_G096	3.13	90.2	0.04	<dl	0.07	0.54	<dl	<dl	<dl	0.81	<dl
MG-10	SJ10_G097	<dl	<dl	0.04	<dl	0.17	0.86	3.32	<dl	0.06	2.73	<dl
MG-10	SJ10_G098	0.68	24.2	0.15	1.30	<dl	0.97	<dl	<dl	<dl	0.37	0.61
MG-10	SJ10_G099	1.19	57.2	0.04	0.13	0.08	0.63	2.78	0.00	<dl	0.09	<dl
MG-10	SJ10_G100	2.48	18.8	0.02	0.09	<dl	0.50	0.50	0.00	<dl	0.78	5.89
MG-10	SJ10_G101	1.96	87.0	<dl	0.09	505	0.67	<dl	<dl	<dl	0.10	<dl
MG-10	SJ10_G102	2.19	<dl	<dl	0.12	0.05	<dl	2.83	0.00	<dl	0.09	0.39
MG-10	SJ10_G103	3.40	183	0.05	0.09	0.08	0.52	<dl	<dl	<dl	0.15	1.09
MG-10	SJ10_G104	0.33	<dl	0.16	0.12	<dl	0.42	<dl	<dl	<dl	4.45	<dl
MG-10	SJ10_G105	<dl	135	0.07	0.14	0.10	0.82	2.95	<dl	<dl	0.19	<dl

Sample	Measurement	Y	Zr	Nb	Mo	Ag	Sn	Hf	Ta	W	Pb	Th
MG-10	SJ10_G106	0.30	17.7	<dl	0.07	<dl	0.48	<dl	<dl	<dl	0.05	<dl
MG-10	SJ10_G107	<dl	<dl	0.26	0.09	0.06	0.65	<dl	0.03	<dl	0.18	0.45
MG-10	SJ10_G108	0.14	<dl	0.02	<dl	0.06	<dl	1.00	0.00	<dl	0.03	<dl
MG-10	SJ10_G109	<dl	20.1	0.03	0.40	0.07	0.60	0.69	0.00	<dl	0.20	<dl
MG-10	SJ10_G110	1.29	30.5	0.16	<dl	0.06	0.75	<dl	0.01	<dl	0.08	0.09
MG-10	SJ10_G111	<dl	21.5	0.18	0.10	<dl	0.64	0.77	<dl	0.16	1.80	0.21
MG-10	SJ10_G112	0.06	6.82	0.82	0.15	0.07	5.19	<dl	<dl	<dl	0.12	<dl
MG-10	SJ10_G113	0.83	<dl	0.04	0.09	0.08	0.48	<dl	<dl	<dl	1.00	2.14
MG-10	SJ10_G114	0.88	36.2	<dl	0.09	<dl	0.66	<dl	<dl	<dl	0.05	0.49
MG-10	SJ10_G115	<dl	96.7	0.01	<dl	<dl	0.35	<dl	<dl	<dl	0.87	0.63
MG-10	SJ10_G116	1.65	43.7	0.04	0.09	<dl	0.71	<dl	<dl	<dl	1.56	<dl
MG-10	SJ10_G117	1.95	68.3	0.04	<dl	<dl	0.63	<dl	<dl	<dl	0.06	0.22
MG-10	SJ10_G118	0.50	33.8	0.26	<dl	<dl	0.60	1.05	0.00	0.03	0.04	0.14
MG-10	SJ10_G119	0.71	42.9	0.03	0.08	<dl	0.43	1.29	<dl	<dl	0.06	0.24

Sample	Measurement	Mg	Al	Si	Ca	Sc	Ti	V	Cr	Mn	Co	Ni	Cu	Zn	Ga	Ge
MG-12	SJ12_G001	143	550	3481	213	1.22	738	697	291	660	79.6	139	2655	233	6.27	13.0
MG-12	SJ12_G002	173	1296	3537	186	<dl	453	867	94.2	1211	88.9	132	391	253	15.4	11.1
MG-12	SJ12_G003	195	664	2590	172	0.64	656	908	34.9	1189	83.4	143	933	234	15.7	14.2
MG-12	SJ12_G004	76.4	453	1558	244	0.62	619	804	178	1024	85.1	133	125	216	12.4	9.43
MG-12	SJ12_G005	366	1214	2961	135	0.84	750	675	609	524	79.3	141	584	129	7.03	11.1
MG-12	SJ12_G006	356	2666	6343	360	1.98	1465	678	669	624	77.8	144	1892	144	8.92	12.6
MG-12	SJ12_G007	142	700	2532	116	1.13	717	794	13.2	1103	84.8	124	1053	252	16.1	10.9
MG-12	SJ12_G008	173	524	3157	146	1.19	1155	764	353	899	69.7	127	1752	156	8.85	14.2
MG-12	SJ12_G009	234	582	3784	236	7.42	676	738	344	751	64.6	140	1434	149	7.14	13.9
MG-12	SJ12_G010	539	1364	4768	331	1.40	2208	836	75.5	845	81.5	140	3048	240	9.89	23.3
MG-12	SJ12_G011	135	836	2545	133	<dl	514	902	80.2	1128	83.2	140	578	252	14.4	13.9
MG-12	SJ12_G012	263	1911	3608	<dl	1.24	513	835	114	1397	88.8	133	869	284	18.0	11.4
MG-12	SJ12_G013	145	776	2255	166	0.68	721	884	15.5	1217	77.8	137	1061	245	14.2	12.9
MG-12	SJ12_G014	244	1992	5152	313	1.29	1069	743	508	755	78.1	139	1181	182	8.45	16.7
MG-12	SJ12_G015	225	1020	3609	158	0.74	1165	853	93.3	1206	84.6	130	2323	248	14.0	14.6
MG-12	SJ12_G016	181	1109	3774	244	0.68	1150	756	342	848	75.4	144	1994	146	7.50	16.2
MG-12	SJ12_G017	139	716	3715	608	0.86	2459	784	654	929	105	144	1520	144	7.69	16.5
MG-12	SJ12_G018	81.5	604	2443	265	<dl	405	711	8811	1469	101	141	797	3581	8.95	11.7
MG-12	SJ12_G019	1005	6035	12385	175	2.51	1029	822	85.0	839	77.0	143	1328	162	15.7	22.5
MG-12	SJ12_G020	116	479	1938	131	0.78	1977	746	670	886	98.2	132	1485	140	7.74	14.0
MG-12	SJ12_G021	96.8	302	2136	109	0.74	344	689	153	611	73.5	135	674	130	7.29	9.97
MG-12	SJ12_G022	125	513	2474	109	0.65	534	734	300	740	99.1	147	1033	150	8.50	10.9

Sample	Measurement	Y	Zr	Nb	Mo	Ag	Sn	Hf	Ta	W	Pb	Th
MG-12	SJ12_G001	21.4	287	3.55	5.88	3.86	<dl	<dl	0.14	2.42	649	<dl
MG-12	SJ12_G002	1.83	46.1	0.39	2.06	<dl	<dl	1.01	<dl	0.84	165	1.02
MG-12	SJ12_G003	2.08	37.5	1.50	11.2	0.45	<dl	1.07	0.03	4.20	556	6.26
MG-12	SJ12_G004	2.79	16.4	0.93	0.77	<dl	<dl	<dl	0.08	<dl	89.8	0.96
MG-12	SJ12_G005	11.0	237	2.44	1.27	<dl	<dl	5.88	0.19	<dl	362	<dl
MG-12	SJ12_G006	17.6	408	6.08	5.39	0.36	1.60	<dl	0.51	1.80	649	<dl
MG-12	SJ12_G007	3.55	46.2	1.69	10.2	<dl	<dl	<dl	<dl	3.06	520	<dl
MG-12	SJ12_G008	5.40	75.1	4.26	15.9	<dl	1.58	2.80	0.26	4.40	1031	43.9
MG-12	SJ12_G009	3.75	39.5	2.23	13.8	0.46	<dl	<dl	<dl	3.80	763	<dl
MG-12	SJ12_G010	17.6	203	9.74	4.68	1.36	3.21	6.41	0.60	<dl	1337	83.3
MG-12	SJ12_G011	1.90	15.7	0.87	6.72	<dl	<dl	<dl	<dl	<dl	310	3.09
MG-12	SJ12_G012	4.83	60.2	1.18	5.08	0.50	<dl	<dl	<dl	1.69	320	3.66
MG-12	SJ12_G013	4.08	30.8	1.87	24.3	0.40	1.88	1.36	0.04	<dl	543	9.56
MG-12	SJ12_G014	13.4	152	3.02	7.64	0.57	<dl	<dl	<dl	1.65	1047	<dl
MG-12	SJ12_G015	10.1	88.1	4.28	10.4	0.75	<dl	<dl	<dl	<dl	764	<dl
MG-12	SJ12_G016	9.96	61.5	4.13	9.12	0.46	<dl	3.21	<dl	<dl	724	<dl
MG-12	SJ12_G017	6.26	82.9	9.05	8.58	<dl	<dl	<dl	0.58	3.10	1240	93.6
MG-12	SJ12_G018	2.50	31.8	1.07	7.04	0.37	<dl	1.02	0.09	1.91	463	<dl
MG-12	SJ12_G019	16.0	<dl	4.27	3.19	0.57	2.05	4.00	0.24	1.85	498	<dl
MG-12	SJ12_G020	5.22	79.1	8.54	8.51	0.47	1.76	<dl	0.47	3.12	1143	85.8
MG-12	SJ12_G021	1.98	18.6	0.82	6.64	<dl	<dl	0.71	0.03	<dl	487	<dl
MG-12	SJ12_G022	5.14	22.2	1.50	6.52	0.56	1.98	1.41	0.08	1.68	731	14.8

Sample	Measurement	Mg	Al	Si	Ca	Sc	Ti	V	Cr	Mn	Co	Ni	Cu	Zn	Ga	Ge
MG-13	SJ13_G001	442	1096	5148	429	1.64	159	350	2252	1177	81.0	182	957	187	5.34	9.73
MG-13	SJ13_G002	200	950	4312	446	1.41	102	366	13360	1722	95.7	214	6380	312	6.86	9.40
MG-13	SJ13_G003	352	1076	2782	547	0.70	131	321	59.9	1343	80.9	164	168	163	4.73	5.08
MG-13	SJ13_G005	2398	20642	76912	291	6.45	362	260	20.8	946	86.7	155	20.7	98.1	16.7	2.81
MG-13	SJ13_G007	160	907	2467	172	0.78	104	322	1003	1149	75.8	179	37.5	140	4.75	5.08
MG-13	SJ13_G009	90.3	430	<dl	308	0.93	104	289	<dl	1338	85.1	150	191	174	5.65	12.8
MG-13	SJ13_G012	244	367	4237	1757	0.50	2258	300	320	1107	74.6	172	71.2	127	4.28	6.23
MG-13	SJ13_G014	2867	3981	23543	21089	5.70	22171	341	380	1422	89.1	159	470	204	6.95	30.4
MG-13	SJ13_G017	13935	13691	38744	17083	9.41	18752	360	709	2350	93.0	176	2688	331	23.3	107

Sample	Measurement	Y	Zr	Nb	Mo	Ag	Sn	Hf	Ta	W	Pb	Th
MG-13	SJ13_G001	7.42	14.2	0.20	3.79	26.2	<dl	0.30	0.02	3.41	920	4.08
MG-13	SJ13_G002	7.50	4.75	0.31	2.07	2406	<dl	<dl	<dl	<dl	490	2.96
MG-13	SJ13_G003	1.12	4.57	0.24	0.78	1.89	<dl	<dl	<dl	0.30	19.3	<dl
MG-13	SJ13_G005	0.96	11.3	1.18	<dl	<dl	3.33	0.47	<dl	<dl	38.9	6.67
MG-13	SJ13_G007	2.01	5.60	0.18	<dl	0.40	<dl	0.16	<dl	0.40	154	<dl
MG-13	SJ13_G009	6.36	9.32	0.12	2.64	0.36	<dl	0.40	0.01	0.96	290	<dl
MG-13	SJ13_G012	23.2	7.61	7.29	1.31	<dl	1.59	<dl	0.94	0.42	77.0	17.3
MG-13	SJ13_G014	229	42.4	55.6	1.48	0.44	6.64	1.78	<dl	<dl	377	<dl
MG-13	SJ13_G017	171	141	66.6	3.53	47.6	12.1	6.27	3.40	5.76	201	<dl

Sample	Measurement	Mg	Al	Si	Ca	Sc	Ti	V	Cr	Mn	Co	Ni	Cu	Zn	Ga	Ge
MG-14	14_G001	522	3762	42318	1603	\	804	25.8	1149	7590	49.8	261	19385	74.6	11.2	22.6
MG-14	14_G002	1116	7224	41450	12015	\	151	27.3	2661	9942	41.7	470	17104	206	13.4	16.0
MG-14	14_G003	183	597	2769	208	\	90.8	480	6.80	251	87.4	225	42.7	127	3.61	9.51
MG-14	14_G004	59.8	226	5126	<dl	\	40.4	394	156	201	83.0	233	6.8	93.8	2.96	5.59
MG-14	14_G005	78.0	518	2391	<dl	\	61.8	462	1426	214	86.9	236	16.6	104	3.20	5.73
MG-14	14_G006	71.6	224	888	<dl	\	117	536	57.3	387	98.3	260	13.3	175	4.42	4.72
MG-14	14_G007	55.1	235	989	<dl	\	95.2	549	172	363	97.3	275	16.9	177	4.87	6.18
MG-14	14_G008	66.6	810	3174	<dl	\	241	525	306	318	112	241	32.5	160	4.13	7.87
MG-14	14_G009	35.3	129	591	<dl	\	52.0	456	449	227	88.8	225	5.1	137	3.05	4.95
MG-14	14_G010	73.1	298	1255	<dl	\	80.0	555	37.3	285	91.7	250	10.5	144	3.67	3.71
MG-14	14_G011	1265	7478	27711	250	\	832	402	333	349	81.3	206	53.8	146	6.25	7.85
MG-14	14_G012	61.6	599	2759	124	\	99.3	483	503	235	90.1	217	17.1	119	3.26	6.02
MG-14	14_G013	57.6	1049	8033	221	\	131	449	23.1	224	83.2	262	33.3	131	3.37	5.44
MG-14	14_G014	204	728	3759	385	\	948	514	26.9	315	102	260	75.9	191	4.77	12.0
MG-14	14_G015	65.9	340	1288	<dl	\	69.6	460	88.4	279	83.9	210	23.5	139	3.18	5.43
MG-14	14_G016	48.1	131	813	<dl	\	51.7	539	24.5	250	95.7	233	9.1	135	3.52	4.38
MG-14	14_G017	175	1081	94857	159	\	98.2	363	470	188	78.6	220	3.5	79.4	3.58	3.86
MG-14	14_G018	113	839	49297	139	\	92.0	432	520	197	95.0	222	29.4	93.4	3.40	6.23
MG-14	14_G019	54.8	149	654	<dl	\	114	354	206	191	77.9	170	5.1	92.5	2.71	4.04
MG-14	14_G020	127	754	3073	341	\	123	429	695	191	91.0	191	83.3	82.2	3.25	6.51
MG-14	14_G021	33.0	111	565	<dl	\	98.7	504	5.10	276	92.8	229	6.0	121	3.25	3.87
MG-14	14_G022	198	1322	3751	133	\	216	566	116	430	186	269	28.9	206	5.62	6.60
MG-14	14_G023	61.3	3616	12575	216	\	108	457	605	163	94.5	201	13.9	93.5	3.41	6.37
MG-14	14_G024	25.4	85.1	487	<dl	\	44.0	445	114	202	88.4	202	2.0	94.2	2.87	4.39
MG-14	14_G025	24.5	98.6	5724	150	\	281	448	915	191	95.7	219	1.8	98.2	3.08	5.07
MG-14	14_G026	9574	15680	30584	340	\	2309	548	2375	572	143	354	52.0	1596	9.86	7.68

Sample	Measurement	Mg	Al	Si	Ca	Sc	Ti	V	Cr	Mn	Co	Ni	Cu	Zn	Ga	Ge
MG-14	14_G027	113	648	2195	<dl	\	112	418	407	197	89.5	203	35.3	95.8	3.49	4.32
MG-14	14_G028	245	1217	4521	456	\	233	430	274	418	91.7	244	343	83.8	3.69	4.44
MG-14	14_G029	58.0	922	2634	166	\	249	489	60.9	283	85.4	281	31.6	159	3.78	4.48
MG-14	14_G030	227	7122	2926	<dl	\	473	484	48025	1802	143	207	28.4	30215	7.22	6.80
MG-14	14_G031	58.9	134	808	<dl	\	70.4	464	104	218	90.9	210	8.8	103	3.12	4.50
MG-14	14_G032	99.8	930	5822	1620	\	50.4	411	282	590	79.9	204	518	112	3.20	5.28
MG-14	14_G033	499	5223	11109	162	\	221	518	104	338	88.4	264	43.1	184	7.67	5.37
MG-14	14_G034	54.5	303	1208	<dl	\	171	482	196	256	105	247	24.1	137	3.26	5.58
MG-14	14_G035	41.5	283	1180	<dl	\	142	456	257	247	81.4	228	7.7	121	3.29	4.61
MG-14	14_G036	266	5316	19746	384	\	142	420	739	217	83.5	186	23.2	83.6	5.26	3.45
MG-14	14_G037	139	2364	7033	314	\	281	487	274	360	104	259	52.7	208	4.77	7.03
MG-14	14_G038	51.6	719	2195	259	\	130	436	383	282	94.1	216	34.6	139	3.39	7.75
MG-14	14_G039	426	8767	23035	398	\	331	411	205	207	78.9	218	22.3	99.0	4.41	5.74
MG-14	14_G040	75.3	1787	5077	475	\	301	454	29.7	307	103	248	39.1	179	4.74	6.89
MG-14	14_G041	138	2190	6228	474	\	559	513	225	408	127	248	70.7	200	5.09	8.19
MG-14	14_G042	62.7	682	41188	<dl	\	54.5	447	284	202	93.8	213	22.5	93.0	2.91	6.14
MG-14	14_G043	124	797	1831	<dl	\	78.9	505	3014	321	95.9	260	0.58	157	4.16	3.52
MG-14	14_G044	70.5	494	1260	<dl	\	92.3	479	330	248	89.6	216	3.2	126	3.50	4.39
MG-14	14_G045	65.0	180	1782	<dl	\	1653	430	141	217	81.6	200	2.8	99.6	2.86	3.79
MG-14	14_G046	48.8	185	783	<dl	\	53.7	463	259	217	91.0	218	9.0	110	3.25	4.26
MG-14	14_G047	43.8	487	1499	447	\	113	328	154	181	77.3	207	56.1	67.3	2.50	5.67
MG-14	14_G048	280	9531	43714	277	\	126	301	261	206	78.5	210	59.9	83.4	4.09	4.89
MG-14	14_G049	182	765	10210	4218	\	136	378	528	835	78.8	222	971	120	3.71	4.79
MG-14	14_G050	257	920	4030	2116	\	223	376	460	379	85.1	204	762	96.4	3.62	4.60
MG-14	14_G051	97.0	545	1823	194	\	144	578	27.4	450	103	280	105	187	4.96	8.79
MG-14	14_G052	328	2262	6276	<dl	\	121	451	1665	261	81.2	234	35.3	128	4.66	7.34

Sample	Measurement	Mg	Al	Si	Ca	Sc	Ti	V	Cr	Mn	Co	Ni	Cu	Zn	Ga	Ge
MG-14	14_G053	34.9	102	<dl	146	\	133	543	25.7	275	194	285	29.0	129	3.46	4.67
MG-14	14_G054	75.9	169	746	<dl	\	60.4	542	350	264	94.3	252	8.3	140	3.88	3.92
MG-14	14_G055	59.3	251	4377	176	\	105	456	115	195	80.2	228	5.4	113	2.69	4.16
MG-14	14_G056	51.4	453	1345	<dl	\	75.9	500	121	270	96.3	227	20.0	135	3.60	6.05
MG-14	14_G057	45.0	130	901	<dl	\	135	558	29.4	271	179	246	21.6	135	3.78	5.27
MG-14	14_G058	3209	4387	11353	339	\	633	370	442	375	91.3	188	238	123	5.00	6.33
MG-14	14_G059	114	776	2116	216	\	307	519	889	305	77.9	290	16.4	188	4.65	3.92
MG-14	14_G060	45.7	279	1134	<dl	\	69.0	441	113	246	81.8	225	9.7	104	2.99	4.08
MG-14	14_G061	28.9	121	3472	<dl	\	104	521	113	264	95.8	258	5.5	118	3.61	3.25
MG-14	14_G062	41.9	425	1939	<dl	\	199	395	178	170	81.1	216	24.7	79.2	2.67	4.36
MG-14	14_G063	48.4	186	850	<dl	\	72.1	438	30.3	209	79.4	202	3.1	122	2.96	3.75
MG-14	14_G064	68.4	398	1454	<dl	\	109	509	5.66	278	83.3	281	38.0	167	3.96	7.83
MG-14	14_G065	37.7	128	646	<dl	\	60.8	390	217	181	80.9	202	2.4	90.6	2.66	3.75
MG-14	14_G066	176	537	2053	1313	\	130	462	248	390	93.6	213	195	99.3	3.71	4.47
MG-14	14_G067	53.5	251	1181	188	\	176	562	279	346	116	245	34.5	159	4.25	6.29
MG-14	14_G068	85.3	1179	5674	591	\	677	546	165	390	117	236	165	206	4.69	16.1
MG-14	14_G069	5965	6432	20927	217	\	1598	454	444	311	101	252	31.5	237	7.24	8.49
MG-14	14_G070	104	1196	3480	332	\	105	515	58.2	300	93.8	260	37.7	166	3.85	8.23
MG-14	14_G071	160	1104	2423	225	\	513	429	90.5	223	79.9	213	21.5	111	3.47	7.85
MG-14	14_G072	51.4	92.5	623	<dl	\	42.8	401	75.9	210	80.1	198	4.2	81.0	2.49	3.60
MG-14	14_G073	95.6	723	1725	278	\	118	533	1691	316	96.5	242	10.9	140	3.82	5.34
MG-14	14_G074	188	782	4135	898	\	118	347	382	488	79.7	234	1051	95.8	3.59	8.93
MG-14	14_G075	67.8	349	1226	<dl	\	128	554	35.3	337	78.2	269	39.6	145	3.42	6.00
MG-14	14_G076	59.5	391	1128	<dl	\	91.3	511	102	344	76.9	272	24.4	152	3.44	5.82
MG-14	14_G077	37.5	113	744	<dl	\	147	598	25.0	317	142	259	33.8	152	3.89	4.67
MG-14	14_G078	56.0	731	2312	308	\	413	487	51.4	333	95.7	244	36.2	169	4.00	7.74

Sample	Measurement	Mg	Al	Si	Ca	Sc	Ti	V	Cr	Mn	Co	Ni	Cu	Zn	Ga	Ge
MG-14	14_G079	46.3	212	930	<dl	\	132	552	21.7	306	200	257	27.0	159	4.12	5.67
MG-14	14_G080	61.9	141	878	<dl	\	91.0	524	381	289	91.3	243	101	126	3.61	5.57
MG-14	14_G081	199	2380	6780	404	\	499	498	233	322	89.0	270	36.0	134	4.65	7.18
MG-14	14_G083	52.0	435	1197	<dl	\	54.5	436	32.0	228	81.2	216	8.1	113	2.86	5.62
MG-14	14_G084	77.7	4056	41276	<dl	\	4750	383	314	157	82.7	238	3.7	76.4	3.08	5.42
MG-14	14_G085	83.2	716	16294	<dl	\	124	402	511	185	85.4	251	4.4	169	2.67	5.95
MG-14	14_G086	411	2005	5015	<dl	\	260	366	934	190	80.3	199	6.9	108	3.58	5.67
MG-14	14_G087	661	4145	14605	<dl	\	274	450	715	197	89.8	214	25.1	107	5.62	7.88
MG-14	14_G088	54.8	468	1220	<dl	\	138	463	326	283	83.7	220	26.1	116	3.47	5.44
MG-14	14_G089	45.8	182	983	<dl	\	110	519	174	320	105	241	66.3	124	3.63	5.98
MG-14	14_G090	136	2257	31338	686	\	206	468	231	222	124	196	48.1	116	4.26	7.49
MG-14	14_G091	45.2	141	512	<dl	\	90.5	493	65.6	361	88.5	265	5.6	156	3.91	4.35
MG-14	14_G092	104	1234	3841	<dl	\	60.5	410	298	176	73.6	154	1.2	83.2	2.93	4.32
MG-14	14_G093	80.0	423	1918	140	\	97.9	476	62.0	269	89.2	244	32.5	147	3.02	6.83
MG-14	14_G094	120	676	2189	143	\	57.7	356	218	179	76.0	192	3.0	102	2.87	4.64
MG-14	14_G095	69.2	906	2807	<dl	\	178	510	61.9	316	89.8	242	35.4	139	4.00	6.86
MG-14	14_G096	50.6	714	2254	149	\	286	510	54.6	344	109	243	30.3	170	4.06	6.73
MG-14	14_G097	279	4856	16635	717	\	186	425	178	718	96.8	222	960	104	5.27	7.49
MG-14	14_G098	66.4	254	930	<dl	\	69.6	531	121	303	116	237	54.6	133	3.97	5.56
MG-14	14_G099	132	963	10622	<dl	\	724	489	541	292	91.6	214	12.1	133	3.98	5.79
MG-14	14_G100	61.5	271	945	<dl	\	175	501	454	334	91.6	249	49.7	158	3.72	5.67
MG-14	14_G101	160	1867	23373	<dl	\	99.3	405	245	184	82.3	207	17.9	85.3	3.12	6.15
MG-14	14_G102	175	1232	11758	422	\	116	346	394	190	85.6	221	61.4	81.8	3.71	6.42
MG-14	14_G103	835	868	4206	<dl	\	462	452	82.8	250	159	212	112	142	3.34	6.06
MG-14	14_G104	36.8	147	619	<dl	\	51.0	505	338	225	91.0	226	3.6	113	3.06	4.35
MG-14	14_G105	46.8	179	771	<dl	\	124	484	456	229	91.1	215	5.5	108	3.21	5.02

Sample	Measurement	Mg	Al	Si	Ca	Sc	Ti	V	Cr	Mn	Co	Ni	Cu	Zn	Ga	Ge
MG-14	14_G106	179	724	2622	408	\	224	466	1389	234	97.7	254	22.1	109	3.32	6.68
MG-14	14_G107	127	380	1449	231	\	87.1	477	8.34	263	83.1	242	34.7	141	3.20	9.76
MG-14	14_G108	52.7	371	1082	<dl	\	140	511	8.33	274	95.2	242	15.5	131	4.08	5.79
MG-14	14_G109	4831	7988	50906	326	\	589	437	345	249	267	219	61.3	184	7.57	8.75
MG-14	14_G110	137	1358	33510	414	\	96.9	369	165	169	113	246	68.6	92.7	3.03	12.6
MG-14	14_G111	85.6	446	8575	300	\	193	372	263	233	80.7	208	87.6	80.8	3.15	7.43
MG-14	14_G112	54.3	225	799	<dl	\	274	509	99.9	276	85.1	287	5.0	146	3.27	4.26
MG-14	14_G113	73.6	280	1566	<dl	\	169	509	493	301	183	279	42.4	148	3.57	7.93
MG-14	14_G114	81.3	593	2570	277	\	142	427	38.1	218	82.3	234	42.2	125	3.14	11.9
MG-14	14_G115	39.7	158	638	<dl	\	143	519	250	301	105	290	40.4	147	3.60	5.38
MG-14	14_G116	17.9	69.2	34663	<dl	\	75.7	395	217	156	77.2	235	3.3	99.1	2.44	5.36
MG-14	14_G117	776	1524	6298	171	\	3907	385	252	176	81.0	233	6.9	110	3.36	5.74
MG-14	14_G118	49.5	560	1832	<dl	\	356	541	52.2	378	96.6	268	27.8	150	3.99	5.32
MG-14	14_G119	40.0	150	576	<dl	\	57.8	451	182	246	82.2	224	5.1	140	3.01	4.35
MG-14	14_G120	51.3	1033	9402	<dl	\	227	472	24.0	262	90.2	244	39.4	120	3.63	9.16
MG-14	14_G121	46.0	202	564	<dl	\	321	534	24.9	349	92.6	272	9.8	185	4.84	3.99
MG-14	14_G122	57.4	928	2764	333	\	306	445	167	313	80.4	228	41.4	138	3.37	7.08

Sample	Measurement	Y	Zr	Nb	Mo	Ag	Sn	Hf	Ta	W	Pb	Th
MG-14	14_G001	17.4	\	7.18	59.9	0.61	111	\	\	7.65	5.15	3.70
MG-14	14_G002	2.13	\	2.03	47.9	0.74	106	\	\	<dl	11.6	<dl
MG-14	14_G003	0.87	\	0.19	5.98	<dl	3.88	\	\	<dl	92.1	5.96
MG-14	14_G004	<dl	\	<dl	0.96	<dl	0.61	\	\	0.06	15.0	0.23
MG-14	14_G005	0.78	\	0.11	2.15	<dl	0.45	\	\	<dl	79.6	<dl
MG-14	14_G006	0.40	\	0.08	3.03	<dl	0.36	\	\	0.84	108	<dl
MG-14	14_G007	1.13	\	0.08	5.01	0.03	<dl	\	\	<dl	54.4	<dl
MG-14	14_G008	<dl	\	0.71	5.51	0.03	0.55	\	\	<dl	89.7	<dl
MG-14	14_G009	0.20	\	<dl	<dl	0.03	0.55	\	\	<dl	30.0	0.49
MG-14	14_G010	0.77	\	0.08	1.21	0.02	0.42	\	\	0.34	68.0	<dl
MG-14	14_G011	3.36	\	1.40	11.2	0.08	2.77	\	\	<dl	446	<dl
MG-14	14_G012	<dl	\	0.16	1.59	0.03	0.62	\	\	<dl	54.5	<dl
MG-14	14_G013	1.61	\	0.22	3.20	<dl	0.55	\	\	1.01	73.1	11.5
MG-14	14_G014	66.7	\	3.42	13.7	0.31	3.14	\	\	<dl	225	<dl
MG-14	14_G015	0.55	\	0.08	6.58	<dl	0.48	\	\	<dl	121	<dl
MG-14	14_G016	0.17	\	<dl	2.58	0.03	<dl	\	\	0.16	56.8	0.21
MG-14	14_G017	0.29	\	0.07	1.22	<dl	0.44	\	\	<dl	14.3	<dl
MG-14	14_G018	1.76	\	0.14	6.45	0.02	9.87	\	\	<dl	139	<dl
MG-14	14_G019	0.99	\	0.18	0.78	0.03	0.34	\	\	<dl	26.9	5.34
MG-14	14_G020	<dl	\	0.21	5.04	<dl	22.3	\	\	<dl	126	<dl
MG-14	14_G021	0.37	\	0.15	1.18	<dl	0.49	\	\	0.51	71.4	2.59
MG-14	14_G022	<dl	\	0.32	2.24	0.44	0.63	\	\	<dl	144	36.1
MG-14	14_G023	17.1	\	0.28	3.10	<dl	0.95	\	\	0.24	130	<dl
MG-14	14_G024	<dl	\	<dl	0.21	0.04	0.80	\	\	<dl	9.30	<dl
MG-14	14_G025	0.33	\	0.57	0.88	<dl	0.53	\	\	<dl	56.9	1.70
MG-14	14_G026	<dl	\	1.91	4.30	0.04	1.86	\	\	<dl	206	<dl

Sample	Measurement	Y	Zr	Nb	Mo	Ag	Sn	Hf	Ta	W	Pb	Th
MG-14	14_G027	<dl	\	0.29	1.39	<dl	33.3	\	\	<dl	95.5	<dl
MG-14	14_G028	<dl	\	1.20	2.82	0.05	14.3	\	\	<dl	114	9.62
MG-14	14_G029	5.20	\	0.59	2.23	<dl	0.75	\	\	<dl	86.9	<dl
MG-14	14_G030	0.99	\	0.16	4.78	0.04	0.54	\	\	<dl	121	1.91
MG-14	14_G031	0.33	\	0.08	1.94	<dl	1.90	\	\	<dl	96.4	4.00
MG-14	14_G032	0.35	\	0.22	4.10	0.09	10.6	\	\	<dl	55.7	<dl
MG-14	14_G033	0.65	\	0.87	2.39	0.07	8.69	\	\	<dl	138	<dl
MG-14	14_G034	3.73	\	0.55	2.15	0.07	0.93	\	\	<dl	128	<dl
MG-14	14_G035	0.40	\	0.23	1.06	<dl	0.69	\	\	<dl	36.1	1.34
MG-14	14_G036	<dl	\	0.22	1.96	0.03	18.0	\	\	<dl	69.9	<dl
MG-14	14_G037	<dl	\	2.77	5.24	0.05	6.59	\	\	<dl	235	<dl
MG-14	14_G038	0.81	\	0.23	4.05	0.04	3.24	\	\	<dl	93.7	7.32
MG-14	14_G039	6.07	\	0.49	2.27	0.06	22.4	\	\	<dl	78.7	<dl
MG-14	14_G040	2.03	\	0.68	3.63	<dl	1.33	\	\	<dl	140	18.1
MG-14	14_G041	34.6	\	1.52	3.93	0.21	1.88	\	\	1.02	233	80.8
MG-14	14_G042	0.43	\	0.08	4.95	<dl	0.59	\	\	0.25	113	4.65
MG-14	14_G043	<dl	\	0.06	<dl	0.04	<dl	\	\	<dl	4.73	<dl
MG-14	14_G044	<dl	\	0.08	0.59	<dl	0.69	\	\	<dl	30.1	<dl
MG-14	14_G045	2.26	\	2.75	0.29	0.04	0.90	\	\	<dl	18.9	<dl
MG-14	14_G046	1.08	\	0.04	2.49	<dl	0.82	\	\	<dl	69.8	<dl
MG-14	14_G047	0.84	\	0.13	1.59	11.4	37.3	\	\	<dl	55.3	8.29
MG-14	14_G048	0.42	\	0.23	1.37	<dl	22.7	\	\	<dl	58.1	8.03
MG-14	14_G049	1.24	\	<dl	2.55	0.13	10.1	\	\	0.50	61.7	<dl
MG-14	14_G050	<dl	\	1.56	3.12	0.05	15.2	\	\	<dl	65.6	7.32
MG-14	14_G051	0.89	\	0.49	5.13	0.14	1.64	\	\	<dl	226	<dl
MG-14	14_G052	<dl	\	0.21	3.32	<dl	0.89	\	\	<dl	116	<dl

Sample	Measurement	Y	Zr	Nb	Mo	Ag	Sn	Hf	Ta	W	Pb	Th
MG-14	14_G053	4.40	\	0.62	33.1	0.16	<dl	\	\	<dl	75.7	8.94
MG-14	14_G054	0.26	\	<dl	1.94	<dl	0.37	\	\	<dl	41.3	0.83
MG-14	14_G055	1.06	\	0.20	2.06	3.26	0.44	\	\	<dl	65.0	<dl
MG-14	14_G056	2.24	\	0.18	10.2	<dl	2.21	\	\	<dl	90.8	<dl
MG-14	14_G057	38.1	\	0.32	0.65	0.20	<dl	\	\	<dl	75.1	<dl
MG-14	14_G058	76.8	\	<dl	6.51	0.06	36.2	\	\	<dl	177	20.1
MG-14	14_G059	<dl	\	0.45	2.76	<dl	0.51	\	\	<dl	168	<dl
MG-14	14_G060	<dl	\	0.09	0.82	0.05	0.80	\	\	0.12	40.4	<dl
MG-14	14_G061	0.28	\	0.07	1.50	0.03	0.61	\	\	<dl	83.0	<dl
MG-14	14_G062	<dl	\	0.25	1.12	0.03	24.7	\	\	<dl	97.8	<dl
MG-14	14_G063	0.16	\	0.06	0.93	<dl	0.98	\	\	<dl	37.0	<dl
MG-14	14_G064	1.18	\	0.29	6.77	<dl	0.37	\	\	<dl	88.2	3.95
MG-14	14_G065	<dl	\	0.11	0.37	<dl	1.36	\	\	<dl	16.2	2.45
MG-14	14_G066	9.36	\	0.29	3.68	0.04	33.7	\	\	<dl	127	<dl
MG-14	14_G067	<dl	\	0.49	2.00	0.34	0.79	\	\	<dl	144	<dl
MG-14	14_G068	99.7	\	<dl	5.40	<dl	3.42	\	\	<dl	600	<dl
MG-14	14_G069	8.54	\	2.81	6.05	<dl	2.67	\	\	<dl	176	<dl
MG-14	14_G070	0.86	\	0.29	3.41	<dl	0.58	\	\	<dl	102	<dl
MG-14	14_G071	0.84	\	2.76	3.26	0.02	17.1	\	\	<dl	95.8	<dl
MG-14	14_G072	0.10	\	0.03	0.21	0.04	0.76	\	\	0.04	8.01	<dl
MG-14	14_G073	<dl	\	<dl	2.82	0.02	0.71	\	\	<dl	147	5.05
MG-14	14_G074	2.45	\	0.43	<dl	0.05	23.0	\	\	1.42	98.0	<dl
MG-14	14_G075	<dl	\	3.04	3.98	<dl	0.75	\	\	<dl	98.7	<dl
MG-14	14_G076	<dl	\	<dl	4.29	<dl	0.61	\	\	<dl	65.6	4.46
MG-14	14_G077	8.65	\	3.75	1.10	<dl	0.89	\	\	<dl	88.0	<dl
MG-14	14_G078	50.7	\	0.85	1.92	0.19	0.88	\	\	<dl	123	<dl

Sample	Measurement	Y	Zr	Nb	Mo	Ag	Sn	Hf	Ta	W	Pb	Th
MG-14	14_G079	<dl	\	1.58	2.72	0.04	0.75	\	\	0.27	59.2	8.53
MG-14	14_G080	<dl	\	0.10	2.81	0.05	<dl	\	\	<dl	94.3	<dl
MG-14	14_G081	<dl	\	0.91	3.90	0.11	0.99	\	\	<dl	213	<dl
MG-14	14_G083	<dl	\	0.06	1.24	0.04	0.62	\	\	<dl	45.0	<dl
MG-14	14_G084	600	\	18.3	0.95	<dl	3.58	\	\	1.77	58.3	20.9
MG-14	14_G085	0.98	\	0.50	1.01	<dl	0.79	\	\	<dl	37.8	<dl
MG-14	14_G086	<dl	\	0.34	2.01	<dl	2.51	\	\	0.22	72.8	<dl
MG-14	14_G087	4.70	\	0.28	5.06	<dl	5.15	\	\	<dl	141	<dl
MG-14	14_G088	1.18	\	0.19	3.60	0.02	3.21	\	\	<dl	158	<dl
MG-14	14_G089	5.83	\	0.58	<dl	0.14	0.48	\	\	<dl	170	<dl
MG-14	14_G090	<dl	\	0.63	5.32	0.03	5.09	\	\	0.33	91.9	<dl
MG-14	14_G091	<dl	\	0.08	1.93	<dl	0.40	\	\	<dl	60.7	<dl
MG-14	14_G092	<dl	\	0.08	0.46	0.03	0.54	\	\	0.09	13.8	<dl
MG-14	14_G093	<dl	\	0.23	8.93	<dl	0.74	\	\	<dl	80.6	<dl
MG-14	14_G094	<dl	\	0.08	1.53	<dl	0.41	\	\	<dl	25.6	<dl
MG-14	14_G095	<dl	\	0.40	3.29	0.07	3.83	\	\	1.48	119	<dl
MG-14	14_G096	<dl	\	0.52	2.09	0.03	1.29	\	\	<dl	107	<dl
MG-14	14_G097	<dl	\	1.62	5.39	0.13	22.4	\	\	0.80	116	14.0
MG-14	14_G098	2.96	\	0.08	<dl	0.05	27.4	\	\	<dl	39.6	<dl
MG-14	14_G099	1.04	\	<dl	14.4	<dl	2.30	\	\	<dl	146	<dl
MG-14	14_G100	<dl	\	0.65	2.39	0.05	0.80	\	\	0.42	269	<dl
MG-14	14_G101	18.0	\	0.16	1.68	<dl	0.72	\	\	0.17	50.6	<dl
MG-14	14_G102	<dl	\	0.20	<dl	<dl	21.1	\	\	<dl	39.2	5.47
MG-14	14_G103	0.80	\	1.06	1.22	<dl	1.39	\	\	<dl	147	<dl
MG-14	14_G104	0.14	\	<dl	1.17	<dl	0.73	\	\	<dl	25.4	<dl
MG-14	14_G105	0.16	\	<dl	1.51	0.06	0.79	\	\	<dl	34.7	1.70

Sample	Measurement	Y	Zr	Nb	Mo	Ag	Sn	Hf	Ta	W	Pb	Th
MG-14	14_G106	1.65	\	0.46	1.58	<dl	11.0	\	\	<dl	111	12.4
MG-14	14_G107	1.58	\	<dl	7.07	0.03	0.75	\	\	<dl	137	<dl
MG-14	14_G108	0.82	\	0.32	2.03	<dl	0.82	\	\	<dl	77.5	1.25
MG-14	14_G109	129	\	0.36	4.18	0.06	1.23	\	\	2.75	118	<dl
MG-14	14_G110	1.64	\	0.41	15.6	0.04	0.51	\	\	<dl	237	9.44
MG-14	14_G111	24.0	\	1.22	2.29	<dl	32.4	\	\	<dl	153	14.9
MG-14	14_G112	0.97	\	0.17	0.91	<dl	0.39	\	\	<dl	58.5	<dl
MG-14	14_G113	<dl	\	0.52	4.81	<dl	0.79	\	\	<dl	224	<dl
MG-14	14_G114	1.35	\	0.36	10.1	0.03	2.24	\	\	0.52	201	6.81
MG-14	14_G115	2.25	\	0.89	1.68	0.12	0.40	\	\	<dl	128	<dl
MG-14	14_G116	0.29	\	0.10	0.58	<dl	0.57	\	\	0.03	59.4	<dl
MG-14	14_G117	2145	\	17.5	1.89	<dl	3.16	\	\	<dl	55.8	35.9
MG-14	14_G118	<dl	\	0.65	2.31	<dl	0.87	\	\	<dl	141	<dl
MG-14	14_G119	0.45	\	0.03	1.08	0.05	0.63	\	\	0.08	31.5	<dl
MG-14	14_G120	<dl	\	0.59	4.46	<dl	0.94	\	\	<dl	162	11.3
MG-14	14_G121	1.22	\	0.50	1.73	0.07	0.86	\	\	0.41	<dl	<dl
MG-14	14_G122	<dl	\	<dl	2.97	<dl	3.37	\	\	<dl	143	<dl

Sample	Measurement	Mg	Al	Si	Ca	Sc	Ti	V	Cr	Mn	Co	Ni	Cu	Zn	Ga	Ge
KG-1	KG1_G001	162	3700	19695	23170	3.86	28913	212	90.0	476	2.50	<dl	1.3	53.4	7.98	6.32
KG-1	KG1_G002	43.9	916	866	7051	0.35	98.3	603	16.9	2717	26.6	5.55	5.3	315	25.6	2.95
KG-1	KG1_G003	26.6	237	386	174	<dl	48.0	593	15.3	3176	29.7	6.26	0.27	249	41.5	3.23
KG-1	KG1_G004	26.2	109	273	48.5	<dl	37.7	535	16.9	2704	28.2	9.05	<dl	128	27.3	2.71
KG-1	KG1_G005	79.5	689	994	97.5	0.48	36.1	545	14.7	2266	25.9	4.84	4.9	175	25.0	2.64
KG-1	KG1_G006	81.3	2118	11504	14084	3.63	19904	130	66.3	458	1.97	<dl	4.3	42.5	9.94	3.33
KG-1	KG1_G007	12.5	124	400	<dl	1.91	8987	133	7.16	413	2.78	<dl	<dl	44.6	10.7	<dl
KG-1	KG1_G008	23.6	1943	3131	2488	7.34	8185	135	21.5	481	2.41	<dl	6.3	41.8	13.1	3.28
KG-1	KG1_G010	33.5	2546	18246	24643	12.4	33989	262	109	721	2.90	<dl	10.6	88.6	9.86	8.42
KG-1	KG1_G011	25.8	406	1001	93.6	<dl	39.2	520	16.5	2553	21.0	6.25	2.1	169	21.5	1.22
KG-1	KG1_G012	19.0	121	569	108	0.25	42.7	778	15.9	2763	24.1	7.18	0.28	117	18.7	3.00
KG-1	KG1_G013	16.0	136	455	76.8	<dl	101	720	17.0	3295	1.20	7.08	<dl	103	32.8	3.50
KG-1	KG1_G014	22.6	621	4855	6290	2.00	13906	219	85.5	394	2.28	0.97	2.0	38.0	8.62	3.06
KG-1	KG1_G015	10.9	105	781	4196	1.95	7454	121	44.2	339	1.71	<dl	2.5	34.3	8.64	1.13
KG-1	KG1_G016	21.2	427	978	44.7	1.23	84.5	405	17.6	1948	26.5	6.86	2.4	142	<dl	1.93
KG-1	KG1_G017	120	2814	16723	21135	7.46	29637	145	69.3	491	1.87	<dl	5.2	42.9	12.3	5.30
KG-1	KG1_G018	8.97	229	1711	<dl	2.07	25.3	683	16.2	3617	37.4	7.79	0.72	188	39.6	1.45
KG-1	KG1_G019	6.63	95.9	1195	56.9	1.29	5931	115	3.39	247	1.89	<dl	<dl	26.7	9.79	1.49
KG-1	KG1_G020	22.3	102	420	<dl	<dl	15.9	730	10.5	1733	39.6	8.85	0.50	279	15.4	1.25

Sample	Measurement	Y	Zr	Nb	Mo	Ag	Sn	Hf	Ta	W	Pb	Th
KG-1	KG1_G001	<dl	90.1	<dl	4.55	<dl	19.1	<dl	9.27	24.1	57.0	<dl
KG-1	KG1_G002	4.30	7.96	0.11	0.27	0.24	<dl	0.25	<dl	0.96	88.9	0.47
KG-1	KG1_G003	0.02	0.20	<dl	<dl	<dl	0.45	216	67.0	<dl	11.3	0.12
KG-1	KG1_G004	<dl	0.04	<dl	<dl	<dl	<dl	163	<dl	<dl	0.10	<dl
KG-1	KG1_G005	0.14	0.12	0.03	<dl	<dl	<dl	<dl	<dl	<dl	38.2	0.44
KG-1	KG1_G006	<dl	2.58	<dl	2.64	<dl	58.4	0.34	<dl	<dl	28.7	0.67
KG-1	KG1_G007	0.01	0.11	3.79	<dl	<dl	19.2	<dl	0.05	<dl	0.19	<dl
KG-1	KG1_G008	46.1	1.62	5.12	<dl	<dl	21.3	<dl	0.08	0.58	2.87	<dl
KG-1	KG1_G010	205	80.2	288	12.2	<dl	44.6	<dl	13.2	<dl	42.9	<dl
KG-1	KG1_G011	0.19	2.14	0.02	0.16	<dl	<dl	0.05	48.0	0.31	40.0	<dl
KG-1	KG1_G012	0.06	0.03	<dl	0.07	<dl	<dl	<dl	<dl	<dl	<dl	<dl
KG-1	KG1_G013	<dl	1.18	0.46	<dl	<dl	0.56	0.13	0.05	<dl	0.17	<dl
KG-1	KG1_G014	27.0	1.42	30.9	13.1	<dl	6.36	<dl	5.57	<dl	21.2	0.51
KG-1	KG1_G015	<dl	1.05	16.8	0.49	<dl	15.3	<dl	0.10	3.59	14.2	<dl
KG-1	KG1_G016	<dl	1567	0.04	<dl	0.18	0.44	<dl	94.0	0.60	34.0	3.91
KG-1	KG1_G017	255	31.3	445	3.46	<dl	45.4	2.44	<dl	<dl	38.0	1.39
KG-1	KG1_G018	<dl	2307	0.06	<dl	0.39	<dl	<dl	<dl	0.08	19.9	2.01
KG-1	KG1_G019	0.08	0.08	3.70	0.18	<dl	22.6	<dl	0.16	0.15	0.18	0.03
KG-1	KG1_G020	0.03	<dl	<dl	<dl	<dl	<dl	<dl	<dl	0.06	5.74	0.41

Sample	Measurement	Mg	Al	Si	Ca	Sc	Ti	V	Cr	Mn	Co	Ni	Cu	Zn	Ga	Ge
OE-1	OE1_G001	24.2	496	2112	305	2.53	4682	84.4	7.23	544	7.34	5.06	<dl	104	12.1	8.82
OE-1	OE1_G002	25.5	621	3418	6316	4.91	5400	114	13.8	540	5.73	5.06	<dl	118	12.3	10.2
OE-1	OE1_G003	63.1	1562	6108	591	5.21	5695	109	11.6	485	4.48	5.29	1.1	125	15.2	9.35
OE-1	OE1_G004	41.4	1288	2636	22698	3.69	6124	166	76.1	575	7.07	8.87	0.69	476	13.7	12.2
OE-1	OE1_G005	13.8	379	2163	301	2.53	5460	113	4.64	375	6.57	3.73	<dl	111	12.9	6.42
OE-1	OE1_G006	66.3	798	2163	127	1.89	5790	228	15.9	451	5.66	2.87	1.0	100	13.8	9.48
OE-1	OE1_G007	321	3729	8167	15259	4.26	5321	176	8.56	476	5.92	2.46	0.62	186	17.3	9.04
OE-1	OE1_G008	24.2	681	2374	274	4.98	4397	109	12.1	501	5.82	2.01	<dl	124	10.7	6.90
OE-1	OE1_G009	749	6963	13624	<dl	3.98	6750	124	14.4	672	11.8	10.7	<dl	215	24.3	6.07
OE-1	OE1_G010	26.8	2003	3206	1028	5.38	23541	178	62.3	676	9.48	6.31	10.3	1931	20.9	7.99
OE-1	OE1_G011	372	3858	9342	297	5.43	6123	119	8.92	336	6.37	6.75	<dl	206	18.0	4.69
OE-1	OE1_G012	71.4	4725	2720	667	9.08	51693	177	47.8	1067	15.5	10.0	3.5	6449	27.5	10.5
OE-1	OE1_G013	245	2671	5652	312	3.68	5158	126	7.99	558	7.09	4.18	14.0	223	17.1	5.14
OE-1	OE1_G014	114	1360	4247	442	5.64	5717	83.1	14.0	657	7.08	5.04	<dl	137	12.6	7.61
OE-1	OE1_G015	28.9	583	2888	242	2.76	5357	104	10.3	439	5.34	3.82	1.3	124	12.5	5.73
OE-1	OE1_G016	158	1733	3950	<dl	2.05	4445	140	16.3	404	5.07	2.46	1.4	172	13.2	2.83
OE-1	OE1_G017	86.7	4858	2523	362	6.42	42617	320	111	4051	19.8	14.6	10.6	7753	38.9	7.80
OE-1	OE1_G018	518	5655	10714	142	5.35	5500	97.9	12.9	333	7.54	4.08	0.55	199	20.5	5.01
OE-1	OE1_G019	1376	13729	25578	6622	10.2	5251	93.2	5.27	691	10.8	34.3	1.6	338	33.4	5.81
OE-1	OE1_G020	41.7	697	2959	235	3.45	5452	125	14.6	300	5.29	4.91	0.60	121	11.2	5.43

Sample	Measurement	Y	Zr	Nb	Mo	Ag	Sn	Hf	Ta	W	Pb	Th
OE-1	OE1_G001	19.9	2.69	39.9	2.29	0.83	61.4	0.34	<dl	77.9	49.7	<dl
OE-1	OE1_G002	106	841	58.6	2.80	0.91	47.1	26.4	<dl	124	79.2	<dl
OE-1	OE1_G003	66.1	7.74	93.3	3.58	0.77	49.1	0.73	<dl	<dl	156	71.3
OE-1	OE1_G004	155	24.1	83.2	8.34	0.77	30.2	0.97	<dl	42.1	96.1	20.2
OE-1	OE1_G005	20.2	3.29	59.7	0.92	<dl	40.7	<dl	1.17	69.4	72.3	<dl
OE-1	OE1_G006	18.3	1.21	58.6	1.31	<dl	67.2	0.09	2.07	65.9	32.4	13.9
OE-1	OE1_G007	152	7.91	63.4	1.50	0.87	63.1	0.14	<dl	93.4	71.8	<dl
OE-1	OE1_G008	<dl	6.34	86.7	2.93	<dl	53.8	0.53	<dl	126	114	<dl
OE-1	OE1_G009	8.35	1.00	19.8	0.97	<dl	23.1	<dl	0.32	33.0	25.4	9.71
OE-1	OE1_G010	<dl	407	69.7	28.7	<dl	54.8	12.9	5.84	<dl	286	49.5
OE-1	OE1_G011	32.7	3.20	85.6	1.93	<dl	38.9	0.17	1.36	<dl	118	41.5
OE-1	OE1_G012	49.7	28.1	75.5	11.6	0.81	28.9	1.79	6.31	16.6	124	14.1
OE-1	OE1_G013	22.0	2.90	67.8	1.78	2.51	39.9	0.19	1.04	89.5	82.8	21.4
OE-1	OE1_G014	70.2	7.59	76.3	3.66	0.68	95.6	<dl	<dl	123	159	<dl
OE-1	OE1_G015	37.8	79.4	68.6	2.67	0.79	51.4	2.69	1.23	117	110	34.7
OE-1	OE1_G016	14.7	1.55	41.8	1.20	0.82	43.2	0.08	<dl	<dl	51.9	<dl
OE-1	OE1_G017	31.7	59.9	89.6	9.01	<dl	28.2	<dl	5.41	11.9	97.2	<dl
OE-1	OE1_G018	<dl	5.45	58.7	1.08	0.70	28.7	<dl	<dl	43.8	91.3	26.1
OE-1	OE1_G019	70.8	8.90	82.2	0.87	<dl	42.5	0.20	0.93	<dl	106	<dl
OE-1	OE1_G020	35.2	10.5	77.0	1.05	0.95	34.0	<dl	0.77	61.5	117	<dl

Sample	Measurement	Mg	Al	Si	Ca	Sc	Ti	V	Cr	Mn	Co	Ni	Cu	Zn	Ga	Ge
OE-2	OE2_001	25.9	1439	55157	301	4.01	16086	2144	2.63	732	<dl	<dl	0.82	44.1	17.0	6.75
OE-2	OE2_002	55.8	910	3421	330	2.21	49.0	1401	9.60	1418	19.6	11.4	95.1	918	40.2	8.30
OE-2	OE2_003	11.5	227	2485	121	1.03	251	1989	3.00	986	25.8	8.23	16.3	1776	27.9	11.0
OE-2	OE2_004	17.4	54.2	1429	<dl	<dl	32.6	1668	6.13	1333	5.20	2.19	<dl	250	22.3	6.19
OE-2	OE2_005	37.1	1598	4932	250	1.39	42.8	1652	15.0	1653	6.51	2.53	25.0	389	29.3	8.64
OE-2	OE2_006	23.3	84.3	1351	<dl	<dl	74.7	1292	<dl	1890	36.9	10.9	<dl	194	29.3	4.58
OE-2	OE2_007	30.3	1589	2503	184	0.56	46.8	1552	3.65	1479	12.4	2.63	16.2	363	38.5	4.91
OE-2	OE2_008	83.5	1672	6431	255	3.02	1167	1712	2.54	1306	5.34	5.98	8.2	313	24.1	7.43
OE-2	OE2_009	62.3	776	3439	<dl	<dl	248	1549	<dl	1294	5.33	5.08	8.3	284	17.7	9.15
OE-2	OE2_010	74.6	328	3641	87.9	0.40	76.0	705	14.4	1801	68.3	55.4	<dl	652	29.9	7.53
OE-2	OE2_011	28.7	392	3160	<dl	0.64	44.9	1547	4.89	1361	9.95	8.01	39.4	446	20.8	8.59
OE-2	OE2_012	158	2072	7096	267	1.62	285	1505	9.83	1386	10.5	14.9	34.4	301	29.3	10.8
OE-2	OE2_013	31.9	679	2914	<dl	0.45	29.3	1421	59.6	844	11.7	16.1	79.0	569	24.2	7.49
OE-2	OE2_014	52.4	1417	4717	248	1.75	189	1545	<dl	1361	3.91	1.75	4.3	397	28.8	6.67
OE-2	OE2_015	41.4	2238	6338	282	2.02	39.0	1468	<dl	1587	11.1	13.5	44.2	415	33.2	10.3
OE-2	OE2_016	192	2756	18486	1602	1.58	131	958	<dl	1039	101	132	197	2236	638	16.4
OE-2	OE2_017	27.2	136	2259	<dl	<dl	81.4	1435	<dl	1143	17.8	2.10	9.2	1276	19.8	6.04
OE-2	OE2_018	61.3	4225	17883	316	1.19	53.5	5215	<dl	1760	17.9	20.7	12.6	618	42.0	5.27
OE-2	OE2_019	26.7	624	3803	160	<dl	32.1	1513	<dl	1374	6.31	3.11	41.7	401	21.5	6.13
OE-2	OE2_020	47.1	619	4068	104	0.40	72.3	1548	<dl	1500	10.7	8.78	33.8	462	23.9	9.51

Sample	Measurement	Y	Zr	Nb	Mo	Ag	Sn	Hf	Ta	W	Pb	Th
OE-2	OE2_001	419	227	288	0.43	0.76	70.9	8.72	<dl	<dl	200	<dl
OE-2	OE2_002	215	717	13.8	0.42	0.48	0.98	26.7	1.12	0.56	315	<dl
OE-2	OE2_003	60.8	19.8	139	0.63	<dl	1.79	1.15	<dl	<dl	557	22.4
OE-2	OE2_004	<dl	173	2.10	0.25	<dl	<dl	8.68	0.35	0.10	0.36	2.85
OE-2	OE2_005	9.64	126	39.9	1.28	0.63	<dl	<dl	0.04	2.94	314	3.79
OE-2	OE2_006	0.51	9.70	0.76	0.38	0.66	1.71	<dl	<dl	<dl	14.4	<dl
OE-2	OE2_007	43.4	40.2	11.9	<dl	<dl	2.39	<dl	0.03	<dl	201	3.07
OE-2	OE2_008	462	40.1	367	0.73	0.62	16.6	1.60	<dl	<dl	134	10.4
OE-2	OE2_009	36.0	121	79.1	0.92	0.63	3.01	3.77	<dl	<dl	65.9	<dl
OE-2	OE2_010	39.8	510	7.57	<dl	<dl	0.87	18.5	0.35	0.50	49.3	61.9
OE-2	OE2_011	50.9	38.7	0.38	0.41	<dl	<dl	1.43	<dl	0.33	209	0.45
OE-2	OE2_012	28.5	89.5	126	0.53	<dl	3.90	3.41	<dl	<dl	312	6.54
OE-2	OE2_013	36.9	22.8	107	0.34	0.67	<dl	0.88	0.04	1.58	123	0.88
OE-2	OE2_014	114	201	138	<dl	<dl	3.33	<dl	<dl	<dl	276	<dl
OE-2	OE2_015	19.6	282	93.6	0.39	0.64	<dl	9.29	0.83	1.84	272	<dl
OE-2	OE2_016	233	133	3.47	0.57	1.70	4.36	7.09	0.29	<dl	1218	<dl
OE-2	OE2_017	7.57	38.2	71.7	0.41	0.67	1.89	1.36	0.15	1.11	263	<dl
OE-2	OE2_018	36.5	6.68	8.29	1.12	0.76	6.42	0.24	0.05	<dl	843	<dl
OE-2	OE2_019	28.9	6.86	7.18	0.64	<dl	1.00	<dl	<dl	<dl	159	0.69
OE-2	OE2_020	37.1	27.5	2.77	<dl	0.56	0.83	<dl	<dl	0.38	97.1	4.66

Appendix VI-B: LA-ICP-MS Excluded Measurements (*n*=30)

Sample	Measurement	Mg	Al	Si	Ca	Ti	V	Cr	Mn	Co	Ni
MG-1	1_G079	1960	101896	4627	<dl	2669	1122	616119	23032	1411	818
MG-1	1_G108	430588	288668	2104321	823323	5436891	2120	3545	121133	407	476
MG-14	14_G082	355043	2816713	**********	421578	2257720	7977	7612	15377	288	577

Sample	Measurement	Cu	Zn	Ga	Ge	Nb	Mo	Ag	Sn	W	Pb	Th
MG-1	1_G079	272	326393	61.3	4.63	<dl	2.39	<dl	1.56	<dl	439	<dl
MG-1	1_G108	17191	2336	145	47.0	18112	94.9	3.49	3011	<dl	5156	3460
MG-14	14_G082	1367	3165	1461	932	3582	<dl	21.7	1719	<dl	133	123

Sample	Measurement	Mg	Al	Si	Ca	Sc	Ti	V	Cr	Mn	Co	Ni	Cu	Zn	Ga	Ge
MG-5	SJ05_G001	**********	8678924	**********	**********	5843	397244	5120	7763	249287	468	2730	1231	14298	2196	514
MG-5	SJ05_G002	213997	**********	**********	155196	2084	10705	1174	<597	8180	173	<439	839	2392	4999	409
MG-5	SJ05_G007	**********	9196513	**********	**********	6497	397758	5029	10429	235258	441	1784	1696	14402	2165	1284
MG-5	SJ05_G009	**********	8596865	**********	**********	6007	390288	4864	8493	245507	365	2416	1583	14103	2104	1281
MG-5	SJ05_G013	**********	5569084	**********	**********	4449	250133	3667	9474	156201	273	1017	2338	7454	1536	<601
MG-5	SJ05_G020	7973217	**********	**********	**********	6727	117308	2090	8016	67834	605	<1373	3916	5712	3356	1498
MG-5	SJ05_G021	**********	4718526	**********	**********	3259	220827	3279	5202	132584	305	382	507	12382	1138	440
MG-5	SJ05_G025	7476753	2897739	**********	**********	42874	528706	20798	19057	80302	<910	<7742	363168	<9610	<3962	<7601
MG-4	SJ4_G005	4062	6826	13351	13303	78.0	387354	5558	541	16880	221	594	198	1058	44.0	5.88
MG-4	SJ4_G006	4596	29557	**********	72467	2221	104526	2956	954	4958	124	587	225	690	61.4	174
MG-4	SJ4_G019	191584	2219179	**********	165905	9581	62219	4079	5972	2405	108	614	2096	3810	1361	2497
MG-4	SJ4_G047	213	2503	61992	910	3.65	114795	368	134	88.5	106	255	2.01	119	4.47	7.07
MG-4	SJ4_G067	405537	1224497	**********	305442	19552	42504	8820	22277	29202	2365	1344	6681	15146	520	3930
MG-4	SJ4_G098	11360	54725	151776	56131	122	580071	2878	169	23389	251	367	33.3	357	40.4	5.99
MG-4	SJ4_G114	64.2	77.0	262121	34.4	2.09	288	268	107	86.5	94.9	238	1.40	97.6	3.19	3.57
MG-13	SJ13_G004	175866	1082131	**********	**********	5034	**********	16884	4500	42743	238	418	228354	2579	808	2231
MG-13	SJ13_G006	440292	3158105	5345494	12275	840	62398	5783	2589	17751	1316	2561	**********	5170	2953	55.7
MG-13	SJ13_G008	390500	7774939	**********	35577	2169	110416	7410	3494	17177	362	639	161	3761	4244	<dl
MG-13	SJ13_G010	3485	92259	170816	124605	20.3	6659	713	141	2605	46.9	97.1	2031	123	44.7	29.2
MG-13	SJ13_G011	10826	50921	**********	37084	478	11452	1586	<dl	3939	22	105	**********	217	181	2480
MG-13	SJ13_G013	322672	1398330	**********	<dl	<dl	52891	3303	<dl	14302	<dl	<dl	1591	4792	1628	<dl
MG-13	SJ13_G015	6995	83813	801051	900392	134	2632629	2210	273	924540	177	46.3	1833314	4008	48.2	133
MG-13	SJ13_G016	10935	35831	115788	28877	10.6	1696	622	1598	3744	78.9	143	3533	361	18.3	40.6
MG-13	SJ13_G018	473943	3447348	**********	416910	1042	515853	5897	3212	21739	481	1100	210	3962	2434	<dl
MG-13	SJ13_G019	449057	3457303	9294687	<dl	940	50947	4881	3796	13244	293	606	<dl	2690	2452	211
MG-10	SJ10_G059	61448	15846	768918	151834	16.5	872	500	578	1092	45.7	110	48.1	131	10.6	7.01
KG-1	KG1_G009	113	8480	85315	128613	17.1	126377	368	151	1787	4.17	<1.97	4.94	68.7	14.0	28.7

Sample	Measurement	Y	Zr	Nb	Mo	Ag	Sn	Hf	Ta	W	Pb	Th
MG-5	SJ05_G001	9413	80991	1230	171	<63.0	2438498	2054	138	133	15903	1987
MG-5	SJ05_G002	18.1	48.9	<17.6	80.0	<53.6	235	<0.00	<2.97	42.8	1774	<4.99
MG-5	SJ05_G007	9626	77171	1412	<154	<109	2062846	2131	120	177	18123	1969
MG-5	SJ05_G009	9313	82344	1225	<85.8	<55.7	3098162	2104	134	127	14343	2193
MG-5	SJ05_G013	6107	52707	887	<108	82.0	4897092	1315	57.2	55.9	4899	1060
MG-5	SJ05_G020	2871	37880	348	<289	<117	2500457	818	53.4	70.8	3974	816
MG-5	SJ05_G021	4957	43551	679	88.2	<41.92	108647	1098	61.2	82.2	12082	1041
MG-5	SJ05_G025	2303	<33660	1233	<1468	**********	7379877	1204	124	103	8421	1173
MG-4	SJ4_G005	6.74	<dl	175	15.5	0.58	57.8	55.6	<dl	<dl	10.9	<dl
MG-4	SJ4_G006	39.7	<dl	60.8	35.0	5.37	215	<dl	<dl	<dl	233	11.1
MG-4	SJ4_G019	231	5160	<dl	<dl	<dl	4717	<dl	<dl	67.0	140	189
MG-4	SJ4_G047	21.6	<dl	386	3.92	<dl	45.2	7.60	<dl	<dl	69.9	<dl
MG-4	SJ4_G067	67.0	<dl	73.6	1084	176	26639	<dl	<dl	<dl	110	<dl
MG-4	SJ4_G098	<dl	1003	350	16.0	0.21	60.3	<dl	<dl	<dl	58.9	<dl
MG-4	SJ4_G114	0.14	11.3	0.68	0.62	0.05	1.22	0.92	0.12	3.32	54.1	1.18
MG-13	SJ13_G004	104423	20869	41595	227	744	3491	<dl	4755	2836	10786	14137
MG-13	SJ13_G006	348	<dl	174	12.0	36565	206	51.4	<dl	127	1189582	139
MG-13	SJ13_G008	12.0	201	160	<dl	<dl	296	<dl	3.76	<dl	272	<dl
MG-13	SJ13_G010	127	678	24.2	14.4	6.79	13.6	16.2	1.92	24.2	684	<dl
MG-13	SJ13_G011	1597	4907	66	<dl	53636	354	<dl	1.09	<dl	30646	13561
MG-13	SJ13_G013	<dl	1086	<dl	1203	<dl	<dl	<dl	<dl	<dl	<dl	<dl
MG-13	SJ13_G015	23128	4523	3653	19.2	77409	207	124	<dl	813	1971	<dl
MG-13	SJ13_G016	39.5	141	6.75	14.2	60.6	35.8	<dl	<dl	16.4	889	90.8
MG-13	SJ13_G018	2126	288	1511	<dl	<dl	155	8.59	67.9	127	149	31.2
MG-13	SJ13_G019	2.94	31.3	107	<dl	<dl	242	<dl	0.96	<dl	32.9	181394
MG-10	SJ10_G059	22.7	300	2.77	<dl	0.67	63.2	17.6	<dl	<dl	35.8	<dl
KG-1	KG1_G009	1617	379	1343	38.0	0.40	174	19.1	66.9	21.8	48.3	4.13

Appendix VI-C: LA-ICP-MS Measurements of NIST-610 and NIST-612 Standard Reference Material

Sample	Measurement	Mg	Al	Si	Ca	Sc	Ti	V	Cr	Mn	Fe	Co	Ni	Cu	Zn	Ga	Ge
KG-1	610_1	440	10430	325802	82181	458	458	452	413	450	444	414	463	439	469	442	450
KG-1	610_2	429	10251	325802	81018	456	457	452	406	437	470	409	457	447	459	430	448
KG-1	610_3	427	10283	325802	81239	451	441	447	404	445	457	407	455	437	452	427	442
KG-1	610_4	434	10249	325802	80586	455	451	442	411	444	522	408	459	440	470	433	452
KG-1	610_5	427	10338	325802	82497	459	445	453	410	447	440	411	461	442	458	436	446
KG-1	610_6	436	10376	325802	81372	452	460	455	404	442	422	412	456	441	454	431	444
MG-1	610_1	424	10156	325802	79381	\	436	439	400	439	450	404	453	442	455	433	442
MG-1	610_2	427	10290	325802	81255	\	456	450	409	441	447	411	460	442	460	431	445
MG-1	610_3	432	10329	325802	81500	\	452	448	410	445	468	411	462	440	457	431	444
MG-1	610_6	442	10519	325802	83510	\	457	458	417	452	470	415	465	448	466	446	461
MG-1	610_7	437	10420	325802	82174	\	449	452	407	445	461	415	461	442	464	436	446
MG-1	610_8	423	10145	325802	79919	\	447	445	406	440	438	405	454	440	456	427	438
MG-1	610_9	423	10204	325802	79956	\	446	441	401	438	463	407	457	439	453	428	443
MG-1	610-4	440	10436	325802	84097	\	467	466	415	450	470	415	460	442	472	437	458
MG-1	610-5	444	10442	325802	82256	\	463	456	409	448	459	408	458	434	459	430	449
MG-10	610_1	433	10334	325802	80928	463	460	450	407	445	526	408	461	450	467	436	449
MG-10	610_2	433	10313	325802	81713	458	455	451	412	447	528	415	465	441	458	438	447
MG-10	610_3	429	10303	325802	81328	455	455	453	412	447	496	411	458	441	464	433	451
MG-10	610_4	434	10355	325802	82054	443	437	448	399	434	304	406	450	431	452	423	441
MG-10	610_5	431	10282	325802	81815	448	438	442	402	442	382	404	448	436	449	426	440
MG-10	610_6	431	10316	325802	81293	452	456	448	409	442	490	409	465	441	459	434	442
MG-10	610_7	432	10314	325802	81050	460	460	454	410	446	516	411	458	442	462	435	447
MG-10	610_8	433	10344	325802	81598	463	457	455	413	450	545	415	465	449	470	439	459
MG-14	610_1	430	10203	325802	80910	\	436	443	399	432	459	404	459	444	459	436	446

Sample	Measurement	Mg	Al	Si	Ca	Sc	Ti	V	Cr	Mn	Fe	Co	Ni	Cu	Zn	Ga	Ge
MG-14	610_2	424	10231	325802	82256	\	457	455	409	445	462	407	453	433	454	428	448
MG-14	610_3	434	10390	325802	80420	\	451	447	411	446	457	412	461	443	464	428	445
MG-14	610_4	437	10467	325802	82410	\	459	458	417	456	458	420	463	437	456	431	451
MG-14	610_5	438	10362	325802	81415	\	459	450	408	445	453	406	456	444	463	441	445
MG-14	610_6	433	10311	325802	81609	\	457	448	406	442	441	410	457	444	462	441	448
MG-14	610_7	440	10424	325802	83197	\	465	460	417	459	473	423	466	450	467	438	450
MG-14	610_8	434	10360	325802	81429	\	447	455	412	444	454	407	464	442	460	436	455
MG-14	610_9	422	10169	325802	80168	\	442	439	398	433	464	403	450	433	455	421	437
MG-4	610_4	442	10447	325802	83210	455	448	461	414	452	426	413	456	439	464	439	453
MG-4	610_5	441	10459	325802	82580	466	465	458	410	449	441	415	467	456	474	444	450
MG-4	612_6	425	10198	325802	80945	451	448	447	408	444	474	408	457	435	453	427	446
MG-4	612_7	436	10370	325802	81594	456	461	456	413	443	460	409	459	445	467	439	450
MG-4	612_8	426	10259	325802	80616	451	442	439	401	439	462	409	456	436	450	424	442
MG-5	610_1	431	10285	325802	82209	457	450	448	407	447	524	412	462	445	468	441	453
MG-5	610_2	434	10417	325802	82047	460	464	455	412	445	383	414	461	449	462	433	445
MG-5	610_3	431	10257	325802	80087	448	442	446	405	439	480	404	453	429	449	424	443
MG-5	610_4	432	10321	325802	81525	455	452	450	408	444	459	410	459	441	460	433	447
MG-6/MG-12/MG-13	610_1	433	10265	326017	81475	457	456	448	405	451	522	415	457	456	463	442	454
MG-6/MG-12/MG-13	610_2	429	10241	329675	81475	457	450	450	388	434	405	402	460	450	454	434	450
MG-6/MG-12/MG-13	610_3	437	10633	326326	81475	451	455	454	430	451	494	420	462	438	462	438	450
MG-6/MG-12/MG-13	610_5	422	10217	322486	81475	456	442	441	404	435	457	399	463	422	464	420	441
MG-6/MG-12/MG-13	610_6	429	10186	325877	81475	449	456	454	408	451	588	421	460	459	457	439	454
MG-6/MG-12/MG-13	610_7	432	10294	326979	81475	454	451	449	399	450	386	408	460	445	457	437	446
MG-6/MG-12/MG-13	610_8	444	10647	329550	81475	462	460	454	418	439	441	413	454	448	462	441	454
MG-6/MG-12/MG-13	610_9	433	10214	321266	81475	454	451	454	416	445	409	407	454	421	461	420	432
MG-9/MG-2	610_1	430	10231	325802	79207	446	453	449	408	442	448	413	464	449	455	435	442

MG-9/MG-2	610_10	424	10167	325802	78513	442	442	434	399	430	443	398	450	435	451	424	436
MG-9/MG-2	610_2	428	10267	325802	80711	451	445	443	404	440	439	408	460	444	458	433	451
MG-9/MG-2	610_3	424	10208	325802	80240	446	440	439	403	441	451	403	451	432	451	421	433

Sample	Measurement	Mg	Al	Si	Ca	Sc	Ti	V	Cr	Mn	Fe	Co	Ni	Cu	Zn	Ga	Ge
MG-9/MG-2	610_4	434	10394	325802	85837	480	475	472	423	462	499	420	464	437	468	436	453
MG-9/MG-2	610_5	446	10620	325802	85174	471	462	465	408	447	500	407	452	435	476	442	464
MG-9/MG-2	610_6	451	10597	325802	84411	471	466	461	414	448	468	418	465	445	480	446	465
MG-9/MG-2	610_7	433	10310	325802	81882	452	449	451	409	443	453	413	459	446	459	433	452
MG-9/MG-2	610_8	423	10201	325802	79964	447	446	445	406	446	436	407	458	436	449	430	439
MG-9/MG-2	610_9	432	10291	325802	80586	452	448	447	409	447	458	416	466	451	460	434	443
OE-1/OE-2/MG-3	610_1	441	10440	328965	81475	464	468	459	420	460	529	424	463	452	461	434	459
OE-1/OE-2/MG-3	610_10	431	10317	331366	81475	458	444	448	403	442	391	413	465	448	458	438	455
OE-1/OE-2/MG-3	610_2	435	10310	326870	81475	451	443	446	411	452	477	417	464	441	461	433	444
OE-1/OE-2/MG-3	610_3	425	10278	328367	81475	458	443	445	393	425	482	399	453	433	457	430	441
OE-1/OE-2/MG-3	610_4	426	10252	325280	81475	448	450	449	404	436	417	403	456	441	454	436	449
OE-1/OE-2/MG-3	610_5	431	10373	323589	81475	455	459	450	414	446	395	409	461	445	460	444	452
OE-1/OE-2/MG-3	610_6	433	10303	322176	81475	451	450	454	404	440	368	405	456	439	471	427	442
OE-1/OE-2/MG-3	610_7	424	10111	313301	81475	446	451	451	411	448	428	399	447	426	463	421	428
OE-1/OE-2/MG-3	610_8	433	10374	329961	81475	462	452	448	405	438	573	411	461	439	444	434	449
OE-1/OE-2/MG-3	610_9	440	10418	327018	81475	456	461	451	417	457	518	420	459	446	472	434	451

Sample	Measurement	Y	Zr	Nb	Mo	Ag	Sn	Hf	Ta	W	Pb	Th
KG-1	610_1	462	453	472	417	251	433	446	454	455	429	462
KG-1	610_2	461	444	463	418	253	430	432	439	437	424	454
KG-1	610_3	463	447	460	415	249	427	427	444	440	425	455
KG-1	610_4	467	446	463	419	252	428	441	449	448	433	458
KG-1	610_5	460	450	470	418	252	431	434	443	441	422	457
KG-1	610_6	459	448	463	415	250	431	432	446	443	424	458
MG-1	610_1	456	\	455	408		424	\	\	\	424	453
MG-1	610_2	458	\		413	254	433	\	\	\	427	\
MG-1	610_3	464	\		418	248	426	\	\	437	419	\
MG-1	610_6	473	\	476	424	256	441	\	\	\	438	\
MG-1	610_7	\	\	466	420	249	429	\	\	\	428	\
MG-1	610_8	\	\	460	411	253	425	\	\	\	424	\
MG-1	610_9	455	\	454		252	424	\	\	431	416	448
MG-1	610-4	473	\	479	429	247	441	\	\	453	437	465
MG-1	610-5	465	\	471	424	242	431	\	\	\	424	458
MG-10	610_1	463	450	466	415	253	433	434	443	440	423	456
MG-10	610_2	465	452	468	421	254	430	438	450	447	429	457
MG-10	610_3	464	450	468	421	253	429	433	446	445	424	455
MG-10	610_4	456	442	458	409	244	427	437	444	444	427	463
MG-10	610_5	453	438	457	415	245	432	433	446	447	431	460
MG-10	610_6	462	446	466	419	252	428	437	447	447	425	455
MG-10	610_7	462	452	466	417	254	433	436	448	444	427	458
MG-10	610_8	471	456	471	419	254	429	433	444	439	422	455
MG-14	610_1	\	\	450	404	247	422	\	\	\	418	\
MG-14	610_2	461	\	464	418	253	430	\	\	\	425	\
MG-14	610_3	466	\	469	422	251	431	\	\	\	427	\

Sample	Measurement	Y	Zr	Nb	Mo	Ag	Sn	Hf	Ta	W	Pb	Th
MG-14	610_4	\	\	478	429	257	433	\	\	\	432	\
MG-14	610_5	462	\	468	415	249	433	\	\	\	432	460
MG-14	610_6	464	\	468	419		435	\	\	\	423	\
MG-14	610_7	\	\	477	422	251	440	\	\	451	433	\
MG-14	610_8	\	\	461	413	250	424	\	\	\	429	\
MG-14	610_9	\	\	455	413	250	425	\	\	\	417	\
MG-4	610_4	472	453	466	417	248	430	447	455	456	440	478
MG-4	610_5	475	464	481	430	255	442	454	468	464	448	485
MG-4	612_6	455	444	460	409	252	430	431	439	437	417	444
MG-4	612_7	464	447	466	426	257	433	433	441	439	427	456
MG-4	612_8	456	443	459	409	244	421	427	442	439	417	448
MG-5	610_1	464	453	466	419	253	433	441	452	\	430	459
MG-5	610_2	463	450	472	421	251	434	438	\	\	423	\
MG-5	610_3	458	440	457	411	249	422	\	\	\	425	\
MG-5	610_4	\	448	465	417	251	430	435	\	\	426	\
MG-6/MG-12/MG-13	610_1	467	452	473	428	258	441	443	443	439	424	458
MG-6/MG-12/MG-13	610_2	464	444	463	403	248	424	426	436	\	420	449
MG-6/MG-12/MG-13	610_3	460	453	465	421	251	438	437	460	451	428	\
MG-6/MG-12/MG-13	610_5	460	448	463	424	251	421	\	443	445	434	\
MG-6/MG-12/MG-13	610_6	468	452	472	423	255	439	439	449	\	430	460
MG-6/MG-12/MG-13	610_7	461	444	455	395	249	433	\	\	438	410	450
MG-6/MG-12/MG-13	610_8	461	451	475	433	253	431	\	450	457	432	460
MG-6/MG-12/MG-13	610_9	457	443	459	416	245	419	434	\	443	432	466
MG-9/MG-2	610_1	453	\	455	411	259	428	\	\	444	432	\
MG-9/MG-2	610_10	\	418	451	406	248	413	420	\		413	\
MG-9/MG-2	610_2	459	546	463	419	255	432	431	\	441	421	455

Sample	Measurement	Y	Zr	Nb	Mo	Ag	Sn	Hf	Ta	W	Pb	Th
MG-9/MG-2	610_3	\	531	454	406	247	413	422	\	\	408	\
MG-9/MG-2	610_4	478	\	484	435	246	451	\	\	\	445	472
MG-9/MG-2	610_5	484	\	486	428	244	442	\	\	\	434	472
MG-9/MG-2	610_6	485	502	484	426	245	443	\	457	\	445	482
MG-9/MG-2	610_7	466	452	467	420	252	429	\	\	\	424	\
MG-9/MG-2	610_8	451	\	453	411	256	430	432	\	437	418	\
MG-9/MG-2	610_9	454	425	461	413	258	428	\	\	450	428	456
OE-1/OE-2/MG-3	610_1	462	451	472	420	254	430	\	450	\	423	459
OE-1/OE-2/MG-3	610_10	465	451	464	422	256	439	436	446	\	427	453
OE-1/OE-2/MG-3	610_2	461	453	470	426	259	431	430	447	\	429	462
OE-1/OE-2/MG-3	610_3	465	446	456	408	246	431	435	443	\	422	449
OE-1/OE-2/MG-3	610_4	462	446	466	422	247	428	\	\	\	431	\
OE-1/OE-2/MG-3	610_5	460	441	458	414	249	431	\	447	445	425	\
OE-1/OE-2/MG-3	610_6	467	454	475	418	246	429	430	\	439	435	463
OE-1/OE-2/MG-3	610_7	453	438	460	401	249	428	437	\	\	419	\
OE-1/OE-2/MG-3	610_8	458	453	462	415	248	423	434	\	\	419	\
OE-1/OE-2/MG-3	610_9	465	445	468	423	256	430	\	\	450	429	461

Sample	Measurement	Mg	Al	Si	Ca	Sc	Ti	V	Cr	Mn	Fe	Co	Ni	Cu	Zn	Ga	Ge
KG-1	612_1	56.5	10671	337021	84254	43.5	43.7	39.5	37.1	38.7	218	34.6	38.4	38.3	38.0	35.4	39.9
KG-1	612_2	56.8	10862	337021	85827	43.9	41.9	39.6	33.8	38.9	204	35.1	39.9	38.4	41.1	36.5	38.0
KG-1	612_3	57.7	10731	337021	84529	43.4	40.6	39.2	38.2	38.9	142	34.8	40.6	37.2	37.4	34.8	39.4
KG-1	612_4	56.8	10814	337021	85999	42.8	39.6	39.1	36.5	40.1	89.9	36.0	40.3	39.4	40.2	36.6	40.5
KG-1	612_5	57.1	10713	337021	84401	41.1	37.6	38.2	36.3	38.8	111	34.4	40.9	37.1	37.8	36.4	38.7
KG-1	612_6	57.8	10808	337021	85397	41.6	43.4	39.1	35.9	39.4	101	35.0	38.6	39.2	38.7	37.6	36.9
MG-1	612_1	58.1	10862	337021	86802	\	44.1	39.6	37.2	38.5	100	35.8	38.5	37.3	40.7	36.7	41.0
MG-1	612_2	57.6	10933	337021	86924	\	40.6	39.7	37.0	39.3	115	35.8	39.2	36.6	40.2	37.0	40.7
MG-1	612_3	59.8	11207	337021	87508	\	43.4	39.3	38.0	40.2	93.8	36.4	39.8	38.2	41.2	37.5	40.5
MG-1	612_5	56.7	10991	337021	85990	\	40.8	37.8	36.6	38.5	94.6	34.4	39.9	35.9	39.9	35.6	37.6
MG-1	612_6	57.0	10780	337021	83989	\	39.0	38.5	37.0	38.4	96.3	34.8	39.6	37.3	38.2	36.2	39.8
MG-1	612-4	59.5	11103	337021	90145	\	42.7	41.0	38.4	39.9	108	35.0	39.6	37.0	40.7	37.9	40.6
MG-10	612_1	57.0	10555	337021	83569	63.7	54.5	38.9	36.9	38.4	301	35.4	38.5	38.6	40.3	36.8	39.1
MG-10	612_2	57.0	10491	337021	83296	63.0	51.8	38.8	35.6	38.6	291	35.0	39.3	38.5	38.5	36.2	40.1
MG-10	612_3	57.3	10674	337021	83504	60.7	55.4	39.2	36.1	38.7	275	35.4	39.8	39.0	39.6	37.0	39.1
MG-10	612_4	57.4	10482	337021	83437	42.6	40.2	39.0	35.7	36.9	127	34.6	38.8	37.8	39.3	36.6	40.4
MG-10	612_5	57.2	10546	337021	83814	39.8	41.1	39.7	37.0	39.7	84.7	35.7	39.9	39.5	39.6	37.4	40.5
MG-10	612_6	56.8	10285	337021	82320	39.5	38.5	38.7	37.3	39.3	125	35.0	37.7	38.3	39.0	36.8	40.7
MG-10	612_7	55.0	10213	337021	81551	39.4	39.3	38.5	37.3	38.5	147	35.0	38.8	37.8	41.1	36.6	41.3
MG-10	612_8	56.2	10205	337021	82785	39.8	40.4	38.3	36.7	37.6	105	34.9	38.4	37.6	38.3	36.3	38.2
MG-14	612_1	58.3	10779	337021	84894	\	40.7	39.7	38.8	40.6	108	35.8	38.6	39.1	38.2	36.4	39.8
MG-14	612_2	55.9	10371	337021	81867	\	40.0	38.3	36.9	38.1	118	35.0	38.9	38.5	37.3	35.3	38.5
MG-14	612_3	56.9	10184	337021	80863	\	39.3	37.8	36.9	38.4	104	35.5	39.2	39.3	36.7	36.2	38.7
MG-14	612_4	56.8	10458	337021	85821	\	41.8	39.6	35.8	38.3	96.6	35.5	39.7	39.6	37.7	38.0	39.7
MG-14	612_5	54.9	9835	337021	75479	\	36.4	37.0	35.1	36.0	92.9	33.4	38.7	38.5	36.6	35.9	40.7
MG-14	612_6	56.1	10015	337021	84750	\	40.0	40.7	38.2	39.7	90.1	35.4	39.6	41.6	39.6	38.8	41.0

Sample	Measurement	Mg	Al	Si	Ca	Sc	Ti	V	Cr	Mn	Fe	Co	Ni	Cu	Zn	Ga	Ge
MG-4	612_6	57.9	10778	337021	83154	40.1	39.9	38.7	37.6	38.3	105	35.4	37.2	38.2	42.1	37.2	40.6
MG-4	612_7	57.0	10742	337021	83523	40.3	39.1	39.3	37.2	38.1	69.6	34.8	40.0	37.8	41.4	36.5	40.7
MG-4	612_8	56.0	10712	337021	84345	40.6	41.6	38.2	37.4	37.7	95.0	35.3	40.4	38.9	39.1	36.3	39.9
MG-4	612_4	57.9	10640	337021	85423	41.1	41.9	39.6	38.2	38.2	104	35.4	38.5	37.9	40.4	37.7	40.1
MG-4	612_5	57.8	10542	337021	83313	40.2	42.0	39.7	37.6	38.4	77.5	34.7	39.9	38.6	40.3	37.1	39.2
MG-5	612_1	54.2	10283	337021	82854	39.1	40.0	37.9	35.3	37.4	109	33.8	38.2	37.2	39.3	37.2	40.1
MG-5	612_2	56.6	10396	337021	83081	40.0	40.9	39.1	37.7	38.6	81.1	35.3	38.6	36.8	38.6	37.0	38.9
MG-5	612_3	57.3	10578	337021	84267	40.0	41.0	38.3	37.4	39.1	102	35.4	38.2	36.5	39.5	36.5	39.6
MG-5	612_4	56.9	10414	337021	85066	41.2	40.5	39.8	36.7	50.8	85.7	35.0	40.0	39.8	38.5	38.0	41.0
MG-6/MG-12/MG-13	612_1	57.6	10489	330756	81475	55.6	51.1	38.0	37.1	37.2	214	33.8	37.8	35.4	36.9	35.1	38.6
MG-6/MG-12/MG-13	612_2	58.1	10477	326238	81475	55.1	48.9	40.3	36.4	38.7	134	35.0	37.6	36.5	34.9	35.8	39.2
MG-6/MG-12/MG-13	612_5	58.8	10809	342325	85048	48.5	45.5	38.4	40.0	38.4	206	36.1	39.9	37.8	38.0	37.3	40.3
MG-6/MG-12/MG-13	612_6	58.5	10496	338482	85048	46.7	44.3	37.2	35.9	36.9	168	34.2	39.6	37.0	39.7	37.0	42.1
MG-6/MG-12/MG-13	612_7	56.8	10633	337231	85048	47.9	42.6	37.4	37.9	38.7	103	36.1	38.5	37.5	36.2	36.7	39.4
MG-6/MG-12/MG-13	612_8	56.8	10749	338022	85048	46.4	40.7	37.8	38.6	38.0	186	35.3	38.8	38.5	36.6	36.4	41.3
MG-6/MG-12/MG-13	612_9	58.2	10644	341409	85048	52.2	47.4	37.9	37.5	37.6	193	34.7	38.9	37.1	40.5	37.4	38.8
MG-9/MG-2	612_1	56.6	10397	337021	81111	39.2	40.5	37.4	34.8	37.5	81.9	34.1	38.6	36.5	40.4	36.3	38.2
MG-9/MG-2	612_10	57.3	10468	337021	80705	37.7	39.8	37.9	37.1	37.6	85.1	34.1	39.7	38.2	38.8	36.4	38.6
MG-9/MG-2	612_2	56.6	10665	337021	82416	39.3	\	38.6	36.4	38.2	96.7	34.7	38.6	36.9	37.9	36.2	39.1
MG-9/MG-2	612_3	64.9	10624	337021	81771	38.7	39.2	37.6	35.6	37.3	65.5	34.5	36.8	36.0	39.1	36.0	38.6
MG-9/MG-2	612_4	58.4	10760	337021	86486	40.0	41.1	39.7	37.8	39.2	78.6	35.5	39.3	38.8	45.3	37.7	40.5
MG-9/MG-2	612_5	57.5	10658	337021	84969	40.3	41.0	39.3	36.9	38.9	95.4	34.9	38.5	37.7	40.4	37.6	40.2
MG-9/MG-2	612_6	57.6	10588	337021	86621	39.9	39.4	39.4	37.0	38.3	69.3	34.6	39.7	37.1	41.1	36.7	40.6
MG-9/MG-2	612_7	56.9	10552	337021	83696	39.7	40.3	38.6	36.5	38.3	101	35.8	40.4	38.6	40.0	37.4	39.9
MG-9/MG-2	612_8	55.9	10423	337021	81462	37.9	38.2	37.7	36.4	37.7	86.8	34.6	38.6	37.7	37.9	37.0	39.4
MG-9/MG-2	612_9	56.0	10423	337021	81500	37.8	39.3	37.6	36.7	37.7	66.2	34.6	39.2	37.4	38.4	36.8	39.5

Sample	Measurement	Mg	Al	Si	Ca	Sc	Ti	V	Cr	Mn	Fe	Co	Ni	Cu	Zn	Ga	Ge
OE-1/OE-2/MG-3	612_1	56.6	10791	338461	85048	67.7	56.6	38.6	35.0	39.2	346	36.7	40.4	38.3	37.2	36.9	40.5
OE-1/OE-2/MG-3	612_10	57.5	10759	335159	85048	42.5	44.1	38.7	37.0	39.0	188	35.2	43.2	38.1	37.8	36.4	39.6
OE-1/OE-2/MG-3	612_2	56.1	10742	335738	85048	68.1	58.9	38.3	33.4	38.0	351	35.0	40.9	37.8	39.3	36.7	40.5
OE-1/OE-2/MG-3	612_3	55.8	10651	315614	85048	66.0	54.4	38.5	36.1	38.6	386	35.5	40.5	38.8	36.8	37.8	39.7
OE-1/OE-2/MG-3	612_4	59.4	11098	337818	85048	51.2	44.9	41.5	34.6	40.0	212	35.5	41.1	39.5	36.9	38.4	39.0
OE-1/OE-2/MG-3	612_5	55.5	10712	327961	85048	49.4	47.4	39.0	34.7	37.7	191	34.9	37.8	37.1	39.0	37.3	40.2
OE-1/OE-2/MG-3	612_6	56.7	10696	327705	85048	45.6	46.4	38.4	34.4	37.1	99.1	34.0	38.9	38.6	37.7	36.9	38.3
OE-1/OE-2/MG-3	612_7	54.0	10564	323205	85048	44.6	48.3	39.4	35.0	38.0	182	35.0	36.1	35.6	38.1	34.3	38.6
OE-1/OE-2/MG-3	612_8	57.2	10770	334799	85048	45.0	43.4	37.1	37.1	38.6	BDL	35.7	39.2	38.7	36.0	37.6	40.8
OE-1/OE-2/MG-3	612_9	56.0	10738	334158	85048	43.4	42.4	38.0	35.5	38.4	112	35.2	38.0	38.5	36.0	37.3	41.1

Sample	Measurement	Y	Zr	Nb	Mo	Ag	Sn	Hf	Ta	W	Pb	Th
KG-1	612_1	38.7	38.5	38.5	35.2	22.7	39.0	37.7	37.0	37.9	38.6	37.9
KG-1	612_2	39.4	39.4	38.9	37.0	22.7	38.2	36.8	37.6	38.5	39.0	38.5
KG-1	612_3	39.2	38.4	38.4	36.9	22.4	37.3	37.2	37.6	38.6	38.4	38.0
KG-1	612_4	38.7	39.5	38.9	37.5	22.9	38.9	36.9	38.0	38.8	39.5	38.0
KG-1	612_5	38.6	38.6	38.6	35.8	23.3	37.9	37.8	37.3	37.6	38.1	37.9
KG-1	612_6	39.3	38.0	39.3	36.3	23.3	39.1	37.3	38.3	39.2	39.6	38.7
MG-1	612_1	39.6	\	39.1	37.8	21.9	38.3	\	\	\	39.1	\
MG-1	612_2	39.7	\	39.0	36.4	21.7	39.0	\	\	\	38.3	\
MG-1	612_3	\	\	40.1	37.6	21.8	39.3	\	\	38.8	39.5	\
MG-1	612_5	38.7	\	38.9	37.3	21.6	38.5	\	\	38.0	38.5	\
MG-1	612_6	\	\	38.7	35.0	21.8	37.8	\	\	37.4	37.2	\
MG-1	612-4	\	\	39.5	37.8	\	40.0	\	\	\	39.5	\
MG-10	612_1	36.6	36.3	37.4	37.3	22.3	37.6	35.0	35.9	38.3	37.6	35.8
MG-10	612_2	36.7	36.5	37.1	38.2	22.9	38.2	35.5	35.7	37.7	38.7	36.3
MG-10	612_3	37.0	36.9	37.3	36.7	22.4	38.6	35.5	36.3	37.5	38.3	36.0
MG-10	612_4	36.7	36.5	37.4	36.1	22.1	38.3	36.3	36.2	38.2	39.1	36.4
MG-10	612_5	37.2	37.1	38.1	36.3	22.1	38.8	36.5	36.5	39.4	39.3	37.1
MG-10	612_6	36.7	36.8	38.3	36.6	22.4	37.5	35.5	35.8	38.0	38.3	36.0
MG-10	612_7	36.8	36.4	37.7	35.7	22.1	37.5	35.6	35.8	39.0	37.7	35.8
MG-10	612_8	36.2	36.1	37.0	36.1	22.8	37.3	34.8	35.0	36.7	37.7	35.7
MG-14	612_1	39.2	\	39.2	38.1	21.8	38.6	\	\	\	37.7	\
MG-14	612_2	36.3	\	37.4	36.5	21.4	38.1	\	\	\	36.3	\
MG-14	612_3	36.4	\	38.0	37.0	21.0	37.5	\	\	\	37.1	\
MG-14	612_4	37.0	\	38.1	35.9	22.0	39.5	\	\	39.3	39.2	\
MG-14	612_5	32.9	\	35.0	35.7	20.5	37.7	\	\	\	35.3	33.5
MG-14	612_6	35.7	\	35.8	36.0	21.4	39.1	\	\	38.9	38.9	36.9

Sample	Measurement	Y	Zr	Nb	Mo	Ag	Sn	Hf	Ta	W	Pb	Th
MG-4	612_6	38.8	37.5	38.5	36.8	23.1	38.2	37.1	35.7	38.6	38.0	36.8
MG-4	612_7	38.1	38.0	37.9	36.1	23.2	38.7	36.8	35.3	37.9	38.1	35.8
MG-4	612_8	38.8	38.1	39.0	36.5	23.2	38.5	36.5	35.6	38.5	38.3	35.9
MG-4	612_4	38.5	37.4	39.0	36.7	23.5	39.3	37.0	36.0	39.0	39.9	37.3
MG-4	612_5	38.1	37.2	38.2	37.1	23.5	39.6	37.3	36.1	38.8	39.7	37.2
MG-5	612_1	36.4	36.0	37.5	37.0	23.3	38.0	\	\	36.8	37.7	\
MG-5	612_2	37.4	37.6	38.6	37.7	23.1	38.3	\	\	\	39.0	\
MG-5	612_3	37.4	37.6	38.5	35.7	21.7	37.7	\	36.4	37.7	39.1	\
MG-5	612_4	36.7	\	38.8	36.9	23.7	37.6	36.6	\	38.1	39.0	\
MG-6/MG-12/MG-13	612_1	36.7	37.6	38.3	36.2	22.2	37.8	\	\	37.1	38.2	37.6
MG-6/MG-12/MG-13	612_2	37.8	37.6	38.9	35.7	22.9	36.7	\	\	37.7	38.6	\
MG-6/MG-12/MG-13	612_5	38.0	39.2	40.3	37.8	22.4	38.8	38.2	\	\	40.9	38.4
MG-6/MG-12/MG-13	612_6	37.6	37.7	38.4	37.0	22.8	37.3	\	36.6	38.0	39.9	37.5
MG-6/MG-12/MG-13	612_7	37.5	39.1	39.5	36.7	22.7	37.8	36.5	\	\	39.1	36.9
MG-6/MG-12/MG-13	612_8	37.7	37.3	38.3	38.4	23.1	39.7	37.5	37.0	\	41.9	37.3
MG-6/MG-12/MG-13	612_9	39.8	38.9	40.2	38.7	23.3	38.1	36.7	37.2	\	41.3	39.4
MG-9/MG-2	612_1	\	44.1	38.1	35.4	22.7	37.3	34.9	33.6	37.6	36.8	\
MG-9/MG-2	612_10	36.2	\	36.4	35.6	22.5	36.5	\	33.7	37.4	37.2	\
MG-9/MG-2	612_2	37.5	\	37.5	35.7	22.4	37.4	\	\	\	37.3	\
MG-9/MG-2	612_3	37.2	\	37.0	36.7	22.3	36.6	\	\	\	36.6	\
MG-9/MG-2	612_4	\	41.5	39.7	38.1	22.3	39.1	45.2	36.6	\	39.7	\
MG-9/MG-2	612_5	38.2	40.9	39.4	37.2	22.4	39.3	\	\	\	39.7	\
MG-9/MG-2	612_6	38.0	40.9	38.9	38.6	22.3	38.2	\	\	37.5	40.0	\
MG-9/MG-2	612_7	37.4	37.1	38.1	36.9	23.2	38.3	36.7	35.5	39.0	41.3	36.6
MG-9/MG-2	612_8	36.3	34.8	36.6	35.6	23.5	37.0	35.4	34.0	\	38.0	35.5
MG-9/MG-2	612_9	36.6	33.9	37.3	35.2	23.2	37.3	35.0	\	\	37.3	

Sample	Measurement	Y	Zr	Nb	Mo	Ag	Sn	Hf	Ta	W	Pb	Th
OE-1/OE-2/MG-3	612_1	39.7	39.5	39.4	37.9	22.3	39.3	38.2	38.3	39.1	39.1	\
OE-1/OE-2/MG-3	612_10	39.0	38.4	39.3	35.4	23.9	38.6	\	37.4	\	39.6	38.1
OE-1/OE-2/MG-3	612_2	39.5	38.9	38.8	35.9	22.9	37.4	\	\	38.0	39.1	38.7
OE-1/OE-2/MG-3	612_3	39.2	40.8	39.4	36.1	22.6	38.1	37.5	\	37.8	38.5	38.3
OE-1/OE-2/MG-3	612_4	39.5	40.2	41.2	39.8	24.4	40.5	\	\	\	40.6	41.1
OE-1/OE-2/MG-3	612_5	38.6	39.6	39.3	35.0	22.4	39.7	37.8	\	37.4	38.8	38.5
OE-1/OE-2/MG-3	612_6	39.1	39.1	38.1	35.8	22.8	38.7	\	\	37.7	40.0	\
OE-1/OE-2/MG-3	612_7	37.7	38.3	38.2	33.7	21.2	34.9	36.3	\	\	37.8	37.6
OE-1/OE-2/MG-3	612_8	40.0	40.1	39.6	37.1	23.3	40.3	39.3	\	\	40.1	\
OE-1/OE-2/MG-3	612_9	38.3	39.3	38.2	38.8	22.3	38.5	36.9	37.6	39.3	39.8	38.0